Katarzyna Kowalczyk-Gajewska

MICROMECHANICAL MODELLING OF METALS AND ALLOYS OF HIGH SPECIFIC STRENGTH

Abstract

The thesis reports the research effort aimed at the micromechanical description of various phenomena characteristic for elastic-viscoplastic deformations of polycrystalline materials. The attention has been focused on metals and alloys of high specific strength, in which the inelastic deformation at the local level is constrained by an insufficient number of easy deformation modes and the presence of lamellar substructure.

The monograph consists of seven chapters. The first chapter has an introductory character. It outlines the motivation and scope of the thesis and indicates fields of applicability of the results obtained. In Chapter 2 a model of a single crystal deforming by slip and twinning is proposed, together with a new reorientation scheme formulated in order to account for appearance of twin-related orientations in polycrystalline aggregates. In the second part of the chapter an implementation of this model within known scale transition schemes is discussed. The validation of the proposed framework, when modelling the overall response and texture evolution for polycrystalline materials of high specific strength, is presented. In Chapter 3 a theoretical analysis of bounds and self-consistent estimates of overall properties of polycrystals of low symmetry, particularly those characterized by the constrained deformation at the local level, is performed. In the study two invariant decompositions of Hooke's tensors are employed. In Chapter 4 predictions of different extensions of the self-consistent method applicable to non-linear viscoplastic crystals of strong anisotropy are analysed. In Chapter 5 a micromechanical three-scale model of polycrystals of lamellar substructure is discussed, together with its extension to the large strain framework. An influence of the confinement effects induced by lamellar substructure on the overall response of polycrystals is evaluated. In Chapter 6 a new method of sequential linearisation of elastic-viscous response is presented. The procedure developed is applied to extend the self-consistent averaging scheme to elastic-viscoplastic heterogeneous materials. The last chapter recapitulates the most important conclusions and includes an outlook for future research employing the developed modelling tools.

Acknowledgment

Contents

1

Introduction

1.1. Motivation

The monograph is devoted to the modelling of metals and alloys of high specific strength within the micromechanical framework. Metals and alloys exhibiting an advantage of high specific strength and stiffness (e.g. intermetallics, Mg and Ti alloys and others) usually suffer from low ductility and formability which limit their potentially numerous use in industrial applications, cf. Appel and Wagner [6], Agnew et al. [2], Proust et al. [169], Lasalmonie [110], Mróz [141]. The main reason of such a combination of properties is the microstructure. The presented micromechanical approach enables one to relate the microstructure and its evolution with the mechanical inelastic response of the advanced alloys and intermetallics under consideration. The proper understanding of this relation is crucial when designing the elements made of these materials. This is clearly visible when analysing the recent literature on the subject. Recently, a lot of papers appear which deal with the discussed issue, e.g. Agnew et al. [2], Salem et al. [182], Kaschner et al. [81], Proust et al. [170]. There are also research and research&development projects devoted to the metals and alloys of high specific strength, e.g. KMM NoE, Workpackage Intermetallics, in which the author was involved, Integrated Project IMPRESS ("Intermetallic Materials Processing in Relation to Earth and Space Solidification") financed by European Union or "Structural Cast Magnesium Development" and "Magnesium Powertrain Cast Component" sponsored by USCAR and US Department of Energy. Usually, micromechanical modelling is an important component of these projects.

Alloys and intermetallics being the subject of this monograph exhibit the following advantageous properties (compare Table 1.1):

- low density,
- high specific strength and stiffness, also at elevated temperature, and
- good or very good corrosion resistance.

Table 1.1. Specific stiffness (the Young modulus divided by density) and specific strength (ultimate tensile strength (UTS) divided by density) at room temperature for selected alloys.

Material	ρ	E/ρ	UTS/ρ
	[g/cm^3]	[GPa/(g/cm^3)]	[MPa/(g/cm^3)]
AZ31B-H24 (Mg alloy)[1]	1.77	25.3	163.8
Ti-6Al-4V (Ti alloy)[2]	4.43	25.7	214.4
Ti-48Al-2Cr-2Nb (TiAl alloy) [3]	3.9	43.3	115.6
Zircaloy-4(Zr-alloy)[4]	6.55	15.2	78.6-82.6
Al 6061-T6 (Al alloy)[2]	2.7	24.7	114.8
AISI 304 (stainless steel)[5]	8.03	24.0	77.3

The advantageous relation of weight of workpieces made of the considered materials with respect to their mechanical parameters as well as their enhanced durability are the sources of increasing interest for their commercial use. This interest is also driven by a demand for reducing the energy (or fuel) consumption and heightening the requirements concerning the reprocessing of the worn out elements. Contemporary and potential applications include, among others, the following areas:

- *The constructional elements in aerospace and transport industries* - Titanium alloys are used in particularly demanding construction parts such as engine turbine blades. Recently, a growing interest in Mg alloys in car industry is observed, as they could replace the aluminum alloys in the construction of powertrain component, leading to the reduction of car mass as much as 100 kg. At the prototype stage are applications of intermetallics (Ti-Al, Ni-Al), which are tested as potential materials for engine turbine blades, turbochargers elements or valves).

- *The constructional elements in nuclear energy production* - Zr alloys have exceptional corrosion resistance and the low ability to absorb thermal neutrons. Consequently, in modern nuclear reactors fuel cladding is based on zirconium alloys due to their good performance in the environment of water-cooled reactors and their transparency to neutrons.

- *The constructional elements of vessels in chemical and fuel industries* - Zr alloys, potential application of Fe-Al intermetallics.

---

[1] www.eFunda.com, 20.09.2010

[2] ASM Aerospace Specification Metals (www.asm.matweb.com, 20.09.2010)

[3] Reference [3]

[4] ATI WahChang. Allegheny Technologies. Technical Data Sheet (www.wahchang.com, 20.09.2010)

[5] AK Steel Product Data Bulletin, 304/304L stainless steel (www.aksteel.com, 20.09.2010)

- *Biomedical applications* - Due to good bio-compatibility Ti alloys are used in implants and protheses.

Limitations of usage of the considered materials are caused by

- limited ductility and formability at room temperature (Mg alloys, intermetallics);

- high cost of processing due to the necessity of incorporation of the advanced technological processes (Ti and Zr alloys, intermetallics); and

- high sensitivity of properties to the material microstructure, including the strong anisotropy of properties induced by the crystallographic texture, e.g. rolling sheets made of Mg alloys, due to the texture, have two-times lower yield stress in compression along the rolling direction as compared to the direction perpendicular to the rolling plane; on the other hand the texture which is created in the extrusion process of tubular vessels made of Zr alloys has a positive impact on their corrosion resistance in nuclear reactors.

As it is easily deduced, the solution to the problem can be sought by the assessment, with use of a proper micromechanical model, of the relation between the material microstructure and the phenomena taking place at a micro-scale on one hand, and the macroscopic material response on the other hand. The modelling framework presented in this book, supported and verified in experiments, can help to answer the following questions:

- How the activation of subsequent deformation modes influences the ductility and formability of materials?

- How the lamellar microstructure, created by processing or evolving due to the applied load, determines the material response?

- What is, both qualitatively and quantitatively, the relation between the anisotropic properties of material on one hand, and the crystallographic texture or orientation of lamellar substructure on the other hand? And, because of that;

- What microstructure, in view of morphology and crystallographic texture, should be created, if possible, in order to obtain the material of desired properties?

It should be emphasized that the potential applications of the micro-macro transition schemes discussed and developed in this monograph are much wider than the analysis of metallic materials of high specific strength and stiffness. The developed framework can be applied to estimate the properties of any material of heterogeneous microstructure, thus also composites.

1.2. The aim and scope of the monograph

As already discussed above, metals and alloys exhibiting an advantage of high specific strength and stiffness usually suffer from low ductility and formability, and the main reason of such a combination of properties is the microstructure. In the majority of described materials one has to do with a low lattice symmetry (e.g. hexagonal close-packed (hcp) or tetragonal) and, consequently, with a limited number of easy plastic deformation modes. In many cases the Taylor condition is not fulfilled, that is there are less than five independent easy slip systems. The lack of easy slip systems is partially compensated by another deformation mechanism - twinning, cf. Christian and Mahajan [36], Appel and Wagner [6]. Similar combination of phenomena taking place at the micro-level can be observed for Zr alloys or FeAl intermetallics which, although do not enjoy high specific strength, are characterized by exceptional corrosion resistance.

It is also common for many of the above mentioned metals and intermetallics to exhibit the lamellar substructure which can be the result of a thermal treatment (e.g. in the case of two-phase $\alpha_2 + \gamma$-TiAl) or can be created by deformation twinning. Appearance of this type of microstructure influences the activity of subsequent deformation mechanisms promoting those which are favourably oriented with respect to the laminate morphology, cf. Lebensohn et al. [113], Proust et al. [169]. Both, the lack of fulfilment of the Taylor condition by a set of possible easy slip systems and the confinement effects induced by the lamellar substructure result in the constrained deformation at the local level of a single grain.

Twinning and limited number of easy slip systems in the low symmetry metals result in the development of strong crystallographic textures upon mechanical processing, e.g. rolling (Agnew et al. [2], Pospiech et al. [168], [167], McCabe et al. [129]) or extrusion (Wang and Huang [211]). The pronounced texture is the source of the strong anisotropy of mechanical properties of the produced components.

In view of the above observations micromechanics seems to provide a natural tool enabling understanding and description of a relation between the microstructure of the above materials and their macroscopic (overall) properties.

The aim of the study is the development of micromechanical modelling tools suitable for the analysis of elastic-(visco)plastic deformations of polycrystalline metals and alloys of high specific strength and stiffness. The novel aspects of the reported research concern:

- the constitutive description of coupling between basic inelastic deformation mechanisms, which are slip and twinning, influencing creation and

evolution of a lamellar substructure, evolution of crystallographic texture and, consequently, the macroscopic response of a material;

- implementation of the proposed model of single grain deforming by slip and twinning within different micro-macro transition schemes and its validation regarding the predictions of the overall response and the texture development;

- theoretical and numerical analysis of the influence of the confinement effects, imposed on the deformation at the local level and caused by violation of the Taylor condition and the presence of a lamellar substructure, on the effective properties of polycrystals; and

- the proposal of a new method of micro-macro transition between the considered scales of the constitutive description for elastic-viscoplastic materials.

Coupling between slip and twinning

Coupling between slip and twinning which participate in realization of the imposed plastic deformation path manifests in the following relations:

- Current activity of twinning mechanism influences the current activity of slip (dislocations) and vice-versa, while the intensity of these interactions depends on the current orientation of acting deformation systems with respect to each other.

- Twinning results in lattice reorientation in a part of a considered grain and the appearance of a phase with a new orientation (a twin-related phase) influences the activity of slip (dislocations) and twinning systems in a non-reoriented phase (a matrix phase).

- Twinning leads to the evolution of a lamellar substructure in the material. Its morphology influences in the directional way, the activity of the individual deformation mechanisms. This effect is particularly apparent when the strain path is changed.

- The crystallographic texture image in a polycrystal is changing due to an appearance of twin-related orientations in the polycrystalline aggregate.

The proper description of these interactions is a serious scientific challenge. Due to an increasing interest in the analysed materials, this subject has been undertaken in many papers, e.g. Kalidindi [75], Kalidindi [76], Karaman et al. [79], Proust et al. [169, 170], Kowalczyk-Gajewska [97]; however, the complete solution to the problem still remains an open issue. One of the main goals of this

work is to contribute with author's own experience to the discussed problem. It seems that in order to account for the indicated aspects of coupling between deformation mechanisms when constructing the constitutive model, one should focus on:

- formulation of the condition of lattice reorientation due to twinning which preserves the number of reoriented crystallites in the representative aggregate at a level consistent with the current volume fraction of twins and consequently enables one a proper modelling of texture evolution; and

- formulation of hardening rules which describe the evolution of activity of the individual slip and twin systems.

These hardening rules should account for:

- the interactions of slip-slip, slip-twin, twin-slip and twin-twin types on the physically-motivated grounds, cf. Kalidindi [76], Karaman et al. [79], Kocks and Mecking [90], e.g. using: a concept of a main-free path for dislocation, a relation between the critical shear stress for the considered deformation mechanism and the dislocations density as well as its decomposition into the statistically stored dislocations and geometrically necessary dislocations;

- the influence of the current relative orientation of slip and twin systems (among others, they should predict the higher latent hardening for non-coplanar systems);

- a directional Hall-Petch mechanism with respect to the evolving or existing lamellar substructures; and

- the change in the nature of active and non-active slip and twin systems in modelling of their mechanical characteristics after the reorientation.

In view of the above requirements

- a new reorientation condition, concurrent with respect to the existing approaches of Tomé et al. [200], Kalidindi [75], Staroselsky and Anand [186] and Proust et al. [169] is formulated and

- hardening rules accounting for the above mentioned coupling between slip and twinning are proposed.

In the proposed approach it is necessary to apply the large elastic-(visco)-plastic deformation framework. It enables one to study crystallographic texture evolution as well as to follow the reorientation of lamellar substructures. It should be underlined that in the case of the analysed materials, anisotropy of their

thermo-mechanical properties and those connected with corrosion resistivity, induced by crystallographic texture, is usually much more significant that in the case of metals of high lattice symmetry.

Micro-macro transition schemes

According to the principles of micromechanics the overall response of a polycrystalline material is assessed in two stages: a description of the deformation mechanisms at the micro-scale i.e. the level of a single grain, and then performing a micro-macro transition. In the case of polycrystalline metals with cubic symmetry of the lattice, the Taylor model [199] is most widely used as a scale transition scheme when studying the material response and the crystallographic texture evolution, e.g. Mathur and Dawson [128], Kalidindi and Anand [77], Kowalczyk and Gambin [95]. The approach assumes a uniform strain distribution in the polycrystalline aggregate. In spite of the considerable simplification of a real behaviour of polycrystalline metals of high symmetry, the Taylor model proved to produce acceptable results when compared with experiments. However, application of this model to the analysis of metals of low symmetry, with a limited number of easy slip systems, leads to a significant overestimation of the overall and local stresses in the polycrystal. It is due to the fact that, within the model, the redistribution of deformation between favourably and unfavourably oriented crystallites in a representative element under consideration is impossible.

Another way of performing the micro-macro transition is the self-consistent (SC) model which ensures a more accurate agreement with the experimental results than the Taylor model. The SC scheme allows one to take into account heterogeneity of deformation when going from grain to grain, cf. Nemat-Nasser [144], Molinari [136]. This micro-macro transition scheme was originally formulated for linearly elastic materials, cf. Kröner [107], Hill [66, 67], and relies on the Eshelby solution [49] of the inclusion problem. In a nutshell, in the SC model, the effective (overall) properties are derived by analysing the problem of a single grain interacting with the surrounding homogenized (uniform) matrix of the overall, yet unknown, moduli. Such an approach seems to be particularly well-suited in the case of polycrystals for which the representative volume element is the grain aggregate. There is a well-known limitation of the SC method encountered when analysing composite materials of high contrast in phase properties, e.g. a composite with voids or rigid inclusions, indicated by Budiansky [23]. One can expect analogous difficulties with the application of the SC scheme to the assessment of the effective properties of polycrystals

with locally constrained deformation. This issue is thoroughly analysed in the thesis, first analytically for polycrystals described by linear constitutive laws, and then numerically for non-linear laws, leading to some important and original conclusions. When deriving the corresponding analytical solutions, two invariant decompositions of fourth-order Hooke's tensors are utilized (see Appendix A).

An extension of the self-consistent method in the case of non-linear constitutive equations, e.g. for (visco)plastic or elastic-(visco)plastic materials is not straightforward. The specification of a linearization procedure of the non-linear relations is required, cf. Hill [67], Nemat-Nasser [144], Molinari [136], Chaboche et al. [29]. There exist many possible solutions of the above mentioned issue, however, they neglect the elastic part of deformation, cf. Hutchinson [69], Molinari et al. [138], Lebensohn et al. [113], Kiryk and Petryk [84], Masson et al. [127]; they are characterized by a high level of complexity and use numerically demanding mathematical tools (e.g. the numerical inverse of Laplace transform performed incrementally), cf. Masson and Zaoui [126], Bornert et al. [19], Pierard and Doghri [162], Paquin et al. [155] or propose some ad-hoc approximation of an interaction equation without referring to some physical motivation, cf. Paquin et al. [155], Molinari [136], Mercier and Molinari [133]. At the same time, the main problem usually encountered when using the known linearization schemes is the prediction of a too stiff macroscopic response as compared to the experimental one, cf. Molinari et al. [139], Chaboche et al. [29].

Linearization of equations which describe the material behaviour, required to make use of the Eshelby solution, is particularly difficult in the case of an elastic-viscoplastic material model due to appearance of the strain and the strain-rate in the constitutive relation at the same time. In this thesis a new method is proposed for the description of elastic-viscoplastic heterogeneous materials, called the *sequential* linearization method, which seems to be computationally effective and has some physical motivation. In the proposed approach the linearization of a relation between the total increment of strain and the increment of stress (or stress itself) is replaced by the sequence of linearizations connected with the decomposition of the material response into the elastic and viscous parts. It should be noticed that such a decomposition has its justification in the real behaviour of material. Therefore, one expects a better evaluation of the obtained overall response with respect to experiments. As it is shown further the main challenge when constructing the proposed transition scheme is the specification of an appropriate way of subdividing the material response into these two parts. It should be underlined that the developed method can find its application for a wider class of heterogeneous materials, e.g. composites.

As it has been already mentioned, in the analysed materials one can have to do with the lamellar substructures. Their presence indicates that, besides two traditional levels in micromechanics, viz.: a micro-scale level of a single grain (here single lamella) and a macro-scale level of a polycrystalline sample, it is necessary to introduce an intermediate level corresponding to the scale of a lamellar grain, called in this thesis a metagrain. Under standard assumptions concerning the proper separation of scales, cf. Nemat-Nasser and Hori [145], the equations describing the transition from the micro-level of a single lamella to the level of a metagrain correspond to the classical relations for the laminates (layered composites), cf. El Omri et al. [47], Stupkiewicz and Petryk [190]. Adopting these relations within the large deformation formalism one should take into account the change of the orientation of the interface between subsequent lamellae. Moreover, in the case of the considered materials, usually one has to do with the lamellar substructure which results from the activity of the twinning mechanism. Therefore, when formulating the model, one should also address the question how the mutual orientations of crystallographic lattice in subsequent lamellae change during the process, having in mind the fact that initially they are strictly related by the geometry of the relevant twin system as discussed by Kowalczyk-Gajewska [98].

The developed constitutive description of coupling between deformation mechanisms as well as the applied scale transition method are the two main backbones of a micromechanical model of polycrystalline metals of high specific strength. The model enables the analysis of the influence of microstructure and its evolution on the macroscopic (overall) response of a material element and, particularly, on the induced anisotropy connected with texture, cf. Agnew et al. [2], Kowalczyk and Gambin [95], Kowalczyk-Gajewska et al. [106]. Analysis of such mutual relations is important from the point of view of future applications of these materials. It also enables one to predict the material properties of metals in view of preceding forming processes, especially plastic forming ones. Consequently, the proposed micromechanical approaches provide tools which could help to design these processes.

Let us express at this point a few remarks concerning the fundamentals of micromechanical modelling. The main advantage of this approach is that it provides explicit relation between phenomena taking place at the local level of observation (in the considered context - the level of single grain) and the macroscopic, overall level (here, the level of polycrystal). Using this modelling tool we assume that the micro-mechanisms and microstructure of the considered materials are properly recognized and described by parameters with a clear physical interpretation. Therefore, it is evident that the predictions of the

developed micromechanical model will be the better the more knowledge about these local features is gathered. The quality of predictions is also influenced by the proper selection of the representative volume element (RVE) for averaging. This issue is not discussed in the monograph, one can find the conditions of representativeness of element in many textbooks and articles on the subject, e.g. Nemat-Nasser and Hori [145], Li and Wang [120]. In a nutshell, such a representative element should contain a sufficiently large number of micro-elements to be statistically representative and, on the other hand, it should be small enough to be treated as a material point at the macro-scale. It should be stressed that the notions of *micro* and *macro* used within micromechanics, in general have nothing to do with the absolute dimensions of micro-elements and the RVE. The relative relation between the length scales associated with both levels matters, i.e. in the considered context the size of RVE must be by orders of magnitude larger than the typical grain size. Finally, multi-scale analysis might be computationally expensive, therefore, when analysing the complicated boundary value problems for the considered materials, one should combine the micromechanical approach with phenomenological approaches, employing the first one only at the most crucial points of the analysis.

The monograph consists of seven chapters including this introductory chapter. Next five chapters present the subsequent issues indicated above, namely:

- In Chapter 2 an own model of a single crystal deforming by slip and twinning is presented, together with a new reorientation scheme developed in order to account for appearance of twin-related orientations in polycrystalline aggregates. In the second part of the chapter an incorporation of this model into known scale transition schemes is discussed and the validation of the developed framework in modelling of overall response and texture evolution for polycrystalline materials of high specific strength is presented.

- In Chapter 3 the theoretical analysis of bounds and self-consistent estimates of overall properties of polycrystals of low symmetry, particularly those characterized by the constrained deformation at the local level, is presented. Originality of this study lies in the use of invariant decompositions of fourth-order tensors.

- In Chapter 4 different extensions of the self-consistent method applicable to non-linear viscoplastic crystals of strong anisotropy are analysed.

- In Chapter 5 a micromechanical three-scale model of polycrystals of lamellar substructure is developed, together with its extension to the large strain framework. An influence of the confinement effects induced by la-

mellar substructure on the overall response of polycrystals is thoroughly evaluated.

- In Chapter 6 a new method of sequential linearization of elastic-viscous response is proposed with the aim to obtain an efficient homogenization scheme which is able to yield results of comparable quality to the approaches requiring much higher computational effort. The method is applied to predict the behaviour of viscoelastic heterogeneous materials.

Each of these chapters starts with an introductory section in which relevant literature on the subject is reviewed. The section which closes each chapter summarizes the main results pointing at their original aspects. The last chapter recapitulates the most important conclusions and includes an outlook for future research employing the developed modelling tools. Chapter 7 provides also the concise list of the original contributions of the author presented in the thesis.

Both unpublished and published results of the author are reported in the monograph. The reference to the respective article is always given. Part of results presented in Chapter 2, i.e.: formulation of a new reorientation scheme and a hardening rule as well as the validation of the model for low SFE fcc materials, was published in Kowalczyk-Gajewska [100]. Research presented in Chapter 3 concerning the Voight and Reuss bounds, as well as the self-consistent estimates of linear properties of untextured polycrystals have been reported in Kowalczyk-Gajewska [99]. Preliminary results concerning the problems discussed in Chapter 5 were presented at conferences, cf. Kowalczyk-Gajewska and Roos [105], Kowalczyk-Gajewska [98, 101]. The development of the sequential linearization method for elastic-viscous materials reported in Chapter 6 is the joint work with Professor Henryk Petryk.

1.3. Notation

Throughout the monograph the so-called "tensor" notation is used. If it is found necessary some of expressions are supplementarily provided in the indicial notation using components of tensors in some orthonormal basis. Notation conventions are as follows:

- Scalars are in mathematical italics, e.g. α, E, σ_Y.

- For vectors and second-order tensors boldface roman or greek symbols are used (meaning should be clear from the context), e.g. $\mathbf{n}$, $\mathbf{F}$, $\boldsymbol{\sigma}$.

- The blackboard style is used for the fourth-order tensors, e.g. $\mathbb{L}$, $\mathbb{A}$.

Table 1.2. Notation used for operations between tensors (summation convention applies), $\mathbf{v}, \mathbf{n}$ - vectors, $\mathbf{A}, \mathbf{B}$ - second-order tensors, $\mathbb{A}, \mathbb{B}$ - fourth-order tensors.

"Tensor" notation	Indicial notation
$\mathbf{v} \cdot \mathbf{n}$, $\mathbf{A} \cdot \mathbf{B}$, $\mathbb{A} \cdot \mathbb{B}$ (a scalar product)	$v_i n_i$, $A_{ij} B_{ij}$, $A_{ijkl} B_{ijkl}$
$\mathbf{A} \cdot \mathbf{n} = \mathbf{An}$, $\mathbb{A} \cdot \mathbf{n} = \mathbb{A}\mathbf{n}$, $\mathbb{A} \cdot \mathbf{B}$	$A_{ij} n_j$, $A_{ijkl} n_l$, $A_{ijkl} B_{kl}$
$\mathbf{n} \cdot \mathbf{A} = \mathbf{nA}$, $\mathbf{n} \cdot \mathbb{A} = \mathbf{n}\mathbb{A}$, $\mathbf{B} \cdot \mathbb{A}$	$A_{ij} n_i$, $A_{ijkl} n_i$, $A_{ijkl} B_{ij}$
$\mathbf{v} \otimes \mathbf{n}$, $\mathbf{A} \otimes \mathbf{B}$, $\mathbb{A} \otimes \mathbb{B}$	$v_i n_j$, $A_{ij} B_{kl}$, $A_{ijkl} B_{mnrs}$
$\mathbf{A} \otimes \mathbf{n}$, $\mathbb{A} \otimes \mathbf{n}$, $\mathbb{A} \otimes \mathbf{B}$	$A_{ij} n_k$, $A_{ijkl} n_m$, $A_{ijkl} B_{nm}$
$\mathbf{n} \otimes \mathbf{A}$, $\mathbf{n} \otimes \mathbb{A}$, $\mathbf{B} \otimes \mathbb{A}$	$n_i A_{jk}$, $n_i A_{jklm}$, $B_{ij} A_{klmn}$
$\mathbf{AB}$, $\mathbb{A} \circ \mathbb{B}$	$A_{ij} B_{jk}$, $A_{ijkl} B_{klmn}$

The second-order and fourth-order identity tensors are denoted as $\mathbf{I}$ and $\mathbb{I}$, respectively. Their components in any orthonormal basis are found to be δ_{ij} and $\delta_{ik}\delta_{jl}$. For the subspace of symmetric second-order tensors the identity operation is realized by the symmetrized $\mathbb{I}$ denoted as $\mathbb{I}^S$ of components $\frac{1}{2}(\delta_{ik}\delta_{jl} + \delta_{il}\delta_{kj})$. Notation used for different operations between tensors of different order is collected in Table 1.2.

The transpose of a second-order tensor $\mathbf{A}$ of components A_{ij} is denoted by $\mathbf{A}^{\mathrm{T}}$ and it indicates a tensor of components A_{ji}. The transpose of a fourth-order tensor $\mathbb{A}$ of components A_{ijkl} is denoted by $\mathbb{A}^{\mathrm{T}}$ and it indicates a tensor of components A_{klij}. The inverses of second- and fourth-order tensors are denoted by $\mathbf{A}^{-1}$ and $\mathbb{A}^{-1}$, respectively and they are defined as follows:

$$\mathbf{A}^{-1}\mathbf{A} = \mathbf{A}\mathbf{A}^{-1} = \mathbf{I}, \quad \mathbb{A}^{-1} \circ \mathbb{A} = \mathbb{A} \circ \mathbb{A}^{-1} = \mathbb{I}. \tag{1.1}$$

In micromechanical models relevant tensorial fields are considered at the local (micro) level and at the overall (macro) level. In this work, when analysing material response at different levels, the general convention has been assumed that the local fields, such as stress, strain or strain-rates fields, are denoted by small letters, e.g.: $\boldsymbol{\sigma}$, $\boldsymbol{\varepsilon}$, $\mathbf{d}$; while the corresponding overall fields are denoted by capital letters, e.g.: $\boldsymbol{\Sigma}$, $\mathbf{E}$, $\mathbf{D}$.

Throughout the monograph, for the brevity of presentation, abbreviations for some expressions have been used. Some of these acronyms are well-established in the literature (e.g. FEM), however, some of them are new. They are always expanded at the first use in the text, nevertheless for the convenience of the reader we provide below the complete list of them with their expansions in an alphabetical order:

- AF - affine (self-consistent scheme),
- fcc - face-centered cubic,

- FE(M) - a finite element (method),
- FFT - the fast Fourier transforms,
- hcp - hexagonal close-packed,
- HEM - a homogenized equivalent medium,
- IPC -in-plane compression,
- IPT -in-plane tension,
- MFP - the main free path,
- MT - the Mori-Tanaka (method),
- PSC - plane strain compression,
- PST - a poly-synthetically twinned (crystal, material),
- PTR - the predominant twin reorientation (scheme),
- PTVC - the probabilistic twin volume consistent (reorientation scheme),
- RD - the rolling direction,
- RVE - a representative volume element,
- SA - the Staroselsky and Anand (reorientation scheme),
- SC - self-consistent (scheme, method),
- SFE - a stacking fault energy,
- SMA -shape memory alloys,
- SMC - simple compression,
- ST - secant (self-consistent scheme),
- TD - the transverse (to rolling) direction,
- TG - tangent (self-consistent scheme),
- TTC - through thickness compression.

2

Modelling of crystals
of high specific strength

2.1. Introduction

For metals which deform plastically by crystallographic slip, the constitutive framework to study material response and texture evolution at large plastic deformations by means of crystal plasticity is well established. There exist rate-dependent formulations originating in the work of Asaro and Needleman [8] and developed by Kalidindi et al. [78], Lebensohn and Tomé [112], Nemat-Nasser et al. [146], Marin and Dawson [124], and rate-independent models originating in the works of Hill and Rice [68], Asaro [7] and developed e.g. by Anand and Kothari [5], Delannay et al. [40]. Within the rate-independent formulation of crystal plasticity, the known computational difficulty related to the selection of active slip systems and uniqueness of plastic flow exists, which is addressed in different ways. The oldest possibilities are the minimum internal work principle and the maximum plastic dissipations principle due to Taylor [199] and Bishop and Hill [16, 17], respectively. The issue is discussed in detail in reviews by Anand and Kothari [5],Havner [61], Van Houtte et al. [207], Busso and Cailletaud [27]. One of the remedies for the problem was proposed by Gambin [53], where a crystal plasticity model with the regularized Schmid law was formulated. In its mathematical structure, the model is similar to the rate-dependent formulation with the power-law relating the rate of slip on the considered slip system to the corresponding resolved shear stress as proposed by Asaro and Needleman [8], but it is independent of the assumed time scale. The model proved to produce acceptable results concerning texture evolution and material response of face-centered cubic (fcc) metals for different deformation paths, cf. Kowalczyk [94], Kowalczyk and Gambin [95], Kowalczyk-Gajewska et al. [106].

In this chapter, the incorporation of twinning into the constitutive model of a single grain presented by Gambin [53, 54] and Kowalczyk and Gambin [95] is

discussed. In order to account for the appearance of twin-related orientations, a new reorientation scheme, a Probabilistic Twin Volume Consistent (PTVC) scheme, is developed. It maintains the number of reoriented grains consistent with the accumulated deformation by twinning within the polycrystalline element. A hardening rule describing slip-twin interactions is also proposed. First, model performance concerning material response and texture evolution are studied for low stacking fault energy (SFE) fcc materials and then applied to metals and alloys of high specific strength. It is concluded that the results obtained by the developed model are in good accordance with experiments. The performance of the developed reorientation scheme has been compared to the modification of Van Houtte's scheme [203] proposed by Staroselsky and Anand [186]. It has been also incorporated into the visco-plastic self-consistent (VPSC) model of Lebensohn and Tomé [112].

Though in the case of metals of medium and high SFE (like copper or aluminum), dislocation slip is the main mechanism of plastic deformation at room temperature, experiments indicate, cf. Heye and Wassermann [64], Asgari et al. [9], El-Danaf et al. [46], Karaman et al. [79], that for low SFE metals like brass, MP35N alloy or Hadfield steel, the effect of mechanical twinning is significant. As it was discussed in the literature (English and Chin [48], Heye and Wassermann [64], Asgari et al. [9], Staroselsky and Anand [186], Kalidindi [76], El-Danaf et al. [45, 46]), the main issues and challenges involved in modelling of low SFE metals are differences in deformation textures, especially in plane strain compression (the copper-type texture vs. the brass-type texture), as compared to high SFE metals (e.g. copper or aluminum) and strong differences in the strain-stress behaviour of materials in different deformation paths. In the literature these facts are mainly attributed to the activity of twinning mechanism, through:

- the volume effect, cf. Heye and Wassermann [64], Van Houtte [203], Staroselsky and Anand [186],

- the microstructural effect, cf. Leffers and Van Houtte [118], Leffers and Juul Jensen [116], Leffers and Ray [117], and

- the influence of shear banding, cf. Duggan et al. [42], El-Danaf et al. [45], El-Danaf et al. [46], Kalidindi [76].

Furthermore, Kalidindi [76] developed a simple model of shear banding in plane strain compression in which initiation of micro-shear banding was correlated with the volume fraction of twins. This hypothesis was supported by the experimental observations reported by Asgari et al. [9]. Authors found that the production of extremely thin deformation twins led to the reduction of slip-

length and consequently, to the stress concentration at the twin-matrix interface. The level of stress concentration was supposed to be so high that dislocations eventually cut through the twins and resulted in initiation of micro-scale shear banding. The hypothesis of massive initiation of micro-scale shear banding for some critical volume fraction of primary twins, cf. Kalidindi [76], allows one to reconcile two explanations for differences in the behaviour of low and high SFE metals: increasing volume fraction of twins formed due to continuing strain path changes leads to the initiation of micro-shear banding and destabilization of microstructure. This hypothesis is not far from the arguments of Leffers and Juul Jensen [116] who suggested that the formation of the brass-type texture was not the volume effect of the appearance of twin-related orientations itself, but rather the result of planar flow induced by the developed lamellar microstructure which eventually may lead to the micro-shear banding. The latter explanation is supported by experimental measurements which show that the twin volume fraction in the considered materials is insufficient for the development of the brass-type texture only via contribution of twins to the texture image, cf. Leffers and Van Houtte [118], Leffers and Ray [117]. For a recent extensive review on the issue of transition from the copper-type texture to the brass-type texture, one is referred to Leffers and Ray [117], where also a vast collection of literature on the subject is provided.

Twinning mechanism is also a significant mechanism of plastic deformation at room temperature in the case of hcp materials such as magnesium, zirconium or Ti alloys, cf. Agnew et al. [2], Salem et al. [182], Karaman et al. [79], Kaschner et al. [81], Staroselsky and Anand [187], and intermetallics, cf. Mecking et al. [131], Marketz et al. [125], Fischer et al. [50]. For these materials of high specific strength, twinning enables to compensate for the lack of five independent slip systems required for a general shape change of volume elements. Initiation of twinning is therefore beneficial for the stress reduction and enhancement of ductility. On the other hand, twinning has a marked effect on texture evolution and hardening response of these metals and alloys. The limited number of easy slip systems in the low symmetry metals results in the development of a strong crystallographic textures upon mechanical processing, e.g. rolling, cf. Agnew et al. [2], Pospiech et al. [168], Pospiech [167], McCabe et al. [129] or extrusion, cf. Wang and Huang [211]. It is particularly true for magnesium alloys, for which the group of easy basal slip provides only two independent systems per grain. The pronounced texture is the source of the strong anisotropy of mechanical properties of the produced components.

The chapter is organized as follows. In the next section the basic material data for the considered metals, established on the basis of literature, are col-

lected. They concern the elastic constants of single crystals, the set of possible slip and twin systems as well as the classification of these plastic deformation mechanisms in view of easiness of their initiation. Section 2.3 is devoted to the description of twinning as far as it plays a significant role in plastic deformation of materials of high specific strength. First, a review of existing approaches is provided and then an original proposal, concerning modelling of texture evolution and the hardening phenomenon, is outlined. Finally, in the last section the results of simulations, compared with available experimental results, are presented and discussed for low SFE materials and then for metals and alloys of high specific strength.

Some of results presented in this chapter in Sec. 2.3 and 2.4.3 were published by the author, see Kowalczyk-Gajewska [100]. Here, more details concerning the model development as well as its validation for metals and alloys of high specific strength are included.

2.2. Lattice symmetry and basic material data

In this section we will discuss briefly the basic material properties of the considered materials.

In Table 2.1 the independent components of the elastic stiffness tensor $\mathbb{L}^e$ for single crystals are collected. For materials of the hexagonal lattice symmetry (hcp), the stiffness and compliance tensors in the linear elastic law,

$$\boldsymbol{\sigma} = \mathbb{L}^e \cdot \boldsymbol{\varepsilon}, \quad \boldsymbol{\varepsilon} = \mathbb{M}^e \cdot \boldsymbol{\sigma}, \quad \mathbb{M}^e = \mathbb{L}^{e-1}, \tag{2.1}$$

have the form equivalent to the transverse isotropy case with 5 independent components in anisotropy axes ($\mathbf{e}_3$ is coaxial with main axis of symmetry), i.e $L_{1111}, L_{1122}, L_{1133}, L_{3333}, L_{1313}$. Note that due to material symmetry remaining additional non-zero components are $L_{2222} = L_{1111}$, $L_{2233} = L_{1133}$, $L_{2323} = L_{1313}$ and $L_{1212} = L_{1111} - L_{1122}$. In the case of crystal of tetragonal symmetry (e.g. γ-TiAl) additionally L_{1212} is independent. Note that metals such as copper and aluminum, used in this study as reference materials, are fcc materials of cubic symmetry with three independent components of $\mathbb{L}^e$: $L_{1111} = L_{2222} = L_{3333}$, $L_{1122} = L_{1133} = L_{2233}$, $L_{1212} = L_{1313} = L_{2323}$. They are the materials of high symmetry. Elastic anisotropy of single crystals and polycrystals of fibre texture is studied in more detail in Chapter 3.

The sets of slip and twin systems relevant for the material under consideration also depend on the crystal symmetry. They are specified in terms of the
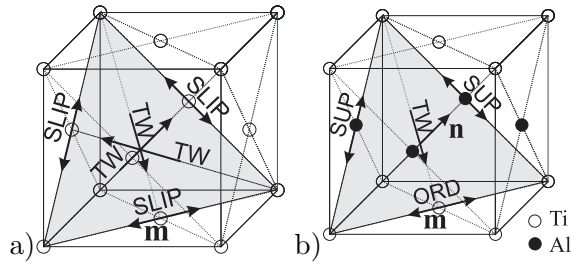
Fig. 2.1. Geometry of slip and twin systems: a) fcc unit cell b) γ-TiAl unit cell.
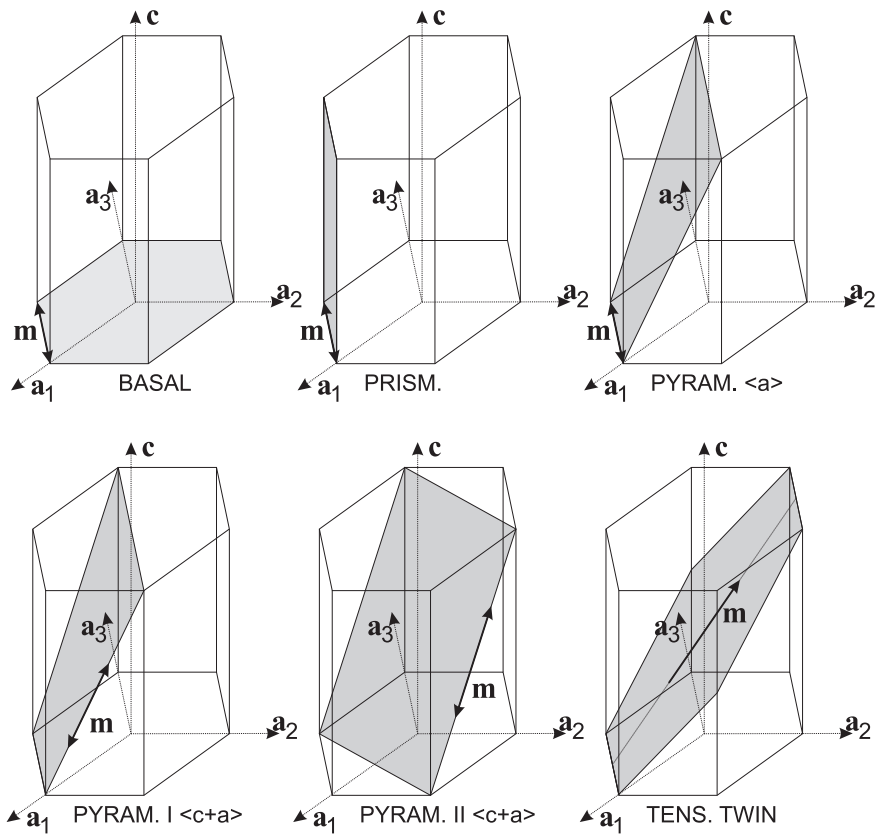
Fig. 2.2. Geometry of basic slip and twin systems for hcp naterials of $c/a < \sqrt{3}$.

Table 2.1. Elastic constants [GPa], c/a ratio and density ρ [g/cm^3] of single crystals for selected metals and alloys of high specific stiffness and some reference fcc materials.

Material	L_{1111}	L_{1122}	L_{1133}	L_{3333}	L_{1313}	L_{1212}	c/a	ρ
Mg [12]	59.3	25.7	21.4	61.5	16.4		1.624	1.74
Zn [12]	163.7	36.4	53.0	63.5	38.8		1.856	7.13
Zr [224]	143.5	72.5	65.4	164.9	32.1		1.593	6.5–6.55
Ti [196, 227]	163.9	91.3	68.9	181.6	47.2	(35.9)	1.587	4.5
α_2-Ti$_3$Al [197, 227]	175	88.7	62.3	220	62.6	(44.2)	0.81	4.2
γ-TiAl [6, 195]	183	74.1	74.4	178	105	78.4	1.04	3.8
Cu [12]	171.0	122.0			69.1			8.8–8.95
Al [12]	186	157			42			2.6–2.8

Miller indices using the standard notation for vectors normal to the slip plane and slip directions, cf. Kocks et al. [88], namely:

- For fcc crystals one has to do with 12 slip systems $\{111\}\langle110\rangle$ and 12 twin systems $\{111\}\langle\bar{2}11\rangle$ with characteristic twinning shear $\gamma^{TW} = 1/\sqrt{2}$ (see Fig. 2.1a).

- γ-TiAl has fcc like structure (see Fig. 2.1b), therefore the geometry of slip systems remains the same. However, due to the spatial distribution of Ti and Al atoms, they are subdivided into two groups, cf. Appel and Wagner [6]: 4 ordinary dislocations $\{111\}\langle1\bar{1}0]$ and 8 super dislocations $\{111\}\langle10\bar{1}]$. It is observed in experiments [6] that super-dislocations are more difficult to initiate than ordinary dislocations. Note that there are only 3 ordinary dislocations which are independent, while there are 5 independent slip systems within super-dislocation group. Furthermore, there are only 4 twin systems: $\{111\}\langle11\bar{2}]$.

- For hcp metals the set of possible slip systems includes five categories: 3 basal $(0001)\langle11\bar{2}0\rangle$, 3 prismatic $\{1100\}\langle11\bar{2}0\rangle$, 6 pyramidal $\langle a\rangle$ $\{1\bar{1}01\}\langle11\bar{2}0\rangle$, 12 pyramidal I $\langle c+a\rangle$ $\{10\bar{1}1\}\langle11\bar{2}3\rangle$ and 6 pyramidal II $\langle c+a\rangle$ $\{1122\}\langle11\bar{2}3\rangle$ (see Fig. 2.2). Depending on c/a ratio, either tensile twin systems $\{10\bar{1}2\}\langle10\bar{1}1\rangle$ $(c/a < \sqrt{3})$ or compressive twin systems $\{10\bar{1}2\}\langle10\bar{1}1\rangle$ $(c/a > \sqrt{3})$, with the characteristic twinning shear $\gamma^{TW} = \sqrt{3}/(c/a) - (c/a)/\sqrt{3}$, operate, cf. Christian and Mahajan [36][1]. Lattice parameter c/a for the considered materials is placed in the second last column of Table 2.1. Usually different levels of resolved shear stresses

---

[1]As reported by Christian and Mahajan [36] all hcp metals twin on $\{10\bar{1}2\}$ plane although additional twinning modes are also observed, e.g. contraction and double twinning modes for magnesium on $\{10\bar{1}1\}$ and $\{10\bar{1}1\} - \{10\bar{1}2\}$ planes, respectively, cf. Koike [91], Jiang et al. [74], Jiang and Jonas [73] or on $\{11\bar{2}2\}$ plane in titanium, cf. Wu et al. [223].

are required to initiate the subsequent types of deformation modes and, depending on the material, categories are subdivided into the easy ones and hard ones. In most cases the group of easy slip systems does not fulfil the Taylor condition (that is, there are less than five independent slip system in this group). Information related to this issue is collected in Table 2.2.

Table 2.2. Properties of slip systems categories for hcp metals (i - number of independent slip systems within the category).

Category	basal	prism.	pyram. $\langle a \rangle$	pyram. $\langle c + a \rangle$
i	2	4	4	5
Easy for	Mg	Ti, Zr,α_2-Ti$_3$Al		

2.3. Description of coupling between slip and twinning

2.3.1. Existing approaches

In modelling of twinning, as compared to modelling of a crystallographic slip, one should account for its polarized character (unidirectionality), the appearance of new twin-related orientations within the grain, and its influence via the slip-twin coupling on the hardening phenomenon. The early works on that issue were reported by Chin et al. [32] and Van Houtte [203]. Nowadays growing interest in hcp metals, such as magnesium or titanium alloys and intermetallics characterized by high specific stiffness, resulted in development of rate-dependent models, e.g. Lebensohn et al. [113], Kalidindi [75], Karaman et al. [79], and rate-independent models, e.g. Staroselsky and Anand [186], Staroselsky and Anand [187] of crystal plasticity accounting for twinning. Some details of these formulations will be discussed below and compared with the proposed model further in this chapter.

Texture development

It seems that the first author who addressed the issue of the appearance of new twin-related orientations during the simulations of texture evolution was Van Houtte [203]. He made use of a probabilistic reorientation condition. This condition states that at the moment when the maximum increment of volume fraction Δf^r over $r = 1, ..., N$ of twins accumulated in all possible twin systems in the considered strain increment is greater than a certain number ξ, the

crystallographic orientation of the considered crystal is replaced by the twin-related orientation. The number ξ is randomly generated from the set $[\xi_0, 1]$ and $0 < \xi_0 < 1$. Consequently, at each stage of the calculations, the grain has a unique orientation corresponding to the matrix one, or to the twin-related one (it is not subdivided into matrix and twin parts). Which of these two orientations is selected is decided with the use of the outlined probabilistic reorientation condition. The applied method enables one to avoid increasing the number of orientations during modelling of deformation process; however, it requires initially a larger number of orientations to model the aggregate in a statistically meaningful sense as pointed out by Tomé et al. [200]. Moreover, as the condition takes into account the increment of twinning shear in the recent deformation step, it may happen that reorientation will not take place according to the most active twin system during the whole deformation process. The other drawback of the method is the fact that the volume fraction of reoriented grains does not follow exactly the accumulated volume fraction of twins resulting from the description of twinning activity in the aggregate. The Van Houtte method was modified by Staroselsky and Anand [186]. There the reorientation condition is formulated with use of the maximum of the total volume fractions of twins f^r accumulated during the whole deformation process up to the considered time step. The condition takes into account the history of deformation by twinning, though the volume fraction of twin-related orientations in the aggregate is inconsistent with the predicted accumulated deformation by twinning (see Sec. 2.4.3).

The other methods developed to account for twin-related orientations in computations of texture evolution were discussed by Tomé et al. [200] and by Kalidindi [75]. Tomé et al. [200] proposed two ways of tackling the issue. The first proposal, called a Predominant Twin Reorientation (PTR) scheme, replaces the probabilistic reorientation condition by the deterministic one. In this scheme the threshold value in the reorientation condition depends on: the total volume fraction of twins accumulated as the deformation proceeds in the whole polycrystalline element, the volume fraction of grains that were reoriented in the calculation up to the considered deformation step, and two constants identified in single crystal experiments. The procedure maintains the twinned volume fraction at a level that is consistent with shear activity of twins contributing to the deformation, however, similarly to Van Houtte's condition and its modification due to Staroselsky and Anand [186], requires larger number of grains to model the aggregate. Moreover, the identification of two additional constants is needed which influence the twin accumulation (see Sec. 2.4.4). This criterion of reorientation was used, e.g., by Karaman et al. [79], Agnew et al. [2] and

Kaschner et al. [81]. The second proposal, called a Volume Fraction Transfer scheme, is the part of an alternative method of computing the texture evolution. In this method, during the deformation process the set of orientations remains fixed while the associated volume fractions are allowed to evolve. Note that for both these schemes the decision about the reorientation requires the analysis of the whole polycrystalline aggregate, therefore they are not applicable to a finite element (FE) model of polycrystal.

All these methods are formally capable of prediction of secondary and subsequent twinning events. The question, if such events are really admitted for the considered material and the deformation process, is addressed by the description of mechanical characteristics of the grain after reorientation due to twinning (see the discussion further in this section and Sec. 2.3.4).

Kalidindi [75] has formulated the time-integration scheme for crystal plasticity equations in which all calculations are performed in a relaxed configuration. In order to account for twinning, the matrix grain orientation and all the twin-related orientations are predefined in this configuration in terms of the initial orientation of a lattice. The iso-deformation gradient assumption for the twinned and untwinned regions of the grain is applied, and the stress is calculated as the volume average of the stresses different in these regions. As the deformation proceeds, the volume fractions of twinned regions increase. The matrix part of the grain deforms plastically by slip and twinning, while twinning is not allowed in the twinned regions. An implicit assumption in this model is that all of the twinned regions of the crystal belonging to a particular twin system would have a single lattice orientation in the current configuration, independently of the instances when they are created. This model could be applied to the FE model of polycrystal. Progressive growth of a twin inside the parent grain has been also accounted for by the so-called composite grain model developed by Proust et al. [169]. In the latter model the overall stress tensor and strain-rate tensor for a composite grain is distributed between matrix and twin lamellae according to relations valid for the laminate (see Chapter 5). These two more accurate descriptions have been achieved by introduction of an additional level of microstructure, which increases the computational cost.

Constitutive description

In the conventional crystal plasticity slip on the considered slip system r, defined by a unit normal $\mathbf{n}^r$ to the slip plane and a slip direction $\mathbf{m}^r$, is initiated when the resolved shear stress $\tau^r = \mathbf{m}^r \cdot \boldsymbol{\sigma} \cdot \mathbf{n}^r$ reaches the critical value τ_c^r. Chin and coworkers [32] were the first who applied a similar condition for twinning

initiation, cf. Christian and Mahajan [36], Fischer et al. [50]. This condition was later confirmed by experiments. Initiation and selection of an active twin system was recently studied in the so-called "latent hardening experiments" performed on fcc single crystals reported by Szczerba et al. [193]. Using the results, the Schmid rule for twinning initiation was expressed in the form of three conditions that have to be satisfied simultaneously, namely:

- The ratio of the resolved shear stress to the critical shear stress of a twin system, τ^l/τ_c^l, is greater than that of any other slip system.

- τ^l is greater than a minimum stress τ_{c0}^l necessary for twinning to occur.

- τ^l satisfies the sense of a twin shear, that is, $\tau^l = \mathbf{m}^l \cdot \boldsymbol{\sigma} \cdot \mathbf{n}^l > 0$.

Tensor $\boldsymbol{\sigma}$ is the Cauchy stress, while $\mathbf{m}^l$ and $\mathbf{n}^l$ denote a twinning shear direction and a unit normal to the twinning shear plane for the twin system l, respectively.

Slip occurs by motion of dislocations that have to overcome both the short-range and long-range obstacles. Accumulation of dislocations makes its further movement more and more difficult. This qualitative description of physical nature of slip is captured in the framework of crystal plasticity by the hardening rule for the critical resolved shear stress τ_c^r. The evolution of τ_c^r depends also on the interactions between slip and twin systems, cf. Staroselsky and Anand [186], Karaman et al. [79], Kalidindi [76]. As it is observed in experiments, cf. Asgari et al. [9], El-Danaf et al. [46], Karaman et al. [79], twin boundaries can be treated as grain boundaries, especially with increasing strain. Near twin boundaries dislocations in the matrix form pile-ups leading to stress concentrations. Therefore, it is believed that this geometrical constraint on deformation in the form of matrix-twin interfaces, provides the high strain hardening especially for the non-coplanar slip and twin systems. Karaman et al. [79] reported also that in most low SFE fcc materials with high concentration of solute atoms, twins clustered to form bundles a few tenths to a few micrometers thick with thin layers of matrix between them. These twins do not grow to form thicker twins and they are stable after unloading. Also Asgari et al. [9] report that twinning is initiated after some amount of initial strain, and then the twin content steadily increases, but at larger strains it appears to reach the saturation value considerably lower than unity. Contrary to low SFE materials, Mg alloys twin more easily and the lamellar substructure with constant thickness of matrix/twin lamellae does not develop. For example, experimental data show that after 10% of in-plane compression of AZ31B sheet with basal texture, almost 90% of material has twinned and that twins 'coalesce' inside the grains, cf. Proust et al. [170].

Modelling of hardening in the presence of twinning remains an open issue. Some proposals were outlined by Staroselsky and Anand [186], Karaman et

al. [79] and Kalidindi [76], and for hexagonal materials by Kaschner et al. [81], Kaschner et al. [82], Proust et al. [169] and Wu et al. [223]. The point of departure for the hardening rule developed in this chapter is the proposal discussed by Karaman et al. [79]. In this model, a geometrical effect of twin boundaries on hardening is accounted for by a term which is proportional to $f^{\text{TW}}/(1 - f^{\text{TW}})$, where f^{TW} is the current volume fraction of twins. The corresponding proportionality factor is specified by the constant K_0 and the inverse of the average thickness of twin lamellae t. When polycrystalline materials are considered, an additional term is introduced which depends on the average grain size d. Thus one finds two length-scale parameters present in this model: t and d.

Use of the reorientation condition requires also to decide if slip and twinning may take place in the grains reoriented by twinning (that is if secondary twinning events are possible), and what is the level of slip and twin resistances after the reorientation. In the early works on modelling of twinning within the large strain formalism, cf. Van Houtte [203], Tomé et al. [200], the coupling between twinning and a hardening phenomenon was not considered. Experimental observations by Asgari et al. [9] and Karaman et al. [79] on low SFE materials indicate that twinning and slip within the twinned regions is at least more difficult than in the untwinned part and, moreover, slip in the twinned regions can be severely restricted to the planes that are coplanar with the matrix-twin boundary. Consequently, the increased resistance of twinned material is explained by the Hall-Petch type effects induced by the directional reduction of the main free path (MFP) in twin lamellae, cf. Mahajan and Chin [123]. Alternative explanation is provided by Basinski's mechanism [11]. According to the latter explanation twinned regions are harder because the glissile dislocations before twinning are converted into sessile dislocations due to the twinning shear transformation. Both mechanisms were recently evaluated by Salem et al. [183] for high purity titanium. The results indicated validity of the latter mechanisms for this hcp material since microhardness tests have shown that twins were significantly harder than matrix, while nanoidentation measurements indicated no clear correlation between the hardness of twins and slip distance/twin thickness. In order to account for the above-mentioned observations, Staroselsky and Anand [186] have assumed that after the reorientation the values of τ_c^r for all twin systems are equal to the value of τ_c for the twin system, according to which the reorientation takes place, while the values of τ_c^r for all slip systems are then equal to the value of τ_c for the slip system coplanar with the reorientation twin system. According to these formulations, twinning is admissible in the reorientated grains what corresponds to the possibility of twinning in the twinned part of the grain. Twinning was enabled only in the matrix part of the

considered grain by Kalidindi [75, 76]. The values of slip and twin resistances were increased by 20% in the reoriented grains by Karaman et al. [79]. Another observations concerning the mechanical characteristics of twinned material have been reported for magnesium by Wang and Huang [211] and Proust et al. [170]. This material shows high propensity to twinning and grain can be even totally transformed by its activity. Upon the strain-path change twinned grains can detwin easily. Experimental data reported by Lou et al. [122] suggest that de-twinning may be even easier to initiate than twinning as far as the twin already exists within the material, so no nucleation is necessary. As concerns twin-slip interactions in hcp materials, it was also observed for magnesium that prior deformation by slip does not prevent deformation by twinning when the strain path is changed, although the stress level at which twinning is activated can be increased by a presence of dislocations.

2.3.2. Kinematics description

The model formulation begins with the description of kinematics. The large strain formulation of the crystal plasticity theory is applied, cf. Asaro [7], Anand and Kothari [5]. The multiplicative decomposition of the total deformation gradient $\mathbf{F}$ into the elastic part $\mathbf{F}^e$ and the plastic part $\mathbf{F}^p$ is used, cf. Lee [115], Duszek-Perzyna and Perzyna [43]. It results in the additive decomposition of the velocity gradient $\mathbf{l}$:

$$\mathbf{F} = \mathbf{F}^e \mathbf{F}^p \Longrightarrow \mathbf{l} = \dot{\mathbf{F}}\mathbf{F}^{-1} = \mathbf{l}^e + \mathbf{l}^p\,, \tag{2.2}$$

where

$$\mathbf{l}^p = \mathbf{F}^e \dot{\mathbf{F}}^p (\mathbf{F}^p)^{-1}(\mathbf{F}^e)^{-1} = \mathbf{F}^e \hat{\mathbf{l}}^p (\mathbf{F}^e)^{-1} \tag{2.3}$$

and 'dot' over the quantity denotes its material derivative. The elastic and plastic parts of the velocity gradient, $\mathbf{l}^e$ and $\mathbf{l}^p$, can be decomposed into their symmetric and skew-symmetric parts - the corresponding strain-rate tensors, $\mathbf{d}^e$ and $\mathbf{d}^p$, and spin tensors, $\boldsymbol{\omega}^e$ and $\boldsymbol{\omega}^p$, namely:

$$\mathbf{l}^e = \mathbf{d}^e + \boldsymbol{\omega}^e, \quad \mathbf{l}^p = \mathbf{d}^p + \boldsymbol{\omega}^p\,, \tag{2.4}$$

It is generally accepted to assume that during the elastic regime, crystallographic lattice and the material undergo the same deformation, while plastic deformation does not alter the lattice geometry and orientation. Moreover, the observation that the elastic deformations are usually much smaller than the inelastic ones is used when formulating the model of mechanical response of metals.

First, it is often assumed that the elastic strains are sufficiently small to neglect their influence on the lattice distortion, therefore, lattice reorientation is described as

$$\mathbf{a} = \mathbf{F}^e \mathbf{a}_0 = \mathbf{R}^e \mathbf{a}_0 \Longrightarrow \dot{\mathbf{a}} = \dot{\mathbf{R}}^e (\mathbf{R}^e)^{\mathrm{T}} \mathbf{a} \cong \dot{\mathbf{a}} = \boldsymbol{\omega}^e \mathbf{a}, \qquad (2.5)$$

where $\mathbf{a}$ is an arbitrary crystallographic direction and the rotation tensor $\mathbf{R}^e$ results from the polar decomposition of $\mathbf{F}^e$. Furthermore, in particular, when we are interested in the response of polycrystal for the regime of large deformations, we can assume that the elastic strains are negligible as compared to the plastic strains so that the elastic part of the deformation gradient $\mathbf{F}^e$ is restricted to the rigid rotation $\mathbf{R}^e$. Such a form of the deformation gradient results in the additive decomposition of the velocity gradient $\mathbf{l}$ into the skew-symmetric elastic spin $\boldsymbol{\omega}^e$, the skew-symmetric plastic spin $\boldsymbol{\omega}^p$ and the symmetric rate of plastic deformation tensor $\mathbf{d}^p$. In the examples presented in Section 2.4 of this chapter the elastic deformations are neglected, however, in the formulation of the constitutive model the way of incorporation of elasticity is discussed.

In the original formulation of crystal plasticity, plastic deformation occurs only by slip. As it was discussed in Section 2.2 of this chapter, the set of slip systems $\{\mathbf{n}^r, \mathbf{m}^r\}$, $r = 1, \ldots, M$, depends on the lattice type. The diad $\mathbf{m}^r \otimes \mathbf{n}^r$ is called the Schmid tensor. Its symmetric part will be denoted by $\mathbf{P}^r$, while the skew-symmetric part by $\mathbf{W}^r$.
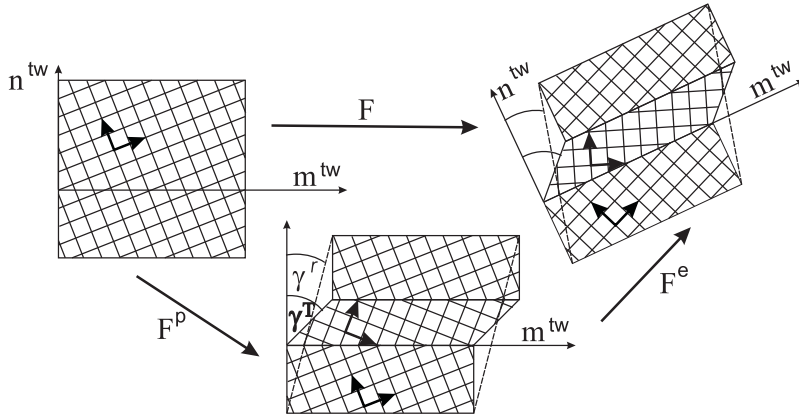
Fig. 2.3. Single grain deforming by twinning.

As far as twinning is concerned, similarly to slip it is also realized by simple shear, see Fig. 2.3; however, in this case only some volume fraction of a matrix grain is sheared on the specified twin plane in the specified twin direction

with the specified amount of shear γ^{TW}. As a result, the twinned sub-grain is formed. By 'specified' plane, direction or an amount of shear we mean that these quantities are determined by the lattice geometry. Contrary to the slip mechanism, twinning is unidirectional. As it is explained by Fischer et al. [50], due to the lattice geometry much more energy is needed to move an atom in a reverse direction. The twinned volume fraction has a different, but specified lattice orientation with respect to the matrix grain, though the lattice orientation in the matrix grain is also unaltered. In the analysed cases the crystallographic direction $\mathbf{a}^{\text{TW}}$ in the twinned part of the grain is related to the corresponding crystallographic direction $\mathbf{a}^{\text{M}}$ in the matrix grain via the relation due to Van Houtte [203]

$$\mathbf{a}^{\text{TW}} = \mathbf{R}^{\text{TW}}\mathbf{a}^{\text{M}} = (2\mathbf{n} \otimes \mathbf{n} - \mathbf{I})\mathbf{a}^{\text{M}}, \tag{2.6}$$

where $\mathbf{n}$ is the unit vector normal to the twinned plane (the interface between matrix and twinned part of a crystal). Note that the orthogonal tensor $\mathbf{R}^{\text{TW}}$ describes the rotation around $\mathbf{n}$ by the angle π. For more detailed discussion concerning twinning see the review by Christian and Mahajan [36].

In order to account for twinning in the developed crystal plasticity model, we follow the standard procedure, cf. Chin et al. [32], Kalidindi [75] Staroselsky and Anand [186]. Twinning is described as a unidirectional slip mode. The rate of pseudo-slip $\dot{\gamma}^l_{(t)}$ is connected with the rate of volume fraction $\dot{f}^l$ of the twinned part created by the twin system l according to the formula

$$\dot{\gamma}^l_{(t)} = \gamma^{\text{TW}}\dot{f}^l. \tag{2.7}$$

Denoting the rate of slip by $\dot{\gamma}^l_{(t)}$, the plastic part of the velocity gradient is then described as follows:

$$\mathbf{l}^p = \sum_{k=1}^{2M} \dot{\gamma}^k_{(s)}\mathbf{m}^k \otimes \mathbf{n}^k + \sum_{l=1}^{N} \dot{\gamma}^l_{(t)}\mathbf{m}^l \otimes \mathbf{n}^l = \sum_{r=1}^{2M+N} \dot{\gamma}^r\mathbf{m}^r \otimes \mathbf{n}^r. \tag{2.8}$$

To unify the description of slip and twinning mechanisms in the above formula, the slip in $\mathbf{m}$ is distinguished from the slip in $-\mathbf{m}$ direction, and $\dot{\gamma}^r$ denotes the rate of shear in the r-th deformation mode. The total volume fraction of twins created within the matrix grain in all twin systems should not exceed unity, that is

$$f^{\text{TW}} = \sum_{l=1}^{N} f^l = \frac{1}{\gamma^{\text{TW}}} \sum_{l=1}^{N} \gamma^l_{(t)} \leqslant 1. \tag{2.9}$$

On the basis of experimental observations, some authors argue that when a certain initial plastic strain is achieved, the twin volume fraction will be steadily

increasing but at larger strains it will reach a saturation value considerably lower than unity, cf. Asgari et al. [9], Kalidindi [76], Salem et al. [182].

As it was discussed in the Introduction, one of the issues connected with modelling of twinning in the context of texture evolution is accounting for the appearance of new twin-related orientations. In this paper a new method, the PTVC scheme, which originates in the Van Houtte reorientation condition is developed. It takes into account the history of the deformation process and maintains the twinned volume fraction at a level that is consistent with shear activity of twins contributing to the deformation. On the other hand, contrary to the PTR scheme, the PTVC scheme does not require the analysis of the whole polycrystalline aggregate and the identification of any additional constants or parameters. Similarly, as in the case of Van Houtte's and PTR schemes, initially the number of grains in the aggregate must be larger than in simulations of crystal plasticity without twinning. It must be also stressed that since the grain is reoriented instantaneously, the model does not account for a growth of a twin inside the grain as in more advanced models of Kalidindi [75] and Proust et al. [169].
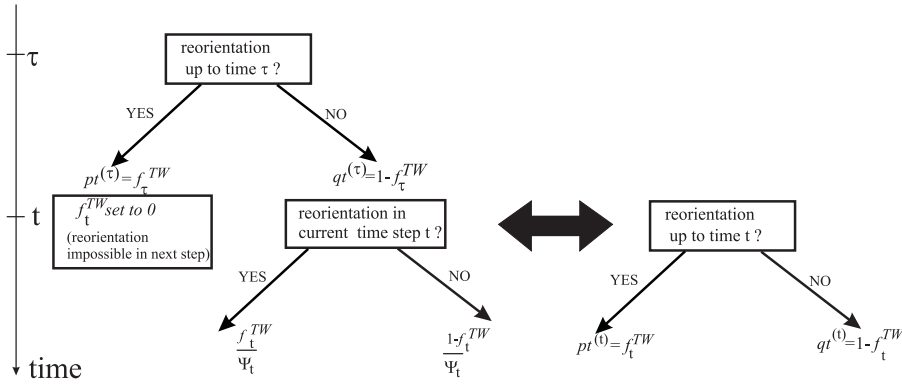
Fig. 2.4. Illustration of an application of a rule of mathematical induction for assessing the Ψ_t value. Probability of reorientation of a grain at time t calculated according to the left and right-hand diagrams must be equal.

The idea of the proposed criterion is to preserve the probability of reorientation for the considered deformation level as close as possible to the current volume fraction of twins in the grain. Assume that the reorientation condition is checked each time the volume fraction of twins f^{TW} (2.9) increases by Δf. Initially, when $f^{\mathrm{TW}} = \Delta f$, the threshold value ξ is polled randomly from the set $[0, 1]$ ($\xi_0 = 0$). If we follow the Staroselsky and Anand [186] modification of the Van Houtte [203] concept, ξ is each time polled from $[0, 1]$; it may be shown

that the probability of reorientation in the k-th step (that is when $f_k^{\mathrm{TW}} = k\Delta f$) *under the condition that reorientation has not taken place in previous steps*, is

$$p_{reorient}^{(k)} = \left[\prod_{i=0}^{k-1}(1 - i\Delta f)\right] k\Delta f\,, \tag{2.10}$$

while the total probability of reorientation in n steps (so the reorientation in any step $k \leqslant n$) is

$$pt_{reorient}^{(n)} = \sum_{k=1}^{n} p_{reorient}^{(k)}. \tag{2.11}$$

It is easy to note that depending on the frequency of checking the reorientation condition, sooner or later the probability of reorientation will inevitably approach unity, independently of the current volume fraction of twins. This moment is retarded if the threshold value is polled from the set $[\xi_0, 1]$ ($\xi_0 > 0$). Therefore, it is proposed to poll the threshold value ξ from the set $[0, \Psi_t]$ which varies as deformation proceeds and it is adjusted in a way to fulfil

$$pt_{reorient}^{(t)} = f_t^{\mathrm{TW}}, \tag{2.12}$$

that is to maintain $pt_{reorient}^{(t)}$ for the time step t consistent with the current volume fraction of twins f_t^{TW}. Fig. 2.4 presents the diagrams allowing us to assess the Ψ_t value with use of a rule of mathematical induction. In order to fulfil the requirement (2.12), the following relation must hold:

$$pt_{reorient}^{(\tau)} + qt_{reorient}^{(\tau)}\frac{f_t^{\mathrm{TW}}}{\Psi_t} = pt_{reorient}^{(t)} \implies f_\tau^{\mathrm{TW}} + (1 - f_\tau^{\mathrm{TW}})\frac{f_t^{\mathrm{TW}}}{\Psi_t} = f_t^{\mathrm{TW}}, \tag{2.13}$$

which enables us to specify Ψ_t as

$$\Psi_t = f_t^{\mathrm{TW}}\frac{1 - f_\tau^{\mathrm{TW}}}{f_t^{\mathrm{TW}} - f_\tau^{\mathrm{TW}}}\,, \tag{2.14}$$

with the additional assumption that the reorientation condition is checked only if $f_t^{\mathrm{TW}} > f_\tau^{\mathrm{TW}}$ and τ denotes the previous time step. Summing up, the grain will be reoriented at the considered deformation level if the current accumulated volume fraction of twins f_t^{TW} is greater than ξ randomly polled from the set $[0, \Psi_t]$. When the condition is true, the whole crystal is reoriented according to the twin system for which the value of f^l ($l = 1, .., N$) is maximum and then all the volume fractions f^l and the total volume fraction f^{TW} are re-initialized to zero.

It must be noted that, since reorientation takes place according to the most active twin system, the orientations of the twinned regions corresponding to other twin systems are lost. However, with only a small modification of the procedure one may account also for these orientations. To achieve this goal if the reorientation condition is true, the second polling procedure is performed. This time the number ξ_2 is polled from the set $[0, 1]$. If $\xi_2 < (f^{r,max}/f^{\mathrm{TW}})$ then the reorientation is performed as previously, otherwise it takes place according to the second most active twin system from the point of view of shear activity. Similarly to the original Van Houtte method, the PTVC scheme is formally capable of predicting secondary and subsequent twinning events.

2.3.3. Rate-independent and rate-dependent constitutive models

Taking into account both, elastic and plastic parts of deformation, within the large strain regime, requires an advanced tensorial apparatus such as the objective rates of the corresponding tensor fields, cf. Ogden [151], Simo and Hughes [185]. Two types of models exist in the literature on finite strain elasto-plasticity of crystals. First ones are based on the velocity-based approach and the additive decomposition of the velocity gradient. They use hypoelastic law. The second ones are based on the incremental displacement-based framework and the multiplicative decomposition of $\mathbf{F}$. They use hyperelastic law.

In the displacement-based formulation, the hyperelastic law is formulated between the conjugated stress and strain measures. Observing that the elastic part of deformation is small, this law is taken as a linear one, cf. Anand and Kothari [5], Kalidindi [75],

$$\mathbf{T}^* = \frac{\partial W^e}{\partial \mathbf{E}^*} = \mathbb{L}^e \cdot \mathbf{E}^*, \tag{2.15}$$

where W^e is the elastic free energy and $\mathbb{L}^e$ is the fourth-order tensor of elastic moduli. A pair $\{\mathbf{E}^*, \mathbf{T}^*\}$ is built by the elastic Green strain measure and the conjugated elastic stress calculated as

$$\mathbf{E}^* = \frac{1}{2}(\mathbf{F}^{e\mathrm{T}}\mathbf{F}^e - \mathbf{I}), \quad \mathbf{T}^* = (\mathbf{F}^e)^{-1}(J^e\boldsymbol{\sigma})(\mathbf{F}^e)^{-\mathrm{T}}, \quad J^e = \det \mathbf{F}^e. \tag{2.16}$$

In the computational procedure, similarly to the widely-used return map algorithm of phenomenological elasto-plasticity, the notion of the trial elastic state is used, obtained by freezing the plastic deformation derived at time t, $\mathbf{F}^{e(tr)}(t + \Delta t) = \mathbf{F}(t + \Delta t)(\mathbf{F}^p(t))^{-1}$, for which the corresponding trial stress at time $t + \Delta t$, is calculated with use of (2.15). The current plastic part of the

deformation gradient is assessed from the evolution equation for $\mathbf{F}^p$ integrated with the use of the exponential map,

$$\dot{\mathbf{F}}^p = \hat{\mathbf{l}}^p \mathbf{F}^p \Rightarrow \mathbf{F}^p(t + \Delta t) = \exp(\Delta t \hat{\mathbf{l}}^p(t + \Delta t))\mathbf{F}^p(t)\,. \qquad (2.17)$$

This formulation is rather not well suited for the application in the self-consistent micro-macro transition scheme which requires the linearization of the constitutive rule.

In the velocity-based formulation of elasto-plasticity of crystals the following objective lattice corotational rate of the Cauchy stress is introduced,

$$\boldsymbol{\sigma}^{\star\triangledown} = \dot{\boldsymbol{\sigma}} - \boldsymbol{\omega}^e \boldsymbol{\sigma} + \boldsymbol{\sigma}\boldsymbol{\omega}^e\,, \qquad (2.18)$$

and under the assumption of small elastic stretches the evolution equation for the Cauchy stress is linear and has the form of Anand and Kothari [5]

$$\boldsymbol{\sigma}^{\star\triangledown} = \mathbb{L}^e \cdot \mathbf{d}^e = \mathbb{L}^e \cdot \Big(\mathbf{d} - \sum_{r=1}^{2M+N} \dot{\gamma}^r \mathbf{P}^r\Big)\,. \qquad (2.19)$$

As this formulation is well suited for further applications in the self-consistent micro-macro transition schemes, it will be developed in more detail in this section.

Now, let us move to the description of (visco)plasticity. We consider rate-independent and rate-dependent formulations. Within the first class, a crystal plasticity model with the single yield surface F, known also as the regularized Schmid law, is used, cf. Gambin [54], Kowalczyk and Gambin [95]. This yield surface has the following form:

$$F(\boldsymbol{\sigma}) = \frac{1}{2n} \sum_{r=1}^{2M+N} \left(\frac{\tau^r}{\tau_c^r}\right)^{2n} - \frac{m}{2n} = 0\,, \qquad (2.20)$$

where m is a parameter defined below and n is a material constant. In order to account for unidirectionality of twinning, and to unify the description of slip and twin mechanisms for the computational reasons, the definition of τ^r has been modified as follows:

$$\tau^r = \langle \mathbf{m}^r \cdot \boldsymbol{\sigma} \cdot \mathbf{n}^r \rangle\,, \quad \text{where} \quad \langle x \rangle = \begin{cases} x & \text{if} \quad x > 0, \\ 0 & \text{if} \quad x \leqslant 0. \end{cases} \qquad (2.21)$$

Moreover, the definition of the parameter m has to be modified (compare the original formulation by Gambin [54]). This parameter describes the size of the

yield surface and it is now calculated as

$$m = \frac{1}{2M+N} \sum_{q=1}^{2M+N} \sum_{r=1}^{2M+N} \left(2\frac{\tilde{\tau}_c^q}{\tau_c} \langle \mathbf{P}^q \cdot \mathbf{P}^r \rangle \right)^{2n} \tag{2.22}$$

and

$$\tilde{\tau}_c^q = \min_r \left\{ \frac{\tau_c^r}{2\langle \mathbf{P}^q \cdot \mathbf{P}^r \rangle}, \quad \langle \mathbf{P}^q \cdot \mathbf{P}^r \rangle > 0 \right\}, \tag{2.23}$$

where $\mathbf{P}^r$ is the symmetrized diad $\mathbf{m}^r \otimes \mathbf{n}^r$. This definition of m enables to make the size of the yield surface close to the Schmid polyhedron. Note that such a modification of m is also beneficial for the description of materials with significantly different values of τ_c^r for different slip systems.

The following flow rule for the plastic part of strain-rate tensor $\mathbf{d}^p$ is associated with the yield surface (2.20),

$$\mathbf{d}^p = \dot{\lambda} \sum_{r=1}^{2M+N} \frac{1}{\tau_c^r} \left(\frac{\tau^r}{\tau_c^r} \right)^{2n-1} \mathbf{P}^r \equiv \dot{\lambda}\mathcal{F}. \tag{2.24}$$

Note that a shear rate on the considered slip system or a rate of pseudo-slip on twin system can be identified as

$$\dot{\gamma}^r = \dot{\lambda}\frac{1}{\tau_c^r} \left(\frac{\tau^r}{\tau_c^r} \right)^{2n-1}; \tag{2.25}$$

therefore, the plastic spin is calculated as follows

$$\boldsymbol{\omega}^p = \dot{\lambda} \sum_{r=1}^{2M+N} \frac{1}{\tau_c^r} \left(\frac{\tau^r}{\tau_c^r} \right)^{2n-1} \mathbf{W}^r \equiv \dot{\lambda}\mathcal{H}. \tag{2.26}$$

The function $\dot{\lambda}$ is the non-negative plastic multiplier which is derived from the consistency condition for the yield surface (2.20). For the plastic multiplier $\dot{\lambda}$ and the yield function $F(\boldsymbol{\sigma})$ classical Kuhn-Tucker conditions are fulfilled, cf. Gambin and Kowalczyk [55]. In its mathematical structure the model specified by a constitutive relation (2.25) is similar to the rate-dependent formulation of Hutchinson [69] and Asaro and Needleman [8], where the equation analogous to (2.25) has the form

$$\dot{\gamma}^r = v_0 \left(\frac{\tau^r}{\tau_c^r} \right)^{\bar{n}}, \quad \bar{n} = 2n - 1. \tag{2.27}$$

However, the reference velocity v_0, which is a material parameter in the latter approach, is replaced in (2.25) by $\dot{\lambda}$. Therefore, similarly as in the classical

theory of plasticity, the model specified by (2.20)-(2.25) is rate-independent. On the other hand, when $\bar{n} \to \infty$ in (2.27), we approach the rate insensitive limit. Accordingly, the power law (2.27) with high value of $\bar{n}$ is often referred as a viscoplastic[2] regularization of the rate-independent plasticity.

With use of the flow rule (2.24) the evolution equation (2.19) takes the form

$$\boldsymbol{\sigma}^{\star\triangledown} = \mathbb{L}^e \cdot (\mathbf{d} - \dot{\lambda}\boldsymbol{\mathcal{F}}) . \tag{2.28}$$

The specification of $\dot{\lambda}$ as a function of the strain-rate depends on the applied hardening law for τ_c^r. We address the issue of hardening in the next subsection. In general, for the presented crystal plasticity with a single yield surface, one can write

$$\dot{\tau}_c^r = \dot{\lambda} h^r(\boldsymbol{\sigma}), \quad \frac{\dot{m}}{2n} = \dot{\lambda} h_m(\boldsymbol{\sigma}) , \tag{2.29}$$

where $h^r(\boldsymbol{\sigma})$ and $h_m(\boldsymbol{\sigma})$ are functions to be specified for the assumed hardening model, and $\dot{\lambda}$ is derived as

$$\dot{\lambda} = \frac{\boldsymbol{\mathcal{F}} \cdot \mathbb{L}^e \cdot \mathbf{d}}{\boldsymbol{\mathcal{F}} \cdot \mathbb{L}^e \cdot \boldsymbol{\mathcal{F}} + h_{pl}(\boldsymbol{\sigma})} , \tag{2.30}$$

where

$$h_{pl}(\boldsymbol{\sigma}) = \sum_{r=1}^{2M+N} \left(\frac{\tau^r}{\tau_c^r} \right)^{2n} \frac{h^r(\boldsymbol{\sigma})}{\tau_c^r} + h_m(\boldsymbol{\sigma}) . \tag{2.31}$$

Introducing $\dot{\lambda}$ into the constitutive equation (2.28), the following formula is obtained:

$$\boldsymbol{\sigma}^{\star\triangledown} = \left(\mathbb{L}^e - \frac{(\boldsymbol{\mathcal{F}} \cdot \mathbb{L}^e) \otimes (\boldsymbol{\mathcal{F}} \cdot \mathbb{L}^e)}{\boldsymbol{\mathcal{F}} \cdot \mathbb{L}^e \cdot \boldsymbol{\mathcal{F}} + h_{pl}(\boldsymbol{\sigma})} \right) \cdot \mathbf{d} \equiv \mathbb{L}^{ep} \cdot \mathbf{d} , \tag{2.32}$$

where the fourth-order tensor $\mathbb{L}^{ep}$ of elastic-plastic moduli has all symmetries of the elasticity tensor with respect to the permutation of indices.

Instead of the Cauchy stress $\boldsymbol{\sigma}$, the Kirchhoff stress $\boldsymbol{\tau} = J\boldsymbol{\sigma}$, ($J = \det \mathbf{F}$) is used in the model formulations by Asaro [7] and Molinari [135]. In such a case, under other assumptions unchanged all the equations developed previously remain valid with the Cauchy stress $\boldsymbol{\sigma}$ replaced by the Kirchhoff stress $\boldsymbol{\tau}$.

_____

[2]Following e.g. Molinari et al. [139] and Lebensohn et al. [114] the notion "viscoplastic" or "viscoplasticity" will be used in the thesis with respect to the rate-dependent material response governed by the non-linear power law (2.27), although the condition for the initiation of the viscous flow is not introduced into the model.

If we do not neglect the lattice distortion during the elastic deformation, the evolution of the considered slip or twin direction and slip or twin plane is described as follows

$$\dot{\mathbf{m}}^r = \mathbf{l}^e \mathbf{m}^r, \quad \dot{\mathbf{n}}^r = -\mathbf{l}^{e\mathrm{T}} \mathbf{n}^r . \tag{2.33}$$

Still using the Kirchhoff stress $\boldsymbol{\tau}$, we re-write the evolution equation (2.28) using the Zaremba-Jaumann derivative of stress in the form

$$\boldsymbol{\tau}^\nabla = \boldsymbol{\tau}^{\star\nabla} - \boldsymbol{\omega}^p \boldsymbol{\tau} + \boldsymbol{\tau}\boldsymbol{\omega}^p = \mathbb{L} \cdot \mathbf{d} - \dot{\lambda}\boldsymbol{\mathcal{G}} , \tag{2.34}$$

where

$$\boldsymbol{\mathcal{G}} \equiv \mathbb{L} \cdot \boldsymbol{\mathcal{F}} + \boldsymbol{\mathcal{H}}\boldsymbol{\tau} - \boldsymbol{\tau}\boldsymbol{\mathcal{H}} . \tag{2.35}$$

Use of the evolution equations (2.33) affects also the development of the consistency condition. If we neglect the change of the scalar product $\mathbf{P}^r \cdot \mathbf{P}^q$, then the plastic multiplier is given by

$$\dot{\lambda} = \frac{\boldsymbol{\mathcal{G}} \cdot \mathbb{L}^e \cdot \mathbf{d}}{\boldsymbol{\mathcal{G}} \cdot \boldsymbol{\mathcal{F}} + h_{pl}(\boldsymbol{\tau})} . \tag{2.36}$$

By substituting $\dot{\lambda}$ into Eq. (2.34) we obtain the following rate form of the constitutive equation

$$\boldsymbol{\tau}^\nabla = \left(\mathbb{L}^e - \frac{1}{\boldsymbol{\mathcal{G}} \cdot \boldsymbol{\mathcal{F}} + h_{pl}(\boldsymbol{\tau})} \boldsymbol{\mathcal{G}} \otimes \boldsymbol{\mathcal{G}} \right) \cdot \mathbf{d} \equiv \mathbb{L}^{ep\tau} \cdot \mathbf{d} \tag{2.37}$$

and the current tangent modulus $\mathbb{L}^{ep\tau}$ has all the symmetries of the elasticity tensor.

Equations (2.32) or (2.37) are the basis for the development of a incremental self-consistent scheme following the Hill proposal [66]. This issue will be discussed in more detail in Chapter 4.

2.3.4. Hardening phenomenon

Following the reasoning presented by Karaman et al. [79] and taking into account the experimental observations discussed in Sec. 2.3.1, the following form of the hardening rule is proposed:

$$\dot{\tau}_c^r = H_{(ss)}^r \sum_{q=1}^{M} h_{rq}^{(ss)} \dot{\gamma}^q + H_{(st)}^r \sum_{q=2M+1}^{2M+N} h_{rq}^{(st)} \dot{\gamma}^q, \tag{2.38}$$

$$\dot{\tau}_c^{r+M} = \dot{\tau}_c^r \quad \text{where} \quad r \leqslant M,$$

$$\dot{\tau}_c^r = H_{(ts)}^r \sum_{q=1}^{M} h_{rq}^{(ts)} \dot{\bar{\gamma}}^q + H_{(tt)}^r \sum_{q=2M+1}^{2M+N} h_{rq}^{(tt)} \dot{\gamma}^q, \qquad (2.39)$$

$$\text{where} \quad r > 2M \,,$$

and $\dot{\bar{\gamma}}^q = \dot{\gamma}^q + \dot{\gamma}^{q+M}$. The hardening sub-matrices $h_{rq}^{(\alpha\beta)}$ account for the interactions of the deformation mechanisms of the slip-slip, slip-twin, twin-slip and twin-twin types. These matrices have been assumed as follows, cf. Asaro and Needleman [8], Anand [4]:

$$h_{rq}^{(\alpha\beta)} = q^{(\alpha\beta)} + (1 - q^{(\alpha\beta)})|\mathbf{n}^r \cdot \mathbf{n}^q|. \qquad (2.40)$$

Thanks to the applied form, it is possible to distinguish between the hardening due to slip or twinning on coplanar and non-coplanar systems, where $q^{(\alpha\beta)}$ describe the corresponding latent-hardening ratios. The functions $H_{(\alpha\beta)}^r$ describe the hardening of the r-th slip system or the r-th twin system due to activity of other slip or other twin systems. These functions are here assumed as follows. For the hardening of the r-th slip system due to activity of slip systems the Voce-type law with saturation is prescribed in the form used by Kalidindi et al. [78], namely,

$$H_{(ss)}^r = h_0^{ss} \left(1 - \frac{\tau_c^r}{\tau_{sat}^r}\right)^\beta . \qquad (2.41)$$

This law accounts for the athermal statistical storage of moving dislocations and dynamic recovery. Quantities h_0^{ss}, τ_{sat}^r and β are material parameters. For $\beta = 1$ the exponential hardening rule is obtained. For the hardening of r-th slip system due to twinning activity, the following relation is used:

$$H_{(st)}^r = \frac{h_0^{st}}{\tau_c^r} \left(\frac{f^{\mathrm{TW}}}{f_{sat}^{st} - f^{\mathrm{TW}}}\right) , \qquad (2.42)$$

which accounts for geometrical effects of twin boundaries in reducing the MFP distance. Quantities h_0^{st} and $f_{sat}^{st} \leqslant 1$ are material parameters. At this stage, the hardening of twin systems due to slip activity is neglected or accounted for by the simplified linear law ($H_{(ts)}^r \doteq const$), while the hardening of the r-th twin system due to activity of twin systems is assumed similarly as in (2.42), namely,

$$H_{(tt)}^r = \frac{h_0^{tt}}{\tau_c^r} \left(\frac{f^{\mathrm{TW}}}{f_{sat}^{tt} - f^{\mathrm{TW}}}\right). \qquad (2.43)$$

The formulation of evolution equations (2.42) and (2.43) follows the concept of Karaman et al. [79], leading to the same variation of τ_c with increasing twin

volume fraction; however, introduction of a parameter $f_{sat}^{tt} < 1$ enables one to describe the saturation of the volume fraction of twins below unity. Schematically, evolution of τ_c due to slip activity and twin activity is presented in Figs 2.5a and 2.5b, respectively. Contrary to the proposals of Karaman et al. [79] and Proust et al. [169], there are no explicit length-scale parameters in this model, therefore material parameters, such as $h_0^{\alpha\beta}$ and initial values of τ_c^α are supposed to depend on the grain size e.g. according to the Hall-Petch relation.
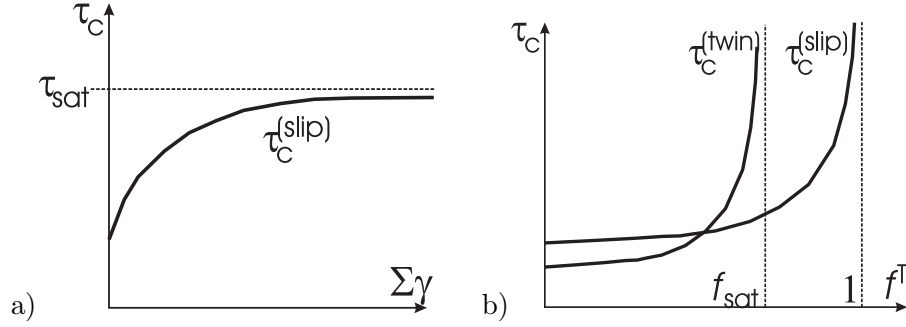
Fig. 2.5. Schematic view of evolution of critical shear stress τ_c due to slip activity (a) and due to twin activity ($f_{sat}^{st} = 1$) (b).

The applied hardening scheme without taking into account the reorientation works as follows. Suppose that slip is initiated for the lower level of stress than twinning, then f^{TW} for some time remains zero, while the material hardens according to the rule (2.41), Fig. 2.5a. If $H_{(ts)}^r = 0$, twin resistance is kept constant and eventually it is lower than active slip resistance, so twinning is initiated. It corresponds to the initial part of the process when plastic deformation is supposed to occur predominantly by slip. After the initiation, due to the applied hardening form, twinning is favoured with respect to slip until the twin volume fraction approaches f_{sat}, Fig. 2.5b. This corresponds to the strain regime for which twinning is observed. Then, after saturation of twinning, again slip will be favoured. Note that the number of parameters in the developed hardening rule is similar or even reduced as compared to the existing approaches by Staroselsky and Anand [186], Kalidindi [76], Karaman et al. [79], Wu et al. [223] and Proust et al. [170].

Concerning the constitutive descriptions of a grain after reorientation due to twinning, the experimental observations indicating increase of its resistance to deformation for low SFE materials are taken into account (see Sec. 2.3.1). Consequently, in the proposed model, after the reorientation the values of τ_c^r for all twin systems are equal to the value of $k\tau_c^q$, $k > 1$ for the twin system

q, according to which the reorientation takes place. The value of τ_c^r for all slip systems which are non-coplanar with the reorientation twin system assumes then the value higher than for the slip system coplanar with the reorientation twin system. In this case twinning in the twinned grains (that is secondary twinning) can be impossible ($k \gg 1$) or at least very difficult to occur. For magnesium alloys, for which we observe high propensity to twinning and, after the strain path is changed, extensive detwinning, different specifications are used (see the corresponding example in Sec. 2.4.4).

2.4. Validation of the model

2.4.1. Preliminary analysis of active deformation modes

It is not a trivial task to establish the suitable relation between the critical shear stresses for different categories of deformation modes relevant for the material. In most cases it requires simultaneous theoretical and experimental analysis. Usually a set of mechanical tests for different deformation paths, supplemented by the measurements of crystallographic texture evolution, is performed, cf. Agnew et al. [2], Proust et al. [170]. On the other hand theoretical analysis allows one to predict the deformation modes which are suspected to be active during the performed tests. Combining both, and verifying the results by additional tests, one is able to establish mechanical characteristic of the single deformation mode. Below we present such a theoretical analysis that should precede the planning of the testing strategy.

Fcc materials

Fcc materials are materials of high symmetry. Only two types of modes are possible: slip and twinning. Let us define the ratio $\alpha \equiv \tau_c^{twin}/\tau_c^{slip}$. If we calculate the resolved shear stresses for shear specified by one of the slip system, e.g.:

$$\boldsymbol{\sigma}_I^{test} = \tau(\mathbf{m}^{slip} \otimes \mathbf{n}^{slip} + \mathbf{n}^{slip} \otimes \mathbf{m}^{slip}),\tag{2.44}$$

where, for example,

$$m_i^{slip} = \frac{1}{\sqrt{3}}(1,1,1), \quad n_i^{slip} = \frac{1}{\sqrt{2}}(-1,1,0)\tag{2.45}$$

and apply the Schmid condition to find the value of $\tau = \tau_Y$ at yielding of a single crystal we obtain

$$\frac{\tau_Y^I}{\tau_c^{slip}} = \min\{1, \frac{2}{\sqrt{3}}\alpha\}.\tag{2.46}$$

Fig. 2.6. The yield stress in tension and compression in different directions in the crystal planes {001} and {011} for fcc crystal with the current value of $\alpha = 0.9$ Polar plots (the direction of an arrow marked in the figure (a) is coaxial with the direction of tension/compression, while its length indicates the magnitude of the corresponding yield stress).

On the other hand, if we calculate the resolved shear stresses for shear coaxial with one of the twin systems, e.g.:

$$\boldsymbol{\sigma}_{II}^{test} = \tau(\mathbf{m}^{twin} \otimes \mathbf{n}^{twin} + \mathbf{n}^{twin} \otimes \mathbf{m}^{twin}), \qquad (2.47)$$

$$m_i^{twin} = \frac{1}{\sqrt{3}}(1,1,1), \quad n_i^{twin} = \frac{1}{\sqrt{6}}(1,1,-2), \qquad (2.48)$$

we obtain

$$\frac{\tau_Y^{II}}{\tau_c^{slip}} = \min\{\frac{2}{\sqrt{3}}, \alpha\}. \qquad (2.49)$$

One concludes that twinning is not initiated for any deformation path as long as $\alpha > 2/\sqrt{3}$. For fcc materials slip is easier to initiate than twinning for not pre-strained crystal ($\alpha < 1$), therefore twinning is observed after some amount of accumulated plastic deformation. Critical shear stress for slip increases due to hardening, and then twinning can be given way.

This phenomenon has been utilized by Szczerba et al. [193] in their latent-hardening experiments. In these experiments validity of the Schmid rule for twinning has been verified in two-step uniaxial tension experiments. Knowing the value of α, one can study which of modes is active at yielding when single fcc crystal is tested in uniaxial tension or compression at different direction **k** with respect to the single crystal axes. As an example, the values of the yield stress in tension and compression in any direction in the crystal plane {001} and in the crystal plane {011} are presented in Fig. 2.6 in the form of polar plots. Ratio $\alpha = 0.9$ has been assumed, so one should understand this figure as valid for some idealized pre-strain material. For not pre-strained material ($\alpha > 1$) the thin curve for slip lies inside the thick curve for twin indicating that only slip mode is active.

Looking at the figures, first we note tension-compression asymmetry resulting from unidirectionality of twinning. Second, depending on the direction of tension or compression, yielding of the material will be specified either by the critical shear stress for slip or by the critical shear stress for twinning, e.g.:

- Take plane {001} and $\mathbf{k} = \mathbf{a}_1$, then yielding in tension takes place by slip and the yield stress σ_Y is specified as

$$\sigma_Y^{k=(100)} = \sqrt{6}\tau_c^{slip} \,. \tag{2.50}$$

- Take plane {001} and direction $\mathbf{k} = (110)$ then yielding in tension takes place by twinning and the yield stress is specified as

$$\sigma_Y^{k=(110)} = 3/2\sqrt{2}\tau_c^{twin} \,. \tag{2.51}$$

Overall anisotropy of a yield stress is not strong.

γ-TiAl intermetallic

Intermetallic γ-TiAl has an insufficient number of easy slip systems. Three types of modes are possible: ordinary dislocations, super-dislocations and twinning. Super-dislocations, a hard mode, are necessary in order to realize some of the deformation paths for single crystal. Let us denote the ratios:
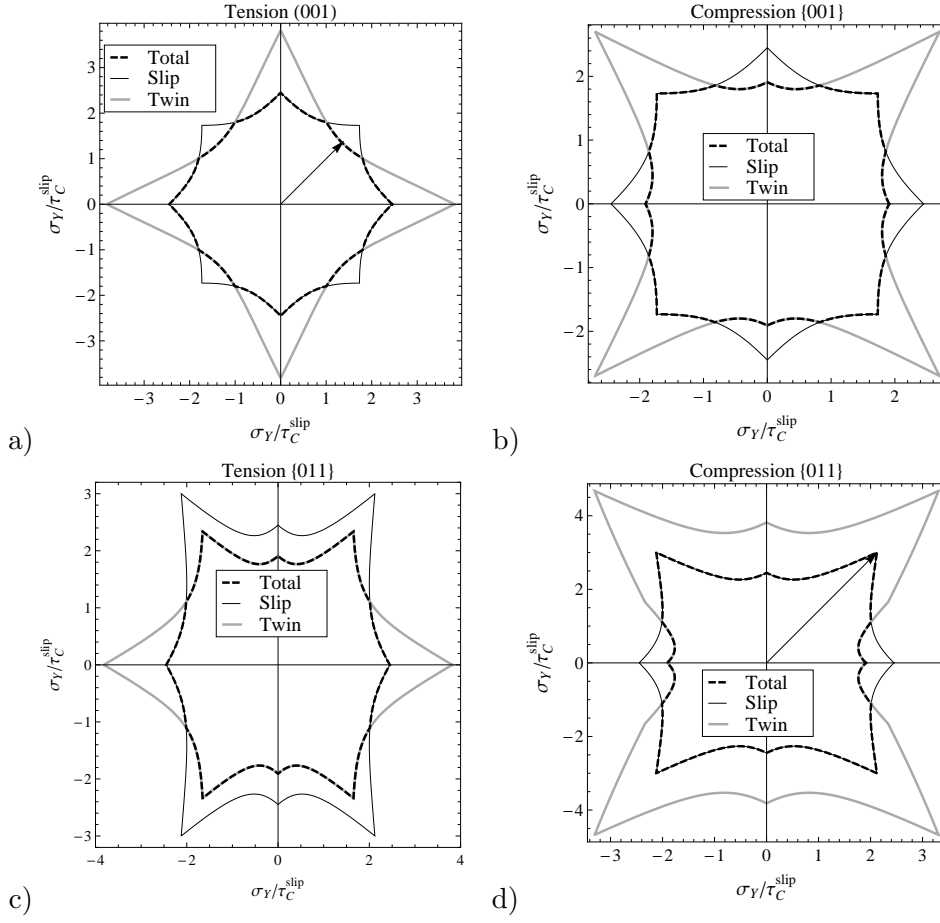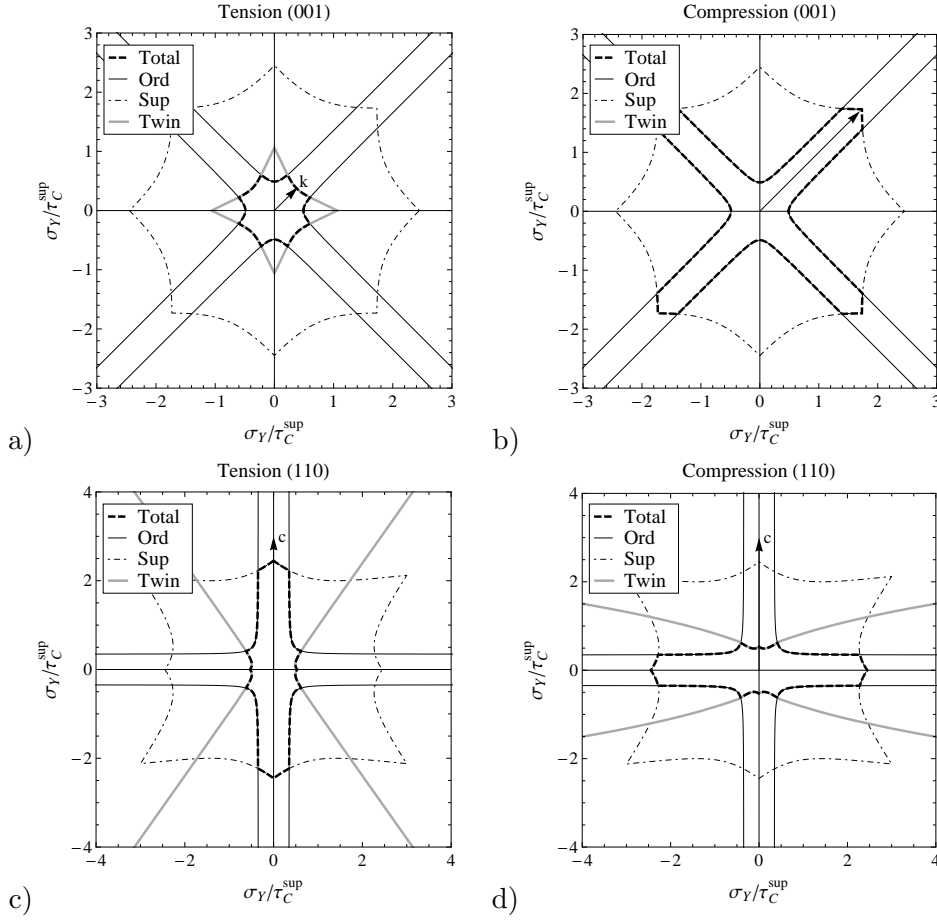
Fig. 2.7. The yield stress in tension and compression in different directions in the crystal planes (001) and (110) for the γ-TiAl single crystal with the assumed values of $\alpha^{ord} = 0.2$ and $\alpha^{tw} = 0.25$. Polar plots (the direction of an arrow marked in the figure (a) is coaxial with direction of tension/compression, while its length indicates the magnitude of the corresponding yield stress).

$\alpha^{ord} \equiv \tau_c^{ord}/\tau_c^{sup}$, $\alpha^{tw} \equiv \tau_c^{tw}/\tau_c^{sup}$ and perform similar analysis as for fcc material. For some combinations of these ratios, twinning and ordinary dislocations will never be initiated. Calculating the yield stresses for shear specified by one of the slip systems belonging to ordinary and super-dislocations, respectively, and for shear specified by one of the twin systems it is obtained:

$$\frac{\tau_Y^I}{\tau_c^{sup}} = \min\{\alpha^{ord}, 2, 3\sqrt{3}\alpha^{tw}\}, \quad \frac{\tau_Y^{II}}{\tau_c^{sup}} = \min\{2\alpha^{ord}, 1, \frac{2}{\sqrt{3}}\alpha^{tw}\}, \qquad (2.52)$$

$$\frac{\tau_Y^{III}}{\tau_c^{sup}} = \min\{3\sqrt{3}\alpha^{ord}, \frac{2}{\sqrt{3}}, \alpha^{tw}\}. \tag{2.53}$$

One concludes that ordinary dislocations are not initiated if $\alpha^{ord} > 2$, while twinning is not initiated if $\alpha^{tw} > 2/\sqrt{3}$. Extended study on deformation modes in γ-TiAl and the influence of their potential activity on the morphology of the yield surface has been performed by Mecking et al. [131]. Most of the experiments indicate that $\alpha^{ord} < \alpha^{tw} < 1$, cf. Appel and Wagner [6].

Let us also analyse the case of uniaxial tension and compression for this material. Similarly, as for a fcc material, the analysis can serve as a basis for the establishment of a mechanical characteristics concerning each mode in experiments performed on γ-TiAl single crystals or strongly textured polycrystals, see e.g. Schillinger et al. [184]. As previously, we present the results for uniaxial tension and compression at any angle in crystallographic planes (001) and (110) (as usual the third axis is the **c** axis).

Comparing with the fcc material, one observes much stronger anisotropy of the yield stress and much stronger tension-compression asymmetry. The highest differences between tensile and compressive yield stresses are expected for **c** direction and directions perpendicular to **c**.

Hcp materials

As indicated in Sec. 2.2 there are six categories of slip and twin systems possible for hcp material, therefore characterization of mechanical behaviour of a single grain is for this case more complex than for previously discussed materials. Among slip systems the pyramidal $\langle a \rangle$ and pyramidal $\langle c+a \rangle$ systems are the hard modes while prismatic slip (Ti, Zr, α_2-TiAl) or basal slip (Mg) and tensile or compressive twinning are easier to initiate. Note that pyramidal $\langle c+a \rangle$ slip systems are necessary in order to fulfil the condition of five independent slip systems and thus to realize some of the deviatoric deformation paths for single crystal. Analysis presented below concerns magnesium ($c/a = 1.624$). First we focus on the hard modes and then we will analyse all modes together.

Considering only the hard modes let us calculate the yield stress for shear specified subsequently by one of the slip systems belonging to prismatic, pyramidal $\langle a \rangle$ and pyramidal $\langle c+a \rangle$ categories. Denoting $\alpha^{prism} \equiv \tau_c^{prism}/\tau_c^{pyr\langle c+a \rangle}$ and $\alpha^{pyr\langle a \rangle} \equiv \tau_c^{pyr\langle a \rangle}/\tau_c^{pyr\langle c+a \rangle}$, we obtain:

$$\frac{\tau_Y^I}{\tau_c^{pyr\langle c+a \rangle}} = \min\{\alpha^{prism}, 1.13\alpha^{pyr\langle a \rangle}, 2.59\}, \tag{2.54}$$

$$\frac{\tau_Y^{II}}{\tau_c^{pyr\langle c+a\rangle}} = \min\{1.13\alpha^{prism}, \alpha^{pyr\langle a\rangle}, 2.24\}, \tag{2.55}$$

$$\frac{\tau_Y^{III}}{\tau_c^{pyr\langle c+a\rangle}} = \min\{2.59\alpha^{prism}, 2.24\alpha^{pyr\langle a\rangle}, 1\}. \tag{2.56}$$

One concludes that, taking into account only hard modes, prismatic slip is not initiated if $\alpha^{prism} > 2.59$ and pyramidal $\langle a\rangle$ slip is not initiated if $\alpha^{pyr\langle a\rangle} > 2.24$. The values of the yield stress in uniaxial tension and compression in the direction coaxial with the prismatic crystallographic planes $\{10\bar{1}0\}$ and the basal plane (0001), respectively, obtained for the hypothetical case when only hard modes act, are presented in Fig. 2.8a and b. The presented curves were obtained assuming equal critical shear stresses for all hard modes, that is $\alpha^{prism} = \alpha^{pyr\langle a\rangle} = 1$.

Fig. 2.8. The yield stress in tension/compression in different directions in the crystal planes $\{10\bar{1}0\}$ (a) and (0001) (b) for the Mg single crystal - only hard slip modes and $\alpha^{prism} = \alpha^{pyr\langle a\rangle} = 1$ (polar plots).

Now, let us group all hard modes together and analyse them in conjunction with the basal slip and tensile twinning. Denoting $\alpha^{basal} \equiv \tau_c^{basal}/\tau_c^{hard}$ and $\alpha_{twin} \equiv \tau_c^{twin}/\tau_c^{hard}$, and calculating the yield stress for simple shears specified by one of the basal systems and the tensile twinning systems, respectively; we find:

$$\frac{\tau_Y^{I}}{\tau_c^{pyr\langle c+a\rangle}} = \min\{\alpha^{basal}, 17.95\alpha^{twin}, 2.12\}, \tag{2.57}$$

$$\frac{\tau_Y^{II}}{\tau_c^{pyr\langle c+a\rangle}} = \min\{17.95\alpha^{basal}, \alpha^{twin}, 1.24\}. \tag{2.58}$$

One concludes that basal slip is not initiated if $\alpha^{basal} > 2.12$, while tensile twinning is not initiated if $\alpha^{twin} > 1.24$. As basal slip is an easy mode, for which the critical shear stress is evaluated to be a few times lower than for hard modes, the condition of its initiation is naturally fulfilled for magnesium alloys. Initiation of tensile twinning is usually more probable for the processes taking place at room temperature.
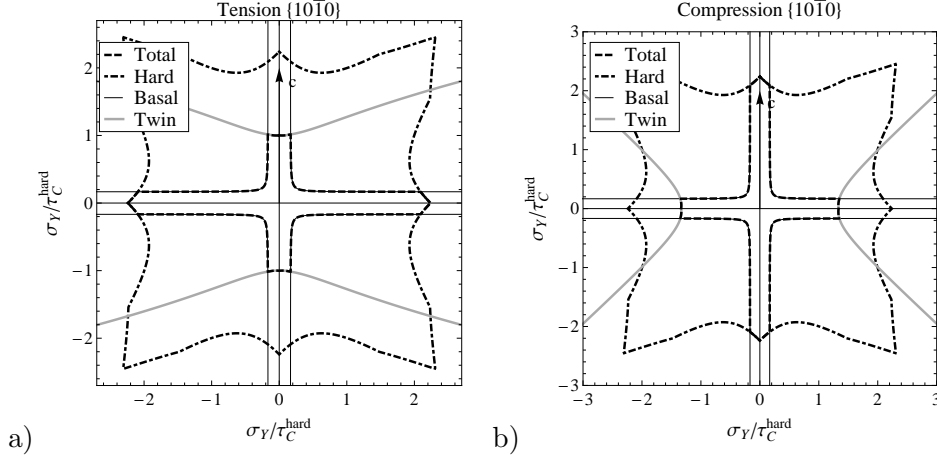
Fig. 2.9. The yield stress in tension (a) and compression (b) in different directions in the crystal planes $\{10\bar{1}0\}$ for the Mg single crystal - all modes and $\alpha^{prism} = \alpha^{pyr\langle a\rangle} = 1$, $\alpha^{bas} = 1/6$, $\alpha^{tw} = 0.5$ (polar plots).

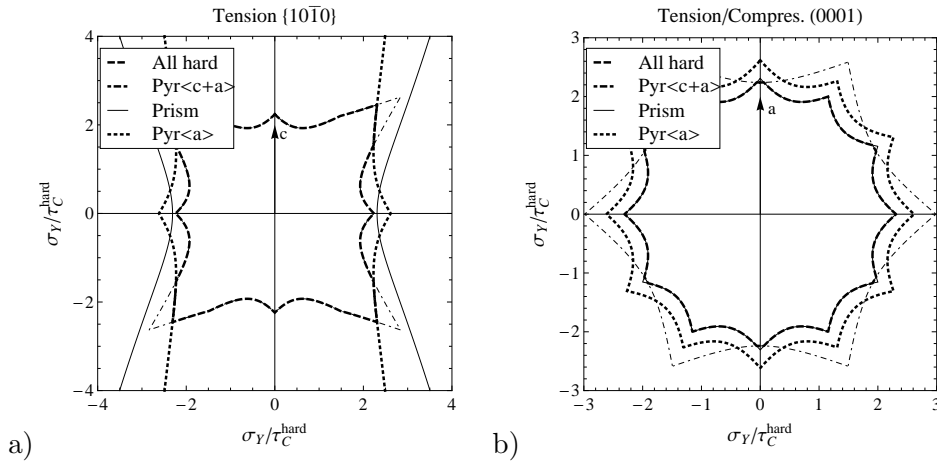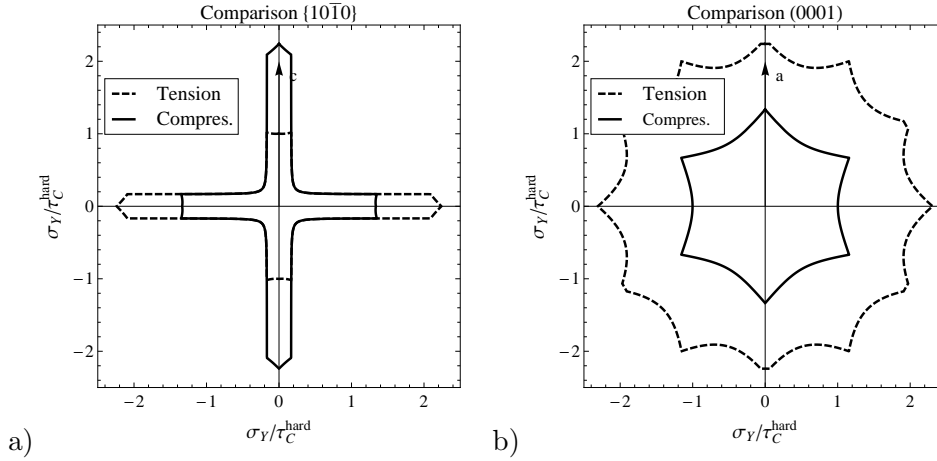
Fig. 2.10. The tension-compression a-symmetry for different directions in the crystal planes $\{10\bar{1}0\}$ (a) and (0001) (b) for Mg single crystal - all modes and $\alpha^{prism} = \alpha^{pyr\langle a\rangle} = 1$, $\alpha^{bas} = 1/6$, $\alpha^{tw} = 0.5$ (polar plots).

Analysing uniaxial tension and compression experiments, we find that, as concerns tension in directions coaxial with basal plane of single crystal, neither basal slip nor tensile twinning can be initiated. For the uniaxial compression process in this plane, activation of tensile twinning reduces the value of a yield stress, at least for some directions in this plane, as long as the value of $\alpha^{twin} < 0.84$, Fig. 2.10b. The yield stress for uniaxial tension and compression in the directions coaxial with prismatic planes $\{10\bar{1}0\}$ is reduced by activation of easy basal modes, except for directions which are aligned, or are close to be aligned, with **c** axis and directions perpendicular to **c** axis, Fig. 2.9. Furthermore, tensile twinning reduces the yield stress in uniaxial tension in **c** direction, Fig. 2.9a.

It is seen that necessity of activation of hard modes for some of loading directions is the source of high anisotropy of Mg alloys of strong textures (e.g. basal texture) observed in experiments. As concerns twinning, the identified critical shear stress is usually lower than for hard modes, however much higher than for easy basal mode, cf. Agnew et al. [2], Agnew and Duygulu [1]. In the case of Mg and Ti alloys, on the basis of experimental evidences usually only four types of modes are selected for further analysis, namely: basal, prismatic and pyramidal $\langle c + a \rangle$ slip, and tensile twinning.

2.4.2. Description of polycrystalline aggregate

The proposed model will now be validated regarding its predictions of an overall stress-strain curve and the texture evolution for polycrystalline low SFE fcc materials, titanium aluminides of near gamma microstructure and magnesium alloys. The presented analysis is performed at the material point at the level of a polycrystalline sample. Since we are interested in the behaviour at large plastic deformations, the elastic strains are neglected and rigid-(visco)plastic model of single grain is used. Consequently, at a level of single grain, under the assumption that the local total velocity gradient is known, we solve the flow rule with definitions (2.27) or (2.25), supplemented by a yield condition in the latter case, in order to obtain the local stress $\boldsymbol{\sigma}^g$. As the representative volume element (RVE) for this macroscopic material point, the grain aggregate composed of NG grains, with the imposed initial distribution of lattice orientations, is assumed.

Different micro-macro transition rules between the level of single grain and the level of polycrystalline sample will be considered. First, as a micro-macro transition rule the Taylor hypothesis is applied assuming that the velocity gradient $\mathbf{l}^g$ in every grain is the same and equal to the macroscopic velocity gra-

dient **L**. The macroscopic stress is calculated as follows:

$$\boldsymbol{\Sigma} = \sum_{g=1}^{NG} \nu^g \boldsymbol{\sigma}^g \, , \tag{2.59}$$

where ν^g is the volume fraction of grains with the orientation g in RVE. The Taylor model has an appealing virtue of computational simplicity and it proved to give results of first-order agreement with experiments in many analyses of single-phase fcc materials, e.g. Staroselsky and Anand [186], Kalidindi and Anand [77], especially concerning the texture evolution and the polycrystal response for large strain regime. Therefore, it is a natural first step for studying the prediction ability of the proposed models. It is also used here in order to compare the results with those of Staroselsky and Anand [186] as far as prediction of the brass-type texture is concerned. Note that the Taylor model is also used as a scale transition rule between three considered levels of microstructure by Kalidindi [75, 76].

In reality strains vary within the grain aggregate and within the single grain. The proposed model of a single crystal may be applied for any micro-macro transition scheme used recently in numerical simulations of polycrystals. In particular, using the self-consistent transition scheme one may account for the heterogeneity of deformation from grain to grain, cf. Lebensohn and Tomé [112], Karaman et al. [79], Kaschner et al. [81], Proust et al. [169], while using the FE-model of a polycrystalline aggregate it is possible to observe also the deformation heterogeneity within the single grain. In these more advanced multi-scale models, analysing the value of volume fraction of twins across the considered volume element, it is possible to study the space distribution of twinning activity. Taking into account the strain heterogeneity from grain to grain is important in the case of modelling of twinning. As it was discussed in Sec. 2.3.1, matrix-twin interfaces produce constraints on deformation which could be restricted to the planar flow within the twinned part, cf. Leffers and Juul Jensen [116]. Such a behaviour cannot be described by the Taylor model that requires five independent slip systems in order to realize an imposed macroscopic velocity gradient in every grain. Therefore, the PTVC scheme and the proposed hardening description have been also implemented and tested within the well-known VPSC (viscoplastic self-consistent) formulation developed by Lebehsohn and Tomè, described in detail in [112, 201], and originating from the idea of Molinari et al. [138]. This model uses the rate-dependent power law (2.27). In order to preserve the rate-insensitive character of constitutive rule, the reference shear rate has been scaled to the macroscopic strain-rate. In simulations we have used the different

variants of the VPSC model. Different formulations of the self-consistent transition scheme for non-linear models of viscoplasticity of crystals will be discussed in detail in Chapter 4 (see also Masson et al. [127]), therefore above only basic facts concerning the description of plastic or viscoplastic polycrystal have been provided.

2.4.3. Low SFE fcc materials

Hadfield steel

In Karaman et al. [79] the stress-strain response of Hadfield steel (composition: Mn 12.34%, C 10.3% and Fe balance) with fcc slip and twin systems was studied. The results of a tension experiment at room temperature performed on the single crystal orientation $[\bar{1}11]$ concern the stress-strain curve and the texture evolution. These results have been used to identify the material parameters for the presented model and to study the performance of the developed PTVC reorientation scheme. Similarly to Karaman et al. [79], a very small linear hardening due to slip-slip and twin-slip interactions has been assumed. It corresponds to the solid solution strengthening. On the other hand, the role of matrix-twin boundaries created during the process is identified as a main mechanism of hardening. After the reorientation, the value of the slip resistance increases by 10% for non-coplanar slip systems, while the value of the twin resistance increases by 20% for all twin systems. Initially, the ratio $\tau_{c0}^{twin} : \tau_{c0}^{slip}$ was assumed as $1.172 : 1.0$. Note that the $[\bar{1}11]$ orientation is symmetric. Theoretically three twin systems with the Schmid factor 0.314 and 6 slip systems with the Schmid factor 0.272 are equivalent and potentially active, depending on the current ratio $\tau_c^{slip} : \tau_c^{twin}$. In order to reproduce the experimental observations which indicated that initially only one twin system is active, a slightly smaller τ_c was assigned to the corresponding twin resistance. All material parameters describing hardening are collected in Table 2.3.

Table 2.3. Material parameters for Hadfield steel; $\tau_{c0}^{slip} = 105$ MPa (single crystal), $\tau_{c0}^{slip} = 150$ MPa (fine-grained polycrystal).

interactions	$h_0^{\alpha\beta} \, [\tau_{c0}^{slip}]$ single/polycrystal	$f_{sat}^{\alpha\beta}$	$q^{(\alpha\beta)}$
slip-slip	0.1/1.2	—	1.6
slip-twin	3.8	0.85	1.6
twin-slip	0.1/1.2	—	1.6
twin-twin	3.8	0.8	1.6
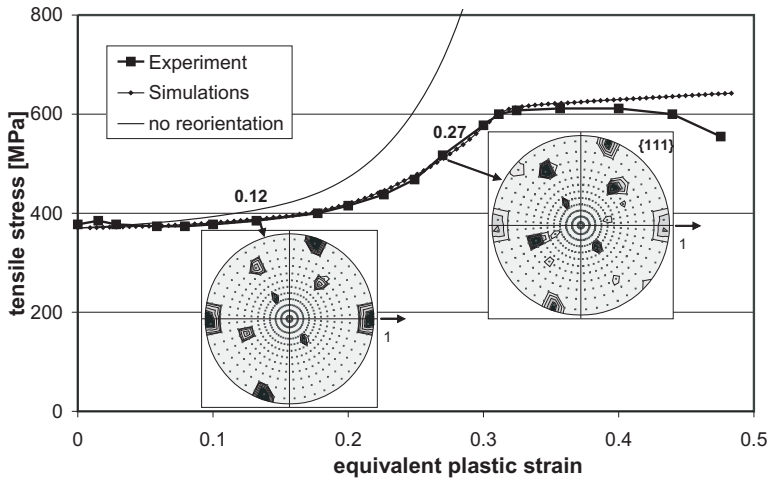
Fig. 2.11. Tension stress - equivalent strain curves ($\dot{\bar{\varepsilon}}_{eq} = \sqrt{\frac{2}{3}\mathbf{D}^p \cdot \mathbf{D}^p}$) and texture evolution of the orientation [$\bar{1}$11] in Hadfield steel (aggregate of 400 grains, PTVC scheme). Axis 1 corresponds to the tension direction. Experimental data reported in [79].
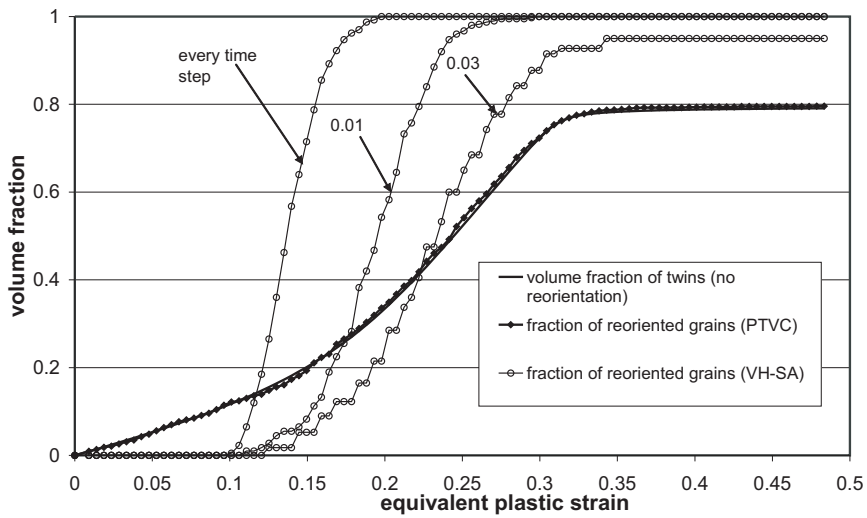
Fig. 2.12. Fraction of reoriented grains ($NG_{reorient}/NG$) predicted by the PTVC scheme and the SA scheme with different frequency of checking the reorientation condition ($\xi_0 = 0.04$). Orientation [$\bar{1}$11] of Hadfield steel under tension (aggregate of 400 grains).
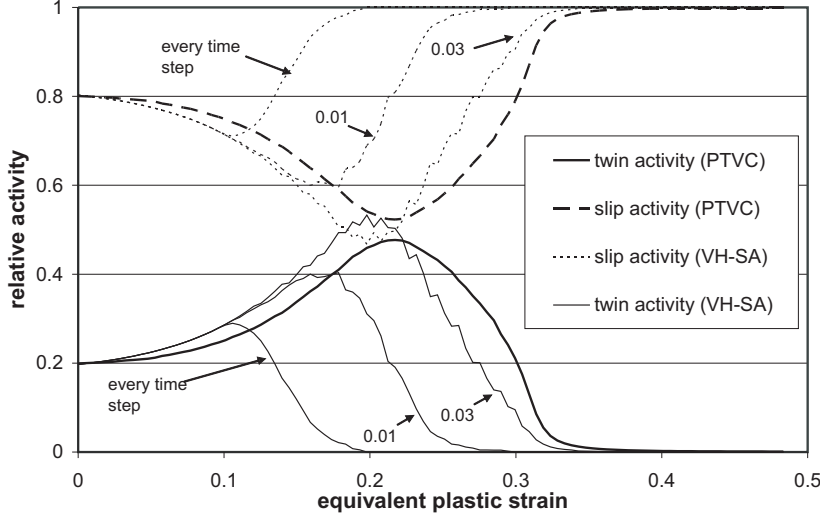
Fig. 2.13. Relative slip and twin activity in tension of the orientation [1̄11] of Hadfield steel predicted by the PTVC scheme and the SA scheme with different frequency of checking the reorientation condition ($\xi_0 = 0.04$).

The results of simulation are presented in Figures 2.11-2.13. The applied description of hardening allows us to fit very well experimentally obtained strain-stress response. The texture image is also well reproduced (compare experimental data of Karaman et al. [79]). Initially, slip is a dominant mechanism and the hardening is small, then as activity of twinning increases, the created twin-matrix boundaries cause the increase of stress, and finally, when twinning activity is halted and material deforms only by slip, again the hardening is small. Note that twinning is active from the beginning of the process, however, its relative activity, predicted by the developed model, changes during the process and it is maximum for the strain interval 0.15-0.25, compare Fig. 2.13. The following definitions of relative activities are used:

$$\alpha^{slip} = \frac{\sum_{r=1}^{2M} \dot{\gamma}^r}{\sum_{r=1}^{2M+N} \dot{\gamma}^r}, \quad \alpha^{twin} = \frac{\sum_{r=2M+1}^{2M+N} \dot{\gamma}^r}{\sum_{r=1}^{2M+N} \dot{\gamma}^r}. \tag{2.60}$$

Let us analyse the performance of the developed PTVC reorientation scheme and compare it with the Staroselsky and Anand modification [186] of Van Houtte's scheme which is denoted as a SA scheme. In Fig. 2.12 the evolution of a twin volume fraction predicted by the developed model, obtained when there is no reorientation, is confronted with the fraction of reoriented grains
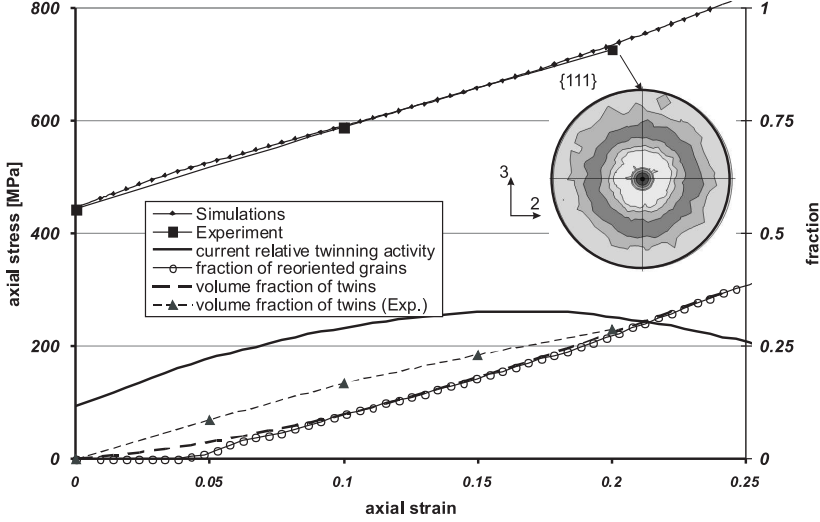
Fig. 2.14. Mechanical response of polycrystalline Hadfield steel deformed in tension (axis 1 corresponds to the tension direction) - aggregate of 3000 grains (average diameter $100\mu m$), random initial texture. Experimental data reported in [79].

in the aggregate according to the PTVC scheme and the SA scheme. In the case of the PTVC scheme, the fraction of reoriented grains follows very well the volume fraction of twins, since it has been the basic assumption of the developed model. In the case of the SA scheme $\xi_0 = 0.04$ was assumed. It is shown that predictions of the SA scheme depend on the frequency of checking the reorientation condition. When the condition is checked every time step, after the volume fraction of the most active twin system f^l_{max} reaches ξ_0, the number of reoriented grains increases rapidly and all grains in the aggregate are reoriented very soon. When the frequency is smaller, that is when the condition is checked every time when the increment of twin volume fraction Δf is equal to 0.01 or 0.03, respectively, the number of reoriented grains increases more slowly and can saturate at a lower level due to the applied hardening description. It may be shown that the predicted mechanical response in this case is affected by the additional parameters describing the reorientation scheme, such as ξ_0 and Δf. It is not the case for the PTVC scheme. In the latter case the mechanical response is governed only by the hardening rule which describes the current relative activity of the corresponding twin and slip systems and the assumption on the slip and twin resistances after the reorientation.

Simulations have been also performed for Hadfield steel polycrystals. Good agreement with experimental results concerning the stress-strain curve reported

in Karaman et al. [79] for the aggregates of different grain sizes was observed. It was achieved by scaling the initial resolved shear stresses according to the Hall-Petch relation and by introducing an additional linear term in the hardening rule (2.41) describing the influence of grain boundaries on the reduction of the MFP distance. Other parameters identified for the single crystal have not been altered. As an example, results for the aggregate of fine grains (an average diameter $d = 100\mu m$) with the initial random texture are collected in Fig. 2.14. The Taylor model of polycrystal has been applied. Note that the predicted and experimental curves for a twin volume fraction are not far from each other.

70-30 brass

Experiments for 70-30 brass indicate the contribution of twinning into the plastic deformation, cf. Asgari et al. [9], El-Danaf et al. [46]. Material parameters have been adjusted independently for the Taylor model and for the tangent variant of VPSC scheme, with use of a strain-stress curve obtained for the plane strain compression experiment reported by Kalidindi [76]. They are collected in Table 2.4. In the yield condition (2.20) and the power law (2.27) $n = 16$ has been prescribed and it has been assumed that further twinning in the reoriented grains is strongly restricted while slip resistances for non-coplanar slip systems are increased by 10% after reorientation. Following Staroselsky and Anand [186] and Kalidindi [76] it has been assumed that twin resistances are initially significantly higher than slip resistances, specifically $\tau_{c0}^{slip} : \tau_{c0}^{twin} = 30$ MPa : 202.5 MPa for the Taylor model and $\tau_{c0}^{slip} : \tau_{c0}^{twin} = 34.5$ MPa: 189.75 MPa for the VPSC model. Twin-slip interactions have been neglected at this stage ($H_{ts}^r = 0$). The aggregate composed of grain with 1500 different orientations, with initially random distribution in the orientation space, has been considered.

Table 2.4. Material parameters for 70-30 brass.

interactions	averaging	$h_0^{(\alpha\beta)}$ [MPa]	τ_{sat} [MPa] / $f_{sat}^{\alpha t}$	a	$q^{(\alpha\alpha)}$
slip-slip	Taylor	252	330	2.3	1.6
	VPSC	431.25	362.25	2.3	1.6
slip-twin	Taylor	69	0.8	—	1.6
	VPSC	79.35	0.8	—	1.6
twin-twin	Taylor	36	0.6	—	1.6
	VPSC	41.4	0.6	—	1.6

Plane strain compression (PSC) and simple compression (SMC) processes have been analysed, specified by the imposed total velocity gradient in the form

$$[L_{ij}^{PSC}] = \frac{v_0}{\sqrt{2}} \begin{bmatrix} 1 & 0 & 0 \\ 0 & 0 & 0 \\ 0 & 0 & -1 \end{bmatrix}, \quad [L_{ij}^{SMC}] = \frac{3v_0}{\sqrt{6}} \begin{bmatrix} \frac{1}{2} & 0 & 0 \\ 0 & \frac{1}{2} & 0 \\ 0 & 0 & -1 \end{bmatrix}, \quad \text{in} \quad \{\mathbf{e}_i\}.$$

In Fig. 2.15 the macroscopic equivalent Von Mises stress-equivalent strain curves are presented. In the case of the Taylor model, the level of stress for simple compression is overpredicted as compared to the experimental results. The similar trend was observed in computations reported by Kalidindi [76], where a more advanced twinning model was used, but with conjunction with the Taylor averaging as well. Better accordance with the experiment, at least as far as the stress level is concerned, is obtained when the VPSC scale transition is applied for polycrystal. The latter formulation admits heterogeneous flow from grain to grain; therefore, the planar flow is possible for reoriented grains.

One observes that till the moment when twinning begins to play a significant role (compare Figs 2.15-2.17) in the realization of plastic deformation, curves predicted by the model with twinning and the model without twinning are very similar. When accumulation of dislocations makes slip more difficult then twinning is given way and a macroscopic hardening modulus is temporarily reduced. After the reorientation of a sufficiently large amount of grains, due to the assumed model for the mechanical characterization of reoriented grains, one has to do with a significant increase of macroscopic hardening. The reduction of strain hardening caused by initiation of twinning as compared to the conventional model accounting only for slip, depends on the type of strain path. It is higher for plane strain compression than for simple compression. Note that the difference between the stress-strain curves for plane strain compression and simple compression for the conventional model results mainly from the shape of the yield surface which is of the Tresca polyhedron type, not of the Huber-von Mises cylinder. In the case of a model with twinning, this effect is supplemented by a different contribution of twinning depending on the strain path. The current relative activity of twinning depends on the strain path as well, Fig. 2.17a and b. It is especially apparent in the case of the self-consistent averaging where, in accordance with experiments, the contribution of twinning is considerably lower for simple compression than for plane strain compression.

In Figs 2.16 and 2.17 the PTVC scheme is compared with the SA scheme. Also for the polycrystalline material the number of reoriented grains follows the volume fraction of twins in the case of the PTVC scheme. In the case of the SA scheme we have assumed $\xi_0 = 0.15$ and studied the results for $\Delta f = 0.01$

Plane Strain Compression (PSC)

a)

Simple Compression (SMC)

b)
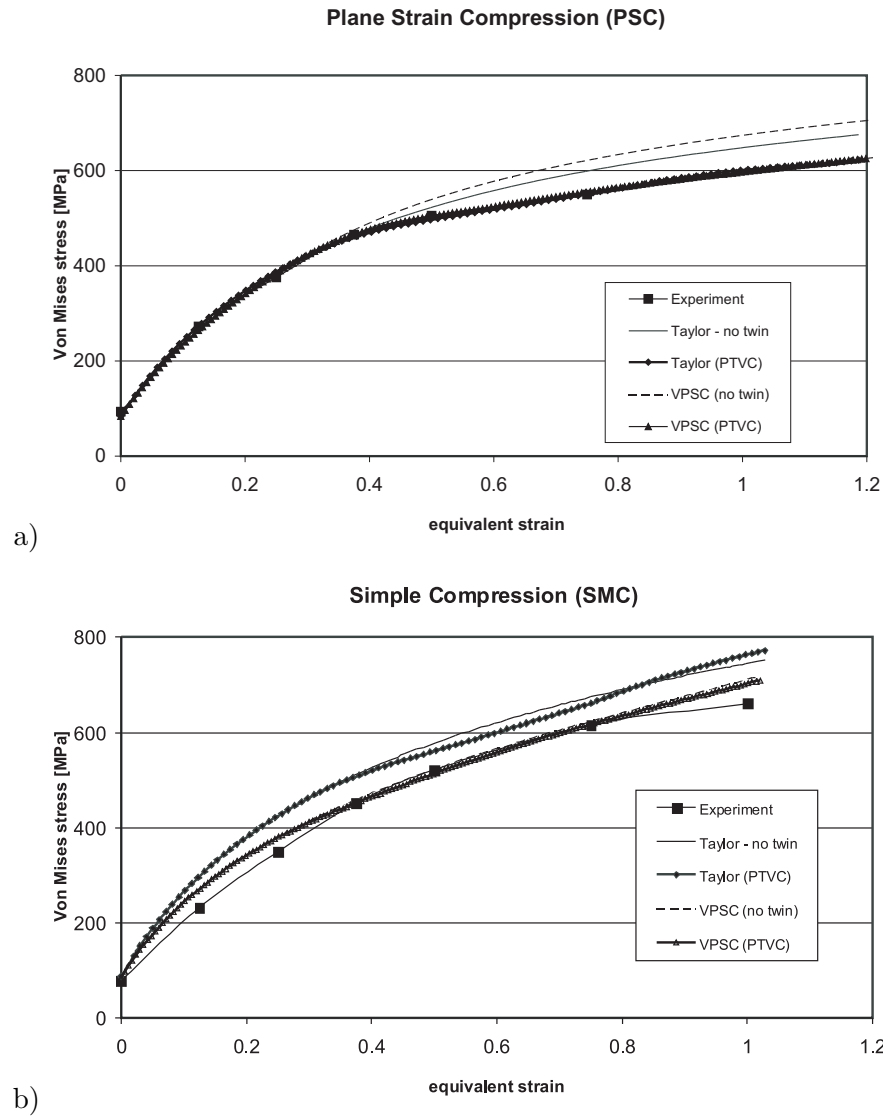
Fig. 2.15. Equivalent von Mises stress - equivalent strain curves: a) plane strain compression, b) simple compression of 70-30 brass.
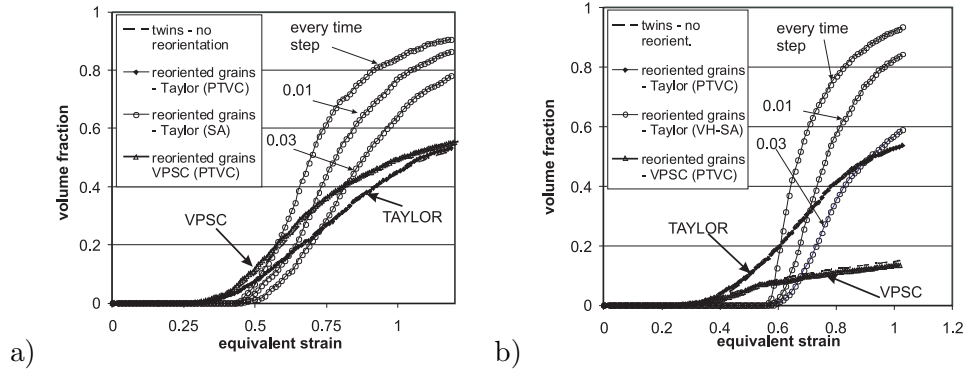
Fig. 2.16. Volume fractions of reoriented grains according to the PTVC scheme and the SA scheme with different frequency of checking the reorientation condition: a) plane strain compression, b) simple compression of 70-30 brass.
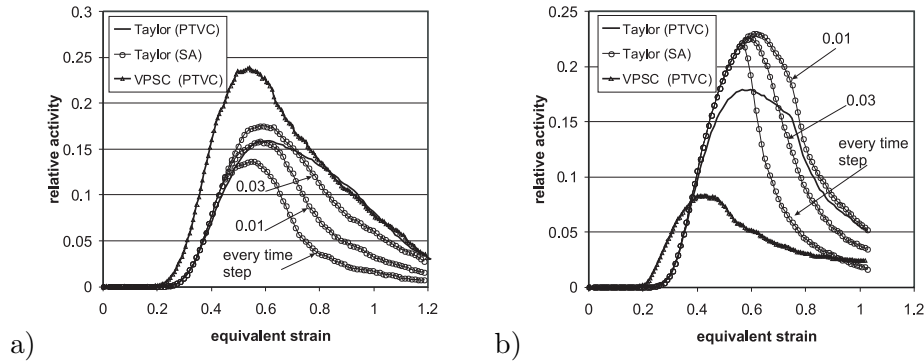
Fig. 2.17. Current relative activity of twinning according to the PTVC scheme and the SA scheme with different frequency of checking the reorientation condition: a) plane strain compression, b) simple compression of 70-30 brass.

and 0.03 as well as in the case when the reorientation condition is checked in every time step. When the SA scheme is used, the number of reoriented grains strongly increases when f^{TW} reaches $\xi_0 = 0.15$ and it quickly becomes overpredicted as compared to the twin volume fraction. Moreover, the parameters assumed for the reorientation condition $(\xi_0, \Delta f)$ affect the relative twinning activity and, therefore, the stress-strain curve.

In Figs 2.18-2.21 the influence of twinning and the applied reorientation scheme on texture development is analysed and compared with the results
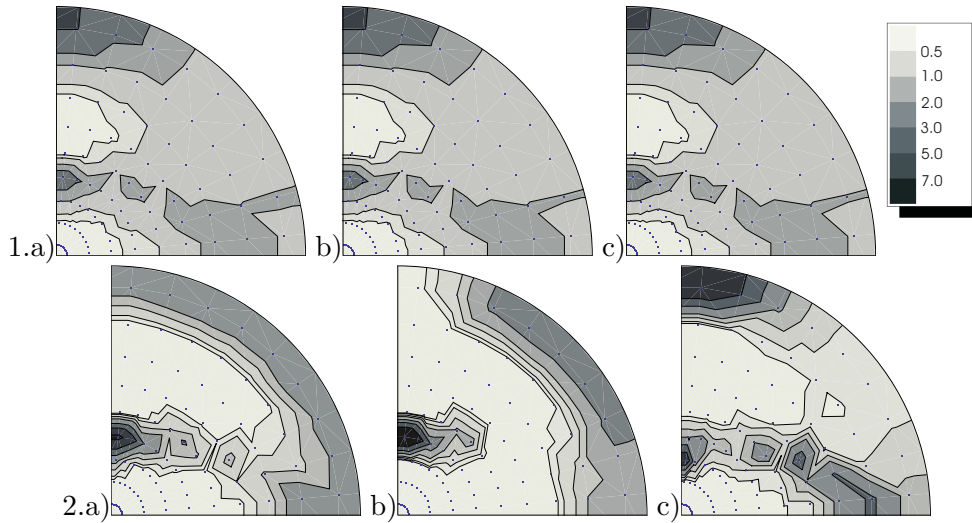
Fig. 2.18. Plane strain compression (Taylor model). Pole figure {111}, stereographic projection: 1. $\varepsilon_{eq} = 0.35$, 2. $\varepsilon_{eq} = 1.2$ (a) model with twinning - the PTVC scheme (b) the SA scheme (reorientation checked in every time step) (c) model without twinning. Contours at multiplicities of random distribution indicated by the legend.
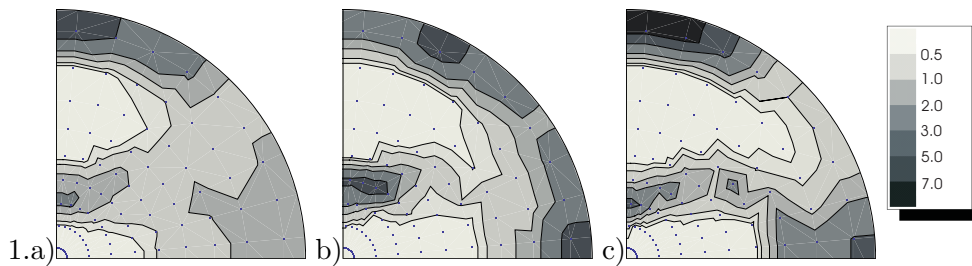
Fig. 2.19. Plane strain compression. Pole figure {111}, stereographic projection: (a) VPSC model with twinning - PTVC scheme, $\varepsilon_{eq} = 0.35$ (b) VPSC model - PTVC scheme, $\varepsilon_{eq} = 1.2$ (c) VPSC model without twinning. Contours at multiplicities of random distribution indicated by the legend.

for conventional crystal plasticity with only slip mechanism. Textures for simple compression are close to each other for all models. Significant difference in texture images is observed for plane strain compression which could be understood as an idealization of a rolling process. Two types of texture obtained for the models with twinning and for the conventional model correspond to two types of rolling texture that are experimentally observed and widely discussed, that is the brass-type texture and the copper-type texture, cf. Staroselsky and Anand [186], Kalidindi [76], Kocks et al. [88], Leffers
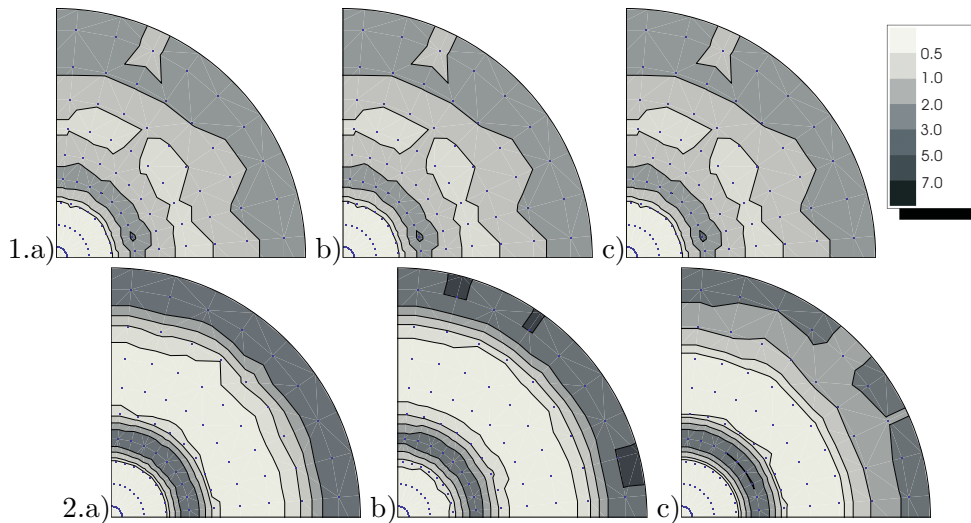
Fig. 2.20. Simple compression (Taylor model). Pole figure {111}, stereographic projection: 1. $\varepsilon_{eq} = 0.3$, 2. $\varepsilon_{eq} = 1.0$ (a) model with twinning - the PTVC scheme (b) the SA scheme (re-orientation checked in every time step) (c) model without twinning. Contours at multiplicities of random distribution indicated by the legend.
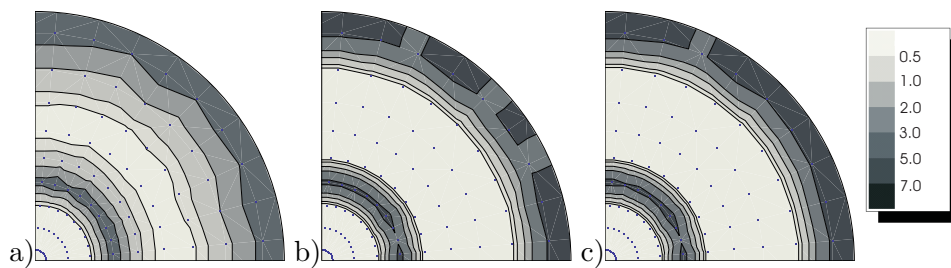
Fig. 2.21. Simple compression. Pole figure {111}, stereographic projection: (a) VPSC model with twinning - PTVC scheme, $\varepsilon_{eq} = 0.3$ (b) VPSC model - PTVC scheme, $\varepsilon_{eq} = 1.0$ (c) VPSC model without twinning. Contours at multiplicities of random distribution indicated by the legend.

and Juul Jensen [116], Leffers and Ray [117]. Such an effect of the appearance of a large fraction of twin-related orientations in the RVE is known from other contributions on simulations of texture in the presence of twinning (e.g. Van Houtte [203], Staroselsky and Anand [186], Kalidindi [75]). Accordingly, a brass component in texture image is especially strong in the case of the SA scheme (compare also the results of Staroselsky and Anand [186]), because almost all grains are reoriented at the final stage of computations (see Fig. 2.16). It is the effect of the described inconsistency between twin activity and the number

of reoriented grains. In the case of the PTVC scheme the difference in the intensity of a brass component as compared to the computations without twinning is also noticeable, though much less pronounced because the number of reoriented grains is smaller, and agrees with the predicted twinning activity. Note that the difference is observed even though the volume fraction of reoriented grains is still higher (50-60%) as compared with those observed in reality (from a few percent up to 20%, cf. Leffers and Ray [117]). Similarly, as concerns the stress-strain response, in the case of texture, better predictions are obtained for the self-consistent model of polycrystal. Note that the applied tangent VPSC formulation with increasing n tends to the Sachs model of polycrystal admitting the planar flow in the grains, cf. Lebensohn and Tomé [112]. Therefore, these results support the arguments presented by Leffers and Juul Jensen [116], Leffers and Ray [117] and Kalidindi [76] that the brass-type texture is more the effect of a lamellar microstructure induced by twinning and leading to the localized planar flow and, eventually, micro-shear banding, than the volume effect of twin-related orientations.

Analysis of the results indicates the necessity of more accurate description of the relation between the developing microstructure and the material response in the presence of twinning. To some extent, this relation is accounted for by the three-scale composite grain model of Proust et al. [169]. However, it is believed that within the proposed two-scale model, there is still a possibility to incorporate microstructural effects, especially by refining the description of directional mechanical characteristics of reoriented grains.

2.4.4. Materials of high specific strength

Near gamma TiAl intermetallics

Within KMM NoE project (www.kmm-noe.org) the properties of γ-TiAl intermetallics were investigated. The commercially processed γ-TiAl of Ti-48Al-2Cr-2Nb composition was provided by one of the industrial partners in the network. Analysis by scanning electron microscopy (SEM) and neutron diffraction measurements indicated that the provided material has near gamma equiaxed microstructure without texture NoE [149]. Samples were made of this material and tested in tension and compression at room temperature using different strain-rates [148]. Though limit strains in tension did not exceed 3%, in compression tests strain up to 35% was achieved. Thus, it is possible to compare these results with predictions of the developed model in large strain regime. Moreover, during the experiments it was concluded that the influence of strain-rate

was not significant when the strain-rate remains moderate $(0.4 - 0.004[1/s])$. Unfortunately, the final texture after compression was not measured. Therefore the identification of material parameters is supported by the results concerning the texture reported by Wang et al. [210] (see Fig. 2.23). They were obtained for near gamma TiAl in similar condition after compression up to 30%.

As it will be shown below, the texture image for the deformation path considered is strongly influenced by the relative activities of ordinary dislocations, super-dislocations and twinning. In the developed model this activity is governed by the initial ratio of the corresponding critical shear stresses and their evolution (specified by the hardening rule) during the process. It must be stressed here that the set of experiments performed within the project is definitely insufficient to argue that the identified values are the optimum ones for the material. However, literature on the subject, e.g. Appel and Wagner [6], Mróz [141], does not provide such a set of values as well, even for the most basic parameter which seems to be the relative ratio $\tau_c^{ord} : \tau_c^{sup} : \tau_c^{twin}$ of the initial critical shear stresses. Therefore, the main goal of the analysis presented below is to identify the important factors influencing the behaviour of this material of high specific strength as well as to study the performance of the developed model. With the use of this example we will also compare the predictions of the PTVC scheme with those of the PTR scheme.

Table 2.5. Identified material parameters for γ-TiAl of near gamma microstructure (material tested within KMM NoE project [148]). Identification performed for the Taylor model of polycrystal, $\tau_{c0}^{ord} = 77.5$ MPa, $n = 20$ in (2.25) ($\bar{n} = 39$ in (2.27)).

Mode	Interaction	$\tau_{c0}[\tau_{c0}^{ord}]$	$h_0[\tau_{c0}^{ord}]$	$\tau_{sat}[\tau_{c0}^{ord}]/f_{sat}$	a	q
Ord.	slip-slip	1.0	6.0	25.	1.1	1.0
	slip-twin	—	1.0	1.0	—	1.6
Super.	slip-slip	5.0	6.0	500.	1.1	1.0
	slip-twin	—	1.0	1.0	—	1.6
Twin	twin-slip	—	0.	—	—	0.0
	twin-twin	1.25	6.0	0.4	—	1.6

First, material parameters have been identified assuming the Taylor model of polycrystal. The values have been established aiming at correct prediction of compression texture and the reproduction of the experimental stress-strain curve for the lowest strain-rate. Material parameters obtained in this way are collected in Table 2.5. The simulated stress-strain response in compression and the calculated final texture are presented in Figs 2.22 and 2.26, respectively.

a)
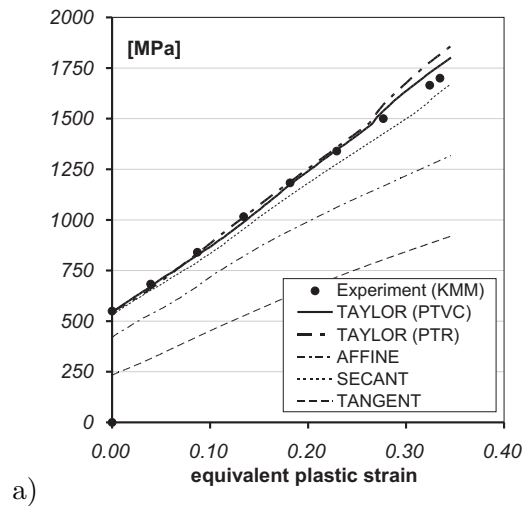
Fig. 2.22. Simple compression: axial stress vs. equivalent plastic strain curves, material parameters from Table 2.5.

a)
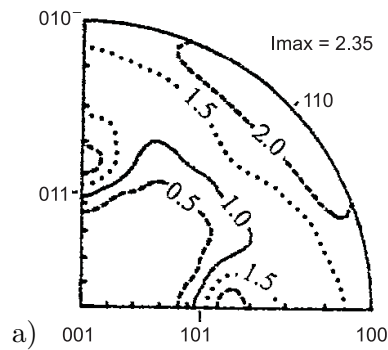
Fig. 2.23. Inverse Pole Figure after compression at room temperature of 30% thickness reduction determined by the maximum entropy method (details see [210]).

As described by Wang et al. [210], the experimentally obtained inverse pole figure of compression axis $\mathbf{e}_3$ contains two important components: the first one is 10° away from $\langle 101]$ directions with a spread of 5° in the pole figure and with a volume fraction of 15%; the second one is a strong $\langle hk0 \rangle$ fibre texture running from $\langle 010]$ to $\langle 100]$ directions with a volume fraction of 40%, although, as seen in Fig. 2.23, the poles belonging to this fibre show tendency to concentrate around $\langle 110]$ direction. Consequently, compression texture of γ-TiAl shows asymmetry between the components $\langle h0k]$ and $\langle hk0]$, not observed for fcc materials for which one expects equal concentration of poles around all $\langle 110 \rangle$ directions. This

asymmetry could be related to a different status of ordinary dislocations and superdislocations. Below we confirm this conclusion of Wang et al. [210] with the use of the proposed model. Furthermore, in the paper of Bartels et al. [10] the fact that the first maximum is shifted from $\langle 101]$ to another orientation, identified in the latter paper with $\langle 302]$ directions, is explained by the twinning activity. The same reason is invoked for the explanation of the appearance of orientations around $\langle 100]$. These conclusions will be also confirmed by the simulations.
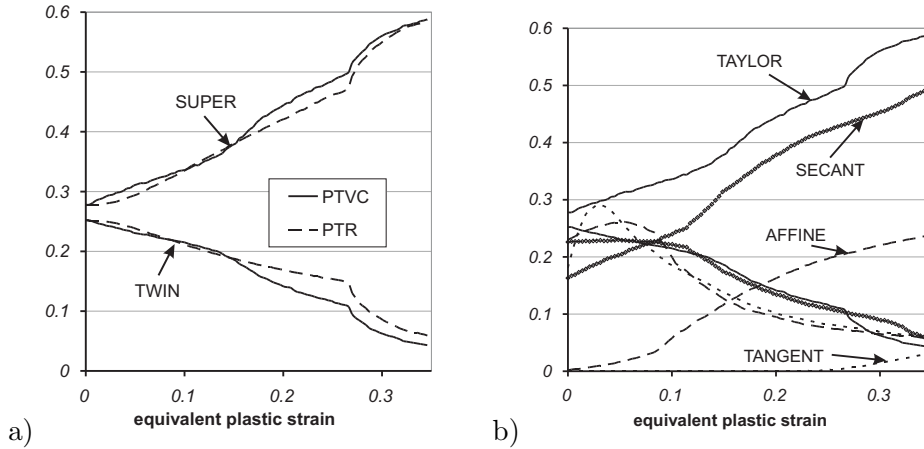
Fig. 2.24. Current relative activities of twinning and superdislocation modes: (a) comparison of PTVC and PTR schemes for Taylor model; (b) comparison of different scale transition rules (PTVC scheme, curves with descriptions are for superdislocations), material parameters from Table 2.5.

Let us analyse the results of simulations of compression process. First, let us study predictions obtained with use of the Taylor model of polycrystal. In Fig. 2.24 the variation of the current relative activities of superdislocations and twinning during the process are presented. Although, the initial critical shear stress for superdislocations is five times higher than for ordinary dislocations, and four times higher than for twinning, quite high activity of this hard mode is predicted by the model. This activity increases in the course of deformation due to decreasing activity of twinning, which is caused by hardening and limited ability of this mode to carry the deformation. In Fig. 2.26 the final texture is presented in the form of inverse pole figure (001). As it is seen the model is able to reproduce the presence of $\langle hk0]$ fibre, however, the texture component $\langle 302]$ is not predicted. Instead of this component we observe the concentration of poles between $\langle 001]$ and $\langle 101]$ directions. It seems that this deficiency of predictions
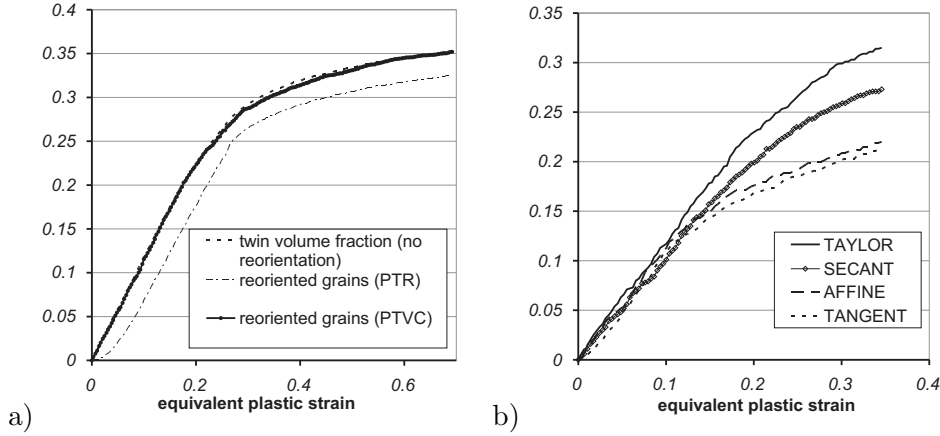
Fig. 2.25. Volume fraction of reoriented grains in compression: (a) Comparison of PTVC and PTR schemes for Taylor model; (b) comparison of different scale transition rules (PTVC scheme), material parameters from Table 2.5.

can be attributed to the general inability of the Taylor model to reproduce some details of texture. Note that the compression texture for fcc material obtained with use of the Taylor model predicts shifting of the main component towards the $\langle 001]$ direction from the correct $\langle 101]$ direction, cf. Kocks et al. [88]. In view of this observation, we have decided to consider more refined VPSC schemes. Before analysing the results obtained with the use of self-consistent models of polycrystal let us compare the results obtained with the use of the proposed PTVC scheme of reorientation and the PTR scheme proposed by Tomé et al. [200]. As it has been explained in the preceding sections, the latter scheme requires establishment of the additional material constants which specify the accumulated twin volume fractions at which the twin-induced reorientation of grains starts and ends. These two values have been assumed as $\gamma_{init}^{TW} = 0$ and $\gamma_{end}^{TW} = 0.35$ in accordance with corresponding values in a self-hardening rule for twinning, cf. Table 2.5. We observe that fraction of reoriented grains follows roughly the evolution of twin volume fraction, however, the agreement between the two is less satisfactory than in the case of the PTVC scheme.

Now, let us look at the results obtained with the same local material parameters but with the secant, affine and tangent VPSC models of polycrystal. Relation between these estimates of the overall stress level reported in the literature, cf. Masson et al. [127] is confirmed also in our calculations, that is the stress level predicted by the secant model is close to the Taylor model for high value of n exponent, the stress level predicted by the tangent model is the

Fig. 2.26. Simple compression. Inverse Pole figure (001), stereographic projection: (a) the Taylor model - the PTVC scheme, (b) the Taylor model - the PTR scheme, $\varepsilon_{eq} = 0.3$, material parameters from Table 2.5. Contours at multiplicities of random distribution indicated by the legend.
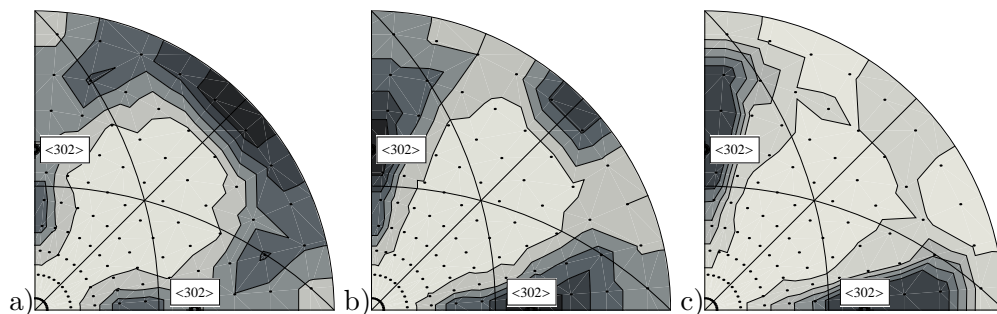
Fig. 2.27. Simple compression. Inverse pole figure (001), stereographic projection: (a) Secant, (b) Affine, (c) Tangent VPSC models with the PTVC scheme, $\varepsilon_{eq} = 0.3$, material parameters from Table 2.5. Contours at multiplicities of random distribution indicated by the legend in Fig. 2.26.

lowest, while the affine model predicts the stress level between the predictions of secant and tangent models. The reason for such relations between the corresponding predictions is clearly seen in Fig. 2.24 where the relative activities of modes are depicted. While the twinning activity for all models is comparable, the activity of the hard superdislocation mode is strongly influenced by the employed averaging scheme. We observe that activity of superdislocations in the case of the secant VPSC model is comparable with that predicted by the Taylor model, while activity of superdislocations are almost not observed for the tangent VPSC model. The differences in activities have direct impact on the obtained textures which are presented in Fig. 2.27. Looking at these figures we can see that the $\langle hk0]$ fibre component in texture is connected with the activity of superdislocations (it almost disappears for the tangent model) while twinning moves $\langle 101]$ component towards $\langle 302]$ component. Proper prediction

of the location of this component is observed only for the affine and tangent VPSC models. In Fig. 2.25b we present the evolution of twin volume fraction (i.e. the fraction of reoriented grains in the aggregate) for all models. It is the highest for the Taylor model and the lowest for the affine and tangent models.

Table 2.6. Identified material parameters for γ-TiAl of near gamma microstructure (material tested within KMM NoE project [148]). Identification performed for the VPSC affine model of polycrystal, $\tau_{c0}^{ord} = 142$ MPa, $n = 20$ in (2.25) ($\bar{n} = 39$ in (2.27)).

Mode	Interaction	$\tau_{c0}[\tau_{c0}^{ord}]$	$h_0[\tau_{c0}^{ord}]$	$\tau_{sat}[\tau_{c0}^{ord}]/f_{sat}$	a	q
Ord.	slip-slip	1.0	5.0	20.	1.1	1.0
	slip-twin	—	1.0	1.0	—	1.6
Super.	slip-slip	2.0	5.0	45.	1.1	1.0
	slip-twin	—	1.0	1.0	—	1.6
Twin	twin-slip	—	0.	—	—	0.0
	twin-twin	1.1	4.0	0.5	—	1.6
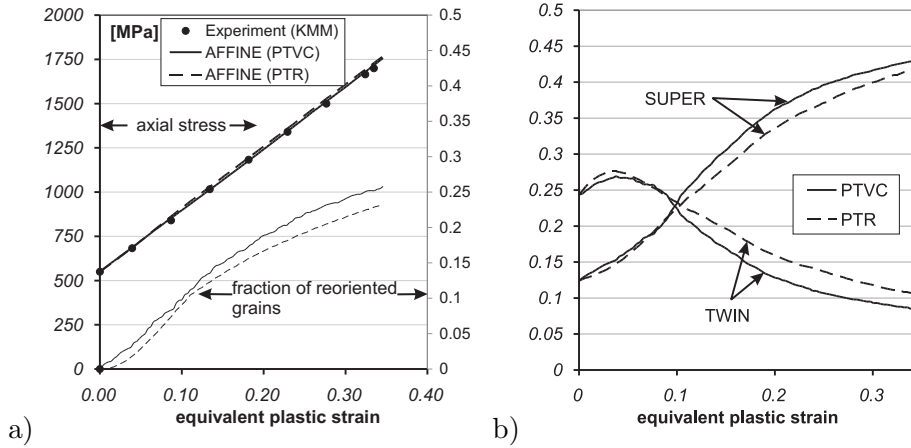
Fig. 2.28. (a) Stress-strain curves and evolution of fraction of reoriented grains fraction; (b) Current relative activities of super-dislocations and twinning. Simple compression, affine model, PTVC and PTR schemes, material parameters from Table 2.6.

Taking the above observations into account, we have decided to perform the identification of material parameters once more, this time using the affine VPSC model of polycrystal. The resulting values are collected in Table 2.6. In order to reproduce the $\langle hk0]$ fibre component in texture image we have set the critical shear stress for superdislocations only two times higher than that for ordinary dislocations. In order to increase propensity to twinning, the critical shear stress for twinning is only 10% higher than τ_c^{ord}, and value of f_{sat} is increased
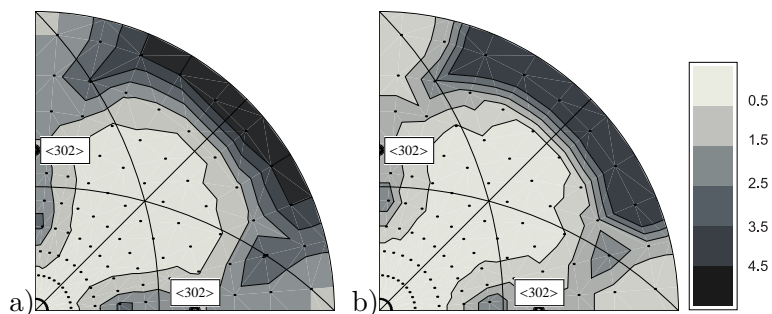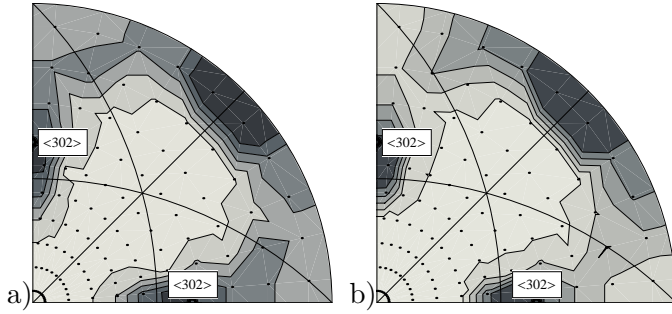
Fig. 2.29. Simple compression. Inverse Pole figure (001), stereographic projection: (a) Affine VPSC model - PTVC scheme, (b) Affine VPSC model - PTR scheme, $\varepsilon_{eq} = 0.3$, material parameters from Table 2.6. Contours at multiplicities of random distribution indicated by the legend in Fig. 2.26.

to 0.5 in a self-hardening function for twinning mode. The results concerning stress-strain curve, twin volume fraction and relative activities are presented in Fig. 2.28, while the final texture in Fig. 2.29. Good agreement concerning two main components of texture reported by Wang et al. [210] is observed.

As it is seen, the overall behaviour of γ-TiAl is very much influenced by the local properties of the single crystal. Consequently, it could be expected that the experiments performed on single crystals or polycrystals with strong textures are very much needed in order to assess more accurately the properties of the material. As it has been reported by Bartels et al. [10] and Schillinger et al. [184], the strong modified cube texture has been observed in sheets that were hot rolled from prealloyed, high isostatic pressed powder compacts of Ti– 47 at.% Al–4 at.%(Cr, Mn, Nb, Si, B) and annealed at 1000^oC for 1 h. Microstructure of the described sheet material was fine grained and equiaxed and consisted of γ-grains with a small amount of α_2 phase. In the case of the modified cube texture the c-axis of γ-TiAl lattice is aligned in the transverse direction (TD), while a-axes are aligned with the rolling direction (RD) and the normal direction (ND). Below we present the results concerning the uniaxial tension and compression in TD and RD directions of material with such texture. They have been obtained with the use of the proposed model and the material parameters from Table 2.6. In order to reflect the experimental observations, the initial texture (see Fig. 2.32a) has been generated using the random number generator build-in the Mathematica package assuming the normal distribution of orientation with a mean value corresponding to the modified ideal cube texture, specified by Euler angles $\{0^o, 90^o, 0^o\}$, and a standard deviation equal to 9° in order to be closer to the experimental observations.

In Fig. 2.30 the stress-strain curves for uniaxial tension and compression in RD and TD obtained with the use of the model are presented. Obviously,
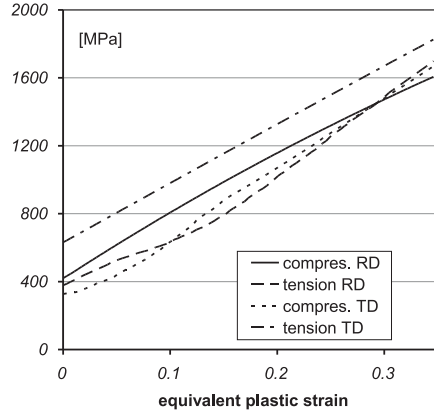
Fig. 2.30. Stress-strain curves for uniaxial tension or compression of aggregate of modified cube texture, material parameters from Table 2.6.

a)   b)
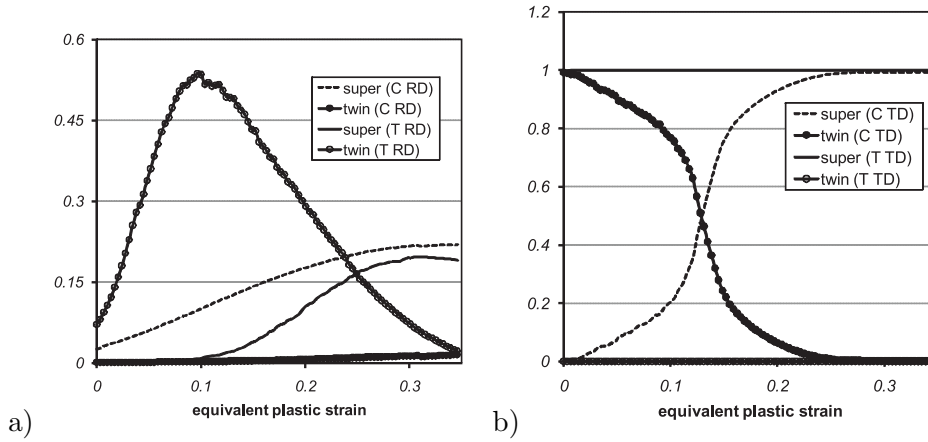
Fig. 2.31. Current relative activities of superdislocations and twinning for an aggregate of modified cube texture in uniaxial tension or compression in (a) RD, (b) TD. Material parameters from Table 2.6 are used.

in reality the strains up to 40% in tension would not be achieved due to poor ductility of TiAl. The numerical simulations are performed up to this level in order to study the hardening behaviour and modes activity predicted by the developed approach. The following relation between initial yield stresses in subsequent tests is predicted:

$$Y_{TD}^t > Y_{RD}^c > Y_{RD}^t > Y_{TD}^c \,, \qquad (2.61)$$

which agrees qualitatively with the experimental results reported by Schillinger et al. [184]. Concerning the quantitative agreement of model predictions and the reported experiments, the relative values of the corresponding yield stresses are compared in Table 2.7. The significant discrepancy between measured and calculated values is observed only for the value of the yield stress in tension in TD.

Table 2.7. Relative yield stresses for a sheet with modified cube texture.

Load direction	Relative yield stress	
	Experiment	Simulations
Compr. TD (Y_{TD}^c)	1.0	1.0
Tension RD (Y_{RD}^t)	1.16	1.16
Compr. RD (Y_{RD}^c)	1.32	1.29
Tension TD (Y_{TD}^t)	1.35	1.93
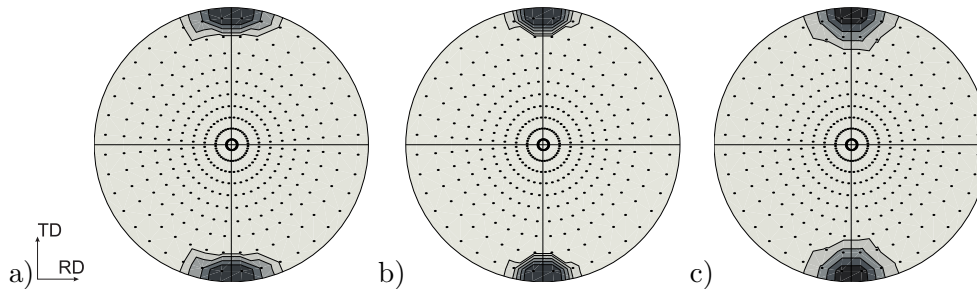
Fig. 2.32. Pole figure (001), stereographic projection: (a) initial (modified cube texture); (b) after uniaxial tension in TD (c) after uniaxial compression in RD. Subsequent contours are at 5, 15, 30, 45 multiplicity of random texture. Material parameters from Table 2.6 are used.
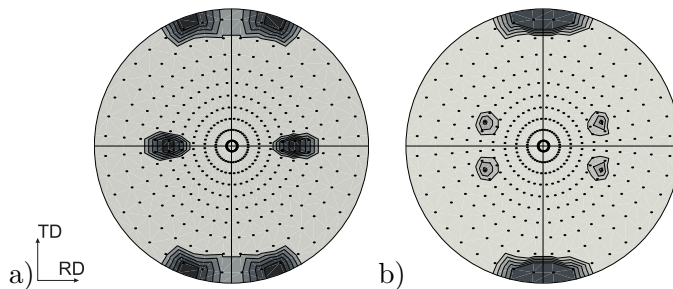
Fig. 2.33. Pole figure (001), stereographic projection: (a) after uniaxial compression in TD (b) after uniaxial tension in RD. Subsequent contours are at 5, 7.5, 10, 12.5, 15 multiplicity of random texture. Material parameters from Table 2.6 are used.

The predicted anisotropy of a yield stress can be explained considering the results for γ-TiAl single crystal presented in Section 2.4.1 in Figs 2.7. For the ideal cube texture, assuming that τ_c^{sup} is sufficiently high, we find:

$$Y_{TD}^c = \frac{3\sqrt{2}}{2}\tau_c^{tw}, \quad Y_{RD}^t = Y_{RD}^c = \sqrt{6}\tau_c^{ord}, \quad Y_{TD}^t = \sqrt{6}\tau_c^{sup}. \tag{2.62}$$

Consequently, one expects:

- high activity of twinning in compression in TD,
- high activity of ordinary dislocations in tension or compression in RD, and
- high activity of superdislocations in tension in TD.

In general, results of simulations presented in Fig. 2.31 agree with the above expectations. However, because in the considered aggregate grains are scattered around the ideal orientation, in the case of tension in RD we observe also some activity of twinning, while for compression in RD some activity of superdislocations. It explains why the yield stress in compression is higher than in tension for this direction. Furthermore, substituting the identified values of τ_c^{sup} and τ_c^{tw} into the theoretical relation (2.62) we find:

$$Y_{TD}^c = 2.33\tau_c^{ord}, \quad Y_{RD}^t = Y_{RD}^c = 2.45\tau_c^{ord}, \quad Y_{TD}^t = 4.89\tau_c^{ord}, \tag{2.63}$$

so the lowest value of Y_{TD}^c is well justified contrary to what is argued by Schillinger et al. [184].

In Figs 2.32-2.33 the final textures for the considered processes are presented. The activity of twinning in compression in TD, and to smaller extent in tension in RD, manifests by the appearance of new twin-related orientations in both cases. Activity of twinning in the case of tension in RD increases with deformation due to the lack of latent hardening due to slip for this mode. The possibility of twinning activation together with the dominant ordinary slip can explain the higher limit strains achieved in tension in RD than in TD observed by Schillinger et al. [184].

Mg alloys

As already discussed, in the case of Mg alloys (metal of hcp unit cell) up to six categories of slip and twin systems are relevant. They are subdivided into easy and hard ones. In the example presented below we consider three types of slip systems: basal, prismatic and pyramidal $\langle c + a \rangle$, and tensile twinning. In some papers compressive twin systems are considered as well, e.g. Koike [91],

Jiang et al. [74], Lou et al. [122], Jiang and Jonas [73], however, the volume fractions produced by these twin systems are much smaller than those resulting from tensile twins, therefore they do not contribute significantly to the texture image. As far as strain along **c**-axis can only be accommodated by pyramidal $\langle c+a \rangle$ slip (a hard mode) or unidirectional twinning (only for extension along **c** axis), magnesium alloys of strong textures show high asymmetry and anisotropy in mechanical properties.

In subsection 2.4.1 it has been demonstrated that, depending on the loading direction, different deformation modes are activated for Mg single crystal. As deformation proceeds, the relative activities of modes change due to crystallographic lattice reorientation, especially due to twin-related reorientation, and hardening phenomenon governed by slip-slip and slip-twin interactions. As it has been mentioned earlier in this chapter, magnesium alloys exhibit also high propensity to detwinning when the strain path is changed. This example will serve us to demonstrate the ability of the developed framework to reproduce the complex hardening pattern and detwinning.

Similarly as in the case of TiAl, experiments performed on single crystals or polycrystals with strong texture are particularly useful when studying the mechanical characteristics of subsequent types of deformation modes, e.g. Jiang et al. [74], Jiang and Jonas [73], Proust et al. [170]. In this subsection the proposed model will be tested for the wide collection of data presented in Proust et al. [170]. These data concern commercial alloy AZ31B (3 wt% Al, 1 wt% Zn and balance Mg) sheet material. The material was heat treated to reduce the presence of mechanical twins. After this procedure it had an equiaxed grain structure with an average grain size of 13 μm and exhibited initial basal texture. The following two sets of mechanical tests have been reported for this material:

1. Monotonic deformation experiments

   - through-thickness compression (**TTC**),
   - in-plane tension (**IPT**), and
   - in-plane compression (**IPC**).

2. Experiments with strain path change

   - pre-strain in TTC up to 5% and 10% and then reloading in IPC (**TTC5% + IPC**, **TTC10% + IPC**), and
   - pre-strain in IPC up to 5% and 10% and then reloading in TTC (**IPC5% + TTC**, **IPC10%+TTC**).

The tests were performed at room temperature and with a strain-rate of $5 \times 10^{-3} s^{-1}$. The final texture of each deformed sample was measured. By

studying the initial and final textures the twin volume fractions in deformed samples were evaluated. Details of experimental procedures can be found in Proust et al. [170].
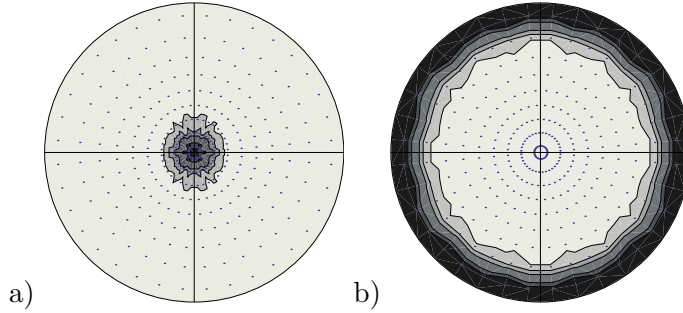
Fig. 2.34. Initial basal texture assumed in simulations: a) pole figure (0001), b) pole figure $\{10\bar{1}0\}$. Contours are at 1, 2, 3, 5, 7 multiplicities of random distribution of orientations.

Using these data the identification of material parameters present in the developed model has been performed. To this end the VPSC code [201] has been used, into which the developed hardening model and the PTVC reorientation scheme have been implemented. The code was developed by Tomé and Lebensohn in Los Alamos National Laboratory (USA). The initial basal texture assumed in simulations is presented in Fig. 2.34[3]. The texture was represented by the set of 500 orientations. The loading process in subsequent experiments has been imposed using mixed strain/stress conditions, namely the following components of velocity gradients and stress tensors in sheet axes have been imposed for TTC, IPT and IPC processes, respectively:

$$L_{ij} = \dot{\varepsilon} \begin{bmatrix} \cdot & 0 & 0 \\ 0 & \cdot & 0 \\ 0 & 0 & -1 \end{bmatrix}, \quad \sigma_{ij} = \begin{bmatrix} 0 & \cdot & \cdot \\ \cdot & 0 & \cdot \\ \cdot & \cdot & \cdot \end{bmatrix}, \quad (2.64)$$

$$L_{ij} = \dot{\varepsilon} \begin{bmatrix} 1 & 0 & 0 \\ 0 & \cdot & 0 \\ 0 & 0 & \cdot \end{bmatrix}, \quad \sigma_{ij} = \begin{bmatrix} \cdot & \cdot & \cdot \\ \cdot & 0 & \cdot \\ \cdot & \cdot & 0 \end{bmatrix}, \quad (2.65)$$

---

[3]The initial texture has been generated with the use of Mathematica package and as such is only an approximation of an actual initial texture of a sheet studied by Proust et al. [170]. In particular, the assumed initial texture is approximately axisymmetric, while for the actual texture of tested material some asymmetry is observed, see Fig. 1(a) in [170].

$$L_{ij} = \dot{\varepsilon} \begin{bmatrix} -1 & 0 & 0 \\ 0 & \cdot & 0 \\ 0 & 0 & \cdot \end{bmatrix}, \quad \sigma_{ij} = \begin{bmatrix} \cdot & \cdot & \cdot \\ \cdot & 0 & \cdot \\ \cdot & \cdot & 0 \end{bmatrix}. \tag{2.66}$$

a)

b)
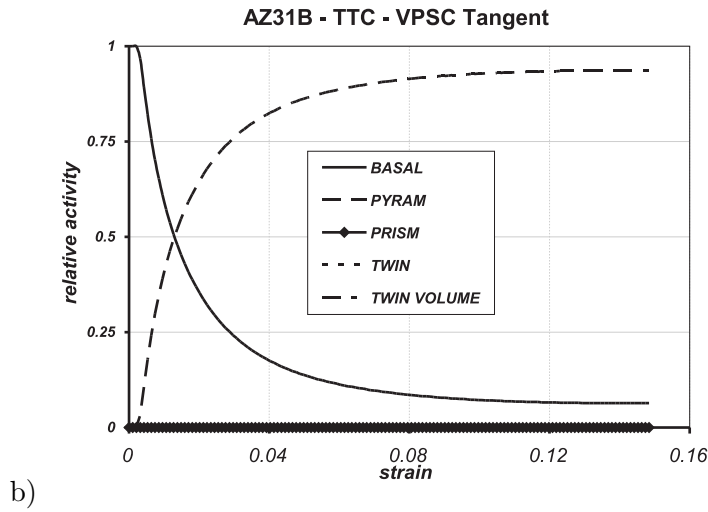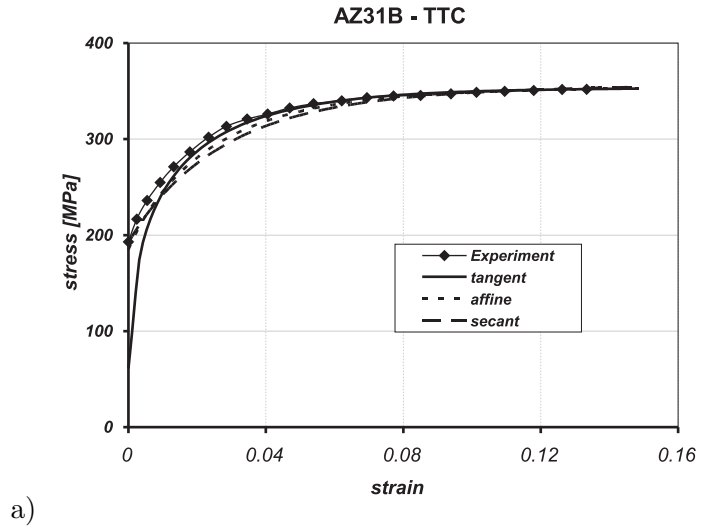
Fig. 2.35. Through thickness compression (TTC) of Mg alloy sheet - experiment reported in [170] and simulations with the use of the proposed model (for material parameters see Table 2.8) and different variants of the VPSC scheme: a) stress-strain curves, b) relative activity of deformation modes for the tangent VPSC scheme.
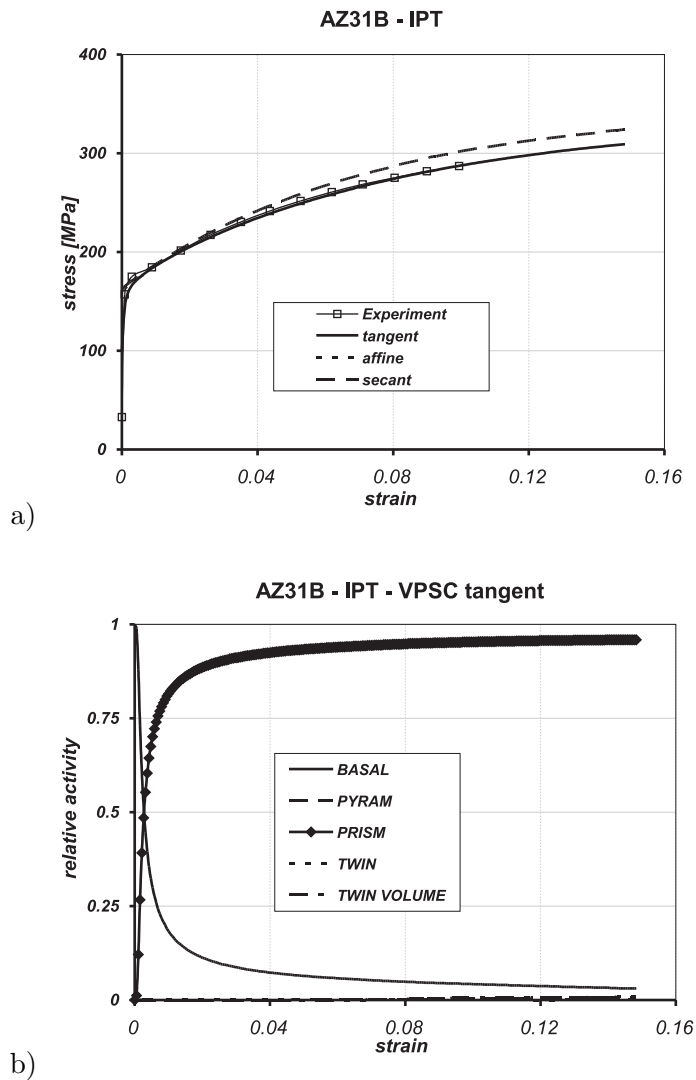
Fig. 2.36. In-plane tension (IPT) of Mg alloy sheet - experiment reported in [170] and simulations with the use of the proposed model (for material parameters see Table 2.8) and different variants of the VPSC scheme: a) stress-strain curves, b) relative activity of deformation modes for the tangent VPSC scheme.
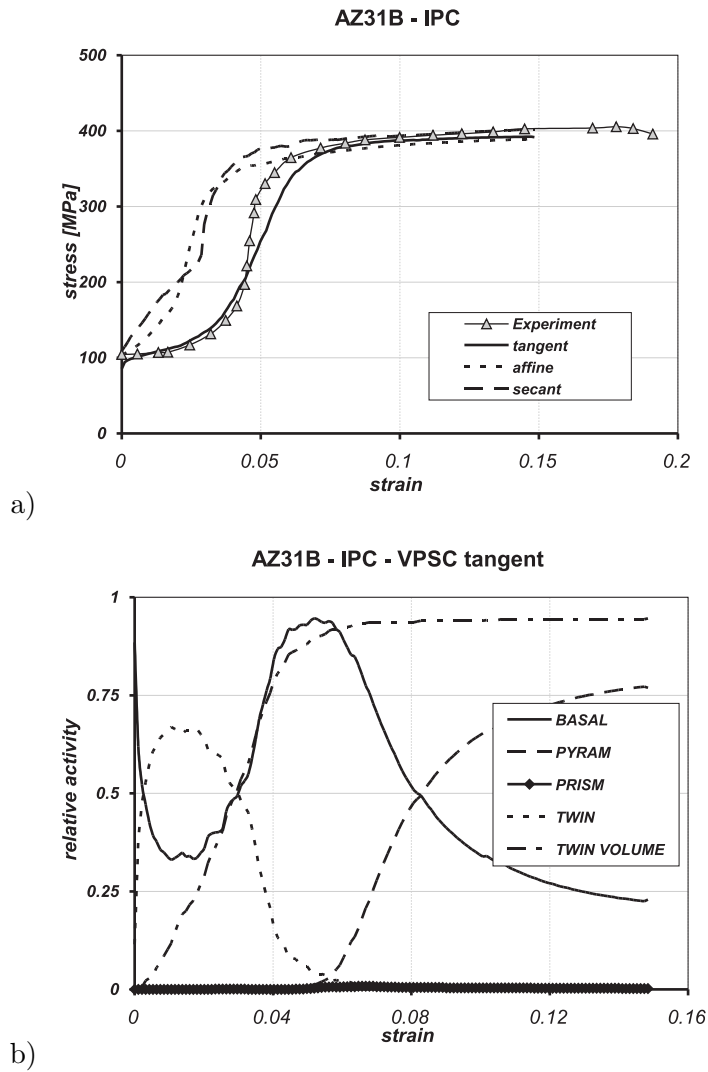
Fig. 2.37. In-plane compression (IPC) of Mg alloy sheet - experiment reported in [170] and simulations with the use of the proposed model (for material parameters see Table 2.8) and different variants of the VPSC scheme: a) stress-strain curves, b) relative activity of deformation modes for the tangent VPSC scheme.

Table 2.8. Identified material parameters for AZ31B Mg alloy. Identification performed using the VPSC tangent model of polycrystal, $\bar{n} = 20$ and $v_0 = 5 \times 10^{-6}[1/s]$ in (2.25) and $\beta = 1$ in (2.41) for slip-slip interactions.

Mode	Interaction	τ_{c0} [MPa]	h_0 [MPa]	τ_{sat}/f_{sat} [MPa]/−	μ −	q basal	q prism.	q pyram. twin
basal	slip-slip	2.9	301.6	81.2	1.5	1.0	1.0	0.5
	slip-twin	—	10^{-5}	0.4	—		1.6	
prism.	slip-slip	52.2	609.0	97.9	2.0	1.0	1.0	1.0
	slip-twin	—	10^{-5}	1.0	—		1.6	
pyram.	slip-slip	67.9	1885	120.4	2.0	1.0	1.0	1.0
	slip-twin	—	10^{-5}	2.0	—		1.4	
twin	twin-slip	—	72.5	—	—	0.0	0.0	1.0
	twin-twin	31.9	10^{-5}	0.95	0.75		1.4	

Let us look at the performed experiments from the point of view of activity of the considered deformation modes. Taking into account the analysis of Mg single crystal presented in Subsection 2.4.1, the following observations are important:

- In the case of the TTC experiment, as far as crystallites are strained along directions close to the **c** axis, one expects strong activity of pyramidal $\langle c + a \rangle$ slip systems. Because orientation of **c** axis within the aggregate is scattered around an ideal alignment with the normal to the sheet plane, one observes also the substantial activity of an easy basal mode. Consequently, this test is used to establish the self-hardening function for pyramidal and basal modes as well as latent hardening ratio between these two modes (see Fig. 2.35).

- In the case of the IPT experiment, for the ideal basal texture, one expects strong activity of a prismatic mode. Again, in the case of the assumed texture, the prismatic mode will be accompanied by an easy basal mode. Consequently, this test is used to identify mechanical characteristic of prismatic and basal modes and their interactions (see Fig. 2.36[4]).

- In the case of the IPC experiment, tensile twinning is supposed to be the most active mode. Accordingly, it is reported by [170] that after 10% strain the volume fraction of twins reaches 90% of an aggregate. As in previous cases, due to the orientations scatter, the basal slip will be also active. As concerns the part of the grain which has been reoriented due to twinning, **c** axis in twinned part is at almost 90° degree with respect

---

[4]Convergence of the numerical solution was lost for the affine VPSC scheme and the assumed material parameters when simulating an IPT process.

to its original orientation in the matrix part, cf. Wang and Huang [211], therefore the twinned grains are preferably oriented for pyramidal $\langle c+a \rangle$ slip. Consequently, this test is used to identify hardening curve for a twinning mode, interaction between basal slip and twinning as well as the resistance to pyramidal slip in the reoriented grains (see Fig. 2.37).

- In view of the above observations, the TTC experiments followed by the IPC reloading enable one to assess the effect of accumulation of dislocations in TTC on subsequent twinning activation in IPC. Consequently, this test has served mainly to characterize the latent hardening of twinning due to slip activity (see Figs 2.38a and 2.39).

- The IPC experiment followed by TTC reloading is well suited for studying detwinning. The grains reoriented by twinning in IPC are preferably oriented for secondary twinning (detwinning) during subsequent TTC. As reported by Proust et al. [170], the material is twin free after 10% of TTC reloading. This means that twins which have been created during IPC pre-strain are detwinned completely during TTC reloading. Consequently, the results of this test are used mainly to assess the resistance to twinning (i.e. detwinning) in the grains after the reorientation (see Figs 2.38b and 2.40).

The best approximation to experimental results by the developed model has been achieved with a set of parameters collected in Table 2.8 and the tangent variant of VPSC scheme. As concerns the mechanical characteristics of modes after the reorientation, we set the corresponding values of the critical shear stresses $\tau_c^{(\alpha)}$ as equal to $\mu^{(\alpha)}\tau_{c0}^{(\alpha)}$, where $\tau_{c0}^{(\alpha)}$ is the initial value. Use of initial values instead of the values of $\tau_c^{(\alpha)}$ just before the reorientation is justified by the fact that twins that form in Mg alloys are coarse and can encompass the total volume of the grain.

The predicted activity of easy basal slip in the subsequent deformation processes varies between the variants of the SC averaging scheme developed for the non-linear polycrystals (see Figs 2.41 and 2.42). It is the highest for the tangent variant and the lowest for the secant variant. The theoretical explanation of this fact can be found in Chapter 4. In general, the secant scheme for high n value provides predictions close to the Taylor model, which imposes the same deformation in every grain of the considered aggregate, thus for some unfavourably oriented grains five independent slip systems are required. On the other hand, the tangent variant tends to the Sachs bound which admits redistribution of deformation between the grains enabling deformation by single slip in many grains. Consequently, in the case of the tangent model deformation starts with
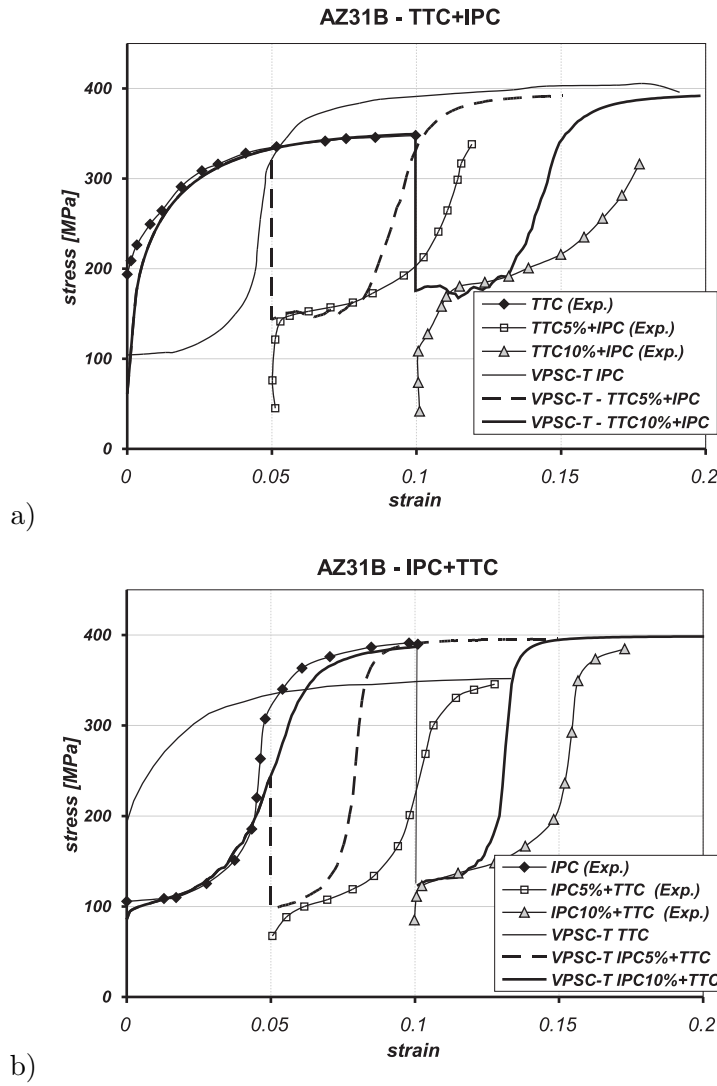
Fig. 2.38. Deformation processes of Mg alloy sheet with strain path change - experimental results reported in [170] and simulations by the proposed model (material parameters in Table 2.8) and the tangent variant of the VPSC scheme): a) TTC followed by IPC, b) IPC followed by TTC.

a)

b)
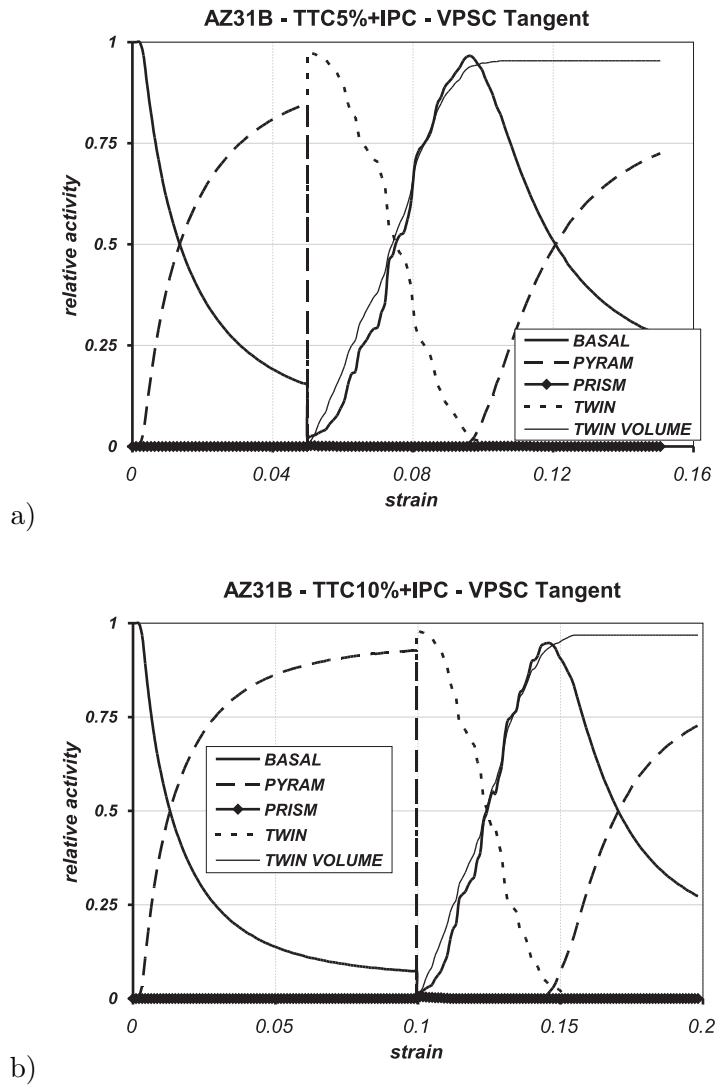
Fig. 2.39. The relative activity of deformation modes in TTC followed by IPC predicted by the proposed model (the tangent VPSC scheme) a) TTC up to 5% of strain, b) TTC up to 10% of strain.

a)

b)
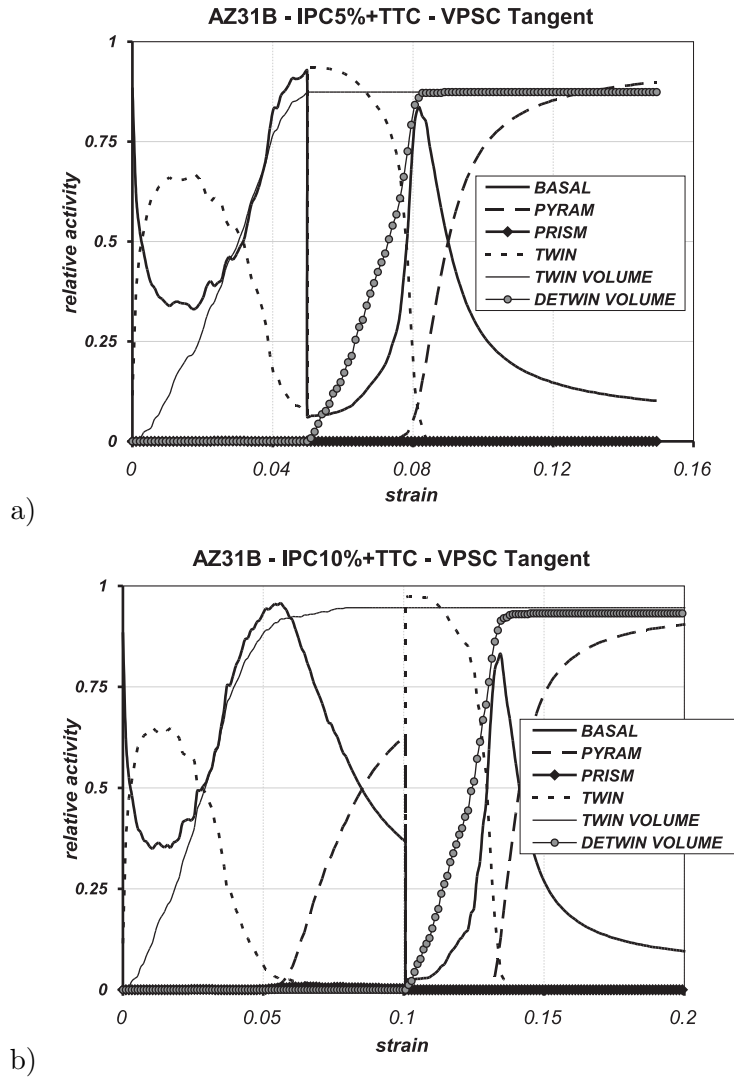
Fig. 2.40. The relative activity of deformation modes in IPC followed by TTC predicted by the proposed model (the tangent VPSC scheme) a) IPC up to 5% of strain, b) IPC up to 10% of strain.

a)

b)
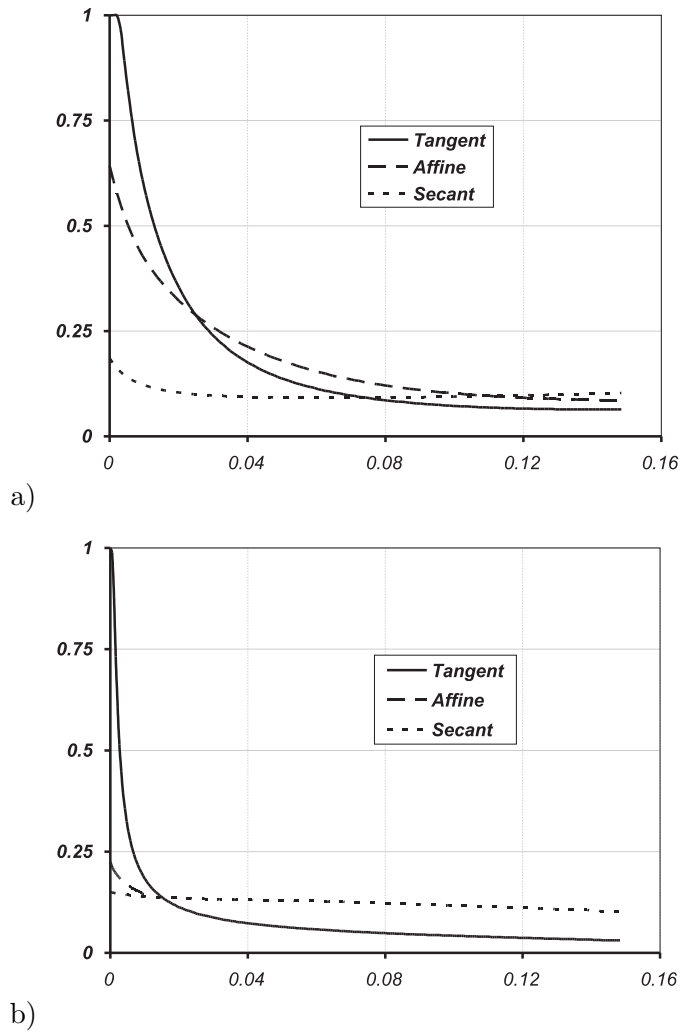
Fig. 2.41. Comparison of predicted activity of deformation modes for different VPSC variants a) basal slip in TTC, b) basal slip in IPT, c) basal slip and twinning in IPC, d) pyramidal slip and the volume fraction of reoriented grains in IPC.

a)

b)
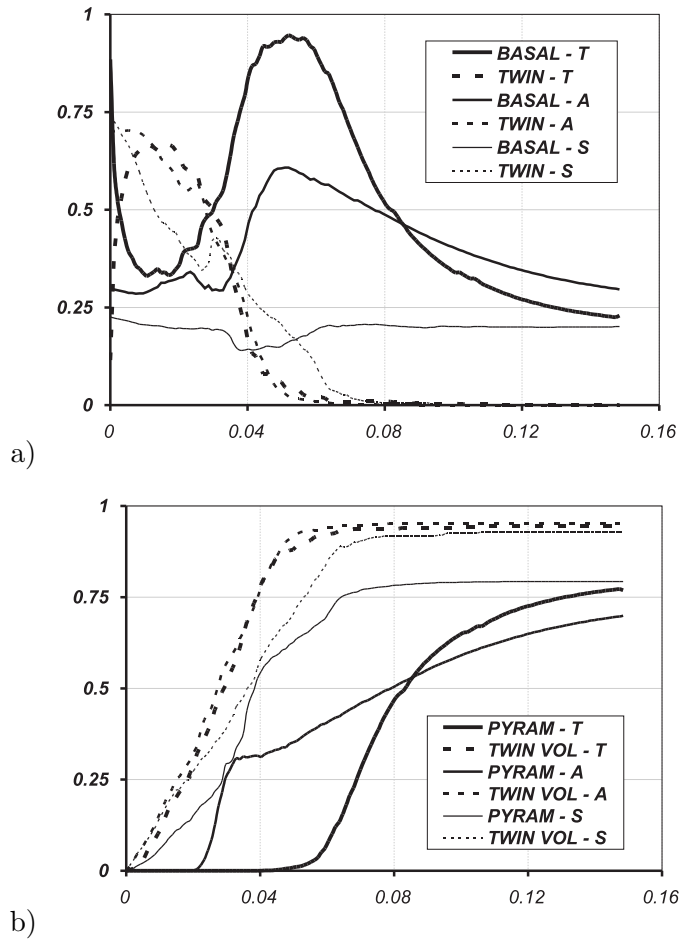
Fig. 2.42. Comparison of predicted activity of deformation modes for different VPSC variants
a) basal slip in TTC, b) basal slip in IPT, c) basal slip and twinning in IPC, d) pyramidal
slip and the volume fraction of reoriented grains in IPC.

activation of an easy basal mode. Then, strong self and latent hardening due to
slip is observed which, in the TTC and IPT processes, leads to the activation
of hard pyramidal or prismatic modes, respectively. In the case of the IPC pro-
cess deformation again starts with activation of a basal mode which soon after
that is accompanied by twinning. Low overall hardening rate for polycrystal
at the beginning of the process suggests low latent hardening ratio responsible
for interactions between basal slip and twinning. Further rapid increase of an
overall hardening rate is connected with an increasing amount of twin-related
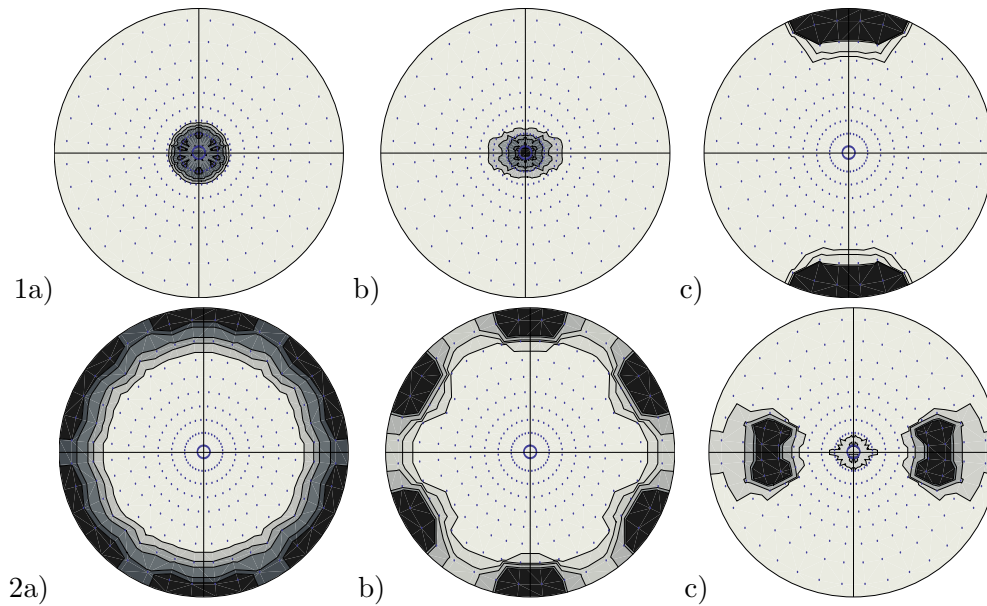
Fig. 2.43. Texture evolution in monotonic deformation processes: (a)-TTC, (b)-IPT, (c)-IPC, predicted by the proposed model (tension/compression direction in in-plane experiments is aligned along vertical axis of pole figure, the tangent VPSC model is used), 1. (0001) pole figure at the end of the process, 2. $\{10\bar{1}0\}$ pole figure at the end of the process. Contours are at 1, 2, 3, 5, 7 multiplicities of random texture.

orientations favourably oriented for activation of hard pyramidal slip. In the case of monotonic processes, good agreement between experimental results and model predictions is observed. Texture evolution is also well predicted (compare Fig. 2.43 and the corresponding Figure 2, page 865 in [170]). Note that reorientation due to substantial twinning activity is apparent when looking at Fig. 2.43c which presents the texture after 10% of IPC. Basal texture is almost totally replaced by the twin-related texture components.

In the case of the processes with a strain path changes the agreement between experiment and the model is less satisfactory. The long plateaus observed for both experiments after the reloading, which correspond to the strain regime of comparable activity of slip (most probably basal) mode and twinning within the aggregate, are much shorter in the case of the model. As it is seen in Fig. 2.39 model predicts that during this regime the deformation is almost totally realized by twinning. It leads to the rapid increase of the overall hardening rate caused by the appearance of twin-related orientations. Insufficient activity of the basal slip when the strain path is changed is caused by strong hardening of this mode
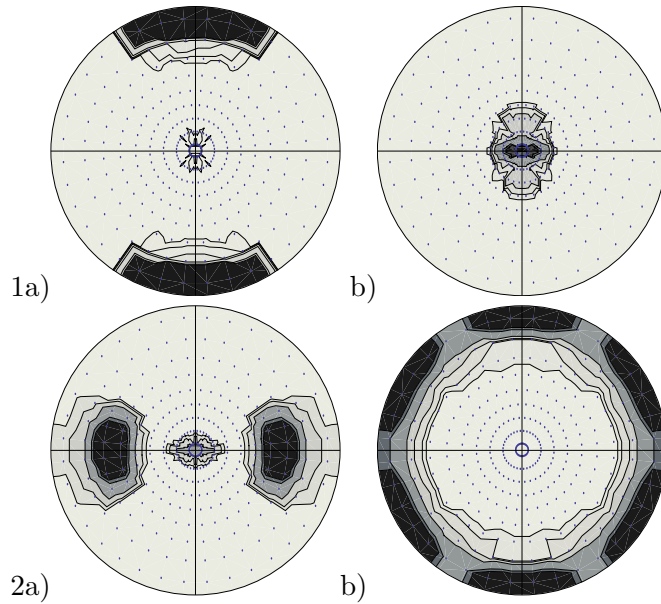
Fig. 2.44. Texture evolution in deformation processes with strain path change: (a)-TTC+IPC, (b)-IPC+TTC, predicted by the proposed model (tension/compression direction in in-plane experiments is aligned along vertical axis of pole figure, the tangent VPSC model is used) 1. (0001) pole figure, 2. $\{10\bar{1}0\}$ pole figure. Contours are at 1, 2, 3, 5, 7 multiplicities of random texture.

due to increase of dislocation density during the pre-strain in TTC predicted by the model, Fig. 2.39. Note that it is also true for the pre-strain in IPC since in the grains reoriented by twinning during IPC one observes substantial activity of basal and then pyramidal modes before the strain path is changed, Fig. 2.40. In spite of the above drawbacks some agreement between the model and experiment is observed. This concerns also the texture prediction, Fig. 2.44. In particular, for the IPC process followed by TTC, we observe zero volume fraction of twin-related orientations with respect to the initial basal texture.

Comparable level of agreement between model predictions and experimental results has been reported for the most sophisticated, three-scale composite grain model by Proust et al. [170]. It indicates that improvement of the description should be sought by further refinement of hardening description, mainly by an incorporation of the Baushinger effect due to the slip reversal upon reloading, cf. Karaman et al. [80], and the change in hardening rate when the developed dislocation substructure is cut-through after the strain path is changed, cf. Peeters et al. [156], Beyerlein and Tomè [15], Petryk and Stupkiewicz [159].

2.5. Conclusions

In this chapter the incorporation of twinning into a rate-independent crystal plasticity with the regularized Schmid law and a power-law viscoplastic model has been presented. The influence of slip-twin interactions on the macroscopic material response has been discussed and, using the concepts of Karaman et al. [79] and Kalidindi [76], the concise hardening rule accounting for these couplings has been proposed. The capabilities of the approach have been demonstrated on the variety of examples, namely a single orientation of Hadfield steel and polycrystalline 70-30 brass (low SFE materials), γ-TiAl of random texture and strong cube texture, and Mg alloy of basal texture subjected to the large deformation processes. The results for a polycrystal have been obtained with the use of Taylor's averaging scheme and different variants of the viscoplastic self-consistent (VPSC) model. It has been shown that by applying the proposed framework the main features of mechanical response of metals deforming by slip and twinning can be captured, also when simulating the processes with a strain path change. Although the proposed model is simpler than the three-scale composite grain model developed by Proust et al. [169], its predictions are of comparable agreement with experimental data. Further improvement of the approach developed can be achieved by refinement of the hardening description with the aim to include the kinematic hardening effects and re-building of the dislocation substructure when the direction of a plastic flow is changed.

In simulations of texture development, the issue of the appearance of twin-related orientations has been addressed. A new probabilistic reorientation scheme, the PTVC scheme, has been developed which maintains the number of reoriented grains consistent with the accumulated deformation by twinning within the polycrystal, contrary to the scheme applied by Staroselsky and Anand [186]. Thanks to this feature, the use of this scheme enables better assessment of contribution of twinning to the deformation texture image. Moreover, the PTVC scheme does not require identification of any additional parameters, which is the case for the PTR scheme proposed by Tomé et al. [200] (the PTR scheme is used as a standard procedure in the VPSC code). Relative simplicity of PTVC scheme and its independence from the applied model of polycrystal should be underlined. For all analysed examples the developed reorientation scheme allows one to reproduce well textures measured experimentally.

3

Estimates of overall properties
of linear polycrystals of low symmetry

3.1. Introduction

Assessment of overall properties of heterogenous materials on the basis of a knowledge about its microstructure and local properties is the central problem of contemporary micromechanics which has its practical and theoretical aspects. This problem attracts researchers since the fifties of the previous century. Many important results and developments have been obtained and proposed since then, cf. Christensen [34], Nemat-Nasser and Hori [145], Kocks et al. [88], Li and Wang [120]. The present monograph deals with the special class of heterogeneous materials which are the polycrystalline aggregates. In this chapter different estimates of overall properties of such materials are considered. Particularly, we are interested in crystals of low symmetry with an insufficient number of easy slip systems.

In the chapter crystals described by linear constitutive rules are considered. For a brevity they will be further called *linear* crystals. Analytical solutions for uniform strain upper and uniform stress lower bounds are provided. Moreover, more rigorous bounds, resulting from the theorems of minimum potential energy and of minimum complementary energy, proposed by Hashin and Shtrikman [59, 60] are also analysed. The detailed theoretical treatment of these bounds as well as its generalizations are presented by Walpole [208] and Willis [220, 221]. Here, the attention is focused on polycrystals composed of grains of low symmetry. With such conditions one has to do when considering metals of high specific strength or stiffness. Two types of textures are discussed:

1. **Random** texture (i.e. no texture) leading to the isotropic overall behaviour, and

2. **Fibre** textures leading to the transversely isotropic overall behaviour.

Mechanical behaviour of grains is arbitrarily anisotropic and described by linear constitutive law relating strain and stress measure, encompassing for example linearly elastic, but also linearly viscous materials.

Next, the so-called self-consistent (SC) estimates of overall properties are considered. In the self-consistent scheme, a single crystal is treated as a spherical or ellipsoidal inclusion embedded in an infinite medium of unknown properties. For the theoretical formulations concerning a self-consistent method one is referred to Appendix B, or the classical papers by Kröner [107], Hill [66], Willis [220], Walpole [208]. Below, the SC estimates are found for a crystal of general anisotropy and of a spherical shape. Special attention is paid to the materials in which anisotropic grains are volumetrically isotropic. Existence and uniqueness of the obtained solutions are discussed. Reductions of above estimates for incompressible materials or materials with constrained modes of deformation are also derived. One of the most interesting results of this section is the fact that a finite SC estimate of an overall shear modulus of incompressible untextured polycrystal exists only if locally the constrained deviatoric space is one-dimensional. Consider, for example, a viscous crystal deforming by slip with a constitutive rule (2.27), where $n = 1$. The above result means that the SC estimate of an overall flow stress of an untextured polycrystal of such a material is finite only if locally there are at least four independent slip systems. It is the counterpart of the widely known Taylor condition of five independent slip systems, which guaranties acceptable solutions obtained by means of uniform strain hypothesis. The result is important as far as metals or alloys of high specific strength and stiffness, such as magnesium or titanium alloys and intermetallics, are concerned. The utility of the obtained results is presented on the examples of these materials.

Some of the derived results are already known in the literature. Upper and lower bounds in the concise form have been provided by Walpole [208]. Quartic equation for self-consistent estimate of an overall shear modulus for cubic crystals has been found already by Hershey in 1954 (independently by Kröner [107]), and then reduced to the cubic one e.g. Kröner [107], Hill [66], Willis [220]. Hexagonal crystals have been studied by Kneer [86]. Qui and Weng [171] have discussed the influence of grain morphology on the self-consistent estimates for overall properties of such crystals. For hexagonal, trigonal and tetragonal crystals implicit equations for these estimates, depending on the components of a local stiffness tensor, were provided in different forms by Pham [160, 161] and Berryman [12]. The Hashin-Shtrikman bounds have been provided for different crystal symmetries, e.g. by Peselnick and Meister [157], Watt [213], Pham [161], Berryman [12] (see also the literature cited there).

The originality of the analysis presented lies mainly in the method applied. In order to obtain the solutions, the spectral and harmonic decompositions of fourth-order Hooke's tensor are used simultaneously. Thanks to that, the important feature of the derived solutions is that they are expressed by means of invariants of local stiffness (compliance) tensors. To the author's best knowledge, the presented analysis concerning incompressible crystals and crystals with constrained deformation modes is also new. In Appendix A the spectral and harmonic decompositions of Hooke's tensor are briefly recalled, introducing the required notation. More details concerning the spectral theorem one may find in Rychlewski [177], Cowin and Mehrabadi [37], Chadwick et al. [30]. The harmonic decomposition is presented by Forte and Vianello [51] and Rychlewski [178, 179, 180]. The reader is referred to these publications for more details.

The analysis of linear crystals presented in this chapter contains the results published by the author in [99]. Here, additionally, the Hashin-Shtrikman bounds and polycrystals of fibre texture are considered.

3.2. Problem statement

Assume a single-phase polycrystal with components (i.e. grains) of arbitrary anisotropy with the same properties, although with axes of symmetry $\{\mathbf{a}_k\}$ rotated with respect to each other (see Fig. 3.1). Moreover, let the orientations ϕ^c of these components be distributed within the considered representative volume element in two distinct ways, namely:

1. *Randomly* - It means that macroscopically polycrystalline material can be treated as isotropic.

2. *Having one of the crystallographic directions, say* $\mathbf{n}$, *common for all crystals (fibre texture)* - Macroscopically polycrystal can be then described as transversely isotropic.

Locally the constitutive relation between the stress tensor $\boldsymbol{\sigma}$ and strain tensor (or strain-rate tensor) $\boldsymbol{\varepsilon}$ is linear, that is:

$$\boldsymbol{\varepsilon} = \mathbb{M} \cdot \boldsymbol{\sigma}, \quad \boldsymbol{\sigma} = \mathbb{L} \cdot \boldsymbol{\varepsilon}, \quad \mathbb{L} = \mathbb{M}^{-1}, \tag{3.1}$$

where $\mathbb{L}$ and $\mathbb{M}$ are stiffness and compliance tensors, respectively. Macroscopic relations for the averaged fields $\mathbf{E} = \langle \boldsymbol{\varepsilon} \rangle$ and $\boldsymbol{\Sigma} = \langle \boldsymbol{\sigma} \rangle$ are assumed to be linear as well, namely,

$$\mathbf{E} = \bar{\mathbb{M}} \cdot \boldsymbol{\Sigma}, \quad \boldsymbol{\Sigma} = \bar{\mathbb{L}} \cdot \mathbf{E}, \quad \bar{\mathbb{L}} = \bar{\mathbb{M}}^{-1}, \tag{3.2}$$
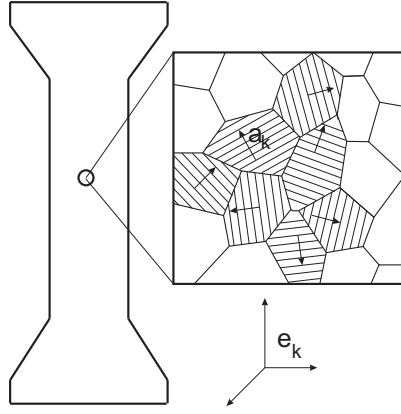
Fig. 3.1. Polycrystalline element.

where $\bar{\mathbb{L}}$ and $\bar{\mathbb{M}}$ are overall stiffness and compliance tensors, respectively. More-over, all the introduced fourth-order tensors have the symmetries with respect to the permutation of indices of Hooke's tensor. Note that major symmetry of the constitutive tensor originates from the assumption of existence of a strain potential.

In view of the above assumptions for the local stiffness and compliance tensors, the spectral decomposition (A.2) can be applied:

$$\mathbb{L}(\phi^c) = \sum_{K=1}^{MK} h_K \mathbb{P}_K(\phi^c), \quad \mathbb{M}(\phi^c) = \sum_{K=1}^{MK} \frac{1}{h_K} \mathbb{P}_K(\phi^c), \tag{3.3}$$

where ϕ^c denotes orientation of local axes $\{\mathbf{a}_k\}$ with respect to some macrosco-pic frame $\{\mathbf{e}_k\}$ specified by, e.g, three Euler angles. Moreover,

$$\mathbb{P}_K(\phi^c) = \mathbf{Q}(\phi^c) \star \mathbb{P}_K(0) \tag{3.4}$$

and $\mathbf{Q}(\phi^c) \star (\cdot)$ denotes the rotation operation for a n-th order tensor, $\mathbf{Q}(\phi^c)$ is the second-order orthogonal tensor, and $\mathbb{P}_K(0)$ is the projector for some selected $\mathbf{Q}_0 \in \mathcal{Q}_{tex}$, where $\mathcal{Q}_{tex}$ is the space of admissible orientations for the considered texture. In the case of no texture, for example, one can select $\mathbf{Q}_0 = \mathbf{I}$, so the crystals for which the local and macroscopic frames $\{\mathbf{a}_k\}$ and $\{\mathbf{e}_k\}$ coincide (see Fig. 3.1).

Now, for each of projectors $\mathbb{P}_K$, the harmonic decomposition of a fourth-order tensor (A.13) can be applied,

$$\mathbb{P}_K(\phi^c) = \eta_K^{\mathrm{P}} \mathbb{I}_{\mathrm{P}} + \eta_K^{\mathrm{D}} \mathbb{I}_{\mathrm{D}} + \mathbb{A}_K^{\mu}(\phi^c) + \mathbb{A}_K^{\nu}(\phi^c) + \mathbb{H}_K(\phi^c), \tag{3.5}$$

where specifically

$$\eta_K^{\mathrm{P}} = \frac{1}{3}\mathbf{I} \cdot \mathbb{P}_K(\phi^c) \cdot \mathbf{I} = \frac{1}{3}\mathbf{I} \cdot \mathbb{P}_K(0) \cdot \mathbf{I}, \quad \eta_K^{\mathrm{D}} = \frac{1}{5}(m_K - \eta_K^{\mathrm{P}}), \qquad (3.6)$$

$$\mathbb{A}_K^\mu(\phi^c) = \mathbb{A}^\mu(\boldsymbol{\mu}_{\mathrm{D}K}(\phi^c)), \quad \mathbb{A}_K^\nu(\phi^c) = \mathbb{A}^\nu(\boldsymbol{\nu}_{\mathrm{D}K}(\phi^c)) \qquad (3.7)$$

and m_K is the multiplicity of the corresponding modulus h_K.

The following identities are also important in the outlined analysis. Let $\mathbf{h}$ be any second-order deviator and $\mathbb{H}$ any fourth-order fully symmetric and traceless tensor. Specifying corresponding rotated tensors as

$$\mathbf{h}(\phi^c) = \mathbf{Q}(\phi^c) \star \mathbf{h}, \quad \mathbb{H}(\phi^c) = \mathbf{Q}(\phi^c) \star \mathbb{H}, \qquad (3.8)$$

one can prove that

$$\langle \mathbf{h}(\phi^c) \rangle_{\mathcal{Q}} = \mathbf{0}, \quad \langle \mathbb{H}(\phi^c) \rangle_{\mathcal{Q}} = \mathbb{O}, \qquad (3.9)$$

where $\langle \cdot \rangle_{\mathcal{Q}}$ denotes an average over the whole orientation space. If the orientation is specified by three Euler angles $\phi^c = \{\varphi_1, \psi, \varphi_2\}$, then this averaging is performed according to the following formula, cf. Bunge [25]:

$$\langle \cdot \rangle_{\mathcal{Q}} = \frac{1}{8\pi^2} \int_0^{2\pi} \int_0^{\pi} \int_0^{2\pi} (\quad \cdot \quad) \sin \psi \mathrm{d}\varphi_1 \mathrm{d}\psi \mathrm{d}\varphi_2. \qquad (3.10)$$

If averaging is performed over the subset $\mathcal{Q}_{\mathbf{n}}$ of $\mathcal{Q}$ corresponding to the fibre texture[1] with the crystallographic direction $\mathbf{n}$ common for all crystals, one can prove that (the decomposition (A.42) is used):

$$\langle \mathbf{h}(\phi^c) \rangle_{\mathcal{Q}_{\mathbf{n}}} = (\mathbf{h} \cdot \mathbf{d}_{\mathbf{n}})\mathbf{d}_{\mathbf{n}}, \quad \langle \mathbb{H}(\phi^c) \rangle_{\mathcal{Q}_{\mathbf{n}}} = (\mathbb{H} \cdot \mathbb{H}_{\mathbf{n}})\mathbb{H}_{\mathbf{n}}, \qquad (3.12)$$

where tensors $\mathbf{d}_{\mathbf{n}}$ and $\mathbb{H}_{\mathbf{n}}$ are specified by (A.28) and (A.29), respectively. In the considered case, the orientation of a crystal is specified by $\mathbf{n}$ and the angle φ specifying rotation of a crystal around $\mathbf{n}$. Averaging over the orientations subspace $\mathcal{Q}_{\mathbf{n}}$ is performed as follows,

$$\langle \cdot \rangle_{\mathcal{Q}_{\mathbf{n}}} = \int_0^{2\pi} (\quad \cdot \quad)\mathrm{d}\varphi. \qquad (3.13)$$

---

[1]Subset $\mathcal{Q}_{\mathbf{n}}$ of $\mathcal{Q}$ is specified as

$$\mathcal{Q}_{\mathbf{n}} = \{\mathbf{I}, -\mathbf{I}, \mathbf{R}_{\mathbf{n}}^\varphi\}, \qquad (3.11)$$

where $\mathbf{R}_{\mathbf{n}}^\varphi$ is the tensor of rotation around $\mathbf{n}$ about any angle $\varphi \in \langle 0, 2\pi \rangle$.

Interesting and important subgroup of the considered materials are the materials for which $\mathbf{I}$ is the eigenstate of $\mathbb{L}$ and $\mathbb{M}$. Materials with such a property are called *volumetrically isotropic*, cf. Burzyński [26], since its response to a hydrostatic stress state is the change of volume without the change of shape, similarly as in the case of isotropic materials. Let us denote the Kelvin bulk modulus of $\mathbb{L}$ by h^{P}; then spectral decompositions (3.3) for the considered subclass of materials take the form

$$\mathbb{L}(\phi^c) = h^{\mathrm{P}}\mathbb{I}_{\mathrm{P}} + \sum_{K=2}^{MK} h_K \mathbb{P}_K(\phi^c),\tag{3.14}$$

$$\mathbb{M}(\phi^c) = \frac{1}{h^{\mathrm{P}}}\mathbb{I}_{\mathrm{P}} + \sum_{K=2}^{MK} \frac{1}{h_K}\mathbb{P}_K(\phi^c),\tag{3.15}$$

where

$$\mathbb{P}_K(\phi^c) = \eta_K^{\mathrm{D}}\mathbb{I}_{\mathrm{D}} + \mathbb{A}_K^{\nu}(\phi^c) + \mathbb{H}_K(\phi^c), \quad \sum_{K=2}^{MK} \mathbb{P}_K(\phi^c) = \mathbb{I}_{\mathrm{D}}\tag{3.16}$$

and specifically

$$\eta_K^{\mathrm{D}} = \frac{1}{5}m_K, \quad \sum_{K=2}^{MK} m_K = 5, \quad \mathbb{A}_K^{\nu}(\phi^c) = \mathbb{A}_K^{\nu}(\boldsymbol{\nu}_{\mathrm{D}K}(\phi^c)).\tag{3.17}$$

For macroscopically isotropic material its overall stiffness and compliance tensors have the form:

$$\bar{\mathbb{L}} = \bar{h}^{\mathrm{P}}\mathbb{I}_{\mathrm{P}} + \bar{h}^{\mathrm{D}}\mathbb{I}_{\mathrm{D}}, \quad \bar{\mathbb{M}} = \frac{1}{\bar{h}^{\mathrm{P}}}\mathbb{I}_{\mathrm{P}} + \frac{1}{\bar{h}^{\mathrm{D}}}\mathbb{I}_{\mathrm{D}},\tag{3.18}$$

where $\bar{h}^{\mathrm{P}} = 3\bar{K}$ is the overall Kelvin bulk modulus, while $\bar{h}^{\mathrm{D}} = 2\bar{\mu} = 2\bar{G}$ is the overall Kelvin shear modulus. Below we use notation *the bulk modulus* and *the shear modulus* for these quantities, but one should note the slight difference with respect to $\bar{K}$ and $\bar{G}$ which are usually called by these names[2]. Above formulae are at the same time spectral and harmonic decompositions of macroscopic

---

[2]Kelvin's bulk and shear moduli are related to the macroscopic Young modulus $\bar{E}$ and the Poisson ratio $\bar{\nu}$ according to the well-known relations

$$\bar{E} = \frac{3\bar{h}^{\mathrm{P}}\bar{h}^{\mathrm{D}}}{2\bar{h}^{\mathrm{P}} + \bar{h}^{\mathrm{D}}}, \quad \bar{\nu} = \frac{\bar{h}^{\mathrm{P}} - \bar{h}^{\mathrm{D}}}{2\bar{h}^{\mathrm{P}} + \bar{h}^{\mathrm{D}}}.\tag{3.19}$$

constitutive tensors. In the next subsections, when discussing polycrystals of random texture, we derive the upper and lower bounds for $\bar{h}^{\mathrm{P}}$ and $\bar{h}^{\mathrm{D}}$ as well as their self-consistent estimates.

Spectral decompositions of macroscopic stiffness and compliance tensors corresponding to transverse isotropy are specified by relations (A.5) and (A.31) discussed in Appendix A, that is:

$$\bar{\mathbb{L}}^{ti} = \bar{h}_1\mathbb{P}_1^{ti}(\bar{\xi}) + \bar{h}_2\mathbb{P}_2^{ti}(\bar{\xi}) + \bar{h}_3\mathbb{P}_3^{ti} + \bar{h}_4\mathbb{P}_4^{ti}\,, \tag{3.20}$$

$$\bar{\mathbb{M}}^{ti} = \frac{1}{\bar{h}_1}\mathbb{P}_1^{ti}(\bar{\xi}) + \frac{1}{\bar{h}_2}\mathbb{P}_2^{ti}(\bar{\xi}) + \frac{1}{\bar{h}_3}\mathbb{P}_3^{ti} + \frac{1}{\bar{h}_4}\mathbb{P}_4^{ti}\,, \tag{3.21}$$

and below bounds and self-consistent estimates will be derived for moduli $\bar{h}_k$ and a distributor $\bar{\xi}$, when discussing polycrystals of fibre texture.

3.3. Upper and lower bounds

The simplest upper bound for averaged properties of polycrystal is obtained by taking

$$\boldsymbol{\varepsilon} = \mathbf{E} \tag{3.22}$$

everywhere in the polycrystal, cf. Willis [220]. Such an upper bound is called the Voigt bound for elastic materials, or the Taylor bound for rigid-plastic or visco-plastic materials. By averaging Eq. $(3.1)_2$ and applying the hypothesis (3.22), one obtains

$$\bar{\mathbb{L}} = \langle \mathbb{L}(\phi^c)\rangle\,, \quad \bar{\mathbb{M}} = \bar{\mathbb{L}}^{-1} = \langle \mathbb{L}(\phi^c)\rangle^{-1}\,. \tag{3.23}$$

The simplest lower bound for averaged properties of polycrystal is obtained by taking

$$\boldsymbol{\sigma} = \boldsymbol{\Sigma} \tag{3.24}$$

everywhere in the polycrystal. Such a lower bound is called the Reuss bound for elastic materials, or the Sachs bound for rigid-plastic or viscoplastic materials. Averaging $(3.1)_1$ and applying the hypothesis (3.24), one obtains

$$\bar{\mathbb{M}} = \langle \mathbb{M}(\phi^c)\rangle\,, \quad \bar{\mathbb{L}} = \bar{\mathbb{M}}^{-1} = \langle \mathbb{M}(\phi^c)\rangle^{-1}\,. \tag{3.25}$$

More rigorous bounds, resulting from the theorems of minimum potential energy and of minimum complementary energy have been derived by Hashin and Shtrikman, who formulated the variational principle called by their names, cf. Hashin and Shtrikman [59, 60], Willis [220, 221], Walpole [208]. The Hashin-Shtrikman principle is the variational principle specifically designed for

heterogeneous solids of moduli $\mathbb{L}(\mathbf{x})$. In order to measure the difference between responses of homogeneous and inhomogeneous materials, some reference homogeneous solid of constant stiffness moduli $\mathbb{L}_0$ is introduced. The principle is derived by considering two boundary value problems: the first one for the reference homogeneous solid and the second one for the actual heterogeneous solid, assuming the same boundary conditions. Solutions to these two problems, in terms of strain fields, are denoted by ε_0 and ε, respectively. The following functional is defined (an argument $\mathbf{x}$ is omitted):

$$\Pi(\mathbf{p}, \varepsilon_d) \equiv \frac{1}{2} \int_V \left(\varepsilon_0 \cdot \mathbb{L}_0 \cdot \varepsilon_0 - \mathbf{p} \cdot (\Delta\mathbb{L})^{-1} \cdot \mathbf{p} + \mathbf{p} \cdot \varepsilon_d + 2\mathbf{p} \cdot \varepsilon_d \right) dV , \quad (3.26)$$

where

$$\Delta\mathbb{L} = \mathbb{L} - \mathbb{L}_0 , \quad \mathbf{p} = \Delta\mathbb{L} \cdot \varepsilon , \quad \varepsilon_d = \varepsilon - \varepsilon_0 . \quad (3.27)$$

The principle states that:

1. Π is stationary if the inhomogenenous equilibrium equation (the subsidiary condition) is satisfied:

$$\operatorname{div}(\mathbb{L}_0 \cdot \varepsilon_d + \mathbf{p}) = \operatorname{div}(\mathbb{L} \cdot \varepsilon - \mathbb{L}_0 \cdot \varepsilon_0) = \mathbf{0} , \quad (3.28)$$

2. Π has a global minimum (maximum) if $\Delta\mathbb{L}$ is negative (positive) definite.

The physical meaning of Π is the strain energy stored inside the heterogeneous solid if the strain field ε and the polarisation field $\mathbf{p}$ are exact solutions to the analysed boundary value problem. The exposition of the Hashin-Shtrikman principle provided above is based on that of Li and Wang [120].

It can be demonstrated that, in view of this principle, some $\tilde{\mathbb{L}}$ provides an upper (lower) bound on tensor of effective properties $\bar{\mathbb{L}}$ according to the following implications:

$$\boldsymbol{\gamma} \cdot (\tilde{\mathbb{L}}(\mathbb{L}_0) - \bar{\mathbb{L}}) \cdot \boldsymbol{\gamma} \geqslant (\leqslant)0 \quad \text{if} \quad \bigwedge_{\phi^c \in \mathcal{Q}_{tex}} \boldsymbol{\gamma} \cdot (\mathbb{L}_0 - \mathbb{L}(\phi^c)) \cdot \boldsymbol{\gamma} \geqslant (\leqslant)0 , \quad (3.29)$$

where $\boldsymbol{\gamma}$ is any strain state. The $\mathbb{L}_0$ is a stiffness tensor for some reference material of the same symmetry as $\bar{\mathbb{L}}$. For the analysed polycrystalline materials of grains with the same shape and orientation, an estimator $\tilde{\mathbb{L}}$ is specified as

$$\tilde{\mathbb{L}} = \left\langle (\mathbb{L}(\phi^c) + \mathbb{L}_*(\mathbb{L}_0))^{-1} \right\rangle^{-1} - \mathbb{L}_*(\mathbb{L}_0) , \quad (3.30)$$

where $\mathbb{L}_*(\mathbb{L}_0)$ is the Hill tensor specified by (B.3-B.4) for the assumed shape of inclusions[3] and properties of a reference material $\mathbb{L}_0$. Note that right-hand

---

[3]If overall properties are isotropic it can be shown that bounding estimates (3.30) are valid for arbitrary shape of inclusions, cf. Christensen [34], with the isotropic $\mathbb{L}_*$ specified by (B.7-B.8).

side of an inequality in implication (3.29) is equivalent to positive (negative) definiteness of the tensor $\mathbb{L}_0 - \mathbb{L}(\phi^c)$ for any ϕ^c.

The bounds formulated above are subsequently specified for polycrystals of random and fibre textures.

3.3.1. Random texture

By introducing decompositions (3.3) and (3.5) into (3.23) it has been demonstrated by Kowalczyk-Gajewska [99] that

$$\bar{h}_{\mathrm{UP}}^{\mathrm{P}} = \sum_{K=1}^{MK} h_K \eta_K^{\mathrm{P}}, \quad \bar{h}_{\mathrm{UP}}^{\mathrm{D}} = \sum_{K=1}^{MK} h_K \eta_K^{\mathrm{D}}. \tag{3.31}$$

It can be shown that $1/3\bar{h}_{\mathrm{UP}}^{\mathrm{P}}$ is equal to the average bulk modulus of polycrystal, cf. Kocks et al. [88]. In the case of volumetrically isotropic materials, above formulae reduce to

$$\bar{h}_{\mathrm{UP*}}^{\mathrm{P}} = h^{\mathrm{P}}, \quad \bar{h}_{\mathrm{UP*}}^{\mathrm{D}} = \frac{1}{5} \sum_{K=2}^{MK} h_K m_K, \tag{3.32}$$

so the macroscopic bulk modulus is equal to the local one.

Performing similar calculations for the lower bound solution one arrives at, cf. Kowalczyk-Gajewska [99],

$$\bar{h}_{\mathrm{LO}}^{\mathrm{P}} = \left(\sum_{K=1}^{MK} \frac{\eta_K^{\mathrm{P}}}{h_K} \right)^{-1}, \quad \bar{h}_{\mathrm{LO}}^{\mathrm{D}} = \left(\sum_{K=1}^{MK} \frac{\eta_K^{\mathrm{D}}}{h_K} \right)^{-1}. \tag{3.33}$$

It can be shown that $3\bar{h}_{\mathrm{LO}}^{\mathrm{P}}$ is equal to the inverse of an average compressibility modulus, cf. Kocks et al. [88]. In the case of the volumetrically isotropic materials above formulae reduce to

$$\bar{h}_{\mathrm{LO*}}^{\mathrm{P}} = h^{\mathrm{P}}, \quad \bar{h}_{\mathrm{LO*}}^{\mathrm{D}} = 5 \left(\sum_{K=2}^{MK} \frac{m_K}{h_K} \right)^{-1}, \tag{3.34}$$

so again the macroscopic bulk modulus is equal to the local one. Since upper and lower bounds for the bulk modulus coincide, $\bar{h}^{\mathrm{P}} = h^{\mathrm{P}}$ is the exact value.

One should note that the derived upper and lower bounds depend only on local Kelvin moduli h_K, their multiplicity and $MK - 1$ independent values η_K^{P}, that is, on maximum 11 independent functions of 21 components of a local stiffness tensor. All these functions are invariants of the local elasticity tensor, cf.

Kowalczyk-Gajewska and Ostrowska-Maciejewska [102]. Specific formulae for $\left\{\bar{h}^{\mathrm{P}}_{\mathrm{UP/LO}}, \bar{h}^{\mathrm{D}}_{\mathrm{UP/LO}}\right\}$ for all local symmetry groups covered by the fourth-order tensor are collected in Kowalczyk-Gajewska [99]. It should be underlined that analytical formulae for lower and upper bounds specified by assumptions (3.22) and (3.24) for arbitrarily anisotropic crystal are already known in the literature, e.g. Walpole [208], Kocks et al. [88], Cowin et al. [38]. The originality of result derived by the author in [99] lies mainly in the method applied, enabling the specification of them in terms of invariants of $\mathbb{L}$ coming from its spectral and harmonic decompositions applied subsequently. As it is shown further, the proposed procedure can be also applied for the derivation of the Hashin-Shtrikman bounds and the self-consistent estimates.

Procedure of deriving the Hashin-Shtrikman bounds involves two important steps, namely:

1. An appropriate selection of a reference material $\mathbb{L}_0$ which does not violate condition of positive (negative) definiteness of $\Delta\mathbb{L}(\phi^c) = \mathbb{L}_0 - \mathbb{L}(\phi^c)$, and at the same time provides the best possible upper (lower) bound[4].

2. Specification of $\tilde{\mathbb{L}}$ according to the formula (3.30) with use of the selected $\mathbb{L}_0$.

Procedure is not as straightforward as derivation of the Voigt and Reuss bounds, because in general the local tensor $\mathbb{L}(\phi^c)$ and the isotropic Hill tensor $\mathbb{L}_*(\mathbb{L}_0)$ specified by (B.7), as well as overall tensor $\tilde{\mathbb{L}}$, do not commute. Two steps simplify considerably if locally the material is volumetrically isotropic and the latter property holds.

Volumetrically isotropic crystals

As it was obtained for the uniform strain and uniform stress bounds, the local bulk modulus $h^{\mathrm{P}} = \bar{h}^{\mathrm{P}}$. Therefore also $\tilde{h}^{\mathrm{P}}_{\mathrm{UP}} = \tilde{h}^{\mathrm{P}}_{\mathrm{LO}} = h^{\mathrm{P}}$, and also $h^{\mathrm{P}}_0 = h^{\mathrm{P}}$. One can show that $\tilde{\mathbb{L}}$ specified by (3.30) is monotonous function of $h^{\mathrm{P}}_0, h^{\mathrm{D}}_0$, cf. Berryman [12], therefore the upper (lower) bound is the closest when the bulk and shear moduli of a reference material are as small (large) as possible. Consider that

$$\Delta\mathbb{L}(\phi^c) = \sum_{K=2}^{MK} (h^{\mathrm{D}}_0 - h_K)\mathbb{P}^{(K)}(\phi^c)\,, \tag{3.35}$$

---

[4]The quality of bounds is assessed in view of the norm $\|\tilde{\mathbb{L}}\|$.

therefore it is easy to see that

$$\bigwedge_{\phi^c \in \mathcal{Q}} \boldsymbol{\gamma} \cdot \Delta\mathbb{L}(\phi^c) \cdot \boldsymbol{\gamma} \geqslant (\leqslant) 0 \iff h_0^{\mathrm{D}} \geqslant \max_{K>1}\{h_K\} \quad (h_0^{\mathrm{D}} \leqslant \min_{K>1}\{h_K\}). \quad (3.36)$$

Consequently the upper and lower bounds $\tilde{\mathbb{L}}_{\mathrm{HS}}$ are obtained by setting, respectively, $h_0^{\mathrm{D}} = \max_{K>1}\{h_K\}$ and $h_0^{\mathrm{D}} = \min_{K>1}\{h_K\}$, in the following formula derived from (3.30) with use of (3.9):

$$\tilde{h}_{\mathrm{HS}}^{\mathrm{D}} = 5 \left(\sum_{K=2}^{MK} \frac{m_K}{h_K + h_*^{\mathrm{D}}(h^{\mathrm{P}}, h_0^{\mathrm{D}})} \right)^{-1} - h_*^{\mathrm{D}}(h^{\mathrm{P}}, h_0^{\mathrm{D}}). \quad (3.37)$$

Anisotropic crystals

Now, let us consider anisotropic crystals which are not volumetrically isotropic. To this end let us re-write (3.3) as follows:

$$\mathbb{L}(\phi^c) = \underbrace{\sum_{K=1}^{NK} h_K \mathbb{P}_K(\phi^c)}_{\hat{\mathbb{L}}(\phi^c)} + \sum_{K=NK+1}^{MK} h_K \mathbb{P}_K(\phi^c), \quad (3.38)$$

$$\mathbb{M}(\phi^c) = \underbrace{\sum_{K=1}^{NK} \frac{1}{h_K}\mathbb{P}_K(\phi^c)}_{\hat{\mathbb{M}}(\phi^c)} + \sum_{K=N+1}^{MK} \frac{1}{h_K}\mathbb{P}_K(\phi^c), \quad (3.39)$$

where projectors $\mathbb{P}_K(\phi^c)$ for $K = NK+1, ..., MK$ into deviatoric eigen-subspaces commute with $\mathbb{I}_{\mathrm{P}}$, while $\mathbb{P}_K(\phi^c)$ for $K = 1, ..., NK$ do not. Note that

$$\sum_{K=1}^{NK} \mathbb{P}_K(\phi^c) = \hat{\mathbb{P}}(\phi_c) = \mathbb{I}_{\mathrm{P}} + \hat{\mathbb{P}}_{\mathrm{D}}(\phi_c), \quad (3.40)$$

where $\hat{\mathbb{P}}(\phi_c)$ and $\hat{\mathbb{P}}_{\mathrm{D}}(\phi_c)$ fulfil $\mathbb{P} \circ \mathbb{P} = \mathbb{P}$, so these fourth-order tensors are projectors. Both commute with $\mathbb{I}_{\mathrm{P}}$, and

$$\hat{\mathbb{L}}(\phi^c) = \hat{\mathbb{P}}(\phi^c) \circ \mathbb{L}(\phi^c), \quad (3.41)$$

while $\hat{\mathbb{M}}(\phi^c)$ is a partial inverse of $\hat{\mathbb{L}}(\phi^c)$.

With use of the above notation, $\Delta\mathbb{L}(\phi^c)$ is specified as

$$\Delta\mathbb{L}(\phi^c) = \Delta\hat{\mathbb{L}}(\phi^c) + \sum_{K=NK+1}^{MK} (h_0^{\mathrm{D}} - h_K)\mathbb{P}_K(\phi^c), \quad (3.42)$$

and $\Delta\hat{\mathbb{L}}(\phi^c) = \hat{\mathbb{L}}_0 - \hat{\mathbb{L}}(\phi^c)$. The requirement of semi-positive (semi-negative) definiteness of the tensor $\Delta\mathbb{L}(\phi^c)$ is fulfilled when

$$\bigwedge_{\phi^c \in \mathcal{Q}_{tex}} \boldsymbol{\gamma} \cdot \Delta\hat{\mathbb{L}}(\phi^c) \cdot \boldsymbol{\gamma} \geqslant (\leqslant)0 \quad \text{and} \quad h_0^{\mathrm{D}} \geqslant \max_{K>NK}\{h_K\} \quad (h_0^{\mathrm{D}} \leqslant \min_{K>NK}\{h_K\}).$$
(3.43)

Above inequalities specify an admissible set $\mathcal{A}_0 \in R^2$ of pairs $\{h_0^{\mathrm{P}}, h_0^{\mathrm{D}}\}$ for the reference isotropic tensor $\mathbb{L}_0$. Now, we derive estimator $\tilde{\mathbb{L}}$ for the selected pair of these scalars. Let us denote

$$\hat{\mathbb{R}}(\phi^c) = (\hat{\mathbb{L}}(\phi^c) + \hat{\mathbb{L}}_*(\mathbb{L}_0))^{-1}$$
(3.44)

and perform its harmonic decomposition,

$$\hat{\mathbb{R}}(\phi^c) = \hat{\mu}^{\mathrm{P}}\mathbb{I}_{\mathrm{P}} + \hat{\mu}^{\mathrm{D}}\mathbb{I}_{\mathrm{D}} + \hat{\mathbb{R}}(\phi^c)_{ani},$$
(3.45)

as well as harmonic decompositions (3.16) of deviatoric projectors $\mathbb{P}_K$ for $K > NK$. After introducing above decompositions into (3.30) and using the property (3.9) one finds

$$\tilde{h}^{\mathrm{P}} = \frac{1}{\hat{\mu}^{\mathrm{P}}} - h_*^{\mathrm{P}}, \quad \tilde{h}^{\mathrm{D}} = \left(\hat{\mu}^{\mathrm{D}} + \sum_{K=NK+1}^{MK} \frac{m^K}{5(h_K + h_*^{\mathrm{D}})}\right)^{-1} - h_*^{\mathrm{D}}.$$
(3.46)

The closest upper (lower) bound on isotropic $\tilde{\mathbb{L}}$ is obtained for a pair $\{h_0^{\mathrm{P}}, h_0^{\mathrm{D}}\} \in \mathcal{A}_0$ for which function $F_0 = \|\tilde{\mathbb{L}}\|^2$ specified as

$$F_0(h_0^{\mathrm{P}}, h_0^{\mathrm{D}}) = \tilde{h}^{\mathrm{P}}(h_0^{\mathrm{P}}, h_0^{\mathrm{D}})^2 + 5\tilde{h}^{\mathrm{D}}(h_0^{\mathrm{P}}, h_0^{\mathrm{D}})^2$$
(3.47)

reaches minimum (maximum).

Let us specify the Hashin-Shtrikman bounds for the materials in which $N = 2$ and corresponding h_1 and h_2 are of multiplicity one. In such a case there exists a uniquely defined (within the sign) deviatoric second order tensor $\mathbf{d}(\phi^c)$ of a unit norm such that

$$\widehat{\mathbb{P}}_{\mathrm{D}}(\phi^c) = \mathbf{d}(\phi^c) \otimes \mathbf{d}(\phi^c), \quad \mathbb{P}_K(\phi^c) \cdot \mathbf{d}(\phi^c) = \mathbf{0}, \quad K = N+1, \dots, MK$$
(3.48)

and

$$\hat{\mathbb{L}}(\phi^c) = L_{11}\mathbb{I}_{\mathrm{P}} + L_{22}\widehat{\mathbb{P}}_{\mathrm{D}}(\phi^c) + \frac{1}{\sqrt{3}}L_{12}\left(\mathbf{I} \otimes \mathbf{d}(\phi^c) + \mathbf{d}(\phi^c) \otimes \mathbf{I}\right).$$
(3.49)

One can show that quantities L_{11}, L_{22} and $(L_{12})^2$ are invariants of the local elasticity tensor, since they are specified as follows:

$$L_{11} = \frac{1}{3}\mathbf{I} \cdot \mathbb{L}(0) \cdot \mathbf{I} = h_1\eta_1^{\mathrm{P}} + h_2\eta_2^{\mathrm{P}} > 0\,, \tag{3.50}$$

$$L_{22} = \mathbf{d}(0) \cdot \mathbb{L}(0) \cdot \mathbf{d}(0) = h_1 + h_2 - L_{11}^c > 0\,, \tag{3.51}$$

$$(L_{12})^2 = L_{11}L_{22} - h_1h_2 > 0\,. \tag{3.52}$$

It can be easily checked that L_{11} provides the Voigt-type upper bound (3.31) for an overall bulk modulus. With use of above definitions one can show that the condition of semi-positive (semi-negative) definiteness of the tensor $\Delta\hat{\mathbb{L}}(\phi^c)$ is equivalent to the condition of semi-positive (semi-negative) definiteness of the 2×2 matrix of the form

$$\begin{bmatrix} h_0^{\mathrm{P}} - L_{11} & -L_{12} \\ -L_{12} & h_0^{\mathrm{D}} - L_{22} \end{bmatrix}\,, \tag{3.53}$$

which, using the fact that $\mathbb{L}$ is positive definite, implies the following inequalities:

$$h_0^{\mathrm{P}} \geqslant (\leqslant)L_{11}, \quad h_0^{\mathrm{D}} \geqslant (\leqslant)L_{22}, \quad h_0^{\mathrm{P}} \geqslant (\leqslant)L_{11} + \frac{(L_{12})^2}{h_0^{\mathrm{D}} - L_{22}}\,. \tag{3.54}$$

The admissible subspaces of h_0^{P} and h_0^{D} specified by above inequalities and (3.43) are presented in Fig. 3.2.

For the specified h_0^{P} and h_0^{D}, estimators (3.30) read

$$\tilde{h}^{\mathrm{P}} = L_{11} - \frac{(L_{12})^2}{L_{22} + h_*^{\mathrm{D}}}, \quad \tilde{h}^{\mathrm{D}} = 5\left(\frac{h_*^{\mathrm{P}} + L_{11}}{J_*} + \sum_{K=NK+1}^{MK} \frac{m^K}{(h_K + h_*^{\mathrm{D}})}\right)^{-1} - h_*^{\mathrm{D}}\,, \tag{3.55}$$

where

$$J_* = (L_{11} + h_*^{\mathrm{P}})(L_{22} + h_*^{\mathrm{D}}) - (L_{12})^2\,. \tag{3.56}$$

It can be shown that the function $F_0(h_0^{\mathrm{P}}, h_0^{\mathrm{D}})$ specified by (3.47) and the above formulae are monotonous functions of their arguments, therefore the closest upper (lower) bound is obtained for values laying on the boundary of the admissible set of solutions marked in Fig. 3.2 a-b (c-d) by a thick black line. Points on this line fulfil equation

$$h_0^{\mathrm{P}} = h_0^{\mathrm{P}}(h_0^{\mathrm{D}}) = L_{11} + \frac{(L_{12})^2}{h_0^{\mathrm{D}} - L_{22}}, \quad \text{and} \quad h_0^{\mathrm{D}} \geqslant h_{max}(\leqslant h_{min})\,, \tag{3.57}$$
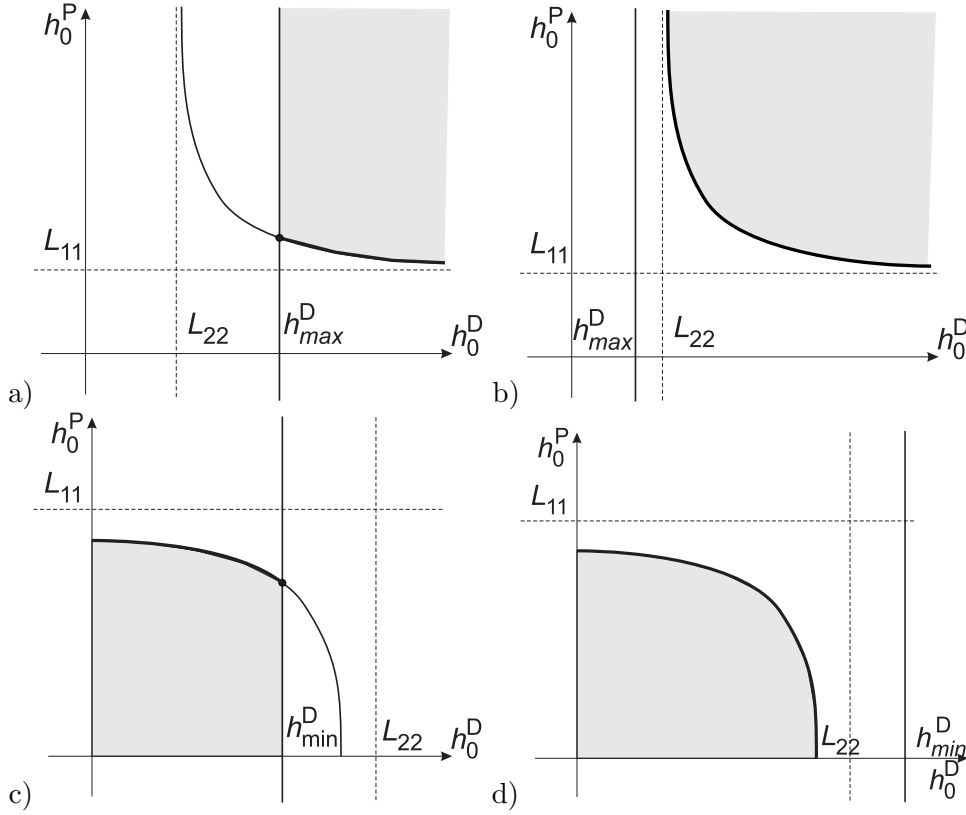
Fig. 3.2. The admissible subspaces of h_0^P and h_0^D specified by (3.54) when calculating the Hashin-Shtrikman bounds for random polycrystal of local properties defined by (3.38) and (3.49): a) $h_{max}^D > L_{22}$ (UP), b) $h_{max}^D < L_{22}$ (UP), c) $h_{min}^D < L_{22}$ (LO), d) $h_{min}^D > L_{22}$ (LO).

where $h_{max} = \max\{h_{max}^D, L_{22}\}$ ($h_{min} = \min\{h_{min}^D, L_{22}\}$). Denote by $\hat{h}_0^D$ the solution of the following extremum condition:

$$\frac{dF_0}{dh_0^D} = \frac{\partial F_0}{\partial h_0^D} + \frac{\partial F_0}{\partial h_0^P}\frac{dh_0^P}{dh_0^D} = \frac{\partial F_0}{\partial h_0^D} - \frac{(L_{12})^2}{(h_0^D - L_{22})^2}\frac{\partial F_0}{\partial h_0^P} = 0\,. \qquad (3.58)$$

If $\hat{h}_0^D \geqslant h_{max}(\leqslant h_{min}$ and $\hat{h}_0^D \geqslant 0)$, then the closest upper (lower) bound on $\bar{\mathbb{L}}$ will be obtained for the isotropic reference material with moduli $\{h_0^P(\hat{h}_0^D), \hat{h}_0^D\}$. If it is not the case, one should take isotropic material with moduli $\{h_0^P(h_{max}), h_{max}\}$ ($\{h_0^P(h_{min}), h_{min}\}$). Note that for $h_{max} \to L_{22}$ one has $h^P \to \infty$, so the reference material is incompressible.

3.3.2. Fibre texture

Fibre texture results in the overall transverse isotropy. Let us first derive Voigt and Reuss bounds. Denote by $\mathbf{n}$ the crystallographic direction common for all crystallites in the representative aggregate and calculate $\bar{\mathbb{L}}_{\mathrm{UP}}$ according to (3.23),

$$
\begin{aligned}
\langle \mathbb{L}(\phi^c) \rangle_{\mathcal{Q}_{\mathbf{n}}} &= \left\langle \sum_{K=1}^{MK} h_K \mathbb{P}_K(\phi^c) \right\rangle_{\mathcal{Q}_{\mathbf{n}}} = \\
&= \left(\sum_{K=1}^{MK} h_K \eta_K^{\mathrm{P}} \right) \mathbb{I}_{\mathrm{P}} + \left(\sum_{K=1}^{MK} h_K \eta_K^{\mathrm{D}} \right) \mathbb{I}_{\mathrm{D}} + \\
&\quad + \sum_{K=1}^{MK} h_K \left\langle \mathbb{A}_K^{\mu}(\phi^c) \right\rangle_{\mathcal{Q}_{\mathbf{n}}} + \sum_{K=1}^{MK} h_K \left\langle \mathbb{A}_K^{\nu}(\phi^c) \right\rangle_{\mathcal{Q}_{\mathbf{n}}} \\
&\quad + \sum_{K=1}^{MK} h_K \left\langle \mathbb{H}_K(\phi^c) \right\rangle_{\mathcal{Q}_{\mathbf{n}}} .
\end{aligned}
\tag{3.59}
$$

Now, using decompositions (A.42) one finds

$$
\langle \mathbb{A}_K^{\mu}(\phi^c) \rangle_{\mathcal{Q}_{\mathbf{n}}} = \mathbb{A}^{\mu}(\langle \boldsymbol{\phi}_K(\phi^c) \rangle_{\mathcal{Q}_{\mathbf{n}}}) = (\boldsymbol{\phi}_K(0) \cdot \mathbf{d}_n) \mathbb{A}^{\mu}(\mathbf{d}_n) = \hat{\alpha}_K^{\mu} \mathbb{A}^{\mu}(\mathbf{d}_n), \tag{3.60}
$$

$$
\langle \mathbb{A}_K^{\nu}(\phi^c) \rangle_{\mathcal{Q}_{\mathbf{n}}} = \mathbb{A}^{\nu}(\langle \boldsymbol{\rho}_K(\phi^c) \rangle_{\mathcal{Q}_{\mathbf{n}}}) = (\boldsymbol{\rho}_K(0) \cdot \mathbf{d}_n) \mathbb{A}^{\nu}(\mathbf{d}_n) = \hat{\alpha}_K^{\nu} \mathbb{A}^{\nu}(\mathbf{d}_n), \tag{3.61}
$$

$$
\langle \mathbb{H}_K(\phi^c) \rangle_{\mathcal{Q}_{\mathbf{n}}} = (\mathbb{H}_K(0) \cdot \mathbb{H}_{\mathbf{n}}) \mathbb{H}_{\mathbf{n}} = \hat{\eta}_K^{\mathrm{H}} \mathbb{H}_{\mathbf{n}} . \tag{3.62}
$$

Introducing these relations into (3.59) and comparing with (A.31), one specifies

$$
\bar{h}_{\mathrm{UP}}^{\mathrm{P}} = \sum_{K=1}^{MK} h_K \eta_K^{\mathrm{P}}, \quad \bar{h}_{\mathrm{UP}}^{\mathrm{D}} = \sum_{K=1}^{MK} h_K \eta_K^{\mathrm{D}}, \tag{3.63}
$$

$$
\bar{\alpha}_{\mathrm{UP}}^{\mu} = \sum_{K=1}^{MK} h_K \hat{\alpha}_K^{\mu}, \quad \bar{\alpha}_{\mathrm{UP}}^{\nu} = \sum_{K=1}^{MK} h_K \hat{\alpha}_K^{\nu}, \quad \bar{\eta}_{\mathrm{UP}}^{\mathrm{H}} = \sum_{K=1}^{MK} h_K \hat{\eta}_K^{\mathrm{H}} . \tag{3.64}
$$

Using (A.29) and (A.32) one finds upper bounds on $\bar{h}_K$:

$$
\bar{h}_{3\mathrm{UP}} = \bar{h}_{\mathrm{UP}}^{\mathrm{D}} - \frac{2}{\sqrt{6}} \bar{\alpha}_{\mathrm{UP}}^{\nu} + \frac{1}{\sqrt{70}} \bar{\eta}_{\mathrm{UP}}^{\mathrm{H}}, \quad \bar{h}_{4\mathrm{UP}} = \bar{h}_{\mathrm{UP}}^{\mathrm{D}} + \frac{1}{\sqrt{6}} \bar{\alpha}_{\mathrm{UP}}^{\nu} - \frac{4}{\sqrt{70}} \bar{\eta}_{\mathrm{UP}}^{\mathrm{H}} , \tag{3.65}
$$

while remaining two Kelvin moduli $\bar{h}_{1\mathrm{UP}}$ and $\bar{h}_{2\mathrm{UP}}$ are obtained as eigenvalues of the following 2×2 matrix

$$
\begin{bmatrix}
\bar{h}_{\mathrm{UP}}^{\mathrm{P}} & \sqrt{3} \bar{\alpha}_{\mathrm{UP}}^{\mu} \\
\sqrt{3} \bar{\alpha}_{\mathrm{UP}}^{\mu} & \bar{h}_{\mathrm{UP}}^{\mathrm{D}} + \frac{2}{\sqrt{6}} \bar{\alpha}_{\mathrm{UP}}^{\nu} + \frac{6}{\sqrt{70}} \bar{\eta}_{\mathrm{UP}}^{\mathrm{H}}
\end{bmatrix} .
\tag{3.66}
$$

The stiffness distributor $\bar{\xi}_{\text{UP}}$ is obtained by finding eigenstates of this matrix. If we put the eigenstates in the following form:

$$\boldsymbol{\omega}_1 = \frac{1}{\sqrt{3}} \cos \Phi \mathbf{I} + \sin \Phi \mathbf{d_n}, \quad \boldsymbol{\omega}_2 = -\frac{1}{\sqrt{3}} \sin \Phi \mathbf{I} + \cos \Phi \mathbf{d_n}, \tag{3.67}$$

then[5]

$$\bar{\xi}_{\text{UP}} = \frac{1}{3} \operatorname{tg} \Phi. \tag{3.68}$$

Derivation of a lower bound for $\bar{\mathbb{L}}$ in the case of a fibre texture follows similar procedure, leading to the following relations being counterparts of (3.63) and (3.64):

$$^M \bar{h}_{\text{LO}}^{\text{P}} = \sum_{K=1}^{MK} \frac{1}{h_K} \eta_K^{\text{P}}, \quad ^M \bar{h}_{\text{LO}}^{\text{D}} = \sum_{K=1}^{MK} \frac{1}{h_K} \eta_K^{\text{D}}, \tag{3.69}$$

$$^M \bar{\alpha}_{\text{LO}}^{\mu} = \sum_{K=1}^{MK} \frac{1}{h_K} \hat{\alpha}_K^{\mu}, \quad ^M \bar{\alpha}_{\text{LO}}^{\nu} = \sum_{K=1}^{MK} \frac{1}{h_K} \hat{\alpha}_K^{\nu}, \quad ^M \bar{\eta}_{\text{LO}}^{\text{H}} = \sum_{K=1}^{MK} \frac{1}{h_K} \hat{\eta}_K^{\text{H}}, \tag{3.70}$$

with an important note that now, the above quantities are related to the harmonic decomposition (A.31) of a compliance tensor $\bar{\mathbb{M}}$, therefore the lower bounds for the Kelvin moduli $\bar{h}_K^{LO}$ are obtained as

$$\frac{1}{\bar{h}_{3\text{LO}}} = {}^M \bar{h}_{\text{LO}}^{\text{D}} - \frac{2}{\sqrt{6}} {}^M \bar{\alpha}_{\text{LO}}^{\nu} + \frac{1}{\sqrt{70}} {}^M \bar{\eta}_{\text{LO}}^{\text{H}}, \tag{3.71}$$

$$\frac{1}{\bar{h}_{4\text{LO}}} = {}^M \bar{h}_{\text{LO}}^{\text{D}} + \frac{1}{\sqrt{6}} {}^M \bar{\alpha}_{\text{LO}}^{\nu} - \frac{4}{\sqrt{70}} {}^M \bar{\eta}_{\text{LO}}^{\text{H}} \tag{3.72}$$

and inverses of $\bar{h}_{1\text{LO}}$ and $\bar{h}_{2\text{LO}}$ and the corresponding distributor $\bar{\xi}_{\text{LO}}$ are obtained as a solution of an eigenproblem for the matrix (3.66), where the subscript UP is replaced by the subscript LO.

Formulae simplify considerably when we deal with volumetrically isotropic material, because in such a case $\eta_K^{\text{P}} = 0$ for $K > 1$ and $\hat{\alpha}_K^{\mu} = 0$ for all K. It is then easily verified that

$$\bar{h}_{1\text{UP}*} = h^{\text{P}}, \quad \bar{h}_{2\text{UP}*} = \bar{h}_{\text{UP}}^{\text{D}} + \frac{2}{\sqrt{6}} \bar{\alpha}_{\text{UP}}^{\nu} + \frac{6}{\sqrt{70}} \bar{\eta}_{\text{UP}}^{\text{H}}, \quad \bar{\xi}_{\text{UP}*} = 0, \tag{3.73}$$

while $\bar{h}_{3\text{UP}*}$ and $\bar{h}_{4\text{UP}*}$ are given by (3.65) and $\bar{h}_{\text{UP}}^{\text{D}}$ is specified by $(3.32)_2$. Correspondingly, for lower bounds one obtains

$$\bar{h}_{1\text{LO}*} = h^{\text{P}}, \quad \bar{h}_{2\text{LO}*} = \frac{1}{{}^M \bar{h}_D^{LO} + \frac{2}{\sqrt{6}} {}^M \bar{\alpha}_2^{LO} + \frac{6}{\sqrt{70}} {}^M \bar{\eta}_{\text{LO}}^{\text{H}}}, \quad \bar{\xi}_{\text{LO}*} = 0, \tag{3.74}$$

---

[5]In order to avoid non-unique result one should order the obtained eigenvalues in the way that ensures $\cos^2 \Phi > \sin^2 \Phi$.

while $\bar{h}_{3\text{LO}*}$ and $\bar{h}_{4\text{LO}*}$ are given by (3.71-3.72) and $\bar{h}_{\text{LO}}^{\text{D}}$ is specified by an inverse of $(3.34)_2$. As it is seen, the polycrystal is also volumetrically isotropic and, moreover, the upper and lower bounds on $\bar{h}_1$ coincide with the local bulk modulus specifying the exact value of $\bar{h}_1$. Let us add at this point that with use of a harmonic decomposition it can be easily shown that this property holds for a polycrystal of any texture as long as constituent grains are volumetrically isotropic. It is worth noting that for crystals of cubic symmetry the Voigt and Reuss bounds on properties of polycrystals of fibre texture take relatively simple forms, because one has in this case $\hat{\alpha}_K^\mu = \hat{\alpha}_K^\nu = 0$ for all K (here, $K = 1, 2, 3$, compare Böhlke and Bertram [18])

Now, let us discuss the Hashin-Shtrikman bounds. In the case of fibre texture, the two steps needed to derive these bounds are more complicated. First, in general $\mathbb{L}(\phi^c)$ and $\mathbb{L}_0$ can have no common symmetries, therefore finding the appropriate $\mathbb{L}_0$ is not a trivial task. Next, it can be seen from the definitions (B.3-B.4) that the symmetry of the Hill tensor $\mathbb{L}_*(\mathbb{L}_0)$ is a joined symmetry of an ellipsoid and the stiffness tensor $\mathbb{L}_0$. In the case of macroscopic transverse isotropy and spherical shape of grains, the Hill tensor has also transverse isotropy. Unfortunately, an integration present in the specification (B.4) cannot be performed analytically. One can only reduce it to the integration over a single angle, cf. Hutchinson [69], Kiryk [83]. In general, five non-zero independent components of $\mathbb{L}_*(\mathbb{L}_0)$ in overall anisotropy axes are functions of corresponding components of an overall stiffness tensor $\mathbb{L}_0$. It should be stressed that, even if the macroscopically material is volumetrically isotropic, the corresponding Hill tensor does not enjoy this property in general. These facts cause that the averaging present in formula (3.30) is more difficult to perform than in the case of the Voigt and Reuss bounds. Derivations are similar to those presented below, when finding the self-consistent estimates in the case of fibre texture.

3.4. Self-consistent estimates

Self-consistent estimate of an overall behaviour of polycrystal relies on Eshelby's solution for the ellipsoidal inclusion embedded in the infinite medium. Here, a single grain is considered as an inclusion while the medium has averaged, yet unknown, properties of a polycrystal (see Appendix B). Following Hill's formulation [66] of a self-consistent procedure one finds the following localization equation for local strain:

$$\boldsymbol{\varepsilon} = \mathbb{A} \cdot \mathbf{E}, \quad \mathbb{A} = (\mathbb{L} + \mathbb{L}_*)^{-1} \circ (\bar{\mathbb{L}} + \mathbb{L}_*), \quad \langle \mathbb{A} \rangle = \mathbb{I}^S, \qquad (3.75)$$

where $\mathbb{A}$ is the localization tensor and $\mathbb{L}_*$ is the Hill tensor which depends on the shape of inclusion and the averaged properties $\bar{\mathbb{L}}$. Furthermore, it is shown that

$$\bar{\mathbb{L}} = \langle \mathbb{L} \circ \mathbb{A} \rangle \;, \tag{3.76}$$

which is an implicit equation since $\mathbb{A}$ depends on $\bar{\mathbb{L}}$. In our analysis we assume that grains have the same spherical shape and the same properties. Therefore, instead of (3.76) for derivation of $\bar{\mathbb{L}}$, the equivalent equation is utilized, namely

$$\langle (\bar{\mathbb{L}} - \mathbb{L}) \circ \mathbb{A} \rangle = \mathbb{O}. \tag{3.77}$$

Another implicit formula for derivation of $\bar{\mathbb{L}}$ is obtained with analogy to (3.30), viz.:

$$\bar{\mathbb{L}} = \left\langle (\mathbb{L}(\phi^c) + \mathbb{L}_*(\bar{\mathbb{L}}))^{-1} \right\rangle^{-1} - \mathbb{L}_*(\bar{\mathbb{L}}) \,. \tag{3.78}$$

Usually, one of the above formulae is solved numerically to find the self-consistent estimate of the average properties of a polycrystal. An iterative procedure applied to solve the equation (3.78), in which $\mathbb{L}_*$ is calculated with use of approximation of $\bar{\mathbb{L}}$ from the previous iteration, with e.g. the Voigt upper bound being the starting value, leads to $\bar{\mathbb{L}}$ possessing the minor and major symmetries.

3.4.1. Random texture

In the case of macroscopic isotropy and a spherical shape of grains, the Hill tensor is specified by (B.7-B.8) with $\{h_0^{\mathrm{P}}, h_0^{\mathrm{D}}\}$ replaced by $\{\bar{h}^{\mathrm{P}}, \bar{h}^{\mathrm{D}}\}$. Introducing appropriate formulae for $\mathbb{A}$ one notices that the inversion present in the formula $(3.75)_2$ is not straightforward unless all $\mathbb{P}_K(\phi^c)$ commute with $\mathbb{I}_{\mathrm{P}}$. All $\mathbb{P}_K(\phi^c)$ commute with $\mathbb{I}_{\mathrm{P}}$ if material is volumetrically isotropic. Let us first consider this class of materials.

Volumetrically isotropic crystals

Introducing formulae (3.14) into $(3.75)_2$, the localization tensor is specified as

$$\mathbb{A}(\phi^c) = \frac{\bar{h}^{\mathrm{P}} + h_*^{\mathrm{P}}}{h^{\mathrm{P}} + h_*^{\mathrm{P}}} \mathbb{I}_{\mathrm{P}} + \sum_{K=2}^{MK} \frac{\bar{h}^{\mathrm{D}} + h_*^{\mathrm{D}}}{h_K + h_*^{\mathrm{D}}} \mathbb{P}_K(\phi^c) \tag{3.79}$$

and

$$(\bar{\mathbb{L}} - \mathbb{L}(\phi^c)) \circ \mathbb{A}(\phi^c) =$$

$$= \underbrace{\frac{(\bar{h}^{\mathrm{P}} - h^{\mathrm{P}})(\bar{h}^{\mathrm{P}} + h_*^{\mathrm{P}})}{h^{\mathrm{P}} + h_*^{\mathrm{P}}}}_{\alpha^{\mathrm{P}}} \mathbb{I}_{\mathrm{P}} + \sum_{K=2}^{MK} \underbrace{\frac{(\bar{h}^{\mathrm{D}} - h_K)(\bar{h}^{\mathrm{D}} + h_*^{\mathrm{D}})}{h_K + h_*^{\mathrm{D}}}}_{\alpha_K} \mathbb{P}_K(\phi^c) = \tag{3.80}$$

$$= \alpha^{\mathrm{P}} \mathbb{I}_{\mathrm{P}} + \sum_{K=2}^{MK} \alpha_K \left(\frac{m_K}{5} \mathbb{I}_{\mathrm{D}} + \mathbb{A}_K^{\nu}(\phi^c) + \mathbb{H}_K(\phi^c) \right) .$$

Performing averaging over the whole orientation space we find that the self-consistent estimates for $\bar{h}^{\mathrm{P}}$ and $\bar{h}^{\mathrm{D}}$ are obtained from the set of two equations

$$\alpha^{\mathrm{P}} = \frac{(\bar{h}^{\mathrm{P}} - h^{\mathrm{P}})(\bar{h}^{\mathrm{P}} + h_*^{\mathrm{P}})}{h^{\mathrm{P}} + h_*^{\mathrm{P}}} = 0 , \tag{3.81}$$

$$\sum_{K=2}^{MK} \alpha_K m_K = (\bar{h}^{\mathrm{D}} + h_*^{\mathrm{D}}) \sum_{K=2}^{MK} \frac{(\bar{h}^{\mathrm{D}} - h_K) m_K}{h_K + h_*^{\mathrm{D}}} = 0 . \tag{3.82}$$

In view of positive definiteness of the local and macroscopic constitutive tensors, the first equation gives

$$\bar{h}^{\mathrm{P}} = h^{\mathrm{P}} , \tag{3.83}$$

which confirms the result of the previous subsection. Introducing (B.8) into the second equation, one can reduce it to the polynomial equation of odd degree $2MK - 3$ of the form:

$$\sum_{K=2}^{MK} (\bar{h}^{\mathrm{D}} - h_K) m_K \prod_{L=2(L \neq K)}^{MK} w^L(h_L, \bar{h}^{\mathrm{P}}, \bar{h}^{\mathrm{D}}) = 0 , \tag{3.84}$$

where

$$w^L(h_L, \bar{h}^{\mathrm{P}}, \bar{h}^{\mathrm{D}}) = 4(\bar{h}^{\mathrm{D}})^2 + 3(\bar{h}^{\mathrm{P}} + 2h_L)\bar{h}^{\mathrm{D}} + 2h_L\bar{h}^{\mathrm{P}} . \tag{3.85}$$

Eq. (3.84) serves to obtain $\bar{h}^{\mathrm{D}}$. We look for $\bar{h}^{\mathrm{D}}$ among positive real roots of this polynomial. It is important to note that the solution depends only on the values of local Kelvin moduli and their multiplicity, so the invariants of local stiffness tensor $\mathbb{L}$. Moreover, it should be stressed that knowledge about the multiplicity of Kelvin moduli is not necessary - formally one can solve this equation as a 9-degree one setting all $m_K = 1$ and assuming that all h_K are different:

$$\sum_{k=0}^{9} a_k (\bar{h}^{\mathrm{D}})^k = 0 . \tag{3.86}$$

One can show that coefficients a_k depend then on the invariant h^{P} and other invariants of deviatoric part of the stiffness tensor of the forms which are independent of the ordering of the local Kelvin moduli. Analysis of coefficients a_k leads to the conclusion that polynomial (3.86) has always single positive real root (for details see Kowalczyk-Gajewska [99]). Consequently, the admissible solution exists and is unique.

Anisotropic crystals

Using spectral decompositions (3.38)-(3.39) and formulae (3.40)-(3.41), it is found that

$$(\bar{\mathbb{L}} - \mathbb{L}) \circ \mathbb{A} = \underbrace{(\hat{\bar{\mathbb{L}}} - \hat{\mathbb{L}}) \circ \hat{\mathbb{A}}}_{\hat{\mathbb{R}}(\phi^c)} + \sum_{K=NK+1}^{MK} \underbrace{\frac{(\bar{h}^{\mathrm{D}} - h_K)(\bar{h}^{\mathrm{D}} + h_*^{\mathrm{D}})}{h_K + h_*^{\mathrm{D}}}}_{\alpha_K} \mathbb{P}_K(\phi^c) , \quad (3.87)$$

where

$$\hat{\mathbb{A}}(\phi^c) = (\hat{\mathbb{L}}(\phi^c) + \hat{\mathbb{L}}_*(\phi^c))^{-1} \circ (\hat{\bar{\mathbb{L}}}(\phi^c) + \hat{\mathbb{L}}_*(\phi^c)) , \quad (3.88)$$

$$\hat{\mathbb{L}}^*(\phi^c) = \hat{\mathbb{P}}(\phi^c) \circ \mathbb{L}_* = h_*^{\mathrm{P}} \mathbb{I}_{\mathrm{P}} + h_*^{\mathrm{D}} \hat{\mathbb{P}}_{\mathrm{D}}(\phi^c) , \quad (3.89)$$

$$\hat{\bar{\mathbb{L}}}(\phi^c) = \hat{\mathbb{P}}(\phi^c) \circ \bar{\mathbb{L}} = \bar{h}^{\mathrm{P}} \mathbb{I}_{\mathrm{P}} + \bar{h}^{\mathrm{D}} \hat{\mathbb{P}}_{\mathrm{D}}(\phi^c) . \quad (3.90)$$

An inverse in (3.88) is the partial inverse. Harmonic decompositions of projectors $\mathbb{P}_K$, $(K = NK + 1, ...MK)$ and of the symmetric part of $\hat{\mathbb{R}}(\phi^c)$:

$$\hat{\mathbb{R}}^s(\phi^c) = \hat{\alpha}^{\mathrm{P}} \mathbb{I}_{\mathrm{P}} + \hat{\alpha}^{\mathrm{D}} \mathbb{I}_{\mathrm{D}} + \hat{\mathbb{A}}^\mu(\phi^c) + \hat{\mathbb{A}}^\nu(\phi^c) + \hat{\mathbb{H}}(\phi^c), \quad (3.91)$$

are now performed. After averaging over the whole orientation space, two scalar equations which correspond to (3.82) are obtained:

$$\tilde{\alpha}^{\mathrm{P}} = 0 , \quad (3.92)$$

$$\tilde{\alpha}^{\mathrm{D}} + \sum_{K=NK+1}^{MK} \alpha_K m_K = 0 . \quad (3.93)$$

Similarly, like in the case of the Hashin-Shtrikman bounds, let us specify above equations for the materials in which $NK = 2$ and corresponding h_1 and h_2 are of multiplicity one. Introducing (3.49-3.52) into (3.88)-(3.90), after some algebra, it is found that

$$\tilde{\alpha}^{\mathrm{P}} = \frac{(\bar{h}^{\mathrm{P}} + h_*^{\mathrm{P}})((L_{12})^2 + (\bar{h}^{\mathrm{P}} - L_{11})(h_*^{\mathrm{D}} + L_{22}))}{(h_*^{\mathrm{P}} + L_{11})(h_*^{\mathrm{D}} + L_{22}) - (L_{12})^2} , \quad (3.94)$$

$$\widetilde{\alpha}^{\mathrm{D}} = \frac{(\bar{h}^{\mathrm{D}} + h_*^{\mathrm{D}})((L_{12})^2 + (h_*^{\mathrm{P}} + L_{11})(\bar{h}^{\mathrm{D}} - L_{22}))}{(h_*^{\mathrm{P}} + L_{11})(h_*^{\mathrm{D}} + L_{22}) - (L_{12})^2} \tag{3.95}$$

and Eqs. (3.92)-(3.93) are equivalent to

$$(L_{12})^2 + (\bar{h}^{\mathrm{P}} - L_{11})(h_*^{\mathrm{D}} + L_{22}) = 0 \,, \tag{3.96}$$

$$\frac{(L_{12})^2 + (h_*^{\mathrm{P}} + L_{11})(\bar{h}^{\mathrm{D}} - L_{22})}{(h_*^{\mathrm{P}} + L_{11})(h_*^{\mathrm{D}} + L_{22}) - (L_{12})^2} + \sum_{K=3}^{MK} \frac{(\bar{h}^{\mathrm{D}} - h_K)m_K}{h_K + h_*^{\mathrm{D}}} = 0 \,. \tag{3.97}$$

Due to relations (B.8), contrary to volumetrically isotropic materials, $\bar{h}^{\mathrm{P}}$ cannot be calculated independently of $\bar{h}^{\mathrm{D}}$.

The class of materials considered above is not artificial. All materials of transverse (hexagonal), trigonal and tetragonal symmetry belong to the considered group. All single crystals in Table 2.4 fall into this category. For these materials deviatoric tensor **d** is specified as (compare definition (A.28))

$$\mathbf{d} = \pm \frac{1}{\sqrt{6}} (3\mathbf{m} \otimes \mathbf{m} - \mathbf{I}) \,, \tag{3.98}$$

where **m** is the unit vector coaxial with the main axis of local symmetry. Formulae for self-consistent estimates for these classes of single crystal anisotropy have been provided by Berryman [12] in the form of implicit equations which are equivalent to (3.96) and (3.97). In Berryman [12] the quantity denoted as G_{eff}^V is introduced which is called "uniaxial shear energy" per unit volume for a unit applied shear strain. It is easily verified that $2G_{eff}^V = L_{22}$.

3.4.2. Fibre texture

Due to the same reasons as those invoked when discussing the Hashin-Shtrikman bounds for polycrystals of fibre texture, derivation of a self-consistent estimate of $\bar{\mathbb{L}}$ is more complicated.

In the case of fibre texture we find that the formula (3.78) on $\bar{\mathbb{L}}$ is more convenient for our purposes. Accordingly, we look for overall moduli $\bar{h}_K^{SC}$ and overall stiffness distributor $\bar{\xi}^{SC}$ solving the following non-linear tensorial equation:

$$\left(\bar{\mathbb{L}}(\bar{h}_{K\mathrm{SC}}, \bar{\xi}_{\mathrm{SC}}) + \mathbb{L}_*(\bar{h}_{K\mathrm{SC}}, \bar{\xi}_{\mathrm{SC}})\right)^{-1} - \left\langle \left(\mathbb{L}(\phi^c) + \mathbb{L}_*(\bar{h}_{K\mathrm{SC}}, \bar{\xi}_{\mathrm{SC}})\right)^{-1} \right\rangle_{\mathcal{Q}_\mathbf{n}} = 0 \,, \tag{3.99}$$

which reduces to the set of five non-linear scalar equations. Due to inverses present in above equation and the fact that tensors $\mathbb{L}_*$, $\bar{\mathbb{L}}$ and $\mathbb{L}(\phi^c)$, in general,

do not commute, specification of these scalar equations is not as straightforward as in the case of random texture. Below we only sketch an applied procedure. Denote

$$\mathbb{R}(\phi^c) = (\mathbb{L}(\phi^c) + \mathbb{L}_*(\bar{h}_{KSC}, \bar{\xi}_{SC}))^{-1} \qquad (3.100)$$

and perform spectral decomposition of $\mathbb{R}(0) = p_K \mathbb{P}_K^{(R)}(0)$ and harmonic decomposition of projectors $\mathbb{P}_K^{(R)}(0)$ in order to obtain, in a way analogous to that followed in derivation of an upper and lower bounds, MK sets of five scalars $\{\tilde{\eta}_K^P, \tilde{\eta}_K^D, \tilde{\alpha}_K^\mu, \tilde{\alpha}_K^\nu, \tilde{\eta}_K^H\}$. After using the property (3.12) we find:

$$\begin{aligned}
\langle \mathbb{R}(\phi^c) \rangle_{\mathcal{Q}_\mathbf{n}} &= \sum_{K=1}^{MK} p_K \tilde{\eta}_K^P \mathbb{I}_P + \sum_{K=1}^{MK} p_K \tilde{\eta}_K^D \mathbb{I}_D + \\
&+ \sum_{K=1}^{MK} p_K \tilde{\alpha}_K^\mu \mathbb{A}_\mathbf{n}^\mu + \sum_{K=1}^{MK} p_K \tilde{\alpha}_K^\nu \mathbb{A}_\mathbf{n}^\nu + \sum_{K=1}^{MK} p_K \tilde{\eta}_K^H \mathbb{H}_\mathbf{n} .
\end{aligned} \qquad (3.101)$$

We underline that all scalar quantities in the above formulae, in general depend on $\bar{h}_{KSC}$ and $\bar{\xi}_{SC}$. Similarly, denoting

$$\bar{\mathbb{R}} = (\bar{\mathbb{L}}(\bar{h}_{KSC}, \bar{\xi}_{SC}) + \mathbb{L}_*(\bar{h}_{KSC}, \bar{\xi}_{SC}))^{-1} \qquad (3.102)$$

and performing harmonic decompositions of $\bar{\mathbb{R}}$ one specifies five scalar equations resulting from (3.99), viz.:

$$\bar{h}^P(\bar{\mathbb{R}}) - \sum_{K=1}^{MK} p_K \tilde{\eta}_K^P = 0 , \quad \bar{h}^D(\bar{\mathbb{R}}) - \sum_{K=1}^{MK} p_K \tilde{\eta}_K^D = 0 , \qquad (3.103)$$

$$\bar{\alpha}^\mu(\bar{\mathbb{R}}) - \sum_{K=1}^{MK} p_K \tilde{\alpha}_K^\mu = 0 , \quad \bar{\alpha}^\nu(\bar{\mathbb{R}}) - \sum_{K=1}^{MK} p_K \tilde{\alpha}_K^\nu = 0 , \quad \bar{\eta}^H(\bar{\mathbb{R}}) - \sum_{K=1}^{MK} p_K \tilde{\eta}_K^H = 0 .$$
$$(3.104)$$

These equations simplify when $\mathbb{L}(0)$ and $\bar{\mathbb{L}}$ have some common external symmetries.

3.5. Materials with constraints

3.5.1. Incompressible materials

It was shown by Kowalczyk-Gajewska and Ostrowska-Maciejewska [103] that incompressible materials can be viewed as a special case of the volumetrically isotropic materials for which the bulk modulus is infinite,

$$h^P \to \infty . \qquad (3.105)$$

Solutions for upper and lower bounds as well as the self-consistent estimate presented in previous sections indicate that macroscopic bulk modulus is equal to the local one independently of crystallographic texture. Therefore, we also have

$$\bar{h}^{\mathrm{P}} \to \infty \,. \tag{3.106}$$

As far as the remaining Kelvin moduli are concerned, the solution depends on texture.

Random texture

The Voigt and Reuss bounds for an overall shear modulus $\bar{h}^{\mathrm{D}}$ are not changed and specified by Eqs. $(3.32)_2$ and $(3.34)_2$. Similarly, formula (3.37) for Hashin-Shtrikman bound on $\bar{h}^{\mathrm{D}}$ remains unaffected with an exception that

$$h_*^{\mathrm{P}} = \lim_{h_0^{\mathrm{P}} \to \infty} h_*^{\mathrm{P}} = 2h_0^{\mathrm{D}}, \quad h_*^{\mathrm{D}} = \lim_{h_0^{\mathrm{P}} \to \infty} h_*^{\mathrm{D}} = \frac{3}{2}h_0^{\mathrm{D}} \,. \tag{3.107}$$

The self-consistent estimate for the macroscopic shear modulus is also obtained with use of the above limit values for h_*^{P} and h_*^{D}, so Eq. (3.82) reduces to

$$5\bar{h}^{\mathrm{D}} \sum_{K=2}^{MK} \frac{(\bar{h}^{\mathrm{D}} - h_K)m_K}{2h_K + 3\bar{h}^{\mathrm{D}}} = 0, \quad \sum_{K=2}^{MK} m_K \leqslant 5 \,. \tag{3.108}$$

This equation, due to the assumptions $h_K > 0$ and $\bar{h}^{\mathrm{D}} > 0$, is equivalent to the following polynomial equation of MK-1 degree:

$$\sum_{K=2}^{MK} (\bar{h}^{\mathrm{D}} - h_K)m_K \prod_{L=2(L \neq K)}^{MK} (2h_K + 3\bar{h}^{\mathrm{D}}) = 0 \,. \tag{3.109}$$

One can prove that this polynomial has always exactly one real root which is positive. Consequently, the solution exists and is unique. Eq. (3.109), similarly to volumetrically isotropic materials, can be formulated with the use of invariants of the local stiffness tensor, cf. Kowalczyk-Gajewska [99].

Fibre texture

We have already found that the polycrystalline material of any texture composed of the volumetrically isotropic grains inherits the latter property. Therefore, the Voigt and Reuss bounds on the bulk modulus coincide, and in the case of incompressible crystals one has

$$\bar{h}_{1\mathrm{UP}*} = \bar{h}_{1\mathrm{LO}*} = \bar{h}^{\mathrm{P}} \to \infty \,. \tag{3.110}$$

The bounds on the deviatoric moduli $h_{K\mathrm{UP}*}$ and $h_{K\mathrm{LO}*}$, where $K = 2, 3, 4$, remain the same as for volumetrically isotropic materials. As concerns the Hashin-Shtrikman bounds and the self-consistent estimates, as already pointed out by Hutchinson [69], the limit analysis of the Hill tensor of transverse isotropy analogous to specification (3.107) does not lead to any utilizable conclusion, therefore one can only study these bounds and estimates numerically by considering volumetrically isotropic materials with a bulk modulus set to be much higher than the other moduli.

3.5.2. Materials with restricted deformation modes

It was shown by Kowalczyk-Gajewska and Ostrowska-Maciejewska [103] that the subspace of restricted deformation modes is the eigenspace of the corresponding constitutive fourth-order tensor. The dimension of this subspace is denoted by m^*, where m^* is also the multiplicity of the infinite Kelvin modulus $h^* \to \infty$. Consequently, spectral decompositions (3.3) have the form:

$$\mathbb{L}(\phi^c) = h^* \mathbb{P}^*(\phi^c) + \sum_{K=2}^{MK} h_K \mathbb{P}_K(\phi^c)\,, \tag{3.111}$$

$$\mathbb{M}(\phi^c) = \underbrace{\frac{1}{h^*}}_{\to 0} \mathbb{P}^*(\phi^c) + \sum_{K=2}^{MK} \frac{1}{h_K}\mathbb{P}_K(\phi^c) = \sum_{K=2}^{MK} \frac{1}{h_K}\mathbb{P}_K(\phi^c)\,. \tag{3.112}$$

Below we consider only the case of random polycrystal, since not much can be said regarding the fibre texture. In the latter case, solution will depend on the relation between local symmetry of $\mathbb{P}^*(0)$ with respect to macroscopic transverse isotropy.

Random texture

Formulae for an upper bound for macroscopic bulk and shear moduli are re-written as

$$\bar{h}_{\mathrm{UP}}^{\mathrm{P}} = h^* \eta^{\mathrm{P}*} + \sum_{K=2}^{MK} h_K \eta_K^{\mathrm{P}}, \quad \bar{h}_{\mathrm{UP}}^{\mathrm{D}} = h^* \eta^{\mathrm{D}*} + \sum_{K=2}^{MK} h_K \eta_K^{\mathrm{D}}\,. \tag{3.113}$$

It is seen that $\bar{h}_{\mathrm{UP}}^{\mathrm{P}}$ is finite only when $\eta^{\mathrm{P}*} = 0$ (it means that the subspace $\mathcal{P}^*$ generated by $\mathbb{P}^*$ is the subspace of deviatoric tensors), while the modulus $\bar{h}_{\mathrm{UP}}^{\mathrm{D}}$ is finite when $\eta^{\mathrm{D}*} = 0$ which is equivalent to $\eta^{\mathrm{P}*} = m^*$. Apparently,

both situations cannot take place simultaneously and $\bar{h}_{\mathrm{UP}}^{\mathrm{D}}$ is finite only when $m^* = \eta_{\mathrm{P}*} = 1$. It is the case when material is incompressible.

Formulae for lower bounds are re-written as

$$\bar{h}_{\mathrm{LO}}^{\mathrm{P}} = \left(\underbrace{\frac{\eta^{\mathrm{P}*}}{h^*}}_{\to 0} + \sum_{K=2}^{MK} \frac{\eta_K^{\mathrm{P}}}{h_K} \right)^{-1} = \left(\sum_{K=2}^{MK} \frac{\eta_K^{\mathrm{P}}}{h_K} \right)^{-1}, \tag{3.114}$$

$$\bar{h}_{\mathrm{LO}}^{\mathrm{D}} = \left(\underbrace{\frac{\eta^{\mathrm{D}*}}{h^*}}_{\to 0} + \sum_{K=2}^{MK} \frac{\eta_K^{\mathrm{D}}}{h_K} \right)^{-1} = \left(\sum_{K=2}^{MK} \frac{\eta_K^{\mathrm{D}}}{h_K} \right)^{-1} \tag{3.115}$$

and both are finite provided that there exists at least one K for which h_K is finite, and simultaneously

$$\eta_K^{\mathrm{D}} \neq 0 \quad \text{and} \quad \eta_K^{\mathrm{D}} \neq 0. \tag{3.116}$$

If additional restrictions have been imposed on the incompressible materials, as far as an upper bound is concerned, both macroscopic moduli are infinite so there is no upper bound, while there exists a lower bound for an overall shear modulus as long as some modes of deformation are not restricted. Similar conclusions are true for the Hashin-Shtrikman bounds.

Let us pass to self-consistent estimates for volumetrically isotropic materials with constrained deformation modes. We begin with the situation when the space of constrained deformation is the subspace of the deviatoric second-order tensors. As previously, m^* denotes the dimension of this subspace and, at the same time, the multiplicity of the corresponding Kelvin modulus h^*. Consequently, the estimate (3.83) for the overall bulk modulus is still valid. Introducing (3.111), Eq. (3.84) can be re-written as follows:

$$\frac{(\bar{h}^{\mathrm{D}} - h^*)m^*}{2h^*(h^{\mathrm{P}} + 3\bar{h}^{\mathrm{D}}) + \bar{h}^{\mathrm{D}}(3h^{\mathrm{P}} + 4\bar{h}^{\mathrm{D}})} + \sum_{K=3}^{MK} \frac{(\bar{h}^{\mathrm{D}} - h_K)m_K}{w^K(h_K, h^{\mathrm{P}}, \bar{h}^{\mathrm{D}})} = 0. \tag{3.117}$$

Taking the limit for $h^* \to \infty$ we are left with

$$\frac{-m^*}{2(h^{\mathrm{P}} + 3\bar{h}^{\mathrm{D}})} + \sum_{K=3}^{MK} \frac{(\bar{h}^{\mathrm{D}} - h_K)m_K}{w^K(h_K, h^{\mathrm{P}}, \bar{h}^{\mathrm{D}})} = 0, \tag{3.118}$$

which, under assumptions that $\bar{h}^{\mathrm{D}} > 0$ and $h_K > 0$, is equivalent to the polynomial equation of degree $2(MK - 2)$:

$$
\sum_{K=3}^{MK} 2(\bar{h}^{\mathrm{D}} - h_K)(h^{\mathrm{P}} + 3\bar{h}^{\mathrm{D}})m_K \prod_{L=3(L\neq K)}^{MK} w^L(h_L, \bar{h}^{\mathrm{P}}, \bar{h}^{\mathrm{D}}) +
$$
$$
- m^* \prod_{K=3}^{MK} w^K(h_K, \bar{h}^{\mathrm{P}}, \bar{h}^{\mathrm{D}}) = 0 \,. \tag{3.119}
$$

A positive, finite solution to the above polynomial equation exists and is unique as long as $m^* \leqslant 2$. In other words, a finite self-consistent estimate for the overall shear modulus exists as long as the dimension of a space of restricted (constrained) deviatoric deformation modes is not greater than two.

Now, let us consider incompressible materials in which additionally some subspace of deviatoric deformation modes is constrained. As it has been already shown, the overall bulk modulus is infinite in this case. Let us re-write Eq. (3.108) as follows:

$$
5\bar{h}^{\mathrm{D}} \frac{(\bar{h}^{\mathrm{D}} - h^*)m^*}{2h^* + 3\bar{h}^{\mathrm{D}}} + 5\bar{h}^{\mathrm{D}} \sum_{K=3}^{MK} \frac{(\bar{h}^{\mathrm{D}} - h_K)m_K}{2h_K + 3\bar{h}^{\mathrm{D}}} = 0, \quad \sum_{K=3}^{MK} m_K \leqslant 4 \,, \tag{3.120}
$$

where, as previously, m^* denotes the dimension of the constrained subspace of deviatoric deformation modes (due to incompressibility, total dimension of the space of constrained deformation modes is $m^* + 1$). Now we take a limit of this equation for $h^* \to \infty$ and find the counterpart of polynomial equation (3.109),

$$
\sum_{K=3}^{MK} 2(\bar{h}^{\mathrm{D}} - h_K)m_K \prod_{L=3(L\neq K)}^{} (2h_L + 3\bar{h}^{\mathrm{D}}) -
$$
$$
- m^* \prod_{K=3}^{} (2h_K + 3\bar{h}^{\mathrm{D}}) = 0 \,, \tag{3.121}
$$

which is of degree $MK - 2$. A positive, finite solution to the above polynomial equation exists and is unique only if $m^* = 1$. In other words, in the case of incompressible materials the self-consistent estimate for the overall shear modulus is finite only when the subspace of restricted deviatoric modes is one-dimensional.

3.6. Examples

3.6.1. Elastic properties

First, we apply the derived formulae to evaluate bounds and self-consistent estimates of elastic properties of selected polycrystalline metals and alloys. Elastic constants for single crystals of these materials are collected in Table 2.1 in Chapter 2. In Table 3.1 we provide the invariants resulting from spectral and harmonic decompositions of the corresponding local elasticity tensor for these materials. The following conclusions result from the analysis of this table:

- All analysed metals and alloys, with exception of Zn, are close to be volumetrically isotropic materials (ξ is close to zero). Note that Cu and Al, being cubic materials, are volumetrically isotropic exactly.

- In view of the above property, the elastic anisotropy degree can be assessed comparing the Kelvin moduli h_2 to h_6. For example, one observes that elastic anisotropy of Mg or Al crystals is not strong, and it is strong for Zn or Cu.

Table 3.1. Kelvin moduli h_K [GPa], η_1^{P}, a stiffness distributor ξ and $\Phi = \arctan(3\xi)$ obtained by spectral decomposition of the local elasticity tensor for single crystals of selected materials.

Material	h_1	h_2	h_3	h_4	$h_5 = h_6$	η_1^{P}	ξ	Φ [^{o}]
Mg	105.7	40.8	33.6		32.8	0.9998	-0.0051	-0.87
Zn	233.2	30.4	127.3		77.6	0.961	-0.0674	-11.43
Zr	286.4	94.5	71.0		64.2	0.9988	0.0117	2.01
Ti	322.6	114.2	72.6		94.4	0.9999	-0.0035	-0.61
α_2-Ti$_3$Al	332.6	151.1	86.4		125.2	0.9977	0.0161	2.77
γ-TiAl	330.0	105.1	108.9	156.8	210	0.9999	-0.0033	-0.56
Cu	415.0	49.0	138.2			1	0	0
Al	228.9	46.5	56.6			1	0	0

In Tables 3.2 and 3.3 bounds and self-consistent estimates of the bulk modulus $\bar{h}^{\mathrm{P}}$ and the shear modulus $\bar{h}^{\mathrm{D}}$, calculated with the use of the derived formulae for an *untextured polycrystal*, are collected. They are presented with an accuracy to six digits in order to demonstrate the quality of bounds. Such an accuracy is of course irrelevant in view of the accuracy which can be achieved in experiments when establishing elastic constants for single crystals. As far as the value of distributor ξ for all analysed cases is close to zero, the obtained bounds on the bulk modulus are very narrow with exception of Zn for which value of ξ is the highest. As it could be expected, the bounds on the shear modulus are

Table 3.2. Upper and lower bounds and a self-consistent estimate of the bulk modulus $\bar{h}^{\mathrm{P}}$ [GPa] of untextured polycrystals.

Material	$h^{\mathrm{P}}_{\mathrm{LO}}$	$h^{\mathrm{P}}_{\mathrm{LO/HS}}$	$h^{\mathrm{P}}_{\mathrm{SC}}$	$h^{\mathrm{P}}_{\mathrm{UP/HS}}$	$h^{\mathrm{P}}_{\mathrm{UP}}$
Mg	105.676	105.687	105.688	105.688	105.700
Zn	184.753	202.441	212.708	215.681	225.233
Zr	285.687	285.898	285.910	285.940	286.167
Ti	322.490	322.509	322.510	322.513	322.533
α_2-Ti$_3$Al	331.693	331.892	331.918	331.952	332.200
γ-TiAl	329.887	329.911	329.914	329.917	329.933
Cu	415.0				
Al	228.9				

Table 3.3. Upper and lower bounds and a self-consistent estimate of shear modulus $\bar{h}^{\mathrm{D}}$ [GPa] of untextured polycrystals.

Material	$h^{\mathrm{D}}_{\mathrm{LO}}$	$h^{\mathrm{D}}_{\mathrm{LO/HS}}$	$\bar{h}^{\mathrm{D}}_{\mathrm{SC}}$	$h^{\mathrm{D}}_{\mathrm{UP/HS}}$	$h^{\mathrm{D}}_{\mathrm{UP}}$
Mg	34.479	34.594	34.597	34.606	34.720
Zn	68.251	75.860	81.151	82.931	89.633
Zr	71.536	72.223	72.259	72.352	73.027
Ti	86.976	88.263	88.370	88.514	89.653
α_2-Ti$_3$Al	109.265	111.880	112.180	112.556	114.900
γ-TiAl	144.533	150.338	151.355	152.239	158.173
Cu	89.333	89.574	92.608	94.374	94.440
Al	52.076	52.328	52.340	52.348	52.560

narrower when the elastic anisotropy is weaker. It is observed that the Hashin-Shtrikman bounds are usually considerably better than the Voigt and Reuss bounds. It seems that exceptional behaviour of Zn has its source in a high c/a ratio as compared to other materials under consideration, see Table 2.1.

In Table 3.4 the self-consistent estimates of an overall Young modulus $\bar{E}$ and a shear modulus $\bar{G} = 1/2\bar{h}^{\mathrm{D}}$ are compared with the corresponding experimental values for random polycrystals available in the literature. As it can be concluded, the self-consistent estimate is usually in good agreement with experimental values.

Now, let us consider the polycrystals of fibre textures. For all analysed materials of Table 2.1 we have derived the formulae for the upper Voigt bound and the lower Reuss bound on the overall transversely isotropic elasticity tensor $\bar{\mathbb{L}}$. We have also derived the Hill type estimate of the this tensor defined in the tensorial way,

$$\bar{\mathbb{L}}_{\mathrm{H}} = \frac{1}{2} \left(\bar{\mathbb{L}}_{\mathrm{UP}} + \bar{\mathbb{L}}_{\mathrm{LO}} \right) . \tag{3.122}$$

Table 3.4. Comparison of the Young modulus $\bar{E}$ [GPa] and the shear modulus $\bar{G}$ [GPa] obtained with use of the self-consistent estimate of $\bar{h}^{\mathrm{P}}$ and $\bar{h}^{\mathrm{D}}$ with experimental values available in the literature for untextured polycrystals.

Material	E_{SC}	G_{SC}	E_{exp}	G_{exp}
Mg	44.6	17.3	44.7 [212]/41.3 [12]	16/15.8
Zn	102.2	40.6	102.96 [12]	41.2 [12]
Zr	96.2	36.1	91.34 [225]/96 [226]	36 [226]
Ti	116.6	44.2	116 [152]	44 [152]
α_2-Ti$_3$Al	143.9	56.1	144 [227]	56[227]
γ-TiAl	184.7	75.7	185 [227]	76 [227]
Cu	125.0	46.3	123.0/123.05[12]	45.5/45.6 [12]
Al	70.5	26.2	70.3/71.0[12]	26.1/26.5 [12]

Note that due to the non-zero stiffness distributor $\bar{\xi}$, this definition results in

$$\bar{h}_K \neq \frac{1}{2}(\bar{h}_{K\mathrm{UP}} + \bar{h}_{K\mathrm{LO}}), \quad \text{for} \quad K = 1, 2. \tag{3.123}$$

The variation of bounds and the Hill estimate on the Kelvin moduli and the stiffness distributor $\bar{\xi}$ for subsequent metals and alloys of hexagonal symmetry with respect to the fibre direction $\mathbf{n}$ are presented in Figs 3.3-3.5. Angle ϕ is the angle between the direction $\mathbf{n}$ and the local anisotropy axis $\mathbf{c}$. Note that $\mathbf{n}$ is the overall anisotropy axis. As it can be observed, similarly as in the case of random texture, quality of bounds depends on the intensity of local anisotropy, therefore, the bounds are narrow for Mg polycrystal, while they are the widest for Zn polycrystal. Similarly, the intensity of overall anisotropy is correlated with the intensity of the local one. One should note that for $\phi = 0$ the local $\mathbb{L}$ and overall $\bar{\mathbb{L}}$ are the same. The other feature common for elastic properties of polycrystals of fibre texture composed of hexagonal crystals is the fact that there exist such fibre directions $\mathbf{n}$ for which corresponding polycrystalline material is volumetrically isotropic. One notes that, as far as locally material is also transversely isotropic, all tensors $\phi_K(\phi^c)$ in harmonic decomposition are proportional to $\mathbf{d_c}$ (Eq. (3.98)), where $\mathbf{c}$ is the direction of the main axis of local anisotropy, therefore

$$\phi_K(0) \cdot \mathbf{d_n} \sim \mathbf{d_c} \cdot \mathbf{d_n} = \frac{1}{2}(3\cos^2\phi - 1). \tag{3.124}$$

Consequently, the values of $\bar{\alpha}_{\mathrm{UP}}^{\mu}$ and $^{M}\bar{\alpha}_{\mathrm{LO}}^{\mu}$ are equal to zero, independently of the value of the local Kelvin moduli, if

$$\cos^2\phi = \frac{1}{3}. \tag{3.125}$$

Fig. 3.3. Elastic properties of Mg and Zn polycrystals of fibre texture. Bounds and the Hill estimate on stiffness distributor $\bar{\xi}$ (a), the Kelvin modulus $\bar{h}_1$ (b), and the Kelvin moduli $\bar{h}_K$ ($K = 2, ..., 4$) (c). The Kelvin moduli $\bar{h}_K, K = 2, 3, 4$ are scaled by a self-consistent estimate of shear modulus $\bar{h}_{SC}^D$ while the Kelvin modulus $\bar{h}_1$ is scaled by a self-consistent estimate of the bulk modulus $\bar{h}_{SC}^P$ for untextured polycrystals (see Tables 3.3 and 3.2).

As it has been already discussed, the anisotropy degree of a polycrystal of fibre texture can be approximately assessed by a relative difference in the Kelvin moduli $\bar{h}_2, ..., \bar{h}_4$, provided that the polycrystal is close to be volumetrically isotropic. If it is not the case, one can study the directional Young modulus, cf. Ostrowska-Maciejewska and Rychlewski [153], defined as follows:

$$\bar{E}(\mathbf{m}) = \left((\mathbf{m} \otimes \mathbf{m}) \cdot \bar{\mathbb{M}} \cdot (\mathbf{m} \otimes \mathbf{m})\right)^{-1} , \tag{3.126}$$

Fig. 3.4. Elastic properties of Zr and Ti polycrystals of fibre texture. Bounds and the Hill estimate on stiffness distributor $\bar{\xi}$ (a), the Kelvin modulus $\bar{h}_1$ (b), and the Kelvin moduli $\bar{h}_K$ ($K = 2, ..., 4$) (c). The Kelvin moduli $\bar{h}_K, K = 2, 3, 4$ are scaled by a self-consistent estimate of shear modulus $\bar{h}_{SC}^D$, while the Kelvin modulus $\bar{h}_1$ is scaled by a self-consistent estimate of the bulk modulus $\bar{h}_{SC}^P$ for untextured polycrystals (see Tables 3.3 and 3.2).

where $\mathbf{m}$ is any direction in 3 dimensional space. In the case of the overall transverse isotropy the value of $\bar{E}(\mathbf{m})$ depends only on the relative orientation of $\mathbf{m}$ and $\mathbf{n}$ - the main axis of macroscopic anisotropy. In Fig. 3.6 the value of the directional Young modulus is presented for polycrystals of three different fibre textures. In general, it is found that the strongest anisotropy is observed when the main axes of local and macroscopic anisotropy coincide.

The variation of the Hill estimate of the Kelvin moduli and of the stiffness distributor $\bar{\xi}$ for Al and Cu metals of cubic symmetry and tetragonal γ-TiAl
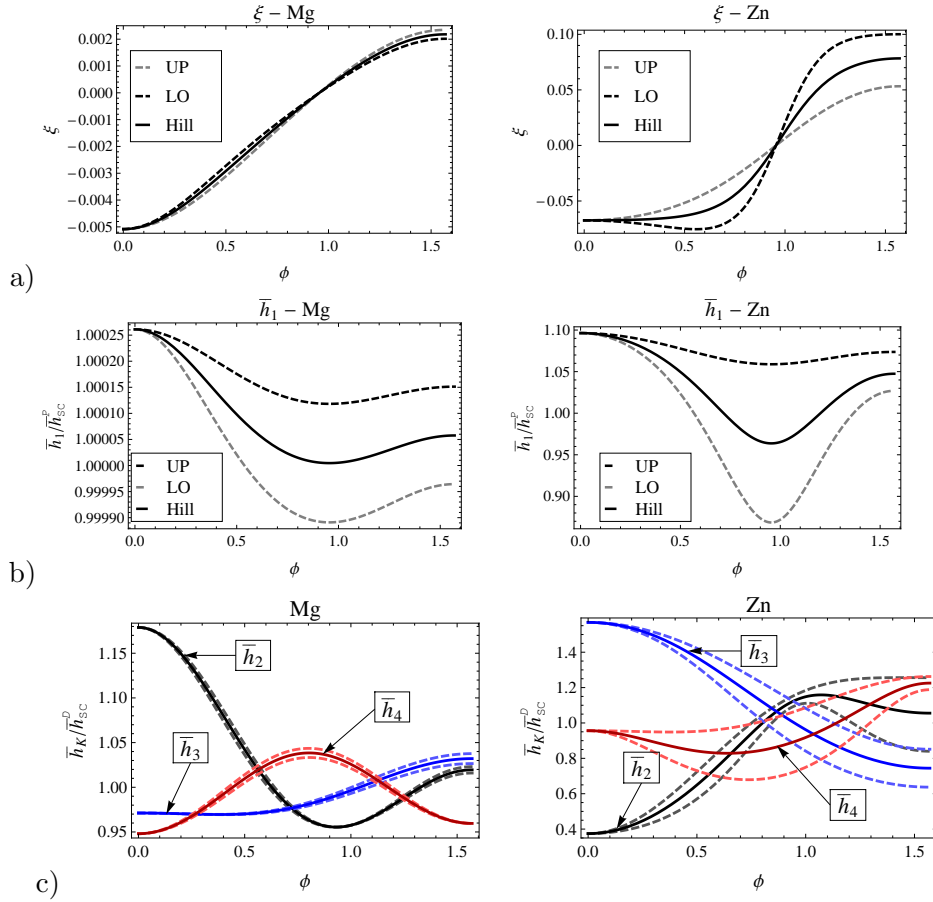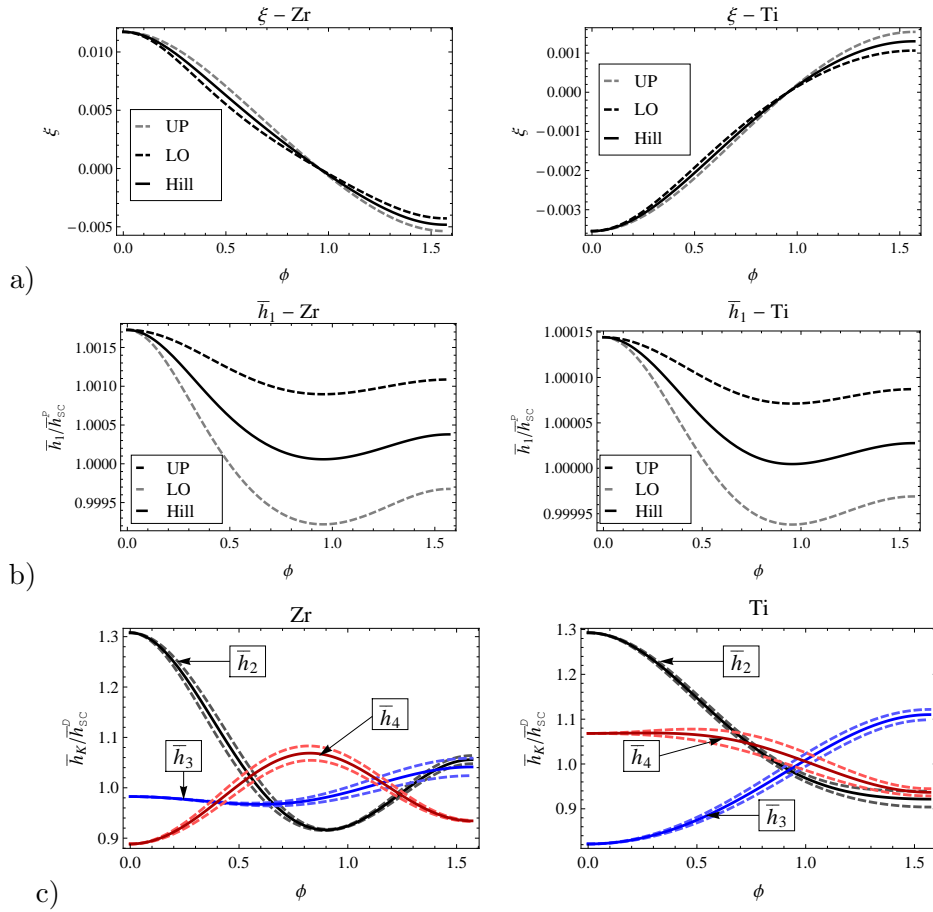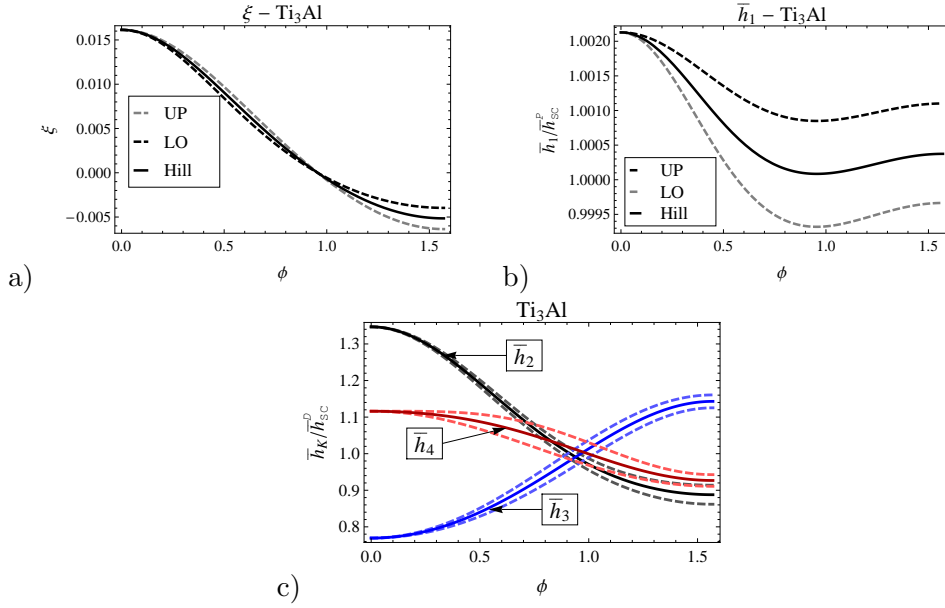
Fig. 3.5. Elastic properties of Ti$_3$Al polycrystals of fibre texture. Bounds and the Hill estimate on stiffness distributor $\bar{\xi}$ (a), the Kelvin modulus $\bar{h}_1$ (b), and the Kelvin moduli $\bar{h}_K$ ($K = 2, ..., 4$) (c). The Kelvin moduli $\bar{h}_K, K = 2, 3, 4$ are scaled by a self-consistent estimate of shear modulus $\bar{h}_{SC}^D$, while the Kelvin modulus $\bar{h}_1$ is scaled by a self-consistent estimate of the bulk modulus $\bar{h}_{SC}^P$ for untextured polycrystals (see Tables 3.3 and 3.2).

intermittent polycrystals of fibre texture with respect to the direction $\mathbf{n}$ are presented in Fig. 3.7. For materials of such a symmetry the resulting properties depend on the orientation of $\mathbf{n}$ with respect to all three local anisotropy axes. For selected directions of $\mathbf{n}$, the bounds and the Hill estimates of $\bar{h}_K$ ($K = 2, 3, 4$) are presented in Fig. 3.8. The notation "plane (001)" and "plane (110)" means that $\mathbf{n}$ is coaxial with a crystallographic plane (001) and (110), respectively. Angle ϕ is measured against the one of anisotropy axes, that is $\mathbf{a}_1$ and $\mathbf{a}_3 = \mathbf{c}$, respectively. As it is observed, since local anisotropy of Al is weak, the overall anisotropy of corresponding polycrystal of fibre texture is also weak. Reversely, since the local anisotropy of Cu is strong, the overall anisotropy of polycrystal of fibre texture is also strong. The anisotropy of γ-TiAl is stronger than anisotropy of Al, but weaker than Cu. The directional Young modulus for fibre textures $\langle 001]$ and $\langle 111 \rangle$ is presented in Fig. 3.9. Cubic crystals (Cu,Al) are volumetrically isotropic, therefore, as it has been already shown, $\bar{h}_1$ is equal to the local h^P. γ-TiAl crystal is not volumetrically isotropic, however, the value of a local stiffness distributor ξ is small (see Table 3.1). Consequently,
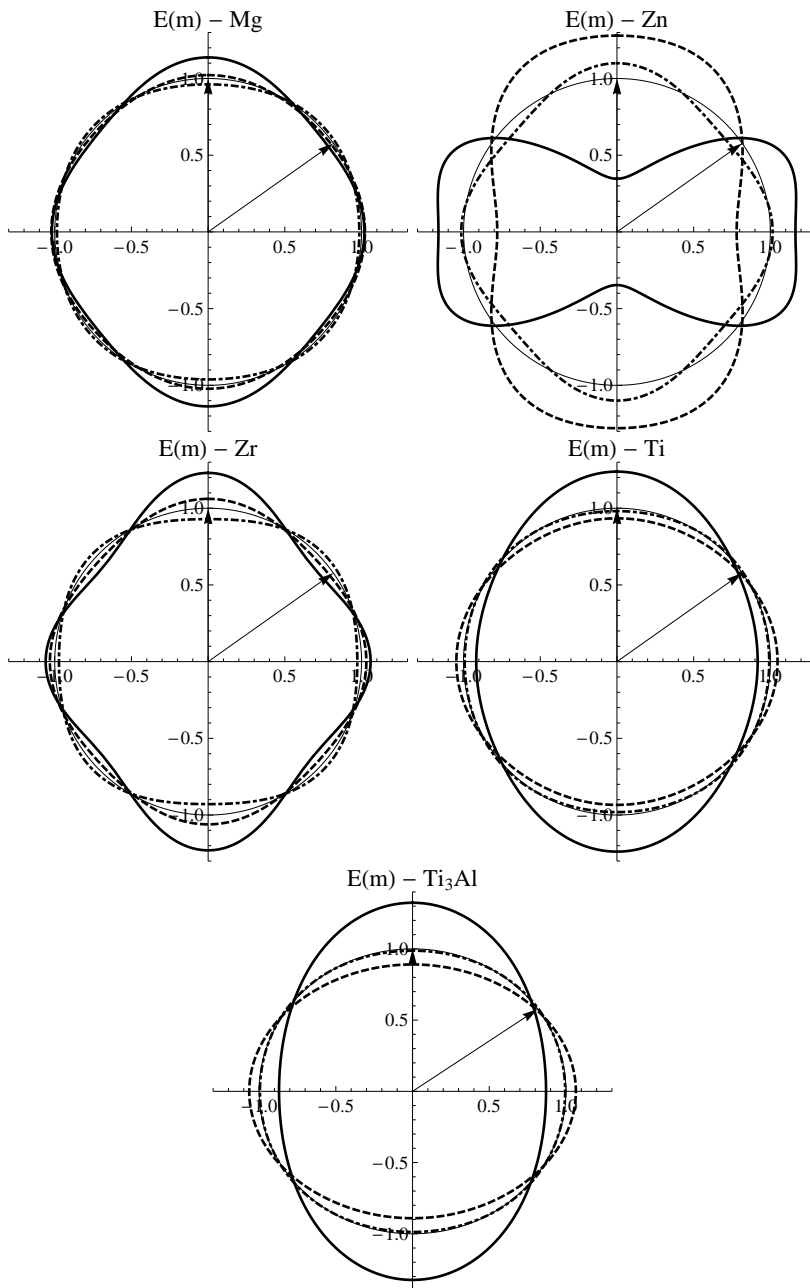
Fig. 3.6. Comparison of anisotropy of the Hill estimate of a directional Young modulus $\bar{E}(\mathbf{m})$ for polycrystals of fibre texture: $\mathbf{n} \cdot \mathbf{c} = 1$ - thick black line, $\mathbf{n} \cdot \mathbf{c} = 1/\sqrt{3}$ (volum. isotropic polycrystal) - thick grey line $\mathbf{n} \cdot \mathbf{c} = 0$ - dashed black line, for various metals of hexagonal symmetry. Thin black line indicates the isotropic behaviour. The value of $\bar{E}(\mathbf{m})$ is scaled by the self-consistent estimate of $\bar{E}$ for untextured polycrystals (see Table 3.4).
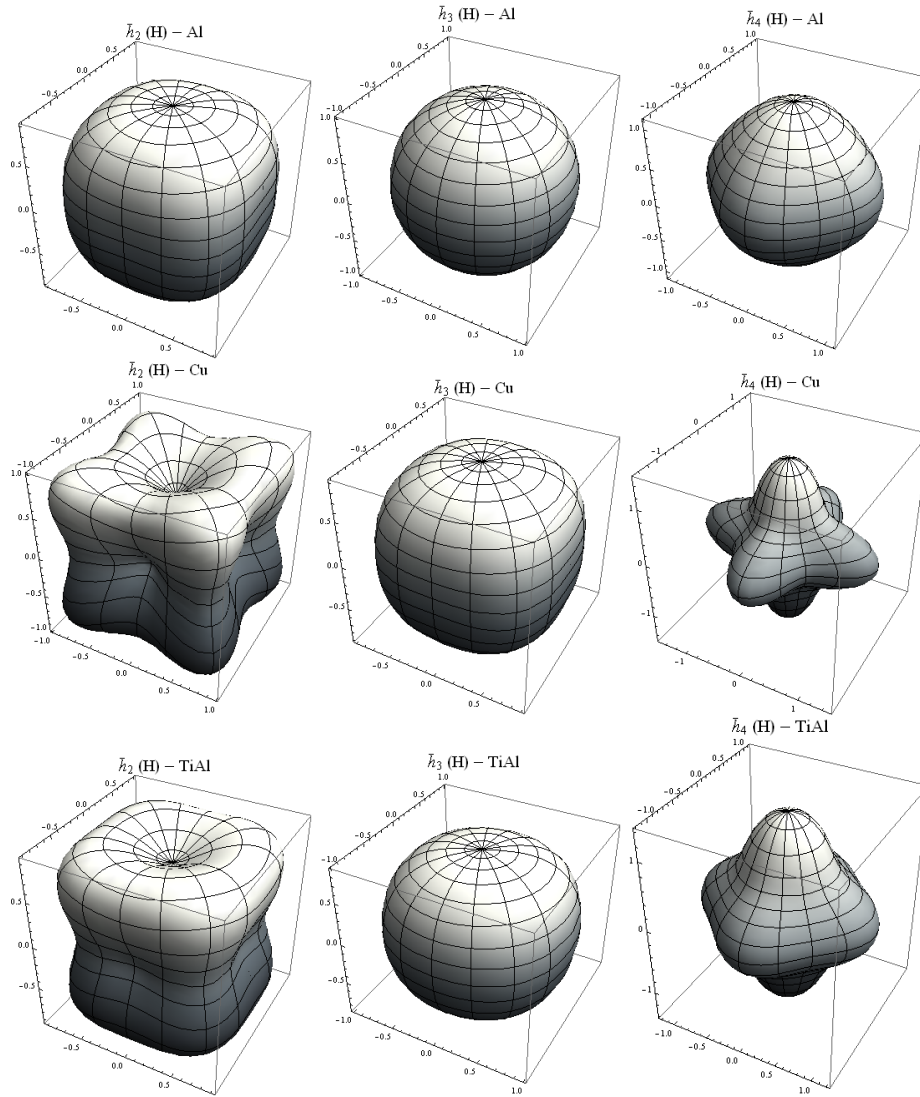
Fig. 3.7. Dependence of the Hill estimate of the overall Kelvin moduli $\bar{h}_K$ ($K = 2, 3, 4$) upon the direction of fibre texture $\mathbf{n}$ for Al, Cu and γ-TiAl polycrystals. The value of $\bar{h}_K$ is scaled by the self-consistent estimate of $\bar{h}_{\mathrm{SC}}^{\mathrm{D}}$ for untextured polycrystals (see Table 3.3).
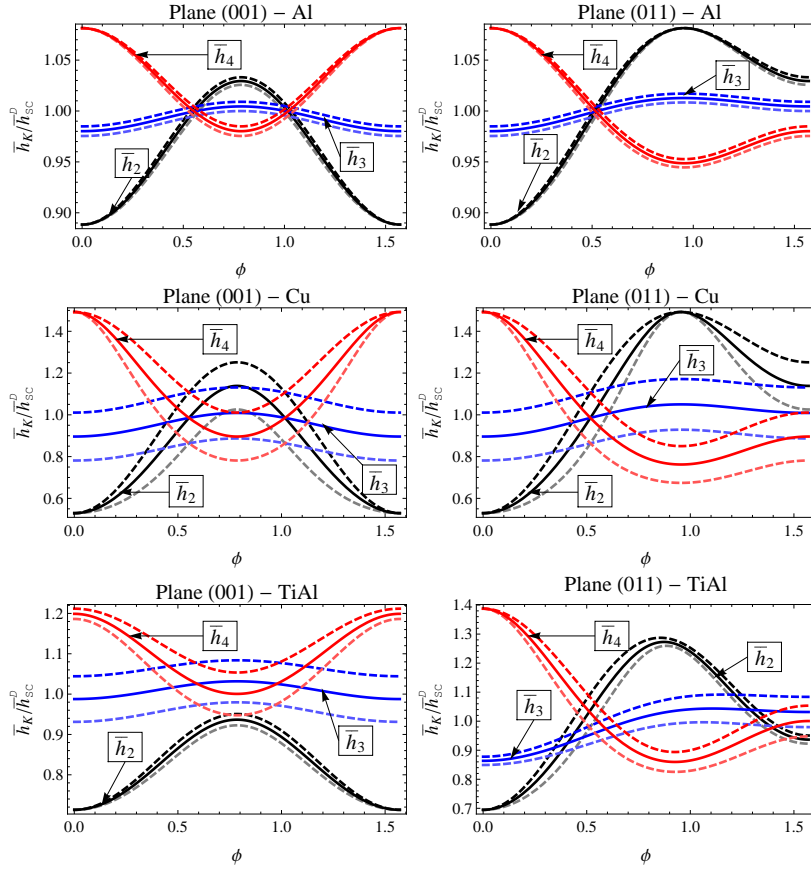
Fig. 3.8. Elastic properties of Al, Cu and γ-TiAl polycrystals of selected fibre textures. Bounds and the Hill estimate for the Kelvin moduli $\bar{h}_K$ ($K = 2, ..., 4$). Values are scaled by the self-consistent estimate of shear modulus $\bar{h}_{\mathrm{SC}}^{\mathrm{D}}$ for untextured polycrystals.

although values of bounds and estimates for $\bar{h}_1$ vary with $\mathbf{n}$, these variations do not exceed 0.012% of $\bar{h}_{\mathrm{SC}}^{\mathrm{P}}$. Note that the property specified by (3.124)-(3.125) is also valid for materials of trigonal and tetragonal (γ-TiAl) symmetries.

The Hashin-Shtrikman bounds and self-consistent estimates for the elastic properties of polycrystals of fibre textures have not been provided since in all cases the Voigt and Reuss bounds are relatively narrow and the Hill estimate is supposed to approximate the overall properties with an acceptable accuracy.

E(m) − Al

E(m) − Cu

E(m) − TiAl

Fig. 3.9. Comparison of anisotropy of the Hill estimate of a directional Young modulus $\bar{E}(\mathbf{m})$ for Al, Cu and γ-TiAl polycrystals of fibre texture: (001] - a thick black line and $\langle 111 \rangle$ - a thick grey line. A thin black line indicates the isotropic behaviour. The value of $\bar{E}(\mathbf{m})$ is scaled by the self-consistent estimate of $\bar{E}$ for untextured polycrystals (see Table 3.4).
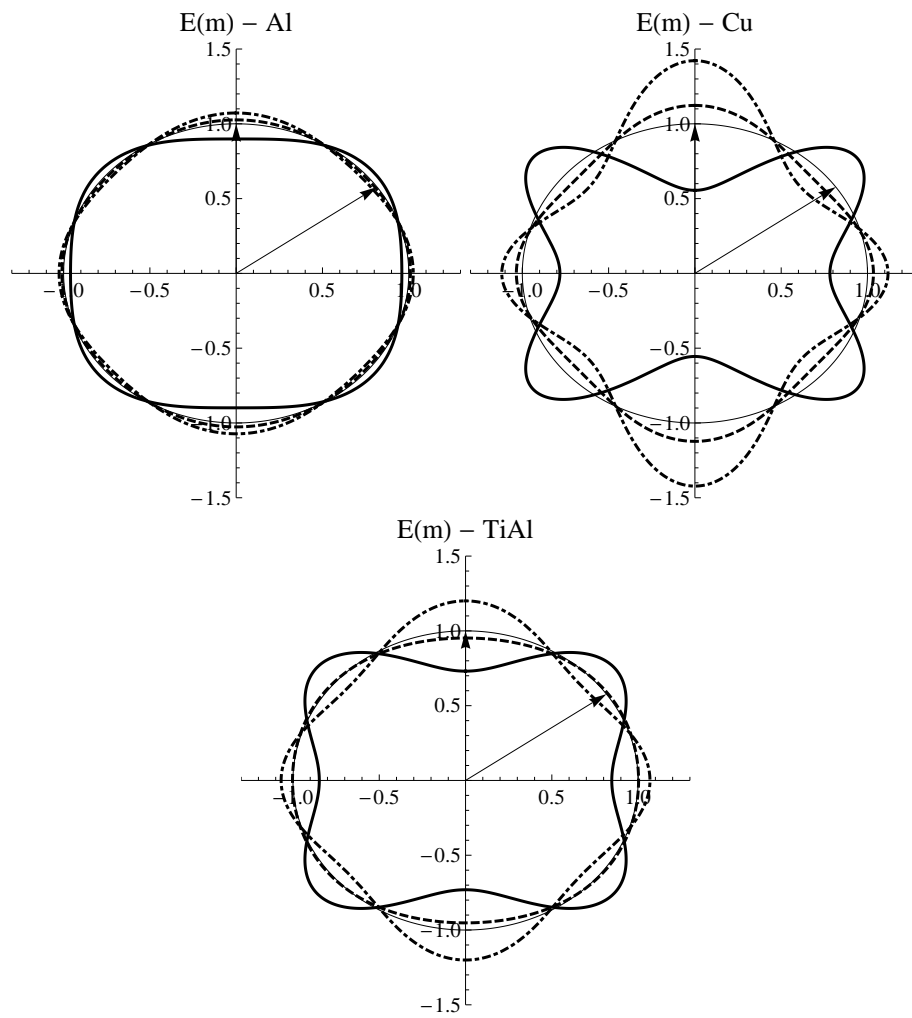
3.6.2. Linear viscous properties

As it will be shown below, the results concerning materials with the constrained deformation modes are very useful when considering the inelastic deformations of polycrystalline metals with an insufficient number of easy slip systems. To this end we consider incompressible linear viscous materials described by (2.27) where $n = 1$. Note that usually $n > 1$ is identified for the analysed materials. Then single crystal is described by a non-linear constitutive law. Consequently, derivation of bounds and self-consistent estimates requires an appropriate linearization of a problem and the solutions depend on a loading scheme. The non-linear case will be considered in the next chapter. Let us only say that for $n > 1$ estimates are found numerically by discretization of the orientation space, e.g. Hutchinson [69], Nebozhyn et al. [143], Bornert et al. [19]. In these calculations knowledge about the analytical solutions for the linear case $n = 1$ is beneficial from the point of view of verification of the applied numerical procedures. Moreover, it provides good initial approximation to a solution. Furthermore, as it will be shown in the next sections, some of the properties of a solution for the linear case can be transferred to the non-linear case.

Introducing (2.27) with $n = 1$ into (2.8), the local linear viscous relation is obtained in the form:

$$\dot{\boldsymbol{\varepsilon}}^v = \mathbb{M}^v \cdot \boldsymbol{\sigma}, \quad \mathbb{M}^v = v_0 \sum_{r=1}^{M} \frac{1}{\tau_c^r} \mathbf{P}^r \otimes \mathbf{P}^r. \tag{3.127}$$

As it has been discussed in Sec. 2.2, the number M and geometry of slip systems, here included in the definition of the symmetrized Schmid tensor $\mathbf{P}^r$, depend on the geometry of crystallographic lattice of a single crystal. Clearly, material described by (3.127) is incompressible. Note that the constitutive relation (2.27) can be also applied when describing steady creep of the considered polycrystals, cf. Hutchinson [69].

In the case of metals and alloys of high specific strength, the group of easy slip systems usually does not fulfil the Taylor condition. In Nebozhyn et al. [143], on the basis of the analysis of the variational self-consistent estimates for random power-law polycrystals with reduced number $1 < i < 5$ of independent easy slip systems, it was found that the overall flow stress follows the following scaling law:

$$\bar{\sigma}_Y \sim \left(\rho_{hard}\right)^{\frac{4-i}{2}}, \tag{3.128}$$

where $\rho_{hard} = \tau_c^{hard}/\tau_c^{easy}$. This law is independent of the exponent n. Before analysing the examples we will show that such a scaling law could be easily deduced from the analytic formula (3.109) for linear polycrystals.

Assume the crystal with easy and hard categories of slip modes and with the critical shear stress for the hard modes much higher than for the easy ones. For the purpose of the analysis of a scaling law, without introducing significant approximations, the local viscous compliance (3.127) can be written as

$$\mathbb{M}^v = \frac{1}{h_{easy}}\mathbb{P}_2 + \frac{1}{h_{hard}}\mathbb{P}_3 \,, \tag{3.129}$$

where $m^{(2)}$ - multiplicity of h_{easy} is equal to i in the scaling law (3.128). Projectors $\mathbb{P}_K$ $(K = 2, 3)$ depend on crystal symmetry and fulfil (3.16). For such a specification of $\mathbb{M}^v$ the equation (3.109) reduces to the following quadratic equation:

$$3\bar{h}^2 + \underbrace{(\eta(m - 3) + 2 - m)}_{b(\eta,m)}\bar{h} - 2\eta = 0 \,, \tag{3.130}$$

where $\bar{h} = \frac{\bar{h}_{SC}^D}{h_{easy}}$, $\eta = \frac{h_{hard}}{h_{easy}}$, $m = m^{(2)} = i$, with the positive root

$$\bar{h} = \frac{-b(\eta, m)}{6} + \frac{|b(\eta, m)|}{6}\underbrace{\sqrt{1 + \frac{24\eta}{b(\eta, m)^2}}}_{f(\eta,m)} \,. \tag{3.131}$$

For $m \neq 3$ the function $f(m, \eta)$ can be expanded into a power series around $1/\eta \to 0$. These expansions introduced into (3.131), after neglecting terms of order $1/\eta^2$ and smaller, lead to the following approximation of $\bar{h}$ for high values of η,

$$\bar{h} \approx \begin{cases} \frac{2}{3}(\eta + 1) & \text{for } m = 1 \,, \\ \frac{1}{3}\eta + 2 & \text{for } m = 2 \,, \\ 2 & \text{for } m = 4 \,. \end{cases} \tag{3.132}$$

For $m = 3$ formula (3.131) reduces to

$$\bar{h} = \frac{1}{6}(1 + \sqrt{1 + 24\eta}) \sim \sqrt{\eta} \,. \tag{3.133}$$

It is seen that the scaling law proposed in Nebozhyn et al. [143] is confirmed by the above analytical derivations. Moreover, the above result provides additional information. First, we observe that the scaling law for $m = 1$ is the same as for $m = 2$. Second, the linear approximation of $\bar{h}$ for $m = 1, 2$ is provided and the finite limit value for $m = 4$ is specified. The quality of linear approximations for $m = 1, 2$ is illustrated in Fig. 3.10.
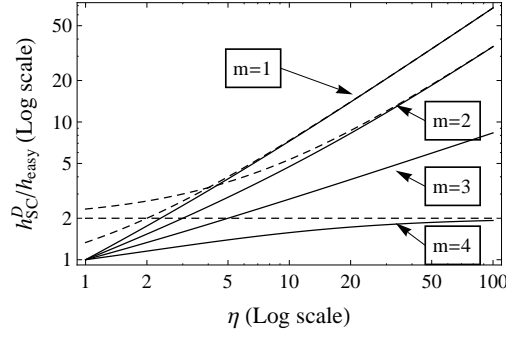
Fig. 3.10. A self-consistent estimate of viscous $\bar{h}_{\mathrm{SC}}^{\mathrm{D}}$ for an untextured polycrystal with reduced number m of independent easy slip systems - exact solutions (continuous line) and approximate ones (dashed line) for large values of $\eta = h_{hard}/h_{easy}$.

Results presented below are derived for bounds and a self-consistent estimate of the overall viscous shear modulus $\bar{h}^{\mathrm{D}}$ for fcc polycrystals, γ-TiAl polycrystal of near-gamma microstructure and hcp Mg polycrystals of random texture assuming $n = 1$. We also find the bounds and estimates on the moduli $\bar{h}_2, \bar{h}_3, \bar{h}_4$ describing the properties of the above polycrystals of different fibre textures. It is worth explaining here the meaning of the subsequent Kelvin moduli for the latter case. Analyzing the form of the projectors $\mathbb{P}_K$ for transverse isotropy (Appendix A), one finds that for the polycrystal of fibre texture:

- the value of the overall flow stress in tension/compression along the **n** direction is governed by the Kelvin viscous modulus $\bar{h}_2$,

- the value of the overall flow stress in shear in the plane perpendicular to **n** is governed by the modulus $\bar{h}_3$, and

- the value of the overall flow stress in shear in the plane containing **n** is governed by the modulus $\bar{h}_4$.

Fcc polycrystals

Single crystal of a fcc unit cell has 12 slip systems of the same type ($\tau_c^r = \tau_c$), see Sec. 2.2. One finds

$$\mathbb{M}^v = \frac{v_0}{\tau_c} \left(\frac{1}{h_2} \mathbb{P}_2 + \frac{1}{h_3} \mathbb{P}_3 \right), \quad h_2 = \frac{1}{2}, \quad h_3 = \frac{3}{2}, \tag{3.134}$$

where h_2 is of multiplicity $m_2 = 2$ and $h_3 > h_2$ of multiplicity $m_3 = 3$, and $\mathbb{P}_2$ and $\mathbb{P}_3$ are specified as for cubic symmetry, cf. Kowalczyk-Gajewska and

Ostrowska-Maciejewska [104]. Using formulas (3.32), (3.34), (3.37) and (3.84), one finds for a polycrystal of random texture:

$$\bar{h}_{\text{LO}}^{\text{D}} = \frac{5}{6}, \quad \bar{h}_{\text{LO/HS}}^{\text{D}} = \frac{21}{22}, \quad \bar{h}_{\text{SC}}^{\text{D}} = 1, \quad \bar{h}_{\text{UP/HS}}^{\text{D}} = \frac{43}{42}, \quad \bar{h}_{\text{UP}}^{\text{D}} = \frac{11}{10} \left[\frac{\tau_c}{v_0} \right].$$

(3.135)

Equivalent solution was obtained by Hutchinson [69].
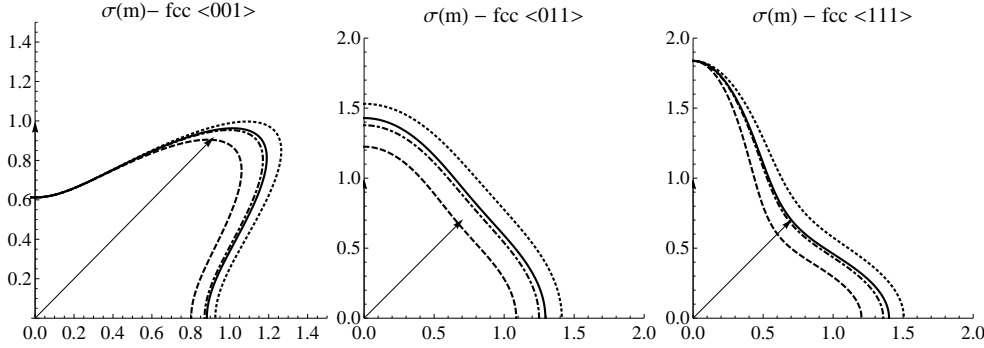
Fig. 3.11. A directional overall flow stress $\sigma_Y(\mathbf{m})/\tau_c$ for fcc polycrystal of fibre texture (parametric plot): a) $\langle 001 \rangle$, b) $\langle 011 \rangle$, c) $\langle 111 \rangle$; dashed and dotted lines - upper and lower bounds (Voigt and Reuss), a dashed-dotted line - the Hill estimate, a continuous line - the self-consistent estimate.

Using the derived formulae one can also study the polycrystals of different fibre textures. As representative results we present upper and lower bounds and a self-consistent estimate on the overall flow stress in tension (compression) of a polycrystal in any direction $\mathbf{m}$ specified by the angle θ measured with respect to the fibre direction $\mathbf{n}$. Three fibre textures are analysed in Fig. 3.11, namely $\langle 001 \rangle$, $\langle 111 \rangle$ and $\langle 011 \rangle$. It is observed that the self-consistent and Hill estimates are close to each other.

γ-TiAl intermetallic

Titanium aluminide of near gamma microstructure can be modelled as a polycrystal composed of spherical grains. Single crystal has a fcc-like unit cell with 12 possible slip systems subdivided into two groups: 4 ordinary dislocations and 8 super-dislocations (for details see Sec. 2.2). Denoting $\rho = \frac{\tau_c^{sup}}{\tau_c^{ord}}$ one finds

$$\mathbb{M}^v = \frac{v_0}{\tau_c^{ord}} \left(\frac{1}{h_2}\mathbb{P}_2 + \frac{1}{h_3}\mathbb{P}_3 + \frac{1}{h_4}\mathbb{P}_4 + \frac{1}{h_5}\mathbb{P}_5 \right).$$

(3.136)

Projectors $\mathbb{P}_K$ are specified as for volumetrically isotropic material of tetragonal symmetry, cf. Kowalczyk-Gajewska and Ostrowska-Maciejewska [103, 104], and

$$h_2 = \frac{\rho}{2}, \quad h_3 = \frac{3\rho}{2+4\rho}, \quad h_4 = \frac{3\rho}{2}, \quad h_5 = \frac{3\rho}{1+\rho}, \tag{3.137}$$

where h_5 is of multiplicity $m_5 = 2$. Variation of local moduli h_K with ρ is presented in Fig. 3.12a. One observes that for $\rho < 1$ one has $h^{\mathrm{D}}_{min} = h_2$ and $h^{\mathrm{D}}_{max} = h_5$, while for $\rho \geqslant 1$ one has $h^{\mathrm{D}}_{min} = h_3$ and $h^{\mathrm{D}}_{max} = h_4$.

Random texture. Using formulae (3.32), (3.34) and (3.37) one finds upper and lower bounds while the self-consistent estimate is the single positive real root of the polynomial equation of degree 4, see Kowalczyk-Gajewska [99]. Fig. 3.12b presents the solution of the above equation for different values of ρ, together with the corresponding upper and lower bounds. It is observed in experiments, cf. Appel and Wagner [6], that super-dislocations are more difficult to initiate than ordinary dislocations, therefore $\rho > 1$ is physically meaningful.

a)   b)
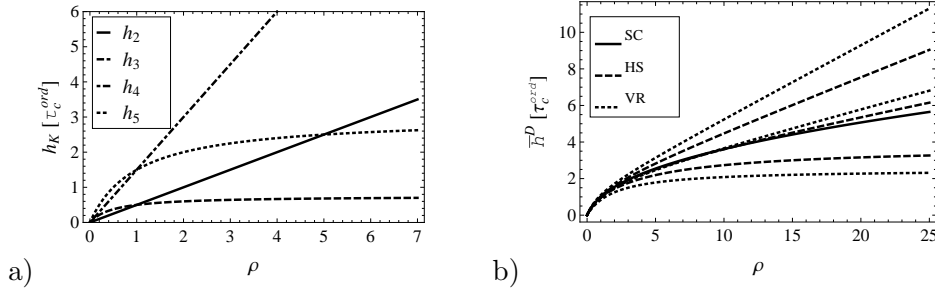
Fig. 3.12. γ-TiAl polycrystal of random texture: a) the local Kelvin moduli; b) bounds and estimates of an overall viscous stiffness ($\rho = \tau_c^{sup}/\tau_c^{ord}$). VR - the Voigt and Reuss bounds, HS - the Hashin-Shtrikman bounds, SC - the self-consistent estimate.

Now, let us examine the limit situation when $\rho \longrightarrow \infty$, which means that the inelastic deformation is possible only by ordinary dislocations. In this case the subspace of deviatoric strain-rate tensors which are possible to be realized by this reduced set of slip systems is three-dimensional. Taking the limit values of h_K, one obtains

$$h_2 = h_4 \longrightarrow \infty, \quad h_3 = \frac{3}{4}, \quad h_5 = 3, \tag{3.138}$$

therefore the multiplicity of the infinite deviatoric Kelvin modulus is two. According to the analysis performed in the preceding subsection, a finite self-consistent estimate does not exist in such a case and a self-consistent estimate

for increasing value of ρ follows the scaling law (3.133). The limited number of easy slip systems is the main source of poor ductility of titanium alumini- des, which inhibits its industrial use in spite of its high specific strength and stiffness. As it has been already discussed in Chapter 2, the lack of easy slip systems is partially balanced by the activation of twinning mechanism. Howe- ver, twin systems cannot be directly included in the presented analysis since, due to their unidirectionality, they introduce non-linearity into the constitutive relation, even for $n = 1$. Influence of twinning will be considered in the next section.
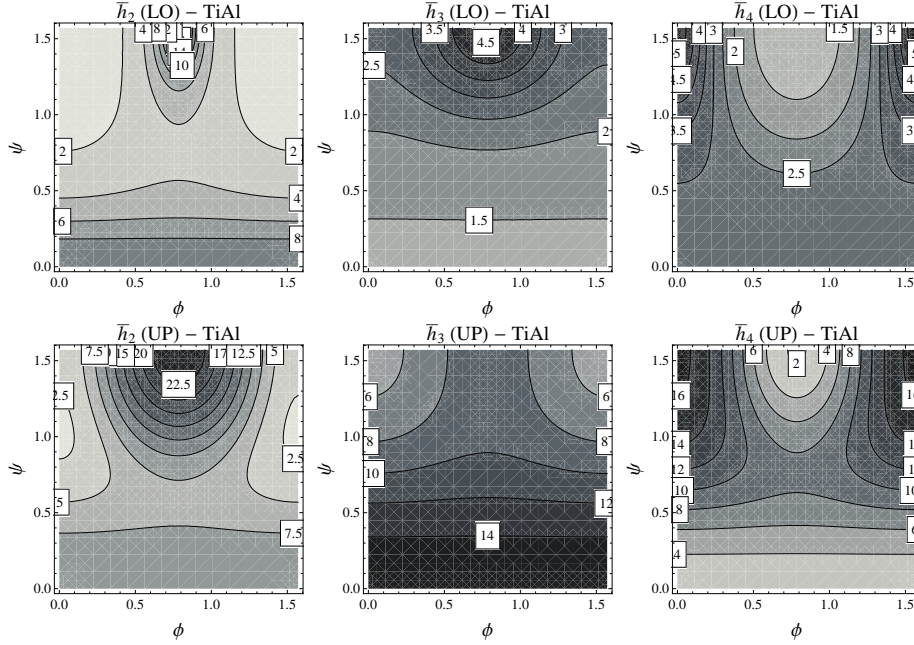
Fig. 3.13. Bounds on the overall moduli $\bar{h}_K$ for TiAl polycrystal of $\rho = 20$ and fibre textures specified by $\mathbf{n}(\phi, \psi)$. UP,LO - the upper (Voigt) and lower (Reuss) bounds.

Fibre textures. Dependence of upper and lower bounds on the Kelvin moduli $\bar{h}_K$, describing the incompressible viscous TiAl polycrystal of fibre texture, upon the direction $\mathbf{n}$ of a fibre is presented in Fig. 3.13 for $\rho = 20$. The fibre direction is specified with respect to the local crystal axes $\{\mathbf{a}_k\}$ by two angles, namely,

$$n_k = (\cos(\phi)\sin(\psi), \sin(\phi)\sin(\psi), \cos(\psi)). \tag{3.139}$$

Fig. 3.13 enables us to select the representative fibre directions for further analysis. The limit analysis of an analytical result obtained in Sec. 3.3 for $\rho \to \infty$
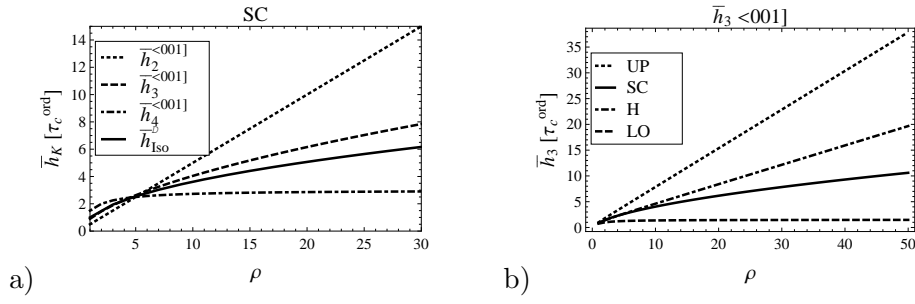
Fig. 3.14. TiAl polycrystal of $\langle 001]$ fibre texture: a) the self-consistent estimates of $\bar{h}_K$, b) bounds (UP,LO) and estimates (H - Hill, SC - self-consistent) of $\bar{h}_3$, $\rho = \tau_c^{sup}/\tau_c^{ord}$.
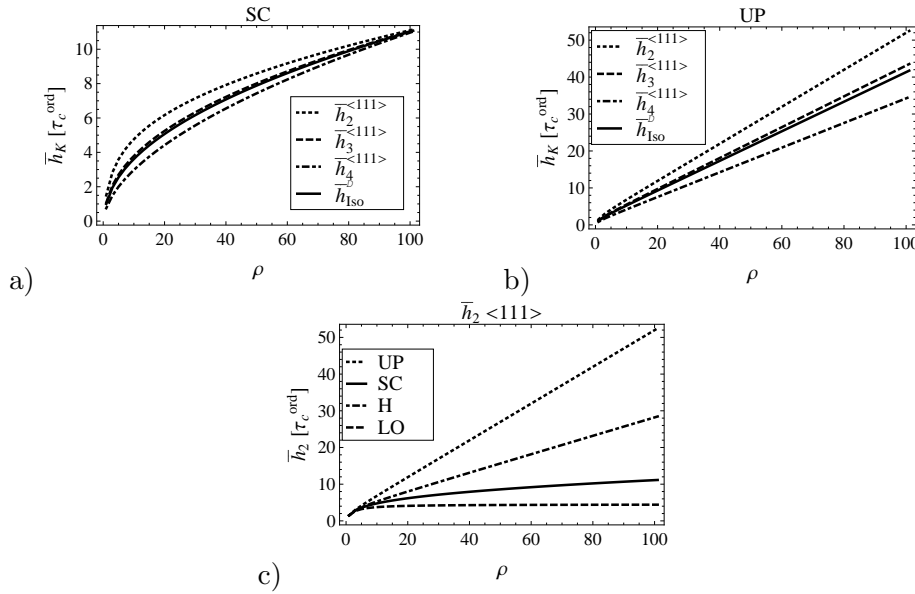
Fig. 3.15. TiAl polycrystal of $\langle 111 \rangle$ fibre texture: a) the self-consistent estimates of $\bar{h}_K$, b) the upper bound on $\bar{h}_K$, c) bounds (UP,LO) and estimates (H - Hill, SC - self-consistent) on $\bar{h}_2$, $\rho = \tau_c^{sup}/\tau_c^{ord}$.

indicates that the lower bound on $\bar{h}_2$ is infinite when $\mathbf{n}$ is coaxial with crystallographic directions $\langle 001]$ or $\langle 110]$. On the other hand, upper bounds for some of the other Kelvin moduli can be finite for $\rho \rightarrow \infty$ in the case of these fibre textures. In view of this observation and properties of the solution visible in Fig. 3.13, the fibre textures $\langle 001]$ ($\psi = 0$), $\langle 111 \rangle$ ($\phi = \pi/4, \psi = \mathrm{arc\,tg}(\sqrt{2})$) and $\langle 110]$ ($\phi = \pi/4, \psi = \pi/2$) have been selected for further analysis.

In the case of fibre texture $\langle 001]$, local and macroscopic anisotropy have a common symmetry axis. One finds that macroscopic moduli $\bar{h}_2$ and $\bar{h}_4$ coincide

then with the local moduli h_2 and h_5, respectively. In Fig. 3.14a the variation of self-consistent estimates of $\bar{h}_K$ with ρ is presented. The figure indicates increase of macroscopic anisotropy with increasing ρ. In Fig. 3.14b the bounds and estimates of $\bar{h}_3$ are presented. It is observed that for high value of ρ the self-consistent estimate differs considerably from the Hill estimate.
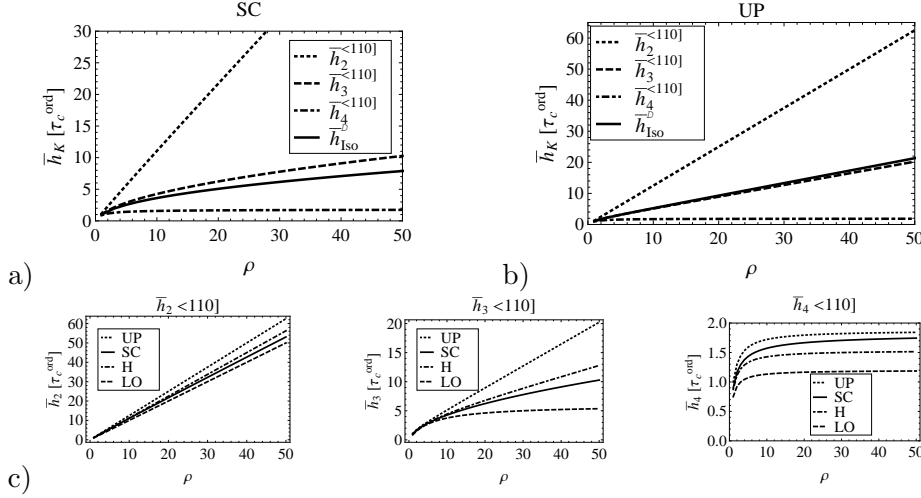
Fig. 3.16. TiAl polycrystal of $\langle 110]$ fibre texture: a) the self-consistent estimates of $\bar{h}_K$, b) upper bound of $\bar{h}_K$, c) bounds (UP,LO) and estimates (H - Hill, SC - self-consistent) on $\bar{h}_K$, $\rho = \tau_c^{sup}/\tau_c^{ord}$.

In the case of fibre texture $\langle 111 \rangle$ there is no common symmetry axis for local and macroscopic anisotropy. In Fig. 3.15a the variation of self-consistent estimates of $\bar{h}_K$ upon ρ is presented. It is observed that for an increasing value of ρ the estimated overall anisotropy decreases and behaviour of a polycrystal tends to be that of an untextured polycrystal. Such a tendency is not observed when analysing upper and lower bounds (see Fig. 3.15b). In Fig. 3.15c the bounds and estimates of $\bar{h}_2$ are compared for different values of ρ. Plots for remaining two moduli are qualitatively similar. Again, for high value of ρ, the difference between the Hill estimate and the self-consistent estimate is high. Note that although an increase of the SC estimate of $\bar{h}_K$ is much slower than the Hill estimate it does not reach any finite value for $\rho \to \infty$.

Fibre texture $\langle 110]$ is illustrated in Figs 3.16. In this case, for $\rho \to \infty$, the lower bound on $\bar{h}_2$ is infinite, while there exists the finite upper bound on $\bar{h}_4$. Consequently, for increasing ρ, the γ-TiAl polycrystal of this texture is highly anisotropic.
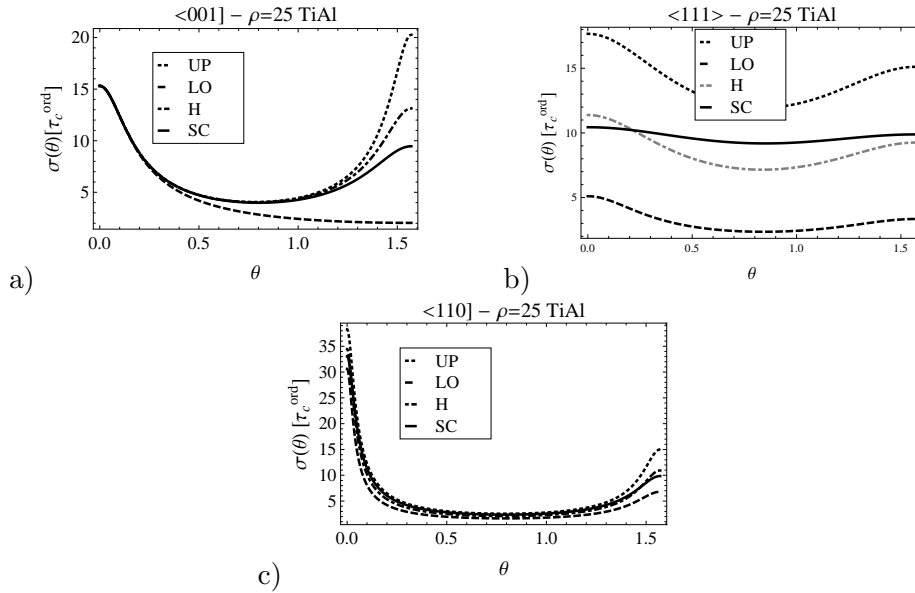
Fig. 3.17. Bounds (UP,LO) and estimates (H - Hill, SC - self-consistent) of the directional overall flow stress for the TiAl polycrystal of fibre texture and $\rho = 25$: a) $\langle 001]$, b) $\langle 110]$, c) $\langle 111 \rangle$.

For the analysed three fibre textures and $\rho = 25$, the dependence of a directional overall flow stress in tension in the direction specified by an angle θ measured with respect to fibre direction $\mathbf{n}$ is presented in Fig. 3.17. It is seen that the strong anisotropy of polycrystals of $\langle 001]$ and $\langle 110]$ fibre textures is confirmed.

Hcp Mg polycrystals

The Mg single crystal of a hcp lattice structure has hexagonal symmetry. Usually four groups of slip systems are reported for magnesium, cf. Agnew et al. [2], Staroselsky and Anand [187]: 3 basal, 3 prismatic, 6 pyramidal $\langle a \rangle$ and 6 pyramidal $\langle c + a \rangle$ (for details see Sec. 2.2). Only basal slip systems are considered to be the easy ones; however, the subspace of deviatoric strain-rate states which are possible to take place by this reduced set of slip systems is two-dimensional. Addition of prismatic or pyramidal $\langle a \rangle$ slip systems (or both of them) makes this subspace four-dimensional. Only the set of pyramidal $\langle c + a \rangle$ slip systems covers the whole deviatoric space. Again, due to the reasons explained above, twinning mechanism is not considered.

Let us denote

$$\rho_1 = \frac{\tau_c^{prism.}}{\tau_c^{basal}}, \quad \rho_2 = \frac{\tau_c^{pyram.\langle a \rangle}}{\tau_c^{basal}}, \quad \rho_3 = \frac{\tau_c^{pyram.\langle c+a \rangle}}{\tau_c^{basal}} . \tag{3.140}$$

If all 18 slip systems can be initiated, by using (3.127) one obtains the local viscous compliance tensor in the form

$$\mathbb{M}^{vp} = \underbrace{\frac{9d^2}{(1+d^2)^2\rho_3}}_{1/h_2} \mathbb{P}_2 + \underbrace{\frac{3}{4}\left(\frac{1}{\rho_1} + \frac{8d^2}{(3+4d^2)\rho_2} + \frac{2d^2}{(1+d^2)^2\rho_3}\right)}_{1/h_3} \mathbb{P}_3 +$$

$$+ \underbrace{\left(\frac{3}{4} + \frac{9}{(6+8d^2)\rho_2} + \frac{3(1-d^2)^2}{2(1+d^2)^2\rho_3}\right)}_{1/h_4} \mathbb{P}_4 , \tag{3.141}$$

where d is a c/a ratio describing lattice geometry (see Table 2.1), while projectors $\mathbb{P}_K$ are specified as for a volumetrically isotropic material of transverse isotropy (Appendix A).

Random texture. Identifying h_K, $K = 2, 3, 4$, as indicated by (3.141), where h_2 is of multiplicity one and h_3, h_4 of multiplicity 2, one easily obtains lower and upper bounds by using Eq. $(3.32)_2$ and Eq. $(3.34)_2$ as well as the self-consistent estimate from the cubic equation, see Kowalczyk-Gajewska [99].

It is interesting to analyse some special cases of the above solutions, corresponding to the situations when some of the groups of slip systems are excluded, in other words they are very difficult to initiate. First, let us consider two limit situations: $\rho_3 \rightarrow \infty$ and $\rho_1 = \rho_2 \rightarrow \infty$, corresponding to blocking pyramidal $\langle c+a \rangle$ or prismatic+pyramidal $\langle a \rangle$ sets of slip systems, respectively. For the first case, the local Kelvin moduli are:

$$\rho_3 \rightarrow \infty \Rightarrow h_2 \rightarrow \infty, \quad h_3 = \frac{4(3+4d^2)}{9(1+4d^2)}\rho_1, \quad h_4 = \frac{4(3+4d^2)\rho_1}{3(6+(3+4d^2)\rho_1)}, \tag{3.142}$$

and since the infinite local modulus h_2 is of multiplicity one, a finite self-consistent estimate can be found from the quadratic equation, see Kowalczyk-Gajewska [99]. The corresponding upper bound is infinite, while the lower bounds exists. Resulting values are presented in Fig. 3.18a. In the second case the

local Kelvin moduli are:

$$\rho_1 = \rho_2 \to \infty \;\Rightarrow\; h_2 = \frac{(1+d^2)^2}{9d^2}\rho_3, \quad h_3 = \frac{2(1+d^2)^2}{3d^2}\rho_3,$$

$$h_4 = \frac{4(1+d^2)^2\rho_3}{3(2(1-d^2)^2 + (1+d^2)^2\rho_3)},$$

so all of them are finite and bounds and a self-consistent estimate can be found. Results are presented in Fig. 3.18b.

a)   b)
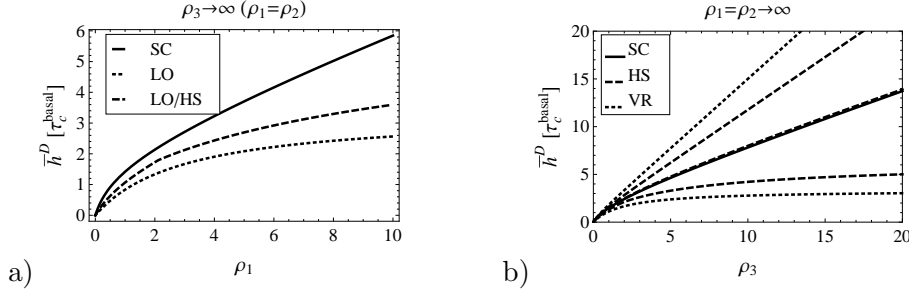
Fig. 3.18. Bounds and self-consistent estimate of an overall viscous shear modulus of a hcp Mg random polycrystal for a) $\rho_3 \to \infty$ (pyramidal $\langle c+a \rangle$ slip systems are blocked) b) $\rho_1 = \rho_2 \to \infty$ (prismatic and pyramidal $\langle a \rangle$ slip systems are blocked); both Hill-type estimates almost coincide with the SC estimate. VR - the Voigt and Reuss bounds, HS - the Hashin-Shtrikman bounds, SC - the self-consistent estimate.

It is easy to see that if all slip systems except of the easy ones are blocked (that is $\rho_1 \to \infty$, $\rho_2 \to \infty$ and $\rho_3 \to \infty$), then only the local Kelvin modulus h_4 is finite, therefore a finite self-consistent estimate of $\bar{h}^{\mathrm{D}}$ does not exist.

Let us add that finite self-consistent estimates can be also found for the cases when both prismatic and pyramidal $\langle c+a \rangle$ slip systems are blocked ($\rho_1 \to \infty$ and $\rho_3 \to \infty$) or when both pyramidal $\langle a \rangle$ and pyramidal $\langle c+a \rangle$ slip systems are blocked ($\rho_2 \to \infty$ and $\rho_3 \to \infty$).

Self-consistent estimates for the single crystal with different groups of slip systems blocked are compared in Fig. 3.19. Surprisingly, although pyramidal $\langle c+a \rangle$ slip systems are sufficient to realize any deviatoric strain-rate state, the self-consistent estimate for $\bar{h}^{\mathrm{D}}$ in the case when only basal and pyramidal $\langle c+a \rangle$ slip systems can operate is higher than for the case, when pyramidal $\langle c+a \rangle$ slip systems are blocked, while other groups of slip systems can be activated with the same level of corresponding critical shear stresses. It means that in the former case, the polycrystal is more stiff than in the latter. Moreover, one can also observe that activation of the pyramidal $\langle a \rangle$ slip systems is more beneficial,
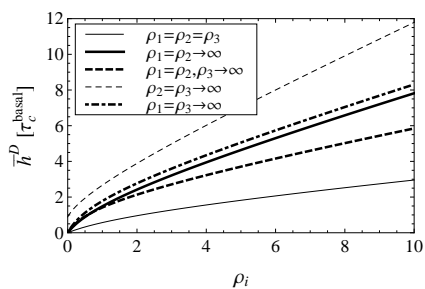
Fig. 3.19. Comparison of self-consistent estimates of an overall viscous shear modulus of a Mg random polycrystal for different active sets of slip systems.

from the point of view of polycrystal ductility, than activation of the prismatic slip systems.
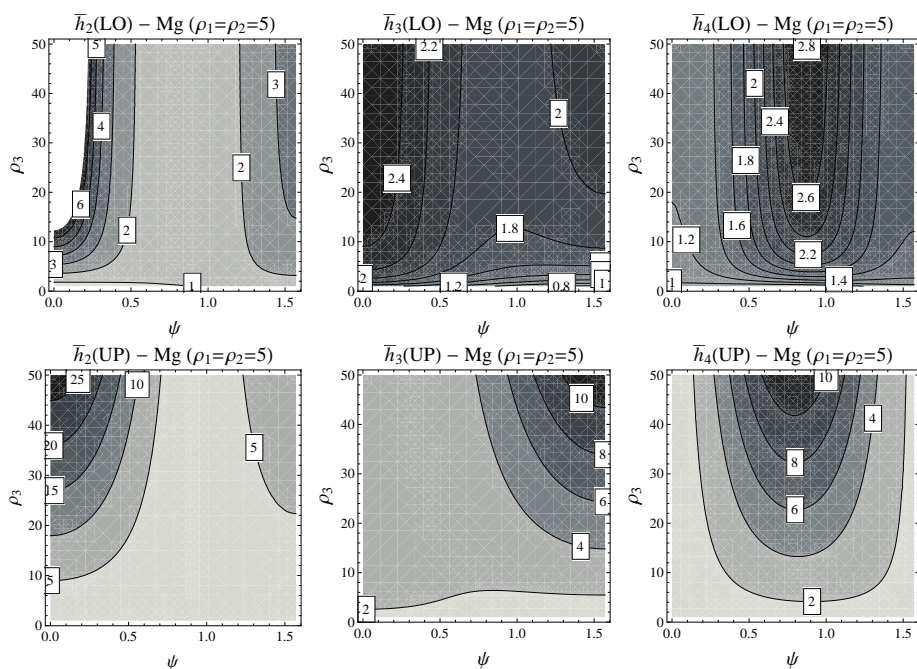
Fig. 3.20. Bounds on the overall moduli $\bar{h}_K$ for Mg polycrystal of $\rho_1 = \rho_2 = 5$ and fibre textures specified by $\mathbf{n}(\psi)$.

Fibre textures. The fibre textures for the Mg polycrystal will be now analysed for $\rho_1 = \rho_2 = 5$ and for different values of ρ_3. For this case, as it was demonstrated above, in the limit of $\rho_3 \to \infty$, the finite SC estimate of $\bar{h}^D$ exists

for random polycrystal. Polycrystals of fibre textures for other combinations of properties can be analysed in the same way. In Fig. 3.20 we present maps of bounds on the overall Kelvin moduli $\bar{h}_K$ for different fibre directions specified by $\cos\psi = \mathbf{n}\cdot\mathbf{c}$ and different values of ρ_3. On the basis of these plots we find it interesting to consider fibre textures: $\langle 0001]$ (basal texture), $\langle 1100]$ (this texture approximately corresponds to the fully twinned basal texture), $\langle 1012]$ (all orientations for this texture have a common twinning plane). As it is seen in Fig. 3.20, for each of above cases one of the Kelvin moduli tends to an extreme value.
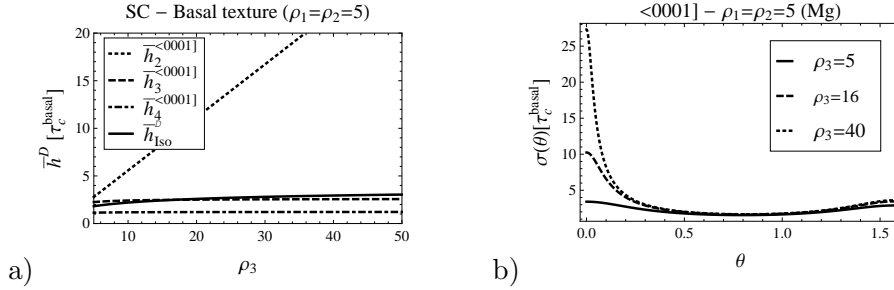
Fig. 3.21. Mg polycrystal of basal texture $\langle 0001]$: a) the Kelvin moduli $\bar{h}_K$, b) a directional flow stress in tension/compression; $\rho_1 = \rho_2 = 5$.

Note that for the basal texture, in the analysed linear case, the local and overall properties coincide. Therefore, bounds and self-consistent estimates will be analysed only for the latter two cases. In the case of basal texture one observes strong anisotropy of properties when ρ_3 increases (see Fig. 3.21)

As it is observed in Figs 3.22 and 3.23, in the case of fibre textures $\langle 1100]$ and $\langle 1102]$, the anisotropy of polycrystal is much weaker than in the case of basal texture. Moreover, as ρ_3 tends to infinity, one observes considerable discrepancy between the Hill estimate and the self-consistent estimate. With increasing ρ_3, the self-consistent estimates of all $\bar{h}_K$ increase very slowly.

3.7. Conclusions

In this chapter bounds and self-consistent estimates on elastic and viscoplastic properties of polycrystalline materials of low symmetry, described by linear constitutive laws, have been studied.

With use of the spectral and harmonic decompositions of Hooke's tensors, new expressions for bounds and self-consistent (SC) estimates have been derived for untextured polycrystals and polycrystals of fibre textures composed
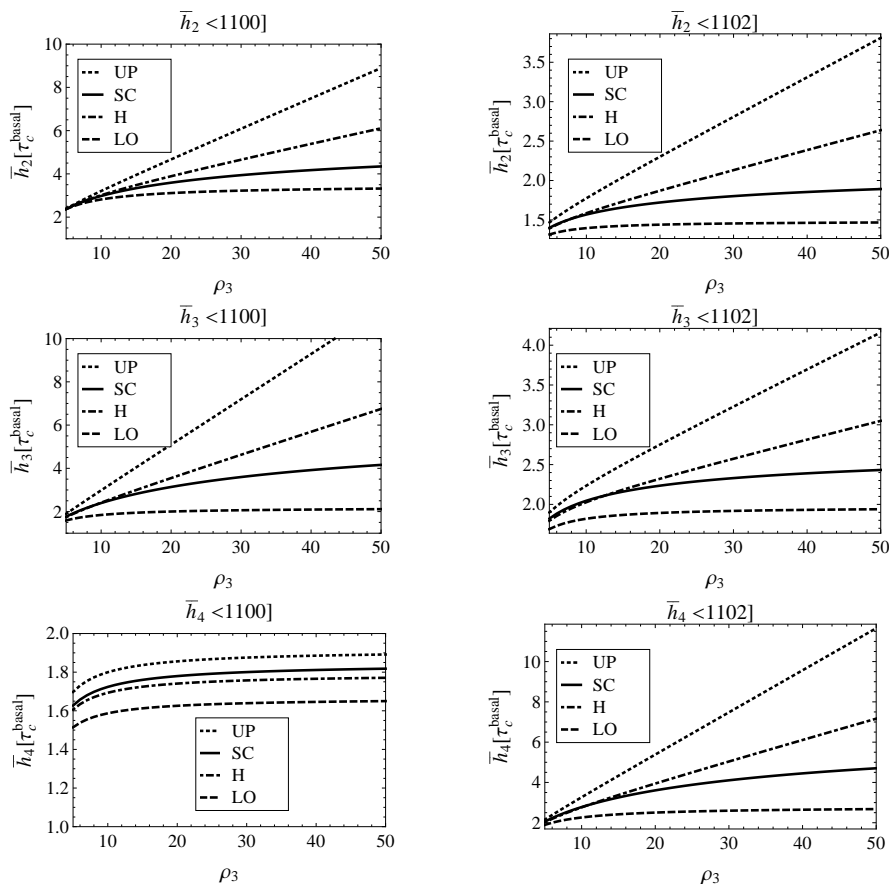
Fig. 3.22. Mg polycrystal of ⟨1100] (left) and ⟨1102] (right) fibre textures, bounds (UP,LO) and estimates (H - Hill, SC - self-consistent) on $\bar{h}_K$, $\rho_1 = \rho_2 = 5$.
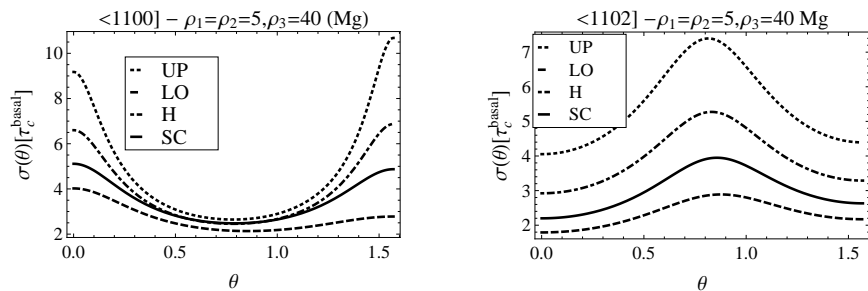
Fig. 3.23. Bounds (UP,LO) and estimates (H - Hill, SC - self-consistent) of the directional overall flow stress for Mg polycrystal of fibre texture, $\rho_1 = \rho_2 = 5$ and $\rho_3 = 40$: a) ⟨1100] b) ⟨1102].

of elements of arbitrary anisotropy. For the wide class of anisotropic crystals, corresponding formulae for SC estimates have been provided in the form of polynomial equations with coefficients depending on the invariants of a local stiffness tensor. Incompressible materials and materials with constrained deformation modes have been considered.

It should be noted that the spectral and harmonic decompositions of Hooke's tensors are relatively new mathematical tools, cf. Rychlewski [176, 178], Cowin and Mehrabadi [37], Forte and Vianello [51]. Its simultaneous application, first to the analysis of the stiffness/compliance tensors, and then to bounds and estimates of overall properties of polycrystalline materials, is not found in the literature. The use of invariants of fourth-order tensors resulting from the decompositions employed, allows us to demonstrate that the existence of a finite SC estimate for an overall shear modulus for an untextured polycrystal depends on the dimension of a subspace of constrained deviatoric deformation. It has been shown that the above property of SC scheme is important for the case of linear viscous polycrystals of low symmetry with an insufficient number of easy slip systems. This original analytical result indicates that the crystal should have at least four independent slip systems in order to have a finite self-consistent estimate of an overall flow stress. It is the counterpart of the well-known Taylor condition.
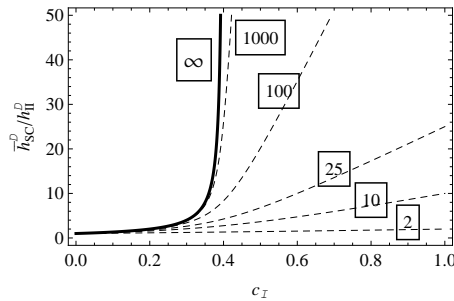
Fig. 3.24. Self-consistent estimate of an overall shear modulus for a two-phase isotropic incompressible material for increasing ratio of local shear moduli $h_{\mathrm{I}}^{\mathrm{D}}/h_{\mathrm{II}}^{\mathrm{D}}$ as a function of the volume fraction of phase I.

Analogy can be also drawn with the limitation of the self-consistent method concerning the assessment of the effective properties of two-phase incompressible materials indicated by Budiansky already in 1965 [23]. He demonstrated that the overall stiffness of the material with rigid inclusions was infinite if volume fraction of inclusions exceeded 2/5 (see Fig. 3.24). One can wonder if the result, proven in Sec. 3.4 for polycrystals with an insufficient number of easy
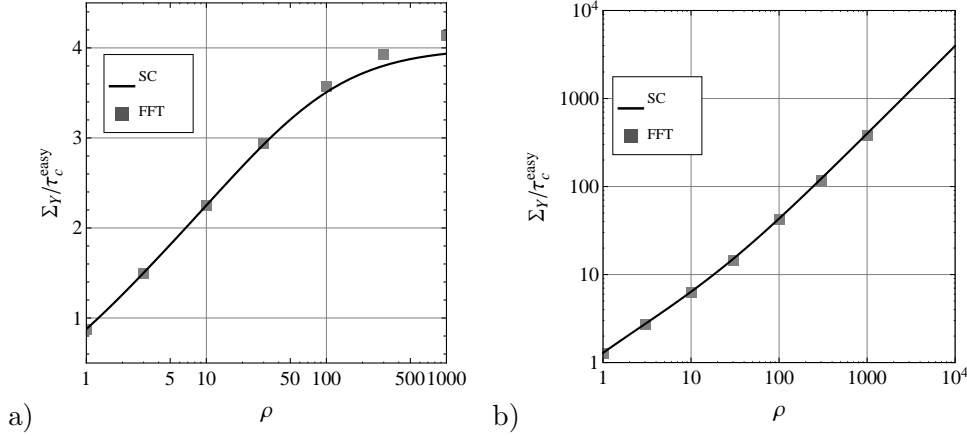
Fig. 3.25. The overall flow stress for untextured, linearly viscous polycrystals with 'equiaxed' (spherical) grains as functions of the grain anisotropy specified by $\rho = \tau_c^{hard}/\tau_c^{easy}$ obtained by a self-consistent method and numerically, using FFT technique: (a) Zr-type polycrystal with one-dimensional subspace of hard modes; (b) ice-type polycrystal with three-dimensional subspace of hard modes. Results obtained by FFT reported after [114].

slip systems, indicates similar limitation of the self-consistent method applied to such materials or represents their real behaviour. Although a definite answer to this question is not yet established, some support for the latter possibility can be found in Lebensohn et al. [114]. In that paper an accuracy of SC estimates of the linear and non-linear visoplastic properties of untextured polycrystals with equiaxed grains has been assessed for the local law specified by (3.127). To accomplish this task, SC approximations have been compared with the results obtained by numerical calculations for ensembles of polycrystals. In these calculations the technique based on the fast Fourier transforms (FFT) has been employed. In view of the posed question, particularly interesting are the results obtained for linear hcp polycrystals of c/a ratios corresponding to Zr and ice in which slip modes can be divided into the easy and hard groups. We cite these results in Fig. 3.25a and b. As $\tau_c^{hard}/\tau_c^{easy}$ increases to infinity, the subspace of constrained deviatoric deformation is one-dimensional and three-dimensional, respectively. One observes that the FFT solution agrees with the demonstrated property of a self-consistent approximation. It is recalled that this approximation predicts a finite estimate in the first case, and an infinite value in the second case.

4

Analysis of existing averaging schemes for non-linear constitutive laws

4.1. Introduction

In this chapter we turn our attention to the polycrystalline materials described by non-linear constitutive laws. Inelastic deformations of polycrystals by slip or twinning are often described with use of a viscoplastic regularization. Accordingly, the non-linear relation is used between the shear rate on the considered slip or twin system and the corresponding resolved shear stress. As it has been written in Sec. 2.3, most often the Norton-type power law (2.27), originally proposed for a steady creep process in Hutchinson [69], is applied. It leads to the relation between the inelastic strain-rate and stress, $\dot{\boldsymbol{\varepsilon}}^{in} = \mathbf{f}(\boldsymbol{\sigma})$, which is homogeneous of degree n, and n is an inverse of strain-rate sensitivity exponent. Estimates of polycrystal properties, e.g. an overall flow stress, are obtained assuming some micro-macro transition scheme, e.g. Hutchinson [69], Molinari et al. [139], Masson et al. [127]. Most widely used is the Taylor hypothesis, which imposes equal $\dot{\boldsymbol{\varepsilon}}^{in}$ in every grain. As demonstrated by Hill, the assumption provides an upper bound on the overall flow stress. On the other hand, similarly to a linear case, the Sachs hypothesis of equal stress in every grain provides a lower bound. As it was already discussed, the Taylor model, although quite successful when fcc materials of high symmetry are considered, fails for strongly anisotropic crystals of low symmetry. These crystals usually do not fulfil the Taylor condition about 5 independent easy slip systems. The description can be improved by applying generalizations of the self-consistent method. However, application of this transition scheme in the case of a non-linear constitutive rule is not straightforward and not unique, mainly due to different possible methods of linearization needed in order to apply the Eshelby solution (Appendix B). Furthermore, as it was demonstrated in Chapter 3 for the linear case ($n = 1$), the lack of 4 easy slip systems causes that the finite self-

consistent estimate of overall flow stress does not exist. If this result holds also for the non-linear case, the problem encountered when applying the Taylor hypothesis may not be overcome. In this chapter we discuss and compare different self-consistent schemes proposed for polycrystals and analyse their predictions for strongly anisotropic constituents. Influence of twinning is also considered. Presented numerical results will concern γ-TiAl and Mg polycrystals.

In order to apply the Eshelby solution (Appendix B), required for the derivation of the improved self-consistent estimate of overall non-linear properties, linearization of the local constitutive equation has to be performed. Generally, the procedure of deriving these estimates consists of the following four steps:

1. Linearization of the local non-linear constitutive rule.

2. Postulation of the overall linearized relation between the averaged strain and stress measures in the following affine (thermoelastic-like) form:

$$\mathbf{E} = \bar{\mathbb{M}} \cdot \mathbf{\Sigma} + \mathbf{E}^{\text{res}}, \quad \mathbf{E} = \langle \boldsymbol{\varepsilon} \rangle, \quad \mathbf{\Sigma} = \langle \boldsymbol{\sigma} \rangle, \qquad (4.1)$$

   where $\bar{\mathbb{M}}$ and $\mathbf{E}^{\text{res}}$ are yet-unknown the overall compliances and the overall eigenstrain, respectively. In some cases strain and stress measures are replaced by the strain-rate or the strain increment and the stress-rate or the stress increment.

3. Application of the Eshelby solution to the matrix of the yet-unknown overall compliances $\bar{\mathbb{M}}$ (i.e. a homogenized equivalent medium) and specification of the interaction equation (B.2).

4. Finding the concentration tensors $\mathbb{A}$ and $\mathbb{B}$ such that Eqs. (B.11-B.12) and (B.19-B.20) hold.

Different linearization methods and the resulting self-consistent estimates have been proposed in the literature. The first group of methods is applicable to rate-independent models of elastic-plastic crystals, cf. Kröner [108], Budiansky and Wu [24], Hill [66], Hutchinson [70], Berveiller and Zaoui [14], Iwakuma and Nemat-Nasser [72], Lipinski et al. [121], while the second group is applicable to rate-dependent rigid-viscoplastic models, cf. Hutchinson [69], Weng [214], Molinari et al. [138], Lebensohn and Tomé [112], de Botton and Ponte Castañeda [39], Kiryk and Petryk [84], Masson et al. [127]. The subsequent methods differ mainly by the definition of the stiffness moduli of the homogenized equivalent medium (HEM), to which the Eshelby solution is applied. There are also models developed for the elastic-viscoplastic polycrystals. They will be discussed in Chapter 6.

Below we will consider in more detail some of schemes relevant to the rate-independent models. Next, we will formulate the incremental self-consistent

scheme for polycrystals described locally by the regularized Schmid law discussed in Chapter 2 within the large strain regime. In this chapter we also provide the critical review of the self-consistent models for rigid-viscoplastic polycrystals, underlining the differences between the derived estimates which are usually not clearly indicated in the literature. Then we find the predictions of these models for γ-TiAl and Mg crystals with an insufficient number of easy slip systems. Analyzing the results, we are particularly interested in how the properties concerning estimates for linear polycrystals with constraints proven in Chapter 3, are transferred to the non-linear case. Moreover, contrary to the preceding chapter, influence of twinning activity on the overall properties will be discussed.

4.2. Elastic-plastic polycrystals

In general, two types of self-consistent models exist for elastic-plastic polycrystal, originating in Kröner [108] and Hill [66] proposals, respectively. In the first model (see also Budiansky and Wu [24]) the inelastic strain $\boldsymbol{\varepsilon}^p$ is identified with the eigenstrain $\boldsymbol{\varepsilon}^{\mathrm{res}}$ in the affine relation (B.1), therefore the local moduli $\mathbb{L} = \mathbb{M}^{-1}$ are identified with the tensor of elastic moduli $\mathbb{L}^e$. In the second method, called the incremental self-consistent scheme, the basic local law (B.1) relates the strain-rate and stress-rate and the local moduli are identified with the instantaneous elastic-plastic tangent moduli $\mathbb{L}^{ep}$ and there is no eigenstrain. Below we formulate these two frameworks for the rate-independent crystal elasto-plasticity with the regularized Schmid law presented in Chapter 2.

4.2.1. The Kröner self-consistent model

The Kröner model was formulated for small strain regime. Using the additive decomposition of the total strain into the plastic part and the elastic part, local behaviour of a single crystal can be specified as

$$\boldsymbol{\sigma} = \mathbb{L}^e \cdot (\boldsymbol{\varepsilon} - \boldsymbol{\varepsilon}^p) = \mathbb{L}^e \cdot \boldsymbol{\varepsilon} + \boldsymbol{\sigma}^{\mathrm{res}}\,, \qquad (4.2)$$

or inversely,

$$\boldsymbol{\varepsilon} = \mathbb{M}^e \cdot \boldsymbol{\sigma} + \boldsymbol{\varepsilon}^p\,, \qquad (4.3)$$

where $\boldsymbol{\sigma}^{\mathrm{res}} = -\mathbb{L}^e \cdot \boldsymbol{\varepsilon}^p$. The plastic strain $\boldsymbol{\varepsilon}^p$ and $\boldsymbol{\sigma}^{\mathrm{res}}$ are now an eigenstrain and an eigenstress, respectively. We assume that they are uniform within each grain. Note that (4.2) and (4.3) have an affine form. The evolution of local plastic strain is specified by the flow rule (2.24), where $\mathbf{d}^p$ is replaced by $\dot{\boldsymbol{\varepsilon}}^p$.

The corresponding yield surface (2.20) and the consistency condition enable the derivation of the plastic multiplier $\dot{\lambda}$.

In accordance with (4.2), at the macroscopic level of polycrystal, it is assumed that the average stress $\boldsymbol{\Sigma}$ and the average strain $\mathbf{E}$ are related by the following affine law:

$$\boldsymbol{\Sigma} = \bar{\mathbb{L}}^e \cdot (\mathbf{E} - \mathbf{E}^p) = \bar{\mathbb{L}}^e \cdot \mathbf{E} + \boldsymbol{\Sigma}^{\text{res}} \tag{4.4}$$

or inversely,

$$\mathbf{E} = \bar{\mathbb{M}}^e \cdot \boldsymbol{\Sigma} + \mathbf{E}^p, \tag{4.5}$$

where $\mathbf{E}^p$ is an overall plastic strain. Application of the Eshelby solution for the homogeneous equivalent medium of the stiffness moduli $\bar{\mathbb{L}}^e$ provides the following interaction relation

$$\boldsymbol{\sigma} - \boldsymbol{\Sigma} = -\mathbb{L}_*(\bar{\mathbb{L}}^e) \cdot (\boldsymbol{\varepsilon} - \mathbf{E}), \tag{4.6}$$

and the concentration relations take the form (B.11-B.12), where tensors $\mathbb{L}$ are identified with elasticity tensors $\mathbb{L}^e$. The overall stiffness is calculated using (B.19), while the overall plastic strain is specified by (B.22). All above relations can be also written in terms of the increments of strain and stress.

The computational advantage of the method is the fact that the overall stiffness, together with the concentration tensors $\mathbb{B}$ and $\mathbb{A}$, can be calculated once at the beginning of the process. However, as far as it is assumed that the interactions between the matrix and the inclusions are purely elastic, the predicted response of polycrystal is usually too stiff, especially for the advanced plastic flow. It can be checked that when the strain increment is almost purely plastic, then the model predictions tend to the Taylor model.

There exist generalizations of this approach, e.g. Berveiller and Zaoui [14], Wierzbanowski [218], Lipinski et al. [121], Cailletaud [28], Wierzbanowski et al. [219], in which stiff elastic interactions between matrix (HEM) and inclusions (grains) are softened by the introduction of some tuning parameters. Another extension of the Kröner method is the Transformation Field Analysis, cf. Dvorak and Benveniste [44], Chaboche et al. [29], in which, besides the interactions between matrix and inclusion, the interactions between inclusions are also taken into account. In the latter method the main difficulty is the assessment of the influence tensors, which account for such interactions.

4.2.2. The incremental self-consistent model

Another method of more accurate establishment of the overall properties of elastic-plastic polycrystals at small strains using the self-consistent framework,

has been proposed by Hill [66] and then extended to large strains by Iwakuma and Nemat-Nasser [72]. In this subsection we formulate the incremental self-consistent model for the regularized Schmid law, first within the small strain framework, and then for large strain regime. In the case of small strains the required affine relation between the stress-rate and the strain-rate takes the form:

$$\dot{\boldsymbol{\sigma}} = \left(\mathbb{L}^e - \frac{(\boldsymbol{\mathcal{F}} \cdot \mathbb{L}^e) \otimes (\boldsymbol{\mathcal{F}} \cdot \mathbb{L}^e)}{\boldsymbol{\mathcal{F}} \cdot \mathbb{L}^e \cdot \boldsymbol{\mathcal{F}} + h_{pl}(\boldsymbol{\sigma})} \right) \cdot \dot{\boldsymbol{\varepsilon}} = \mathbb{L}^{ep} \cdot \dot{\boldsymbol{\varepsilon}} \,, \tag{4.7}$$

where $\boldsymbol{\mathcal{F}}$ and $h_{pl}(\boldsymbol{\sigma})$ are defined by Eq. (2.24) and Eq. (2.31), respectively, while the fourth-order tensor of the instantaneous elastic-plastic moduli $\mathbb{L}^{ep}$ has all symmetries (A.1) of Hooke's tensor. Note that the lattice rotation is neglected and the additive decomposition of the velocity gradient corresponds to the additive decomposition of the rate of strain. The latter quantity is now identified with a symmetric part of the displacement gradient. As it is seen, the tensor of the tangent elastic-plastic moduli depends on the stress and, in general, it is position dependent, even for a homogeneous body.

In correspondence with (4.7) we assume that the overall behaviour of a polycrystalline aggregate is governed by the following affine constitutive equation between the rate of average stress $\dot{\boldsymbol{\Sigma}}$ and the rate of average strain $\dot{\mathbf{E}}$:

$$\dot{\boldsymbol{\Sigma}} = \bar{\mathbb{L}}^{ep} \cdot \dot{\mathbf{E}} \,, \tag{4.8}$$

where the fourth-order tensor $\bar{\mathbb{L}}^{ep}$ of the overall instantaneous elastic-plastic moduli is uniform and it has all symmetries of the Hooke tensor.

Accordingly, the corresponding interaction equation resulting from the Eshelby solution for the HEM of the moduli $\bar{\mathbb{L}}^{ep}$ assumes the form:

$$\dot{\boldsymbol{\sigma}} - \dot{\boldsymbol{\Sigma}} = -\mathbb{L}^{ep}_*(\bar{\mathbb{L}}^{ep}) \cdot (\dot{\boldsymbol{\varepsilon}} - \dot{\mathbf{E}}) \,, \tag{4.9}$$

and the concentration relation for the strain-rate and the relation for $\bar{\mathbb{L}}^{ep}$ are derived as

$$\dot{\boldsymbol{\varepsilon}} = \mathbb{A}^{ep} \cdot \dot{\mathbf{E}} = (\mathbb{L}^{ep} + \mathbb{L}^{ep}_*)^{-1}(\bar{\mathbb{L}}^{ep} + \mathbb{L}^{ep}_*) \cdot \dot{\mathbf{E}} \,, \quad \bar{\mathbb{L}}^{ep} = \langle \mathbb{L}^{ep} \mathbb{A}^{ep} \rangle \,. \tag{4.10}$$

Specifying the overall elastic-plastic moduli we assume that the local fields are uniform within the grains, which is an approximation to real behaviour of material.

Extension of the incremental self-consistent framework to the large strain requires reformulation of a local relation. According to Nemat-Nasser [144], the constitutive equations that relate the rate of the nominal stress $\mathbf{S} = J\mathbf{F}^{-1}\boldsymbol{\sigma}$ (the

transpose of the first Piola-Kirchhoff stress tensor) and the rate of deformation gradient are best suited for the formulation of the incremental self-consistent scheme within the large strain formalism. Moreover, to simplify description, it is also advisable to assume the current configuration as a reference one. In such a case one has

$$\mathbf{F} = \mathbf{I}, \quad J = \det \mathbf{F} = 1, \quad \mathbf{S} = \boldsymbol{\sigma} \tag{4.11}$$

and

$$\dot{\mathbf{F}} = \mathbf{l}\mathbf{F} = \mathbf{l}, \quad \dot{J} = (\text{tr}\mathbf{l})J = \text{tr}\mathbf{l}, \tag{4.12}$$

$$\dot{\mathbf{S}} = \dot{J}\mathbf{F}^{-1}\boldsymbol{\sigma} + J\mathbf{F}^{-1}\dot{\boldsymbol{\sigma}} + J\dot{\mathbf{F}}^{-1}\boldsymbol{\sigma} = (\text{tr}\mathbf{l})\boldsymbol{\sigma} + \dot{\boldsymbol{\sigma}} - \mathbf{l}\boldsymbol{\sigma}. \tag{4.13}$$

In terms of $\dot{\mathbf{S}}$, the rate of Cauchy stress can be expressed as

$$\dot{\boldsymbol{\sigma}} = \dot{\mathbf{S}} - (\text{tr}\mathbf{l})\mathbf{S} + \mathbf{l}\mathbf{S} = \dot{\mathbf{S}} + \mathbb{G}^3 \cdot \mathbf{l}, \quad G^3_{ijkl} = \delta_{ik}S_{lj} - S_{ij}\delta_{kl}. \tag{4.14}$$

Making use of the definition of the corotational rate (2.18), we re-write (2.32) as

$$\dot{\boldsymbol{\sigma}} = \mathbb{L}^{ep} \cdot \mathbf{d} + \boldsymbol{\omega}^e\boldsymbol{\sigma} - \boldsymbol{\sigma}\boldsymbol{\omega}^e. \tag{4.15}$$

With the use of (2.2)-(2.4), (2.26) and (2.30) the second part of this equation may be expanded as follows:

$$\boldsymbol{\omega}^e\boldsymbol{\sigma} - \boldsymbol{\sigma}\boldsymbol{\omega}^e = \boldsymbol{\omega}\boldsymbol{\sigma} - \boldsymbol{\sigma}\boldsymbol{\omega} - \underbrace{\frac{(\mathcal{H}\boldsymbol{\sigma} - \boldsymbol{\sigma}\mathcal{H}) \otimes (\mathbb{L}^e \cdot \mathcal{F})}{\mathcal{F} \cdot \mathbb{L}^e \cdot \mathcal{F} + h_{pl}(\boldsymbol{\sigma})}}_{=\mathbb{G}^2} \cdot \mathbf{d} =$$

$$= \mathbb{G}^1 \cdot \boldsymbol{\omega} - \mathbb{G}^2 \cdot \mathbf{d}, \quad G^1_{ijkl} = \delta_{ik}\sigma_{lj} - \sigma_{ik}\delta_{jl}, \tag{4.16}$$

where $\mathcal{H}$ is defined by Eq. (2.26) and the fourth-order tensors $\mathbb{G}^1$ and $\mathbb{G}^2$ do not exhibit all the symmetries of the Hooke tensor.

Using Eqs (4.13)-(4.16), it is now possible to formulate a local affine relation between the rate of nominal stress and the velocity gradient,

$$\dot{\mathbf{S}} = \mathbb{K}^{ep} \cdot \mathbf{L}, \tag{4.17}$$

where

$$\mathbb{K}^{ep} = \mathbb{L}^{ep} - \mathbb{G}^2 + \mathbb{G}^1 \circ \mathbb{I}^a - \mathbb{G}^3, \quad I^a_{ijkl} = \frac{1}{2}(\delta_{ik}\delta_{jl} - \delta_{il}\delta_{jk}). \tag{4.18}$$

The fourth-order tensor $\mathbb{K}^{ep}$ does not exhibit symmetries of Hooke's tensor, particularly it does not exhibit the major symmetry: $K^{ep}_{ijkl} \neq K^{ep}_{klij}$.

When the Kirchhoff stress is used in the formulation of a single grain model (see Section 2.3.3), under assumptions (4.11), it is obtained

$$\mathbf{S} = \boldsymbol{\tau}\dot{\mathbf{S}} = \dot{\boldsymbol{\tau}} - \mathbf{l}\boldsymbol{\tau}, \quad \dot{\boldsymbol{\tau}} = \dot{\mathbf{S}} + \mathbf{l}\mathbf{S} = \dot{\mathbf{S}} + \mathbb{G}^{3\tau} \cdot \mathbf{l}, \quad G^{3\tau}_{ijkl} = \delta_{ik}S_{lj}. \qquad (4.19)$$

Other specifications leading to the affine incremental law (4.17) remain valid with the Cauchy stress replaced by the Kirchhoff stress.

When the lattice distortions are taken into account (Eq. (2.33)), the affine relation between the rate of the nominal stress and the velocity gradient is expressed as follows:

$$\dot{\mathbf{S}} = \mathbb{L}^{ep\tau} \cdot \mathbf{d} + \mathbb{G}^1 \cdot \boldsymbol{\omega} - \mathbb{G}^{3\tau} \cdot \mathbf{l} = (\mathbb{L}^{ep\tau} + \mathbb{G}^1 \circ \mathbb{I}^a - \mathbb{G}^{3\tau}) \cdot \mathbf{l} = \mathbb{K}^{ep\tau} \cdot \mathbf{l}, \quad (4.20)$$

where $\mathbb{K}^{ep\tau}$ is not symmetric and $\mathbb{L}^{ep\tau}$ is specified by Eq. (2.37).

In accordance with (4.17), the constitutive rule describing the overall behaviour of polycrystal is assumed as follows:

$$\dot{\bar{\mathbf{S}}} = \bar{\mathbb{K}}^{ep} \cdot \mathbf{L}, \quad \mathbf{L} = \langle \mathbf{l} \rangle, \quad \bar{\mathbf{S}} = \langle \mathbf{S} \rangle. \qquad (4.21)$$

where $\bar{\mathbf{S}}$ is a macroscopic nominal stress. The Eshelby framework for HEM of pseudo-moduli $\bar{\mathbb{K}}^{ep}$ is now employed to find the interaction equation of the form (see Appendix B):

$$\dot{\mathbf{S}} - \dot{\bar{\mathbf{S}}} = -\mathbb{K}^{ep}_*(\bar{\mathbb{K}}^{ep}) \cdot (\mathbf{l} - \mathbf{L}), \qquad (4.22)$$

where the generalized Hill tensor $\mathbb{K}^{ep}_*(\bar{\mathbb{K}}^{ep})$ is specified by (B.3) with $\mathbb{L}_0$ replaced by $\bar{\mathbb{K}}^{ep}$ and the polarisation tensor specified by (B.25). Let us underline that because the tensor of local pseudo-moduli $\mathbb{K}^{ep}$ is not symmetric with respect to permutation of indices specified by $(A.1)_4$, there is no reason for $\bar{\mathbb{K}}^{ep}$ to be symmetric in this respect as well. Consequently, the existence and uniqueness of the solution to the related Eshelby problem is not guaranteed, cf. Molinari [135], Nemat-Nasser [144].

The aggregate behaviour can be analysed for the assumed macroscopic velocity gradient $\bar{\mathbf{L}}(t)$ or for the assumed macroscopic Cauchy stress $\boldsymbol{\Sigma}(t)$ and $\dot{\boldsymbol{\Sigma}}(t)$. In the latter case we should also assume the macroscopic spin tensor $\bar{\mathbf{W}}(t)$.

As it can be seen, application of the self-consistent scheme in the case of rate-independent model of single crystal, especially for large strain regime, is complex. Computational difficulties arise mainly from the fact that the loading-unloading and consistency conditions must be verified for each grain. Consequently, results of application of the above formulation for polycrystals are rarely found in the literature, e.g. in Iwakuma and Nemat-Nasser [72]. Recently, interesting results for fcc polycrystals obtained by employing the incremental self-consistent model within the small strain regime have been reported by Yoshida

et al. [228]. Authors compared the predictions obtained with the use of the standard and regularized Schmid models of single crystal. They showed that, although the overall stress-strain curves delivered with the use of the Taylor model for both local descriptions do not differ, the significant difference can be observed in the case of the incremental self-consistent scheme. It is argued that the latter fact can be explained by the difference in the local tangent moduli. For the advanced plastic flow the predictions of SC scheme and the regulari-zed Schmid law tend to the Taylor model predictions. For the same regime of plastic flow and the classical Schmid law, the overall stress level for polycrystal predicted by the SC scheme is reduced by about 15% as compared to the Taylor model.

4.3. Viscoplastic polycrystals

4.3.1. Comparison of different self-consistent schemes

The improvement of the predictions of the overall response of polycrystals for the advanced inelastic deformations, and at the same time simplifications of the related computational procedure, can be achieved when neglecting elasticity and using the non-linear viscous regularization of plastic flow of crystals.

Consequently, following the analysis of steady creep of polycrystals perfor-med by Hutchinson [69], the attention of researchers is focused on the rigid-viscoplastic crystals described by the non-linear laws relating the strain-rate tensor $\mathbf{d}$ to the stress tensor $\boldsymbol{\sigma}$,

$$\mathbf{d} = \mathbf{d}^{vp} = \mathbf{f}(\boldsymbol{\sigma}, \tau_c) \,. \tag{4.23}$$

The special case of these materials are metals for which locally the power-law (2.27) can be applied and, using Eq. (4.23), the local constitutive law is specified as [1]

$$\mathbf{d} = v_0 \sum_{r=1}^{2M+N} \left(\frac{\tau^r}{\tau_c^r} \right)^n \mathbf{P}^r, \quad \tau^r = \langle \boldsymbol{\sigma} \cdot \mathbf{P}^r \rangle \,. \tag{4.24}$$

It can be verified that the function $\mathbf{f}$ specified as above is homogeneous of degree n with respect to $\boldsymbol{\sigma}$, thus

$$\mathbf{f}(\alpha\boldsymbol{\sigma}) = \alpha^n \mathbf{f}(\boldsymbol{\sigma}), \quad \frac{\partial \mathbf{f}(\boldsymbol{\sigma})}{\partial \boldsymbol{\sigma}} \cdot \boldsymbol{\sigma} = n\mathbf{f}(\boldsymbol{\sigma}) \,. \tag{4.25}$$

As $n \to \infty$, the rate-insensitive limit is approached.

---

[1]In order to simplify the notation a bar over n is omitted in this section.

One can introduce a tensor of tangent compliances for the law (4.23), viz.:

$$\mathbb{M}^{tg} \equiv \frac{\partial \mathbf{f}}{\partial \boldsymbol{\sigma}}, \tag{4.26}$$

which in the case of the power-law reads

$$\mathbb{M}^{tg} = n v_0 \sum_{r=1}^{2M+N} \frac{1}{\tau_c^r} \left(\frac{\tau^r}{\tau_c^r} \right)^{n-1} \mathbf{P}^r \otimes \mathbf{P}^r. \tag{4.27}$$

As it is seen, the fourth-order tensor $\mathbb{M}^{tg}$ exhibits all minor and major symmetries of Hook's tensor (A.1). For $n = 1$, the linear relation (3.127) is recovered. With use of the tangent compliance (4.26), a secant compliance for the power law can be defined as

$$\mathbb{M}^{sc} \equiv \frac{1}{n} \mathbb{M}^{tg} \Rightarrow \mathbf{d} = \mathbb{M}^{sc} \cdot \boldsymbol{\sigma}. \tag{4.28}$$

In general, for a non-homogeneous tensor function $\mathbf{f}$, definition of $\mathbb{M}^{sc}$ is not unique as discussed by Molinari et al. [139]. Note that for $n = 1$ one has $\mathbb{M}^{sc} = \mathbb{M}^{tg} = \mathbb{M}^{vp}$. The difference between tangent and secant compliances for the analysed power law is schematically depicted in Fig. 4.1. As it is easily noticed, for the presented one-dimensional case, one has $M^{sc} < M^{tg}$.
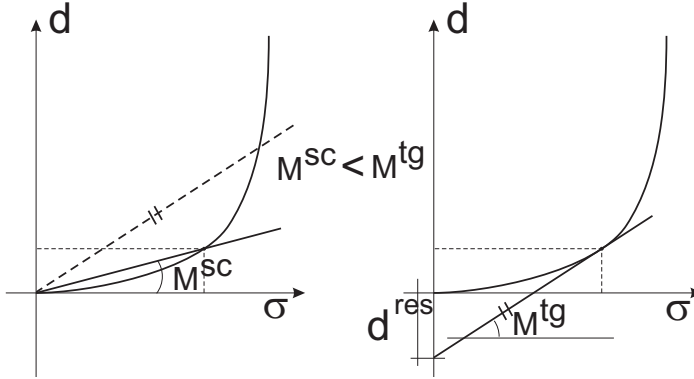
Fig. 4.1. Linearization of the power law - secant and viscous compliances.

In order to apply the Eshelby solution required for the self-consistent-type estimation of the effective response for a non-linear polycrystal, linearization of the constitutive law (4.23) has to be performed. Different proposals can be found in the literature. The most common are the following three:

1. Secant scheme proposed by Hutchinson [69] and extended by Kiryk [83], Kiryk and Petryk [84],

2. Tangent scheme proposed by Molinari et al. [138] and Lebensohn and Tomé [112], and

3. Affine scheme developed by Masson et al. [127].

They will be analysed in detail below within the small strain framework when the lattice rotation is not taken into account. Under this assumption, the strain-rate $\mathbf{d}$ can be identified with $\dot{\boldsymbol{\varepsilon}}$. At the end of this section we discuss generalization of the methods to finite strain regime. The above terminology concerning the classification of subsequent methods follows Masson et al. [127]. It is also adopted in the widely used VPSC code of Tomé and Lebensohn [201] and generally accepted in the contemporary literature on the subject, e.g. Mercier and Molinari [133].

Other proposals for estimating an overall response of non-linear polycrystalline materials can be also found in the literature. They originate in the extensions of the Hashin-Shtrikman variational principle to the non-linear composites by Talbot and Willis [194], Ponte Castañenda [165], Ponte Castañenda and Suquet [166] and are denoted as variational estimates, e.g. de Botton and Ponte Castañeda [39], Nebozhyn et al. [143]. The recent proposals belonging to this group are the so-called second-order estimates, e.g. Bornert et al. [19]. Within these variational methods it is necessary to formulate a viscoplastic potential for an appropriately selected reference homogeneous material. Let us note that the affine scheme can be also formulated with the use of this variational approach.

Secant scheme

Analyzing the steady creep of polycrystals Hutchinson [69], inspired by Hill's idea of the incremental SC model, proposed to take time-derivative of law (4.23) in the case when $\tau_c = const$ (no hardening),

$$\dot{\mathbf{d}} = \mathbb{M}^{tg}(\boldsymbol{\sigma}, \tau_c^r) \cdot \dot{\boldsymbol{\sigma}}, \tag{4.29}$$

and he has shown that in the case of the power-law (4.24) and the proportional loading it could be integrated. As an outcome it is obtained that

$$\mathbf{d} = \mathbb{M}^{sc}(\boldsymbol{\sigma}, \tau_c^r) \cdot \boldsymbol{\sigma}. \tag{4.30}$$

Using the proved property that the homogeneity of degree $n+1$ of a local stress potential f defined such that

$$\mathbf{d} = \mathbf{f}(\boldsymbol{\sigma}, \tau_c^r) = \frac{\partial f(\boldsymbol{\sigma}, \tau_c^r)}{\partial \boldsymbol{\sigma}} \Rightarrow \mathbb{M}^{tg} = \frac{\partial^2 f}{\partial \boldsymbol{\sigma} \partial \boldsymbol{\sigma}}, \tag{4.31}$$

is transferred to an overall stress potential F, cf. Hill and Rice [68], one can postulate for the overall strain-rate $\mathbf{D}$ and stress $\boldsymbol{\Sigma}$ that

$$\mathbf{D} = \bar{\mathbb{M}}^{sc} \cdot \boldsymbol{\Sigma}, \quad \bar{\mathbb{M}}^{sc} = \frac{1}{n} \frac{\partial^2 F}{\partial \boldsymbol{\Sigma} \partial \boldsymbol{\Sigma}} = \frac{1}{n} \bar{\mathbb{M}}^{tg} . \tag{4.32}$$

Neglecting the fluctuations of the local fields within the grains and then applying the Eshelby solution for the ellipsoidal inclusion embedded in HEM of compliances $\bar{\mathbb{M}}^{sc}$, one obtains interaction equation of the form

$$\mathbf{d} - \mathbf{D} = -\mathbb{M}^{sc}_* \cdot (\boldsymbol{\sigma} - \boldsymbol{\Sigma}) , \tag{4.33}$$

where the inverse of Hill tensor $\mathbb{M}^{sc}_*$ depends on inclusion shape and macroscopic compliances $\bar{\mathbb{M}}^{sc}$ via relations (B.3-B.4). By substituting laws (4.29) and (4.32) into (4.33) one obtains:

$$\boldsymbol{\sigma} = \mathbb{B}^{sc} \cdot \boldsymbol{\Sigma}, \quad \mathbb{B}^{sc} = (\mathbb{M}^{sc}_* + \mathbb{M}^{sc})^{-1} \circ (\mathbb{M}^{sc}_* + \bar{\mathbb{M}}^{sc}) . \tag{4.34}$$

For grains (inclusions) of the same shape and orientations $\langle \mathbb{B}^{sc} \rangle = \mathbb{I}$. Using the SC scheme assumption $\mathbf{D} = \langle \mathbf{d} \rangle$ and the above relations it is obtained

$$\mathbf{d} = \mathbb{M}^{sc} \cdot \boldsymbol{\sigma} = (\mathbb{M}^{sc} \circ \mathbb{B}^{sc}) \cdot \boldsymbol{\Sigma} \Longrightarrow \bar{\mathbb{M}}^{sc} = \langle \mathbb{M}^{sc} \circ \mathbb{B}^{sc} \rangle , \tag{4.35}$$

where $\mathbb{B}^{sc}$ is the concentration tensor. Alternatively the Eshelby solution can be applied to $\dot{\mathbf{d}}$ and $\dot{\boldsymbol{\sigma}}$ fields and HEM described by the overall tangent compliance. Both possibilities give equivalent results due to the properties (4.28) and (4.32) as far as the following relations are true:

$$\mathbb{M}^{tg}_* = n\mathbb{M}^{sc}_*, \quad \mathbb{B}^{tg} = \mathbb{B}^{sc} . \tag{4.36}$$

In Kiryk [83] and Kiryk and Petryk [84] the above idea was extended in order to account for a work-hardening phenomenon when modelling rate-dependent plasticity of polycrystals in the absence of elastic strains. Assuming the evolution of τ^r_c in a general manner, i.e.:

$$\dot{\tau}^r_c = h^r(\boldsymbol{\sigma}, \tau^q_c) , \tag{4.37}$$

the counterpart of (4.29) is

$$\mathbf{d} = \mathbb{M}^{tg} \cdot \dot{\boldsymbol{\sigma}} + \underbrace{\sum_q \frac{\partial \mathbf{f}(\boldsymbol{\sigma}, \tau^r_c)}{\partial \tau^q_c} h^q(\boldsymbol{\sigma}, \tau^r_c)}_{= \dot{\mathbf{d}}^{\text{res}}} . \tag{4.38}$$

This relation has a thermoelastic-like linearized form. In the case of the power law (4.24), the residual strain-rate $\dot{\mathbf{d}}^{\text{res}}$ is specified as

$$\dot{\mathbf{d}}^{\text{res}} = -n \sum_{r=1}^{M} v_0 \frac{1}{\tau_c^r} \left(\frac{\tau^r}{\tau_c^r} \right)^n h^r(\boldsymbol{\sigma}, \tau_c^q) \mathbf{P}^r . \tag{4.39}$$

Accordingly, the overall relation is postulated as

$$\dot{\mathbf{D}} = \bar{\mathbb{M}}^{tg} \cdot \dot{\boldsymbol{\Sigma}} + \dot{\mathbf{D}}^{\text{res}} . \tag{4.40}$$

Applying the Eshelby solution, the concentration relation can be specified, namely,

$$\dot{\boldsymbol{\sigma}} = \mathbb{B}^{tg} \cdot \dot{\boldsymbol{\Sigma}} + (\mathbb{M}^{tg} + \mathbb{M}_*^{tg})^{-1} \cdot (\dot{\mathbf{D}}^{\text{res}} - \dot{\mathbf{d}}^{\text{res}}) , \tag{4.41}$$

where $\mathbb{B}^{tg}$ and $\bar{\mathbb{M}}^{tg}$ are the same as for the original secant model (relations (4.36) and (4.35)). Additionally, an overall quantity $\dot{\mathbf{D}}^{\text{res}}$ is found to be[2]

$$\dot{\mathbf{D}}^{\text{res}} = \langle (\mathbb{B}^{tg})^T \cdot \dot{\mathbf{d}}^{\text{res}} \rangle . \tag{4.42}$$

When implementing the model, it is assumed that the stress field and internal variables τ_c^r are known at the end of preceding time step t. Accordingly, one can compute local tangent compliances $\mathbb{M}^{tg}$ and the reference rates of strain-rate $\dot{\mathbf{d}}^{\text{res}}$. For the considered strain programme, using the above equations, one is able to find the corresponding quantities at $t + \Delta t$. As it is seen, the procedure requires some initial condition imposed on the local stresses. In Kiryk [83] it has been proposed to derive them by applying the Hutchinson secant model, namely,

$$\boldsymbol{\sigma}_{init} = \mathbb{B}_{init}^{sc} \cdot \boldsymbol{\Sigma}_{init}, \quad \boldsymbol{\Sigma}_{init} = \langle \boldsymbol{\sigma}_{init} \rangle, \quad \mathbf{D}_{init} = \mathbb{M}_{init}^{sc} \cdot \boldsymbol{\Sigma}_{init} . \tag{4.43}$$

The form of the above initial conditions can have an impact on the predicted response of polycrystal.

Tangent scheme

The tangent scheme, proposed by Molinari et al. [138] and extended by Lebensohn and Tomé [112] can be applied only to the constitutive relation for which the stress potential is a homogeneous function of degree $n + 1$. Adopting

---

[2]The procedure for deriving $\dot{\mathbf{D}}^{\text{res}}$ is the same as the one employed by [119] to find the overall coefficient of thermal expansion. The overall plastic strain in the Kröner model is found equivalently.

the idea of an approximation of function by the Taylor series, the local relation is linearized in the following way[3]

$$\mathbf{d} = \mathbb{M}^{tg}(\boldsymbol{\sigma}, \tau_c^r) \cdot \boldsymbol{\sigma} + \mathbf{d}^{\mathrm{res}}, \tag{4.44}$$

where $\mathbb{M}^{tg}$ is specified by (4.26). Using the definition (4.28) of secant compliances for homogeneous functions, the above relation can be re-written as

$$\mathbf{d} = n\mathbb{M}^{sc}(\boldsymbol{\sigma}, \tau_c^r) \cdot \boldsymbol{\sigma} + \mathbf{d}^{\mathrm{res}}, \quad \mathbf{d}^{\mathrm{res}} = (1 - n)\mathbb{M}^{sc}(\boldsymbol{\sigma}, \tau_c) \cdot \boldsymbol{\sigma}. \tag{4.45}$$

An overall constitutive relation is postulated as[4]

$$\mathbf{D} = \bar{\mathbb{M}}^{\tilde{tg}} \cdot \boldsymbol{\Sigma} + \mathbf{D}^{\mathrm{res}}, \tag{4.46}$$

and using (4.32) it can be re-written as

$$\mathbf{D} = n\bar{\mathbb{M}}^{\tilde{sc}} \cdot \boldsymbol{\Sigma} + \mathbf{D}^{\mathrm{res}}, \quad \mathbf{D}^{\mathrm{res}} = (1 - n)\bar{\mathbb{M}}^{\tilde{sc}} \cdot \boldsymbol{\Sigma}. \tag{4.47}$$

Now, the Eshelby solution is applied to the ellipsoidal inclusion embedded in the HEM of compliances $n\bar{\mathbb{M}}^{\tilde{sc}}$, therefore the interaction equation assumes the form

$$\mathbf{d} - \mathbf{D} = -n\mathbb{M}^{\tilde{sc}}_* \cdot (\boldsymbol{\sigma} - \boldsymbol{\Sigma}), \tag{4.48}$$

where the inverse of the Hill tensor $\mathbb{M}^{\tilde{sc}}_*$ depends on the inclusion shape and the macroscopic moduli $\bar{\mathbb{M}}^{\tilde{sc}}$ via the classical relations (see Appendix B). Introducing laws (4.45) and (4.47), together with the specifications of $\mathbf{d}^{\mathrm{res}}$ and $\mathbf{D}^{\mathrm{res}}$, one obtains

$$\boldsymbol{\sigma} = \mathbb{B}^{\tilde{sc}} \cdot \boldsymbol{\Sigma}, \quad \mathbb{B}^{\tilde{sc}} = (n\mathbb{M}^{\tilde{sc}}_* + \mathbb{M}^{sc})^{-1} \circ (n\mathbb{M}^{\tilde{sc}}_* + \bar{\mathbb{M}}^{\tilde{sc}}). \tag{4.49}$$

For grains with the same shape and orientation $\langle \mathbb{B}^{\tilde{sc}} \rangle = \mathbb{I}$. Using the SC scheme assumption $\mathbf{D} = \langle \mathbf{d} \rangle$ and the above relations, it is obtained

$$\mathbf{d} = \mathbb{M}^{sc} \cdot \boldsymbol{\sigma} = (\mathbb{M}^{sc} \circ \mathbb{B}^{\tilde{sc}}) \cdot \boldsymbol{\Sigma} \implies \bar{\mathbb{M}}^{\tilde{sc}} = \langle \mathbb{M}^{sc} \circ \mathbb{B}^{\tilde{sc}} \rangle. \tag{4.50}$$

Let us stress that in general

$$\mathbb{M}^{\tilde{sc}} \neq \mathbb{M}^{sc}, \quad \mathbb{M}^{\tilde{sc}}_* \neq \mathbb{M}^{sc}_*, \quad \mathbb{B}^{\tilde{sc}} \neq \mathbb{B}^{sc}. \tag{4.51}$$

---

[3]The quantity $\mathbf{d}^{\mathrm{res}}$ in (4.44) has in general nothing to do with $\dot{\mathbf{d}}^{\mathrm{res}}$ in (4.38).

[4]A tilde over the superscripts "tg" and "sc" indicates the difference with respect to the corresponding quantities in the secant scheme.

Since the components of $\mathbb{M}_*^{\tilde{s}c}$ are of the order of components of $\mathbb{M}^{\tilde{s}c}$, we notice that for $n \to \infty$ (the rate-insensitive limit)

$$\mathbb{M}_*^{\tilde{s}c} + \frac{1}{n}\mathbb{M}^{sc} \to \mathbb{M}_*^{\tilde{s}c}, \quad \mathbb{M}_*^{\tilde{s}c} + \frac{1}{n}\mathbb{M}^{\tilde{s}c} \to \mathbb{M}_*^{\tilde{s}c}, \tag{4.52}$$

therefore

$$\mathbb{B}^{\tilde{s}c} = (n\mathbb{M}_*^{\tilde{s}c} + \mathbb{M}^{sc})^{-1} \circ (n\mathbb{M}_*^{\tilde{s}c} + \bar{\mathbb{M}}^{\tilde{s}c}) =$$
$$= (\mathbb{M}_*^{\tilde{s}c} + \frac{1}{n}\mathbb{M}^{sc})^{-1} \circ (\mathbb{M}_*^{\tilde{s}c} + \frac{1}{n}\bar{\mathbb{M}}^{\tilde{s}c}) \to \mathbb{I}^S. \tag{4.53}$$

As a consequence, for large n the solution obtained with the use of the tangent scheme tends to the lower bound (the Sachs model) and it is observed that for high values of n the tangent scheme provides too soft response as compared with the experiments. To address this drawback Molinari and Toth [137] (see also Molinari [135]) proposed the improvement of the model in which, instead of the local rate sensitivity exponent n, some effective $1 \leqslant n^{\text{eff}} \leqslant n$ was applied in the interaction equation (4.48). Consequently, the concentration tensor $\mathbb{B}^{\tilde{s}c}$ assumes the form

$$\mathbb{B}^{\tilde{s}c} = (n^{\text{eff}}\mathbb{M}_*^{\tilde{s}c} + \mathbb{M}^{sc})^{-1} \circ (n^{\text{eff}}\mathbb{M}_*^{\tilde{s}c} + \bar{\mathbb{M}}^{\tilde{s}c}). \tag{4.54}$$

Such a generalization of the tangent model appeared to be also useful when considering multi-phase polycrystals with phases of different n exponents or one-phase polycrystals with deformation modes of different rate sensitivity, e.g. slip and twinning.

Affine scheme

Similarly to the tangent scheme, in the frame of an affine scheme the local relation is linearized in the way specified by (4.44) and (4.45), where $\mathbb{M}^{tg}$ is specified by (4.26). An overall constitutive relation is postulated as[5]

$$\mathbf{D} = \bar{\mathbb{M}}^{tg} \cdot \mathbf{\Sigma} + \mathbf{D}^{\text{res}}, \tag{4.55}$$

and using (4.32) it can be re-written as

$$\mathbf{D} = n\bar{\mathbb{M}}^{sc} \cdot \mathbf{\Sigma} + \mathbf{D}^{\text{res}}. \tag{4.56}$$

---

[5]A tilde over the superscript "tg" is now not added, since for the same local stresses, the compliance $\bar{\mathbb{M}}^{tg}$ in (4.55) should be equal to that in the secant scheme.

Contrary to tangent scheme, the quantity $\mathbf{D}^{\mathrm{res}}$ is not specified by $(4.47)_2$ and has to be established with the use of the rules of self-consistent transition scheme.

The Eshelby solution is applied for the ellipsoidal inclusion embedded in the HEM of compliances $n\bar{\mathbb{M}}^{sc} = \bar{\mathbb{M}}^{tg}$, therefore, the interaction equation has the form

$$\mathbf{d} - \mathbf{D} = -n\mathbb{M}^{sc}_* \cdot (\boldsymbol{\sigma} - \boldsymbol{\Sigma}) = -\mathbb{M}^{tg}_* \cdot (\boldsymbol{\sigma} - \boldsymbol{\Sigma}),\qquad(4.57)$$

where the inverse of the Hill tensor $\mathbb{M}^{sc}_*$ (or $\mathbb{M}^{tg}_*$) depends on inclusion shape and macroscopic compliances $\bar{\mathbb{M}}^{sc}$ (or $\bar{\mathbb{M}}^{tg}$) via classical relations. Introducing laws (4.45) and (4.56) one obtains

$$\boldsymbol{\sigma} = \mathbb{B}^{tg} \cdot \boldsymbol{\Sigma} - (\mathbb{M}^{tg}_* + \mathbb{M}^{tg})^{-1} \cdot (\mathbf{d}^{\mathrm{res}} - \mathbf{D}^{\mathrm{res}}),\qquad(4.58)$$

where the concentration tensor is specified by $(4.34)_2$ and relations (4.36) are true. Note that in the case of affine model, contrary to the secant and tangent models, one can have non-zero local stresses $\boldsymbol{\sigma}$ under overall stress $\boldsymbol{\Sigma} = \mathbf{0}$.

Using the assumption of the self-consistent scheme: $\mathbf{D} = \langle\mathbf{d}\rangle$ and the above concentration relation, it is found that

$$\bar{\mathbb{M}}^{tg} = \langle\mathbb{M}^{tg} \circ \mathbb{B}^{tg}\rangle \qquad (\bar{\mathbb{M}}^{sc} = \langle\mathbb{M}^{sc} \circ \mathbb{B}^{sc}\rangle)\qquad(4.59)$$

and

$$\mathbf{D}^{\mathrm{res}} = \langle(\mathbb{B}^{tg})^T \cdot \mathbf{d}^{\mathrm{res}}\rangle = \langle(\mathbb{B}^{sc})^T \cdot \mathbf{d}^{\mathrm{res}}\rangle.\qquad(4.60)$$

Discussion

Let us compare the tangent scheme and the affine scheme. Note that, if we use for a local $\mathbf{d}^{\mathrm{res}}$ the relation

$$\mathbf{d}^{\mathrm{res}} = (1-n)\mathbb{M}^{sc} \cdot \boldsymbol{\sigma} = \frac{1-n}{n}\mathbb{M}^{tg} \cdot \boldsymbol{\sigma}\qquad(4.61)$$

and substitute (4.61) into (4.60), but together with the concentration relation (4.49) valid for the tangent scheme, we obtain

$$\mathbf{D}^{\mathrm{res}} = (1-n)\langle(\mathbb{B}^{\tilde{s}c})^T \circ \mathbb{M}^{sc} \cdot \boldsymbol{\sigma}\rangle = (1-n)\langle(\mathbb{B}^{\tilde{s}c})^T \circ \mathbb{M}^{sc} \circ \mathbb{B}^{\tilde{s}c}\rangle \cdot \boldsymbol{\Sigma}.\qquad(4.62)$$

On the other hand, if we expand the expression (4.47) for $\mathbf{D}^{\mathrm{res}}$ defined as in the tangent scheme, we arrive at

$$\mathbf{D}^{res*} = (1-n)\bar{\mathbb{M}}^{\tilde{s}c} \cdot \boldsymbol{\Sigma} = (1-n)\langle\mathbb{M}^{sc} \circ \mathbb{B}^{\tilde{s}c}\rangle \cdot \boldsymbol{\Sigma},\qquad(4.63)$$

thus the difference is

$$\mathbf{D}^{res} - \mathbf{D}^{res*} = (1 - n)\left(\langle(\mathbb{B}^{\tilde{sc}})^T \circ \mathbb{M}^{sc} \circ \mathbb{B}^{\tilde{sc}}\rangle - \langle\mathbb{M}^{\tilde{sc}} \circ \mathbb{B}^{\tilde{sc}}\rangle\right) \cdot \boldsymbol{\Sigma}. \qquad (4.64)$$

It vanishes for any $\boldsymbol{\Sigma}$ if the quantity in parentheses is zero. Recall now the Hill postulate, cf. Hill [65], Li and Wang [120]

$$\langle\boldsymbol{\sigma} \cdot \mathbf{d}\rangle - \langle\boldsymbol{\sigma}\rangle \cdot \langle\mathbf{d}\rangle = \int_{\partial V} (\mathbf{t} - \langle\boldsymbol{\sigma}\rangle\mathbf{n}) \cdot (\mathbf{v} - \langle\mathbf{d}\rangle\mathbf{x})dS, \qquad (4.65)$$

where $\mathbf{t}$ is the traction vector. For macro-uniform boundary conditions applied on the boundary of RVE, i.e. $\mathbf{t} = \boldsymbol{\Sigma} \cdot \mathbf{n} = \langle\boldsymbol{\sigma}\rangle \cdot \mathbf{n}$ or $\mathbf{v} = \mathbf{D} \cdot \mathbf{x} = \langle\mathbf{d}\rangle \cdot \mathbf{x}$, the postulate takes the form

$$\langle\boldsymbol{\sigma} \cdot \mathbf{d}\rangle = \langle\boldsymbol{\sigma}\rangle \cdot \langle\mathbf{d}\rangle = \boldsymbol{\Sigma} \cdot \mathbf{D}. \qquad (4.66)$$

By introducing into (4.66): the local relation (4.45) expressed in terms of the secant compliance, the concentration relation $(4.49)_1$ for the local stress derived for the tangent scheme, as well as the postulated overall relation for the tangent scheme, it is obtained

$$\boldsymbol{\Sigma} \cdot \langle(\mathbb{B}^{\tilde{sc}})^T \circ \mathbb{M}^{sc} \circ \mathbb{B}^{\tilde{sc}}\rangle \cdot \boldsymbol{\Sigma} = $$
$$\boldsymbol{\Sigma} \cdot \langle(\mathbb{B}^{\tilde{sc}})^T\rangle \circ \langle\mathbb{M}^{sc} \circ \mathbb{B}^{\tilde{sc}}\rangle \cdot \boldsymbol{\Sigma} = \boldsymbol{\Sigma} \cdot \bar{\mathbb{M}}^{\tilde{sc}} \cdot \boldsymbol{\Sigma}, \qquad (4.67)$$

therefore the difference (4.64) vanishes, under fulfilment of $\langle\mathbb{B}^{\tilde{sc}}\rangle = \mathbb{I}$, if the Hill condition is true. When deriving the Hill postulate, the real local fields are analysed. In the self-consistent method the approximated fields are used, in particular the piecewise-uniform distribution of local fields within the heterogeneities (grains) is assumed. Consequently, the difference specified by (4.64) may not vanish. Within the same method the difference between the two quantities (4.62) and (4.63) should be small since the fulfilment of the Hill condition indicates representativeness of the grain aggregate.

The difference between the methods can be explained by the way in which the concentration relations (4.49) and (4.58) are derived and the overall quantities are specified. In order to make it more clear recall the relation (3.30) for the estimates of overall moduli derived using the Hashin-Shtrikman variational principle. In this formula $\mathbb{L}_0$ denotes moduli of a so-called reference medium. For properly selected $\mathbb{L}_0$, bounds on $\bar{\mathbb{L}}$ are obtained; however, an estimate $\tilde{\mathbb{L}}$ of $\bar{\mathbb{L}}$ is derived for an arbitrary $\mathbb{L}_0$. In particular, if $\mathbb{L}_0$ is identified with $\tilde{\mathbb{L}}$ one obtains the self-consistent estimate by solving the resulting implicit equation,

cf. Walpole [208]. Let us specify the tangent and secant schemes approximations of overall moduli in the form equivalent to (3.30), namely,

$$\mathbb{L}^{\tilde{s}c} = \left\langle \left(\mathbb{L}^{sc} + \mathbb{L}_* \left(\frac{1}{n} \mathbb{L}^{\tilde{s}c} \right) \right)^{-1} \right\rangle^{-1} - \mathbb{L}_* \left(\frac{1}{n} \mathbb{L}^{\tilde{s}c} \right) \tag{4.68}$$

and

$$\mathbb{L}^{sc} = \left\langle \left(\mathbb{L}^{sc} + \mathbb{L}_* \left(\mathbb{L}^{sc} \right) \right)^{-1} \right\rangle^{-1} - \mathbb{L}_* \left(\mathbb{L}^{sc} \right) , \tag{4.69}$$

where $\mathbb{L}^{sc} = (\mathbb{M}^{sc})^{-1}$, $\bar{\mathbb{L}}^{sc} = (\bar{\mathbb{M}}^{sc})^{-1}$, $\bar{\mathbb{L}}^{\tilde{s}c} = (\bar{\mathbb{M}}^{\tilde{s}c})^{-1}$ and inverses are partial inverses taken accounting for tensor symmetries and incompressibility. In view of the above formulae, the tensors $\mathbb{L}^{\tilde{s}c}$ and $\mathbb{L}^{sc}$ can be interpreted as the estimates derived by assuming a reference homogenized medium of moduli $\frac{1}{n}\mathbb{L}^{\tilde{s}c}$ and $\mathbb{L}^{sc}$, respectively. For isotropic materials it has been proved that an estimate $\tilde{\mathbb{L}}$ is a monotonous function of $\mathbb{L}_0$. It is argued that the result should be transferred also to the anisotropic case, cf. Walpole [208]. Since for $n > 1$ one has $\frac{1}{n}\mathbb{L}^{\tilde{s}c} < \mathbb{L}^{\tilde{s}c}$, it suggests that the tangent scheme should provide the softer response than secant (and affine) schemes, while estimates derived with use of n^{eff} should lie somewhere in-between. The predictions of the affine scheme should be softer than those of the secant scheme for the same reasons for which the presence of inelastic strains reduces the stress level predicted by the Kröner model.

The above conclusions are confirmed by numerical results. Usually overall quantities such as, for example, overall flow stress in tension Σ_Y, obtained with use of the subsequent methods fulfil the relation

$$\Sigma_Y^{LO} < \Sigma_Y^{TG} < \Sigma_Y^{AF} < \Sigma_Y^{ST} < \Sigma_Y^{UP} . \tag{4.70}$$

In Table 4.1 the basic formulae for the analysed methods are collected.

Figure 4.2 presents the comparison of the overall flow stress in tension of the untextured fcc polycrystal derived for various averaging methods and for increasing value of the exponent n. In order to reduce the number of factors influencing the results, only slip systems are considered and equal τ_c is assumed for each slip system. Due to crystal symmetry and polycrystalline sample symmetry[6], the grain aggregate has been represented by a set of 36 orientations. As it is seen for $n = 1$, all self-consistent methods coincide (it is the case of a linear polycrystal considered in previous section). As n increases, the solution

---

[6]In the case of an untextured polycrystal, the sample symmetry corresponds to the symmetry of a deformation process. In the case of uniaxial tension or compression one has to do with axial symmetry that is the overall transverse isotropy.

Table 4.1. Basic self-consistent schemes for non-linear viscoplastic polycrystals. Subsequent rows provide: (1) the linearized form of local relation, (2) the postulated linearized overall relation, (3) the interaction equation (4) $\overline{\text{underline{derived} overall properties, (5)}}$ the stress concentration tensor $\mathbb{B}$.

Secant (ST)	Tangent (TG)	Affine (AF)
$\mathbf{d} = \mathbb{M}^{sc} \cdot \boldsymbol{\sigma}$	$\mathbf{d} = n\mathbb{M}^{sc} \cdot \boldsymbol{\sigma} + \mathbf{d}^{\text{res}}$	$\mathbf{d} = n\mathbb{M}^{sc} \cdot \boldsymbol{\sigma} + \mathbf{d}^{\text{res}}$
$(\dot{\mathbf{d}} = \mathbb{M}^{tg} \cdot \dot{\boldsymbol{\sigma}})$	$\mathbf{d}^{\text{res}} = (1-n)\mathbb{M}^{sc} \cdot \boldsymbol{\sigma}$	$\mathbf{d}^{\text{res}} = (1-n)\mathbb{M}^{sc} \cdot \boldsymbol{\sigma}$
$\mathbf{D} = \bar{\mathbb{M}}^{sc} \cdot \boldsymbol{\Sigma}$	$\mathbf{D} = n\bar{\mathbb{M}}^{\tilde{s}c} \cdot \boldsymbol{\Sigma} + \mathbf{D}^{\text{res}} = \bar{\mathbb{M}}^{\tilde{s}c} \cdot \boldsymbol{\Sigma}$	$\mathbf{D} = n\bar{\mathbb{M}}^{sc} \cdot \boldsymbol{\Sigma} + \mathbf{D}^{\text{res}}$
	$(\mathbf{D}^{\text{res}} = (1-n)\bar{\mathbb{M}}^{\tilde{s}c} \cdot \boldsymbol{\Sigma})$	
$\mathbf{d} - \mathbf{D} = -\mathbb{M}^{sc}_* \cdot (\boldsymbol{\sigma} - \boldsymbol{\Sigma})$	$\mathbf{d} - \mathbf{D} = -n\mathbb{M}^{\tilde{s}c}_* \cdot (\boldsymbol{\sigma} - \boldsymbol{\Sigma})$	$\mathbf{d} - \mathbf{D} = -n\mathbb{M}^{sc}_* \cdot (\boldsymbol{\sigma} - \boldsymbol{\Sigma})$
$\bar{\mathbb{M}}^{sc} = \langle \mathbb{M}^{sc} \circ \mathbb{B}^{sc} \rangle$	$\bar{\mathbb{M}}^{\tilde{s}c} = \langle \mathbb{M}^{sc} \circ \mathbb{B}^{\tilde{s}c} \rangle$	$\bar{\mathbb{M}}^{sc} = \langle \mathbb{M}^{sc} \circ \mathbb{B}^{sc} \rangle$
		$\mathbf{D}^{\text{res}} = \langle (\mathbb{B}^{sc})^T \cdot \mathbf{d}^{\text{res}} \rangle$
$\mathbb{B}^{sc} = (\mathbb{M}^{sc}_* + \mathbb{M}^{sc})^{-1}$	$\mathbb{B}^{\tilde{s}c} = (n\mathbb{M}^{\tilde{s}c}_* + \mathbb{M}^{sc})^{-1}$	$\mathbb{B}^{sc} = (\mathbb{M}^{sc}_* + \mathbb{M}^{sc})^{-1}$
$\circ(\mathbb{M}^{sc}_* + \bar{\mathbb{M}}^{sc})$	$\circ(n\mathbb{M}^{\tilde{s}c}_* + \bar{\mathbb{M}}^{\tilde{s}c})$	$\circ(\mathbb{M}^{sc}_* + \bar{\mathbb{M}}^{sc})$

Fig. 4.2. Estimates of the normalized overall flow stress $\Sigma^{ref} = \frac{v_0}{\dot{\varepsilon}_{eq}} \frac{\Sigma_Y}{\tau_c}$ $(\dot{\varepsilon}_{eq} = \sqrt{\frac{2}{3}\mathbf{D} \cdot \mathbf{D}})$ of fcc polycrystal of random texture in uniaxial tension. Comparison of different self-consistent schemes for viscoplastic crystals described by the power law. Macroscopic transverse isotropy is assumed.
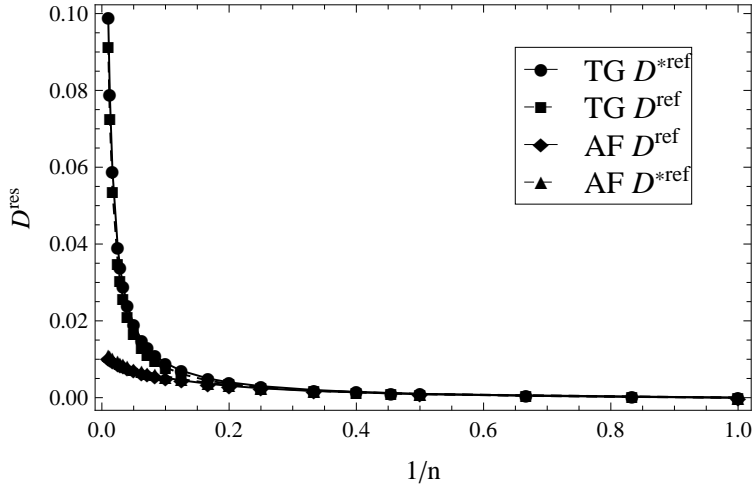
Fig. 4.3. The magnitude of an overall reference strain $D^{\mathrm{res}} = |\mathbf{D}^{\mathrm{res}}|$ in uniaxial tension for the fcc polycrystal of random texture. Comparison of the tangent scheme and the affine SC scheme for viscoplastic crystals described by the power law. Macroscopic transverse isotropy is assumed.

obtained with the use of the secant scheme tends to the solution of the Taylor model, while the solution obtained with the use of the tangent model tends to the solution of the Sachs model. The overall flow stress predicted by the affine method lies below the corresponding prediction of the secant model, although the difference between these two estimates is not substantial. Fig. 4.3 presents the magnitude of reference strain-rates $\mathbf{D}^{\mathrm{res}}$ and $\mathbf{D}^{*\mathrm{res}}$ defined, respectively, by (4.60) and (4.47). In the formulae the overall secant stiffness and the concentration tensors are calculated as for the tangent (TG) and affine (AF) schemes, respectively. As discussed above, within the same scheme, the quantities do not differ substantially which indicates approximate fulfilment of the Hill condition, and therefore representativeness of the analysed grain aggregate for the considered problem. On the other hand, the difference between the residual strain-rate $\mathbf{D}^{\mathrm{res}}$ calculated for the tangent and affine methods for large values of n is significant.

4.3.2. Application to crystals of low symmetry

Now, we will analyse the predictions of the self-consistent schemes discussed in previous sections for the non-linear viscoplastic polycrystals of low symmetry. Similarly to the case of linear polycrystals studied in Section 3.6, we will use

the examples of γ-TiAl and Mg crystals. Particularly, we would like to address the question if the properties of the self-consistent estimate discussed for the linear case are transferred for $n > 1$ in the power law. We will also study the influence of twinning.
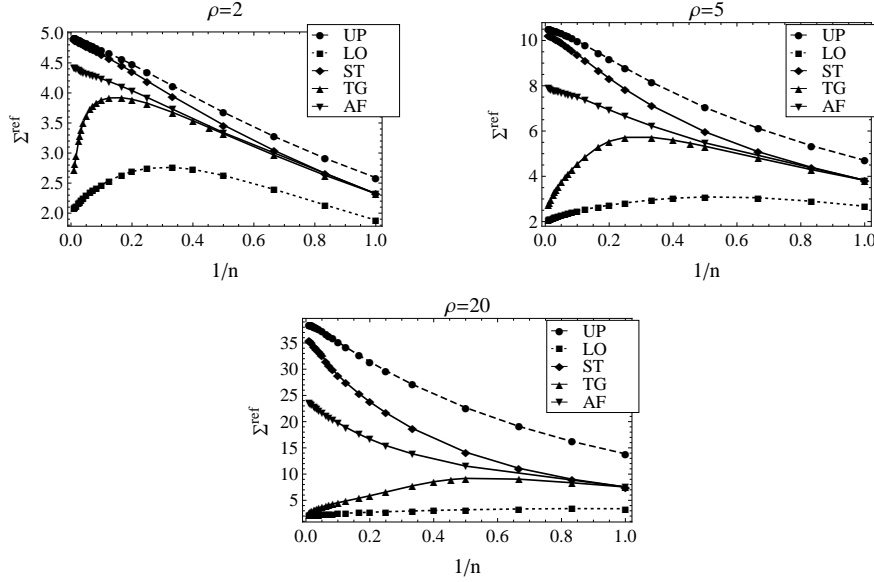
Fig. 4.4. Estimates of the normalized overall flow stress $\Sigma^{ref} = (v_0/\dot{\varepsilon}_{eq})(\Sigma_Y/\tau_c^{ord})$ $(\dot{\varepsilon}_{eq} = \sqrt{\frac{2}{3}\mathbf{D}\cdot\mathbf{D}})$ in uniaxial tension for the γ-TiAl polycrystal of random texture. Comparison of different self-consistent schemes for viscoplastic crystals described by the power law. Macroscopic transverse isotropy is assumed.

γ-TiAl intermetallic

First, let us consider the case when only slip systems are active and analyse the estimates of overall properties for the increasing value of $\rho = \tau_c^{sup}/\tau_c^{ord}$. Note that as $\rho \to \infty$ there are only three independent slip systems, so as it has been proved in Sec. 3.5, for $n = 1$ and random texture, the self-consistent estimate of an overall viscous stiffness is infinite. In Fig. 4.4 the dependence of the value of the overall flow stress in tension on the exponent n is presented for different models and different values of ρ (note that $\rho = 1$ corresponds to the case of fcc polycrystal, presented in previous subsection, Fig. 4.2).

One concludes that as ρ increases, and so the inelastic anisotropy of a single crystal, the difference between estimates obtained by different self-consistent
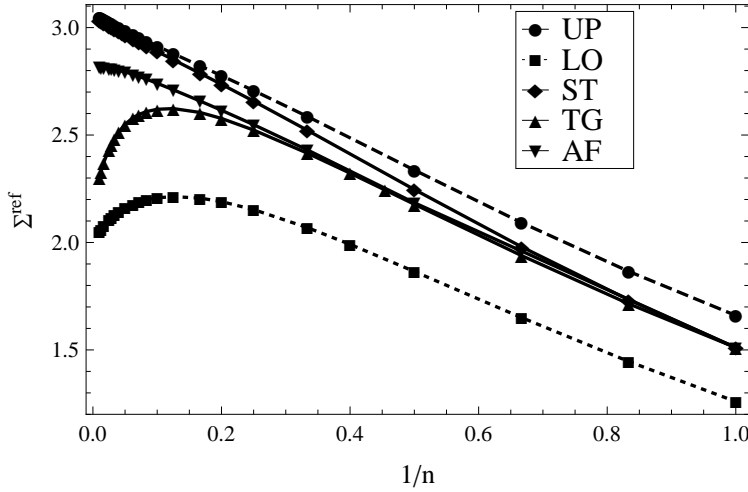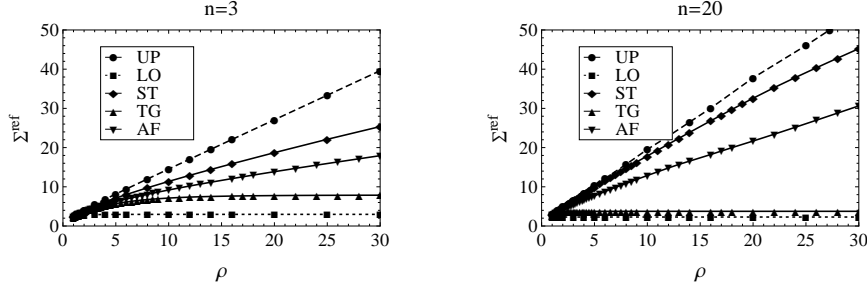
Fig. 4.5. Estimates of the normalized overall flow stress $\Sigma^{ref} = (v_0/\dot{\varepsilon}_{eq})(\Sigma_Y/\tau_c^{ord})$ $(\dot{\varepsilon}_{eq} = \sqrt{\frac{2}{3}\mathbf{D}\cdot\mathbf{D}})$ in uniaxial tension for the γ-TiAl polycrystal of random texture for increasing value of ρ, for $n=3$ and $n=20$. Comparison of different self-consistent schemes for viscoplastic crystals described by the power law. Macroscopic <u>transverse isotropy</u> is assumed.

schemes increases for high values of n. However, the relation (4.70) observed for the fcc polycrystal remains valid. As $1/n \to 0$ (rate independent limit) the secant (ST) estimates tend to the Taylor (UP) bound, the tangent (TG) estimates tend to the Sachs (LO) bound, while the affine (AF) estimates lie somewhere in-between, being closer to the secant estimates.

In Fig. 4.5 the predictions of averaging methods for increasing value of ρ and two values of n are demonstrated. One observes that as ρ increases the estimates obtained with the use of the secant and affine models increase without reaching any finite value in the limit, so they exhibit the properties of the self-consistent solution for the linear case. On the other hand, the estimate obtained by the tangent model stabilizes at some finite value, similarly to the solution of the Sachs model.

In Figs 4.6-4.8 the influence of twinning on the value of the overall flow stress in tension Σ_Y^t and compression Σ_Y^c of the γ-TiAl polycrystal of random texture is studied (note that for the polycrystal which deforms only by slip one has $\Sigma_Y^t = \Sigma_Y^c$). In general, twinning does not change the relation (4.70) between estimates of Σ_Y obtained with the use of the discussed methods. As it could be expected, possibility of activation of twinning mechanisms reduces the value of Σ_Y^c as compared to the value estimated for a polycrystal for which twinning is not taken into account, but for the same value of ρ, Fig. 4.6. The lower is the ratio $\rho_{tw} = \tau_c^{tw}/\tau_c^{ord}$, the higher is reduction of Σ_Y^c. Such a reduction takes place for both, compression and tension. For γ-TiAl, the calculated value of the overall flow stress in tension is lower than in compression, independently of the method applied. The difference is usually not substantial, being more significant for lower ρ and lower n values. In Figs 4.7 and 4.8 the effect of unidirectionality of twinning is analysed. Besides the overall flow stress in tension and compression

Fig. 4.6. The influence of twinning on the estimates of the overall flow stress in compression, $\Sigma^{ref} = (v_0/\dot{\varepsilon}_{eq})(\Sigma_Y^c/\tau_c^{ord})$ $(\dot{\varepsilon}_{eq} = \sqrt{\frac{2}{3}\mathbf{D}\cdot\mathbf{D}})$, obtained by different averaging schemes for the TiAl polycrystal of random texture.

for polycrystal deforming by slip and twinning, we present the corresponding curve for polycrystal composed of grains made of hypothetical material for which the geometry of shear modes is the same as for a real γ-TiAl crystal; however, modes of geometry of twin systems act as slip systems (i.e. shear on these systems can take place in both directions). One observes that in the latter case the estimated overall flow stress is much lower than in the case of unidirectional twin systems.

Fig. 4.7. The difference between the estimates of the overall flow stress in compression, $\Sigma^{ref} = (v_0/\dot{\varepsilon}_{eq})(\Sigma_Y^c/\tau_c^{ord})$, and tension, $\Sigma^{ref} = (v_0/\dot{\varepsilon}_{eq})(\Sigma_Y^t/\tau_c^{ord})$ $(\dot{\varepsilon}_{eq} = \sqrt{\frac{2}{3}\mathbf{D}\cdot\mathbf{D}})$, induced by twinning in the case of local visco-plastic power law with $n = 1$ (different averaging schemes, the γ-TiAl polycrystal, $\rho = 20$). Reference curve - a crystal with twinning replaced by slip of the same geometry.

Mg polycrystals

Similarly as for TiAl, we start with the case when only slip systems are active. Without loss of generality, we restrict to three classes of slip systems: basal, prismatic and pyramidal $\langle c+a \rangle$ (see Section 2.2). Furthermore, throughout the presented examples, we assume

$$\rho_1 = \frac{\tau_c^{prism.}}{\tau_c^{basal}} = 5\,, \qquad (4.71)$$

and we analyse the dependence of results on the value of $\rho_3 = \tau_c^{pyram.\langle c+a \rangle}/\tau_c^{basal}$. Note that when $\rho_3 \to \infty$, there are four independent slip systems and, as it has been demonstrated in Section 3.5, in the case of linear polycrystal $(n = 1)$ of random texture, a finite self-consistent estimate of overall properties exists.

As observed in Fig. 4.9, similarly to the TiAl polycrystal, difference between subsequent estimates increases with ρ_3 satisfying relation (4.70). It is observed that for high ρ_3 the difference between the Taylor upper bound and the secant model is significant. Moreover, for ρ_3 high enough, the affine estimate becomes almost independent of n.
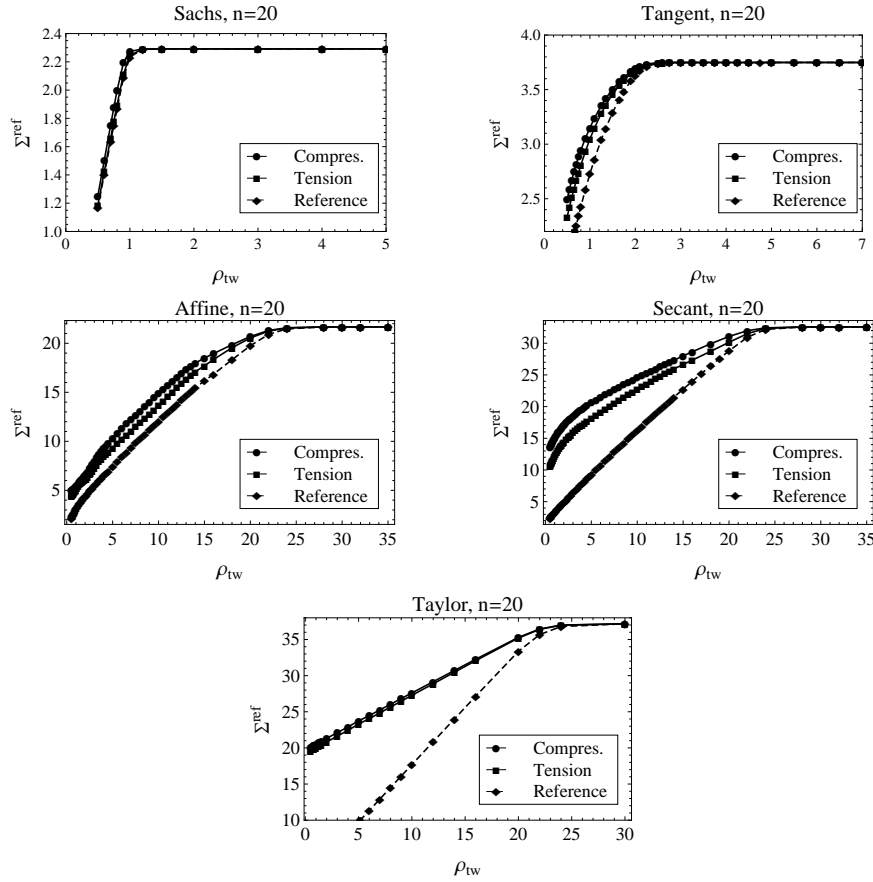
Fig. 4.8. The difference between the estimates of the overall flow stress in compression, $\Sigma^{ref} = (v_0/\dot{\varepsilon}_{eq})(\Sigma_Y^c/\tau_c^{ord})$, and tension, $\Sigma^{ref} = (v_0/\dot{\varepsilon}_{eq})(\Sigma_Y^t/\tau_c^{ord})$ ($\dot{\varepsilon}_{eq} = \sqrt{\frac{2}{3}\mathbf{D}\cdot\mathbf{D}}$), induced by twinning in the case of local viscoplastic power law with $n = 20$ (different averaging schemes, the γ-TiAl polycrystal, $\rho = 20$). A reference curve - a crystal with twinning replaced by slip of the same geometry.

In Fig. 4.10 the behaviour of the subsequent averaging methods for increasing value of ρ_3 and two values of n is demonstrated. One observes that all self-consistent estimates for increasing ρ_3 reach some finite values in the limit, therefore one can conclude that the property proved for $n = 1$ is inherited by these self-consistent estimates in the case of a non-linear viscoplastic polycrystal. In bottom-left Fig. 4.9 the dependence of this limit value on the exponent n is shown. Recall that the finite Taylor upper bound for the case when $\rho_3 \to \infty$ does not exist.

In Figs 4.11-4.13 the influence of twinning on the value of the overall flow stress in tension, Σ_Y^t, and compression, Σ_Y^c, is compared. Pyramidal $\langle c + a\rangle$
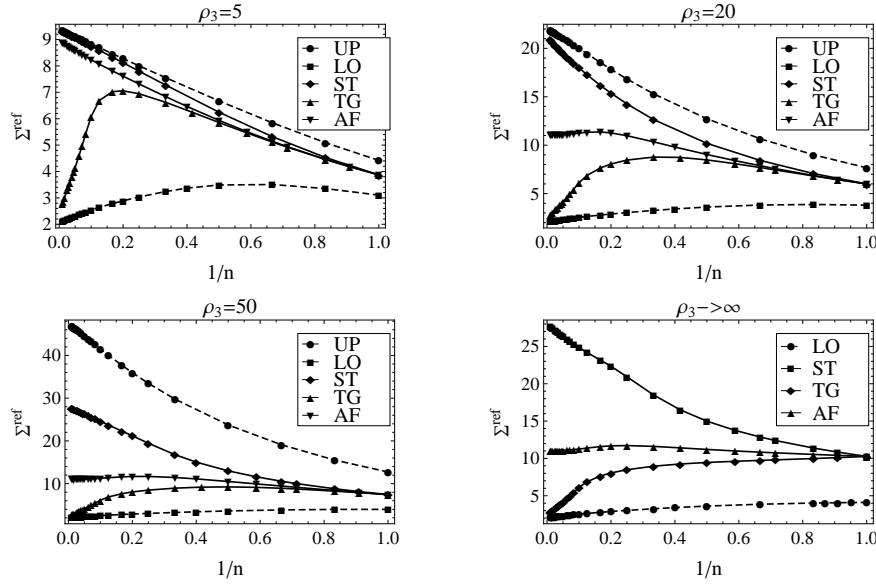
Fig. 4.9. Estimates of the normalized overall flow stress $\Sigma^{ref} = (v_0/\dot{\varepsilon}_{eq})(\Sigma_Y/\tau_c^{basal})$ ($\dot{\varepsilon}_{eq} = \sqrt{\frac{2}{3}\mathbf{D}\cdot\mathbf{D}}$) in uniaxial tension for the Mg polycrystal of random texture. Comparison of different self-consistent schemes for viscoplastic crystals described by the power law. Macroscopic transverse isotropy is assumed.
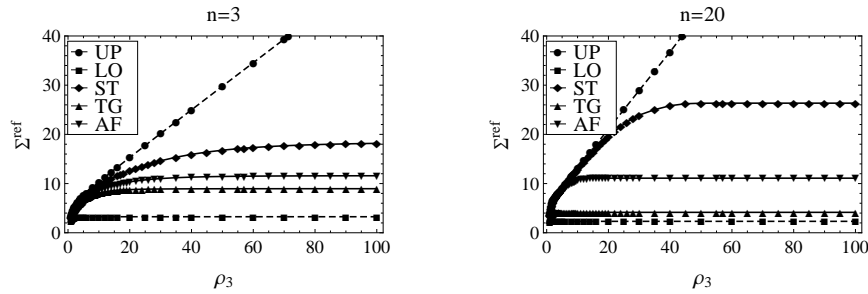
Fig. 4.10. Estimates of the normalized overall flow stress $\Sigma^{ref} = (v_0/\dot{\varepsilon}_{eq})(\Sigma_Y/\tau_c^{basal})$ ($\dot{\varepsilon}_{eq} = \sqrt{\frac{2}{3}\mathbf{D}\cdot\mathbf{D}}$) in uniaxial tension for the Mg polycrystal of random texture for increasing value of ρ_3, for $n = 3$ and $n = 20$. Comparison of different self-consistent schemes for viscoplastic crystals described by the power law. Macroscopic transverse isotropy is assumed.
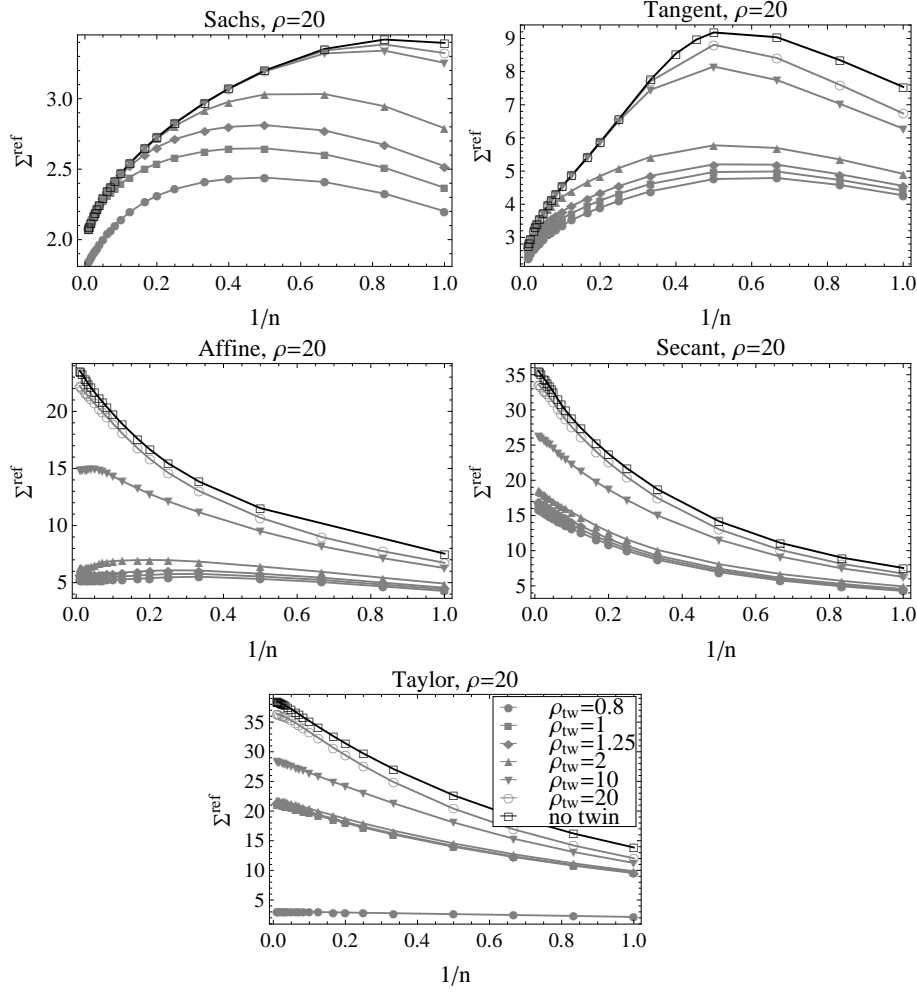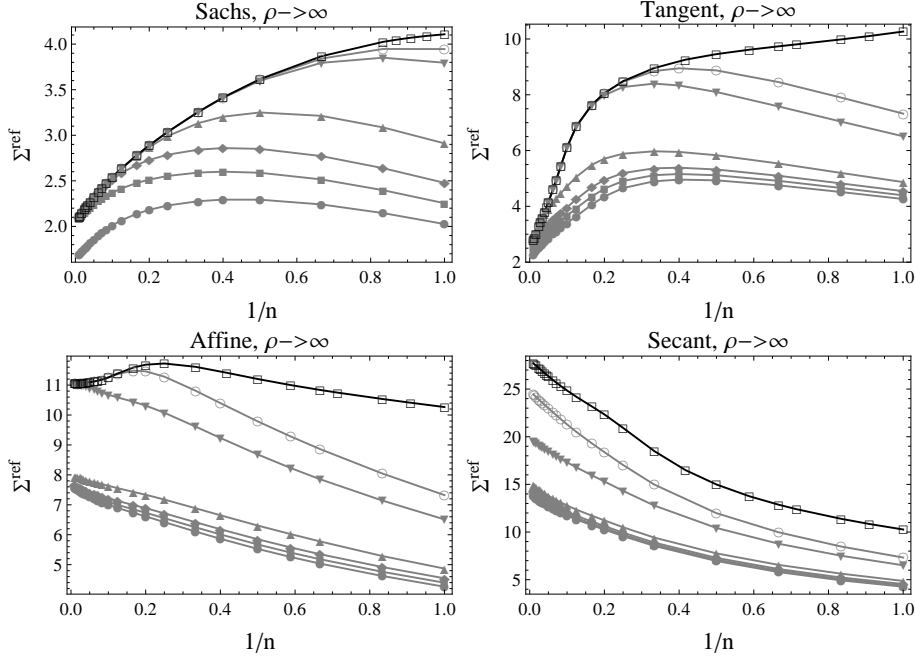
Fig. 4.11. The influence of twinning on the estimates of the overall flow stress in compression, $\Sigma^{ref} = (v_0/\dot{\varepsilon}_{eq})(\Sigma_Y^c/\tau_c^{basal})$ ($\dot{\varepsilon}_{eq} = \sqrt{\frac{2}{3}\mathbf{D}\cdot\mathbf{D}}$), obtained by different averaging schemes for the Mg polycrystal of random texture (lines denoted as in Fig. 4.6).
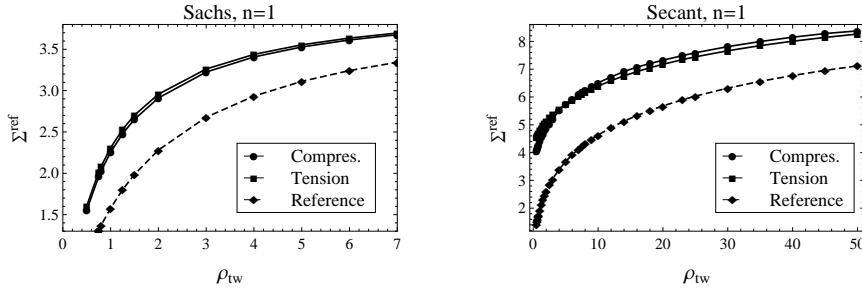
Fig. 4.12. The difference between the estimates of the overall flow stress in compression, $\Sigma^{ref} = (v_0/\dot{\varepsilon}_{eq})(\Sigma_Y^c/\tau_c^{basal})$, and tension, $\Sigma^{ref} = (v_0/\dot{\varepsilon}_{eq})(\Sigma_Y^t/\tau_c^{basal})$ ($\dot{\varepsilon}_{eq} = \sqrt{\frac{2}{3}\mathbf{D}\cdot\mathbf{D}}$), induced by twinning in the case of local visco-plastic power law with $n = 1$ (Sachs lower bound and self-consistent estimate are shown, the Mg polycrystal (no pyramidal slip, $\rho_3 \to \infty$)). A reference curve - a single crystal with twinning replaced by slip of the same geometry.
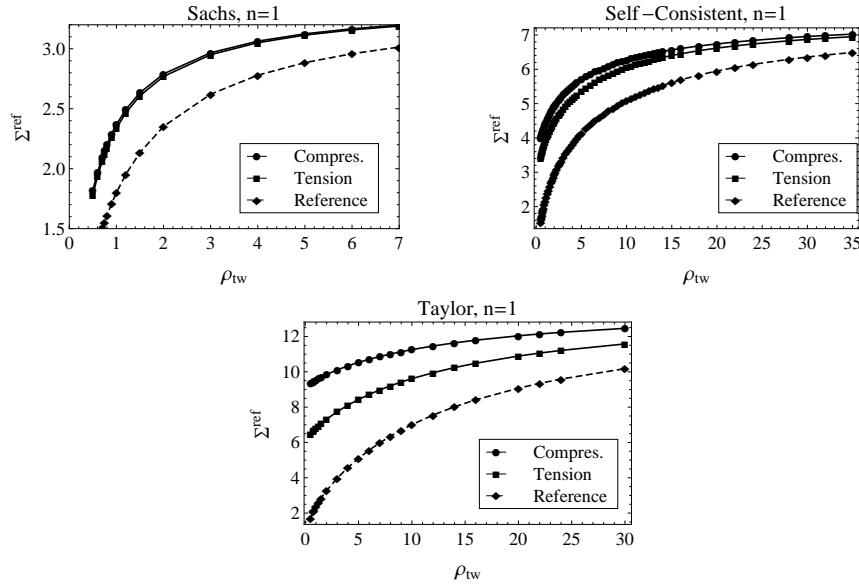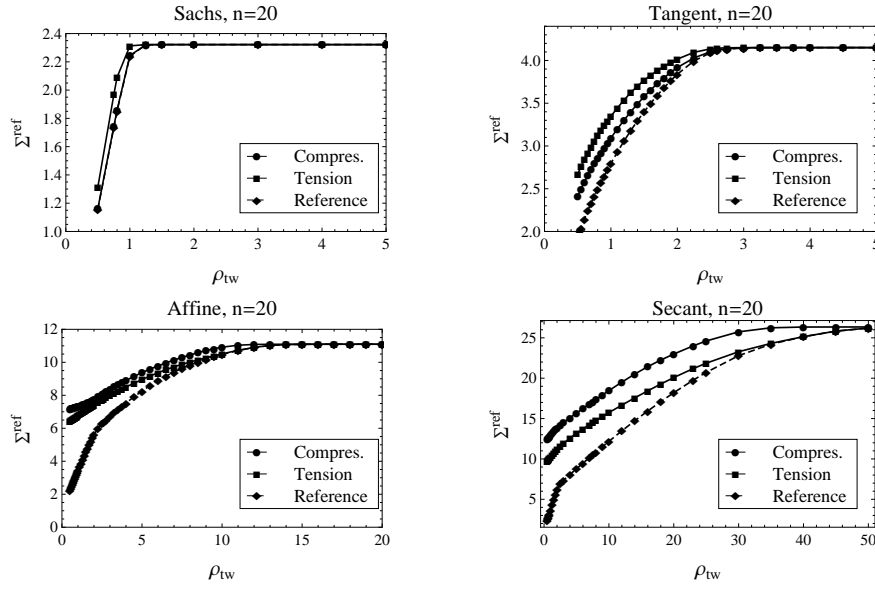
Fig. 4.13. The difference between the estimates of the overall flow stress in compression, $\Sigma^{ref} = (v_0/\dot{\varepsilon}_{eq})(\Sigma_Y^c/\tau_c^{basal})$, and tension, $\Sigma^{ref} = (v_0/\dot{\varepsilon}_{eq})(\Sigma_Y^t/\tau_c^{basal})$ $(\dot{\varepsilon}_{eq} = \sqrt{\frac{2}{3}\mathbf{D} \cdot \mathbf{D}})$, induced by twinning in the case of local visco-plastic power law with $n = 20$ (different averaging schemes, the Mg polycrystal of random texture, $\rho_3 \to \infty$). Reference curve - a single crystal with twinning replaced by slip of the same geometry.

slip systems have not been taken into account $(\rho_3 \to \infty)$, therefore we do not present the results for the Taylor scheme. Contrary to the result obtained for the γ-TiAl polycrystal, depending on the averaging scheme, Σ_Y^t can be greater or lower than Σ_Y^c, and moreover, even for the same averaging scheme this relation can be different for different values of ρ_{tw}. Similarly to the case of γ-TiAl, the value of the overall flow stress, due to unidirectionality of twinning, is higher than for the hypothetical crystal in which twinning is replaced by slip of the same geometry.

4.3.3. Finite strain regime

The self-consistent models discussed above are easily adopted to the analysis of large strain and texture evolution, cf. Lebensohn and Tomé [112], Molinari et al. [139]. One can show that, as a result of the Eshelby solution, the gradient of the velocity field induced in the inclusion by the eigenstrain-rate $\mathbf{d}^*$ is

$$\tilde{\mathbf{l}} = \mathbf{l} - \mathbf{L} = (\mathbb{T} \circ \bar{\mathbb{M}}^{-1}) \cdot \mathbf{d}^*, \tag{4.72}$$

where the tensor $\mathbb{T}$ is the not-symmetrized polarisation tensor specified by (B.4). Let us define the tensor $\hat{\mathbb{P}}$ such that

$$\hat{P}_{ijmn} = \frac{1}{4}\left(T_{ijmn} - T_{jimn} + T_{ijnm} - T_{jimn}\right) , \tag{4.73}$$

then decomposition of (4.72) into symmetric and skew-symmetric parts provides the relations

$$\tilde{\mathbf{d}} = \mathbf{d} - \mathbf{D} = (\mathbb{P} \circ \bar{\mathbb{M}}^{-1}) \cdot \mathbf{d}^* , \tag{4.74}$$

$$\tilde{\boldsymbol{\omega}} = \boldsymbol{\omega} - \boldsymbol{\Omega} = (\hat{\mathbb{P}} \circ \bar{\mathbb{M}}^{-1}) \cdot \mathbf{d}^* . \tag{4.75}$$

By introducing (4.74) into (4.75) one obtains

$$\boldsymbol{\omega} - \boldsymbol{\Omega} = \hat{\mathbb{P}} \circ \mathbb{P}^{-1} \cdot (\mathbf{d} - \mathbf{D}) . \tag{4.76}$$

After assessing the total local spin $\boldsymbol{\omega}$, provided that the local stress field is known, one can calculate the lattice spin, and consequently the texture evolution.

Assuming that the overall strain programme $\mathbf{L}(t)$ is imposed, the computational procedure consists of the following steps:

- The local and overall stresses are calculated with the use of the interaction equations valid for the selected linearization scheme, i.e. (4.33), (4.48) or (4.57), and local and overall constitutive rules. The derivations are not straightforward, as the local and overall compliances depend non-linearly on stress fields. Usually some version of Newton-Raphson method is applied, which employs outer and inner loops for iterations. In the outer loop over iterations K the overall compliance $\bar{\mathbb{M}}$ is assessed by solving one of the implicit equations (B.20)-(B.21). In the inner loop for the approximated $\bar{\mathbb{M}}^{(K)}$, obtained in the current iteration K of the outer loop, we solve the interaction equations in order to find corresponding values of local and overall stress and strain-rate fields.

- For the local strain-rates, stresses and imposed $\mathbf{L}(t)$, the local total spins, plastic spins and lattice spins are calculated using (4.76), (2.2), (2.4) and (2.26).

- The current values of grain orientations and internal variables τ_c^r are updated.

The above generalizations of the self-consistent method for non-linear viscoplastic polycrystals are implemented in the widely used VPSC code [201], which has been utilized in Chapter 2 to study the stress-strain response and texture evolution in metals and alloys subjected to large deformation processes.

4.4. Conclusions

The chapter has been devoted to the analysis of existing extensions of a self-consistent averaging scheme in the case of the non-linear constitutive laws.

First, elastic-plastic (rate-independent) polycrystals have been considered. A short review on the generalizations of the Kröner method as well as the Hill incremental scheme has been provided. The original outcome of this section is the formulation of the incremental scheme for estimation of a mechanical response of the elastic-plastic polycrystal within the large strain regime, in conjunction with the regularized Schmid law.

Next, a critical review of existing methods for estimation of averaged properties of non-linear viscoplastic polycrystals has been performed. The attention has been focused on three most widely applied generalizations of a self-consistent model, namely: secant, tangent and affine schemes. The differences between these three micro-macro transition methods have been emphasized, which are usually not clearly indicated in the literature. All these schemes have been evaluated for the selected random polycrystals of low symmetry, i.e. the γ-TiAl and Mg untextured aggregates of equiaxed grains. We have found that the condition for the existence of a finite self-consistent estimate derived for a linear law seems to hold for $n \to \infty$ in the case of secant and affine schemes, while the tangent scheme behaves as the lower bound in this case. Similar observations for other polycrystals with an insufficient number of easy slip systems have been reported in the literature as well, e.g. Hutchinson [71], Nebozhyn et al. [143], Bornert et al. [19], Lebensohn et al. [114]. Here, in contrast to the cited papers, twinning mode has been included in the analysis which enabled us to assess tension/compression asymmetry predicted by the analysed schemes. In this respect, it has been found that in the case of random polycrystal the difference in the yield stress in tension and compression is not significant. As expected, possibility of activation of twinning reduces the yield stress of a polycrystal as compared to the same material with only slip systems active. However, unidirectionality of twinning causes that this reduction is less pronounced than in the case of addition of slip of the same geometry. The observed differences are more pronounced for the secant and affine schemes than for the tangent scheme.

5

Metals of lamellar substructure

5.1. Introduction

In some metals or alloys of high specific strength, due to e.g. particular conditions during processing, a lamellar substructure of grains develops. In the case of these materials one can distinguish three levels of microstructure (Fig. 5.1), namely:

1. Level of an individual lamella,
2. Level of a lamellar grain, which will be called a *metagrain*, build of colonies of thin parallel plates,
3. Level of polycrystalline material.

For proper separation of these three levels of microstructure, enabling one the formulation of a three-scale micromechanical model, it is required that the thickness of an individual lamella is considerably smaller than the average size of a metagrain, which itself is much smaller than the characteristic dimension of a polycrystalline sample.

As concerns (visco)plastic properties of the material, it is observed that the small thickness of the lamellae induces confinement effects (the Hall-Petch effects) by reducing the distance of a main free path for dislocations, cf. Appel and Wagner [6]. These effects are usually taken into account by a morphological differentiation of the plastic deformation modes, such as slip or twinning. Consequently, one defines, cf. Lebensohn et al. [113]:

- *longitudinal* modes, for which plane and direction of shearing are parallel to the lamellae interface specified by a unit normal $\mathbf{n}$,

$$\mathbf{n}^r_{LONG} \cdot \mathbf{n} = 1, \quad \mathbf{m}^r_{LONG} \cdot \mathbf{n} = 0, \tag{5.1}$$

- *mixed* modes, for which only the direction of shearing is parallel to the lamellae interface,

$$\mathbf{n}^r_{MIX} \cdot \mathbf{n} \neq 1, \quad \mathbf{m}^r_{MIX} \cdot \mathbf{n} = 0, \tag{5.2}$$
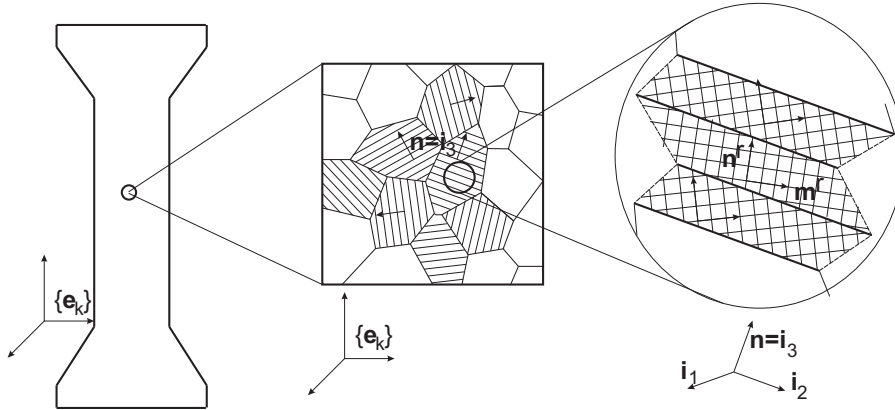
Fig. 5.1. Polycrystal with a lamellar substructure.

- *transversal* modes, for which neither plane nor direction of shearing are parallel to the lamellae interface,

$$\mathbf{n}_{TRANS}^r \cdot \mathbf{n} \neq 1, \quad \mathbf{m}_{TRANS}^r \cdot \mathbf{n} \neq 0. \tag{5.3}$$

If the deformation mode under consideration belongs to the same type, that is in the case of a single crystal one should expect an equal initial critical shear stress τ_c^r, then in the case of a lamellar grain one has

$$\tau_c^{TRANS} = \alpha_T \tau_c^{MIX} = \alpha_T \alpha_M \tau_c^{LONG}, \quad \text{where} \quad \alpha_T \geqslant 1, \quad \alpha_M \geqslant 1. \tag{5.4}$$

These directional confinement effects result in substantial anisotropy of a metagrain. The critical shear stress τ_c^{LONG} is usually assumed to be equal to τ_c for the relevant slip system in the equiaxed grain without the lamellar substructure of the same size as the analysed metagrain.

In metals and alloys of high specific strength the lamellar substructure develops due to the deformation twinning or due to the thermal treatment, as in the case of a $\alpha_2 + \gamma$-TiAl intermetallic. However, this kind of microstructure can be also observed in shape memory alloys and polymers or man-made laminated composites. Consequently, the micromechanical model presented in this chapter shares common concepts with the corresponding modelling frameworks developed for shape memory alloys (SMA), e.g. Stupkiewicz and Petryk [190], semicrystalline polymers, e.g. Nikolov et al. [147], or composites, e.g. El Omri et al. [47], Berryman [13]. In most of these models attention is focused on the linear elasticity or linear elasticity with the eigenstrain (transformation strain in the case of SMA).

The idea of a three-scale model has been also utilized in a family of models developed in order to relax the strong constraints imposed on the deformation by the Taylor scheme. These models introduce the metagrain composed of two brick-shaped adjacent grains (LAMEL model of Van Houtte et al. [206]) or the grain segments (ALAMEL model of Van Houtte et al. [207]), for which compatibility conditions for the velocity gradient are formulated at each of existing interfaces. The slip rates in each grain or each grain segment are found by minimizing the rate of plastic work. It has been found that the latter procedure is equivalent to imposing the stress equilibrium at the interface. The approach originates in the so-called pancake model, cf. Kocks and Chandra [89], Van Houtte [204], Van Houtte et al. [205], which was proposed to account for the change in grain morphology in a unidirectional forming process. The models work within the large strain regime. The compatibility conditions, together with the Taylor transition scheme, govern the texture evolution in the metagrain aggregate. The similar concept has been recently applied in modelling of the polycrystalline SMA by Stupkiewicz and Petryk [191] within the small strain framework.

In the case of lamellar substructure which develops due to the deformation twinning and the thermal treatment or phase transformations, a strict orientation relationship between subsequent lamellae exists. In the small strain regime it is admissible to assume that this relation, as well as the volume fractions of the phases, are preserved during the deformation process. However, when the material is subjected to the large plastic deformation processes, the initial relation can be lost due to the lattice rotation responsible for the texture development. The problem is rarely analysed in the literature. In Tomé et al. [202] the issue of corotation of neighbouring grains, not necessary twin-related ones, was addressed. Within the two-site self-consistent scheme four variants of the corotational schemes have been proposed. In this scheme one considers two ellipsoidal inclusions embedded in an equivalent medium. The idea is that these two inclusions represent two adjacent grains. Two tensorial parameters have been introduced, which govern corotation of material fibres and crystallographic directions in two inclusions. Depending on the specification of these parameters, in subsequent variants it is assumed that: (i) rotations of ellipsoids axes and crystallographic directions are not constrained and follow directly from the applied SC scheme, (ii) the lattice directions in adjacent grains corotate, (iii) the main axes of ellipsoids representing adjacent grains corotate, (iv) the crystallographic planes parallel to the tangent plane of two ellipsoids corotate.

In this chapter the attention is first focused on the scale transition rule between level 1 and level 2. We start with the presentation of an approach for mo-

delling of a lamellar microstructure within a small strain regime, assuming that material is described by linear or non-linear constitutive laws. The presented model uses the general framework developed for laminates (layered composites), cf., e.g. El Omri et al. [47]. Specification of the model will be provided for incompressible materials. The computational issues related to the implementation of the three-scale model, which employs different transition schemes between the level of lamellar grain and the level of polycrystal are presented in more detail. The specification of these procedures in the case of non-linear constitutive laws can be indicated as an original result, as this kind of modelling framework is not common in the literature. The only example we are aware of is the proposal of a composite grain model discussed by Proust et al. [169], but without providing implementation details. The possibility of application of the three-scale model to TiAl polycrystals was also indicated by Lebensohn et al. [113]. The model formulated in this chapter adopts the approach described in the latter paper. However, in Lebensohn et al. [113] only the viscoplastic properties of a metagrain were analysed. Recently, similar modelling scheme has been applied to semi-crystalline polymers by Nikolov et al. [147].

Furthermore, the extension of the presented approach to the case of large deformations will be formulated. In particular, in the presented large strain model, the reorientation of lamellae planes and the evolution of crystallographic texture are taken into account as proposed by Kowalczyk-Gajewska [98]. Due to relative reorientation of lamellae interfaces and crystallographic planes, the character of subsequent deformation modes within the lamellae changes. We account for this effect by introducing the formula for the critical shear stress, which depends on the current orientation of a deformation mode with respect to the lamellar substructure.

The model is applied to predict the response of two-phase $\alpha_2 + \gamma$-TiAl. First, elastic anisotropy and plastic anisotropy of the poly-synthetically twinned (PST) TiAl is analysed. In the second part of the chapter the texture evolution in $\alpha_2 + \gamma$-TiAl polycrystal is computed. In the literature one can find various modelling schemes applied for this two-phase TiAl. Brockman [21] and Werwer and Cornec [215, 216] estimated effective elastic-plastic properties of the corresponding polycrystalline material by combining a laminate model with a finite element method. Roos et al. [173] analysed elastic-viscoplastic behaviour of polycrystal using, as a scale transition between levels 2 and 3, the self-consistent Kröner model with purely elastic interactions between inclusion (identified with a metagrain) and the homogenized effective medium. In these works the models were restricted to the small strain regime. Besides the analysis of $\alpha_2 + \gamma$-TiAl response within the large strain regime, the original outcome

of the research reported in this chapter is the evaluation of the influence of different rules of scale transition between levels 2 and 3 on the estimated overall properties. In particular, different self-consistent estimates developed for non-linear viscoplastic polycrystals are considered.

5.2. Lamellar grain model - small strain framework

5.2.1. Homogenized properties

In this section we restrict ourselves to small strains and rotations. At the interface of a unit normal $\mathbf{n}$ between neighbouring lamellae i and j, a standard condition of continuity of a displacement (velocity) field is fulfilled, implying the following compatibility condition for the small strain (strain-rate) tensor $\boldsymbol{\varepsilon}$,

$$\boldsymbol{\varepsilon}_j = \boldsymbol{\varepsilon}_i + \frac{1}{2}(\mathbf{b} \otimes \mathbf{n} + \mathbf{n} \otimes \mathbf{b}), \tag{5.5}$$

where $\mathbf{b}$ is an arbitrary vector. Furthermore, assumption of equilibrium of traction forces on this interface implies for the stress tensor $\boldsymbol{\sigma}$,

$$\boldsymbol{\sigma}_j \cdot \mathbf{n} = \boldsymbol{\sigma}_i \cdot \mathbf{n}. \tag{5.6}$$

We assume also that the stress and strain fields are uniform within the lamella. As a result of the above conditions, the components of the strain and stress tensors in the lamellae i and j in the basis $\{\mathbf{i}_k\}$, where $\mathbf{i}_3 = \mathbf{n}$ (Fig. 5.1), are related as follows:

$$\varepsilon_{kl}^i = \varepsilon_{kl}^j, \quad \text{for} \quad kl = 11, 22, 12, \tag{5.7}$$

and

$$\sigma_{kl}^i = \sigma_{kl}^j, \quad \text{for} \quad kl = 13, 23, 33. \tag{5.8}$$

Let us define two orthogonal projectors[1], cf. Walpole [208], Petryk [158]:

$$(\mathbb{P}^T)_{ijkl} = \frac{1}{4}\left(2\delta_{ik}n_j n_l + \delta_{jk}n_i n_l + \delta_{il}n_j n_k\right), \quad \mathbb{P}^L = \mathbb{I}^S - \mathbb{P}^T, \tag{5.9}$$

which project into two three-dimensional orthogonal subspaces of second-order tensors. It can be easily verified that relations (5.7-5.8) are equivalent to the following basis-free equations:

$$\mathbb{P}^L \cdot \boldsymbol{\varepsilon}_i = \mathbb{P}^L \cdot \boldsymbol{\varepsilon}_j = \mathbb{P}^L \cdot \boldsymbol{\varepsilon}_{mc}, \quad \mathbb{P}^T \cdot \boldsymbol{\sigma}_i = \mathbb{P}^T \cdot \boldsymbol{\sigma}_j = \mathbb{P}^T \cdot \boldsymbol{\sigma}_{mc}, \tag{5.10}$$

---

[1]The notation $(\cdot)^T$ should not be confused with the notation $(\cdot)^{\mathrm{T}}$ denoting the transpose of a tensor.

where ε_{mc} and $\boldsymbol{\sigma}_{mc}$ are average strain and stress in the metagrain defined as

$$\varepsilon_{mc} = \{\varepsilon_i\}, \quad \boldsymbol{\sigma}_{mc} = \{\boldsymbol{\sigma}_i\}, \quad \{\cdot\} = \sum_{i=1}^{NL} \nu_i(\cdot)_i \tag{5.11}$$

and NL is a number of distinct lamellae in the metagrain; $\nu_i = V_i/V_{mc}$ are their relative volume contents.

It is assumed that the constitutive law between a strain (or a strain-rate) measure and a stress measure in the lamella i is linear, or that it has been linearized according to one of the proposals discussed in Chapter 4, with the corresponding compliance tensor $\mathbb{M}_i$ and the eigenstrain (the reference strain) $\varepsilon_i^{\mathrm{res}}$, namely,

$$\varepsilon_i = \mathbb{M}_i \cdot \boldsymbol{\sigma}_i + \varepsilon_i^{\mathrm{res}}. \tag{5.12}$$

We are looking for the homogenized properties $\mathbb{M}_{mc}$ of a laminated metagrain and the overall eigenstrain (the overall reference strain) in a metagrain, $\varepsilon_{mc}^{\mathrm{res}}$, which relate the average strain ε_{mc} and the stress $\boldsymbol{\sigma}_{mc}$, according to the following affine relation

$$\varepsilon_{mc} = \mathbb{M}_{mc} \cdot \boldsymbol{\sigma}_{mc} + \varepsilon_{mc}^{\mathrm{res}}. \tag{5.13}$$

To this end we follow, to some extent, the derivation presented by El Omri et al. [47] and Stupkiewicz [189] which rely on the decomposition of the second-order tensor into out-of-plane and in-plane parts. This decomposition is realized by the orthogonal projectors (5.9).

Local and average constitutive relations (5.12) and (5.13), in view of (5.10), can be re-written as (no summation convention invoked)

$$\varepsilon_i^L = \varepsilon_{mc}^L \ = \ \mathbb{M}_i^{LL} \cdot \boldsymbol{\sigma}_i^L + \mathbb{M}_i^{LT} \cdot \boldsymbol{\sigma}_{mc}^T + \varepsilon_i^{\mathrm{res}L}, \tag{5.14}$$

$$\varepsilon_i^T \ = \ \mathbb{M}_i^{TL} \cdot \boldsymbol{\sigma}_i^L + \mathbb{M}_i^{TT} \cdot \boldsymbol{\sigma}_{mc}^T + \varepsilon_i^{\mathrm{res}T} \tag{5.15}$$

and

$$\varepsilon_{mc}^L \ = \ \mathbb{M}_{mc}^{LL} \cdot \{\boldsymbol{\sigma}_i^L\} + \mathbb{M}_{mc}^{LT} \cdot \boldsymbol{\sigma}_{mc}^T + \varepsilon_{mc}^{\mathrm{res}L}, \tag{5.16}$$

$$\varepsilon_{mc}^T = \{\varepsilon_i^T\} \ = \ \mathbb{M}_{mc}^{TL} \cdot \{\boldsymbol{\sigma}_i^L\} + \mathbb{M}_{mc}^{TT} \cdot \boldsymbol{\sigma}_{mc}^T + \varepsilon_{mc}^{\mathrm{res}T}, \tag{5.17}$$

where for any second-order symmetric tensor $\mathbf{a}$ and any fourth-order tensor $\mathbb{A}$ we have introduced the notations:

$$\mathbf{a}^L = \mathbb{P}^L \cdot \mathbf{a}, \quad \mathbf{a}^T = \mathbb{P}^T \cdot \mathbf{a}, \quad \mathbf{a}^L + \mathbf{a}^T = \mathbf{a}, \tag{5.18}$$

$$\mathbb{A}^{LL} = \mathbb{P}^L \circ \mathbb{A} \circ \mathbb{P}^L, \quad \mathbb{A}^{LT} = \mathbb{P}^L \circ \mathbb{A} \circ \mathbb{P}^T, \tag{5.19}$$

$$\mathbb{A}^{TL} = \mathbb{P}^T \circ \mathbb{A} \circ \mathbb{P}^L, \quad \mathbb{A}^{TT} = \mathbb{P}^T \circ \mathbb{A} \circ \mathbb{P}^T, \tag{5.20}$$

$$\mathbb{A} = \mathbb{A}^{LL} + \mathbb{A}^{LT} + \mathbb{A}^{TL} + \mathbb{A}^{TT}. \tag{5.21}$$

Using Eqs (5.14)-(5.15), the overall compliance tensor of a metagrain is obtained in the form (no summation convention)

$$\begin{align}
\mathbb{M}_{mc}^{LL} &= \{(\mathbb{M}_i^{LL})^{-1}\}^{-1}, \tag{5.22} \\
\mathbb{M}_{mc}^{LT} &= \{(\mathbb{M}_i^{LL})^{-1}\}^{-1} \circ \{(\mathbb{M}_i^{LL})^{-1} \circ \mathbb{M}_i^{LT}\}, \tag{5.23} \\
\mathbb{M}_{mc}^{TL} &= \{\mathbb{M}_i^{TL} \circ (\mathbb{M}_i^{LL})^{-1}\} \circ \{(\mathbb{M}_i^{LL})^{-1}\}^{-1}, \tag{5.24} \\
\mathbb{M}_{mc}^{TT} &= \{\mathbb{M}_i^{TT} - \mathbb{M}_i^{TL} \circ (\mathbb{M}_i^{LL})^{-1} \circ \mathbb{M}_i^{LT}\} + \tag{5.25} \\
&\quad + \{\mathbb{M}_i^{TL} \circ (\mathbb{M}_i^{LL})^{-1}\} \circ \{(\mathbb{M}_i^{LL})^{-1}\}^{-1} \circ \{(\mathbb{M}_i^{LL})^{-1} \circ \mathbb{M}_i^{LT}\},
\end{align}$$

while the overall eigenstrain is derived as

$$\begin{align}
\boldsymbol{\varepsilon}_{mc}^{\mathrm{res}L} &= \{\boldsymbol{\varepsilon}_i^{\mathrm{res}L}\}, \tag{5.26} \\
\boldsymbol{\varepsilon}_{mc}^{\mathrm{res}T} &= \{\boldsymbol{\varepsilon}_i^{\mathrm{res}T}\} + \{\mathbb{M}_i^{TL} \circ (\mathbb{M}_i^{LL})^{-1} \cdot (\boldsymbol{\varepsilon}_{mc}^{\mathrm{res}L} - \boldsymbol{\varepsilon}_i^{\mathrm{res}L})\}. \tag{5.27}
\end{align}$$

Note that the sign of the inverse of a tensor $\mathbb{M}^{LL}$ denotes a partial inverse performed in the corresponding three-dimensional subspace. Starting from the inverse of local and average constitutive equations relating stress and strain via the stiffness tensors $\mathbb{L}_i = \mathbb{M}_i^{-1}$ and $\mathbb{L}_{mc} = \mathbb{M}_{mc}^{-1}$, the latter tensor is obtained as

$$\begin{align}
\mathbb{L}_{mc}^{LL} &= \{\mathbb{L}_i^{LL} - \mathbb{L}_i^{LT} \circ (\mathbb{L}_i^{TT})^{-1} \circ \mathbb{L}_i^{TL}\} + \tag{5.28} \\
&\quad + \{\mathbb{L}_i^{LT} \circ (\mathbb{L}_i^{TT})^{-1}\} \circ \{(\mathbb{L}_i^{TT})^{-1}\}^{-1} \circ \{(\mathbb{L}_i^{TT})^{-1} \circ \mathbb{L}_i^{TL}\}, \\
\mathbb{L}_{mc}^{LT} &= \{\mathbb{L}_i^{LT} \circ (\mathbb{L}_i^{TT})^{-1}\} \circ \{(\mathbb{L}_i^{TT})^{-1}\}^{-1}, \tag{5.29} \\
\mathbb{L}_{mc}^{TL} &= \{(\mathbb{L}_i^{TT})^{-1}\}^{-1} \circ \{(\mathbb{L}_i^{TT})^{-1} \circ \mathbb{L}_i^{TL}\}, \tag{5.30} \\
\mathbb{L}_{mc}^{TT} &= \{(\mathbb{L}_i^{TT})^{-1}\}^{-1}. \tag{5.31}
\end{align}$$

Localization tensor $\mathbb{A}_i$ and concentration tensor $\mathbb{B}_i$ defined as

$$\boldsymbol{\varepsilon}_i = \mathbb{A}_i \cdot \boldsymbol{\varepsilon}_{mc} + \boldsymbol{\alpha}_i, \quad \boldsymbol{\sigma}_i = \mathbb{B}_i \cdot \boldsymbol{\sigma}_{mc} + \boldsymbol{\beta}_i \tag{5.32}$$

can be also obtained, namely:

$$\begin{align}
\mathbb{B}_{mc}^{LL} &= (\mathbb{M}_i^{LL})^{-1} \circ \mathbb{M}_{mc}^{LL}, \\
\mathbb{B}_{mc}^{LT} &= (\mathbb{M}_i^{LL})^{-1} \circ (\mathbb{M}_{mc}^{LT} - \mathbb{M}_i^{LT}), \\
\mathbb{A}_{mc}^{TL} &= (\mathbb{L}_i^{TT})^{-1} \circ (\mathbb{L}_{mc}^{TL} - \mathbb{L}_i^{TL}), \tag{5.33} \\
\mathbb{A}_{mc}^{TT} &= (\mathbb{L}_i^{TT})^{-1} \circ \mathbb{L}_{mc}^{TT}, \\
\mathbb{B}^{TL} &= \mathbb{O}, \quad \mathbb{B}^{TT} = \mathbb{P}^T, \quad \mathbb{A}^{LT} = \mathbb{O}, \quad \mathbb{A}^{LL} = \mathbb{P}^L,
\end{align}$$

and

$$
\begin{aligned}
\boldsymbol{\alpha}_i^L &= \mathbf{0}, \quad \boldsymbol{\beta}_i^T = \mathbf{0}, \\
\boldsymbol{\alpha}_i^T &= \boldsymbol{\varepsilon}_i^{\mathrm{res}T} - ((\mathbb{L}_i^{TT})^{-1} \circ \mathbb{L}_{mc}^{TT}) \cdot \boldsymbol{\varepsilon}_{mc}^{\mathrm{res}T} - \\
&\qquad (\mathbb{L}_i^{TT})^{-1} \cdot (\mathbb{L}_{mc}^{TL} \cdot \boldsymbol{\varepsilon}_{mc}^{\mathrm{res}L} - \mathbb{L}_i^{TL} \cdot \boldsymbol{\varepsilon}_i^{\mathrm{res}L}), \\
\boldsymbol{\beta}_i^L &= (\mathbb{M}_i^{LL})^{-1} \cdot (\boldsymbol{\varepsilon}_{mc}^{\mathrm{res}L} - \boldsymbol{\varepsilon}_i^{\mathrm{res}L}),
\end{aligned}
\tag{5.34}
$$

where $\mathbb{O}$ is the fourth order tensor of all components equal to zero.

Note that derivation of the homogenized properties of a metagrain is not necessary if our only task is to find local stresses and strains in lamellae under the imposed average strain $\boldsymbol{\varepsilon}_{mc}$ (or stress $\boldsymbol{\sigma}_{mc}$) in the metagrain. Eqs. (5.10), the definitions (5.11) and the local constitutive relations (5.12) constitute the set of $6NL + 3$ equations, sufficient to find $6NL + 3$ independent components of unknowns: $\boldsymbol{\varepsilon}_i^T$, $\boldsymbol{\sigma}_i^L$, $\boldsymbol{\sigma}_{mc}$ (or $\boldsymbol{\varepsilon}_{mc}$). The latter observation is also true if the constitutive relation is non-linear (e.g. the viscoplastic power-law). In the latter case the obtained equations are non-linear and they are solved, e.g, by using the Newton-Raphson method. The specification of the homogenized properties of a metagrain is necessary when we have to do with three-scale (or, in general, multi-scale) modelling. In such a case, compliances $\mathbb{M}_{mc}$ serve as local properties in the self-consistent-type transition scheme between the level of a metagrain and the level of a polycrystalline sample. Computational issues related to the three-scale modelling will be discussed below.

5.2.2. Incompressible materials

Now, let us specify the above relations for incompressible materials. In this case the constitutive law relates the strain (strain-rate) deviator $\mathbf{e}$ with the stress deviator $\mathbf{s}$. Note that for deviators of strain and stress the compatibility condition (5.5) and the equilibrium condition (5.6) lead to

$$
e_{kl}^i = e_{kl}^j, \quad \text{for} \quad kl = 11, 22, 12 \quad \Rightarrow \quad e_{33}^i = -(e_{11}^i + e_{22}^i) = e_{33}^j \tag{5.35}
$$

and

$$
s_{kl}^i = s_{kl}^j, \quad \text{for} \quad kl = 13, 23 \tag{5.36}
$$

for components in the basis $\{\mathbf{i}_k\}$. Our aim is to find the average compliance tensor $\tilde{\mathbb{M}}_{mc}$ of the metagrain that relates average stress deviator $\mathbf{s}_{mc}$ and the average strain deviator $\mathbf{e}_{mc}$. To accomplish this task, with analogy to the preceding derivation, we decompose the five-dimensional space of the symmetric

second-order deviators into two- and three-dimensional orthogonal subspaces with the help of the following two projectors:

$$(\tilde{\mathbb{P}}^T)_{ijkl} = \frac{1}{4} \left(2(\delta_{ik} - n_i n_k) n_j n_l + (\delta_{jk} - n_j n_k) n_i n_l + (\delta_{il} - n_i n_l) n_j n_k \right),$$
$$(5.37)$$
$$\tilde{\mathbb{P}}^L = \mathbb{I}_{\mathrm{D}} - \tilde{\mathbb{P}}^T. \tag{5.38}$$

It can be easily verified that all previous derivations can be repeated for incompressible materials, provided the following change of variables is performed:

$$\mathbb{P}^L \to \tilde{\mathbb{P}}^L, \quad \mathbb{P}^T \to \tilde{\mathbb{P}}^T, \quad \mathbb{M}_i \to \tilde{\mathbb{M}}_i, \quad \mathbb{M}_{mc} \to \tilde{\mathbb{M}}_{mc}, \tag{5.39}$$

$$\boldsymbol{\sigma}_i \to \mathbf{s}_i, \quad \boldsymbol{\varepsilon}_i \to \mathbf{e}_i, \quad \boldsymbol{\sigma}_{mc} \to \mathbf{s}_{mc}, \quad \boldsymbol{\varepsilon}_{mc} \to \mathbf{e}_{mc}. \tag{5.40}$$

Now, the computational procedures related to the implementation of the three-scale model of polycrystals with lamellar substructure will be discussed. In order to encompass in the analysis the general case, the non-linear constitutive rule at a level of single lamellae relating the strain-rate $\mathbf{d}$ and the stress deviator $\mathbf{s}$ is assumed. Three types of transition rules between the levels of metagrain and polycrystal will be considered, namely the Taylor (Voigt) model, the Sachs (Reuss) model and the family of self-consistent models discussed in Chapter 4. When presenting the corresponding algorithms, the process is assumed to be strain-driven ($\mathbf{E}(t)$ is imposed).

The Taylor model. The relations between the overall stress $\boldsymbol{\Sigma}$ and the overall strain-rate $\mathbf{D} = \dot{\mathbf{E}}$ and the corresponding average quantities in the metagrain are

$$\mathbf{D} = \mathbf{d}_{mc}, \quad \boldsymbol{\Sigma} = \langle \boldsymbol{\sigma}_{mc} \rangle, \quad \langle \cdot \rangle = \sum_{mc=1}^{NG} \nu_{mc}(\cdot), \tag{5.41}$$

where NG is the number of metagrains in the polycrystalline aggregate. With the use of relations (5.10) the corresponding set of non-linear equations, which can be solved independently for each metagrain in order to obtain local stress deviators in lamellae, has the form:

$$\mathbf{D}_{(mc)}^L = \mathbf{f}_i^L(\mathbf{s}_i^L, \mathbf{s}_{mc}^T), \quad i = 1, \dots, NL, \tag{5.42}$$
$$\mathbf{D}_{(mc)}^T = \{\mathbf{d}_i^T\} = \{\mathbf{f}_i^T(\mathbf{s}_i^L, \mathbf{s}_{mc}^T)\}, \tag{5.43}$$

and $\mathbf{f}_i^L = \tilde{\mathbb{P}}^L \cdot \mathbf{f}_i$, $\mathbf{f}_i^T = \tilde{\mathbb{P}}^L \cdot \mathbf{f}_i$, etc. Note that projectors $\tilde{\mathbb{P}}^L$ and $\tilde{\mathbb{P}}^T$ change when passing from one metagrain to another because they are functions of $\mathbf{n}$, therefore also parts $\mathbf{D}_{(mc)}^L$ and $\mathbf{D}_{(mc)}^T$ of $\mathbf{D}$ specified by (5.18) are different.

The above set of equations can be solved with use of the Newton-Raphson method. The corresponding set of linear equations solved for the iteration k of the Newton-Raphson procedure is as follows ($i = 1, \ldots, NL$):

$$\mathbf{r}_i^{L(k-1)} = \mathbf{D}_{(mc)}^L - \mathbf{f}_i^{L(k-1)} = \tilde{\mathbb{M}}_i^{LL(k-1)} \cdot \Delta \mathbf{s}_i^{L(k)} + \mathbb{M}_i^{LT(k-1)} \cdot \Delta \mathbf{s}_{mc}^{T(k)},$$

$$\mathbf{r}^{T(k-1)} = \mathbf{D}_{(mc)}^T - \{\mathbf{f}_i^{T(k-1)}\} = \{\tilde{\mathbb{M}}_i^{TL(k-1)} \cdot \Delta \mathbf{s}_i^{L(k)}\} + \{\tilde{\mathbb{M}}_i^{TT(k-1)}\} \cdot \Delta \mathbf{s}_{mc}^{T(k)},$$

where $\tilde{\mathbb{M}}_i^{LL}$, $\tilde{\mathbb{M}}_i^{LT}$, etc., are defined by relations (5.19-5.20) under (5.39) and

$$\tilde{\mathbb{M}}_i = \tilde{\mathbb{M}}_i^{tg}(\mathbf{s}_i) = \frac{\partial \mathbf{f}_i}{\partial \mathbf{s}_i}. \qquad (5.44)$$

In the case of the viscoplastic power law (4.24), the tensor $\tilde{\mathbb{M}}_i^{tg}$ is specified by (4.27). Quantities with index $(k-1)$ are calculated for the approximations of local stress deviators obtained in the previous iteration, while new approximation reads $\mathbf{s}_i^{(k)} = \mathbf{s}_i^{(k-1)} + \Delta \mathbf{s}_i^{(k)}$. The hydrostatic part of stress is found using the boundary condition for the problem under consideration.

The self-consistent models. As it has been discussed in Chapter 4, the computational procedure applied in the case of self-consistent schemes for non-linear polycrystals usually consists of two iteration loops: an outer loop serving to derive overall properties and an inner loop in which local stresses are found for the current approximation of the overall self-consistent compliance $\bar{\mathbb{M}}^{SC}$. Here, we only discuss this inner loop, therefore we assume that, besides $\mathbf{D}$, we know also $\bar{\mathbb{M}}^{SC}$ and the inverse of the corresponding Hill tensor $\mathbb{M}_*^{SC}$ (see Appendix B). Due to particular features of three variants of the self-consistent scheme for non-linear viscoplastic materials discussed in Chapter 4 (i.e. secant, tangent and affine), the corresponding algorithms are similar for the secant and tangent SC schemes and differ for the affine SC scheme, for which the overall reference strain depends directly on local stress deviators. For the first two models the local stress deviator for each metagrain can be found independently, with the use of the following interaction equation

$$\mathbf{d}_{mc} - \mathbf{D} = -\tilde{\mathbb{M}}_*^{SC} \cdot (\mathbf{s}_{mc} - \mathbf{S}), \qquad (5.45)$$

where the overall stress deviator $\mathbf{S}$ is obtained using the overall relation $\mathbf{S} = \mathbb{L}^{SC} \cdot \mathbf{D}$. With the use of the relations (5.10), the set of non-linear equations to be solved in order to obtain local stress deviators takes the form

$(i = 1, ..., NL)^2$:

$$\mathbf{f}_i^L(\mathbf{s}_i^L, \mathbf{s}_{mc}^T) - \mathbf{D}_{(mc)}^L = \tag{5.46}$$
$$= -\mathbb{M}_{*(mc)}^{SC,LL} \cdot (\{\mathbf{s}_i^L\} - \mathbf{S}_{(mc)}^L) - \mathbb{M}_{*(mc)}^{SC,LT} \cdot (\mathbf{s}_{mc}^T - \mathbf{S}_{(mc)}^T),$$

$$\{\mathbf{f}_i^T(\mathbf{s}_i^L, \mathbf{s}_{mc}^T)\} - \mathbf{D}_{(mc)}^T = \tag{5.47}$$
$$= -\mathbb{M}_{*(mc)}^{SC,TL} \cdot (\{\mathbf{s}_i^L\} - \mathbf{S}_{(mc)}^L) - \mathbb{M}_{*(mc)}^{SC,TT} \cdot (\mathbf{s}_{mc}^T - \mathbf{S}_{(mc)}^T).$$

As in the case of the Taylor model, the above set of equations is solved by means of the Newton-Raphson method. In the case of the affine method, local stress deviators are calculated together for all metagrains. The corresponding set of equations consists of NG sets of equations (5.46)-(5.47), where $\mathbf{S}$ is the additional unknown. In order to balance the number of unknowns and the number of equations, this set is supplemented by the following condition

$$\mathbf{S} = \langle \{\mathbf{s}_i\} \rangle. \tag{5.48}$$

The Sachs (Reuss) model. The model assumes $\mathbf{S} = \mathbf{s}_{mc}$ in every metagrain. The derivation of local stress deviators in lamellae, in the case of the Sachs scheme and the strain-driven process, is rather complex when the constitutive law is non-linear. Therefore, similarly to the SC schemes, the algorithm consisting of two loops has been proposed. In the outer loop, the overall stress deviator is derived, and in the inner loop the local stress deviators are found, assuming that the overall stress is known. Within the inner loop, we solve the following set of non-linear equations, independently for each metagrain,

$$\mathbf{f}_1^L(\mathbf{s}_1^L, \mathbf{s}_{mc}^T) = \mathbf{f}_j^L(\mathbf{s}_j^L, \mathbf{s}_{mc}^T), \quad j = 2, \ldots, NL, \tag{5.49}$$
$$\{\mathbf{s}_i^L\} = \mathbf{S}_{mc}^L, \quad \mathbf{s}_{mc}^T = \mathbf{S}_{mc}^T. \tag{5.50}$$

Similarly to the case of previous averaging schemes, the above set is solved with use of the Newton-Raphson method.

5.2.3. Example - PST $\gamma + \alpha_2$-TiAl intermetallic

The microstructure of polysynthetically-twinned (PST) $\gamma + \alpha_2$-TiAl has been described in detail by Appel and Wagner [6] or Werwer and Cornec [215, 216], therefore we will only recapitulate basic facts. In this two phase material a strict

---

[2]A subscript (mc) reflects the fact that the decompositions (5.19)-(5.20) vary when passing between metagrains.

orientation relationship exists between the hexagonal α_2 phase and the fcc-like γ phase of tetragonal symmetry, namely the closely packed planes, (0001) in α_2 and {111} in γ, and the crystallographic directions $\langle 1\bar{1}0 \rangle$ in γ and $\langle 11\bar{2}0 \rangle$ in α_2 are parallel. This relationship is fulfilled by six distinct orientation variants of γ-phase, corresponding to three twin-related pairs, Fig. 5.2.
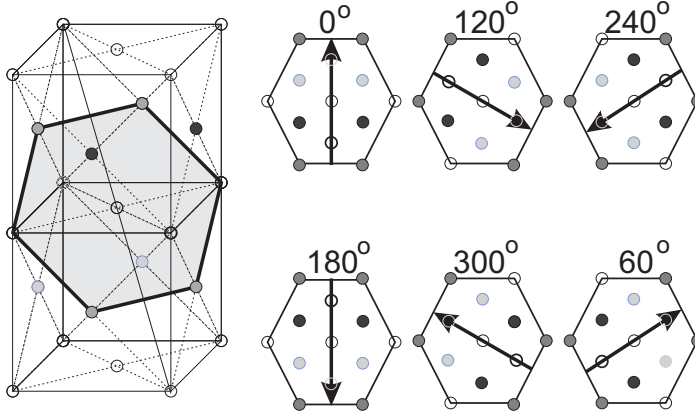
Fig. 5.2. Orientation variants of γ phase in PST $\gamma + \alpha_2$ TiAl crystal (see also [216]).

Let us study mechanical properties of a metagrain made of this material. We start with elastic anisotropy and then turn to inelastic properties. Three types of a laminated unit cell (RVE) for the derivation of the overall properties of a metagrain are considered. They are presented in Fig. 5.3. In the case of RVE1, a laminate is composed of 7 distinct lamellae. In the case of RVE2 and RVE3 the laminated component of RVE is composed of 3 distinct lamellae: one α_2 lamella and two γ lamellae being one of the three twin-related pairs, Fig. 5.2. Subsequently, the overall properties of the metagrain are obtained by assuming equal strain (strain-rate) or equal stress in each of three possible sub-laminates, respectively. Additionally, the upper and lower bounds are derived. They are obtained assuming equal strain or equal stress in each of seven lamellae. They will be denoted by RVEV and RVER in the figures.

In further derivations we assume that six admissible variants of γ lamellae have equal volume fractions, therefore we have, for a laminate of RVE1,

$$\nu_i = \frac{1}{6}(1 - \nu_\alpha) \quad \text{for} \quad i = 1, \ldots, 6, \quad \nu_7 = \nu_\alpha \qquad (5.51)$$

and for an individual laminated component of RVE2 and RVE3:

$$\nu_i = \frac{1}{2}(1 - \nu_\alpha) \quad \text{for} \quad i = 1, 2 \quad (k = 1, 3, 5), \quad \nu_3 = \nu_\alpha. \qquad (5.52)$$
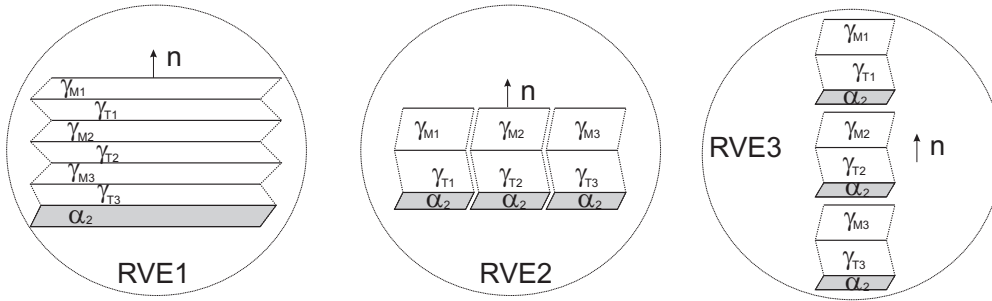
Fig. 5.3. Considered types of RVE for the metagrain.

The overall properties of a metagrain depend on the volume fraction ν_α of α_2 phase.

Elastic properties

The independent components of the elasticity tensors of the single crystals of γ-TiAl and α_2-Ti$_3$Al phases are collected in Table 2.1 in Chapter 2. Independently of ν_α and the assumed type of RVE, the overall elasticity tensor $\mathbb{L}^e_{mc}$ of a metagrain is transversely isotropic (although, the laminated subcomponent for RVE2 and RVE3 is not). The main axis of symmetry is coaxial with the unit normal $\mathbf{n}$ to the lamellae interfaces, therefore the spectral decomposition of $\mathbb{L}^e_{mc}$ has the form (A.5) invoked in Appendix A. Fig. 5.4 presents the variation of the Kelvin moduli and the angle $\Phi(\xi)$ with the volume fraction of α_2 phase for all considered types of RVE. As it is seen, differences between results obtained for three RVEs are almost negligible. Similarly, the upper and lower bounds are quite close to each other, except of the modulus h^{mc}_3 for which they are relatively far from each other. As far as dependence of overall moduli on the volume fraction of α_2 phase is concerned, it has a significant impact on moduli h^{mc}_2 and h^{mc}_3, while moduli h^{mc}_1 and h^{mc}_4 almost do not vary with ν_α. The value of stiffness distributor ξ increases with ν_α, though it remains very small. Consequently, this two-phase material is almost volumetrically isotropic (Appendix A).

Fig. 5.5 presents the overall directional Young modulus (Eq. (3.126)) of PST $\gamma+\alpha_2$-TiAl in the case of the metagrain represented by RVE1 for different values of ν_α. Generally, with the increasing volume fraction of α_2 phase, the Young modulus decreases for any direction. Moreover, the volume fraction of α_2 phase has the most significant impact on the Young modulus in the directions coaxial with the laminate interface. For experimentally observed values of $\nu_\alpha \cong 0.1$ one
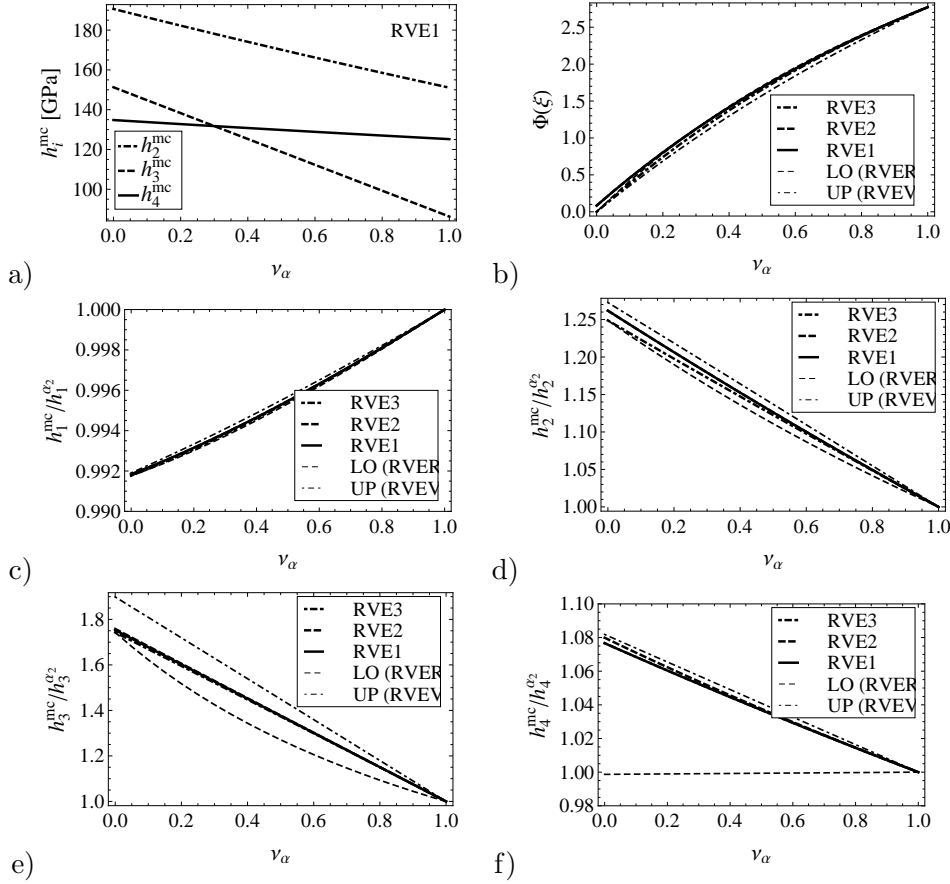
Fig. 5.4. Estimates of the elastic Kelvin moduli and of the elastic stiffness distributor of a metagrain obtained for different models of RVE. Because α_2 phase is also transversely isotropic, the Kelvin moduli h_i^{mc} are scaled by the corresponding moduli $h_i^{\alpha_2}$ in plots c-f.

obtains the relation

$$E(0) > E(90) > E(\phi), \quad \phi \in (30^o, 60^o), \tag{5.53}$$

which is qualitatively confirmed by experiments Kishida et al. [85]. The independent components of the elasticity tensor of PST crystal of TiAl has been measured by Tanaka (see Paidar and Yamaguchi [154] for the respective values). The directional Young modulus corresponding to the measured $\mathbb{L}_{mc}^e$ is marked in Fig. 5.5 by a dashed line. In general, it lies within the theoretically predicted values for relatively small content of α_2 phase (not clearly reported by Paidar and Yamaguchi [154]). The most significant difference is obtained
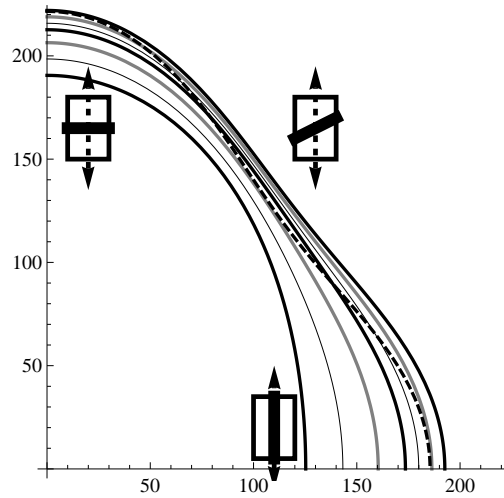
Fig. 5.5. Dependence of the directional Young modulus [GPa] for PST $\gamma + \alpha_2$-TiAl (a single metagrain) on the volume fraction of α_2 phase. The outer line corresponds to $\nu_\alpha = 0$, while the inner line to $\nu_\alpha = 1$. In-between lines are for $\nu_\alpha = \{0.1, 0.2, 0.3, 0.5, 0.75\}$. The dashed curve corresponds to the measured elasticity tensor of PST TiAl [154].

for intermediate directions. Werwer et al. [217] measured the Young modulus $E = 175$ GPa for the polycrystalline TiAl of lamellar microstructure. The extrusion texture of a tested sample indicates the case for which the direction **n** is close to be perpendicular to the tension direction. As it is seen in Fig. 5.5, the experimentally obtained value is reproduced quite well for the reasonable content of α_2 phase (again, not clearly reported by Werwer et al. [217]).

Finally, the overall elastic properties of random polycrystal composed of metagrains are evaluated. In Fig. 5.6 the comparison of bounds and self-consistent estimates (see Chapter 3) of the overall Young modulus and the overall shear modulus are presented as functions of ν_α. Different RVEs denote different models of a metagrain, that is different scale transition rule employed between the level 1 and the level 2. It is seen that for RVE1 the bounds are very narrow and the SC estimate almost coincides with the Hill estimate (the same behaviour is observed for two remaining RVEs presented in Fig. 5.3). For a low content of α_2 phase the scale transition rule between levels 1 and 2 influences more the predicted overall property than the scale transition rule between levels 2 and 3. This trend is reversed for a high content of α_2 phase, as expected. In the figures, the self-consistent estimates of $\bar{E}$ and $\bar{G}$ obtained for the two-phase material without introduction of an additional level of microstructure (denoted as "2 scale (SC)") are also presented. When calculating the latter estimates, the
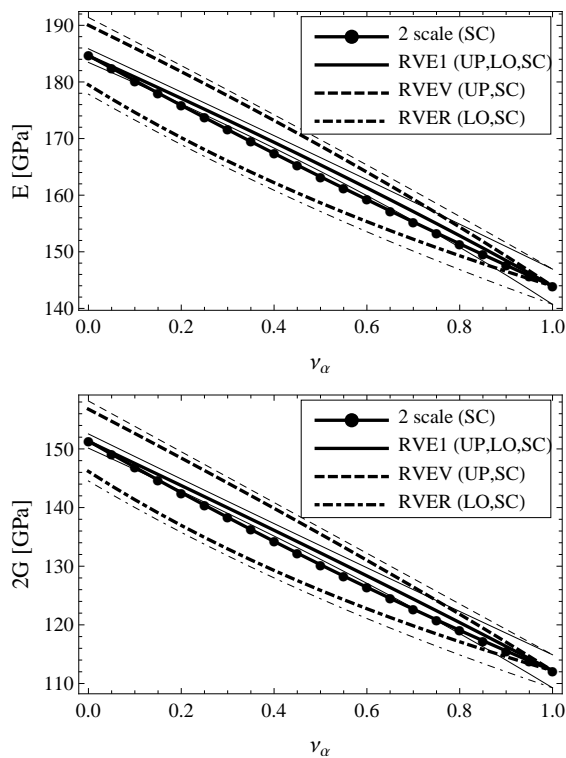
Fig. 5.6. Bounds and self-consistent estimates of the overall Young modulus and the overall shear modulus for untextured polycrystal of two-phase TiAl with lamellar substructure and different models of the metagrain.

orientation relationships between α_2 and γ lamellae are not taken into account. Differences between self-consistent estimates obtained for three-scale and two-scale microstructure are not substantial. They are the strongest for comparable contents of both phases.

Initial yield surface

Now, let us move to the inelastic properties of TiAl of lamellar substructure. First, we will study the anisotropy of an *initial* yield stress of a metagrain induced mainly by the confinement effects discussed in the introduction. We will consider the so-called micro-yielding. To this end we identify *initiation of yielding of a metagrain with initiation of slip or twinning on any of possible systems in any of lamellae.* Similarly to the case of the analysis performed in

Section 2.4.1, initiation of slip or twinning within lamellae is governed by the classical Schmid law. According to the above definition, initiation of yielding of a PST metagrain is equivalent to the limit of elasticity in one of the lamellae, and must be established with the use of a local stress. Consequently, this local stress in the lamellae, under the prescribed overall stress $\boldsymbol{\sigma}_{mc}$, is obtained by employing the concentration equations (5.32), where tensors $\mathbb{B}_i$ are calculated with the use of the elastic compliances, and $\boldsymbol{\beta}_i = \mathbf{0}$. In the examples shown below the PST metagrain is modelled by RVE1.

In Section 2.4.1 the slip and twin systems in γ-phase have been analysed. As concerns α_2 phase, three types of slip systems are usually invoked: basal $(0001)\langle11\bar{2}0\rangle$, prismatic $\{1\bar{1}00\}\langle11\bar{2}0\rangle$ and pyramidal $\langle2c+a\rangle$ $\{11\bar{2}1\}\langle\bar{1}\bar{1}26\rangle$. As reported in the literature, cf. Nakano et al. [142], Koizumi et al. [92], Roos et al. [173], the prismatic slip systems are most easily initiated, while the remaining two groups are difficult to initiate. One should note that the easy prismatic mode, in view of its orientation with respect to the lamellae interface, is the mixed mode, therefore initiation of the plastic yielding within α_2 lamellae requires much higher level of stress than in γ lamellae. The performed study indicates that the hard modes in γ and α_2 phases have no influence on the value of the initial yield stress defined as above, thus in the further analysis the hard modes (super-dislocations in γ phase and two hard modes in α_2 phase) have been neglected. Furthermore, relying on Roos et al. [173], we have assumed

$$\tau_c^{prism} = 2\tau_c^{ord}. \tag{5.54}$$

The value of critical shear stress for twinning mode in single crystal of γ-TiAl is usually close to the value of τ_c^{ord}. In further calculations we have assumed $\rho^{twin} = \tau_c^{twin}/\tau_c^{ord} = 1.1$.

In Fig. 5.7 an identification procedure for confinement parameters α_M and α_T defined by (5.4), is illustrated. As it is shown without the morphological differentiation of the plastic deformation modes ($\alpha_M = \alpha_T = 1$), one is not able to reproduce the strong anisotropy of the uniaxial yield stress of PST metagrain. The experimental data for tension at room temperature of PST in five different directions with respect to **n** has been taken from Appel and Wagner [6]. They concern two-phase PST γ-Ti49Al-alloys without ternary alloying additions (see page 195, Fig. 8 in [6]). It can be verified that α_T, defined by (5.4), does not influence the initial yield stress in the direction perpendicular to **n**, therefore, first, the value of α_M is established with the use of Fig. 5.7a, and then α_T with the use of Fig. 5.7b. The value of the yield stress for the intermediate direction specified by $\phi = 40^o$ is independent of both confinement
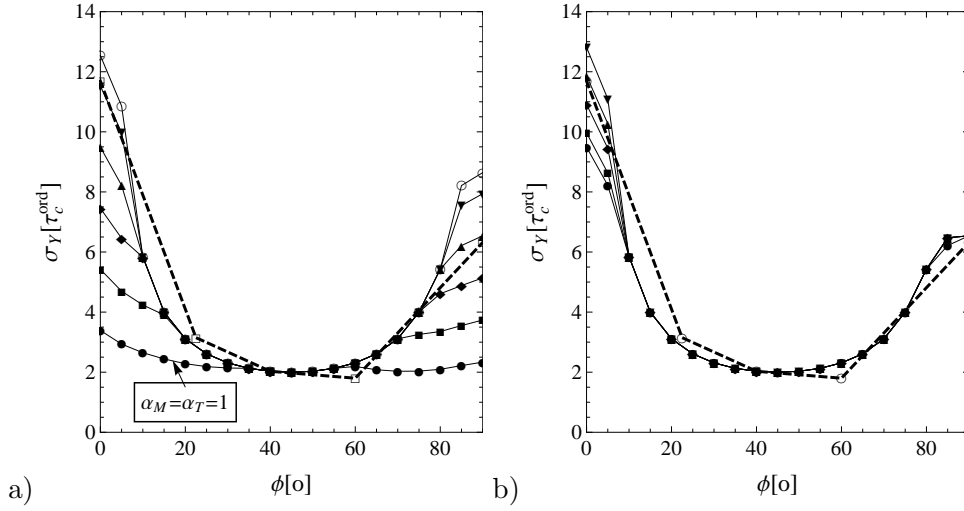
Fig. 5.7. Illustration of the identification procedure for confinement parameters. The directional initial yield stress in tension (ϕ denotes the angle between unit normal to the interface and the loading direction) for a) different values of $\alpha_M = \{1.0, 1.9, 2.5, 3.1, 3.4, 4.0\}$, ($\alpha_T = 1$), b) different values of $\alpha_T = \{1, 1.05, 1.15, 1.25, 1.65\}$ and $\alpha_M = 2.8$; dashed line: experimental data Appel and Wagner [6].

parameters, therefore it has been used as a reference value, where the measured value of $\sigma_Y(40^o) \simeq 100$ MPa. As a result of this identification procedure one finds: $\alpha_M = 2.8$, $\alpha_T = 1.25$ and $\tau_c^{ord} = 50$ [MPa]. Similar values have been established by Lebensohn et al. [113]; however, for a flow stress established with the use of the viscoplastic power law (4.24). In Fig. 5.8 the directional yield stress in compression is presented and compared with the experimental data found by Werwer and Cornec [215]. Details concerning the experiment conditions and material composition were not provided in the reference, nevertheless the agreement with the values obtained with the use of identified parameters is quite good. In Fig. 5.8 the shape of the cross-section of the initial yield surface for the bi-axial stress state is shown. One observes strong anisotropy of this yield surface.

In Fig. 5.9a the influence of volume fraction of α_2 phase on the directional initial yield stress in tension and compression is demonstrated. It is seen that this influence is the most significant when the tension/compression direction is coaxial with the interface of lamella. In Fig. 5.9b the effect of ratio ρ^{twin} is studied. Twining is the source of a tension-compression asymmetry of a yield stress. This asymmetry is the strongest for the direction perpendicular to the lamella interface and is less significant for the intermediate directions. Note also
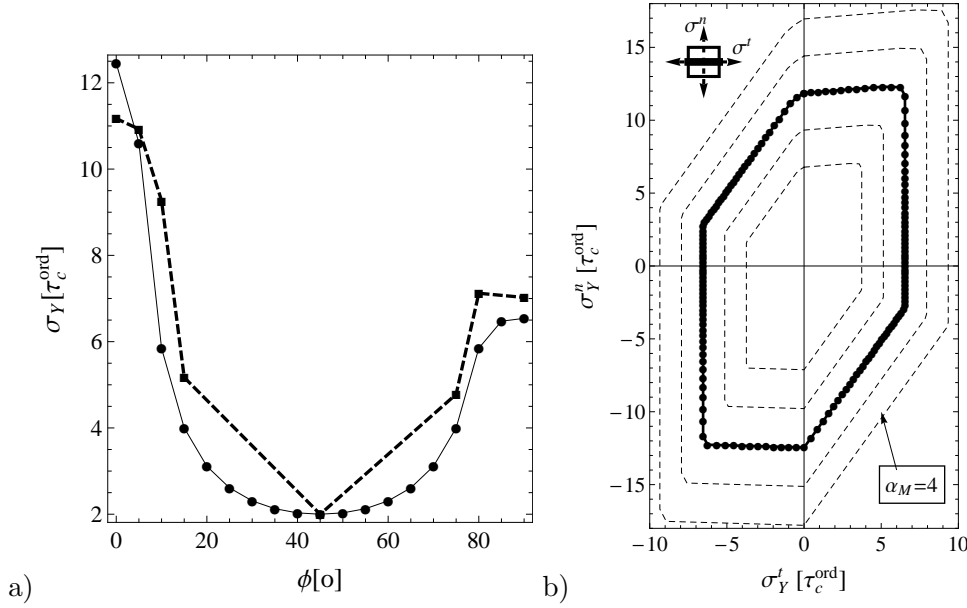
Fig. 5.8. a) The initial yield stress in compression obtained with the use of identified parameters (black line) and experimental data [215] (dashed line); b) the initial yield surface for the biaxial stress state for identified parameters (black line with circles), for different values of $\alpha_M = \{1.6, 2.2, 3.4, 4.0\}$ (dashed lines). Schematic figure presents the orientation of the analysed loading with respect to the lamellae interfaces.

that when τ_c^r for twinning is sufficiently high, then twinning does not influence the initial yielding.

We conclude this point with the derivation of the initial yield surface for untextured polycrystal of lamellar substructure. Initiation of plastic yielding is now identified with initiation of yielding in any metagrain, within any of its constituent lamellae on any of slip or twin systems (compare Hutchinson [70], Brenner et al. [20]). In Fig. 5.10 the obtained yield surface is presented for the identified material parameters and $\rho^{twin} = 1.1$ and $\rho^{twin} = 0.7$. Performed studies indicated that the tension-compression asymmetry of the initial yield surface of polycrystal will be observed for ρ^{twin} lower than one or close to one, see Fig. 5.11a. For the experimentally justified value (i.e. $\rho^{twin} = 1.1$) this asymmetry is not present and, similarly as it has been found for fcc untextured polycrystals by Hutchinson [70], the obtained yield surface is the Tresca polyhedron specified by the condition

$$\bar{\tau}_{max} = \bar{\tau}_0 \,, \tag{5.55}$$
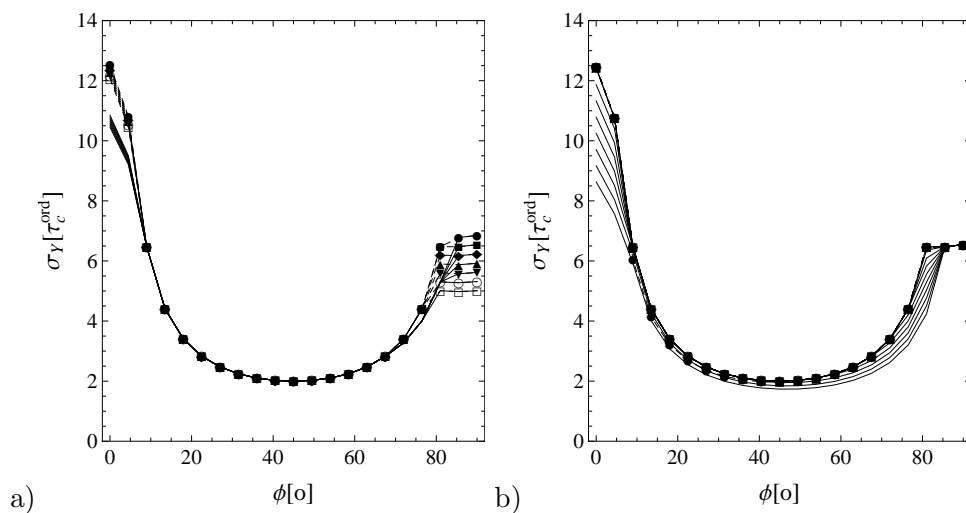
Fig. 5.9. Initial yield stress in tension (continuous black lines) and compression (dashed lines with markers) for a) different values of ν_α, the top curve - $\nu_\alpha = 0$, the bottom curve $\nu_\alpha = 0.7$, spacing $\Delta\nu_\alpha = 0.1$, $\rho^{twin} = 1$; b) different values of $\rho^{twin} = \tau_c^{twin}/\tau_c^{ord}$, the top curve - $\rho^{twin} = 1.2$, the bottom curve $\rho^{twin} = 0.8$, spacing $\Delta\rho^{twin} = 0.05$, $\nu_\alpha = 0.1$. Confinement parameters: $\alpha_T = 1.25$, $\alpha_M = 2.8$.
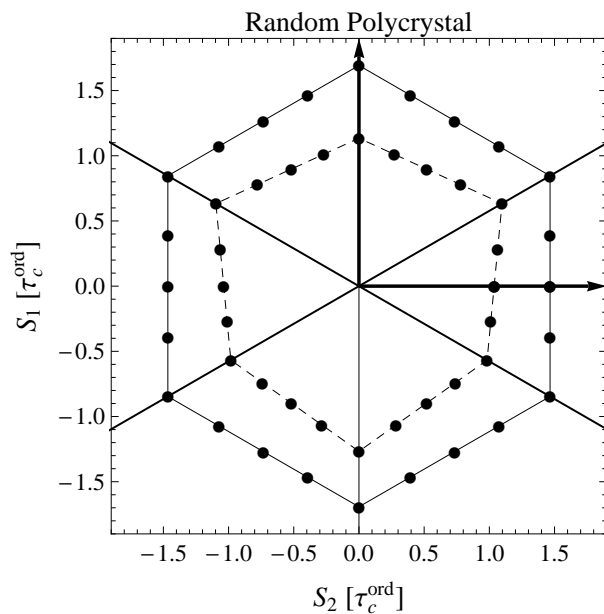
Fig. 5.10. Initial yield surface for utextured polycrystal of $\alpha_2 + \gamma$-TiAl of lamellar substructure in a deviatoric plane ($\alpha_T = 1.25$, $\alpha_M = 2.8$, $\nu_\alpha = 0.1$), continuous line - $\rho^{twin} = 1.1$, dashed line $\rho^{twin} = 0.7$; $S_1 = 1/\sqrt{6}(2\Sigma_3 - \Sigma_1 - \Sigma_2)$, $S_2 = 1/\sqrt{2}(\Sigma_1 - \Sigma_2)$.
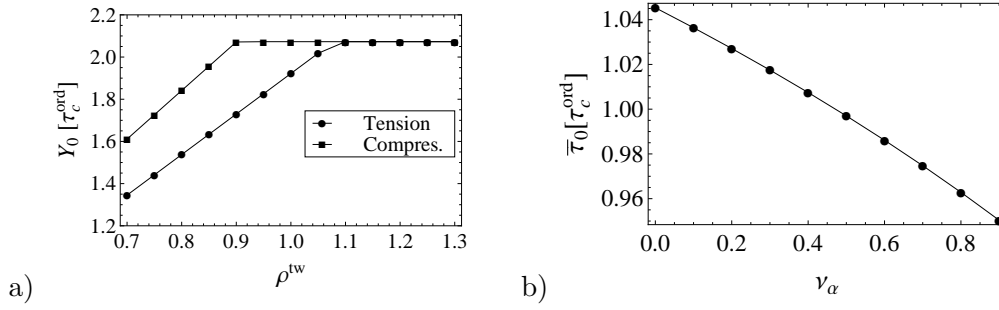
Fig. 5.11. a) Initial yield stress in uniaxial tension and compression for untextured polycrystal of $\alpha_2 + \gamma$-TiAl of lamellar substructure ($\alpha_T = 1.25$, $\alpha_M = 2.8$, $\nu_\alpha = 0.1$) as a function of ρ^{twin}, b) Initial yield stress in shear ($\alpha_T = 1.25$, $\alpha_M = 2.8$, $\nu_\alpha = 0.1$, $\rho^{twin} = 1.1$) as a function of ν_α.

where $\bar{\tau}_{max}$ is the maximum overall shear stress. The size of the yield surface, specified by the parameter $\bar{\tau}_0$, is almost not affected by the confinement parameters. It is governed by the volume fraction of α_2 phase and the value of the critical yield stress on the easiest slip system, see Fig. 5.11b.

Viscoplastic properties

Now, we will study a PST crystal in which the behaviour of single lamellae is governed by the non-linear viscoplastic power-law (4.24). Depending on the value of n, the discussed constitutive model corresponds to the inelastic strain regime for which elastic strains can be neglected, or to the steady creep process. We are interested in the influence of confinement parameters and the introduction of an additional level of microstructure on the estimate of the overall flow stress of untextured polycrystal of lamellar substructure. In the analysis the twinning mode has been neglected, while hard modes (super-dislocations in γ phase and prismatic and pyramidal slip systems in α_2 phase) are taken into account. As it has been verified, the predicted tendencies concerning the analysed phenomena are not changed when twinning is taken into account.

First, we analyse linear polycrystal ($n = 1$). In Fig. 5.12 the Taylor and Reuss bounds and self-consistent estimates are presented for different models of a metagrain, namely:

- A laminate composed of 7 lamellae (RVE1 in Fig. 5.3),

- A laminate composed of 3 lamellae (laminate subcomponent of RVE2 or RVE3 in Fig. 5.3),

- The laminate level neglected (presence of a lamellar substructure is reflected only by the confinement parameters).
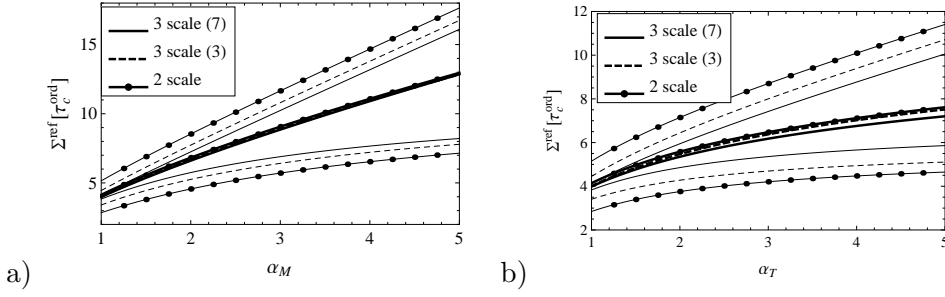
Fig. 5.12. Bounds and self-consistent estimate of a reference overall flow stress in uniaxial tension for the linear viscoplastic $\alpha_2 + \gamma$-TiAl random polycrystal of lamellar substructure as a function of a) α_M ($\alpha_T = 1$), b) α_T ($\alpha_M = 1$). Other parameters: $\nu_\alpha = 0.1$, $\rho_{sup} = 5$, $\rho_{bas} = 6.6$, $\rho_{prism} = 2$, $\rho_{pyr} = 18.2$ taken from [173].
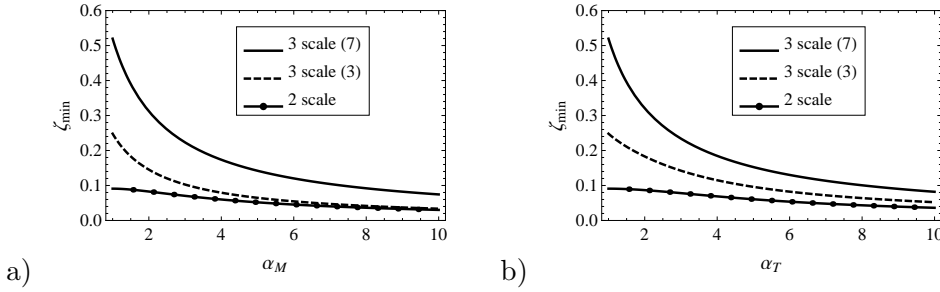
Fig. 5.13. Variation of the Zener-like anisotropy parameters ζ_{min} for two realizations of a metagrain ($\nu_\alpha = 0$) and the individual γ lamella with a) α_M ($\alpha_T = 1$, $\rho_{sup} = 5$), b) α_T ($\alpha_M = 1$, $\rho_{sup} = 5$).

It is observed that when the three-scale models of microstructure are used, then the gap between the upper and lower bounds is reduced as compared to the two-scale model. However, as the value of confinement parameters increases, this reduction is relatively smaller as compared to the total difference between the bounds. It could be explained considering the anisotropy degree of a metagrain in the three-scale model and of an individual lamellae in the two-scale model. In the case of linear volumetrically isotropic material, anisotropy can be qualified

by the set of Zener-like parameters[3]:

$$\zeta_K = \frac{h_K}{h_{max}}, \quad K = 2, ..., MK, \quad MK \leqslant 6,\tag{5.57}$$

where h_K are distinct deviatoric Kelvin moduli obtained by means of the spectral decomposition of an appropriate constitutive fourth order tensor (see Appendix A). The anisotropy degree (strong vs. weak anisotropy) is predominantly governed by the smallest of parameters ζ_K. In Fig. 5.13 the smallest Zener-like anisotropy parameters ζ_{min} as function of confinement parameters are presented for the two considered realizations of a metagrain ($\nu_\alpha = 0$ is assumed) and for the single γ lamella. As it could be observed for small values of α_M and α_T, the anisotropy of both metagrains is considerably weaker than the anisotropy of the individual γ lamella.

The self-consistent estimates obtained for different realizations of lamellar substructure are close to each other.

a)   b)
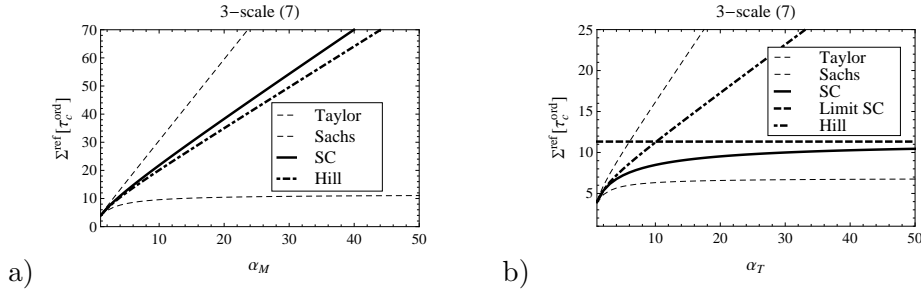
Fig. 5.14. Bounds, Hill's and self-consistent estimates of a reference overall flow stress in uniaxial tension for the linear viscoplastic $\alpha_2 + \gamma$-TiAl untextured polycrystal as a function of a) α_M ($\alpha_T = 1$), b) α_T ($\alpha_M = 1$). Other parameters: $\nu_\alpha = 0.1$, $\rho_{sup} = 5$, $\rho_{bas} = 6.6$, $\rho_{prism} = 2$, $\rho_{pyr} = 18.2$ [173], RVE1 model of metagrain.

As concerns the limit cases, that is $\alpha_M \to \infty$ and $\alpha_T \to \infty$, the property of the self-consistent estimate for incompressible crystal with constrained deformation modes proved in Chapter 3 indicates that:

---

[3]Zener has introduced in [229] the following anisotropy ratio for elastic materials of cubic symmetry expressed in terms of the components of the elasticity tensor in anisotropy axes

$$\zeta = \frac{L_{1111} - L_{1122}}{2L_{1212}},\tag{5.56}$$

which, as can be verified, is the ratio of two deviatoric Kelvin moduli in this case, cf. Kowalczyk-Gajewska and Ostrowska-Maciejewska [104].

- for $\alpha_M \to \infty$, the self-consistent estimate is <u>infinite</u>, because the space of the constrained deviatoric deformation is 3-dimensional,

- for $\alpha_T \to \infty$, the self-consistent estimate is <u>finite</u>, because the space of the constrained deviatoric deformation is 1-dimensional.

These theoretical predictions are confirmed in Fig. 5.14.
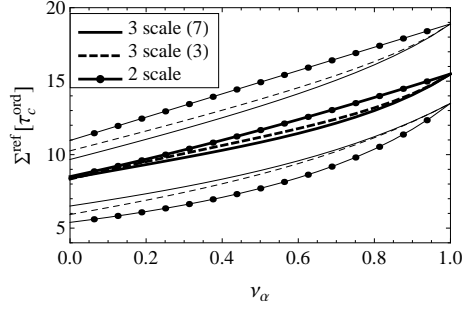
Fig. 5.15. Bounds and self-consistent estimates (notation as in Fig. 5.12) of a reference flow stress in uniaxial tension for the linear viscoplastic untextured $\alpha_2 + \gamma$-TiAl polycrystal as a function of ν_α. Other parameters: $\rho_{sup} = 5$, $\rho_{bas} = 6.6$, $\rho_{prism} = 2$, $\rho_{pyr} = 18.2$ [173], $\alpha_M = 2.7$, $\alpha_T = 1.2$ [113].

In Fig. 5.15 the influence of the volume fraction of α_2 phase on the value of bounds and self-consistent estimates of the overall flow stress are studied for confinement parameters $\alpha_M = 2.7$ and $\alpha_T = 1.2$ identified by Lebensohn et al. [113]. As expected, the overall flow stress increases with increasing ν_α, since initiation of slip in α_2 phase requires a higher level of stress than in γ phase. Difference between the self-consistent estimates obtained for different models of a metagrain is the most substantial for the comparable content of α_2 and γ lamellae.

Now, let us consider the non-linear case. In the analysis, besides twinning, we have also neglected the α_2 phase ($\nu_\alpha = 0$). Similarly as in Chapter 4, we have derived three kinds of self-consistent estimates: secant, tangent and affine ones. In Fig. 5.16 bounds and the three self-consistent estimates are presented for $n = 8$ and increasing values of α_M and α_T parameters for RVE1 model of a metagrain, and the two-scale model of TiAl of lamellar substructure. Comparing the results for both realizations of microstructure, we observe that, for relatively small values of α_T and α_M, all SC estimates, in the case of the three-scale model, are much closer to the upper bound solution than for the two-scale model for which standard relation between the bounds and the three SC estimates is observed (see Section 4.3). As concerns high values of α_M and α_T, one observes,
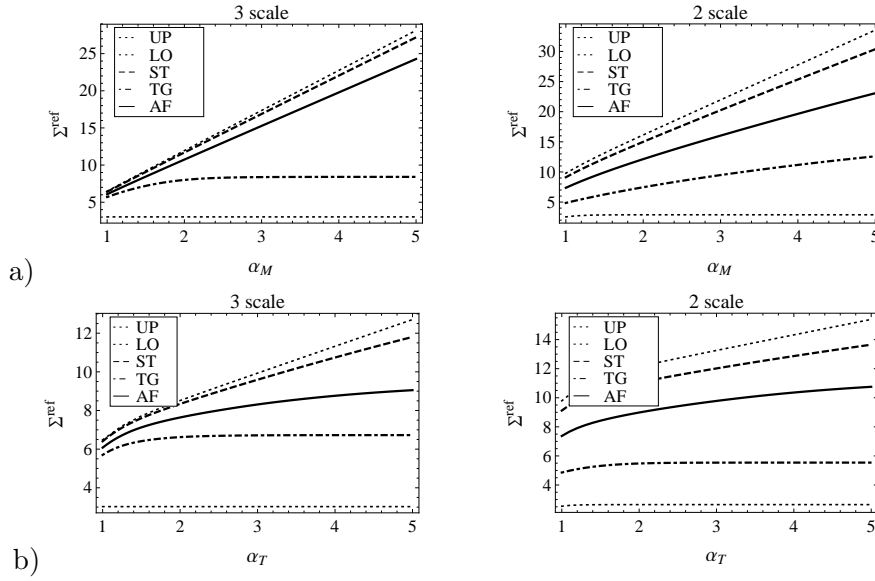
Fig. 5.16. Bounds and non-linear self-consistent estimates ($n = 8$) of a reference overall flow stress in uniaxial tension for the viscoplastic untextured TiAl polycrystal of lamellar substructure as a function of a) α_M ($\alpha_T = 1$), b) α_T ($\alpha_M = 1$). Left - the three-scale model (RVE1), right - the two-scale model. Other parameters: $\nu_\alpha = 0$, $\rho_{sup} = 5$.

for both three-scale and two-scale cases, that all SC estimates tend to finite values as α_T increases, while only the tangent estimates tend to finite value as α_M increases.

By comparing bounds and SC estimates for the two-scale and three-scale models (Fig. 5.17) we find that:

- similarly to the linear case, introduction of the additional laminate level of microstructure narrows the gap between upper and lower bounds, and reduction of the difference between the bounds is relatively more pronounced for low values of confinement parameters;

- as concerns dependence on α_T parameter, the secant and affine SC estimates for the three-scale model are lower than for the two-scale model, while a reverse relation is observed for the tangent SC estimate;

- in the case of dependence of a reference flow stress on α_M parameter, the SC estimates for the two-scale and three-scale models cross each other for some value of α_M, and the corresponding relation between estimates observed for α_T parameter is true only for low values of α_M.
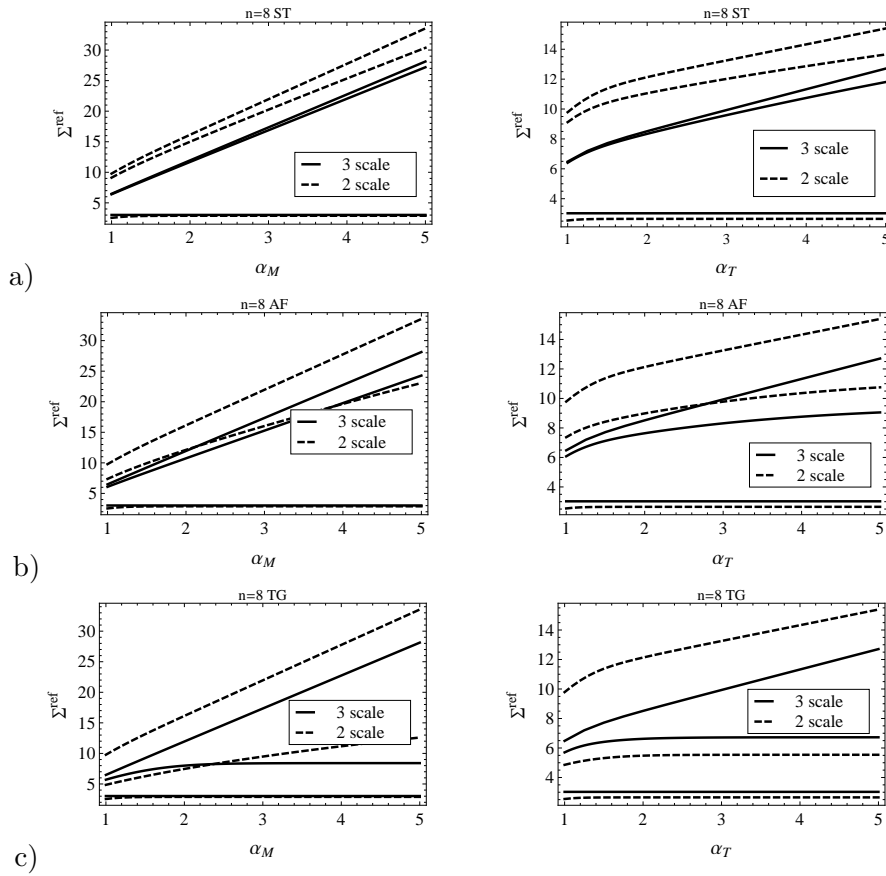
Fig. 5.17. Comparison of bounds and non-linear self-consistent estimates ($n = 8$) of a reference overall flow stress in uniaxial tension for the viscoplastic untextured TiAl polycrystal of lamellar substructure for the three-scale and two-scale models a) secant, b) affine, c) tangent SC estimates. Left - α_M ($\alpha_T = 1$), right - α_T ($\alpha_M = 1$). Other parameters: $\nu_\alpha = 0$, $\rho_{sup} = 5$.

5.3. Evolving microstructure

5.3.1. Model formulation

In order to account for the evolution of microstructure (e.g. the change of interface orientations and the reorientation of crystallographic axes in lamellae) the large strain framework has to be applied. According to the discussion in Chapter 2, we will use the velocity-based formulation in order to address this issue.

The continuity conditions imposed on the velocity field at lamellae interface result in the compatibility condition for the total velocity gradient $\mathbf{l}$ of the form

$$\mathbf{l}_j = \mathbf{l}_i + \mathbf{b} \otimes \mathbf{n} \tag{5.58}$$

being the counterpart of (5.5). Together with the equilibrium condition (5.6) for the Cauchy stress $\boldsymbol{\sigma}$ and the definition of the average velocity gradient and its symmetric part $\mathbf{d}$ and skew-symmetric part $\boldsymbol{\omega}$, i.e.:

$$\mathbf{l}_{mc} = \{\mathbf{l}_i\} \iff \mathbf{d}_{mc} = \{\mathbf{d}_i\} \quad \text{and} \quad \boldsymbol{\omega}_{mc} = \{\boldsymbol{\omega}_i\}, \tag{5.59}$$

supplemented by the assumed constitutive model, they provide sufficient number of equations to derive the local fields $\mathbf{l}_i$ and $\boldsymbol{\sigma}_i$.

Similarly as in the case of small strain framework, one can define orthogonal projectors $\mathbb{P}^L$ and $\mathbb{P}^T$. In contrast to the previously defined projectors, they decompose 9-dimensional space of second-order tensors (not necessarily symmetric) into two subspaces: 6-dimensional space $\mathcal{P}^L$ and 3-dimensional space $\mathcal{P}^T$. These projectors have the form, cf. Petryk [158]:

$$(\mathbb{P}^T)_{ijkl} = \delta_{ik} n_j n_l, \quad \mathbb{P}^L = \mathbb{I} - \mathbb{P}^T, \tag{5.60}$$

where the following relations are true:

$$\mathbb{P}^L \cdot \mathbf{l}_i = \mathbb{P}^L \cdot \mathbf{l}_j = \mathbb{P}^L \cdot \mathbf{l}_{mc}, \quad \mathbb{P}^T \cdot \boldsymbol{\sigma}_i = \mathbb{P}^T \cdot \boldsymbol{\sigma}_j = \mathbb{P}^T \cdot \boldsymbol{\sigma}_{mc}. \tag{5.61}$$

In the case of crystal plasticity, if the elastic strains are neglected, deformation is volume preserving ($\mathrm{tr}\,\mathbf{l}_i = \mathbf{0}$) and the constitutive law relates the stress deviator with the deviatoric strain-rate tensor. Then, similarly to the small strain case, one can introduce the modified projectors:

$$(\tilde{\mathbb{P}}^T)_{ijkl} = (\delta_{ik} - n_i n_k) n_j n_l, \quad \tilde{\mathbb{P}}^L = \mathbb{I} - \mathbb{I}_\mathrm{P} - \tilde{\mathbb{P}}^T. \tag{5.62}$$

It can be easily verified that, as far as the symmetric part of the velocity gradient is concerned, in view of the symmetry of the Cauchy stress, the averaging conditions (5.61) are equivalent to (5.10), where $\dot{\boldsymbol{\varepsilon}}$ is replaced by the strain-rate tensor $\mathbf{d}$ (symmetric part of $\mathbf{l}$). Using these relations and the constitutive law for the individual lamella, one can derive local strain-rates and local stresses.

In the simplest velocity-based framework of viscoplasticity of crystals, the constitutive rules take the form (2.8), with rate-independent specification (2.25) or viscoplastic specification (2.27) discussed in Chapter 2. In the second case

they can be linearized according to one of the methods described in Section 4.3 and thus re-written as follows:

$$\mathbf{d}_i = \mathbf{d}_i^p = \mathbf{f}_i(\boldsymbol{\sigma}_i) = \mathbf{M}(\boldsymbol{\sigma}_i) \cdot \boldsymbol{\sigma}_i + \mathbf{d}_i^{\mathrm{res}}, \tag{5.63}$$

where definitions of $\mathbf{M}(\boldsymbol{\sigma}_i)$ and $\mathbf{d}_i^{\mathrm{res}}$ depend on the applied linearization scheme. Accordingly, homogenized properties of a metagrain are defined as follows:

$$\mathbf{d}_{mc} = \mathbf{M}_{mc} \cdot \boldsymbol{\sigma}_{mc} + \mathbf{d}_{mc}^{\mathrm{res}}. \tag{5.64}$$

The compliance tensor $\mathbf{M}_{mc}$ and the reference strain-rate $\mathbf{d}_{mc}^{\mathrm{res}}$ of laminate are derived using the relations (5.22)-(5.27). They can serve as the corresponding local quantities, when employing one of the SC scale transition schemes between the level of a metagrain and the level of a polycrystalline sample.

Irrespective of which kind of the transition rule is employed between the level 2 and the level 3, the following procedure can be applied in order to derive the local fields $\mathbf{l}_i$ and deviatoric parts $\mathbf{s}_i$ of $\boldsymbol{\sigma}_i$ in lamellae for the known $\mathbf{l}_{mc}$ of the metagrain. First, we solve the following system of non-linear equations:

$$\mathbf{d}_{mc}^L = \mathbf{f}_i^L(\mathbf{s}_i^L, \mathbf{s}_{mc}^T), \quad i = 1, \ldots, NL, \tag{5.65}$$
$$\mathbf{d}_{mc}^T = \{\mathbf{f}_i^T(\mathbf{s}_i^L, \mathbf{s}_{mc}^T)\}, \tag{5.66}$$

in order to find $\mathbf{s}_i$ and $\mathbf{d}_i$. If the flow rule (2.24) of rate-independent model is used, additionally the NL plastic multipliers $\dot{\lambda}_i \geqslant 0$ must be derived. The set of equations (5.65)-(5.66) is then supplemented by the consistency conditions and the Kuhn-Tucker conditions for the regularized Schmid law, cf. Gambin and Kowalczyk [55], in every lamella.

Once the local strain-rates are established, with use of remaining kinematic relations (5.61), one can find the components of local spins in any orthonormal basis such that $\mathbf{i}_3 = \mathbf{n}$, namely:

$$\omega_{12}^i = \omega_{12}^{mc}, \tag{5.67}$$
$$\omega_{13}^i = \omega_{13}^{mc} + d_{13}^i - d_{13}^{mc}, \tag{5.68}$$
$$\omega_{23}^i = \omega_{23}^{mc} + d_{23}^i - d_{23}^{mc}. \tag{5.69}$$

Now, the elastic spins can be calculated using Eqs. (2.2), (2.4), (2.8) and (2.25) or (2.27). The derived elastic spins, responsible for the lattice rotation in the subsequent lamellae belonging to the considered metagrain, are generally different. As a result, the relative orientations of crystallographic lattice in these lamellae change as deformation proceeds. In the case when lamellar microstructure is the result of twinning, initially this relative orientation is specified by

the geometry of the corresponding twinning mode. In view of the above for-
mulation, there is no reason to obey the initial relation (2.6) between crystal
axes in matrix and twin during the process. It should be noted that the initial
relation is satisfied for any deformation path, if the set of plastic deformation
modes is restricted to the longitudinal modes.

The projectors $\mathbb{P}^L$ and $\mathbb{P}^T$ for each metagrain are functions of the current
orientation of lamellae interface defined by a unit normal $\mathbf{n}$. On the other hand,
the deformation path is imposed with respect to the reference sample frame
$\{\mathbf{e}_k\}$, Fig. 5.1. During the large deformation process, the orientation of interface
with respect to the reference sample frame changes. In the frame of the model
we treat the interface as a material surface (compare Raniecki and Mróz [172]),
therefore the change of infinitesimal element of this surface deforms according
to the Nanson formula,

$$\mathrm{d}\mathbf{s} = J_{mc}\mathbf{F}_{mc}^{-\mathrm{T}}\mathrm{d}\mathbf{S}, \quad \mathrm{d}\mathbf{s} = \mathrm{d}s\mathbf{n}, \quad \mathrm{d}\mathbf{S} = \mathrm{d}S\mathbf{N}, \tag{5.70}$$

where the particles which initally make up the interface area represented by $\mathrm{d}\mathbf{S}$
now fill the interface area element represented by $\mathrm{d}\mathbf{s}$, $\mathbf{F}_{mc}$ is the deformation
gradient of a metagrain while $J_{mc} = \det\mathbf{F}_{mc}$. Calculating the material derivative
of (5.70) one has

$$\mathrm{d}\dot{\mathbf{s}} = (\mathrm{tr}\mathbf{l}_{mc}J_{mc}\mathbf{I} - \mathbf{l}_{mc}^{\mathrm{T}})\mathrm{d}\mathbf{s}. \tag{5.71}$$

For incompressible materials this relation reduces to

$$\mathrm{d}\dot{\mathbf{s}} = -\mathbf{l}_{mc}^{\mathrm{T}}.\mathrm{d}\mathbf{s}. \tag{5.72}$$

Now, imagine that in the reference configuration the axis $\mathbf{i}_1$ of a metagrain
frame is coaxial with the material fibre $\mathrm{d}\mathbf{X}$ lying on the interface ($\mathrm{d}\mathbf{X} \cdot \mathbf{N} = 0$).
This line element deforms according to the well-known relation

$$\mathrm{d}\mathbf{x} = \mathbf{F}_{mc}\mathrm{d}\mathbf{X} \Longrightarrow \mathrm{d}\dot{\mathbf{x}} = \mathrm{d}\mathbf{v} = \mathbf{l}_{mc}\mathrm{d}\mathbf{x}. \tag{5.73}$$

Consequently, in the computational scheme, we define the current metagrain
frame $\{\mathbf{i}_k\}$, Fig. 5.1, as follows:

$$\mathbf{i}_3(t) = \mathbf{n}(t) = \frac{\mathrm{d}\mathbf{s}(t)}{|\mathrm{d}\mathbf{s}(t)|}, \quad \mathbf{i}_1(t) = \frac{\mathrm{d}\mathbf{x}(t)}{|\mathrm{d}\mathbf{x}(t)|}. \tag{5.74}$$

Note that if one uses the simple updating in the incremental calculation process,
that is:

$$\mathrm{d}\mathbf{s}(t + \Delta t) = \mathrm{d}\mathbf{s}(t) + \mathrm{d}\dot{\mathbf{s}}(t)\Delta t, \quad \mathrm{d}\mathbf{x}(t + \Delta t) = \mathrm{d}\mathbf{x}(t) + \mathrm{d}\dot{\mathbf{x}}(t)\Delta t, \tag{5.75}$$

then the frame orthogonality may not be satisfied for $t + \Delta t$. Therefore, in order to enforce the orthogonality, the idea of an exponential map is adopted, cf. Simo and Hughes [185]. Expand $d\mathbf{x}(t + \Delta t)$ and $d\mathbf{s}(t + \Delta t)$ around the time instant t and assume that $\mathbf{l}_{mc}$ can be approximated as constant for the considered time increment. As a result, the following updating formula is found for $d\mathbf{x}$ and $d\mathbf{s}$:

$$d\mathbf{x}(t + \Delta t) = (\mathbf{I} + \mathbf{l}_{mc}\Delta t + \frac{1}{2}\mathbf{l}_{mc}^2(\Delta t)^2 + ...)d\mathbf{x}(t) = \exp(\Delta t \mathbf{l}_{mc})d\mathbf{x}(t), \quad (5.76)$$

$$d\mathbf{s}(t + \Delta t) = (\mathbf{I} - \mathbf{l}_{mc}^{\mathrm{T}}\Delta t + \frac{1}{2}(\mathbf{l}_{mc}^{\mathrm{T}})^2(\Delta t)^2 + ...)d\mathbf{s}(t) = \exp(-\Delta t \mathbf{l}_{mc}^{\mathrm{T}})d\mathbf{s}(t), \quad (5.77)$$

and it can be verified that

$$d\mathbf{x}(t + \Delta t) \cdot d\mathbf{s}(t + \Delta t) = d\mathbf{x}(t) \cdot d\mathbf{s}(t) = 0. \quad (5.78)$$

As the crystal axes reorient with respect to the lamellae interfaces, the morphological identification of a deformation mode (5.1)-(5.3) can change, that is, e.g. the longitudinal mode can become the mixed mode etc. In order to account continuously for this change in the computational framework, the following dependence of the critical resolved shear stress on the current orientation of slip or twin system $\{\mathbf{m}^r, \mathbf{n}^r\}$ with respect to the unit vector $\mathbf{n}$ normal to the lamellae interface has been proposed as

$$\hat{\tau}_c^r(\mathbf{n}) = \tau_c^r \left(1 + a_1\sqrt{(1 - |\mathbf{n}^r \cdot \mathbf{n}|)(1 + a_2|\mathbf{m}^r \cdot \mathbf{n}|)}\right), \quad (5.79)$$

where τ_c^r is the critical shear stress for equiaxed microstructure, while a_i are parameters which describe the confinement effects induced by lamellar substructure. Note that according to the above formula, for the longitudinal mode, one has $\hat{\tau}_c^{r,LONG} = \tau_c^r$ and this value can be thought of as the corresponding critical shear stress for the material without lamellar substructure.

5.3.2. Example - TiAl of lamellar substructure

The presented model has been applied to model titanium alluminide of lamellar substructure, discussed also in Subsection 5.2.3. In order to simplify calculations, we have neglected α_2 phase, and hence the metagrain has been modelled as element consisting of two γ lamellae corresponding to one of the twin-related pairs, see Figs 5.2 and 5.3. The Taylor model has been applied as the scale transition rule between the levels of a metagrain and of a polycrystalline element.
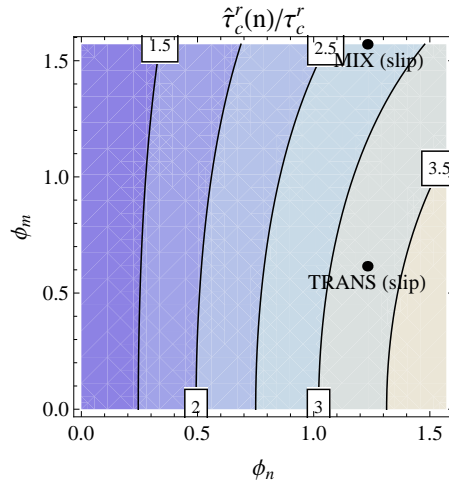
Fig. 5.18. The variation of $\hat{\tau}_c^r(\mathbf{n})$ specified by (5.79) with $\cos(\phi_n) = \mathbf{n}^r \cdot \mathbf{n}$ and $\cos(\phi_m) = \mathbf{m}^r \cdot \mathbf{n}$ for $\alpha_1 = 2.1$ and $\alpha_2 = 0.9$. Thick points indicate the values of this function for mixed and transversal slip modes in γ-TiAl.

Within the KMM NoE project, the commercial TiAl material provided by one of the industrial partners has been characterized. Microstructural characterization indicated that this material has lamellar substructure [149]. The material has been tested in tension and compression [148]. Though limit strains in tension did not exceed 3%, in compression tests deformation up to 35% was achieved. Thus, it is possible to compare these results with predictions of the developed model in large strain regime. Moreover, during the experiments it was concluded that the influence of strain-rate was not significant. It justifies the use of the rate-independent model discussed in Chapter 2. The exponent $n = 8$ for the yield surface (2.20) is assumed. In the computations, the initial critical resolved shear stress for all mechanism varies only due to confinement effects, that is $\tau_c^{ord} = \tau_c^{sup} = \tau_c^{twin}$. The identification of confinement effects performed for TiAl by Lebensohn et al. [113] has been utilized, i.e. the initial values of this parameters are set to $\alpha_M = 2.8$ and $\alpha_T = 1.2$. In order to obtain an approximate agreement between these initial values and the proposed formula (5.79), one identifies that $a_1 = 2.1$ and $a_2 = 0.9$ (see Fig. 5.18). Because the available experimental data are limited to the uniaxial compression test, the number of material parameters has been reduced by assuming a simple model of hardening for the "non-confined" critical shear stress τ_c^r present in (5.79). Accordingly, the latent-hardening ratios $q^{\alpha\beta} = 1$ are assumed for all mechanisms interactions in Eq. (2.40), and the hardening law with saturation (2.41) for self-hardening is adopted.

In the identification procedure the results for the lowest strain-rate at room temperature have been utilized, Fig. 5.19. When analysing the response for large strain regime, the elastic strains are neglected. In the computation, the polycrystalline aggregate containing 500 metagrains of random distribution of orientations with respect to the sample axes (see Fig. 5.20a) has been considered. The identified values of material parameters are collected in Table 5.1.

Table 5.1. Identified material parameters for the commercial TiAl of lamellar substructure.

Mechanism	τ_c^0 [MPa]	h_0 [MPa]	τ_{sat} [MPa]	α
Longitudinal	125.0	7375	1112.5	3.7
Calculated init. yield stress in tension/compres.	863 [MPa] /870.1[MPa]			
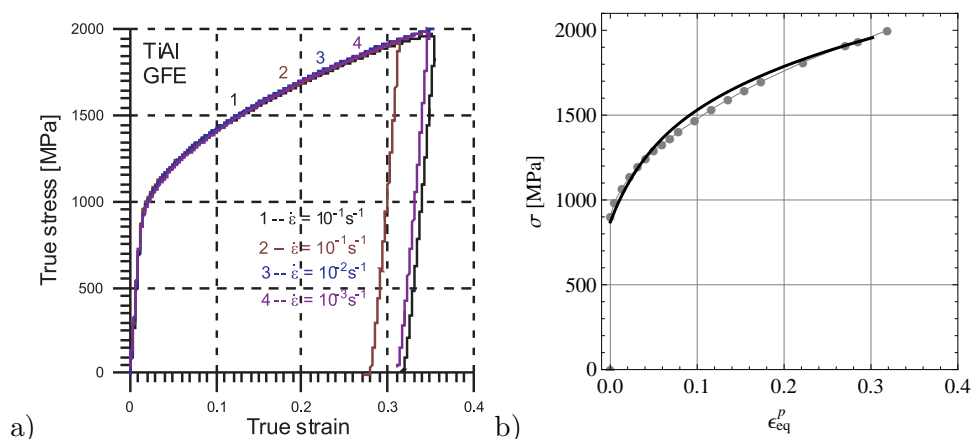
Fig. 5.19. Experimental strain-stress curves for TiAl of lamellar substructure [148] (a) and the comparison of experimental data (grey curve with circles) with computed stress-strain curve (thick black curve) for identified parameters (b).

In Fig. 5.20b the calculated crystallographic texture after 30% compression is presented. Note that the figure shows the stereographic projections of {111} crystallographic planes in all lamellae with respect to the sample directions (compression axis $\mathbf{e}_3$ is perpendicular to the projection plane). This pole figure is not much different from the corresponding pole figure obtained for near gamma TiAl studied in Section 2.4.4.

In Fig. 5.21a the change of the initial relation between crystallographic planes {111} in lamellae and the laminate interface after 30% compression is presented. The direction $\mathbf{i}_3 = \mathbf{n}$ is perpendicular to the projection plane. As it is
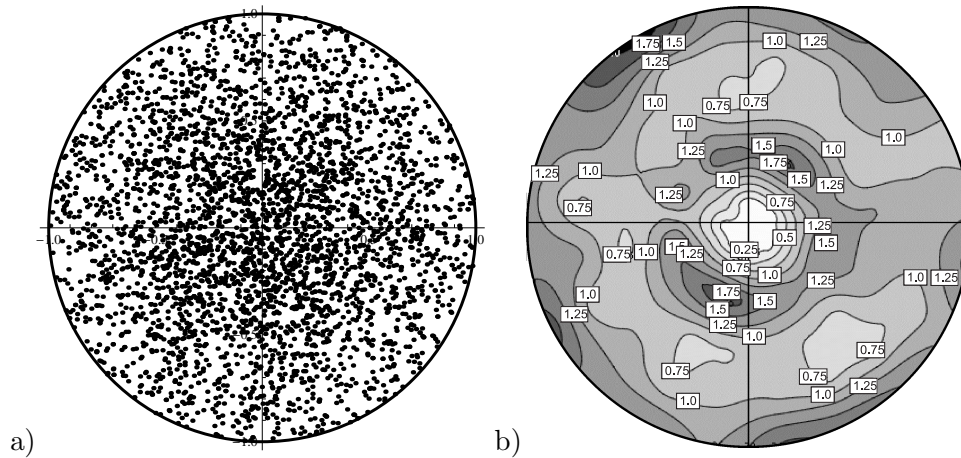
Fig. 5.20. Pole figures {111} (crystal axes vs. sample axes) for compression: a) initial random texture, b) texture for 30% of compression strain.

seen, the applied computational scheme leads to the considerable disturbance of the initial relation marked in Fig. 5.21a by thick grey dots. In Fig. 5.21b the reorientation of lamellae interfaces with respect to the sample frame during the process is presented. Note that initially random distribution of orientations of metagrains with respect to the sample axes has been assumed. Because the Taylor model is employed as a scale transition rule between the level of me-
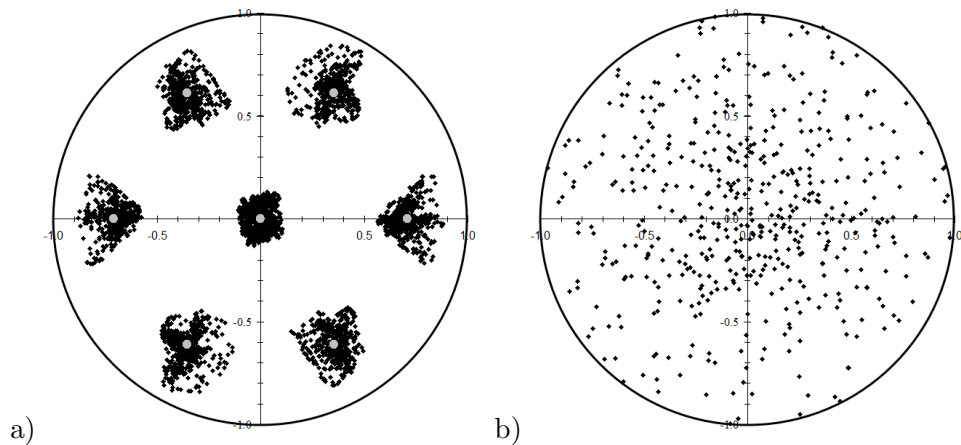
Fig. 5.21. a) Pole figures {111} of crystal axes vs. lamellae axes: grey thick dots - an initial twin-related relation between crystal axes and laminate axes, black dots - the corresponding relation after 30% compression, b) Pole figures {001} of laminate axes vs. sample axes.

tagrain and the overall level, each metagrain undergoes the same compression deformation. Consequently, in view of the assumption that lamellae interfaces are material surfaces, they rotate in such a way that their unit normals gradually align along the compression axis. These computational results concerning evolution of crystallographic texture and reorientation of lamellar substructure should be verified in experiments. Unfortunately, the corresponding measurements within KMM-NoE project were not performed. We were also not able to find the appropriate experimental data in the literature.

Current relative activities of modes
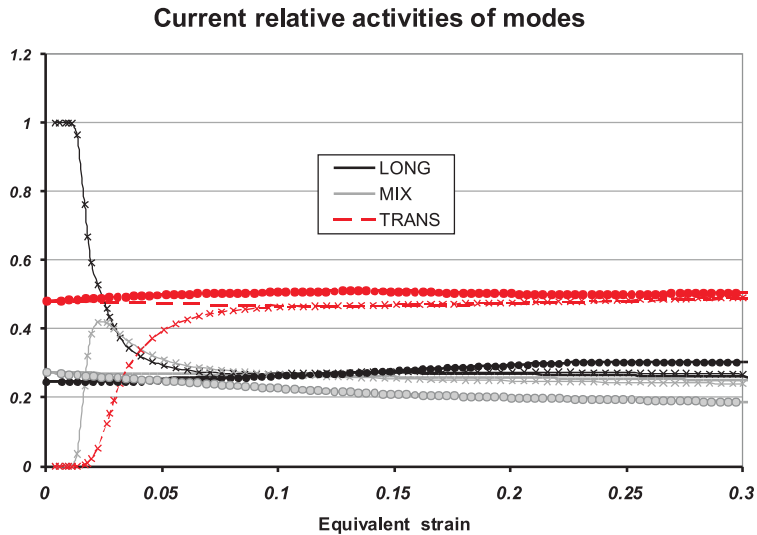
Fig. 5.22. Current relative activity of the morphologically classified modes [150]. Curves with dots - the proposed approach with microstructure evolution, curves without markers - the proposed approach without microstructure evolution, curves with crosses - the elastic-viscoplastic model with the Kröner SC scheme developed in [173].

Fig. 5.22 presents the current relative activity of three types of modes classified in view of their initial orientation with respect to the lamellar substructure. The corresponding quantities have been compared for the proposed approach applied within the large strain framework and the small strain framework, cf. Kowalczyk-Gajewska and Roos [105]. In the first case, we account for the microstructure evolution during the deformation process, while in the second case this effect is neglected. As we can see, the texture evolution slightly increases the activity of easy longitudinal modes. In Fig. 5.22 the equivalent results obtained with the use of the model proposed by Roos et al. [173] are also depicted. The

latter model is the three-scale model developed under the assumption of small strains. It uses elastic-viscoplastic model of single lamellae, a laminate-type transition rule between level 1 and level 2, and the Kröner-type self-consistent averaging scheme between level 2 and the level 3. As it is seen, in view of this approach, initially inelastic deformation is almost solely restricted to the easy longitudinal modes. For this regime, the notion of the initial yield surface studied in Section 5.2.3 would be relevant. As deformation proceeds, other modes come into play and for the advanced deformations the predicted response coincides with the Taylor model prediction, as expected.

5.4. Conclusions

In this chapter the three-scale micromechanical model for polycrystalline metals and alloys of lamellar substructure has been formulated. Within the model, the constitutive behaviour of an individual lamella can be described by the non-linear rule. First, using the general framework developed for layered composites, cf. El Omri et al. [47], Stupkiewicz and Petryk [190], and adopting the known proposals for metals of lamellar substructure due to Lebensohn et al. [113] and Roos et al. [173], the model has been formulated for small strains. Next, the approach has been extended to the large strain regime. In the latter case, the problem of the relative reorientation of lamellae interfaces and crystallographic lattice in lamellae has been discussed. It has been shown that when the scale transition scheme developed for the layered composites is utilized, in which case the lamella interface is thought of as a material surface, then the initial relation between the crystallographic orientations in neighbouring lamellae is lost. Due to relative reorientation of lamellae interfaces and crystallographic planes, the character of subsequent deformation modes within the lamellae changes. We have accounted for this effect by introducing the formula (5.79) for the critical shear stress, which depends on the current orientation of a deformation mode with respect to the lamellar substructure.

The way in which the model is formulated enables one to employ different scale transition rules between the metagrain level and the level of the polycrystalline sample. The computational procedures, not found elsewhere in the literature, are presented. They are related to the implementation of the different variants of scale transition schemes in the case of non-linear constitutive relations.

The capabilities of the model are thoroughly explored using the example of $\alpha_2 + \gamma$-TiAl intermetallic. The elastic, plastic and viscoplastic properties of the

metagrain (i.e. PST crystal) are estimated with the use of different variants of the proposed framework and compared with the available experimental data. The important part of the performed analysis is the study of the so-called confinement effects induced by the existence of lamellar substructure. These effects influence the inelastic deformation, resulting thus in substantial anisotropy of the metagrain.

Moreover, the original outcome of this chapter is the study of bounds and different self-consistent estimates of overall properties of an untextured viscoplastic polycrystal of lamellar substructure. In view of the confinement effects, the polycrystal composed of metagrains with a very fine lamellae spacing can be treated as an incompressible material with the constrained deformation modes. Therefore, theoretical results derived for such materials in Chapter 3 are also applicable in this case. It is also analysed how the introduction of an additional level of microstructure influences the value of bounds and the self-consistent estimates of overall quantities, such as the Young modulus or the yield stress. It is found that if the local anisotropy is relatively weak, incorporation of this additional level into the model narrows substantially the gap between the bounds. However, when the local anisotropy is strong, then the effect is much less pronounced.

As concerns the model performance within the large strain regime, the predictions of the mechanical response and the texture evolution in 30% compression of γ-TiAl of lamellar substructure are presented. This example illustrates also the issue of different reorientation of lamellae interfaces and crystallographic planes which initially coincide. The results concerning the current relative activity of morphologically classified modes are compared for the Taylor model accounting for the microstructure evolution, and the self-consistent Kröner model formulated within the small strain framework by Roos et al. [173]. Both models for the advanced plastic flow predict similar activity of modes. In particular, substantial activity of the hard transversal mode is predicted. This result can be questionable. Predictions might be improved by using one of the nonlinear self-consistent schemes (i.e. secant, tangent or affine) as a scale transition rule between the level of the metagrain and the level of the polycrystalline aggregate.

6

Averaging schemes
for elastic-viscoplastic
heterogeneous materials

6.1. Introduction

Metals and alloys of high specific strength usually suffer from low ductility, therefore, for many deformation processes, the available strains are not large. In view of this observation, description of the material response by means of rigid-viscoplastic models, where elastic strains are neglected, can introduce sometimes too strong simplifications, e.g., when the strain path is changed during the process. Moreover, strong anisotropy of viscoplastic flow related to the presence of easy and hard slip and twin systems within the grain, results in the existence of a considerable intermediate regime during which in the aggregate there are both purely elastic crystallites and those in which inelastic flow has already started. These facts indicate that it is desirable to formulate a model of heterogeneous elastic-viscoplastic materials. The model, when estimating the overall response, should take into account the heterogeneity of the local deformation as well as elastic and viscous interactions between the constituents. In this respect, the approaches utilizing the Eshelby inclusion concept are of interest.

Various averaging schemes which use the concept of an ellipsoidal inhomogeneity in a linearly elastic matrix, originally introduced by Eshelby [49], are available, including extensions to anisotropy, composite or coated inclusions, differential and incremental schemes, etc., cf. Kröner [107], Hashin [57], Kneer [87], Mori and Tanaka [140], McLaughlin [130], Christensen and Lo [35], Willis [220], Walpole [208], Weng [214], Suquet [192], Herve and Zaoui [63], Cherkaoui et al. [31], Nemat-Nasser and Hori [145], Broohm et al. [22]. As it has been discussed in Chapter 4, if the actual material behaviour is non-linear,

then the usual approach is to introduce some kind of linearization, e.g., by using tangent or secant stiffness moduli for the matrix representing an elasto-plastic aggregate, with applications and extensions to elastoplastic polycrystals and composites, cf. Hill [66], Hutchinson [70], Berveiller and Zaoui [14], Tandon and Weng [198], Lipinski et al. [121]. Other types of linearization are used to model rigid-viscoplastic materials, cf. Hutchinson [69], Molinari et al. [138], Cailletaud [28], Lebensohn and Tomé [112], de Botton and Ponte Castañeda [39], Ponte Castañeda [164], Kiryk and Petryk [84], Masson et al. [127], Bornert et al. [19].

However, the linearization becomes more difficult if both elastic and viscous properties of the matrix are to be simultaneously taken into account. For linear viscoelasticity the problem can be solved in an elegant way, at least formally, by using the Stieltjes convolutions and Laplace-type transform, cf. Hashin [58], Christensen [33], Laws and McLaughlin [111], Suquet [192], although the inverse transform may be difficult and numerically time-consuming in a general anisotropic case. Extensions of that formalism to cases when elasticity is accompanied by non-linear viscous properties, as in elastic-viscoplastic materials, lead to rather complex formulations cf. Rougier et al. [175], Masson and Zaoui [126], Pierard and Doghri [162]. As all mean-field approaches to the mechanics of composites and polycrystals are approximate even for strictly linear problems, it is reasonable to look for simpler linearization schemes.

Therefore, approximate linearization schemes for elasto-viscoplasticity, cf. Kouddane et al. [93], Paquin et al. [155], Sabar et al. [181], Molinari [136], Lahellec and Suquet [109], Mercier and Molinari [133], Doghri et al. [41], Wang et al. [209], are of interest. The common task is to approximate the interaction between the matrix material and inhomogeneities without applying the Laplace (or Carson) transform, inversion of which can be cumbersome in a general case. Differences between some of the existing approaches of that type will be illustrated in next sections. Our aim is to develop a related, but conceptually different approach.

The main idea presented in this chapter, not found in the literature, is to abandon the attempts to incorporate both elastic and viscous properties of the matrix in a *single* computational step of an incremental scale-transition scheme. Rather, we propose to use elastic and viscous properties *sequentially* within one incremental step. Accordingly, not a single linear matrix-inhomogeneity problem but two or more different subproblems of that type, with different matrix-inhomogeneity interaction rules, are to be solved separately. The results are combined together to simulate the actual, simultaneously viscous and elastic response of the system to the applied external strain history. It is not

evident that such an approach can work well even for linearly viscoelastic iso-
tropic materials, therefore this question is examined in the present thesis in
more detail. Step-by-step sequential linearization of a strongly non-linear visco-
us/elastic (elasto-viscoplastic) material behaviour requires further development,
and only an illustrative example of moderate non-linearity is presented below.
The attention is restricted to the geometrically linear (small strain) theory. The
predictions of the sequential linearization approach proposed here are compa-
red with other approximations as well as with the exact results obtained by
using the Laplace transform technique and the correspondence principle. As
an example, first a two-phase composite of high contrast in elastic and viscous
properties of the phases is examined, and then the proposed approach is applied
to estimate elastic-viscoplastic response of polycrystals characterized by strong
anisotropy of constituent crystals.

6.2. Linear viscoelastic inhomogeneity problem

6.2.1. Formulation of the sequential approach

We begin with the formulation of the sequential approach to the classical
problem of a linear viscoelastic inhomogeneity[1] in a linear viscoelastic infinite
matrix, both taken to be of the Maxwell type. Accordingly, a local strain-rate
in phase r is decomposed into elastic and viscous parts as follows:

$$\dot{\boldsymbol{\varepsilon}}_r = \dot{\boldsymbol{\varepsilon}}_r^e + \dot{\boldsymbol{\varepsilon}}_r^v, \qquad \dot{\boldsymbol{\varepsilon}}_r^e = \mathbb{M}_r^e \cdot \dot{\boldsymbol{\sigma}}_r, \qquad \dot{\boldsymbol{\varepsilon}}_r^v = \mathbb{M}_r^v \cdot \boldsymbol{\sigma}_r, \qquad (6.1)$$

where $\boldsymbol{\sigma}_r$ is a local stress, $\mathbb{M}_r^e$ and $\mathbb{M}_r^v$ are fixed, diagonally symmetric, positive
definite tensors of elastic and viscous compliances, respectively, and a superim-
posed dot denotes time derivative. The respective stiffness moduli tensors $\mathbb{L}_r^e$
and $\mathbb{L}_r^v$ are defined by $\mathbb{L}_r^e = (\mathbb{M}_r^e)^{-1}$ and $\mathbb{L}_r^v = (\mathbb{M}_r^v)^{-1}$, with the inverses taken
with due account for the minor symmetries.

Let $r = 0$ stands for the (infinite) matrix and $r = i$ for the (ellipsoidal)
inhomogeneity. The external strain imposed on the matrix at infinity is denoted
by $\boldsymbol{\varepsilon}_0$ and is assumed to vary in a prescribed manner with respect to time t,
$\boldsymbol{\varepsilon}_0 = \boldsymbol{\varepsilon}_0(t)$, while the associated stress in the matrix at infinity is denoted by $\boldsymbol{\sigma}_0$.
For the linear *purely elastic* problem ($\mathbb{M}_r^v \equiv \mathbb{O}$), we have the following equation
for the differences between strain-rates and stress-rates in the inhomogeneity

---

[1]Following Eshelby [49], we employ the term "inhomogeneity" in contrast to the term
"inclusion" used to indicate an incompatible eigenstrain without perturbation of compliances
(see Appendix B).

and in the matrix at infinity (see Appendix B),

$$\dot{\boldsymbol{\varepsilon}}_i^e - \dot{\boldsymbol{\varepsilon}}_0 = -\mathbb{M}_*^e \cdot (\dot{\boldsymbol{\sigma}}_i - \dot{\boldsymbol{\sigma}}_0) \,, \tag{6.2}$$

where $\mathbb{M}_*^e$ is the inverse of the Hill tensor (B.3) associated with the matrix moduli $\mathbb{L}_0^e$. The classical solution to (6.2) is expressed in the form:

$$\dot{\boldsymbol{\varepsilon}}_i^e(t) = \mathbb{A}_i^e \cdot \dot{\boldsymbol{\varepsilon}}_0(t) \,, \qquad \mathbb{A}_i^e = \left(\mathbb{I}^S + \mathbb{P}^e \circ (\mathbb{L}_i^e - \mathbb{L}_0^e)\right)^{-1} \qquad \text{if} \quad \mathbb{M}_r^v \equiv \mathbb{O} \,, \tag{6.3}$$

where $\mathbb{P}^e$ is the stress polarisation tensor for the linear elastic problem, defined by Eq. (B.4) for the elastic matrix moduli tensor $\mathbb{L} = \mathbb{L}_0^e$ and for the shape of the ellipsoidal inhomogeneity expressed by $\mathbf{a} = \mathbf{a}_i$.

On the other hand, for the linear *purely viscous* problem ($\mathbb{M}_r^e \equiv \mathbb{O}$) the counterpart of Eq. (6.2) is

$$\dot{\boldsymbol{\varepsilon}}_i^v - \dot{\boldsymbol{\varepsilon}}_0 = -\mathbb{M}_*^v \cdot (\boldsymbol{\sigma}_i - \boldsymbol{\sigma}_0) \,, \tag{6.4}$$

with the solution

$$\dot{\boldsymbol{\varepsilon}}_i^v(t) = \mathbb{A}_i^v \cdot \boldsymbol{\varepsilon}_0(t) \,, \qquad \mathbb{A}_i^v = \left(\mathbb{I}^S + \mathbb{P}^v \circ (\mathbb{L}_i^v - \mathbb{L}_0^v)\right)^{-1} \qquad \text{if} \quad \mathbb{M}_r^e \equiv \mathbb{O} \,. \tag{6.5}$$

Here, $\mathbb{P}^v$ is the stress polarisation tensor for the linear viscous problem, defined by Eq. (B.4) on substituting $\mathbb{L} = \mathbb{L}_0^v$ and $\mathbf{a} = \mathbf{a}_i$.

The question we address now is how to determine $\dot{\boldsymbol{\varepsilon}}_i$, at least approximately, without employing the Laplace transform technique, if none of $\mathbb{M}_r^e$ and $\mathbb{M}_r^v$ vanishes. The key concept here is to consider *sequentially* two linear subproblems within *one* infinitesimal time step:

Subproblem V in which the interaction between the inhomogeneity and matrix is assumed as purely viscous,

Subproblem E in which the interaction between the inhomogeneity and matrix is purely elastic.

For instance, Subproblem V may be thought of as corresponding to a fixed or smoothly varying external stress within an infinitesimal time interval, while Subproblem E corresponds to a suddenly applied infinitesimal increment in external stress or strain at the beginning or end of that interval. All instantaneous changes in Subproblem E are referred to the same infinitesimal time interval as those in Subproblem V and interpreted as purely elastic rates.

The inhomogeneity-matrix interaction equations for Subproblems V and E, in analogy to Eqs. (6.4) and (6.2), are defined by

$$\dot{\boldsymbol{\varepsilon}}_i^{\mathrm{V}} - \dot{\boldsymbol{\varepsilon}}_0^{\mathrm{V}} = -\mathbb{M}_*^v \cdot (\boldsymbol{\sigma}_i - \boldsymbol{\sigma}_0^{\mathrm{V}}) \tag{6.6}$$

and

$$\dot{\boldsymbol{\varepsilon}}_i^{\mathrm{E}} - \dot{\boldsymbol{\varepsilon}}_0^{\mathrm{E}} = -\mathbb{M}_*^e \cdot (\dot{\boldsymbol{\sigma}}_i^{\mathrm{E}} - \dot{\boldsymbol{\sigma}}_0^{\mathrm{E}}) \,, \tag{6.7}$$

respectively. In the most general case, in the above equations only the local stress $\boldsymbol{\sigma}_i$ is treated as known, and the other quantities with a superscript V or E are unknowns. Depending on further assumptions, the unknowns can be eliminated in various ways. Some of them are discussed below.

We introduce the simplifying assumption that

$$\dot{\boldsymbol{\varepsilon}}_i^{\mathrm{V}} = \dot{\boldsymbol{\varepsilon}}_i^v \,, \qquad \dot{\boldsymbol{\varepsilon}}_i^{\mathrm{E}} = \dot{\boldsymbol{\varepsilon}}_i^e \,, \qquad \dot{\boldsymbol{\sigma}}_i^{\mathrm{E}} = \dot{\boldsymbol{\sigma}}_i \,. \tag{6.8}$$

It means that not only the interaction rules, but also the local strain-rates are separated as purely viscous and purely elastic in Subproblems V and E, respectively.

One might adopt a more general point of view that $\dot{\boldsymbol{\varepsilon}}_i^{\mathrm{V}}$ includes also an elastic accommodation strain-rate, constitutively related to the local stress-rate. Such a local stress-rate is, in turn, constitutively related to the second time derivative (acceleration) of a local viscous strain, which need not vanish even if the external strain varies linearly in time. We will show below that in a certain special case an exact solution is obtained using assumption (6.8), which motivates its use here. The influence of elastic accommodation rates is examined in Section 6.3, where the sequential approach to a single inhomogeneity problem is extended to the sequential self-consistent scheme for a viscoelastic multi-phase composite.

Kinematic consistency between the imposed external strain-rate $\dot{\boldsymbol{\varepsilon}}_0$ and those in Subproblems V and E considered jointly is obtained by enforcing the relationship

$$\dot{\boldsymbol{\varepsilon}}_0^{\mathrm{V}} + \dot{\boldsymbol{\varepsilon}}_0^{\mathrm{E}} = \dot{\boldsymbol{\varepsilon}}_0 \,. \tag{6.9}$$

On substituting relationships (6.8) and (6.9) into (6.6) and (6.7), the basic equations for Subproblems V and E reduce to

$$\dot{\boldsymbol{\varepsilon}}_i^v - \dot{\boldsymbol{\varepsilon}}_0^{\mathrm{V}} = -\mathbb{M}_*^v \cdot (\boldsymbol{\sigma}_i - \boldsymbol{\sigma}_0^{\mathrm{V}}) \tag{6.10}$$

and

$$\dot{\boldsymbol{\varepsilon}}_i^e - \dot{\boldsymbol{\varepsilon}}_0 + \dot{\boldsymbol{\varepsilon}}_0^{\mathrm{V}} = -\mathbb{M}_*^e \cdot (\dot{\boldsymbol{\sigma}}_i - \dot{\boldsymbol{\sigma}}_0^{\mathrm{E}}) \,, \tag{6.11}$$

respectively.

Two additional tensor equations are still required. In conjunction with Eqs. (6.6), (6.7), (6.8) and (6.9), two natural variants are:

- Variant I:

$$\boldsymbol{\sigma}_0^{\mathrm{V}} = \mathbb{L}_0^v \cdot \dot{\boldsymbol{\varepsilon}}_0^{\mathrm{V}}, \qquad \dot{\boldsymbol{\sigma}}_0^{\mathrm{E}} = \mathbb{L}_0^e \cdot \dot{\boldsymbol{\varepsilon}}_0^{\mathrm{E}}. \tag{6.12}$$

- Variant II:

$$\boldsymbol{\sigma}_0^{\mathrm{V}} = \boldsymbol{\sigma}_0, \qquad \dot{\boldsymbol{\sigma}}_0^{\mathrm{E}} = \dot{\boldsymbol{\sigma}}_0. \tag{6.13}$$

Variant III specified by relations $\mathbb{M}_0^v \cdot \boldsymbol{\sigma}_0^{\mathrm{V}} + \mathbb{M}_0^e \cdot \dot{\boldsymbol{\sigma}}_0^{\mathrm{E}} = \dot{\boldsymbol{\varepsilon}}_0$ and $\dot{\boldsymbol{\varepsilon}}_0^{\mathrm{V}} = \dot{\boldsymbol{\varepsilon}}_0^v$ (then $\dot{\boldsymbol{\varepsilon}}_0^{\mathrm{E}} = \dot{\boldsymbol{\varepsilon}}_0^e$ which follows from (6.9) and (6.1)) has also been tested. This variant, in the special case of a spherical inhomogeneity and matrix being both of an isotropic and incompressible linearly viscoelastic material, leads to an exact solution based on Laplace transform. However, for compressible materials, the results for Variant III are in a less satisfactory agreement with the exact solution, see Subsection 6.2.5.

After straightforward rearrangements, Variants I and II of the sequential linearization approach to the viscoelastic inhomogeneity/matrix system reduce to the following sets of equations:

- Variant I:

$$\begin{array}{lll} \text{Subproblem V:} & \dot{\boldsymbol{\varepsilon}}_0^{\mathrm{V}} = (\mathbb{A}_i^v)^{-1} \cdot \dot{\boldsymbol{\varepsilon}}_i^v, & (6.14) \\[4pt] \text{Subproblem E:} & \dot{\boldsymbol{\varepsilon}}_i^e = \mathbb{A}_i^e \cdot (\dot{\boldsymbol{\varepsilon}}_0 - \dot{\boldsymbol{\varepsilon}}_0^{\mathrm{V}}). & (6.15) \end{array}$$

- Variant II:

$$\begin{array}{lll} \text{Subproblem V:} & \dot{\boldsymbol{\varepsilon}}_0^{\mathrm{V}} = \dot{\boldsymbol{\varepsilon}}_i^v + \mathbb{M}_*^v \cdot (\boldsymbol{\sigma}_i - \boldsymbol{\sigma}_0), & (6.16) \\[4pt] \text{Subproblem E:} & \dot{\boldsymbol{\varepsilon}}_i^e = (\mathbb{I}^S + \mathbb{M}_*^e \circ \mathbb{L}_i^e)^{-1} \cdot (\dot{\boldsymbol{\varepsilon}}_0 - \dot{\boldsymbol{\varepsilon}}_0^{\mathrm{V}} + \mathbb{M}_*^e \cdot \dot{\boldsymbol{\sigma}}_0) & (6.17) \end{array}$$

In each Variant, the essence of Subproblem V is to estimate the part $\dot{\boldsymbol{\varepsilon}}_0^{\mathrm{V}}$ of external strain-rate $\dot{\boldsymbol{\varepsilon}}_0$ that is intended to correspond to $\dot{\boldsymbol{\varepsilon}}_i^e = \mathbf{0}$ in the inhomogeneity in the current stress state. In Subproblem E, the difference $(\dot{\boldsymbol{\varepsilon}}_0 - \dot{\boldsymbol{\varepsilon}}_0^{\mathrm{V}})$ is used to determine the elastic strain-rate $\dot{\boldsymbol{\varepsilon}}_i^e$ and the corresponding stress-rate $\dot{\boldsymbol{\sigma}}_i$ in the inhomogeneity. Recall that $\dot{\boldsymbol{\varepsilon}}_i^v = \mathbb{M}_i^v \cdot \boldsymbol{\sigma}_i$ and $\dot{\boldsymbol{\sigma}}_0 = \mathbb{L}_0^e \cdot (\dot{\boldsymbol{\varepsilon}}_0 - \mathbb{M}_0^v \cdot \boldsymbol{\sigma}_0)$ are known in the current stress state.

On summing up equations (6.10) and (6.11) and substituting assumptions (6.13) it is found that Variant II leads to the equation equivalent to that postulated by Molinari [136]. The present derivation is different as it is based on the novel sequential linearization method. It is worth noting that in Variant II, after straightforward transformations with the use of Eqs. (6.6)-(6.9) and (6.13), we have the following relationship:

$$\dot{\boldsymbol{\varepsilon}}_0^{\mathrm{V}} - \dot{\boldsymbol{\varepsilon}}_0^v = (\mathbb{M}_i^v + \mathbb{M}_*^v) \cdot (\boldsymbol{\sigma}_i - \mathbb{B}_i^v \cdot \boldsymbol{\sigma}_0), \tag{6.18}$$

where

$$\mathbb{B}_i^v = (\mathbb{M}_i^v + \mathbb{M}_*^v)^{-1} \circ (\mathbb{M}_0^v + \mathbb{M}_*^v) \tag{6.19}$$

is the stress concentration tensor, cf. Eq. (B.12), determined for viscous compliances.

The above variants (including Variant III) exhibit the following desired properties:

- For the initial stage of the deformation process ($t = 0$ and $\boldsymbol{\sigma}_0 = \boldsymbol{\sigma}_i = \mathbf{0}$) the problem defined by Eqs (6.6)-(6.7) reduces to the purely elastic problem (6.3).

- For the limit stage of the proportional deformation process ($t \to \infty$ and $\dot{\boldsymbol{\sigma}}_0 = \dot{\boldsymbol{\sigma}}_i = \mathbf{0}$) the problem defined by Eqs (6.6)-(6.7) reduces to the purely viscous problem (6.5).

- In the special case of the spherical inhomogeneity and matrix being both of isotropic and incompressible linear viscoelastic materials, the solution of Eqs (6.6)-(6.7) coincides with an exact solution obtained using the Laplace transform by Hashin [58], see Subsection 6.2.5.

6.2.2. Extension to the Mori-Tanaka scheme for multiphase composites

The above sequential linearization approach is immediately applicable to multiphase composites in conjunction with the averaging scheme of Mori-Tanaka type [140], widely used in the analysis of linear composite materials. It suffices to define the meaning of strain $\boldsymbol{\varepsilon}_0$ and stress $\boldsymbol{\sigma}_0$ in the above formulae as the corresponding *average* values in the matrix, and impose the conditions:

$$\bar{\boldsymbol{\varepsilon}} = \sum_{i=0}^{N} c_i \boldsymbol{\varepsilon}_i, \quad \bar{\boldsymbol{\sigma}} = \sum_{i=0}^{N} c_i \boldsymbol{\sigma}_i, \quad \sum_{i=0}^{N} c_i = 1, \tag{6.20}$$

where the quantities with a bar, $\bar{\boldsymbol{\varepsilon}}$ and $\bar{\boldsymbol{\sigma}}$, are the overall variables for the composite, N is the number of different phases r occupying ellipsoidal inhomogeneities, average values in the matrix are denoted by index 0, and c_i denote respective volume fractions in the representative volume element (RVE).

The sequential linearization method formulated above, employed within the Mori-Tanaka scheme, results in the following two interaction equations for subproblems Vi and Ei,

$$\dot{\boldsymbol{\varepsilon}}_i^v - \dot{\boldsymbol{\varepsilon}}_0^{\mathrm{V}i} = -\mathbb{M}_*^v \cdot (\boldsymbol{\sigma}_i - \boldsymbol{\sigma}_0^{\mathrm{V}i}), \tag{6.21}$$

$$\dot{\boldsymbol{\varepsilon}}_i^e - \dot{\boldsymbol{\varepsilon}}_0^{\mathrm{E}i} = -\mathbb{M}_*^e \cdot (\dot{\boldsymbol{\sigma}}_i - \dot{\boldsymbol{\sigma}}_0^{\mathrm{E}i}), \tag{6.22}$$

with the additional assumption for every variant:

$$\dot{\varepsilon}_0^{\mathrm{V}i} + \dot{\varepsilon}_0^{\mathrm{E}i} = \dot{\varepsilon}_0 \,, \tag{6.23}$$

where $\dot{\varepsilon}_0$ is the average strain-rate in the matrix. As in Section 6.2.1 above, we have different variants dependent on further specifications, in particular,

- Variant I:

$$\boldsymbol{\sigma}_0^{\mathrm{V}i} = \mathbb{L}_0^v \cdot \dot{\boldsymbol{\varepsilon}}_0^{\mathrm{V}i} \,, \qquad \dot{\boldsymbol{\sigma}}_0^{\mathrm{E}i} = \mathbb{L}_0^e \cdot \dot{\boldsymbol{\varepsilon}}_0^{\mathrm{E}i} \,, \tag{6.24}$$

- Variant II:

$$\boldsymbol{\sigma}_0^{\mathrm{V}i} = \boldsymbol{\sigma}_0 \,, \qquad \dot{\boldsymbol{\sigma}}_0^{\mathrm{E}i} = \dot{\boldsymbol{\sigma}}_0 \,. \tag{6.25}$$

Jointly with the constitutive laws (6.1), the equations above are sufficient to determine the elastic strain-rate in each inhomogeneity in terms of the average strain-rate $\dot{\varepsilon}_0$ in the matrix, in full analogy to Eqs. (6.14)-(6.17).

The final step is to relate $\dot{\varepsilon}_0$ to the overall strain-rate $\dot{\bar{\varepsilon}}$ for the composite by using the rate form of Eq. $(6.20)_1$, viz.:

$$c_0 \dot{\varepsilon}_0 = \dot{\bar{\varepsilon}} - \sum_{i=1}^{N} c_i(\dot{\varepsilon}_i^v + \dot{\varepsilon}_i^e). \tag{6.26}$$

The specific versions of Eq. (6.26) for the above two variants are:

- Variant I:

$$\dot{\varepsilon}_0 = \left(c_0 \mathbb{I}^S + \sum_{i=1}^{N} c_i \mathbb{A}_i^e \right)^{-1} \cdot \left(\dot{\bar{\varepsilon}} - \sum_{i=1}^{N} c_i(\dot{\varepsilon}_i^v - \mathbb{A}_i^e \cdot \dot{\varepsilon}_0^{\mathrm{V}i}) \right), \tag{6.27}$$

- Variant II:

$$
\begin{aligned}
\dot{\varepsilon}_0 = {}& \left(c_0 \mathbb{I}^S + \sum_{i=1}^{N} c_i \mathbb{A}_i^e \right)^{-1} \cdot \Big(\dot{\bar{\varepsilon}} + \\
& - \sum_{i=1}^{N} c_i \left(\dot{\varepsilon}_i^v - (\mathbb{I}^S + \mathbb{M}_*^e \circ \mathbb{L}_i^e)^{-1} \cdot (\dot{\varepsilon}_0^{\mathrm{V}i} + \mathbb{M}_*^e \circ \mathbb{L}_0^e \cdot \dot{\varepsilon}_0^v) \right) \Big),
\end{aligned} \tag{6.28}
$$

where in the last equation the following identity has been used:

$$\mathbb{A}_i^e = (\mathbb{I}^S + \mathbb{M}_*^e \circ \mathbb{L}_i^e)^{-1} \circ (\mathbb{I}^S + \mathbb{M}_*^e \circ \mathbb{L}_0^e).$$

If $\dot{\bar{\varepsilon}}$ is prescribed then the above equations constitute the full set of equations of the sequential linearization approach to a linear viscoelastic multi-phase composite in conjunction with the Mori-Tanaka averaging scheme.

6.2.3. Comparison of different approximation schemes

The above two variants of the sequential approach to a viscoelastic inhomogeneity problem are now compared with the Kröner-Weng [107, 214], Molinari [136] and Paquin et al. [155] approaches. For this purpose we use the relationship between a stress-rate in an ellipsoidal inhomogeneity and a remote stress-rate.

In the case of the Kröner-Weng model the interaction is purely elastic, that is

$$\dot{\boldsymbol{\varepsilon}}_i - \dot{\boldsymbol{\varepsilon}}_0 = -\mathbb{M}_*^e \cdot (\dot{\boldsymbol{\sigma}}_i - \dot{\boldsymbol{\sigma}}_0). \tag{6.29}$$

On substituting the constitutive relationships (6.1) and rearranging, we obtain the following relationship:

$$\dot{\boldsymbol{\sigma}}_i = \mathbb{B}_i^e \cdot \dot{\boldsymbol{\sigma}}_0 - (\mathbb{M}_i^e + \mathbb{M}_*^e)^{-1} \cdot (\dot{\boldsymbol{\varepsilon}}_i^v - \dot{\boldsymbol{\varepsilon}}_0^v), \tag{6.30}$$

where

$$\mathbb{B}_i^e = (\mathbb{M}_i^e + \mathbb{M}_*^e)^{-1} \circ (\mathbb{M}_0^e + \mathbb{M}_*^e) \tag{6.31}$$

is the stress concentration tensor determined for elastic compliances.

The approach discussed by Paquin et al. [155] has been formulated within the self-consistent averaging scheme for heterogeneous materials. The solution for the inhomogeneity problem can be extracted in the limit case when

$$c_i \to 0, \quad \mathbb{A}_0^e \to \mathbb{I}^S, \quad \mathbb{A}_0^v \to \mathbb{I}^S. \tag{6.32}$$

In this case the micro-macro relationship derived by Paquin et al. [155] reduces to

$$\dot{\boldsymbol{\varepsilon}}_i^e = \dot{\boldsymbol{\varepsilon}}_i - \dot{\boldsymbol{\varepsilon}}_i^v = \mathbb{A}_i^e \cdot \left[\dot{\boldsymbol{\varepsilon}}_0 + (\mathbb{S}^e - \mathbb{S}^v) \cdot \delta\dot{\boldsymbol{\varepsilon}}_i^v - (\mathbb{A}_i^v)^{-1} \cdot \dot{\boldsymbol{\varepsilon}}_i^v \right], \tag{6.33}$$

where $\mathbb{S}^e$ and $\mathbb{S}^v$ is the Eshelby tensor for the purely elastic and purely viscous matrix, respectively, $\delta\dot{\boldsymbol{\varepsilon}}_i^v = \dot{\boldsymbol{\varepsilon}}_i^v - \mathbb{A}_i^v \cdot \dot{\boldsymbol{\varepsilon}}_0^v$, and $\dot{\boldsymbol{\varepsilon}}_0^v$ is the remote viscous strain-rate. The respective expression for the stress-rate in the inhomogeneity, in terms of the remote stress-rate, is

$$\dot{\boldsymbol{\sigma}}_i = \mathbb{B}_i^e \cdot \dot{\boldsymbol{\sigma}}_0 - (\mathbb{M}_i^e + \mathbb{M}_*^e)^{-1} \circ \mathbb{H}_i^{\mathrm{PQ}} \cdot ((\mathbb{A}_i^v)^{-1} \cdot \dot{\boldsymbol{\varepsilon}}_i^v - \dot{\boldsymbol{\varepsilon}}_0^v), \tag{6.34}$$

where

$$\mathbb{H}_i^{\mathrm{PQ}} = (\mathbb{I}^S + \mathbb{M}_\circ^e * \mathbb{L}_0^e) \circ (\mathbb{I}^S - (\mathbb{S}^e - \mathbb{S}^v) \circ \mathbb{A}_i^v). \tag{6.35}$$

Note that, similarly to the examined variants of sequential linearization, for the initial and final stages of a proportional deformation process, the rate-solutions for the purely elastic and purely viscous problem, respectively, are recovered.

On the contrary, for the final stage of a proportional deformation process for the Kröner-Weng model, a purely viscous solution of the Eshelby problem is not recovered, as one finds $\dot{\boldsymbol{\varepsilon}}_i^v = \dot{\boldsymbol{\varepsilon}}_0^v$ instead.

In case of Variants I and II of the sequential linearization approach, the expression for the stress-rate in the inhomogeneity takes the form:

$$\dot{\boldsymbol{\sigma}}_i = \mathbb{B}_i^e \cdot \dot{\boldsymbol{\sigma}}_0 - (\mathbb{M}_i^e + \mathbb{M}_*^e)^{-1} \circ \mathbb{H}^K \cdot ((\mathbb{A}_i^v)^{-1} \cdot \dot{\boldsymbol{\varepsilon}}_i^v - \dot{\boldsymbol{\varepsilon}}_0^v), \tag{6.36}$$

where[2]

$$\mathbb{H}^{\mathrm{I}} = \mathbb{I}^S + \mathbb{M}_*^e \circ \mathbb{L}_0^e \quad \text{and} \quad \mathbb{H}^{\mathrm{II}} = \mathbb{I}^S + \mathbb{M}_*^v \circ \mathbb{L}_0^v. \tag{6.39}$$

Consider an incompressible isotropic (elastic and viscous) matrix for which the elastic bulk modulus K_0 is infinite and

$$\mathbb{M}_0^{e/v} = \frac{1}{h_0^{e\mathrm{D}/v}} \mathbb{I}_{\mathrm{D}}, \tag{6.40}$$

with $h_0^{e\mathrm{D}} = 2\mu_0$, $h_0^v = 2\eta_0$, where μ_0 and η_0 are the elastic shear modulus and the viscosity of the matrix, respectively,

$$\mathbb{S}^e = \mathbb{S}^v, \quad \mathbb{M}_*^e \circ \mathbb{L}_0^e = \mathbb{M}_*^v \circ \mathbb{L}_0^v. \tag{6.41}$$

Then, all the three variants of the sequential linearization approach and the Paquin et al. model provide the same concentration relationship as the exact solution obtained by Hashin [58] with use of the Laplace transform and the correspondence principle. This fact was already demonstrated by Mercier et al. [134] for the Paquin et al. [155] and Molinari [136] approaches, the latter being equivalent to the present Variant II of the sequential linearization approach. This particular exact solution is not recovered using the model developed by Sabar et al. [181], which is therefore not analysed below in more detail.

In the case of isotropic elastically compressible materials (viscous incompressibility is still assumed, $\mathbb{M}_r^v = 1/h_r^v \mathbb{I}_{\mathrm{D}}$), for which

$$\mathbb{M}_r^e = \frac{1}{h_r^{e\mathrm{P}}} \mathbb{I}_{\mathrm{P}} + \frac{1}{h_r^{e\mathrm{D}}} \mathbb{I}_{\mathrm{D}}, \quad h_r^{e\mathrm{P}} = 3K_r, \tag{6.42}$$

---

[2]For Variant III tensor $\mathbb{H}^K$ reads

$$\mathbb{H}^{\mathrm{III}} = (\mathbb{M}_*^e \circ \mathbb{L}_0^e) \circ (\mathbb{M}_*^v \circ \mathbb{L}_0^v)^{-1} \circ (\mathbb{I}^S + \mathbb{M}_*^v \circ \mathbb{L}_0^v), \tag{6.37}$$

which for an elastically compressible isotropic material with $\mathbb{M}_r^v = 1/h_r^v \mathbb{I}_D$ and a spherical inhomogeneity can be represented by a single scalar β^{III},

$$\beta^{\mathrm{I}} \leqslant \beta^{\mathrm{III}} = \frac{5 + 15\eta(\nu)}{3 + 4\eta(\nu)} \leqslant \frac{15}{7} \tag{6.38}$$

with $\eta(\nu)$ specified in Eq. (6.45).

and a spherical inhomogeneity, the fourth-order tensor $\mathbb{H}$ in the concentration relationship can be replaced by a single scalar,

$$\dot{\boldsymbol{\sigma}}_i = \mathbb{B}^e \cdot \dot{\boldsymbol{\sigma}}_0 - \beta^K (\mathbb{M}_i^e + \mathbb{M}_*^e)^{-1} \cdot ((\mathbb{A}^v)^{-1} \cdot \dot{\boldsymbol{\varepsilon}}_i^v - \dot{\boldsymbol{\varepsilon}}_0^v), \qquad (6.43)$$

where the coefficient β^K is specified as follows:

$$\beta^K = \begin{cases} \frac{5+10\eta(\nu)}{3+4\eta(\nu)} & \text{if} \quad K = \text{I} \\ \frac{5}{3} & \text{if} \quad K = \text{II(M)} \\ \frac{5+10\eta(\nu)\gamma_v}{3+4\eta(\nu)} & \text{if} \quad K = \text{PQ} \end{cases} \qquad (6.44)$$

and (for a non-negative Poisson ratio ν, $0 \leqslant \eta \leqslant 1$)

$$\eta(\nu) = \frac{1-2\nu}{1+\nu}, \quad \gamma_v = \frac{2+\xi_v}{3+\xi_v}, \quad \xi_v = \frac{h_i^v}{h_0^v}, \quad \gamma_v \in \left(\frac{2}{3}, 1\right). \qquad (6.45)$$
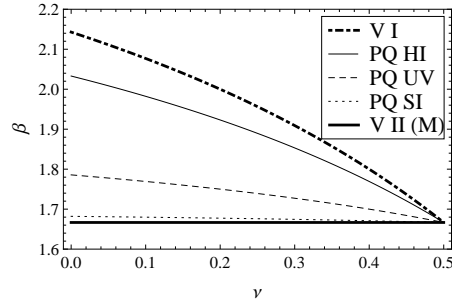
Fig. 6.1. Comparison of coefficients β in the concentration relationship for two variants of the sequential linearization and Paquin et al. (PQ) approaches for isotropic elastically compressible materials and a spherical inhomogeneity; HI (Hard Inclusion) - $h_i^v/h_0^v = 10$, UV (Uniform Viscous properties) - $h_i^v/h_0^v = 1$, SI (Soft Inclusion) - $h_i^v/h_0^v = 0.1$.

The following relation between the coefficients is obtained:

$$\beta^{\text{II}} \leqslant \beta^{\text{PQ}} \leqslant \beta^{\text{I}} \leqslant \frac{10}{7}. \qquad (6.46)$$

If $\frac{h_i^v}{h_0^v} \to 0$ (the inhomogeneity behaves as a void in terms of viscous properties) then the Paquin et al. model coincides with Variant II (the Molinari model), $\beta^{\text{PQ}}(\nu, 2/3) = \beta^{\text{II}}$. On the other hand, if $\frac{h_i^v}{h_0^v} \to \infty$ (the inhomogeneity is elastic) the Paquin et al. model coincides with Variant I, $\beta^{\text{PQ}}(\nu, 1) = \beta^{\text{I}}(\nu)$. Dependence of the coefficient β on the Poisson ratio ν for different models and viscosity ratios is presented in Fig. 6.1.

6.2.4. An exact solution in the Laplace transform space

As shown by Hashin [58] for isotropic materials and by Laws and McLaughlin [111] in a general anisotropic case, the problem of ellipsoidal viscoelastic inhomogeneity embedded in a viscoelastic matrix, both described by the Maxwell-type constitutive law (6.1), can be solved by using the Laplace transform technique and the correspondence principle. Taking the Laplace transform of equations (6.1) for the inhomogeneity ($r = i$) and for the matrix at infinity ($r = 0$), and assuming the initial conditions $\boldsymbol{\varepsilon}_r|_{t=0} = \mathbf{0}$, $\boldsymbol{\sigma}_r|_{t=0} = \mathbf{0}$, we obtain

$$s\hat{\boldsymbol{\varepsilon}}_r(s) = (s\mathbb{M}_r^e + \mathbb{M}_r^v) \cdot \hat{\boldsymbol{\sigma}}_r(s), \tag{6.47}$$

denoting $\hat{f}(s) \equiv \int_0^\infty e^{-st} f(t)\, \mathrm{d}t$, with s as a complex variable.

We will specify the solution for isotropic materials which are *elastically compressible* and viscously incompressible, of elastic compliance tensors specified by Eq. (6.42) and viscous compliance tensors as in Eq. (6.40), and a spherical inhomogeneity. Decompose the strain and stress into hydrostatic and deviatoric parts, denoted by upper indices P and D, respectively. On taking the Laplace transform of equations (6.1) decomposed in this way, we obtain

$$\hat{\boldsymbol{\sigma}}_r^{\mathrm{P}}(s) = \underbrace{h_r^{\mathrm{P}e}}_{\hat{h}_r^{\mathrm{P}}(s)} \hat{\varepsilon}_r^{\mathrm{P}}(s), \quad \hat{\boldsymbol{\sigma}}_r^{\mathrm{D}}(s) = \underbrace{\frac{sh_r^v}{1 + s\frac{h_r^v}{h_r^{\mathrm{D}e}}}}_{\hat{h}_r^{\mathrm{D}}(s)} \hat{\varepsilon}_r^{\mathrm{D}}(s). \tag{6.48}$$

Using the correspondence principle and the Eshelby solution for a spherical inclusion, we obtain, cf. Hashin [58],[3]

$$\hat{\varepsilon}_i^{\mathrm{P}}(s) = \hat{A}_i^{\mathrm{P}}(s)\hat{\varepsilon}_0^{\mathrm{P}}(s), \qquad \hat{A}_i^{\mathrm{P}}(s) = \frac{h_0^{\mathrm{P}e} + 2\hat{h}_0^{\mathrm{D}}(s)}{h_i^{\mathrm{P}e} + 2\hat{h}_0^{\mathrm{D}}(s)} \tag{6.52}$$

---

[3]In the case of the corresponding elastic solution there is

$$\mathbb{A}_i = \alpha^{\mathrm{P}}\mathbb{I}_{\mathrm{P}} + \alpha^{\mathrm{D}}\mathbb{I}_{\mathrm{D}} = \frac{h_0^{\mathrm{P}e} + 2h_0^{\mathrm{D}e}}{h_i^{\mathrm{P}e} + 2h_0^{\mathrm{D}e}}\mathbb{I}_{\mathrm{P}} + \frac{h_0^{\mathrm{D}e} + h_*^{\mathrm{D}e}}{h_i^{\mathrm{D}e} + h_*^{\mathrm{D}e}}\mathbb{I}_{\mathrm{D}}, \tag{6.49}$$

where

$$h_*^{\mathrm{D}e} = h_0^{\mathrm{D}e} \frac{3h_0^{\mathrm{P}e} + 4h_0^{\mathrm{D}e}}{2(h_0^{\mathrm{P}e} + 3h_0^{\mathrm{D}e})}. \tag{6.50}$$

Relations (6.52) and (6.53) can be compared with Eqs (6.34)-(6.37) in [58] using

$$h^{\mathrm{P}} = 3K, \quad h^{\mathrm{D}} = 2\mu, \quad \nu = \frac{h^{\mathrm{P}} - h^{\mathrm{D}}}{2h^{\mathrm{P}} + h^{\mathrm{D}}}. \tag{6.51}$$

and

$$\hat{\varepsilon}_i^{\mathrm{D}}(s) = \hat{A}_i^{\mathrm{D}}(s)\hat{\varepsilon}_0^{\mathrm{D}}(s), \qquad \hat{A}_i^{\mathrm{D}}(s) = \frac{\hat{h}_0^{\mathrm{D}}(s) + \hat{h}_*^{\mathrm{D}}(s)}{\hat{h}_i^{\mathrm{D}}(s) + \hat{h}_*^{\mathrm{D}}(s)}, \qquad (6.53)$$

where

$$\hat{h}_*^{\mathrm{D}}(s) = \hat{h}_0^{\mathrm{D}}(s)\frac{3h_0^{\mathrm{Pe}} + 4\hat{h}_0^{\mathrm{D}}(s)}{2(h_0^{\mathrm{Pe}} + 3\hat{h}_0^{\mathrm{D}}(s))}. \qquad (6.54)$$

Consider the external strain programme specified as follows:

$$\varepsilon_0(t) = \varepsilon_0^{\mathrm{P}}(t)\mathbf{I} + \varepsilon_0^{\mathrm{D}}(t)\mathbf{N}_{\mathrm{D}}, \quad \mathbf{N}_{\mathrm{D}} = \mathrm{const}, \quad \mathrm{tr}\,\mathbf{N}_{\mathrm{D}} = 0, \qquad (6.55)$$

where $\varepsilon_0^{\mathrm{P}}(t), \varepsilon_0^{\mathrm{D}}(t)$ are given scalar functions of time. Thus,

$$\hat{\varepsilon}_0(s) = \hat{\varepsilon}_0^{\mathrm{P}}(s)\mathbf{I} + \hat{\varepsilon}_0^{\mathrm{D}}(s)\mathbf{N}_{\mathrm{D}}. \qquad (6.56)$$

From Eqs. (6.52)-(6.53) it follows that:

$$\hat{\varepsilon}_i^{\mathrm{P}}(s) = \hat{\varepsilon}_i^{\mathrm{P}}(s)\mathbf{I} = \hat{A}_i^{\mathrm{P}}(s)\hat{\varepsilon}_0^{\mathrm{P}}(s)\mathbf{I} \qquad \rightarrow \qquad \hat{\varepsilon}_i^{\mathrm{P}}(s) = \hat{A}_i^{\mathrm{P}}(s)\hat{\varepsilon}_0^{\mathrm{P}}(s), \qquad (6.57)$$

$$\hat{\varepsilon}_i^{\mathrm{D}}(s) = \hat{\varepsilon}_i^{\mathrm{D}}(s)\mathbf{N}_{\mathrm{D}} = \hat{A}_i^{\mathrm{D}}(s)\hat{\varepsilon}_0^{\mathrm{D}}(s)\mathbf{N}_{\mathrm{D}} \qquad \rightarrow \qquad \hat{\varepsilon}_i^{\mathrm{D}}(s) = \hat{A}_i^{\mathrm{D}}(s)\hat{\varepsilon}_0^{\mathrm{D}}(s). \qquad (6.58)$$

Similarly, an 'exact' solution can be derived for the averaged response of a two-phase composite within the Mori-Tanaka-type averaging scheme. Then, the Laplace transform of an *external* strain in Eqs (6.52)-(6.53) is replaced by the Laplace transform of the corresponding *average* strain in the matrix. Moreover, the Laplace transform of Eq. (6.20)$_1$ is used, in the form

$$\hat{\bar{\varepsilon}}(s) = c_i\hat{\varepsilon}_i(s) + (1 - c_i)\hat{\varepsilon}_0(s), \qquad (6.59)$$

where $\hat{\bar{\varepsilon}}(s)$ is prescribed by an equation analogous to Eq. (6.56). After manipulations outlined above for the spherical inhomogeneity problem, in the case of isotropic materials and compressible elasticity, one finds:

$$\hat{\bar{\varepsilon}}_0^{\mathrm{P}/\mathrm{D}}(s) = \frac{\hat{\bar{\varepsilon}}^{\mathrm{P}/\mathrm{D}}(s)}{1 - c_i(1 - \hat{A}_i^{\mathrm{P}/\mathrm{D}}(s))}, \quad \hat{\varepsilon}_i^{\mathrm{P}/\mathrm{D}}(s) = \frac{\hat{A}_i^{\mathrm{P}/\mathrm{D}}(s)\hat{\bar{\varepsilon}}^{\mathrm{P}/\mathrm{D}}(s)}{1 - c_i(1 - \hat{A}_i^{\mathrm{P}/\mathrm{D}}(s))}. \qquad (6.60)$$

6.2.5. Comparison of results for a tension-compression cycle

Quantitative predictions of the approximate schemes from Section 6.2.3 are now compared with the exact solution outlined above for a tension-compression cycle under the constraint of constant *overall* volume (not necessarily in individual phases). This is done for the inhomogeneity problem; results for the

Mori-Tanaka scheme for a two-phase composite would be analogous. As already mentioned, in the case of *fully incompressible* (both for elastic and viscous deformations) isotropic materials of the inhomogeneity and matrix, an exact solution is obtained. Specifically, the solution obtained with the use of the three variants of the sequential approach, as well as of the Paquin et al. model, for an incompressible spherical inhomogeneity problem coincides with the corresponding exact solution obtained with use of the Laplace transform. Therefore, the analysis is performed below for *elastically compressible* materials. A low value of the Poisson ratio is assumed, equal for the matrix and inhomogeneity, since the difference between approximate schemes is then more pronounced, cf. Fig. 6.2. Different elastic and viscous properties of the matrix and spherical inhomogeneity (inclusion) have been examined, namely:

- A hard elastic inclusion in a viscoelastic matrix

- A hard/soft viscoelastic inclusion in a viscoelastic matrix

- A void in viscoelastic matrix

A *hard* and *soft* inclusion means that its elastic and viscous moduli are, correspondingly, higher or lower than respective moduli of the matrix. Isotropic material properties of the matrix are specified by

$$\nu_{0/i} = 0.05\,, \quad E_0 = 200\,\text{MPa}\,, \quad h_0^v = \frac{2}{3}\,\text{MPa} \times \text{s}. \qquad (6.61)$$

The examined cases of inclusion properties are collected in Table 6.1.

Table 6.1. Analysed examples of a spherical inhomogeneity.

Case	E_i/E_0	h_i^v/h_m^v
Hard Elastic Inclusion	10	∞
Hard Inclusion	3	10
Soft Inclusion	1/3	1/10
Void	0	~ 0

The case of void requires more explanation. Mechanical behaviour of a void can be described by the relation $\boldsymbol{\sigma}_i = \mathbf{0}$. Considering the sequential linearization method under $\boldsymbol{\sigma}_i = \mathbf{0}$ assumption, using (6.8), one has for all variants:

$$\dot{\boldsymbol{\varepsilon}}_i^v - \dot{\boldsymbol{\varepsilon}}_0^V = \mathbb{M}_*^v \cdot \boldsymbol{\sigma}_0^V \quad \text{and} \quad \dot{\boldsymbol{\varepsilon}}_i^e - \dot{\boldsymbol{\varepsilon}}_0^E = \mathbb{M}_*^e \cdot \dot{\boldsymbol{\sigma}}_0^E\,. \qquad (6.62)$$

Now, assuming arbitrary but <u>finite or zero (incompressible)</u> $\mathbb{M}_i^v$ one obtains[4] $\dot{\boldsymbol{\varepsilon}}_i^v = \mathbf{0}$ and (6.62) reduces to

$$\dot{\boldsymbol{\varepsilon}}_0^{\mathrm{V}} = -\mathbb{M}_*^v \cdot \boldsymbol{\sigma}_0^{\mathrm{V}} \quad \text{and} \quad \dot{\boldsymbol{\varepsilon}}_i = \dot{\boldsymbol{\varepsilon}}_0^{\mathrm{E}} + \mathbb{M}_*^e \cdot \dot{\boldsymbol{\sigma}}_0^{\mathrm{E}}. \tag{6.63}$$

Let us denote

$$\mathbb{A}_{void}^{e/v} = \mathbb{M}_*^{e/v} \circ (\mathbb{L}_0^{e/v} + \mathbb{L}_*^{e/v}). \tag{6.64}$$

After solving (6.63) with additional relations valid for subsequent variants of the sequential method, the strain-rate of void is specified as

$$\dot{\boldsymbol{\varepsilon}}_i = \begin{cases} \mathbb{A}_{void}^e \cdot \dot{\boldsymbol{\varepsilon}}_0 & \text{for} \quad \text{Variant I} \\ \mathbb{A}_{void}^e \cdot \dot{\boldsymbol{\varepsilon}}_0 - (\mathbb{A}_{void}^e - \mathbb{A}_{void}^v) \cdot \dot{\boldsymbol{\varepsilon}}_0^v & \text{for} \quad \text{Variant II} \\ \mathbb{A}_{void}^e \cdot \dot{\boldsymbol{\varepsilon}}_0 + (\mathbb{A}_{void}^e - \mathbb{A}_{void}^v) \circ \mathbb{M}_0^v \circ \mathbb{L}_*^v \cdot \dot{\boldsymbol{\varepsilon}}_0^v & \text{for} \quad \text{Variant III} \end{cases}. \tag{6.65}$$

Only in the case of Variant II the solution of purely viscous problem, i.e a void in purely viscous matrix, is recovered at infinity for the proportional straining process.

The conditions $\boldsymbol{\sigma}_i = \mathbf{0}$ and $\dot{\boldsymbol{\varepsilon}}_i^v = \mathbf{0}$ substituted into the concentration relation (6.33) valid for the Paquin et al. model result in

$$\dot{\boldsymbol{\varepsilon}}_i = \mathbb{A}_{void}^e \cdot \dot{\boldsymbol{\varepsilon}}_0 - \mathbb{A}_{void}^e \circ \left((\mathbb{A}_{void}^v)^{-1} - (\mathbb{A}_{void}^e)^{-1} \right) \circ \mathbb{A}_i^v \dot{\boldsymbol{\varepsilon}}_0^v, \tag{6.66}$$

so the strain-rate in a void depends on the assumed viscous properties of a inhomogeneity via $\mathbb{A}_i^v$. Considering the solution at infinity, on imposing $\dot{\boldsymbol{\varepsilon}}_0^v = \dot{\boldsymbol{\varepsilon}}_0$ one recovers the exact solution only when $\mathbb{A}_i^v \to \mathbb{A}_{void}^v$, so for $\mathbb{M}_i^v \to \mathbb{O}$.

Now, let us compare these approximated solutions of a void problem with the analytical one in the case of isotropic elastically compressible matrix and the spherical shape of void. In such a case quantities (6.64) are specified as

$$\mathbb{A}_{void}^e = \alpha_{void}^{Pe}\mathbb{I}_{\mathrm{P}} + \alpha_{void}^e\mathbb{I}_{\mathrm{D}}, \quad \mathbb{A}_{void}^v = \mathbb{I}_{\mathrm{P}} + \alpha_{void}^v\mathbb{I}_{\mathrm{D}} = \mathbb{I}_{\mathrm{P}} + \frac{5}{3}\mathbb{I}_{\mathrm{D}}. \tag{6.67}$$

We derive the exact solution to the void problem starting from the interaction equation expressed in the Laplace transform space, cf. Hashin [58], namely,

$$\underbrace{\hat{\sigma}_i^{\mathrm{P/D}}}_{=0} - \underbrace{\hat{\sigma}_0^{\mathrm{P/D}}}_{=\hat{h}_0^{\mathrm{P/D}}(s)\hat{\varepsilon}_0^{\mathrm{P/D}}(s)} = \hat{h}_*^{\mathrm{P/D}}(s)(\hat{\varepsilon}_i^{\mathrm{P/D}}(s) - \hat{\varepsilon}_0^{\mathrm{P/D}}(s)), \tag{6.68}$$

---

[4]In the case when we impose $\mathbb{M}_i^v = \mathbb{O}$ exactly for the inhomogeneity, we are not able to solve Subproblem V as far as $\dot{\boldsymbol{\varepsilon}}_i^v \simeq \infty \cdot \mathbf{0}$ is indefinite.

therefore

$$\hat{\varepsilon}_i^{P/D}(s) = \frac{\hat{h}_*^{P/D}(s) + \hat{h}_0^{P/D}(s)}{\hat{h}_0^{P/D}(s)} \hat{\varepsilon}_0^{P/D}(s) \,. \tag{6.69}$$

One observes that the strain of a void depends only on the (elastic and viscous) mechanical properties of a matrix. Assuming some proportional straining process (6.55), where $\varepsilon_0^P(t) = 0$ and

$$\begin{cases} \varepsilon_0^D(t) = 0 \ \text{ if } \ t < 0 \\ \varepsilon_0^D(t) = t \ \text{ if } \ t \geqslant 0 \end{cases}, \tag{6.70}$$

one has $\hat{\varepsilon}_0^D(s) = 1/s^2$. Note that the remote plastic strain-rate is then specified for $t \geqslant 0$ as

$$\dot{\varepsilon}_0^v(t) = 1 - \exp\left(-\frac{h_0^{De}}{h_0^v}t\right).$$

Using (6.48) and (6.54) in (6.69), inverse of the Laplace transform gives for, $t \geqslant 0$,

$$\varepsilon_i^D(t) = \frac{5}{3}t + \frac{10h_0^v}{9h_0^{De}}\left(1 - \exp\left(-\frac{3h_0^{Pe}}{3h_0^{Pe} + 4h_0^{De}}\frac{h_0^{De}}{h_0^v}t\right)\right) \tag{6.71}$$

and the evolution of the strain-rate of a void is specified as

$$\dot{\varepsilon}_i^D(t) = \alpha_{void}^e - (\alpha_{void}^e - \alpha_{void}^v)\left(1 - \exp\left(-\frac{3h_0^{Pe}}{3h_0^{Pe} + 4h_0^{De}}\frac{h_0^{De}}{h_0^v}t\right)\right). \tag{6.72}$$

Comparing the above relation with (6.65) and (6.66) one finds that Variant II is the closest to the exact solution and differs only by the quantity $(3h_0^{Pe})/(3h_0^{Pe} + 4h_0^{De})$ being the function of the Poisson ratio (both solutions coincide for an incompressible material).

In the computations, void has been modelled as an inhomogeneity with $E_i = 0$ and $h_i^v/h_m^v \to 0$ (a finite value due to numerical reasons), so that $\boldsymbol{\sigma}_i(t) = \mathbf{0}$ follows.

In Figs 6.2 and 6.3 we compare the results obtained using the considered schemes for the tension-compression cycle. Accordingly, as a particular case of Eq. (6.55), the remote strain history $\boldsymbol{\varepsilon}_0(t)$ is assumed as follows:

$$\boldsymbol{\varepsilon}_0(t) = (\varepsilon_1(t) - \varepsilon_2(t))\mathbf{N}_D, \quad \text{where} \quad \begin{cases} \varepsilon_1(t) = 0 & \text{if } \ t < 0 \\ \varepsilon_1(t) = t & \text{if } \ t \geqslant 0 \\ \varepsilon_2(t) = 0 & \text{if } \ t < T \\ \varepsilon_2(t) = 2(t-T) & \text{if } \ t \geqslant T \end{cases} \tag{6.73}$$

with

$$\mathbf{N}_\mathrm{D} = \frac{1}{2}\left(3\mathbf{e}_1 \otimes \mathbf{e}_1 - \mathbf{I}\right), \quad [N_{\mathrm{D}ij}] = \begin{bmatrix} 1 & 0 & 0 \\ 0 & -1/2 & 0 \\ 0 & 0 & -1/2 \end{bmatrix}, \qquad (6.74)$$

$\mathbf{e}_1$ being the tension-compression direction. The corresponding strain-rate history is

$$\dot{\boldsymbol{\varepsilon}}_0(t) = \dot{\varepsilon}_0^\mathrm{D}(t)\mathbf{N}_\mathrm{D}, \quad \text{where} \quad \begin{cases} \dot{\varepsilon}_0^\mathrm{D}(t) = 0 & \text{if} \quad t < 0 \\ \dot{\varepsilon}_0^\mathrm{D}(t) = 1 & \text{if} \quad 0 \leqslant t < T \\ \dot{\varepsilon}_0^\mathrm{D}(t) = -1 & \text{if} \quad t \geqslant T. \end{cases} \quad [1/\mathrm{s}]. \qquad (6.75)$$

The Laplace transform of the strain programme (6.73) is $\hat{\boldsymbol{\varepsilon}}_0(s) = \hat{\varepsilon}_0(s)\mathbf{N}_\mathrm{D}$, with

$$\hat{\varepsilon}_0(s) = \hat{\varepsilon}_1(s) - \hat{\varepsilon}_2(s) = \frac{1}{s^2}\left(1 - 2\exp(-sT)\right). \qquad (6.76)$$

Analytical inversion of the Laplace transform has been performed with the help of *Mathematica* package [222].

Conclusions from the analysis are the following (see Fig. 6.2 and Fig. 6.3):

- For *hard inclusions*, the approximate schemes give results close to each other, with Variant II (Molinari model) being the softest. As the contrast in viscous properties increases (the asymptotic case is the *hard elastic inclusion*), the exact solution is less stiff in the transient regime than the approximate solutions, therefore Variant II provides the best prediction among the approximate schemes examined. As expected for hard inclusions, predictions of the Paquin model are close to Variant I predictions.

- For *soft inclusions*, the exact solution predicts a 'peak' of stress in the transient regime which is not observed for Variant I and III of the sequential model and can be predicted (although usually less intensive than those in the exact solution) by Variant II and the Paquin et al. model. As expected for soft inclusions, predictions of the Paquin el al. model are close to Variant II predictions.

- In the case of Variant I, the evolution of the strain-rate in a *void* coincides with that for the problem of a void in a purely elastic matrix and as such does not agree with an exact solution. Variant II and Paquin et al. model provide good predictions. Similarly to an exact solution, the solution obtained with the use of Variant II is not sensitive to the value of h_i^v/h_m^v ratio, provided $\boldsymbol{\sigma}_i(t) = \mathbf{0}$ is enforced, and in the limit of the proportional straining the purely viscous solution is recovered. This is not
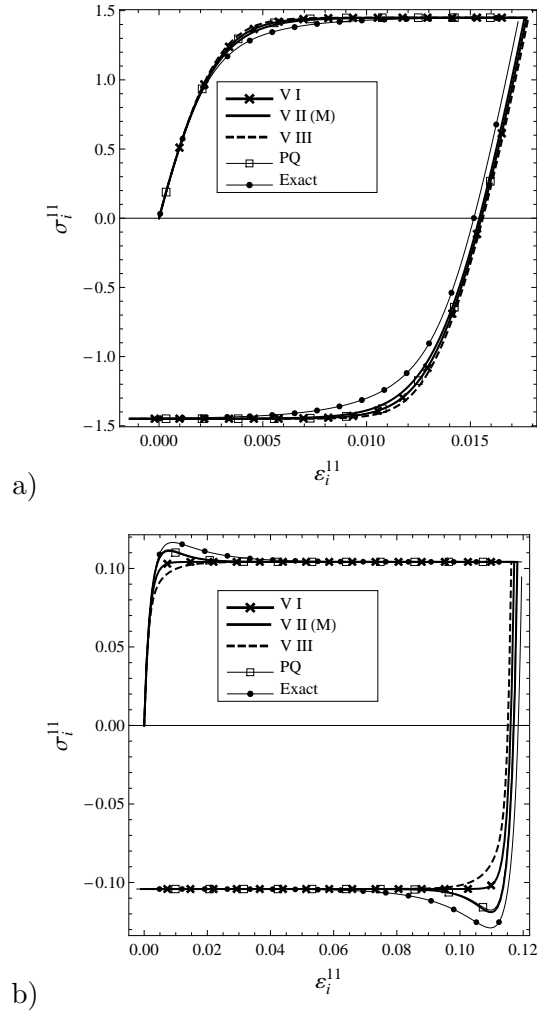
Fig. 6.2. Comparison of the stress-strain loops predicted by different approaches within a spherical inhomogeneity embedded in an infinite matrix subjected to the tension-compression cycle: a) Hard Inclusion, b) Soft Inclusion.

the case for the Paquin et al. model for which results depend on h_i^v/h_m^v ratio. In particular, if one assumes $E_i \to 0$ and $h_i^v/h_m^v \to \infty$, predictions of this model tend to the purely elastic solution for the problem of a void and disagree with an exact solution obtained under these conditions.

- The predictions of the Kröner-Weng model (K) are depicted only in Fig. 6.3. Except of a hard elastic inclusion, for the regimes for which
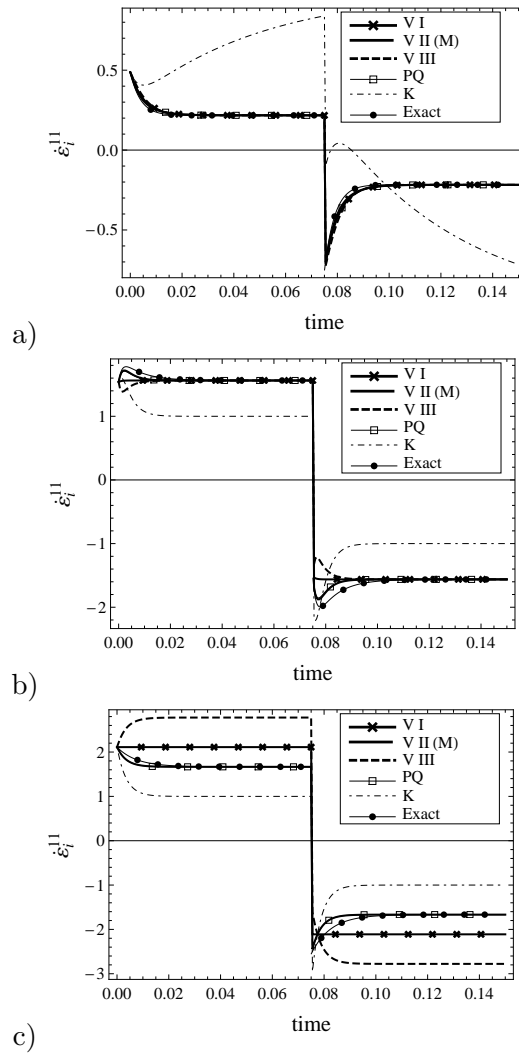
Fig. 6.3. Comparison of strain-rate evolution predicted by different approaches within a spherical inhomogeneity embedded in an infinite matrix subjected to the tension-compression cycle: a) Hard Inclusion, b) Soft Inclusion, c) Void.

the strain-rate of the matrix is almost totally viscous, they tend to the Voigt model assumption, $\dot{\varepsilon}_i = \dot{\varepsilon}_0$. The stress-strain loops obtained with the use of this model are not presented in Fig. 6.2 since the stress level is highly overpredicted (hard inclusion) or underpredicted (soft inclusion) as compared to the exact solution in the regimes dominated by a viscous flow.

On the basis of the performed analysis, Variant II of the sequential method has been selected for further developments as it provides the best predictions in comparison to the exact solution. As indicated above, this variant is equivalent to the Molinari model [136] in the case of a single inhomogeneity problem.

6.3. Self-consistent averaging scheme

6.3.1. Formulation of the sequential approach

Consider now a heterogeneous material composed of N constituents, of volume fractions c_i, which obey the constitutive relation (6.1) with elastic compliances $\mathbb{M}_i^e$ and viscous compliances $\mathbb{M}_i^v$, $i = 1, \ldots, N$. The overall strain-rate and stress-rate are now defined by

$$\bar{\varepsilon} = \langle \varepsilon_i \rangle , \quad \bar{\sigma} = \langle \sigma_i \rangle , \qquad \langle \psi_i \rangle \equiv \sum_{i=1}^{N} c_i \psi_i, \quad \sum_{i=1}^{N} c_i = 1 , \qquad (6.77)$$

where ε_i, σ_i are themselves averages over individual phases.

In the self-consistent treatment of a multi-phase composite investigated below, fluctuations within each phase are disregarded. The change with respect to the single inhomogeneity problem and the Mori-Tanaka scheme addressed above is that the matrix properties are no longer those of any specific phase and are to be replaced by effective properties of the homogenized composite. Denote by $\bar{\mathbb{M}}^e$ and $\bar{\mathbb{M}}^v$ the fourth-order tensors of effective elastic and viscous compliances of the homogenized composite and by $\bar{\mathbb{L}}^e$ and $\bar{\mathbb{L}}^v$ their inverses, determined for the purely elastic and purely viscous problem, respectively. The latter are determined implicitly from the well-known equations:

$$\bar{\mathbb{L}}^e = \langle \mathbb{L}_i^e \circ \mathbb{A}_i^e \rangle, \quad \mathbb{A}_i^e = (\mathbb{I}^S + \mathbb{P}^e \circ (\mathbb{L}_i^e - \bar{\mathbb{L}}^e))^{-1}, \qquad (6.78)$$
$$\bar{\mathbb{L}}^v = \langle \mathbb{L}_i^v \circ \mathbb{A}_i^v \rangle, \quad \mathbb{A}_i^v = (\mathbb{I}^S + \mathbb{P}^v \circ (\mathbb{L}_i^v - \bar{\mathbb{L}}^v))^{-1}, \qquad (6.79)$$

where the concentration tensors $\mathbb{A}_i^e$ and $\mathbb{A}_i^v$ for phase i, in comparison with Eqs (6.3) and (6.5) for the single inhomogeneity embedded in the matrix of prescribed properties, depend now on the overall properties of the homogenized composite rather than of a given matrix. In the case of inhomogeneities of the same shape and orientations, concentration tensors fulfil the identity $\langle \mathbb{A}_i^{e/v} \rangle = \mathbb{I}^S$. It is known that the approximations involved in the above equations themselves may not always be realistic, for instance, for a high contrast between phase properties, cf. Christensen [34], or in the presence of high anisotropy as

discussed in Chapter 3. Our aim here is, however, not to discuss validity of the self-consistent scheme as such for a linear problem, rather, to examine a more difficult viscous/elastic problem in the case when the self-consistent scheme is appropriate for each linear subproblem separately.

In analogy to Variant II of the sequential approach from the preceding section, selected as the best from those considered, in the first subproblem we find an external strain-rate at infinity, $\dot{\boldsymbol{\varepsilon}}_0^{\mathrm{V}i}$, intended to be compatible with the viscous strain-rate $\dot{\boldsymbol{\varepsilon}}_i^v$ that results from a local uniform stress $\boldsymbol{\sigma}_i$ in an ellipsoidal inhomogeneity i. This is done by assuming purely viscous interaction between the inhomogeneity and the homogenized matrix of moduli $\bar{\mathbb{L}}^v$ under remote stress $\boldsymbol{\sigma}_0 = \langle \boldsymbol{\sigma}_i \rangle$. Those *external* strain-rates $\dot{\boldsymbol{\varepsilon}}_0^{\mathrm{V}i}$ depend on the phase index i and differ from each other in general (and also from *overall* quantities independent of i). They are determined for different phases i from the equation for Subproblem Vi :

$$\dot{\boldsymbol{\varepsilon}}_i^v - \dot{\boldsymbol{\varepsilon}}_0^{\mathrm{V}i} = -\bar{\mathbb{M}}_*^v \cdot (\boldsymbol{\sigma}_i - \boldsymbol{\sigma}_0) , \qquad (6.80)$$

where the Hill tensor inverse $\bar{\mathbb{M}}_*^v$ is associated with the viscous effective moduli tensor $\bar{\mathbb{L}}^v$ for the homogenized composite. Upon multiplying Eq. (6.80) by c_i and summing up, we obtain $\langle \dot{\boldsymbol{\varepsilon}}_i^v \rangle = \langle \dot{\boldsymbol{\varepsilon}}_0^{\mathrm{V}i} \rangle$ on account of $\boldsymbol{\sigma}_0 = \langle \boldsymbol{\sigma}_i \rangle$.

On the other hand, the homogenized matrix of effective viscous compliance tensor $\bar{\mathbb{M}}^v$ undergoes viscous flow with the strain-rate $\dot{\boldsymbol{\varepsilon}}_0^v = \bar{\mathbb{M}}^v \cdot \boldsymbol{\sigma}_0$ at infinity, while volume averaging for the purely viscous subproblem gives the overall viscous strain-rate $\langle \dot{\boldsymbol{\varepsilon}}_i^v \rangle$. The difference between $\dot{\boldsymbol{\varepsilon}}_0^v$ and $\langle \dot{\boldsymbol{\varepsilon}}_i^v \rangle$ is to be accommodated elastically. The respective internal elastic accommodation rates in phases are distinguished by a superscript A and obey the elastic constitutive relationships $\dot{\boldsymbol{\sigma}}_i^{\mathrm{A}} = \mathbb{L}_i^e \cdot \dot{\boldsymbol{\varepsilon}}_i^{\mathrm{A}}$.

To retain consistency with Eq. (6.80), we assume that each internal elastic accommodation strain-rate $\dot{\boldsymbol{\varepsilon}}_i^{\mathrm{A}}$ coincides with its external counterpart $\dot{\boldsymbol{\varepsilon}}_0^{\mathrm{A}i}$ for phase i, so that they cancel each other when incorporated into Eq. (6.80), viz.,

$$\dot{\boldsymbol{\varepsilon}}_i^{\mathrm{A}} = \dot{\boldsymbol{\varepsilon}}_0^{\mathrm{A}i} \quad \text{and} \quad (\dot{\boldsymbol{\varepsilon}}_i^v + \dot{\boldsymbol{\varepsilon}}_i^{\mathrm{A}}) - (\dot{\boldsymbol{\varepsilon}}_0^{\mathrm{V}i} + \dot{\boldsymbol{\varepsilon}}_0^{\mathrm{A}i}) = -\bar{\mathbb{M}}_*^v \cdot (\boldsymbol{\sigma}_i - \boldsymbol{\sigma}_0) . \qquad (6.81)$$

Suppose for a moment that the introduced accommodation strain-rates, and consequently the accommodation stress-rates, are known. The purely elastic Subproblem Ei is specified as follows:

$$\dot{\boldsymbol{\varepsilon}}_i^{\mathrm{E}} - \dot{\boldsymbol{\varepsilon}}_0^{\mathrm{E}i} = -\mathbb{M}_*^e \cdot (\dot{\boldsymbol{\sigma}}_i^{\mathrm{E}} - \dot{\boldsymbol{\sigma}}_0^{\mathrm{E}}) , \qquad (6.82)$$

where the elastic contributions with a superscript E represent the differences between total elastic and accommodation terms, viz.,

$$\dot{\boldsymbol{\varepsilon}}_i^{\mathrm{E}} = \dot{\boldsymbol{\varepsilon}}_i^e - \dot{\boldsymbol{\varepsilon}}_i^{\mathrm{A}} , \qquad \dot{\boldsymbol{\sigma}}_i^{\mathrm{E}} = \dot{\boldsymbol{\sigma}}_i - \dot{\boldsymbol{\sigma}}_i^{\mathrm{A}} , \qquad \dot{\boldsymbol{\sigma}}_0^{\mathrm{E}} = \dot{\boldsymbol{\sigma}}_0 - \dot{\boldsymbol{\sigma}}_0^{\mathrm{A}} , \qquad (6.83)$$

with $\dot{\boldsymbol{\varepsilon}}_i^e = \mathbb{M}_i^e \cdot \dot{\boldsymbol{\sigma}}_i$. In analogy to the kinematic consistency condition (6.9), we assume that

$$\dot{\boldsymbol{\varepsilon}}_0^{\mathrm{E}i} = \dot{\boldsymbol{\varepsilon}}_0 - \dot{\boldsymbol{\varepsilon}}_0^{\mathrm{A}i} - \dot{\boldsymbol{\varepsilon}}_0^{\mathrm{V}i} . \tag{6.84}$$

It can easily be shown that the requirements

$$\langle \dot{\boldsymbol{\varepsilon}}_i \rangle = \langle \dot{\boldsymbol{\varepsilon}}_i^v + \dot{\boldsymbol{\varepsilon}}_i^e \rangle = \dot{\boldsymbol{\varepsilon}}_0 , \quad \langle \dot{\boldsymbol{\sigma}}_i \rangle = \dot{\boldsymbol{\sigma}}_0 , \tag{6.85}$$

together with the equations above, lead to

$$\dot{\boldsymbol{\sigma}}_0^{\mathrm{A}} = \left\langle \dot{\boldsymbol{\sigma}}_i^{\mathrm{A}} \right\rangle . \tag{6.86}$$

One can verify that, if $\dot{\boldsymbol{\sigma}}_i^{\mathrm{A}}$ are known, the set of equations (6.80)-(6.85) implies the following equation that relates the local and global responses of the heterogeneous medium:

$$\dot{\boldsymbol{\varepsilon}}_i - \dot{\boldsymbol{\varepsilon}}_0 = -\mathbb{M}_*^v \cdot (\boldsymbol{\sigma}_i - \boldsymbol{\sigma}_0) - \mathbb{M}_*^e \cdot (\dot{\boldsymbol{\sigma}}_i - \dot{\boldsymbol{\sigma}}_0) - \mathbb{M}_*^e \cdot (\dot{\boldsymbol{\sigma}}_i^{\mathrm{A}} - \dot{\boldsymbol{\sigma}}_0^{\mathrm{A}}) . \tag{6.87}$$

It remains, therefore, to estimate the local accommodation stress-rates. There are different possible ways to approximate these quantities.

The simplest way is to neglect the influence of accommodation rates entirely by assuming that

$$\dot{\boldsymbol{\sigma}}_i^{\mathrm{A}} = \dot{\boldsymbol{\sigma}}_0^{\mathrm{A}} . \tag{6.88}$$

Then, Eq. (6.87) reduces to that postulated by Molinari [136] for the self-consistent model for elastic-viscoplastic materials, cf. also Mercier et al. [134], Mercier and Molinari [133].

A more consequent (although still simplified) way is to define the overall elastic accommodation strain-rate and the respective overall accommodation stress-rate as follows:

$$\dot{\boldsymbol{\varepsilon}}_0^{\mathrm{A}} = \dot{\boldsymbol{\varepsilon}}_0^v - \langle \dot{\boldsymbol{\varepsilon}}_i^v \rangle = \dot{\boldsymbol{\varepsilon}}_0^v - \langle \dot{\boldsymbol{\varepsilon}}_0^{\mathrm{V}i} \rangle , \qquad \dot{\boldsymbol{\sigma}}_0^{\mathrm{A}} = \bar{\mathbb{L}}^e \cdot \dot{\boldsymbol{\varepsilon}}_0^{\mathrm{A}} . \tag{6.89}$$

Local accommodation stress-rates can be related to an overall accommodation stress-rate through the viscous concentration tensors $\mathbb{B}_i^v$,

$$\dot{\boldsymbol{\sigma}}_i^{\mathrm{A}} = \mathbb{B}_i^v \cdot \dot{\boldsymbol{\sigma}}_0^{\mathrm{A}} , \tag{6.90}$$

which is consistent with treating the accommodation stress-rates as constitutively related to *viscous strain accelerations* in the calculation step based on interactions of viscous type, cf. the remark in Section 6.2.1. Note that Eq. (6.86) is then satisfied if $\langle \mathbb{B}_i^v \rangle = \mathbb{I}^S$, which is an identity for ellipsoidal inclusions of equal

orientations and aspect ratio. An alternative way, apparently less consequent, is to use elastic concentration tensors instead,

$$\dot{\boldsymbol{\sigma}}_i^{\mathrm{A}} = \mathbb{B}_i^e \cdot \dot{\boldsymbol{\sigma}}_0^{\mathrm{A}} \quad \Longleftrightarrow \quad \dot{\boldsymbol{\varepsilon}}_i^{\mathrm{A}} = \mathbb{A}_i^e \cdot \dot{\boldsymbol{\varepsilon}}_0^{\mathrm{A}}. \tag{6.91}$$

As a result, we obtain three variants of Subproblem A of elastic accommodation in the sequential self-consistent scheme for linearly viscoelastic heterogeneous materials:

- Variant 1 based on Eq. (6.88),
- Variant 2 based on Eqs (6.89) and (6.90),
- Variant 3 based on Eqs (6.89) and (6.91).

After straightforward substitutions, the proposed sequential self-consistent scheme for linear viscoelastic heterogeneous materials is summarized in Table 6.2.

From Eq. (6.89) we obtain

$$\dot{\boldsymbol{\varepsilon}}_0^{\mathrm{A}} = \mathbb{M}_0^v \cdot \boldsymbol{\sigma}_0 - \langle \mathbb{M}_i^v \cdot \boldsymbol{\sigma}_i \rangle. \tag{6.96}$$

It can easily be verified that:

- when viscous properties are uniform then $\dot{\boldsymbol{\varepsilon}}_0^{\mathrm{A}} = \mathbb{O}$ and both Variants 2 and 3 reduce to Variant 1,
- when elastic properties are uniform then $\dot{\boldsymbol{\sigma}}_i^{\mathrm{A}} = \dot{\boldsymbol{\sigma}}_0^{\mathrm{A}}$ and Variants 3 reduces to Variant 1,
- in the limit when volume fraction of one phase tends to 1, predictions of all three Variants 1, 2 and 3 tend to those of Variant II for an inhomogeneity embedded in an infinite matrix analysed in the preceding section.

In general, the three variants provide different predictions. They are compared below by illustrative examples.

6.3.2. Comparison of results

The model is tested for a two-phase incompressible material (data are the same as in Paquin et al. [155] and Mercier and Molinari [133]) subjected to a tension-compression cycle under the constraint of constant overall volume. The overall strain-rate is prescribed in the form:

$$\dot{\boldsymbol{\varepsilon}}_0(t) = \dot{\varepsilon}(t)\mathbf{N}_{\mathrm{D}}, \quad \text{where} \quad \begin{cases} \dot{\varepsilon}(t) = 0 & \text{if} \quad t < 0 \\ \dot{\varepsilon}(t) = 10^{-4} & \text{if} \ 0 \leqslant t < T \\ \dot{\varepsilon}(t) = -10^{-4} & \text{if} \quad t \geqslant T \end{cases} \quad [1/\mathrm{s}], \tag{6.97}$$

Table 6.2. The sequential self-consistent scheme for linear viscoelastic materials

(i) Subproblem V: Determine the external viscous strain-rate $\dot{\boldsymbol{\varepsilon}}_0^{\mathrm{V}i}$ intended to correspond to $\dot{\boldsymbol{\varepsilon}}_i^e = \mathbb{O}$ in the i-th phase in the current stress state, from the equation

$$\dot{\boldsymbol{\varepsilon}}_i^v - \dot{\boldsymbol{\varepsilon}}_0^{\mathrm{V}i} = -\bar{\mathbb{M}}_*^v \cdot (\boldsymbol{\sigma}_i - \boldsymbol{\sigma}_0) \qquad \text{with} \quad \dot{\boldsymbol{\varepsilon}}_i^v = \mathbb{M}_i^v \cdot \boldsymbol{\sigma}_i . \qquad (6.92)$$

(ii) Subproblem A: Determine the overall elastic accommodation rates of strain and stress from the equations

$$\dot{\boldsymbol{\varepsilon}}_0^{\mathrm{A}} = \bar{\mathbb{M}}^v \cdot \boldsymbol{\sigma}_0 - \langle \dot{\boldsymbol{\varepsilon}}_i^v \rangle, \qquad \dot{\boldsymbol{\sigma}}_0^{\mathrm{A}} = \bar{\mathbb{L}}^e \cdot \dot{\boldsymbol{\varepsilon}}_0^{\mathrm{A}} \qquad (6.93)$$

and define the related internal accommodation rates for each phase by

$$\dot{\boldsymbol{\sigma}}_i^{\mathrm{A}} = \mathbb{B}_i \cdot \dot{\boldsymbol{\sigma}}_0^{\mathrm{A}} , \quad \dot{\boldsymbol{\varepsilon}}_i^{\mathrm{A}} = \mathbb{M}_i^e \cdot \dot{\boldsymbol{\sigma}}_i^{\mathrm{A}} \qquad (6.94)$$

using $\mathbb{B}_i = \mathbb{I}^S$, $\mathbb{B}_i = \mathbb{B}_i^v$ or $\mathbb{B}_i = \mathbb{B}_i^e$ in Variant 1, 2 or 3, respectively.

(iii) Subproblem E: Determine the elastic strain-rate $\dot{\boldsymbol{\varepsilon}}_i^e$ and the corresponding stress-rate $\dot{\boldsymbol{\sigma}}_i$ in the i-th phase, from the equations

$$\dot{\boldsymbol{\varepsilon}}_i^e - \dot{\boldsymbol{\varepsilon}}_0 + \dot{\boldsymbol{\varepsilon}}_0^{\mathrm{V}i} = -\bar{\mathbb{M}}_*^e \cdot (\dot{\boldsymbol{\sigma}}_i - \dot{\boldsymbol{\sigma}}_i^{\mathrm{A}} - \dot{\boldsymbol{\sigma}}_0 + \dot{\boldsymbol{\sigma}}_0^{\mathrm{A}}), \quad \dot{\boldsymbol{\sigma}}_i = \mathbb{L}_i^e \cdot \dot{\boldsymbol{\varepsilon}}_i^e , \quad \dot{\boldsymbol{\sigma}}_0 = \langle \dot{\boldsymbol{\sigma}}_i \rangle .$$
$$(6.95)$$

(iv) Select a time step, update $\boldsymbol{\sigma}_i$ and $\boldsymbol{\sigma}_0$, and continue.

where $\mathbf{N}_{\mathrm{D}}$ is specified by Eq. (6.74). Both phases are isotropic with compliances of phases specified by Eq. (6.40) with $h_i^{e\mathrm{D}} = h_i^e$ being a doubled elastic shear modulus and h_i^v a doubled viscosity modulus; a spherical shape of inhomogeneities is assumed. In the first example, the following values of these material parameters are examined:

$$h_1^e = 100\,\mathrm{MPa}, \quad h_2^e = 500\,\mathrm{MPa}, \quad h_1^v = 20\,\mathrm{MPa} \times \mathrm{s}, \quad h_2^v = 2000\,\mathrm{MPa} \times \mathrm{s},$$
$$(6.98)$$

for volume fractions of phase 1 equal to $c_1 = 0.1, 0.25, 0.5, 0.75$.

Note that phase 1 as above is less stiff than phase 2 with respect to the elastic and viscous compliances. Other cases have also been examined, namely,

uniform viscosity with the material parameters

$$h_1^e = 100\,\text{MPa}, \quad h_2^e = 2000\,\text{MPa}, \quad h_1^v = h_2^v = 2000\,\text{MPa} \times \text{s}, \qquad (6.99)$$

and uniform elasticity with

$$h_1^e = h_2^e = 100\,\text{MPa}, \quad h_1^v = 20\,\text{MPa} \times \text{s}, \quad h_2^v = 2000\,\text{MPa} \times \text{s}. \qquad (6.100)$$

In both cases $c_1 = 0.5$ is assumed.
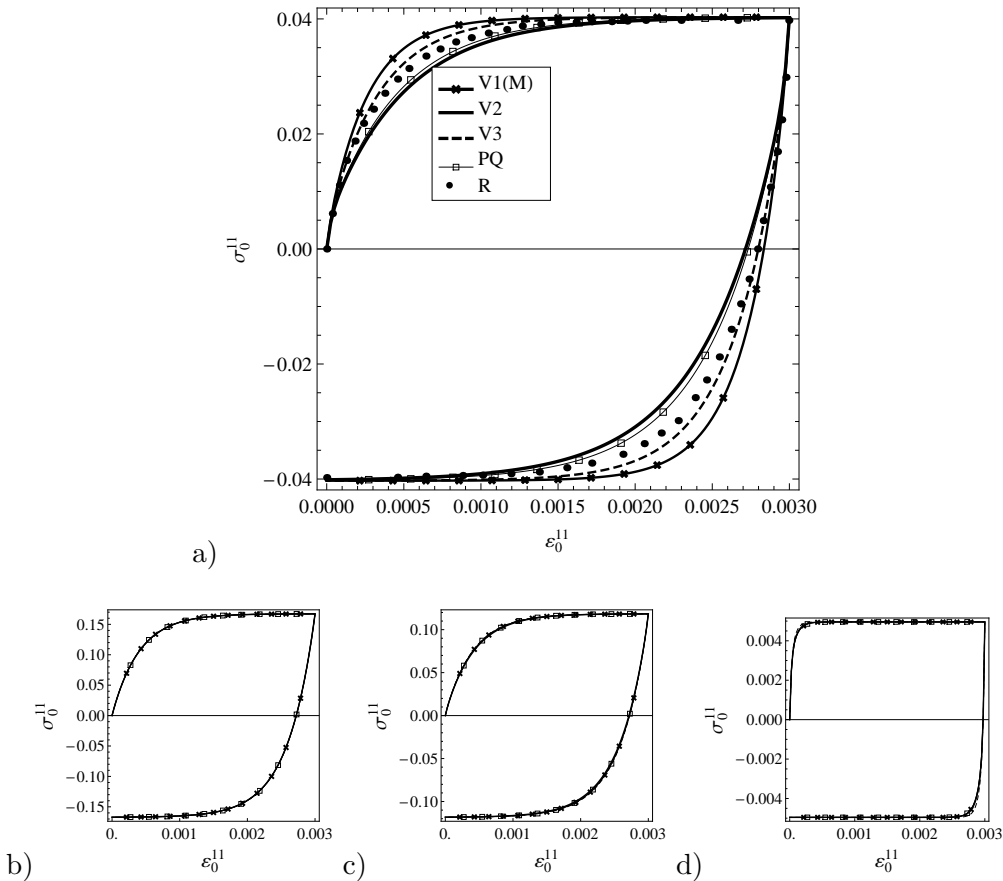
Fig. 6.4. Averaged stress-strain response calculated by different variants of the self-consistent approach for a two-phase material of non-uniform elastic and viscous properties: a) $c_1 = 0.5$, b) $c_1 = 0.1$, c) $c_1 = 0.25$, d) $c_1 = 0.75$.

a)

b)
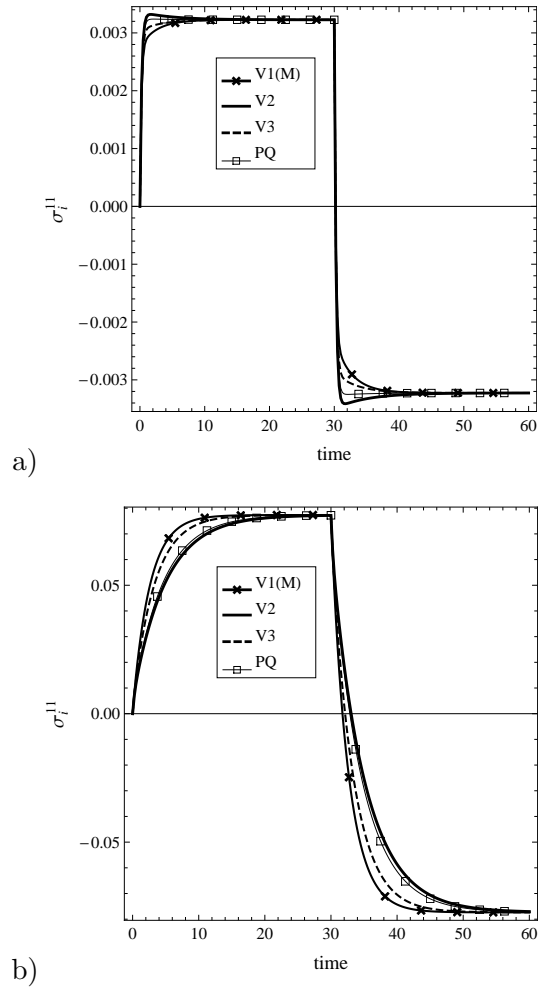
Fig. 6.5. Stress evolution in Phase 1 (a) and Phase 2 (b) of a two-phase material of non-uniform elastic and viscous properties, corresponding to Fig.6.4a ($c_1 = 0.5$).

In Fig. 6.4 the calculated overall stress-strain curves are presented for non-uniform viscous and elastic properties and different volume fractions of phase 1. It has been found that differences between the predictions of the analysed models are best visible in the case of equal volume fractions of phases, therefore in Fig. 6.5 the evolution of local stresses in phases is shown only for this case. Figure 6.6 includes overall stress-strain curves for the cases of uniform elasticity and uniform viscosity. For equal volume fractions of the phases, the
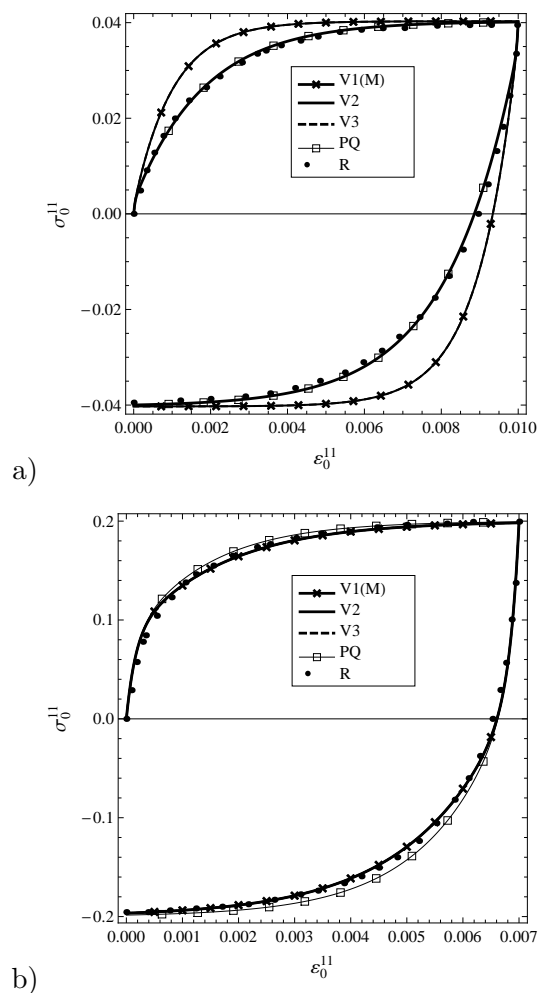
Fig. 6.6. Averaged stress-strain response calculated by different variants of the self-consistent approach for a two-phase material: a) uniform elastic properties (V1=V3), b) uniform viscous properties (V1=V2=V3); $c_1 = 0.5$.

results obtained with the use of the proposed variants (V1,V2,V3) of the self-consistent model employing the sequential linearization method are compared to the exact[5] solution (dented by R) found with the use of Laplace transform by Rougier et al. [174], and to the predictions of the Paquin et al. model (denoted

---

[5]Of course, exact only within the approximations inherent to the self-consistent scheme itself.

a)

b)
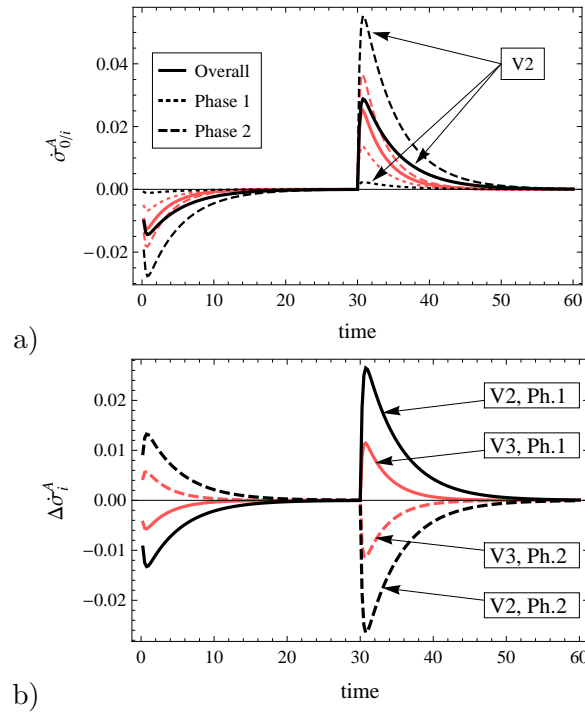
Fig. 6.7. Non-uniform elastic and viscous properties: a) evolution of local and overall accommodation stress-rates for Variant 2 and Variant 3 of the sequential self-consistent model, b) difference $\Delta\dot\sigma_i^A = \dot\sigma_0^A - \dot\sigma_i^A$ (identically zero in Variant 1); $c_1 = 0.5$.

by PQ). In the latter case the concentration relation for the average strain-rate in phase i is of quite a complicated form.

The conclusions from the analysis are the following:

- As it can be seen in Figs 6.4a and 6.5, in the case of non-uniform elastic and viscous properties and equal volume fractions of the phases $(c_1 = 0.5)$, Variant 2 gives a response similar to that for the Paquin et al. model and clearly softer than that for Variant 1 (equivalent to the Molinari model). The former two responses are also closer to, although softer than, the exact solution provided by Rougier et al. [174]. Variant 3 is also satisfactory in this case, although the predicted response is stiffer than in the case of the exact solution.

- Very good agreement of Variant 2 with the exact macroscopic solution, in comparison with the remaining variants of the sequential model, is observed for the case of uniform elastic properties (Fig. 6.6). When the viscous properties are uniform then all three variants collapse into one
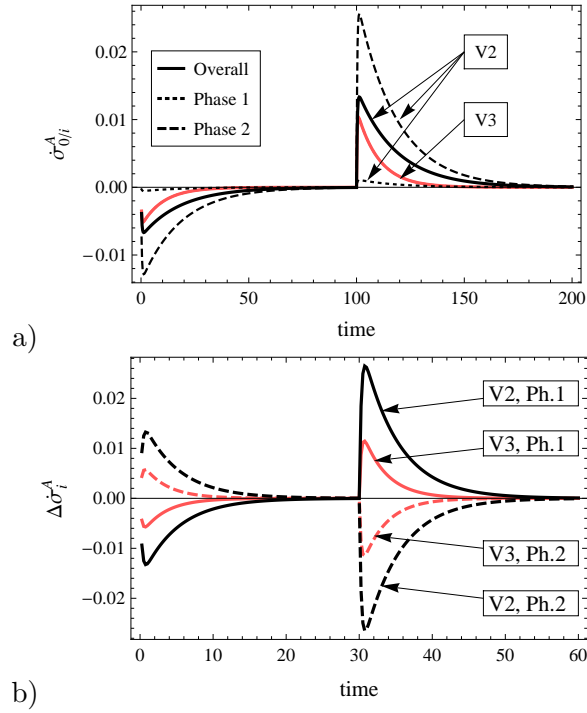
Fig. 6.8. Uniform elastic properties: a) evolution of local and overall accommodation stress-rates for Variant 2 and Variant 3 of the sequential self-consistent model, b) difference $\Delta \dot{\sigma}_i^A = \dot{\sigma}_0^A - \dot{\sigma}_i^A$ (identically zero in Variant 1); $c_1 = 0.5$.

(thus coincide with the Molinari model) and provide good predictions. The Paquin et al. model is also successful in both cases.

- When the volume fraction of one phase is noticeably smaller than that of a second phase then the differences between the macroscopic predictions for the examined models are less visible, cf. Fig. 6.4b-d. If the volume fraction of one phase tends to zero then the problem examined here tends to that of a single inhomogeneity embedded in an infinite matrix, and therefore the predicted responses converge to the exact solution.

The uniform elasticity case is worth being analysed in more detail. It can be seen that in this case the predictions of Variant 1 and 3 are not satisfactory in comparison with the exact solution. This supports the viewpoint that the reduction of the overall stress level within the accommodation step should be related to viscous non-uniformity, as assumed in Variant 2 of the model. It has been checked that, for the case considered, the accommodation strain-rate defined by Eq. (6.89) has an opposite direction than the imposed total strain-rate,

and within a half of cycle its magnitude increases from zero to some maximum value and then decreases again towards zero in the purely viscous limit. The viscous redistribution of the corresponding accommodation stress-rate between the phases, cf. Eq. (6.90), Figs 6.7b and 6.8b, causes the higher/lower reduction of the stress level in the stiffer/softer phase than in the case of the remaining variants. It leads to the acceleration of the viscous flow in the softer phase and to a softer overall response of the composite. The evolution of accommodation terms in Variants 2 and 3 in the case of non-uniform viscous and elastic properties is presented in Figs 6.7a and 6.8a.

On the basis of the analysis performed, Variant 2 of the proposed model is recommended for further use. Variant 1 (equivalent to the Molinari model), due to its relative simplicity, is also worth considering, especially in the case of a small contrast in viscous properties of the phases. It is worth emphasizing that the softening of the macroscopic response in the transient regime, observed for the recommended Variant 2 in comparison with Variant 1, which makes the predictions of the former variant closer to the exact solution, has been achieved here without introducing any additional tuning parameters. The latter technique has been used by Mercier and Molinari [133] in order to improve the Molinari model [136] predictions in this respect.

6.3.3. Extension to non-linear viscosity

The next step is to extend the model to the case of non-linear viscosity,

$$\dot{\boldsymbol{\varepsilon}}_i^v = \mathbf{f}(\boldsymbol{\sigma}_i). \tag{6.101}$$

That extension is not straightforward. In Subproblem V of the sequential approach, a purely viscous problem is solved by using the Eshelby method. When the constitutive law describing viscous behaviour becomes non-linear, some method of linearization of the constitutive law has to be employed. As it has been mentioned in the introduction, different linearization schemes developed for the rigid-viscoplastic materials can be found in the literature. Out of three schemes discussed in Chapter 4, i.e. secant, cf. Hutchinson [69], tangent, cf. Molinari et al. [138], Lebensohn and Tomé [112], and affine cf. Masson et al. [127], we use here the affine one which seems to provide the most accurate predictions, cf. Lebensohn et al. [114]. The selected linearization scheme serves us to find a viscous compliance tensor of homogenized matrix. Consequently, Subproblem V takes the form:

$$\dot{\boldsymbol{\varepsilon}}_i^v - \dot{\boldsymbol{\varepsilon}}_0^{\mathrm{V}i} = -\bar{\mathbb{M}}_*^{v\mathrm{AF}} \cdot \left(\boldsymbol{\sigma}_i - \boldsymbol{\sigma}_0 \right), \tag{6.102}$$

where

$$\dot{\boldsymbol{\varepsilon}}_i^v = \mathbb{M}_i^{v\mathrm{AF}} \cdot \boldsymbol{\sigma}_i + \dot{\boldsymbol{\varepsilon}}_i^{\mathrm{res}}, \quad \mathbb{M}_i^{v\mathrm{AF}} = \frac{\partial \mathbf{f}(\boldsymbol{\sigma}_i)}{\partial \boldsymbol{\sigma}_i}, \quad \dot{\boldsymbol{\varepsilon}}_i^{\mathrm{res}} = \mathbf{f}(\boldsymbol{\sigma}_i) - \mathbb{M}_i^{v\mathrm{AF}} \cdot \boldsymbol{\sigma}_i \quad (6.103)$$

and

$$\bar{\mathbb{M}}^{v\mathrm{AF}} = \langle \mathbb{M}_i^{v\mathrm{AF}} \circ \mathbb{B}_i^{v\mathrm{AF}} \rangle, \quad \mathbb{B}_i^{v\mathrm{AF}} = (\mathbb{M}_i^{v\mathrm{AF}} + \bar{\mathbb{M}}_*^{v\mathrm{AF}})^{-1} \circ (\bar{\mathbb{M}}^{v\mathrm{AF}} + \bar{\mathbb{M}}_*^{v\mathrm{AF}}). \quad (6.104)$$

Additionally, following the affine linearization scheme, it is assumed that

$$\dot{\bar{\boldsymbol{\varepsilon}}}^{\mathrm{res}} = \langle \dot{\boldsymbol{\varepsilon}}_i^{\mathrm{res}} \cdot \mathbb{B}_i^{v\mathrm{AF}} \rangle. \quad (6.105)$$

The Hill tensor inverse $\bar{\mathbb{M}}_*^{v\mathrm{AF}}$ depends on $\bar{\mathbb{M}}^{v\mathrm{AF}}$ and the shape of an inhomogeneity according to the formulae (B.3) and (B.4) in Appendix B.
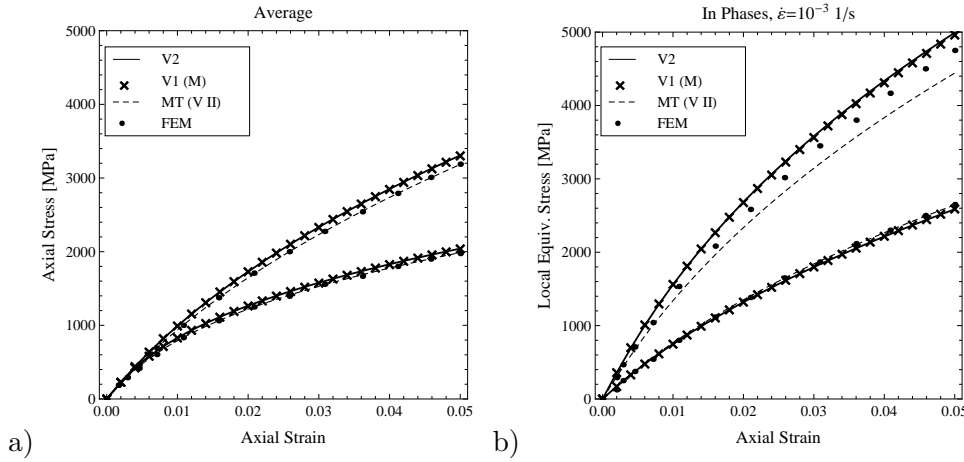
Fig. 6.9. Comparison of the response predicted by the sequential SC and MT models with FEM results taken from [163] for a viscously non-linear two-phase composite in uniaxial tension, $c_i = 0.3$: a) stress-strain curve for the composite at axial strain-rate $\dot{\varepsilon} = 10^{-3}\mathrm{1/s}$ (top curves) and $\dot{\varepsilon} = 10^{-4}\mathrm{1/s}$ (bottom curves), b) stress-strain curve in phases for $\dot{\varepsilon} = 10^{-3}\mathrm{1/s}$ (top curves - inhomogeneity, bottom curves - matrix).

Presence of viscous non-linearity requires also re-consideration of Subproblem A. In the case of Variant 1 we use the formula (6.88) as previously. Variant 2 requires a definition of the overall accommodation strain-rate and respective accommodation stress-rate. Following the reasoning employed previously, we define

$$\dot{\boldsymbol{\sigma}}_0^{\mathrm{A}} = \bar{\mathbb{L}}^e \cdot (\bar{\mathbb{M}}^{v\mathrm{AF}} \cdot \boldsymbol{\sigma}_0 + \dot{\bar{\boldsymbol{\varepsilon}}}^{\mathrm{res}} - \langle \dot{\boldsymbol{\varepsilon}}_i^v \rangle), \quad \dot{\boldsymbol{\sigma}}_i^{\mathrm{A}} = \mathbb{B}_i^{v\mathrm{AF}} \cdot \dot{\boldsymbol{\sigma}}_0^{\mathrm{A}}. \quad (6.106)$$

Numerical tests for moderate non-linearity[6] of the viscosity law have been performed, that is, for a power-type relationship (6.101) with an exponent equal to 1.5. The results for a two-phase material in uniaxial tension obtained by using two variants of the sequential self-consistent (SC) scheme are shown in Fig. 6.9. To enable comparison to other approaches, the constitutive law has been taken the same as that used by Pierard et al. [163] and Mercier and Molinari [133]; details can be found in these references. A spherical shape of inhomogeneities has been assumed. It can be seen in the figures that the difference between Variant 2 and Variant 1 (the latter equivalent to the Molinari model) is hardly visible. The reason for that lies in a relatively small contrast in viscous properties of the phases. As already shown by Mercier and Molinari [133], in the examined case the Mori-Tanaka (MT) averaging scheme applied jointly with the Molinari model (here Variant II of the sequential method) is in the excellent agreement with FEM results reported by Pierard et al. [163] as concerns the average response of the composite, while the self-consistent scheme slightly overestimates the stress level. In turn, the local stress in the stronger phase is somewhat better predicted by the self-consistent model, especially at the advanced stage of the process.

6.3.4. Application to polycrystalline metals of high specific strength

As already indicated in Chapter 3, it is justified to formulate an analogy between the two-phase (or multiphase) composite material of high contrast in properties of the phases (studied in previous subsections of this Chapter) and an untextured polycrystal composed of grains of high anisotropy. In particular, viscous anisotropy is invoked by an insufficient number of easy slip systems characteristic for metals of high specific strength.

Therefore, in this subsection we test the possibility of application of the developed sequential approach to the modelling of polycrystals of high anisotropy. To this end we use the example of untextured polycrystalline γ-TiAl intermetallic of near gamma microstructure, which has been already extensively studied within this thesis. As far as we do not have a suitable set of experimental data available, which is needed to identify parameters and validate the model, the presented results should be treated as preliminary ones. Nevertheless, the analysis enables the comparison of the performance of the

---

[6]The accommodation step in Variant 2 requires further re-consideration in the case of highly non-linear problems. Preliminary calculations have indicated that formula (6.106) at high non-linearity can introduce too strong reduction of the total instantaneous tangent modulus which can lead to overall softening of the homogenized material. This problem requires further study.
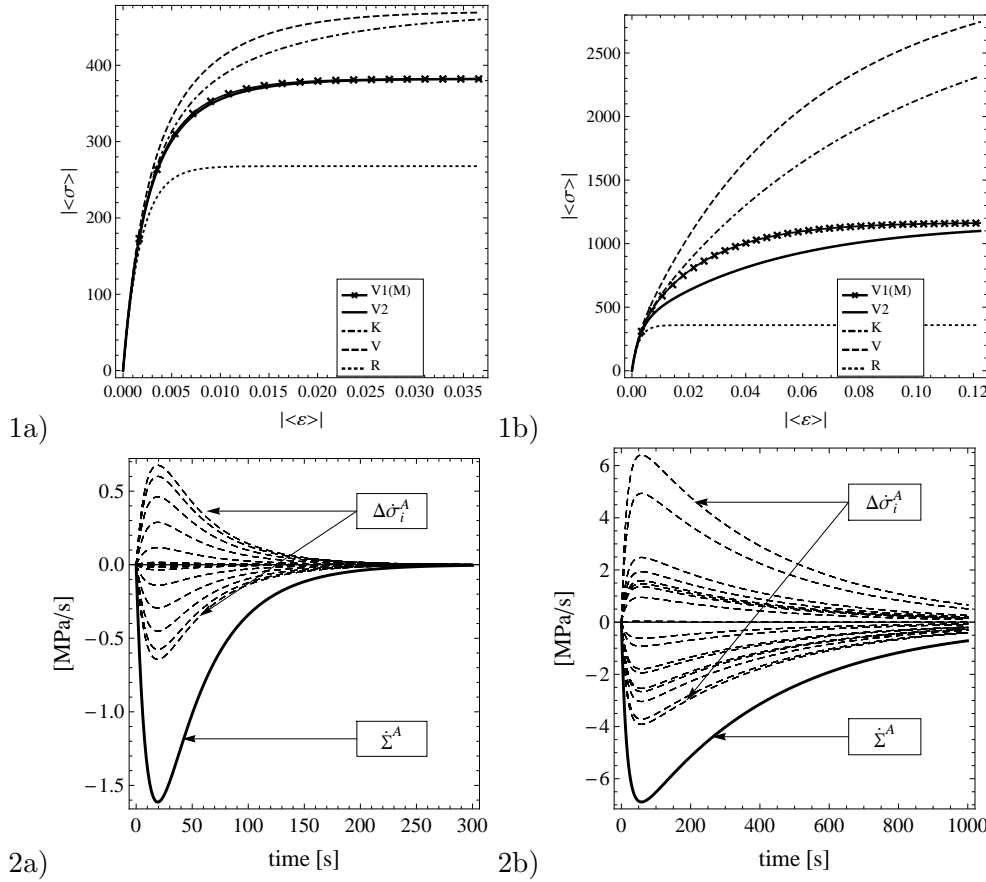
Fig. 6.10. (1) The overall stress-strain curve predicted by different micro-macro transition schemes: V1(M),V2,K - meaning as in previous subsections; V, R - uniform strain (Voigt) and uniform stress (Reuss) schemes. (2) evolution of overall and local accommodation stress-rates for V2 sequential scheme. Polycrystalline γ-TiAl with a) $\tau_c^{sup}/\tau_c^{ord} = 5$ and b) $\tau_c^{sup}/\tau_c^{ord} = 50$; no twinning, $n = 1$, $\tau_c^{ord} = 150$ [MPa].

developed framework with respect to the other approaches available in the literature.

First, we consider a linear polycrystal (i.e. viscous properties are described by Eq. (3.127)) and then a non-linear one (Eq. (4.24)) with high n exponent. The assumed elastic properties of a single crystal of TiAl can be found in Table 2.1.

In Fig. 6.10 we present the overall stress-strain curve predicted by different micro-macro transition schemes for the imposed strain path specified by (6.55)

1a)   1b)

2a)   2b)
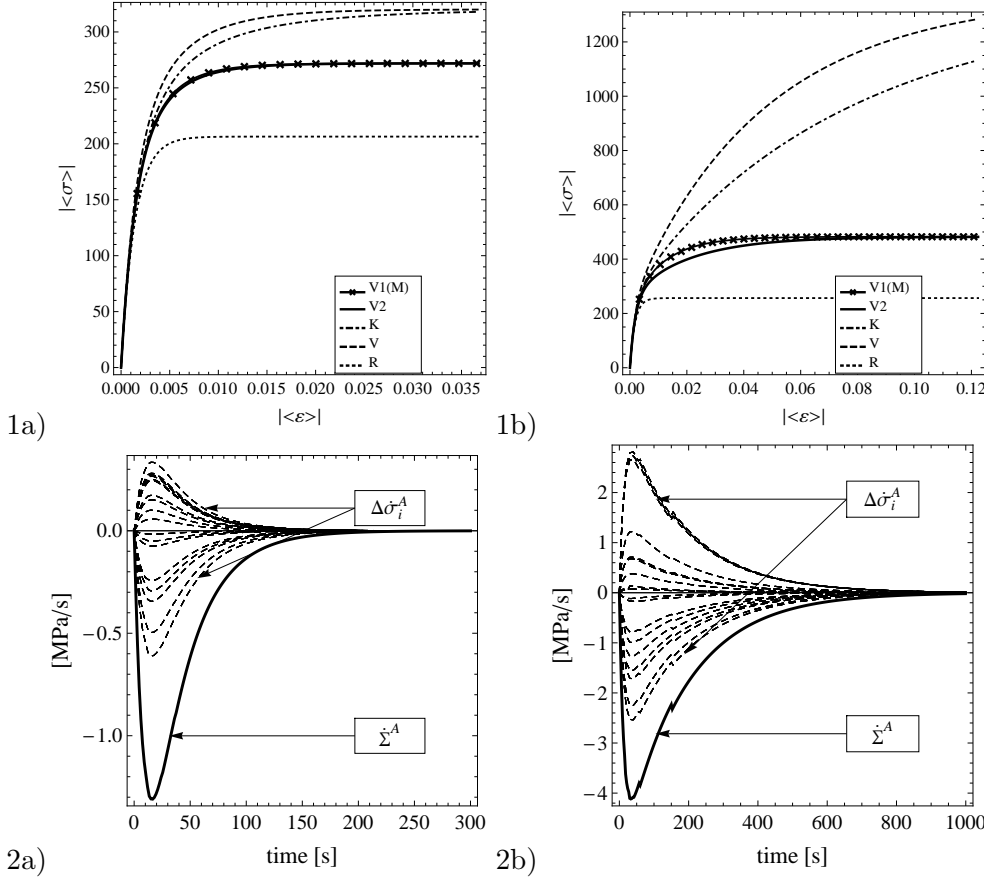
Fig. 6.11. (1) The overall stress-strain curve obtained by different micro-macro transition schemes. Notation as in Fig. 6.10. (2) Evolution of overall and local accommodation stress-rates for V2 sequential scheme. Polycrystalline γ-TiAl with a) $\tau_c^{sup}/\tau_c^{ord} = 5$ and b) $\tau_c^{sup}/\tau_c^{ord} = 50$; $\tau_c^{tw}/\tau_c^{ord} = 1.2$, $n = 1$, $\tau_c^{ord} = 150$ [MPa].

and (6.74) with $\varepsilon_0^{\mathrm{P}}(t) = 0$ and $\varepsilon_0^{\mathrm{D}}(t) = 10^{-4}t$. We have neglected hardening in this example. As it could be expected, when the ratio $\tau_c^{sup}/\tau_c^{ord}$ (the indicator of intensity of viscous anisotropy) is high then the estimated overall response is dramatically different for different averaging schemes[7]. The gap between the predictions of two variants of the sequential method increases with increasing anisotropy factor. Similarly to the case of composite materials, the most noticeable difference is obtained for the transient regime, while for the advanced

---

[7]It is worth recalling that uniform stress and uniform strain schemes are not, in general case, upper and lower bounds of elastic-viscous response, cf. Christensen [34].
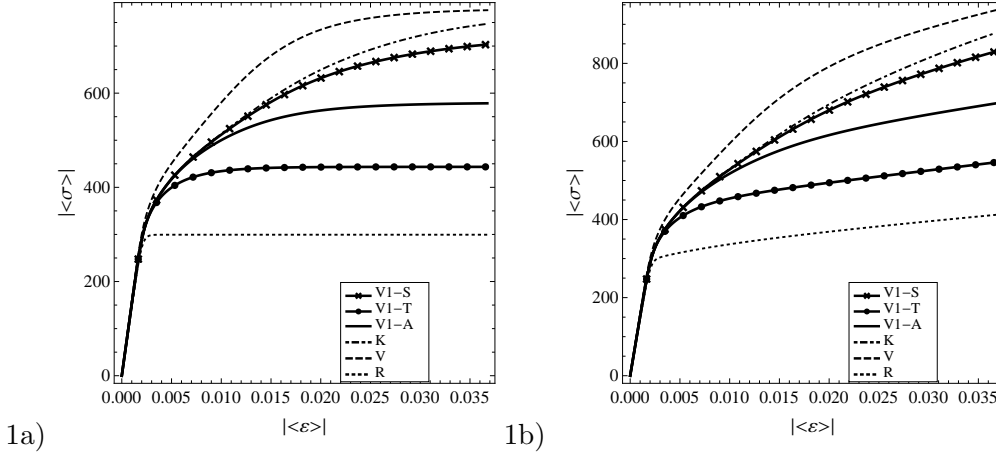
Fig. 6.12. The overall stress-strain curve predicted by different micro-macro transition schemes. Polycrystalline γ-TiAl for $n = 8$, $\tau_c^{sup}/\tau_c^{ord} = 5$, $\tau_c^{tw}/\tau_c^{ord} = 1.2$ and $\tau_c^{ord} = 150$ [MPa]: a) without hardening and b) with linear hardening. Notation as in Fig. 6.10.

viscous flow the solution converges to the purely viscous one. When twinning mechanism is additionally admitted (see Fig. 6.11) we observe narrowing of the gap between estimations of different models, because incorporation of twinning reduces viscous anisotropy of single crystal in the considered case.

In Fig. 6.12 the results for the same polycrystal and the same strain path but for $n = 8$ are presented, both for the case without hardening and for the simple linear hardening of the form:

$$\dot{\tau}_c^r = h^r \dot{\varepsilon}_{eq} \,, \tag{6.107}$$

where $\dot{\varepsilon}_{eq}$ is the equivalent inelastic strain-rate in the considered grain, while h^r is hardening modulus taken to be: 1500 MPa, 7500 MPa and 562.5 MPa for ordinary dislocations, super-dislocations and twinning, respectively. The parameters have been assumed to describe approximately the commercial TiAl intermetallic studied in Chapter 2. Since the anisotropy indicators: $\tau_c^{sup}/\tau_c^{ord} = 5$ and $\tau_c^{tw}/\tau_c^{ord} = 1.2$ are not high, the Variant 1 of the sequential method is only analysed. In contrast to the results presented in Section 6.3.3, three different self-consistent estimates of purely viscous solution are considered: secant (ST), tangent (TG) and affine (AF). It is seen that differences between subsequent methods of averaging are substantial. The predicted transient elastic-viscous regime is the longest for the uniform strain scheme and the shortest for the uniform stress scheme. The corresponding relation between the durations of the transient regime for subsequent variants of the self-consistent method fol-

lows the relation (4.70). For the initial regime of viscous flow, all sub-variants of sequential approach coincide with the Kröner-Weng model. Then, subsequently, the curves corresponding to the tangent, affine and secant subvariants departure from the Kröner-Weng curve stabilizing at some stress level. The Kröner-Weng solution tends to the Voigt solution, as expected. The stress level for the advanced inelastic strains predicted by the particular subvariant of the sequential model is governed by the employed self-consistent scheme for purely viscous solution. The differences between the solutions in the elastic regime are almost negligible as a result of the narrow bounds on elastic properties found for this material (see Sec. 3.6, Tables 3.2 and 3.3).

6.4. Conclusions

In this chapter, a new approach has been proposed to predict the behaviour of viscous/elastic heterogeneous materials. Instead of incorporating both elastic and viscous properties of the constituents in a *single* computational step, we propose to use elastic and viscous properties within an applied averaging scheme *sequentially*. The goal is to obtain an efficient homogenization scheme that is able to generate results comparable to the approaches that require much higher computational effort.

First, the model has been evaluated for the classical problem of an ellipsoidal inhomogeneity embedded in an infinite matrix. Predictions of the outlined variants of the proposed method have been compared with other models available in the literature, and with the exact analytical solution obtained with the use of the Laplace transform and the correspondence principle, in the case of isotropic materials that are viscously and elastically linear and elastically compressible. On the basis of this analysis, the best variant of the sequential decomposition of elastic and viscous responses has been selected for further application into the averaging schemes for heterogeneous materials. It has been found that the selected variant is equivalent to the Molinari model [136] for the inhomogeneity problem.

The sequential linearization concept can be combined with various averaging schemes. The extension to the Mori-Tanaka averaging scheme for a composite is immediate. The major problem in this work has been to adapt the sequential linearization approach to the self-consistent averaging scheme for composite materials. In this case, the sequential approach consists of solving *three* subproblems. It has been demonstrated that an additional accommodation step, besides the viscous and elastic subproblems, is needed in order to estimate the

material response satisfactorily. By examples of an isotropic two-phase mate-
rial, we have shown that the proposed method provides acceptable predictions
in comparison to the existing models. At the end of this chapter, an application
of the developed linearization method to the analysis of polycrystalline metals
of high specific strength has been presented.

7

Summary and outlook

In the present monograph different aspects of micromechanics of metals and alloys of high specific strength have been addressed. In modelling, attention has been focused on the specific features of deformation at the local level, namely coupling between slip and twinning, recognized as main mechanisms of inelastic deformation in these materials, as well as the confinement effects introduced by the lack of independent easy slip systems and the formation of lamellar substructure. The objective has been to develop micromechanical modelling tools suitable for the evaluation of the influence of these phenomena on the macroscopic properties of the analysed materials. The modelling approaches range from the theoretical developments, e.g. analysis of bounds and self-consistent estimates of overall properties of polycrystals by means of invariant decompositions of fourth-order tensors presented in Chapter 3, to numerical calculations of texture evolution and stress-strain response in large deformation processes presented in Chapters 2 and 5. It should be stressed that many of the developed approaches and derived results can be applicable also to other polycrystalline materials with constrained inelastic deformations, not only metals but also e.g. to creep of polar ice, cf. Gilormini et al. [56], Staroszczyk [188] or semi-crystalline polymers, cf. Nikolov et al. [147]. The constitutive framework developed for those materials is in its mathematical structure similar to the one used within crystal plasticity.

Detailed conclusions and summaries pointing at the original aspects of results have been provided at the end of each chapter. Below, we briefly recapitulate the most important findings of the performed studies.

In Chapter 2 the model of single crystal deforming by slip and twinning is presented, originally proposed in Kowalczyk-Gajewska [100], and then applied to evaluate the overall response and texture evolution in different polycrystalline materials. In Sec. 2.3.2 the new reorientation scheme, called a Probabilistic Twin Volume Consistent (PTVC) scheme, has been formulated in order to account for appearance of twin-related orientations in polycrystalline aggregates. The proposal maintains the number of reoriented grains consistent with the

accumulated deformation by twinning within the polycrystal. Moreover, it does not require identification of any additional parameters, which is the case for the PTR scheme proposed by Tomé et al. [200]. Its computational efficiency and independence from the applied model of polycrystal should be underlined. In Sec. 2.3.4 the observed phenomena connected with different slip-twin interactions have been discussed and, adopting the concepts of Karaman et al. [79] and Kalidindi [76], the hardening rule accounting for them has been proposed. The formulated model of single grain deforming by slip and twinning, together with PTVC scheme, have been incorporated within the existing micro-macro transition schemes for polycrystals, namely the classical Taylor model and the viscoplastic self-consistent (VPSC) model, cf. Lebensohn and Tomé [112], Molinari et al. [138]. In Sec. 2.4 the validation of the developed framework has been presented, first for low stacking fault energy metals and alloys (the Hadfield steel and brass), and then for metals and alloys of high specific strength (TiAl intermetallic of near gamma microstructure and Mg alloy). Good agreement with the available experimental results has been observed, both concerning the stress-strain response and predicted textures.

In Chapter 3 the estimates of overall properties of polycrystals of low symmetry (in particular, these characterized by the constrained deformation at the local level) are studied. The theoretical analysis, employing invariant decompositions of Hooke's tensors, of limit bounds and self-consistent estimates is performed in the case of linear constitutive laws. The use of invariant decompositions has allowed us to derive original results concerning these quantities. The new analytical expressions for the Reuss and Voigt bounds as well as the Hashin-Shtrikman bounds are derived for the overall Kelvin bulk and shear modulus of untextured one-phase polycrystal, as well as for four overall Kelvin moduli and the stiffness distributor of one-phase polycrystals of fibre texture. The formulae are expressed in terms of the invariants of the local constitutive tensor. Furthermore, the set of implicit scalar equations for self-consistent estimates of these quantities is found. In the latter case the uniqueness of the solution is examined. In the presented developments the local anisotropy of constituent grains can be arbitrary. The cases of volumetrically isotropic crystals and crystals with constrained deformation (e.g. crystals which do not fulfil the Taylor condition) are studied in more detail. It is proved, for example, that the finite self-consistent estimate of Kelvin shear modulus of random volumetrically isotropic/incompressible polycrystal exists if the dimension of the subspace of constrained deformation is not higher than two/one, respectively. The obtained relations are utilized to derive overall elastic properties of polycrystals of metals listed in Table 2.1, as well as to establish dependence of the overall

reference flow stress on the confinement effects for γ-TiAl and Mg polycrystals.

In Chapter 4 different extensions of the self-consistent (SC) method applicable to non-linear elastic-plastic and viscoplastic crystals of strong anisotropy are discussed. First, the formulation of the incremental self-consistent model within the large strain regime, in conjunction with the rate-independent model of single crystal discussed in Chapter 2, is outlined. Next, three most widely used generalizations of the self-consistent method (i.e. secant, tangent and affine schemes) in the case of rate-dependent model based on the power-law (4.24) are compared. The predictions of these three schemes with respect to Taylor and Sachs bounds are studied for polycrystals of strong local anisotropy induced by an insufficient number of easy slip systems. Moreover, the influence of incorporation of unidirectional twinning mechanism on the value of subsequent estimates is evaluated. Examples of γ-TiAl and magnesium are examined.

In Chapter 5 the micromechanical three-scale model of polycrystals of lamellar substructure has been discussed, together with its extension to the large strain framework. The role of the confinement effects, which are induced on the local inelastic deformation by the presence of a lamellar substructure, on the anisotropic overall response of polycrystals has been thoroughly evaluated. In order to accomplish this task, the confinement parameters (5.4) introduced in Lebensohn et al. [113] have been utilized, which enable us to quantify the directional Hall-Petch effects caused by the layered substructure. In Sec. 5.2, using the general approach developed for layered composites, cf. El Omri et al. [47], the rule for scale transition from the level of single lamella (single grain) to the level of the metagrain has been formulated within the small strain framework. The affine local relation has been assumed, which can be thought of as an actual constitutive law or as a linearised form of a non-linear law. Several scale transition rules have been considered between the level of the metagrain and the level of the polycrystalline sample, namely uniform strain and uniform stress schemes and three generalizations of the self-consistent model in the case of non-linear local law. The original outcome of this part is the discussion of procedures needed for the implementation of the resulting variants of three-scale model. The proposed micromechanical framework has been applied to estimate the overall properties of TiAl intermetallic of lamellar substructure, in particular its elasticity, an initial yield surface and viscoplasticity have been studied. Good accordance with experimental data has been achieved. The important contribution is the evaluation of what is the impact of the introduction into the analysis of the additional level of microstructure on the quality of bounds and the self-consistent estimates. It has been found that taking into account

this intermediate level improves the bounds and lowers the differences between SC estimates; however, this effect has been less pronounced for high values of confinement parameters. In Sec. 5.3 the extension of the discussed three-scale formalism to the large strain framework has been proposed. The important task within this context is the description of the evolution of relative orientation of lamellae interfaces and crystallographic lattice within the lamellae. To this end the interfaces between the lamellae have been recognized as material surfaces which follow the relation (5.70). As in Sec. 5.2, the model has been applied to study the mechanical response and texture evolution in TiAl intermetallic of lamellar substructure in the compression process up to 30% axial strain.

In Chapter 6 the problem of suitable approximation of the interaction between phases in heterogeneous materials that exhibit both viscous and elastic properties has been addressed. A new method of the sequential linearization of elastic-viscous response is proposed to extend the Eshelby result [49] and the self-consistent averaging scheme to the elastic-viscoplastic heterogeneous materials. A novel approach is proposed in which linearised subproblems for an inhomogeneity-matrix system with viscous or elastic interaction rules are solved sequentially within one incremental step. In Sec. 6.2 the Eshelby inclusion problem has been investigated. Different variants of decomposition of elastic-viscous material response have been tested. Using the example of isotropic, elastically compressible and viscously incompressible material, by comparison with the exact solution obtained with the use of the Laplace transform and the correspondence principle, the best variant has been selected. The approach developed has been also compared with relevant models available in the literature, i.e. Molinari [136], Paquin et al. [155], Sabar et al. [181]. It has been found that the selected variant, although established by applying conceptually a different approach, is equivalent to the model proposed by Molinari [136]. In Sec. 6.3 the adaptation of the developed method to the self-consistent scheme has been discussed. It has been demonstrated that in this case an additional accommodation subproblem, besides purely viscous and elastic subproblems, has to be solved in order to estimate the material response satisfactorily. By examples of an isotropic two-phase material it has been shown that the proposed approach provides acceptable predictions in comparison with the existing models. The improvement of predictions as compared to the existing method is particularly significant in the transient regime of comparable rates of elastic and viscous strains and in the case of high contrast between the viscous properties. It indicates that the method will be useful when considering polycrystals of viscously highly anisotropic constituents, e.g. crystals with a limited number of easy slip systems.

In brief, the most important original contributions presented in the monograph are:

- derivation of the constitutive model of single grain deforming by slip and twinning, in which unidirectionality of the latter mechanism and different aspects of slip-twin coupling are taken into account,

- construction of the probabilistic twin volume consistent (PTVC) scheme - the new reorientation scheme for modelling the texture evolution in the presence of twinning,

- incorporation of the proposed model of crystal plasticity including twinning into the existing micro-macro transition schemes, and its validation for polycrystalline metals and alloys of high specific strength with regard to the evaluation of the overall response and the texture evolution in large deformation processes,

- use of invariants of the arbitrarily anisotropic fourth-order tensor of local properties to formulate bounds (uniform strain and stress bounds, the Hashin-Shtrikman bounds) and self-consistent estimates of overall properties of polycrystals,

- the analytical proof of the existence of the finite self-consistent estimates of overall properties for a wide class of polycrystals with constrained deformation at the local level, in the case of linear constitutive laws,

- micromechanical analysis of the effect of a limited number of easy slip systems, unidirectionality of twinning and the presence of lamellar substructure on the quality of different estimates of overall properties of polycrystals described by non-linear constitutive laws,

- the extension of the three-scale micromechanical model of inelastic polycrystal with lamellar substructure to the large strain regime,

- development of the sequential linearization method suitable for the approximation of the interaction between phases and the assessment of the overall response for heterogeneous elastic-viscoplastic materials.

We conclude this final chapter by indicating ongoing research and the future plans concerning the extensions of the discussed models. First, the model of single grain deforming by slip and twinning can be refined. As it has been observed on the example of magnesium, for the processes with strain path change, there is room for the improvement of the predictions by taking into account the kinematic hardening effects and re-building of the dislocation substructure when the direction of plastic flow is changed within the grain. Although the model predictions have been of comparable accuracy with those given by a more

complicated three-scale composite grain model developed by Proust et al. [169], more effort is required in the field of modelling of materials in which the lamellar microstructure induced by twinning is accounted for.

The method employing the invariant decomposition of Hooke's tensor, applied in Chapter 3, proved to be efficient in exploring the properties of bounds and self-consistent estimates of effective properties. Therefore, further studies employing the developed technique concerning predictions of effective properties are worth undertaking. The analysis can be extended, for example, to take into account different shapes of grains, second-order moments, cf. Lebensohn et al. [114], or use of more advanced averaging schemes.

The three-scale model developed in Chapter 5 for the large strain regime, up to now has been implemented only by using the Taylor transition scheme for averaging between the level of the metagrain and the level of polycrystalline sample. Results presented for γ-TiAl of lamellar substructure have indicated that it can lead to unsatisfactory predictions. Therefore, we would like to implement the model in conjunction with one of the generalizations of the self-consistent method developed for the viscoplastic regularization. Moreover, it would be interesting to apply this three-scale model to materials in which lamellar substructure evolves due to the change of volume fractions of subsequent lamellae as is the case for mechanical twinning.

The new method of finding the overall response of elastic-viscoplastic heterogeneous materials proposed in Chapter 6 has been thoroughly evaluated for linear viscosity. The extension and verification of the method for strongly non-linear laws requires further studies. Moreover, it is not clear how the method can be extended in the case of multi-scale microstructure like the one studied in Chapter 5. The developed approach is currently verified in modelling of metal-matrix composites performed within the KomCerMet project (www.komcermet.ippt.gov.pl).

Invariant decompositions
of Hooke's tensor

A.1. Spectral decomposition

Hooke's tensor is the fourth-order tensor with the following symmetries with respect to the permutation of indices:

$$T_{ijkl} = T_{jikl} = T_{ijlk} = T_{klij} \,. \tag{A.1}$$

The last internal symmetry in (A.1) is called the major symmetry. Since, at the same time Hooke's tensor is the symmetric second-order tensor in a six-dimensional Euclidean space, the spectral theorem can be applied to such a tensor, cf. Rychlewski [176, 177], viz.,

$$\mathbb{T} = \sum_{K=1}^{MK} T_K \mathbb{P}_K \,, \tag{A.2}$$

where T_K are $MK \leqslant 6$ mutually different eigenvalues and $\mathbb{P}_K$ are orthogonal projectors into the corresponding subspace $\mathcal{P}_K$ of eigentensors. Orthogonal projectors fulfil

$$\mathbb{P}_K \circ \mathbb{P}_L = \begin{cases} \mathbb{P}_K & \text{if } K = L \\ \mathbb{O} & \text{if } K \neq L \end{cases} , \quad \sum_{K=1}^{MK} \mathbb{P}_K = \mathbb{I}^S \,. \tag{A.3}$$

If T_K is an eigenvalue of multiplicity m_K, then the corresponding projector may be specified in the form

$$\mathbb{P}_K = \sum_{i=1}^{m_K} \boldsymbol{\omega}_i \otimes \boldsymbol{\omega}_i \,, \tag{A.4}$$

where $\{\boldsymbol{\omega}_i\}, i = 1, \ldots, m_K$ constitute a basis in the corresponding m_K-dimensional eigen-subspace $\mathcal{P}_K$ of second-order tensors. It should be stressed that decomposition (A.2) is unique.

The symmetry group of $\mathbb{T}$ is the product of symmetry groups of projectors $\mathbb{P}_K$. More on that issue one finds, for example, in Rychlewski [176, 177], Cowin and Mehrabadi [37], Chadwick et al. [30], Kowalczyk-Gajewska and Ostrowska-Maciejewska [103, 104]. Below we specify the spectral decomposition for transverse isotropy.

The spectral decomposition of $\mathbb{T}$, when it is transversely isotropic, is the following, cf. Cowin et al. [38], Kowalczyk and Ostrowska-Maciejewska [96],

$$\mathbb{T}^{ti} = T_1 \mathbb{P}_1^{ti}(\xi) + T_2 \mathbb{P}_2^{ti}(\xi) + T_3 \mathbb{P}_3^{ti} + T_4 \mathbb{P}_4^{ti}, \tag{A.5}$$

where the eigenvalues T_3 and T_4 are of multiplicity two, and ξ is a so-called stiffness distributor. Similarly to eigenvalues T_K, the stiffness distributor is an invariant of elasticity tensor, cf. Kowalczyk-Gajewska and Ostrowska-Maciejewska [102]. Projectors $\mathbb{P}_3$ and $\mathbb{P}_4$ are functions of a diad $\mathbf{N} = \mathbf{n} \otimes \mathbf{n}$, where $\mathbf{n}$ is a symmetry axis. They are specified as (compare Walpole [208]):

$$\mathbb{P}_3^{ti} = \frac{1}{2} \left([(\mathbf{I} - \mathbf{N}) \otimes (\mathbf{I} - \mathbf{N})]^{T(23)+T(24)} - (\mathbf{I} - \mathbf{N}) \otimes (\mathbf{I} - \mathbf{N}) \right), \tag{A.6}$$

$$\mathbb{P}_4^{ti} = \frac{1}{2} [\mathbf{N} \otimes (\mathbf{I} - \mathbf{N}) + (\mathbf{I} - \mathbf{N}) \otimes \mathbf{N}]^{T(23)+T(24)}, \tag{A.7}$$

where

$$(\mathbb{A}^{T(23)+T(24)})_{ijkl} \equiv (\mathbb{A})_{ikjl} + (\mathbb{A})_{ilkj}. \tag{A.8}$$

The remaining two projectors depend also on the distributor ξ[1],

$$\mathbb{P}_1^{ti} = \frac{1}{3(1+9\xi^2)} \left(\mathbf{I} \otimes \mathbf{I} + \frac{3\xi}{\sqrt{2}} (\mathbf{I} \otimes (3\mathbf{N} - \mathbf{I}) + (3\mathbf{N} - \mathbf{I}) \otimes \mathbf{I}) + \right.$$
$$\left. + \frac{9\xi^2}{2} (3\mathbf{N} - \mathbf{I}) \otimes (3\mathbf{N} - \mathbf{I}) \right), \tag{A.10}$$

$$\mathbb{P}_2^{ti} = \frac{1}{3(1+9\xi^2)} \left(9\xi^2 \mathbf{I} \otimes \mathbf{I} - \frac{3\xi}{\sqrt{2}} (\mathbf{I} \otimes (3\mathbf{N} - \mathbf{I}) + (3\mathbf{N} - \mathbf{I}) \otimes \mathbf{I}) + \right.$$
$$\left. + \frac{1}{2} (3\mathbf{N} - \mathbf{I}) \otimes (3\mathbf{N} - \mathbf{I}) \right), \tag{A.11}$$

---

[1] In order to simplify the results, definition of distributor ξ used in Appendix is slightly different from the one proposed by Kowalczyk-Gajewska and Ostrowska-Maciejewska [102], namely (compare Eq. (4) in [102]),

$$\xi^3 = \sqrt{2}\eta_2 = \sqrt{2}\frac{\det \mathbf{h}_I}{(\operatorname{tr}\boldsymbol{\omega}_I)^3}. \tag{A.9}$$

where

$$\mathbb{P}_1^{ti} + \mathbb{P}_2^{ti} = \frac{1}{3}\mathbf{I} \otimes \mathbf{I} + \frac{1}{6}(3\mathbf{N} - \mathbf{I}) \otimes (3\mathbf{N} - \mathbf{I}) = \mathbb{I}_\mathrm{P} + \mathbb{P}_\mathbf{d}. \qquad (A.12)$$

For transversely isotropic material which is also volumetrically isotropic one has $\xi = 0$.

A.2. Harmonic decomposition

Any Hooke's tensor can be also uniquely decomposed into five pairwise orthogonal parts (belonging to five pairwise orthogonal subspaces), cf. Rychlewski [178, 180], viz.

$$\mathbb{T} = \underbrace{h^\mathrm{P}\mathbb{I}_\mathrm{P} + h^\mathrm{D}\mathbb{I}_\mathrm{D}}_{\text{the isotropic part}} + \underbrace{\mathbb{A}^\mu + \mathbb{A}^\nu + \mathbb{H}}_{\text{the anisotropic part}}, \qquad (A.13)$$

where the first two parts are isotropic and specified by the second-order identity tensor $\mathbf{I}$ and the fourth-order symmetrized identity tensor $\mathbb{I}^S$:

$$\mathbb{I}_\mathrm{P} = \frac{1}{3}\mathbf{I} \otimes \mathbf{I}, \quad \mathbb{I}_\mathrm{D} = \mathbb{I}^S - \frac{1}{3}\mathbf{I} \otimes \mathbf{I}, \qquad (A.14)$$

and two scalars h^P and h^D. Second two parts are specified as linear functions of two second-order deviators $\boldsymbol{\phi}$ and $\boldsymbol{\rho}$, namely[2],

$$\mathbb{A}^\mu(\boldsymbol{\phi}) = \mathbf{I} \otimes \boldsymbol{\phi} + \boldsymbol{\phi} \otimes \mathbf{I}, \qquad (A.16)$$

$$\mathbb{A}^\nu(\boldsymbol{\rho}) = \frac{1}{2}\left[\mathbf{I} \otimes \boldsymbol{\rho} + \boldsymbol{\rho} \otimes \mathbf{I}\right]^{T(23)+T(24)} - \frac{2}{3}\left[\mathbf{I} \otimes \boldsymbol{\rho} + \boldsymbol{\rho} \otimes \mathbf{I}\right] \qquad (A.17)$$

and $\mathbb{H}$ is totally symmetric and traceless.

This decomposition enables the following one to one correspondence

$$\mathbb{T} \longleftrightarrow \left(h^\mathrm{P}, \quad h^\mathrm{D}, \quad \boldsymbol{\phi}, \quad \boldsymbol{\rho}, \quad \mathbb{H}\right). \qquad (A.18)$$

Scalars are calculated as follows:

$$h^\mathrm{P} = \frac{1}{3}\mathbf{I} \cdot \mathbb{T} \cdot \mathbf{I}, \quad h^\mathrm{D} = \frac{1}{5}(\mathrm{Tr}\mathbb{T} - h^\mathrm{P}), \quad h^\mathrm{P} = \frac{1}{3}T_{iikk}, \quad \mathrm{Tr}\mathbb{T} = T_{ikik}, \quad (A.19)$$

---

[2]As shown by Rychlewski [178], there are infinitely many possible definitions of $\mathbb{A}^\mu$ and $\mathbb{A}^\nu$, while their sum remains the same for the considered tensor $\mathbb{T}$. All of them have the form

$$\mathbb{A}^\alpha = \aleph^\alpha \times (\mathbf{I} \otimes \mathbf{a}^\alpha + \mathbf{a}^\alpha \otimes \mathbf{I}), \qquad (A.15)$$

where $\aleph^\alpha$ are independent permutation operations, while $\mathbf{a}^\alpha$ are some second-order deviators depending on the Novozhilov's tensors deviators.

while second-order deviators are calculated with the use of the so-called Novo-zhilov's deviators $\boldsymbol{\mu}_\mathrm{D}$ and $\boldsymbol{\nu}_\mathrm{D}$, namely,

$$\boldsymbol{\phi} = \frac{1}{3}\boldsymbol{\mu}_\mathrm{D}, \quad \boldsymbol{\rho} = \frac{2}{7}(3\boldsymbol{\nu}_\mathrm{D} - 2\boldsymbol{\mu}_\mathrm{D}), \tag{A.20}$$

where $\boldsymbol{\mu}_\mathrm{D}$ and $\boldsymbol{\nu}_\mathrm{D}$ are deviators of the following tensors:

$$\boldsymbol{\mu} = \mathbb{T}\cdot\mathbf{I}, \quad \boldsymbol{\nu} = \mathbb{T}^{T(23)}\cdot\mathbf{I}, \quad \mu_{ij} = T_{ijkk}, \quad \nu_{ij} = T_{ikjk}. \tag{A.21}$$

The symmetry group of the tensor $\mathbb{T}$ is the product of symmetry groups of the tensors $\boldsymbol{\phi}$, $\boldsymbol{\rho}$ (or equivalently of $\boldsymbol{\mu}_\mathrm{D}$, $\boldsymbol{\nu}_\mathrm{D}$) and $\mathbb{H}$.

Because projectors $\mathbb{P}_K$ of the spectral decomposition of $\mathbb{T}$ are the fourth-order tensors, the harmonic decomposition (A.13) of them can be performed, namely,

$$\mathbb{P}_K = \eta_K^\mathrm{P}\mathbb{I}_\mathrm{P} + \eta_K^\mathrm{D}\mathbb{I}_\mathrm{D} + \mathbb{A}_K^\mu + \mathbb{A}_K^\nu + \mathbb{H}_K, \tag{A.22}$$

where specifically

$$\eta_K^\mathrm{P} = \frac{1}{3}\mathbf{I}\cdot\mathbb{P}_K\cdot\mathbf{I}, \quad \eta_K^\mathrm{D} = \frac{1}{5}(m_K - \eta_K^\mathrm{P}), \tag{A.23}$$

$$\mathbb{A}_K^\mu = \mathbb{A}^\mu(\boldsymbol{\mu}_{\mathrm{D}K}), \quad \mathbb{A}_K^\nu = \mathbb{A}^\nu(\boldsymbol{\nu}_{\mathrm{D}K}), \tag{A.24}$$

and m_K is the multiplicity of the corresponding modulus h_K. One should note the following identities:

$$\sum_{K=1}^{MK}\mathbb{P}_K = \mathbb{I}^S \Rightarrow \sum_{K=1}^{MK}\eta_K^\mathrm{P} = 1, \quad \sum_{K=1}^{MK}\eta_K^\mathrm{D} = 1, \quad \sum_{K=1}^{MK}m_K = 6, \tag{A.25}$$

where $0 \leqslant \eta_K^\mathrm{P} \leqslant 1$, $0 \leqslant \eta_K^\mathrm{D} \leqslant 1$ and

$$\sum_{K=1}^{MK}\mathbb{A}_K^\mu = \mathbb{O} \quad \left(\sum_{K=1}^{MK}\boldsymbol{\mu}_{\mathrm{D}K} = \mathbf{0}\right), \quad \sum_{K=1}^{MK}\mathbb{A}_K^\nu = \mathbb{O} \quad \left(\sum_{K=1}^{MK}\boldsymbol{\nu}_{\mathrm{D}K} = \mathbf{0}\right), \tag{A.26}$$

$$\sum_{K=1}^{MK}\mathbb{H}_K = \mathbb{O}. \tag{A.27}$$

The form of decomposition (A.13) is based on the presentations by Rychlew-ski [178, 180]. Different definitions of $\mathbb{A}^\mu$ and $\mathbb{A}^\nu$ have been utilized by Forte and Vianello [51]. Below we specify the harmonic decomposition for transverse isotropy (compare the related analysis by Forte and Vianello [52]).

A second-order deviator of a unit norm which exhibits transverse isotropy has the form which is uniquely specified, within a sign, that is

$$\mathbf{d_n} = \frac{1}{\sqrt{6}}(3\mathbf{N} - \mathbf{I}), \tag{A.28}$$

where $\mathbf{N}$ has been specified in previous subsection of this appendix. Similarly, a fully symmetric and traceless fourth-order tensor of a unit norm, which exhibits transverse isotropy, is uniquely specified, within a sign, namely,

$$\mathbb{H_n} = \frac{1}{\sqrt{70}}\left(6\mathbb{P_d} + \mathbb{P}_3^{ti} - 4\mathbb{P}_4^{ti}\right), \tag{A.29}$$

where

$$\mathbb{P_d} = \mathbf{d_n} \otimes \mathbf{d_n}. \tag{A.30}$$

In view of the above observations one obtains:

$$\mathbb{T}^{ti} = h^{\mathrm{P}}\mathbb{I}_{\mathrm{P}} + h^{\mathrm{D}}\mathbb{I}_{\mathrm{D}} + \alpha^{\mu}\mathbb{A}^{\mu}(\mathbf{d_n}) + \alpha^{\nu}\mathbb{A}^{\nu}(\mathbf{d_n}) + \eta^{H}\mathbb{H_n} \tag{A.31}$$

and

$$\mathbb{A}^{\mu}(\mathbf{d_n}) = \mathbf{I} \otimes \mathbf{d_n} + \mathbf{d_n} \otimes \mathbf{I}, \quad \mathbb{A}^{\nu}(\mathbf{d_n}) = \frac{1}{\sqrt{6}}\left(2\mathbb{P_d} - 2\mathbb{P}_3^{ti} + \mathbb{P}_4^{ti}\right). \tag{A.32}$$

The relations (A.28)-(A.32) show that the fourth-order Hooke tensor describing the properties of transversely isotropic material is uniquely specified by five scalar invariants $\{h^{\mathrm{P}}, h^{\mathrm{D}}, \alpha_1, \alpha_2, \eta^{\mathrm{H}}\}$ and the orientation of symmetry axis $\mathbf{n} \otimes \mathbf{n}$, where

$$\alpha^{\mu} = \boldsymbol{\phi} \cdot \mathbf{d_n}, \quad \alpha^{\nu} = \boldsymbol{\rho} \cdot \mathbf{d_n}, \quad \eta^{\mathrm{H}} = \mathbb{T} \cdot \mathbb{H_n} \tag{A.33}$$

and in the components in any basis $\{\mathbf{e}_k\}$:

$$\alpha^{\mu} = \frac{1}{\sqrt{6}}(h^{\mathrm{P}} - T_{ijkk}n_i n_j), \quad \alpha^{\nu} = \frac{6}{7}\left(\frac{3}{\sqrt{6}}(3T_{ikjk}n_i n_j - T_{ijij}) - 2\alpha_1\right). \tag{A.34}$$

Harmonic decompositions of projectors $\mathbb{P}_K^{ti}$ specified by relations (A.6)-(A.11) result in:

$$\eta_K^{\mathrm{P}} = \left\{ \frac{9\xi^2}{1+9\xi^2}, \frac{1}{1+9\xi^2}, 0, 0 \right\}, \tag{A.35}$$

$$\eta_K^{\mathrm{D}} = \frac{1}{5} \left\{ \frac{1}{1+9\xi^2}, \frac{9\xi^2}{1+9\xi^2}, 2, 2 \right\}, \tag{A.36}$$

$$\alpha_K^{\mu} = \left\{ \frac{\sqrt{3}\xi}{1+9\xi^2}, -\frac{\sqrt{3}\xi}{1+9\xi^2}, 0, 0 \right\}, \tag{A.37}$$

$$\alpha_K^{\nu} = \frac{\sqrt{6}}{7} \left\{ \frac{1}{1+9\xi^2}, \frac{9\xi^2}{1+9\xi^2}, -2, 1 \right\}, \tag{A.38}$$

$$\eta_K^{\mathrm{H}} = \frac{2}{\sqrt{70}} \left\{ \frac{3}{1+9\xi^2}, \frac{27\xi^2}{1+9\xi^2}, 1, -4 \right\}. \tag{A.39}$$

It is easy to verify that above scalars fulfil identities (A.25)-(A.26).

Note that two alternative sets of five invariants are derived in this Appendix for the Hooke tensor of transverse isotropy. It is easy to show that these two sets are related as follows:

$$h^{\mathrm{P}} = \sum_{K=1}^{2} T_K \eta_K^{\mathrm{P}}, \quad h^{\mathrm{D}} = \sum_{K=1}^{4} T_K \eta_K^{\mathrm{D}}, \tag{A.40}$$

$$\alpha^{\mu} = \sum_{K=1}^{2} T_K \alpha_K^{\mu}, \quad \alpha^{\nu} = \sum_{K=1}^{4} T_K \alpha_K^{\nu}, \quad \eta^{\mathrm{H}} = \sum_{K=1}^{4} T_K \eta_K^{\mathrm{H}}. \tag{A.41}$$

Let us note that any second-order deviator $\mathbf{d}$ and any fully symmetric and traceless fourth-order tensor $\mathbb{H}$ can be uniquely decomposed with respect to the diad $\mathbf{n} \otimes \mathbf{n}$ as follows:

$$\mathbf{d} = (\mathbf{d} \cdot \mathbf{d_n})\mathbf{d_n} + \bar{\mathbf{d}}_\mathbf{n}, \quad \mathbb{H} = (\mathbb{H} \cdot \mathbb{H_n})\mathbb{H_n} + \bar{\mathbb{H}}_\mathbf{n}, \tag{A.42}$$

where $\bar{\mathbf{d}}_\mathbf{n} = \mathbf{d} - (\mathbf{d} \cdot \mathbf{d_n})\mathbf{d_n}$ and $\bar{\mathbb{H}}_\mathbf{n} = \mathbb{H} - (\mathbb{H} \cdot \mathbb{H_n})\mathbb{H_n}$.

The Eshelby solution
and a self-consistent model

Eshelby [49] found the analytical solution to the problem of an ellipsoidal inclusion/inhomogeneity V_* embedded into the infinite matrix V. The solution was obtained within the linear elasticity and the small strain framework.
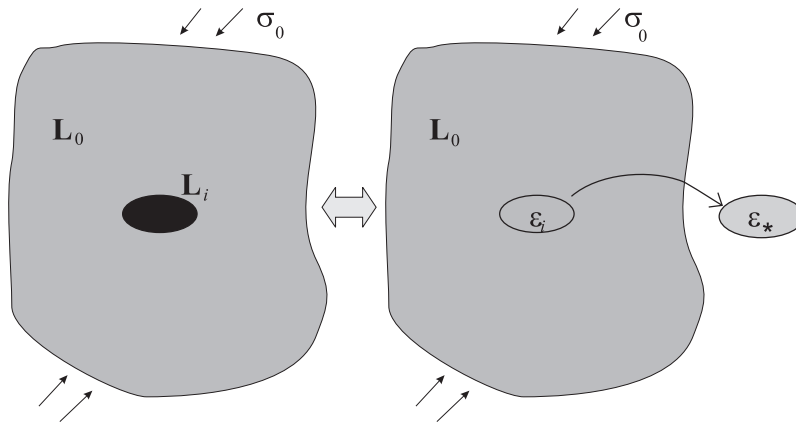
Fig. B.1. Equivalence between the Eshelby inclusion and inhomogeneity problems.

The term *inclusion* is used with respect to the problem of an ellipsoidal subvolume V_* which undergoes a permanent deformation such that, if we remove V_* from V, it assumes the strain $\boldsymbol{\varepsilon}_*$ (see Fig. B.1). The eigenstrain $\boldsymbol{\varepsilon}_*$ can be thought of as, e.g., being the transformation strain for the phase transformation phenomenon. The term *inhomogeneity* is used with respect to the problem of an ellipsoidal subvolume V_* of different properties as those of the surrounding matrix. It can be shown that the second problem can be reduced to the first one by introducing some properly selected eigenstrain, Fig. B.1. Selection of this eigenstrain is done by employing the strain/stress equivalence principle, cf. Li and Wang [120], Nemat-Nasser and Hori [145].

The most remarkable outcome of this analytical solution[1] is that the strain and stress fields in the constrained inclusion are uniform and, under the zero external loading, the strain can be related to the eigenstrain $\boldsymbol{\varepsilon}_*$ by the Eshelby tensor $\mathbb{S}$, viz.,

$$\boldsymbol{\varepsilon}_i = \mathbb{S} \cdot \boldsymbol{\varepsilon}_* \, .$$

Let us recall basic formulae originating in the Eshelby result. Assume an affine relationship between strain and stress tensors,

$$\boldsymbol{\sigma} = \mathbb{L}_r \cdot (\boldsymbol{\varepsilon} - \boldsymbol{\varepsilon}_r^{\text{res}}), \quad \boldsymbol{\varepsilon}_r = \mathbb{M}_r \cdot \boldsymbol{\sigma} + \boldsymbol{\varepsilon}_r^{\text{res}}, \quad \mathbb{L}_r \circ \mathbb{M}_r = \mathbb{I}^S, \qquad \text{(B.1)}$$

where $\mathbb{L}_r$ and $\mathbb{M}_r \equiv \mathbb{L}_r^{-1}$ are given fourth-order stiffness and compliance tensors of an infinite matrix ($r = 0$) or inhomogeneity ($r = i$). As shown by Hill [67], the analytical solution to the inclusion problem provides the following relation between the stress $\boldsymbol{\sigma}_0$ and strain $\boldsymbol{\varepsilon}_0$ at infinity, and their counterparts in inhomogeneity (the stiffness tensor $\mathbb{L}_0$ and the reference strain $\boldsymbol{\varepsilon}_0^{\text{res}}$ should be uniform),

$$\boldsymbol{\sigma}_i - \boldsymbol{\sigma}_0 = -\mathbb{L}_* \cdot (\boldsymbol{\varepsilon}_i - \boldsymbol{\varepsilon}_0) \, , \qquad \text{(B.2)}$$

where $\mathbb{L}_*$ is called the Hill tensor. This fourth order Hooke's tensor is calculated as follows

$$\mathbb{L}_* = \mathbb{P}^{-1} - \mathbb{L}_0 \, . \qquad \text{(B.3)}$$

The polarisation tensor $\mathbb{P}$ is specified by the shape of ellipsoidal inhomogeneity and the matrix properties, cf. Willis [220], namely,

$$\mathbb{P} = \frac{1}{4\pi abc} \int_{|\boldsymbol{\nu}|=1} |\mathbf{a}^{-1} \cdot \boldsymbol{\nu}|^{-3} \left(\boldsymbol{\nu} \otimes (\boldsymbol{\nu}\mathbb{L}_0\boldsymbol{\nu})^{-1} \otimes \boldsymbol{\nu} \right)^{sym} dS \, , \qquad \text{(B.4)}$$

where

$$A_{ijkl}^{sym} \equiv \frac{1}{4} \left(A_{ijkl} + A_{jikl} + A_{ijlk} + A_{klij} \right) \, , \qquad \text{(B.5)}$$

and $\mathbf{a}$ is the second-order tensor of principal values a, b, c, equal to the ellipsoid semi-axes (for a spherical inhomogeneity $a = b = c$ and $\mathbf{a} = a\mathbf{I}$). The integration is over the surface of the unit sphere $|\boldsymbol{\nu}| = 1$. The Eshelby tensor $\mathbb{S}$ reads

$$\mathbb{S} = \mathbb{P} \circ \mathbb{L}_0 = (\mathbb{I}^S + \mathbb{M}_0 \circ \mathbb{L}_*)^{-1} = \mathbb{M}_* \circ (\mathbb{M}_0 + \mathbb{M}_*)^{-1},$$

on using the inverses $\mathbb{M}_0 = \mathbb{L}_0^{-1}$, $\mathbb{M}_* = \mathbb{L}_*^{-1}$.

---

[1]The solution is most easily obtained with use of the Green functions and the Fourier transforms. Details can be found, e.g., in Li and Wang [120].

In the case of an isotropic matrix, i.e. $\mathbb{L}_0 = h_0^{\mathrm{P}}\mathbb{I}_{\mathrm{P}} + h_0^{\mathrm{D}}\mathbb{I}_{\mathrm{D}}$, and the spherical inclusion, the polarisation tensor $\mathbb{P}$ is

$$\mathbb{P} = \frac{1}{h_0^{\mathrm{P}} + 2h_0^{\mathrm{D}}}\mathbb{I}_{\mathrm{P}} + \frac{2(h_0^{\mathrm{P}} + 3h_0^{\mathrm{D}})}{5h_0^{\mathrm{D}}(h_0^{\mathrm{P}} + 2h_0^{\mathrm{D}})}\mathbb{I}_{\mathrm{D}} \,, \tag{B.6}$$

and the Hill tensor takes the form:

$$\mathbb{L}_* = h_*^{\mathrm{P}}\mathbb{I}_{\mathrm{P}} + h_*^{\mathrm{D}}\mathbb{I}_{\mathrm{D}} \,, \tag{B.7}$$

where

$$h_*^{\mathrm{P}} = 2h_0^{\mathrm{D}}, \quad h_*^{\mathrm{D}} = h_0^{\mathrm{D}}\frac{3h_0^{\mathrm{P}} + 4h_0^{\mathrm{D}}}{2(h_0^{\mathrm{P}} + 3h_0^{\mathrm{D}})} \,. \tag{B.8}$$

On substituting the constitutive equations for the inhomogeneity and matrix into Eq. (B.2), the following relationships are derived:

$$\boldsymbol{\sigma}_i = \mathbb{B}_i \cdot \boldsymbol{\sigma}_0 + (\mathbb{M}_i + \mathbb{M}_*)^{-1} \cdot (\boldsymbol{\varepsilon}_0^{\mathrm{res}} - \boldsymbol{\varepsilon}_i^{\mathrm{res}}) \,, \tag{B.9}$$

$$\boldsymbol{\varepsilon}_i = \mathbb{A}_i \cdot \boldsymbol{\varepsilon}_0 - (\mathbb{L}_i + \mathbb{L}_*)^{-1} \cdot (\mathbb{L}_0 \cdot \boldsymbol{\varepsilon}_0^{\mathrm{res}} - \mathbb{L}_i \cdot \boldsymbol{\varepsilon}_i^{\mathrm{res}}) \,, \tag{B.10}$$

where $\mathbb{A}_i$ and $\mathbb{B}_i$ are the strain and stress concentration tensors specified as

$$\mathbb{A}_i = (\mathbb{L}_i + \mathbb{L}_*)^{-1} \circ (\mathbb{L}_0 + \mathbb{L}_*) = (\mathbb{I}^S + \mathbb{P} \circ (\mathbb{L}_i - \mathbb{L}_0))^{-1} \,, \tag{B.11}$$

$$\mathbb{B}_i = (\mathbb{M}_i + \mathbb{M}_*)^{-1} \circ (\mathbb{M}_0 + \mathbb{M}_*) = (\mathbb{I}^S + \mathbb{Q} \circ (\mathbb{M}_i - \mathbb{M}_0))^{-1} \,. \tag{B.12}$$

We note the following notation and connections between the introduced tensors, cf. Hill [66], Walpole [208],

$$\mathbb{T} \equiv (\mathbb{M}_0 + \mathbb{M}_*)^{-1} \circ \mathbb{M}_0 = \mathbb{L}_* \circ (\mathbb{L}_0 + \mathbb{L}_*)^{-1} \,, \tag{B.13}$$

$$\mathbb{Q} \equiv \mathbb{L}_* \circ \mathbb{S} = \mathbb{L}_0 \circ (\mathbb{I}^S - \mathbb{S}) \,, \quad \mathbb{P} = \mathbb{S} \circ \mathbb{M}_0 = (\mathbb{I}^S - \mathbb{S}) \circ \mathbb{M}_* \,, \tag{B.14}$$

$$\mathbb{P} = \mathbb{M}_* \circ \mathbb{T} = \mathbb{M}_0 \circ (\mathbb{I}^S - \mathbb{T}) \,, \quad \mathbb{Q} = \mathbb{T} \circ \mathbb{L}_0 = (\mathbb{I}^S - \mathbb{T}) \circ \mathbb{L}_* \,, \tag{B.15}$$

$$\mathbb{Q}^{-1} = \mathbb{M}_* + \mathbb{M}_0 \,, \quad \mathbb{P} \circ \mathbb{L}_0 + \mathbb{M}_0 \circ \mathbb{Q} = \mathbb{I}^S \,, \tag{B.16}$$

$$\mathbb{L}_i \circ \mathbb{A}_i = \mathbb{B}_i \circ \mathbb{L}_0 \,, \quad \mathbb{M}_i \circ \mathbb{B}_i = \mathbb{A}_i \circ \mathbb{M}_0 \,. \tag{B.17}$$

Considering a composite or a polycrystal in which all constituents, with properties $\mathbb{L}_i$ and residual strains $\boldsymbol{\varepsilon}_i^{\mathrm{res}}$, can be treated on the same footing, one can apply the so-called self-consistent model. Within this model each constituent is identified with an ellipsoidal inclusion embedded in the infinite homogeneous equivalent medium (HEM) of the averaged, yet unknown, properties $\bar{\mathbb{L}}$, cf.
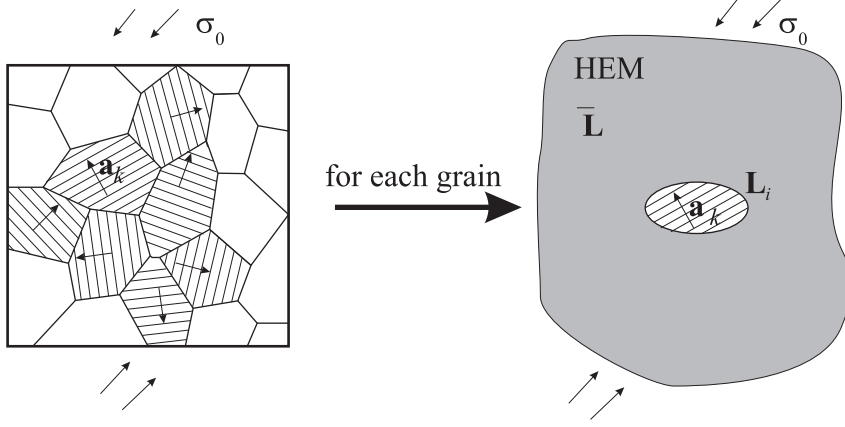
Fig. B.2. Idea of the self-consistent model of polycrystal.

Fig. B.2. The imposed uniform strain follows the constitutive rule of HEM of the form[2]:

$$\varepsilon_0 = \langle \varepsilon \rangle = \bar{\mathbb{L}} \cdot \boldsymbol{\sigma}_0 + \mathbf{E}^{\mathrm{res}} = \bar{\mathbb{L}} \cdot \langle \boldsymbol{\sigma} \rangle + \mathbf{E}^{\mathrm{res}} . \tag{B.18}$$

The overall properties $\bar{\mathbb{L}}$ and $\mathbf{E}^{\mathrm{res}}$ are found applying the Eshelby solution to each constituent and performing the averaging over the representative volume. In the case when all the ellipsoids have the same shape and orientation (hence, tensors $\mathbb{P}(\bar{\mathbb{L}})$, and consequently $\mathbb{L}_*(\bar{\mathbb{L}}), \mathbb{M}_*(\bar{\mathbb{L}}), \mathbb{Q}(\bar{\mathbb{L}}), \mathbb{S}(\bar{\mathbb{L}}), \mathbb{T}(\bar{\mathbb{L}})$ are the same for all inclusions), one obtains implicit formula, viz.,

$$\bar{\mathbb{L}} = \langle \mathbb{L}_i \circ \mathbb{A}_i \rangle, \quad \text{where} \quad \langle \mathbb{A}_i \rangle = \mathbb{I}^S , \tag{B.19}$$

or equivalently,

$$\bar{\mathbb{M}} = \langle \mathbb{M}_i \circ \mathbb{B}_i \rangle, \quad \text{where} \quad \langle \mathbb{B}_i \rangle = \mathbb{I}^S . \tag{B.20}$$

These formulae are also equivalent to

$$\langle (\bar{\mathbb{M}} - \mathbb{M}_i) \circ \mathbb{B}_i \rangle = \mathbb{O}, \quad \langle (\bar{\mathbb{L}} - \mathbb{L}_i) \circ \mathbb{A}_i \rangle = \mathbb{O} . \tag{B.21}$$

The residual strain $\mathbf{E}^{\mathrm{res}}$ is specified as

$$\mathbf{E}^{\mathrm{res}} = \langle \boldsymbol{\varepsilon}_i^{\mathrm{res}} \cdot \mathbb{B}_i \rangle = \langle \mathbb{B}_i^{\mathrm{T}} \cdot \boldsymbol{\varepsilon}_i^{\mathrm{res}} \rangle . \tag{B.22}$$

Note that the major symmetry of the constitutive tensors $\mathbb{L}_i$ and $\bar{\mathbb{L}}$ is assumed.

---

[2]In general $\langle \cdot \rangle$ denotes volume averaging over the representative volume V, i.e $\langle \cdot \rangle = \int_V (\cdot) dV$. For discrete number N of phases in the representative volume it reduces to the summation $\langle \cdot \rangle = \sum_{i=1}^N \nu_i(\cdot)$, where $\nu_i = V_i/V$, while in the case of polycrystalline material it means the averaging over the orientation space (see Chapter 3).

As discussed in Chapter 4, within the large strain regime the elastic-plastic crystal can be described by the incremental linearized relation between the rate of nominal stress and the velocity gradient (e.g. Eq. (4.17)), viz.,

$$\dot{\mathbf{S}} = \mathbb{K}^{ep} \cdot \mathbf{l} \,. \tag{B.23}$$

One should note that the tensor of tangent pseudo-moduli $\mathbb{K}^{ep}$ is not the Hooke tensor (none of the external symmetries (A.1) is guaranteed). The self-consistent model can be applied to find the overall response of polycrystal. The relation for HEM is postulated as

$$\dot{\bar{\mathbf{S}}} = \bar{\mathbb{K}}^{ep} \cdot \mathbf{L} \,. \tag{B.24}$$

Employing the Eshelby solution, all relations developed within the small strain framework remain valid for $\mathbb{L}$ replaced by $\mathbb{K}^{ep}$ and $\bar{\mathbb{L}}$ replaced by $\bar{\mathbb{K}}^{ep}$ with the polarisation tensor defined as

$$\mathbb{P} = \frac{1}{4\pi abc} \int_{|\boldsymbol{\nu}|=1} |\mathbf{a}^{-1} \cdot \boldsymbol{\nu}|^{-3} \left(\boldsymbol{\nu} \otimes (\boldsymbol{\nu} \bar{\mathbb{K}}^{ep} \boldsymbol{\nu})^{-1} \otimes \boldsymbol{\nu} \right)^{T(2143)} dS \,, \tag{B.25}$$

where

$$(A_{ijkl})^{T(2143)} = A_{jilk} \,. \tag{B.26}$$

Let us remind that because the tensor of local tangent moduli $\mathbb{K}^{ep}$ does not exhibit a major symmetry ($K_{ijkl}^{ep} \neq K_{klij}^{ep}$), there is no reason for $\bar{\mathbb{K}}^{ep}$ to exhibit such a symmetry as well. Consequently, the existence and uniqueness of the solution to the related Eshelby problem is not guaranteed, cf. Molinari et al. [139], Nemat-Nasser and Hori [145].

C

Computational issues

As it is common for computational algorithms in mechanics of materials, the fourth-order tensors are represented by square matrices (6×6 if they relate symmetric second-order tensors or 9×9 in a general case) and the second-order tensors are represented by vectors (correspondingly of 6 or 9 components). Instead of using the bases leading to the standard Voigt notation, cf. Christensen [34], or the Kelvin notation, cf. Cowin et al. [38], in the developed procedures the following basis is used, cf. Kowalczyk and Ostrowska-Maciejewska [96]:

$$\mathbf{d}_1 = \frac{1}{\sqrt{3}}\mathbf{I}, \quad \mathbf{d}_2 = \frac{1}{\sqrt{6}}(2\mathbf{m}_3 \otimes \mathbf{m}_3 - \mathbf{m}_1 \otimes \mathbf{m}_1 - \mathbf{m}_2 \otimes \mathbf{m}_2),$$

$$\mathbf{d}_3 = \frac{1}{\sqrt{2}}(\mathbf{m}_1 \otimes \mathbf{m}_1 - \mathbf{m}_2 \otimes \mathbf{m}_2), \quad \mathbf{d}_4 = \frac{1}{\sqrt{2}}(\mathbf{m}_1 \otimes \mathbf{m}_2 + \mathbf{m}_2 \otimes \mathbf{m}_1),$$

$$\mathbf{d}_5 = \frac{1}{\sqrt{2}}(\mathbf{m}_1 \otimes \mathbf{m}_3 + \mathbf{m}_3 \otimes \mathbf{m}_1), \quad \mathbf{d}_6 = \frac{1}{\sqrt{2}}(\mathbf{m}_3 \otimes \mathbf{m}_2 + \mathbf{m}_2 \otimes \mathbf{m}_3), \quad \text{(C.1)}$$

$$\mathbf{d}_7 = \frac{1}{\sqrt{2}}(\mathbf{m}_1 \otimes \mathbf{m}_2 - \mathbf{m}_2 \otimes \mathbf{m}_1), \quad \mathbf{d}_8 = \frac{1}{\sqrt{2}}(\mathbf{m}_1 \otimes \mathbf{m}_3 - \mathbf{m}_3 \otimes \mathbf{m}_1),$$

$$\mathbf{d}_9 = \frac{1}{\sqrt{2}}(\mathbf{m}_3 \otimes \mathbf{m}_2 - \mathbf{m}_2 \otimes \mathbf{m}_3),$$

which naturally decomposes the tensor: first, into its symmetric and skew-symmetric parts, and then, the symmetric part into its hydrostatic and deviatoric parts. Accordingly, for the corresponding representation of a compliance tensor $\mathbb{M}$ in this basis in the case of the volumetrically isotropic material, it is always valid that

$$M_{1K} = 0, \quad K = 2, \ldots, 6, \tag{C.2}$$

and the inverse of M_{11} is the Kelvin bulk modulus. Additionally, for an incompressible material, one obtains $M_{11} = 0$. In such a case problems are analysed within the subspace of deviatoric tensors, and the corresponding matrices are 5×5 (or 8×8) dimensional.

Basis (C.1) is slightly different from the basis of similar property used by Tomé and Lebensohn [201]. Such a selection of the basis is motivated by its particular suitability when analysing a wide group of material anisotropy. Note that for materials of tetragonal symmetry with the main axis of anisotropy coaxial with $\mathbf{m}_3$ and the remaining two axes coaxial with $\mathbf{m}_1$ and $\mathbf{m}_2$, the only non-zero components in the representation of $\mathbb{M}$ are:

$$M_{11}, \quad M_{12}, \quad M_{22}, \quad M_{33}, \quad M_{44}, \quad M_{55} = M_{66} \,. \tag{C.3}$$

If material is transversely isotropic we additionally have $M_{33} = M_{44}$. Thus, if these materials are volumetrically isotropic, the corresponding representations are diagonal. For volumetrically isotropic materials which are orthotropic, we have seven non-zero components:

$$M_{11}, \quad M_{22}, \quad M_{23}, \quad M_{33}, \quad M_{44}, \quad M_{55}, \quad M_{66} \,. \tag{C.4}$$

The change of reference frames $\{\mathbf{m}_k\} \rightarrow \{\tilde{\mathbf{m}}_k\}$ in the three-dimensional physical space, specified by some 3×3 rotation matrix Q_{ij}, implies the change of bases $\mathbf{d}_K(\{\mathbf{m}_k\}) \rightarrow \mathbf{d}_K(\{\tilde{\mathbf{m}}_k\})$. The corresponding transformation of M_{KL} and a_K components is performed with the use of the orthogonal 6×6 matrix $[Q_D^6]$, according to the standard formulae:

$$\tilde{a}_K = [Q_D^6]_{KL} a_L, \quad \tilde{M}_{KL} = [Q_D^6]_{KN} [Q_D^6]_{LM} M_{NM} \,. \tag{C.5}$$

This matrix has the form

$$[Q_D^6] = [Q_D][R^6][Q_D]^T \,, \tag{C.6}$$

where $[R^6] = [R^6(Q_{ij})]$ is the representation of rotation matrix for the Kelvin notation [1] while the orthogonal matrix $[Q_D]$ transforms the representation from the Kelvin basis to the deviatoric basis and has the form

$$[Q_D] = \begin{bmatrix} 1/\sqrt{3} & 1/\sqrt{3} & 1/\sqrt{3} & 0 & 0 & 0 \\ -1/\sqrt{6} & -1/\sqrt{6} & 2/\sqrt{6} & 0 & 0 & 0 \\ 1/\sqrt{2} & -1/\sqrt{2} & 0 & 0 & 0 & 0 \\ 0 & 0 & 0 & 1 & 0 & 0 \\ 0 & 0 & 0 & 0 & 1 & 0 \\ 0 & 0 & 0 & 0 & 0 & 1 \end{bmatrix} \,. \tag{C.7}$$

As it can be easily deduced, for the matrix $[Q_D^6]$ it is always true that

$$[Q_D^6]_{11} = 1, \quad [Q_D^6]_{1K} = 0, \quad [Q_D^6]_{K1} = 0, \quad K = 2, \dots, 6 \,. \tag{C.8}$$

---

[1] The representation of this matrix in terms of Q_{ij} components can be found, e.g., in Mehrabadi et al. [132] or Stupkiewicz [189].

Bibliography

[1]   S. R. Agnew and Ö. Duygulu. Plastic anisotropy and the role of non-basal slip in magnesium alloy AZ31B. *Int. J. Plasticity*, 21:1161–1193, 2005.

[2]   S.R. Agnew, M.H. Yoo, and C.N. Tomé. Application of texture simulation to understanding mechanical behavior of Mg and solid solution alloys containing Li or Y. *Acta Mater.*, 49:4277–4289, 2001.

[3]   I. Agote, J. Coleto, M. Gutiérrez, A. Sargsyan, M. García de Cortazar, M.A. Lagos, I.P. Borovinskaya, A.E. Sytschev, V.L. Kvanin, N.T. Balikhina, S.G. Vadchenko, K. Lucas, A. Wisbey, and L. Pambaguian. Microstructure and mechanical properties of gamma TiAl based alloys produced by combustion synthesis + compaction route. *Intermetallics*, 16: 1310–1316, 2008.

[4]   L. Anand. Single-crystal elasto-viscoplasticity: application to texture evolution in polycrystalline metals at large strain. *Comput. Methods Appl. Mech. Engrg.*, 193:5359–5383, 2004.

[5]   L. Anand and M. Kothari. A computational procedure for rate independent crystal plasticity. *J. Mech. Phys. Solids*, 44(4):525–558, 1996.

[6]   F. Appel and R. Wagner. Microstructure and deformation of two-phase γ-titanium aluminides. *Mater. Sci. Engng. R.*, 22:187–268, 1998.

[7]   R. J. Asaro. Crystal plasticity. *J. Applied Mechanics*, 50:921–934, 1983.

[8]   R. J. Asaro and A. Needleman. Textured development and strain hardening in rate dependent polycrystals. *Acta Metall.*, 33(6):923–953, 1985.

[9]   S. Asgari, E. El-Danaf, S. R. Kalidindi, R. D. Doherty, and C. Necker. Strain hardening regimes and microstructural evolution during large strain compression of low stacking fault energy fcc alloys that form deformation twins. *Metal. Mater Trans. A*, 28:1781–1795, 1997.

[10]   A. Bartels, H. Kestler, and H. Clemens. Deformation behavior of differently processed γ-titanium aluminides. *Mater. Sci. Engng. A*, 329-331: 153–162, 2002.

[11]   Z.S. Basinski, M.S. Szczerba, M. Niewczas, J.D. Embury, and S.J. Basin-
       ski. The transformation of slip dislocations during twinning of copper-
       aluminum alloy crystals. *Rev. Metall.*, 94:1037–1043, 1997.

[12]   J. G. Berryman. Bounds and self-consistent estimates for elastic con-
       stants of random polycrystals with hexagonal, trigonal, and tetragonal
       symmetries. *J. Mech. Phys. Solids*, 53:2141–2173, 2005.

[13]   J. G. Berryman. Bounds and estimates for elastic constants of random
       polycrystals of laminates. *Int. J. Solids Structures*, 42:3730–3743, 2005.

[14]   M. Berveiller and A. Zaoui. An extension of the self-consistent scheme to
       the plastically flowing polycrystals. *J. Mech. Phys. Solids*, 26:325, 1979.

[15]   I.J. Beyerlein and C. N. Tomè. Modeling transients in the mechanical
       response of copper due to strain path changes. *Int. J. Plasticity*, 23:
       640–664, 2007.

[16]   J. F. Bishop and R. Hill. A theory of the plastic distortion of a polycry-
       stalline aggregate under combined stresses. *Philos. Mag.*, 42(Ser. VII):
       414–427, 1951.

[17]   J. F. Bishop and R. Hill. A theoretical derivation of the plastic properties
       of a polycrystalline face-centred metal. *Philos. Mag.*, 42(Ser. VII):1298–
       1307, 1951.

[18]   T. Böhlke and A. Bertram. Isotropic orientation distributions of cubic
       crystals. *J. Mech. Phys. Solids*, 49:2459–2470, 2001.

[19]   M. Bornert, R. Masson, P. Ponte Castañeda, and A. Zaoui. Second-
       order estimates for the effective behaviour of viscoplastic polycrystalline
       materials. *J. Mech. Phys. Solids*, 49:2737–2764, 2001.

[20]   R. Brenner, R.A. Lebensohn, and O. Castelnau. Elastic anisotropy and
       yield surface estimates of polycrystals. *Int. J. Solids Structures*, 46:3018–
       3026, 2009.

[21]   R. A. Brockman. Analysis of elastic-plastic deformation in TiAl polycry-
       stals. *Int. J. Plasticity*, 19:1749–1772, 2003.

[22]   A. Broohm, P. Zattarin, and P. Lipinski. Prediction of mechanical beha-
       viour of inhomogeneous and anisotropic materials using an incremental
       scheme. *Arch. Mech.*, 6:949–967, 2000.

[23]   B. Budiansky. The elastic moduli of some heterogeneous materials. *J.
       Mech. Phys. Solids*, 13:223–227, 1965.

[24]   B. Budiansky and T. T. Wu. Theoretical prediction of plastic strains of
       polycrystals. *Proc. 4th U.S. Nat. Congr. Appl. Mech.*, pages 1175–1185,
       1962. ASME, New York.

[25] H. J. Bunge. *Texture Analysis in Material Science. Mathematical Methods.* London: Butterworths, 1982.

[26] W. T. Burzyński. *Studium nad hipotezami wytężenia.* Lwów, 1928. (także Dzieła Wybrane, t. I, PWN, Warszawa 1982).

[27] E. P. Busso and G. Cailletaud. On the selection of active slip systems in crystal plasticity. *Int. J. Plasticity*, 21:2212–2231, 2005.

[28] G. Cailletaud. A micromechanical approach to inelastic behaviour of metals. *Int. J. Plasticity*, 8:55–73, 1992.

[29] J.L. Chaboche, P. Kanoute, and A. Roos. On the capabilities of mean-field approaches for the description of plasticity in metal-matrix composites. *Int. J. Plasticity*, 21:1409–1434, 2005.

[30] P. Chadwick, M. Vianello, and S. C. Cowin. A new proof that the number of linear elastic symmetries is eight. *J. Mech. Phys. Solids*, 49:2471–2492, 2001.

[31] M. Cherkaoui, H. Sabar, and M. Berveiller. Micromechanical approach of the coated inclusion problem and applications to composite materials. *J. Eng. Mater. Technol.*, 116:274–278, 1994.

[32] G. Y. Chin, W. F. Hosford, and D. R. Mendorf. Accommodation of constrained deformation in f.c.c. metals by slip and twinning. *Proc. R. Soc. A*, 309:433–456, 1969.

[33] R. M. Christensen. Viscoelastic properties of heterogeneous media. *J. Mech. Phys. Solids*, 17:23–41, 1969.

[34] R. M. Christensen. *Mechanics of Composite Materials.* Dover Publications, 2005.

[35] R.M. Christensen and K. H. Lo. On the effective moduli of composite materials: effect of fiber length and geometry at dilute concentrations. *Z. Angew. Math. Phys.*, 24:581, 1979.

[36] J. W. Christian and S. Mahajan. Deformation twinning. *Progress in Materials Science*, 39:1–157, 1995.

[37] S. C. Cowin and M. M. Mehrabadi. Anisotropic symmetries of linear elasticity. *Appl. Mech. Rev.*, 48(5):247–285, 1995.

[38] S.C. Cowin, G. Yang, and M.M. Mehrabadi. Bounds on the effective anisotropic elastic constants. *J. Elasticity*, 57:1–24, 1999.

[39] G. de Botton and P. Ponte Castañeda. Variational estimates for the creep behavior of polycrystals. *Proc. R. Soc. Lond. A*, 448:121–142, 1995.

[40] L. Delannay, R. E. Loge, Y. Chastel, and P. Van Houtte. Prediction of intergranular strains in cubic metals using a multisite elastic-plastic model. *Acta Mater.*, 50:5127–5138, 2002.

[41] I. Doghri, L. Adam, and N. Bilger. Mean-field homogenization of elasto-viscoplastic composites based on a general incrementally affine linearization method. *Int. J. Plasticity*, 26:219–238, 2010.

[42] B. J. Duggan, M. Hatherly, W. B. Hutchinson, and P. T. Wakefield. Deformation structures and textures in cold-rolled 70:30 brass. *Metal. Sci.*, 12:343–351, 1978.

[43] M. K. Duszek-Perzyna and P. Perzyna. Analysis of anisotropy and plastic spin effects on localization phenomena. *Archive of Applied Mechanics*, 68: 352–374, 1998.

[44] G.J. Dvorak and Y. Benveniste. On transformation strains and uniform fields in multiphase elastic media. *Proc. R. Soc. Lond. A*, 437:291—-310, 1992.

[45] E. El-Danaf, S. R. Kalidindi, R. D. Doherty, and C. Necker. Deformation texture transition in brass: critical role of micro-scale shear bands. *Acta Mater.*, 48:2665–2673, 2000.

[46] E. El-Danaf, S. R. Kalidindi, and R. D. Doherty. Influence of deformation path on the strain hardening behavior and microstructure evolution in low sfe fcc metals. *Int. J. Plasticity*, 17:1245–1265, 2001.

[47] A. El Omri, A. Fennan, F. Sidoroff, and A. Hihi. Elastic-plastic homogenization for layered composites. *Eur. J. Mech. A/Solids*, 19:585–601, 2000.

[48] A. T. English and G. Y. Chin. On the variation of wire texture with stacking fault energy in f.c.c. metals and alloys. *Acta Metall.*, 13:1013, 1965.

[49] J.D. Eshelby. The determination of the elastic field of an ellipsoidal inclusion, and related problems. *Proc. Roy. Soc. A*, 241:376–396, 1957.

[50] F. D. Fischer, T. Schaden, F. Appel, and H. Clemens. Mechanical twins, their development and growth. *Eur. J. Mech. A/Solids*, 22:709–726, 2003.

[51] S. Forte and M. Vianello. Symmetry classes for elasticity tensors. *J. Elasticity*, 43:81–108, 1996.

[52] S. Forte and M. Vianello. Functional bases for transversely isotropic and transversely hemitropic invariants of elasticity tensor. *Q. Jl. Mech. Appl. Math.*, 51:543–552, 1998.

[53] W. Gambin. Plasticity of crystals with interacting slip systems. *Engng. Trans.*, 39(3–4):303–324, 1991.

[54] W. Gambin. Refined analysis of elastic–plastic crystals. *Int. J. Solids Structures*, 29(16):2013–2021, 1992.

[55] W. Gambin and K. Kowalczyk. *Plastyczność metali (Plasticity of Metals)*. Oficyna Wydawnicza PW, 2003.

[56] P. Gilormini, M.V. Nebozhyn, and P. Ponte Castañeda. Accurate estimates for the creep behaviour of hexagonal polycrystals. *Acta Mater.*, 49: 329–337, 2001.

[57] Z. Hashin. Theory of mechanical behaviour of heterogeneous media. *Appl. Mech. Rev.*, 17:1–9, 1964.

[58] Z. Hashin. The inelastic inclusion problem. *Int. J. Engng Sci.*, 7:11–36, 1969.

[59] Z. Hashin and S. Shtrikman. On some variational principles in anisotropic and nonhomogeneous elasticity. *J. Mech. Phys. Solids*, 10:335–342, 1962.

[60] Z. Hashin and S. Shtrikman. A variational approach to the theory of the elastic behaviour of polycrystals. *J. Mech. Phys. Solids*, 10:343–352, 1962.

[61] K. S. Havner. *Finite Plastic Deformation of Crystalline Solids*. Cambridge University Press, 1992.

[62] A.V. Hershey. The elasticity of an isotropic aggregate of anisotropic cubic crystals. *J. Appl. Mech.*, 21:236–240, 1954.

[63] E. Herve and A. Zaoui. Modelling the effective behavior of non-linear matrix-inclusion composites. *Eur. J. Mech. A/Solids*, 9:505–516, 1990.

[64] W. Heye and G. Wassermann. The formation of the rolling textures in fcc metals by slip and twinning. *Scripta Metall.*, 2:205–207, 1968.

[65] R. Hill. Elastic properties of reinforced solids: some theoretical principles. *J. Mech. Phys. Solids*, 11:357–372, 1963.

[66] R. Hill. Continuum micro-mechanics of elastoplastic polycrystals. *J. Mech. Phys. Solids*, 13:89–101, 1965.

[67] R. Hill. A self-consistent mechanics of composite materials. *J. Mech. Phys. Solids*, 13:213–222, 1965.

[68] R. Hill and J. R. Rice. Constitutive analysis of elastic–plastic crystals at arbitrary strain. *J. Mech. Phys. Solids*, 20:401–413, 1972.

[69] J. W. Hutchinson. Bounds and self-consistent estimates for creep of polycrystalline materials. *Proc. R. Soc. Lond. A*, 348:101–127, 1976.

[70] J.W. Hutchinson. Elastic-plastic behavior of polycrystalline metals and composites. *Proc. Roy. Soc. Lond. A*, 319:247–272, 1970.

[71] J.W. Hutchinson. Creep and plasticity of hexagonal polycrystals as related to single crystal slip. *Metal. Trans. A*, 8A:1465–1469, 1977.

[72] T. Iwakuma and S. Nemat-Nasser. Finite elastic-plastic deformation of polycrystalline metals. *Proc. R. Soc. Lond. A*, 394:87–119, 1984.

[73] L. Jiang and J. J. Jonas. Effect of twinning on the flow behavior during strain path reversals in two Mg (+Al, Zn, Mn) alloys. *Scripta Mater.*, 58: 803–806, 2008.

[74] L. Jiang, J.J. Jonas, R.K. Mishra, A.A. Luo, A.K. Sachdev, and S. Godet. Twinning and texture development in two Mg alloys subjected to loading along three different strain paths. *Acta Mater.*, 55:3899–3910, 2007.

[75] S. R. Kalidindi. Incorporation of twinning in crystal plasticity models. *J. Mech. Phys. Solids*, 46:267–290, 1998.

[76] S. R. Kalidindi. Modeling anisotropic strain hardening and deformation textures in low stacking fault energy fcc metals. *Int. J. Plasticity*, 17: 837–860, 2001.

[77] S. R. Kalidindi and L. Anand. Macroscopic shape change and evolution of crystallographic texture in pre-textured fcc metals. *J. Mech. Phys. Solids*, 42:459–490, 1994.

[78] S. R. Kalidindi, C. A. Bronkhorst, and L. Anand. Crystallographic texture evolution in bulk deformation processing of fcc metals. *J. Mech. Phys. Solids*, 40:537–569, 1992.

[79] I. Karaman, H. Sehitoglu, A. J. Beaudoin, Y. I. Chumlyakov, H. J. Maier, and C. N. Tomé. Modeling the deformation behavior of Hadfield steel single and polycrystals due to twinning and slip. *Acta Mater.*, 48:2031–2047, 2000.

[80] I. Karaman, H. Sehitoglu, Y. I. Chumlyakov, H. J. Maier, and I. V. Kireeva. The effect of twinning and slip on the Bauschinger effect of Hadfield steel single crystals. *Metal. Mater. Trans. A*, 32A:695–706, 2001.

[81] G. C. Kaschner, C. N. Tomé, I. J. Beyerlein, S. C. Vogel, D. W. Brown, and R. J. McCabe. Role of twinning in the hardening response of zirconium during temperature reloads. *Acta Mater.*, 54:2887–2896, 2006.

[82] G. C. Kaschner, C. N. Tomé, R. J. McCabe, A. Misra, S. C. Vogel, and D. W. Brown. Exploring the dislocation/twin interactions in zirconium. *Mater. Sci. Eng. A*, 463:122–127, 2007.

[83] R. Kiryk. Micromechanical model of viscoplastic polycrystalline materials (in Polish). PhD Thesis 38/1992, IFTR Reports, 1992.

[84] R. Kiryk and H. Petryk. A self-consistent model of rate dependent plasticity of polycrystals. *Arch. Mech.*, 50:247–263, 1998.

[85] K. Kishida, H. Inui, and M. Yamaguchi. Deformation of PST crystals of a TiAl/Ti$_3$Al two-phase alloy at 1000°C. *Intermetallics*, 7:1131–1139, 1999.

[86] G. Kneer. Die elastischen Konstanten quasiisotroper Vielkristallaggregate. *Physica Status Solidi (b)*, 3:K331–K335, 1963.

[87] G. Kneer. Uber die berechnung der Elastizitatsmoduln vielkristalliner Aggregate mit textur. *Phys. Stat. Sol.*, 9, 1965.

[88] U. F. Kocks, C. N. Tomé, and H.-R. Wenk. *Texture and Anisotropy.* Cambridge University Press, II edition, 2000.

[89] U.F. Kocks and H. Chandra. Slip geometry in partially constrained deformation. *Acta Metall.*, 30:695, 1982.

[90] U.F. Kocks and H. Mecking. Physics and phenomenology of strain hardening: the FCC case. *Progress in Materials Science*, 48:171–273, 2003.

[91] J. Koike. Enhanced deformation mechanisms by anisotropic plasticity in polycrystalline Mg alloys at room temperature. *Metal. Mater. Trans. A*, 36A:1689–1696, 2005.

[92] Y. Koizumi, T. Nakano, and Y. Umakoshi. Plastic deformation and fracture behaviour of Ti$_3$Al single crystals deformed at high temperature under cyclic loading. *Acta Mater.*, 47:2019–2029, 1999.

[93] R. Kouddane, A. Molinari, and G.R. Canova. *Proceedings of the International Seminar MECAMAT'91, Fontenblau/France/7-8 August 1991*, chapter Self-consistent modelling of heterogeneous viscoelastic and elastoviscoplastic materials, pages 129–141. A.A.Balkema, 1993.

[94] K. Kowalczyk. Evolution of plastic anisotropy of the polycrystalline materials in large deformation processes. *Engng. Trans.*, 49(4):537–571, 2001.

[95] K. Kowalczyk and W. Gambin. Model of plastic anisotropy evolution with texture-dependent yield surface. *Int. J. Plasticity*, 20:19–54, 2004.

[96] K. Kowalczyk and J. Ostrowska-Maciejewska. Energy-based limit conditions for transversally isotropic solids. *Arch. Mech.*, 54(5-6):497–523, 2002.

[97] K. Kowalczyk-Gajewska. Micromechanical modelling of polycrystalline materials at large plastic deformations. (Modelowanie materiałów polikrystalicznych w zakresie dużych deformacji plastycznych). *CD Proceedings of I Congress of Polish Mechanics*, 2007. In Polish.

[98] K. Kowalczyk-Gajewska. Multiscale modelling of intermetallics of lamellar microstructure at finite strains. *IUTAM Symposium Multi-Scale Plasticity of Crystalline Materials, Nov. 5-9, 2007. Book of Abstracts*, pages 79–80, 2007.

[99] K. Kowalczyk-Gajewska. Bounds and self-consistent estimates of overall properties for random polycrystals described by linear constitutive laws. *Arch. Mech.*, 61(6):475–503, 2009.

[100] K. Kowalczyk-Gajewska. Modelling of texture evolution in metals accounting for lattice reorientation due to twinning. *Eur. J. Mech. Solids/A*, 29:28–41, 2010.

[101] K. Kowalczyk-Gajewska. Comparison of three-scale and two-scale modelling of polycrystalline materials with lamellar substructure. *CD Proceedings of IV European Conference on Computational Mechanics, ECCM 2010, Paris, May 16-21*, 2010.

[102] K. Kowalczyk-Gajewska and J. Ostrowska-Maciejewska. *Mechanics of the 21st Century, Proceedings of the 21st International Congress of Theoretical and Applied Mechanics Warsaw, Poland, 15-21 August 2004*, chapter On the invariants of the elasticity tensor for orthotropic materials. Springer (e-book), 2004.

[103] K. Kowalczyk-Gajewska and J. Ostrowska-Maciejewska. The influence of internal restrictions on the elastic properties of anisotropic materials. *Arch. Mech*, 56:205–232, 2004.

[104] K. Kowalczyk-Gajewska and J. Ostrowska-Maciejewska. Review on spectral decomposition of Hooke's tensor for all symmetry groups of linear elastic material. *Engng. Trans.*, 57:145–183, 2009.

[105] K. Kowalczyk-Gajewska and A. Roos. Intermetallics with lamellar microstructure: finite strain modelling. *Modelling of Microstructure Media II. Abstracts. Łódź, 19.09.2008*, pages 17–19, 2008.

[106] K. Kowalczyk-Gajewska, Z. Mróz, and R. B. Pęcherski. Micromechanical modelling of polycrystalline materials under non-proportional deformation paths. *Arch. Metall. Mater.*, 52:181–192, 2007.

[107] E. Kröner. Berechnung der elastischen Konstanten des Vielkristalls aus

den Konstanten des Einkristalls. *Zeitschrift fur Physik A*, 151:504–518, 1958.

[108] E. Kröner. Zur plastischen Verformung des Vielkristalls. *Acta Met.*, 9: 155–161, 1961.

[109] N. Lahellec and P. Suquet. On the effective behavior of nonlinear inelastic composites: I. Incremental variational principles. *J. Mech. Phys. Solids*, 55:1932–1963, 2007.

[110] A. Lasalmonie. Intermetallics: Why is it so difficult to introduce them in gas turbine engines? *Intermetallics*, 14:1123–1129, 2006.

[111] N. Laws and R. McLaughlin. Self-consistent estimates for viscoelastic creep compliance of composite materials. *Proc. R. Soc. Lond. A*, 359: 251–273, 1978.

[112] R. A. Lebensohn and C. N. Tomé. A self-consistent anisotropic approach for the simulation of plastic deformation and texture development of polycrystals: Application to zirconium alloys. *Acta Metall. Mater.*, 41: 2611–2624, 1993.

[113] R. A. Lebensohn, H. Uhlenhut, C. Hartig, and H. Mecking. Plastic flow of γ-TiAl-based polysynthetically twinned crystals: micromechanical modelling and experimental validation. *Acta Mater.*, 46:229–236, 1998.

[114] R.A. Lebensohn, Y. Liu, and P. Ponte Castañeda. On the accuracy of the self-consistent approximation for polycrystals: comparison with full-field numerical simulations. *Acta Mater.*, 52:5347–5361, 2004.

[115] E. H. Lee. Elastic–plastic deformation at finite strains. *J. Appl. Mech.*, 36(1), 1969.

[116] T. Leffers and D. Juul Jensen. The relation between texture and microstructure in rolled fcc materials. *Text. Microstruct.*, 14–18:933–952, 1991.

[117] T. Leffers and R.K. Ray. The brass-type texture and its deviation from the copper-type texture. *Progress in Materials Science*, 54:351–396, 2009.

[118] T. Leffers and P. Van Houtte. Calculated and experimental orientation distributions of twin lamellae in rolled brass. *Acta metall.*, 37:1191–1198, 1989.

[119] V.M. Levin. On the coefficients of thermal expansion of heterogeneous media. *Mekh. Tverd. Tela (In Russian)*, 88, 1968.

[120] S. Li and G. Wang. *Introduction to Micromechanics and Nanomechanics*. World Scientific, 2008.

[121] P. Lipinski, J. Krier, and M. Berveiller. Elastoplasticite des metaux en grandes deformations: Comportement global et evolution de la structure interne. *Rev Phys. Appl.*, 25:361, 1990.

[122] X.Y. Lou, M. Li, R.K. Boger, S.R. Agnew, and R.H. Wagoner. Hardening evolution of AZ31B Mg sheet. *Int. J. Plasticity*, 23:44–86, 2007.

[123] S. Mahajan and G.Y. Chin. Twin-slip, twin-twin and slip-twin interactions in Co-8 wt.% Fe alloy single crystals. *Acta Metall.*, 21:173–179, 1973.

[124] E. B. Marin and P. R. Dawson. Elastoplastic finite element analyses of metal deformations using polycrystal constitutive model. *Comput. Methods Appl. Mech. Engrg.*, 165:23–41, 1998.

[125] W. T. Marketz, F. D. Fischer, F. Kauffmann, G. Dehm, T. Bidlingmaier, A. Wanner, and H. Clemens. On the role of twinning during room temperature deformation of γ-TiAl based alloys. *Mater. Sci. Eng. A*, 329-331: 177–183, 2002.

[126] R. Masson and A. Zaoui. Self-consistent estimates of the rate-dependent elasto-plastic behaviour of polycrystalline materials. *J. Mech. Phys. Solids*, 47:1543–1568, 1999.

[127] R. Masson, M. Bornert, P. Suquet, and A. Zaoui. An affine formulation for the prediction of the effective properties of non-linear composites and polycrystals. *J. Mech. Phys. Solids*, 48:1203–1227, 2000.

[128] K. K. Mathur and P. R. Dawson. On modelling the development of the crystallografic texture in a bulk forming processes. *Int. J. Plasticity*, 5: 67–94, 1989.

[129] R. J. McCabe, G. Proust, E.K. Cerreta, and A. Misra. Quantitative analysis of deformation twinning in zirconium. *Int. J. Plasticity*, 25:454–472, 2009.

[130] R. McLaughlin. A study of the differential scheme for composite materials. *Int. J. Engrg. Sci.*, 15:237–244, 1977.

[131] H. Mecking, U. F. Kocks, and Ch. Hartig. Taylor factors in materials with many deformation modes. *Scripta Materialia*, 35:465–471, 1996.

[132] M. Mehrabadi, S.C. Cowin, and J. Jaric. Six-dimensional orthogonal tensor representation of the rotation about an axis in three dimensions. *Int. J. Solids Structures*, 32:439–449, 1995.

[133] S. Mercier and A. Molinari. Homogenization of elastic-viscoplastic heterogeneous materials: Self-consistent and Mori-Tanaka schemes. *Int. J. Plasticity*, 25:1024–1048, 2009.

[134] S. Mercier, N. Jacques, and A. Molinari. Validation of an interaction law for the Eshelby inclusion problem in elasto-viscoplasticity. *Int. J. Solids Structures*, 42:1923–1941, 2005.

[135] A. Molinari. *Large plastic deformation of crystalline aggregates*, chapter Self-consistent estimates of plastic and viscoplastic polycrystalline materials, pages 173–245. Springer Wien New York, 1997.

[136] A. Molinari. Averaging models for heterogeneous viscoplastic and elastic viscoplastic materials. *Transactions of the ASME*, 124:62–70, 2002.

[137] A. Molinari and L. Toth. Tuning a self-consistent viscoplastic model by finite element results I: Modelling. *Acta Metall. Mater.*, 42:2453–2458, 1994.

[138] A. Molinari, G.R. Canova, and S. Ahzi. Self-consistent approach of the large deformation polycrystal visco-plasticity. *Acta Metall.*, 35:2983–2994, 1987.

[139] A. Molinari, S. Ahzi, and R. Kouddane. On the self-consistent modeling of elastic-plastic behavior of polycrystals. *Mech. Mater.*, 26:43–62, 1997.

[140] T. Mori and K. Tanaka. Average stress in matrix and average elastic energy of materials with misfitting inclusions. *Acta Metall.*, 21:571–574, 1973.

[141] Z. Mróz, editor. *State of the Art Report on Knowledge-based Multicomponent Materials*, volume 1, Intermetallics: Properties, Modelling and Applications. KMM, 2006.

[142] T. Nakano, B. Ogawa, Y. Koizumi, and Y. Umakoshi. Plastic deformation behaviour and dislocation structure in Ti_3Al single crystals cyclically deforming by prism slip. *Acta Mater.*, 46:4311–4324, 1998.

[143] M. V. Nebozhyn, P. Gilormini, and P. Ponte-Castañeda. Variational self-consistent estimates for cubic viscoplastic polycrystals: the effects of grain anisotropy and shape. *J. Mech. Phys. Solids*, 49:313–340, 2001.

[144] S. Nemat-Nasser. Averaging theorems in finite deformation plasticity. *Mech. Mater.*, 31:493–523, 1999.

[145] S. Nemat-Nasser and M. Hori. *Micromechanics: overall properties of heterogeneous materials*. North-Holland Elsevier, 1999.

[146] S. Nemat-Nasser, L. Ni, and T. Okinaka. A constitutive model for fcc crystals with application to polycrystalline ofhc copper. *Mech. Mater.*, 30:325–341, 1998.

[147] S. Nikolov, R.A. Lebensohn, and D. Raabe. Self-consistent modeling of large plastic deformation, texture and morphology evolution in semi-crystalline polymers. *J. Mech. Phys. Solids*, 54:1350–1375, 2006.

[148] KMM NoE. DNRT 1-1.2-3(a) Complete results of experimental approach and characterization. Internal report, LMT Cachan, University of Metz, IPPT PAN and IMZ PAN, 2007.

[149] KMM NoE. DNRT 1-1.2-4(c) Texture measurements and microstructure determination of TiAl, FeAl materials processed by partners. Internal report, Universita Politecnica delle Marche (A. Manescu and A. Giuliani), 2007.

[150] KMM NoE. DNRT 1-1.3-6(c) Comparison of the predictions of the ONE-RA and IPPT models concerning the macroscopic mechanical response of TiAl (prepared by K. Kowalczyk-Gajewska and H. Petryk (IPPT PAN), Arjen Roos (ONERA), S. Mercier (University of Metz)). Internal report, 2008.

[151] R. W. Ogden. *Non-linear Elastic Deformations*. Dover Publication, Mineola, New York, 2 edition, 1997.

[152] H. Ogi, S. Kai, H. Ledbetter, R. Tarumi, M. Hirao, and K. Takashima. Titanium's high-temperature elastic constants through the hcp–bcc phase transformation. *Acta Mater.*, 52:2075–2080, 2004.

[153] J. Ostrowska-Maciejewska and J. Rychlewski. Generalized proper states for anisotropic elastic materials. *Arch. Mech.*, 53(4-5):501–518, 2001.

[154] V. Paidar and M. Yamaguchi. Constrained deformation of a lamellar structure. *Mater. Sci. Engng A*, 462:460–464, 2007.

[155] A. Paquin, H. Sabar, and M. Berveiller. Integral formulation and self-consistent modelling of elastoviscoplastic behavior of heterogeneous materials. *Arch. Appl. Mech.*, 69:14–35, 1999.

[156] B. Peeters, M. Seefeldt, C. Teodosiu, S.R. Kalidindi, P. Van Houtte, and E. Aernoudt. Work-hardening/softening behaviour of b.c.c. polycrystals during changing strain paths: I. An integrated model based on substructure and texture evolution, and its prediction of the stress-strain behaviour of an IF steel during two-stage strain paths. *Acta Mater.*, 49:1607–1619, 2001.

[157] L. Peselnick and R. Meister. Variational method of determining effective moduli of polycrystals: (A) hexagonal symmetry, (B) trigonal symmetry. *J. Appl. Phys.*, 60:3120–3124, 1986.

[158] H. Petryk. General conditions for uniqueness in materials with multiple mechanisms of inelastic deformation. *J. Phys. Mech. Solids*, 48:367–396, 2000.

[159] H. Petryk and S. Stupkiewicz. A quantitative model of grain refinement and strain hardening during severe plastic deformation. *Mater. Sci. Engng. A*, 444:214–219, 2007.

[160] D.C. Pham. Elastic moduli of perfectly random polycrystalline aggregate. *Philos. Mag. A*, 76:31–44, 1997.

[161] D.C. Pham. Asymptotic estimates on uncertainty of the elastic moduli of completely random trigonal polycrystals. *Int. J. Solids Struct.*, 40: 4911–4924, 2003.

[162] O. Pierard and I. Doghri. An enhanced affine formulation and the corresponding numerical algorithms for the mean-field homogenization of elasto-viscoplastic composites. *Int. J. Plasticity*, 22:131–157, 2006.

[163] O. Pierard, J. LLorca, J. Segurado, and I. Doghri. Micromechanics of particle-reinforced elasto-viscoplastic composites: Finite element simulations versus affine homogenization. *Int. J. Plasticity*, 23:1041–1060, 2007.

[164] P. Ponte Castañeda. Exact second-order estimates for the effective mechanical properties of nonlinear composite materials. *J. Mech. Phys. Solids*, 44:827–862, 1996.

[165] P. Ponte Castañenda. The effective mechanical properties of nonlinear isotropic composites. *J. Mech. Phys. Solids*, 39:45–71, 1991.

[166] P. Ponte Castañenda and P. Suquet. Nonlinear composites. *Adv. Appl. Mech.*, 34:171–302, 1998.

[167] J. Pospiech. Effects in the texture and microstructure in some metals of cubic and hexagonal symmetry caused by the change of the rolling direction. *Acta Metal. Mater.*, 53:83–87, 2008.

[168] J. Pospiech, M. Ostafin, and R. Schwarzer. The effect of rolling geometry on the texture and microstructure in AZ31 and copper. *Acta Metal. Mater.*, 51:37–42, 2006.

[169] G. Proust, C. N. Tomé, and G. C. Kaschner. Modeling texture, twinning and hardening evolution during deformation of hexagonal materials. *Acta Mater.*, 55:2137–2148, 2007.

[170] G. Proust, C.N. Tomé, A. Jain, and S.R. Agnew. Modeling the effect of twinning and detwinning during strain-path changes of magnesium alloy AZ31. *Int. J. Plasticity*, 25:861–880, 2009.

[171] Y.U. Qui and G.J. Weng. Elastic constants of a polycrystal with transversally isotropic grains, and the influence of precipitates. *Mech. Mater.*, 12:1–15, 1991.

[172] B. Raniecki and Z. Mróz. *Inelastic Solids and Structures (Antoni Sawczuk memorial volume)*, chapter On the strain-induced anisotropy and texture in rigid-plastic solids. Prineridge Press, Swansea, U.K., 1990.

[173] A. Roos, J.-L. Chaboche, L. Gelebart, and J. Crepin. Multiscale modelling of titanium aluminides. *Int. J. Plasticity*, 20:811—-830, 2004.

[174] Y. Rougier, C. Stolz, and A. Zaoui. Representation spectrale en viscoèlasticité linéaire de matériaux hétérogènes. *C. R. Acad. Sci. Paris*, 316, Serie II:1517–1522, 1993.

[175] Y. Rougier, C. Stolz, and A. Zaoui. Self-consistent modelling of elastic-viscoplastic polycrystals. *C. R. Acad. Sci. Paris*, 318, Serie II:145–151, 1994.

[176] J. Rychlewski. CEIIINOSSSTTUV. Mathematical structure of elastic bodies. Technical Report 217, Inst. Mech. Probl. USSR Acad. Sci., Moskva, 1983. In Russian.

[177] J. Rychlewski. Unconventional approach to linear elasticity. *Arch. Mech.*, 47(2):149–171, 1995.

[178] J. Rychlewski. A qualitative approach to Hooke's tensors. Part I. *Arch. Mech.*, 52:737–759, 2000.

[179] J. Rychlewski. Elastic waves under unusual anisotropy. *J. Mech. Phys. Solids*, 49:2651–2666, 2001.

[180] J. Rychlewski. A qualitative approach to Hooke's tensors. Part II. *Arch. Mech.*, 53:45–63, 2001.

[181] H. Sabar, M. Berveiller, V. Favier, and S. Berbenni. A new class of micro-macro models for elastic-viscoplastic heterogeneous materials. *Int. J. Solids Structures*, 39:3257–3276, 2002.

[182] A. A. Salem, S. R. Kalidindi, and S. L. Semiatin. Strain hardening due to deformation twinning in α-titanium: Constitutive relations and crystal plasticity modeling. *Acta Mater.*, 53:3495–3502, 2005.

[183] A.A. Salem, S.R. Kalidindi, R.D. Doherty, and S.L. Semiatin. Strain hardening due to deformation twinning in α-Titanium: Mechanisms. *Metal. Mater. Trans. A*, 37A:259–268, 2006.

[184] W. Schillinger, B. Lorenzen, and A. Bartels. Anisotropic mechanical behavior of textured γ-TiAl caused by the directionality of twinning. *Mater. Sci. Engng. A*, 329-331:644–648, 2002.

[185] J.C. Simo and T.J.R. Hughes. *Computational Inelasticity*. Springer, 1998.

[186] A. Staroselsky and L. Anand. Inelastic deformation of polycrystalline face centered cubic materials by slip and twinning. *J. Mech. Phys. Solids*, 46: 671–696, 1998.

[187] A. Staroselsky and L. Anand. A constitutive model for hcp materials deforming by slip and twinning: application to magnesium alloy AZ31B. *Int. J. Plasticity*, 19:1843–1864, 2003.

[188] R. Staroszczyk. A multi-grain model for migration recrystallization in polar ice. *Arch. Mech.*, 61:259–282, 2009.

[189] S. Stupkiewicz. Micromechanics of contact and interphase layers. Habilitation Thesis 2/2005, IFTR Reports, 2005.

[190] S. Stupkiewicz and H. Petryk. Modelling of laminated microstructures in stress-induced martensitic transformations. *J. Phys. Mech. Solids*, 50: 2303–2331, 2002.

[191] S. Stupkiewicz and H. Petryk. A bi-crystal aggregate model of pseudoelastic behaviour of shape-memory alloy polycrystals. *Int. J. Mech. Sci.*, 52:219–228, 2010.

[192] P. Suquet. *Homogenization Techniques for Composite Media*, chapter Elements of homogenization for inelastic solid mechanics, pages 193–278. Springer-Verlag, Berlin, 1985.

[193] M. S. Szczerba, T. Bajor, and T. Tokarski. Is there a critical resolved shear stress for twinning in face-centered cubic crystals? *Philos. Mag.*, 84:481–502, 2004.

[194] D.R.S. Talbot and J.R. Willis. Variational principles for inhomogeneous non-linear media. *IMA J. Appl. Math.*, 35:39–54, 1985.

[195] K. Tanaka. Single-crystal elastic constants of γ-TiAl. *Phil. Mag. Lett.*, 73:71–78, 1996.

[196] K. Tanaka and M. Koiwa. Single-crystal elastic constants of intermetallic compounds. *Intermetallics*, 4:29–39, 1996.

[197] K. Tanaka, K. Okamoto, H. Inui, Y. Minonishi, M. Yamaguchi, and M. Koiwa. Elastic constants and their temperature dependence for the intermetallic compound Ti3Al. *Philos. Mag. A*, 73:1475–1488, 1996.

[198] G.P. Tandon and G.J. Weng. A theory of particle-reinforced plasticity. *ASME J. Appl. Mech.*, 55:126–135, 1988.

[199] G. I. Taylor. Plastic strain in metals. *Journal of Institute of Metals*, 62: 307–324, 1938.

[200] C. N. Tomé, R. A. Lebensohn, and U. F. Kocks. A model for texture development dominated by deformation twinning: application to zirconium alloy. *Acta Metal. Mater.*, 39:2667–2680, 1991.

[201] C.N. Tomé and R.A. Lebensohn. Manual for Code Visco-Plastic Self-Consistent (VPSC). Version 7b. Technical report, Los Alamos National Labolatory, May 2, 2007.

[202] C.N. Tomé, R.A. Lebensohn, and C.T. Necker. Mechanical anisotropy and grain interaction in recrystallized aluminum. *Metal. Mater. Trans. A*, 33A:2635–2648, 2002.

[203] P. Van Houtte. Simulation of the rolling texture and shear texture of brass by the Taylor theory adapted for mechanical twinning. *Acta Metal.*, 26: 591–604, 1978.

[204] P. Van Houtte. On the equivalence of the relaxed Taylor theory and the Bishop-Hill theory for partially constrained plastic deformation of crystal. *Mater. Sci. Eng.*, 55:69–77, 1982.

[205] P. Van Houtte, L. Delannay, and I. Samajdar. Quantitative prediction of cold rolling textures in low carbon steel by means of the LAMEL model. *Textures and Microtextures*, 31:109–149, 1999.

[206] P. Van Houtte, L. Delannay, and S. R. Kalidindi. Comparison of two grain interaction models for polycrystal plasticity and deformation texture prediction. *Int. J. Plasticity*, 18:359–377, 2002.

[207] P. Van Houtte, S. Li, M. Seefeldt, and L. Delannay. Deformation texture prediction: from the Taylor model to the advanced Lamel model. *Int. J. Plasticity*, 21:589–624, 2005.

[208] L. J. Walpole. *Advances in Applied Mechanics*, volume 21, chapter Elastic Behavior of Composite Metarials: Theoretical Foundations, pages 169–236. 1981.

[209] H. Wang, P.D.Wu, C.N.Tomé, and Y. Huang. A finite strain elastic–viscoplastic self-consistent model for polycrystalline materials. *J. Mech. Phys. Solids*, 58:594–612, 2010.

[210] Y.D. Wang, A. Vadon, and J.J. Heizmann. Room temperature compression textures and deformation mechanisms of TiAl-46Al-2V alloy. *Mater. Sci. Eng.*, A222:70–75, 1997.

[211] Y.N. Wang and J.C. Huang. The role of twinning and untwinning in yielding behavior in hot-extruded Mg–Al–Zn alloy. *Acta Mater.*, 55:897–905, 2007.

[212] H. Watanabe, T. Mukai, M. Sugioka, and K. Ishikawa. Elastic and damping properties from room temperature to 673 K in an AZ31 magnesium alloy. *Scripta Mater.*, 51:291–295, 2004.

[213] J.P. Watt. Hashin-Shtrikman bounds on the effective elastic moduli of polycrystals with trigonal $(3, \bar{3})$ and tetragonal $(4, \bar{4}, 4m)$ symmetry. *J. Appl. Phys.*, 36:2879–2884, 1965.

[214] G.J. Weng. Self-consistent determination of time-dependent behavior of metals. *ASME J. Appl. Mech.*, 48:41–46, 1981.

[215] M. Werwer and A. Cornec. Numerical simulation of plastic deformation and fracture in polysynthetically twinned (PST) crystals of TiAl. *Comput. Mater. Sci.*, 19:97–107, 2000.

[216] M. Werwer and A. Cornec. The role of superdislocations for modeling plastic deformation of lamellar TiAl. *Int. J. Plasticity*, 22:1683–1698, 2006.

[217] M. Werwer, R. Kabir, A. Cornec, and K.-H. Schwalbe. Fracture in lamellar TiAl simulated with the cohesive model. *Engng. Fracture Mech.*, 74: 2615–2638, 2007.

[218] K. Wierzbanowski. Computer simulation of rolling texture formation in hcp and orthorombic metals. *Scripta Metall.*, 13:795, 1978.

[219] K. Wierzbanowski, A. Baczmański, and P. Lipinski. *Niejednorodności odkształcenia w procesach przeróbki plastycznej. Seminarium poświęcone 70. rocznicy urodzin Profesora Zdzisława Jasieńskiego.*, chapter Modele sprężysto-plastyczne odkształcenia polikryształu i ich zastosowania., pages 173–190. IMIM PAN, 2005.

[220] J. R. Willis. *Advances in Applied Mechanics*, volume 21, chapter Variational and Related Methods for the Overall Properties of Composites, pages 2–79. 1981.

[221] J.R. Willis. Bounds and self-consistent estimates for the overall properties of anisotropic composites. *J. Mech. Phys. Solids*, 25:185–202, 1977.

[222] S. Wolfram. *The Mathematica Book, 5th ed.* Wolfram Media, 2003.

[223] X. Wu, S.R. Kalidindi, C. Necker, and A.A. Salem. Prediction of crystallographic texture evolution and anisotropic stress–strain curves during large plastic strains in high purity α-titanium using a Taylor-type crystal plasticity model. *Acta Mater.*, 55:423–432, 2007.

[224] F. Xu, R.A. Holt, and M.R. Daymond. Modeling lattice strain evolution during uniaxial deformation of textured Zircaloy-2. *Acta Mater.*, 56:3672–3687, 2008.

[225] J. Xu and S-Q. Shi. Investigation of mechanical properties of ε-zirconium hydride using micro- and nano-indentation techniques. *J. Nucl. Mater.*, 327:165–170, 2004.

[226] S. Yamanaka, K. Yoshioka, M. Uno, M. Katsura, H. Anada, T. Matsuda, and S. Kobayashi. Thermal and mechanical properties of zirconium hydride. *J. Alloys Compunds*, 293-295:23–29, 1999.

[227] M.H. Yoo and C.L. Fu. Physical constants, deformation twinning, and microcracking of titanium aluminides. *Metal. Mater. Trans. A*, 29A:49–63, 1998.

[228] K. Yoshida, R. Brenner, B. Bacroix, and S. Bouvier. Effect of regularization of Schmid law on self-consistent estimates for rate-independent plasticity of polycrystals. *Eur. J. Mech. A/Solids*, 28:905–915, 2009.

[229] C. Zener. *Elasticite et Anelasticite des Metaux*. Dunod, Paris, 1955.

Mikromechaniczne modelowanie metali i stopów o wysokiej wytrzymałości właściwej

Streszczenie

Niniejsza rozprawa poświęcona jest mikromechanicznemu modelowaniu metali i stopów o wysokiej wytrzymałości właściwej. Metale i stopy charakteryzujące się wysokim stosunkiem wytrzymałości i sztywności do gęstości materiału (np. stopy magnezu i tytanu, związki międzymetaliczne Ti-Al), wykazują zwykle niską ciągliwość i formowalność. Te niepożądane cechy ograniczają ich potencjalnie liczne zastosowania w przemyśle (Appel and Wagner [6], Agnew et al. [2], Proust et al. [169], Mróz [141], Lasalmonie [110]). Wskazana kombinacja własności jest wynikiem mikrostruktury. W większości opisywanych materiałów mamy do czynienia z niską symetrią sieci (np. symetrią heksagonalną A3 w przypadku stopów Mg i Ti lub symetrią tetragonalną dla γ-TiAl), a w konsekwencji z niewystarczającą liczbą łatwych systemów poślizgu uruchamiających się podczas deformacji niesprężystych. W wielu przypadkach nie jest spełniony warunek Taylora, to znaczy liczba niezależnych łatwych systemów poślizgu, które są dostępne dla materiału, jest mniejsza od pięciu. Brak ten może być częściowo zrekompensowany przez inny mechanizm deformacji plastycznej - bliźniakowanie, Christian and Mahajan [36]. Analogiczny zespół zjawisk zachodzących na poziomie mikro jest obserwowany w przypadku stopów cyrkonu lub związków międzymetalicznych Fe-Al. Materiały te nie wykazują wysokiej wytrzymałości właściwej ale charakteryzują się wyjątkową odpornością na korozję.

Dla wielu z wyżej wspomnianych metali i związków międzymetalicznych częste jest również występowanie substruktur lamelarnych powstałych na skutek obróbki termicznej (np. $\alpha_2 + \gamma$-TiAl) bądź tworzących się podczas bliźniakowa-

nia mechanicznego. Pojawienie się tego typu mikrostruktury wpływa na aktywność poszczególnych modów deformacji promując te spośród nich, które mają korzystną orientację względem geometrii laminatu (Lebensohn et al. [113], Proust et al. [169]). Oba fakty, to jest niespełnienie warunku Taylora przez zbiór możliwych łatwych systemów poślizgu oraz występowanie kierunkowych efektów typu Halla-Petcha związanych z istnieniem substruktury lamelarnej, wskazują na istnienie więzów nałożonych na deformację niesprężystą na poziomie mikro pojedynczego ziarna.

Na skutek powyższych cech omawianych materiałów, w procesach formowania wyrobów, np. walcowania, tworzą się silne tekstury krystalograficzne, co na poziomie makroskopowym manifestuje się znaczącą anizotropią właściwości.

W świetle powyższych obserwacji mikromechanika wydaje się być naturalnym narzędziem pozwalającym zrozumieć i opisać relację między mikrostrukturą analizowanych materiałów a ich właściwościami makroskopowymi.

Celem rozprawy jest opracowanie różnych metod mikromechanicznej analizy sprężysto-(lepko)plastycznych polikryształów metali i stopów o wysokiej sztywności i wytrzymałości właściwej. Oryginalne aspekty prezentowanych rezultatów to:

- opis konstytutywny pojedynczego ziarna uwzględniający sprzężenia zachodzące pomiędzy mechanizmami poślizgu i bliźniakowania,

- opracowanie nowego schematu reorientacji ziarna na skutek bliźniakowania, służącego modelowaniu ewolucji tekstury krystalograficznej,

- adaptacja zaproponowanego modelu pojedynczego ziarna deformującego się przez poślizg i bliźniakowanie w ramach różnych schematów przejścia mikro-makro i weryfikacja jego przewidywań pod względem makroskopowej odpowiedzi materiału oraz ewolucji tekstury krystalograficznej,

- wykorzystanie niezmienników tensora IV-ego rzędu wynikających z rozkładów inwariantnych takiego tensora do znalezienia nowych zależności opisujących standardowe oszacowania właściwości makroskopowych (oszacowania Voigta i Reussa, Hashina-Shtrikmana, estymator wewnętrznie-zgodny),

- sformułowanie warunków i dowód istnienia wewnętrznie-zgodnego oszacowania właściwości makroskopowych dla szerokiej klasy polikryształów z więzami nałożonymi na deformację na poziomie lokalnym, w przypadku liniowych praw konstytutywnych,

- numeryczne studium wpływu więzów nałożonych na deformację wynikających z niespełnienia warunku Taylora, jednokierunkowości mechanizmu

bliźniakowania oraz występowania substruktur lamelarnych, na makroskopową odpowiedź polikryształów metali opisanych nieliniowymi prawami konstytutywnymi,

- sformułowanie trójskalowego modelu polikryształu o substrukturze lamelarnej w zakresie dużych deformacji niesprężystych,

- opracowanie nowej metody przejścia mikro-makro dla sprężysto-lepkoplastycznych materiałów niejednorodnych bazującej na zaproponowanej sekwencyjnej linearyzacji nieliniowej odpowiedzi materiału.

Rozprawa składa się z siedmiu rozdziałów. Rozdział pierwszy wskazuje motywację do podjęcia dyskutowanego zagadnienia, omawia cel i zakres podjętych badań oraz ich znaczenie, zawiera również uwagi dotyczące notacji zastosowanej w monografii. Ostatni rozdział podsumowuje najważniejsze rezultaty i płynące z nich wnioski oraz wskazuje kierunki możliwych dalszych badań. Praca uzupełniona jest trzema aneksami omawiającymi istotne narzędzia wykorzystane w modelowaniu: rozkład spektralny i harmoniczny tensora czwartego rzędu typu Hooke'a (Rychlewski [176, 178]) rozwiązanie Eshelby'ego oraz podstawy modelu wewnętrznie-zgodnego (*self-consistent*) ciał niejednorodnych (Eshelby [49], Hill [67], Li and Wang [120]), a także zagadnienia związane z implementacją numeryczną proponowanego podejścia. Monografię zamyka spis cytowanej literatury. Zawartość rozdziałów 2-6, stanowiących podstawową treść rozprawy, omówiona jest poniżej.

Modelowanie kryształów deformujących się przez poślizg i bliźniakowanie

Rozdział 2 poświęcony jest uwzględnieniu mechanizmu bliźniakowania w modelu konstytutywnym pojedynczego ziarna wykorzystującym regularyzowane prawo Schmida (Gambin [53, 54], Kowalczyk and Gambin [95]) oraz w modelu bazującym na lepkoplastycznej regularyzacji prawa Schmida za pomocą prawa potęgowego (Asaro and Needleman [8], Hutchinson [69]), jak również zastosowaniu zaproponowanego podejścia do modelowania makroskopowej odpowiedzi materiałów polikrystalicznych i rozwoju tekstury.

Przy modelowaniu bliźniakowania, w odróżnieniu od poślizgu krystalograficznego, należy uwzględnić jego jednokierunkowość, jak również pojawianie się nowych orientacji bliźniaczych. Bliźniakowanie, podobnie jak poślizg, zachodzi przez proste ścięcie materiału, jednakże w tym przypadku ścięciu o zadany kąt ulega jedynie fragment ziarna uzyskując jednocześnie nową orientację sieci krystalograficznej, Christian and Mahajan [36]. Modelując ten mechanizm traktuje się go zwykle jako pseudo-poślizg o prędkości ścinania związanej z przyrostem

udziału objętościowego bliźniaka, nie zapominając, że ścinanie może zajść tylko w jednym kierunku. W kontekście wyznaczania ewolucji tekstury ważne jest uwzględnienie, w sposób efektywny z punktu widzenia procesu obliczeń, pojawiania się w agregacie nowych orientacji. W literaturze można znaleźć kilka propozycji odpowiednich schematów obliczeniowych, cf. Kalidindi [75], Proust et al. [169], Staroselsky and Anand [186], Tomé et al. [200], Van Houtte [203]. Ich krytyczny przegląd zawarty jest w podrozdziale 2.3.1 w części *Ewolucja tekstury (Texture development)*.

W podrozdziale 2.3.2, w ramach opisu kinematyki pojedynczego ziarna, sformułowano własną procedurę reorientacji uwzględniającą pojawianie się orientacji bliźniaczych w rozważanym agregacie polikrystalicznym. Propozycja stara się łączyć zalety poszczególnych metod unikając jednocześnie ich wad, m.in. nie wymaga rozważania całego agregatu ziaren jednocześnie, a zatem jest niezależna od przyjętego schematu przejścia mikro-makro oraz utrzymuje liczbę zreorientowanych ziaren na poziomie konsystentnym z aktualnym udziałem objętościowym fazy bliźniaczej w ziarnach o rozważanej orientacji. Nowa metoda bazuje na idei Van Houtte'a [203] modyfikując kluczowy dla schematu warunek reorientacji ziarna. Według proponowanego modelu, dla rozważanej chwili procesu deformacji, ziarno ulega reorientacji związanej z bliźniakowaniem, jeżeli udział objętościowy bliźniaków zakumulowanych w ziarnie jest dla rozważanej chwili procesu większy od pewnej liczby ξ wygenerowanej losowo z przedziału $[0, \Psi_t]$. Granica przedziału Ψ_t ewoluuje w procesie deformacji według wzoru (2.14).

Począwszy od wczesnych prac China i współpracowników [32] oraz Van Houtte'a [203] inicjacja bliźniakowania opisywana jest przez warunek analogiczny do warunku Schmida dla poślizgu, uwzględniający jednak jednokierunkowość mechanizmu, cf. Christian and Mahajan [36], Szczerba et al. [193]. Wykorzystując powyższe analogie w podrozdziale 2.3.3 zaproponowano modyfikację (2.20)-(2.22) regularyzowanego warunku Schmida (Gambin [54], Kowalczyk and Gambin [95]) pozwalającą na uwzględnienie bliźniakowania.

Obecność bliźniakowania wśród mechanizmów deformacji plastycznej manifestuje się nie tylko w zmianie ewolucji tekstury krystalograficznej, ale również poprzez sprzężenia z mechanizmem poślizgu ujawniające się w charakterze zjawiska umocnienia, to znaczy wzrostu naprężeń krytycznych na poszczególnych systemach poślizgu i bliźniakowania w związku z kumulacją odkształceń plastycznych. Wpływ bliźniakowania jest związany z powstawaniem barier dla ruchu dyslokacji, jakie stanowią tworzące się fazy bliźniacze w ziarnie. Modelowanie zjawiska umocnienia związanego z aktywnością bliźniakowania pozostaje kwestią otwartą. W ostatnich latach pojawiło się wiele prac dedykowanych temu

tematowi, np. Agnew et al. [2], Kalidindi [75, 76], Karaman et al. [79], Proust et al. [170], Salem et al. [182]. Omówiono je w podrozdziale 2.3.1, w części *Opis konstytutywny (Constitutive description)*. Bazując na powyższych propozycjach w podrozdziale 2.3.4 sformułowano prawo umocnienia uwzględniające różne sprzężenia zachodzące pomiędzy poślizgiem a bliźniakowaniem oraz różny charakter zjawiska dla obu mechanizmów, Rys. 2.5. W sformułowaniu zróżnicowane zostało umocnienie utajone dla mechanizmów koplanarnych i niekoplanarnych, cf. formuła (2.40). Dużo uwagi poświęcono również właściwościom, jakie należy przypisać ziarnu po reorientacji indukowanej bliźniakowaniem, biorąc pod uwagę możliwość występowania mechanizmu umocnienia Basińskiego [11], czyli zmiany charakteru dyslokacji swobodnych na zakotwiczone w takim przypadku.

Zaproponowany warunek reorientacji oraz wprowadzone prawo umocnienia zostały zaimplementowane do istniejących schematów przejścia mikro-makro, a mianowicie klasycznego modelu Taylora oraz lepkoplastycznego modelu wewnętrznie zgodnego (VPSC) zaproponowanego przez Molinari et al. [138] i rozwiniętego przez Lebensohn and Tomé [112], stanowiącego podstawę szeroko stosowanego kodu VPSC. Program ten, rozwijany przez Tomé i Lebensohna w Los Alamos National Laboratory (USA), służy symulacji rozwoju tekstury i makroskopowej odpowiedzi materiałów polikrystalicznych. W podrozdziale 2.4 pokazana została weryfikacja podejścia, na początek dla materiałów o sieci A1 i niskiej energii błędu ułożenia (stal Hadfield, mosiądz), a następnie dla materiałów o wysokiej wytrzymałości właściwej (γ-TiAl, stop magnezu). W obliczeniach wyznaczano makroskopową odpowiedź materiału oraz rozwój tekstury dla różnych ścieżek deformacji. Przeprowadzone symulacje wykazały, że zaproponowany model pozwala uzyskać dobrą zgodność z dostępnymi wynikami doświadczalnymi.

Część rezultatów (sformułowanie nowego schematu reorientacji, prawa umocnienia oraz wyniki symulacji dla materiałów o sieci A1 i niskiej energii błędu ułożenia) przedstawionych w Rozdziale 2 została opublikowana w artykule Kowalczyk-Gajewska [100].

Oszacowania liniowych właściwości makroskopowych polikryształów o niskiej symetrii sieci

Rozdział 3 dotyczy metod szacowania właściwości makroskopowych materiałów polikrystalicznych opisanych lokalnie liniowym prawem konstytutywnym, np. prawem Hooke'a.

Określenie makroskopowych, uśrednionych właściwości materiałów niejednorodnych na podstawie znajomości ich mikrostruktury i właściwości lokalnych

to podstawowe zagadnienie rozważane w mikromechanice. Dziedzina ta rozwijana jest od lat 50-tych ubiegłego wieku, a zatem wiele ważnych problemów zostało w tym czasie podjętych i rozwiązanych (Christensen [34], Nemat-Nasser and Hori [145], Kocks et al. [88], Li and Wang [120]). W pracy rozważana jest wybrana klasa materiałów niejednorodnych, a mianowicie polikryształy, w szczególności zaś te zbudowane z kryształów o niskiej symetrii sieci i silnej anizotropii właściwości lokalnych wynikającej np. z niewystarczającej liczby łatwych systemów poślizgu.

Rozdział dotyczy liniowych praw konstytutywnych, w których właściwości materiału opisane są tensorem czwartego rzędu typu Hooke'a. Rozważane są dwa typy rozkładu orientacji w agregacie, a mianowicie:

- brak tekstury (tekstura losowa) prowadzący do izotropii właściwości makroskopowych,

- tekstury włókniste, dla których jeden z kierunków krystalograficznych ma taką samą orientację względem kierunków próbki dla wszystkich ziaren w agregacie. Tekstura taka prowadzi do anizotropii (izotropii poprzecznej) właściwości makroskopowych.

W części 3.3 przeanalizowano ograniczenia dolne i górne na tensor makroskopowych właściwości materiału, zadane odpowiednio przez założenie jednorodnych naprężeń (model Reussa) lub odkształceń (model Voigta) w agregacie polikrystalicznym, jak również bardziej rygorystyczne ograniczenia otrzymywane przy wykorzystaniu zasady Hashina-Shtrikmana. Obok powyższych ograniczeń, w części 3.4 rozważano również oszacowanie otrzymywane przy wykorzystaniu metody wewnętrznie-zgodnej (*self-consistent*) mającej swe źródło w rozwiązaniu Eshelby'ego [49].

Analizując dyskutowane ograniczenia i oszacowanie wewnętrznie-zgodne, można pokazać, że w przypadku makroskopowej izotropii, odpowiednie zależności tensorowe (3.23), (3.25), (3.30) i (3.76) redukują się do dwóch równań skalarnych, a w przypadku izotropii poprzecznej do pięciu równań skalarnych. Wykorzystując inwariantne rozkłady tensora IV-ego rzędu, znaleziono odpowiednie wzory analityczne, pozwalające oszacować np. makroskopowe moduły sztywności dla liniowej sprężystości czy naprężenia płynięcia dla liniowego ustalonego pełzania. Wyprowadzone zależności dotyczą kryształów o dowolnej anizotropii. W przypadku metody wewnętrznie-zgodnej założono dodatkowo kulisty kształt ziaren. Przedyskutowano istnienie i jednoznaczność rozwiązań. Szczególną uwagę poświęcono tym materiałom, w których pojedyncze kryształy są objętościowo izotropowe oraz podano redukcję rozwiązań dla materiałów nieściśliwych i takich, w których na deformację nałożono pewne więzy. Wię-

zy takie mogą na przykład wynikać z niespełnienia warunku Taylora. Jednym z najbardziej istotnych rezultatów podrozdziału jest dowód faktu, że skończony estymator wewnętrznie-zgodny makroskopowego modułu ścinania polikryształu objętościowo izotropowego bez tekstury istnieje tylko wtedy, gdy wymiar podprzestrzeni izochorycznych stanów deformacji na które nałożono więzy jest nie większy od dwóch, a w przypadku polikryształów nieściśliwych, nie większy niż jeden. Wynik ten oznacza m.in., że makroskopowe naprężenie płynięcia izotropowego polikryształu, opisanego lokalnie prawem (3.127), będzie skończone, jeżeli liczba niezależnych systemów poślizgu jest nie mniejsza od czterech.

Niektóre z otrzymanych rezultatów są już znane w literaturze, np. formuły (3.31) i (3.33) na ograniczenia górne i dolne typu Voigta i Reussa podał Walpole [208], wielomianowe równania na estymator wewnętrznie-zgodny modułu ścinania dla materiałów o symetrii kubicznej wyznaczyli Hershey [62], Kröner [107], Hill [66], Willis [220], natomiast ograniczenia Hashina-Shtrikmana i oszacowania właściwości makroskopowych metodą wewnętrznie-zgodną dla kryształów o różnych symetriach sieci wyznaczano w pracach Kneer [86], Peselnick and Meister [157], Watt [213], Pham [161], Berryman [12]. Oryginalny aspekt zależności otrzymanych w ramach rozprawy to ich sformułowanie przy wykorzystaniu niezmienników anizotropowego tensora IV-ego rzędu opisującego właściwości pojedynczego kryształu. Oryginalne są również powyżej dyskutowane wyniki dotyczące redukcji odpowiednich rozwiązań dla materiałów nieściśliwych oraz materiałów z więzami nałożonymi na deformację.

W części 3.6 wyznaczone wzory wykorzystano do oszacowania makroskopowych właściwości sprężystych różnych polikryształów o niskiej symetrii sieci oraz analizy wartości względnego makroskopowego naprężenia płynięcia polikryształów γ-TiAl i Mg w zależności od parametrów opisujących relację między krytycznymi naprężeniami ścinającymi uruchamiającymi łatwe i trudne systemy poślizgu.

Część rezultatów dyskutowanych w Rozdziale 3 została opublikowana w artykule Kowalczyk-Gajewska [99]. W rozprawie rozważania zostały uzupełnione o analizę ograniczeń Hashina-Shtrikmana oraz polikryształy o teksturach włóknistych.

Analiza istniejących schematów uśredniania dla nieliniowych praw konstytutywnych

Rozdział 4 został poświęcony analizie istniejących modyfikacji podejścia wewnętrznie-zgodnego mających na celu rozszerzenie jego stosowalności do nieliniowych równań konstytutywnych. W przypadku nieliniowych modeli konsty-

tutywnych brak jest jednoznacznego rozwiązania tego zagadnienia. Wypracowano wiele podejść służących jak najlepszej aproksymacji rozwiązań uzyskiwanych metodą wewnętrznie-zgodną poprzez różne sposoby linearyzacji równań konstytutywnych, np.: Chaboche et al. [29], Hill [66], Hutchinson [69], Lebensohn and Tomé [112], Masson et al. [127], Molinari et al. [138, 139].

Na początek, w części 4.2, rozważano polikryształy sprężysto-plastyczne. Dokonano krótkiego przeglądu proponowanych podejść mających swe źródła w pracach Krönera [107] i Hilla [66]. Oryginalnym wynikiem tej części pracy jest sformułowanie wewnętrznie-zgodnego przyrostowego schematu Hilla dla modelu pojedynczego kryształu dyskutowanego w Rozdziale 2. Model ten został sformułowany w dużych deformacjach i wykorzystuje regularyzowane prawo Schmida.

Część 4.3 zawiera krytyczną analizą istniejących generalizacji metody wewnętrznie-zgodnej służących wyznaczeniu makroskopowych właściwości polikryształu lepkoplastycznego opisanego prawem potęgowym (4.24), stosowanego również do opisu pełzania ustalonego. Szczególną uwagę poświęcono trzem najczęściej wykorzystywanym wariantom, a mianowicie schematom: siecznemu (Hutchinson [69]), stycznemu (Lebensohn and Tomé [112], Molinari et al. [138]) i afinicznemu (Masson et al. [127]). W ramach analizy uwypuklono różnicę pomiędzy schematami. Następnie, owe trzy schematy zastosowano do wyznaczenia makroskopowych właściwości lepkoplastycznych polikryształów γ-TiAl i Mg o losowej teksturze porównując otrzymane wyniki. Zaobserwowano znaczne różnice pomiędzy przewidywaniami poszczególnych modeli. Różnice te były tym większe, im większa była intensywność anizotropii lokalnej. Intensywność anizotropii lokalnej w analizowanych przypadkach była określona stosunkiem naprężeń ścinających uruchamiających łatwe i trudne systemy poślizgu. Ponadto zaobserwowano, że warunek istnienia skończonego, wewnętrznie-zgodnego oszacowania makroskopowego naprężenia płynięcia, wynikający z rozważań przeprowadzonych dla liniowych praw konstytutywnych, wydaje się obowiązywać również dla praw nieliniowych przy $n \to \infty$ w przypadku schematów siecznego i afinicznego, natomiast wyniki otrzymane przy wykorzystaniu schematu stycznego są wtedy zbieżne z wynikami otrzymywanymi przy wykorzystaniu modelu Sachsa (ograniczenie dolne przy założeniu stałych naprężeń). Podobne wnioski, wysnute na podstawie analizy polikryształów innych metali o niewystarczającej liczbie łatwych systemów poślizgu można również znaleźć w pracach Bornert et al. [19], Hutchinson [71], Lebensohn et al. [114], Nebozhyn et al. [143].

W rozprawie, w odróżnieniu od prac cytowanych powyżej, przeanalizowano również wpływ mechanizmu bliźniakowania, a w szczególności jednokierunkowość tego mechanizmu, na wartość różnych oszacowań typu wewnętrznie-

zgodnego. Stwierdzono, że różnica w makroskopowym naprężeniu płynięcia dla polikryształu o teksturze losowej przy ściskaniu i rozciąganiu nie jest znacząca, Rys. 4.7, 4.8, 4.12 i 4.13. Zgodnie z przewidywaniami, możliwość aktywacji mechanizmu bliźniakowania przy stosunkowo niedużym naprężeniu ścinającym, obniża wartość makroskopowego naprężenia płynięcia w stosunku do polikryształu deformującego się jedynie przez poślizg. Jednokierunkowość bliźniakowania sprawia jednak, że taka redukcja jest mniejsza, niż w przypadku hipotetycznego polikryształu, w którym mielibyśmy do czynienia z mechanizmem poślizgu o tej samej geometrii co analizowany mechanizm bliźniakowania. Obserwowane różnice są większe dla metody siecznej i afinicznej niż dla metody stycznej.

Metale o substrukturze lamelarnej

W analizowanych metalach i stopach mamy do czynienia z substrukturami lamelarnymi. Ich obecność wskazuje na konieczność wprowadzenia oprócz tradycyjnych w mikromechanice dwóch poziomów: skali mikro pojedynczego ziarna i skali makro elementu polikrystalicznego; pośredniego poziomu odpowiadającego skali lamelarnego metaziarna (Rys. 5.1). W Rozdziale 5 przedstawiono trójskalowy model mikromechaniczny pozwalający uwzględnić występowanie tego typu substruktury.

Analizując własności (lepko)plastyczne, należy zauważyć, że mała grubość poszczególnych warstw w metaziarnie może prowadzić do utrudnienia deformacji w ramach warstwy. Jest to efekt typu Halla-Petcha związany z redukcją średniej drogi swobodnej dyslokacji w pewnych kierunkach. W związku z powyższym dostępne, równoważne ze względu na symetrię sieci, systemy poślizgu i bliźniakowania, podlegają zróżnicowaniu ze względu na ich orientację względem morfologii laminatu, a mianowicie można wyróżnić (Lebensohn et al. [113]): mody podłużne (5.1), mody mieszane (5.2) i mody poprzeczne (5.3). Odpowiednie krytyczne naprężenia ścinające uruchamiające poszczególne systemy podlegają relacji (5.4). Podobnie jak niewystarczająca liczba łatwych systemów poślizgu wynikająca z symetrii sieci, więzy nałożone na deformację niesprężystą związane z występowaniem substruktur lamelarnych mogą prowadzić do znaczącego podwyższenia wartości makroskopowego naprężenia płynięcia, jak również prowadzić do silnej anizotropii lokalnych właściwości mechanicznych.

W podrozdziale 5.2 sformułowano schemat przejścia mikro-makro od poziomu pojedynczego ziarna (pojedynczej lameli) do poziomu metaziarna w zakresie małych odkształceń. Założono afiniczne równanie konstytutywne (5.12), które może odpowiadać oryginalnemu równaniu konstytutywnemu (np. liniowej termosprężystości) lub zlinearyzowanej formie nieliniowego związku, np. odpo-

wiednio (4.24) i (4.44). Wykorzystując ogólne podejście sformułowane dla laminatów (El Omri et al. [47]) oraz jego adaptację dla polikryształów o substrukturze lamelarnej (Lebensohn et al. [113], Roos et al. [173]) wyznaczono własności metaziarna (5.22-5.27) o założonym równaniu konstytutywnym (5.13). Podano również redukcję otrzymanych rozwiązań dla materiałów nieściśliwych. Następnie przedyskutowano procedury implementacji zaproponowanego modelu trójskalowego dla nieliniowych związków konstytutywnych i założonych różnych schematów przejścia mikro-makro z poziomu metaziarna do poziomu polikryształu zbudowanego z metaziaren. Rozważane były modele Taylora i Sachsa oraz trzy warianty metody wewnętrznie-zgodnej: sieczny, styczny i afiniczny. Zaprezentowane procedury, przy wskazanej różnorodności metod uśredniania, stanowią oryginalny rezultat pracy.

W części 5.2.3 zaproponowane podejście zostało zastosowane do modelowania $\gamma + \alpha_2$-TiAl o strukturze lamelarnej. Na początek przeanalizowano anizotropię sprężystą metaziarna oraz zależność wartości początkowego naprężenia płynięcia od orientacji substruktury lamelarnej względem kierunku rozciągania lub ściskania. Wykazano dobrą zgodność przewidywań modelu z eksperymentem. Oszacowano również właściwości sprężyste oraz początkową powierzchnię plastyczności dla polikryształu o substrukturze lamelarnej i losowym rozkładzie orientacji metaziaren. Następnie dyskutowano właściwości lepkoplastyczne. Należy zauważyć, że w przypadku modelowania właściwości niesprężystych substruktura lamelarna może zostać uwzględniona tylko poprzez morfologiczne zróżnicowanie modów deformacji (5.1-5.4) przy zachowaniu modelu dwuskalowego, bądź dodatkowo poprzez wprowadzenie pośredniego poziomu rozważań. W związku z powyższym przeanalizowano, jak zmieniają się przewidywania poszczególnych metod uśredniania w zależności od uwzględnienia pośredniego poziomu w obliczeniach oraz intensywności efektów Halla-Petcha opisywanych parametrami α_M i α_T. Zaobserwowano, że wprowadzenie dodatkowego poziomu rozważań mikromechanicznych w ogólności zmniejsza różnicę pomiędzy poszczególnymi oszacowaniami, natomiast efekt ten zanika wraz ze wzrostem parametrów α_M i α_T. Przeprowadzona analiza stanowi oryginalny wkład autorki. Część otrzymanych wyników zaprezentowano w Kowalczyk-Gajewska [101].

W podrozdziale 5.3 przedstawiono propozycję rozszerzenia opracowanego formalizmu na duże deformacje niesprężyste. Stosując formalizm dużych deformacji sprężysto-(lepko)plastycznych przy modelowaniu substruktur lamelarnych, należy uwzględnić ewolucję orientacji interfejsu pomiędzy warstwami laminatu. Struktury lamelarne, z jakimi mamy do czynienia w przypadku analizowanych materiałów, są zwykle pochodnymi aktywności mechanizmu bliźniakowania. Przy formułowaniu modelu takiej mikrostruktury należy zatem odpo-

wiedzieć także na pytanie, w jaki sposób zmieniają się orientacje sieci krystalograficznej w poszczególnych lamelach, pamiętając, iż początkowo są one ze sobą ściśle związane poprzez geometrię danego systemu bliźniakowania. W rozprawie zastosowano rozwiązania zaproponowane w Kowalczyk-Gajewska [98], a mianowicie założono, że interfejs pomiędzy warstwami laminatu jest powierzchnią materialną podlegającą ewolucji zgodnie z (5.70). Ponownie model został zastosowany do modelowania $\gamma + \alpha_2$-TiAl. Wyznaczono makroskopową odpowiedź materiału, rozwój tekstury krystalograficznej oraz reorientację substruktury lamelarnej w procesie ściskania stosując model Taylora dla agregatu metaziaren i sztywno-plastyczny model pojedynczej lameli z regularyzowanym prawem Schmida. Badano zmianę aktywności poszczególnych modów deformacji sklasyfikowanych morfologicznie. Wyniki porównano z odpowiednimi przewidywaniami [150] otrzymanymi przy wykorzystaniu podejścia zaproponowanego przez w [173]. Podejście z pracy [173] jest sformułowane w ramach małych odkształceń (a zatem nie uwzględnia ewolucji mikrostruktury), wykorzystuje metodę wewnętrznie-zgodną Krönera oraz sprężysto-lepkoplastyczny modeli pojedynczego ziarna. Oba podejścia, dla zaawansowanych deformacji plastycznych ($\sim 30\%$) przewidują podobną aktywność poszczególnych modów, w szczególności znaczącą aktywność modów poprzecznych. Ponieważ powyższy wynik można kwestionować, konieczne wydaje się zastosowanie innego schematu przejścia mikro-makro, np. jednej z generalizacji metody-wewnętrznie zgodnej, dla modelu sztywno-plastycznego lub jego lepkoplastycznej regularyzacji.

Schematy przejścia mikro-makro dla sprężysto-lepkoplastycznych materiałów niejednorodnych

Metale i stopy o wysokiej wytrzymałości właściwej wykazują zwykle niską ciągliwość, a zatem dla wielu schematów obciążania (np. jednoosiowego rozciągania) maksymalne obserwowane odkształcenia nie są duże. W związku z powyższym opisywanie odpowiedzi takich materiałów za pomocą modeli sztywno-(lepko)plastycznych, pomijających wpływ odkształceń sprężystych, może wprowadzać zbyt duże uproszczenia, szczególnie w przypadku procesów związanych ze zmianą ścieżki deformacji. Ponadto, w związku z silną anizotropią właściwości lokalnych analizowanych metali i stopów, deformacja na poziomie mikro jest silnie niejednorodna a oddziaływania pomiędzy ziarnami mają złożony, sprężysto-lepki charakter o porównywalnym wpływie obu czynników w dość dużym zakresie deformacji. Wydaje się zatem pożądane sformułowanie modelu sprężysto-lepkoplastycznych materiałów niejednorodnych wykorzystującego koncepcję inkluzji zaproponowaną przez Eshelby'ego [49].

Odpowiednia linearyzacja nieliniowych równań konstytutywnych matrycy, konieczna w celu zastosowania rozwiązania Eshelby'ego a następnie sformułowania odpowiedniego schematu przejścia mikro-makro, jest szczególnie trudna w przypadku materiałów sprężysto-lepkoplastycznych. Związane jest to z występowaniem w równaniach jako zmiennych równocześnie odkształcenia i jego prędkości. W Rozdziale 6 przedstawiono nowe podejście służące zaadaptowaniu metody wewnętrznie-zgodnej do opisu niejednorodnych materiałów sprężysto-lepkoplastycznych.

Problem odpowiedniej linearyzacji równań sprężysto-lepkoplastycznych można rozwiązać w elegancki sposób dla liniowej lepkosprężystości stosując transformaty Laplace'a i zasadę korespondencji, np.: Hashin [58], Christensen [33], Laws and McLaughlin [111], Suquet [192], choć znalezienie transformaty odwrotnej może być w pewnych przypadkach utrudnione. Zastosowanie podobnego podejścia w sytuacji, gdy sprężystości towarzyszy silnie nieliniowa lepkość prowadzi do mocno skomplikowanych zależności, których implementacja wymaga zaawansowanych narzędzi numerycznych, patrz Masson and Zaoui [126], Pierard and Doghri [162], Rougier et al. [175]. W związku z powyższym uznano, że warto rozważyć przybliżone schematy linearyzacji lokalnej odpowiedzi materiału, którą przeprowadza się bez wykorzystywania techniki transformat, cf. Kouddane et al. [93], Paquin et al. [155], Sabar et al. [181], Molinari [136], Lahellec and Suquet [109], Mercier and Molinari [133], Doghri et al. [41].

Oryginalna w stosunku do wyżej wymienionych prac idea, prezentowana w Rozdziale 6, to zrezygnowanie z próby jednoczesnego uwzględnienia sprężystych i lepkich własności matrycy w ramach pojedynczego kroku obliczeniowego w przyrostowym schemacie przejścia mikro-makro. W zamian, proponuje się, aby dla danego kroku uwzględniać własności sprężyste i lepkie sekwencyjnie. Zgodnie z przedstawioną ideą, zamiast rozwiązywać jedno zagadnienie Eshelby'ego dla liniowej matrycy z niejednorodnością, rozwiązuje się sekwencję takich podzagadnień o różnym typie interakcji pomiędzy matrycą a niejednorodnością, w szczególności sprężystych i lepkich (6.6)-(6.7). Całkowita odpowiedź materiału jest następnie wyznaczana przy wykorzystaniu odpowiednich założeń wiążących podproblemy ze sobą. Założenia te stanowią kluczową część modelu. W rozdziale ograniczono się do zakresu małych odkształceń.

Ponieważ nie jest oczywiste, czy zaproponowane podejście daje właściwe rezultaty nawet w przypadku liniowej lepkosprężystości, na początek (podrozdział 6.2.3) opracowane wersje metody, różniące się przyjętymi założeniami wiążącymi, zostały zweryfikowane dla zagadnienia niejednorodności w nieskończonej matrycy. Rozważono przykład izotropowej matrycy i niejednorodność o kształcie sferycznym. Otrzymane wyniki porównano z innymi przybliżonymi

schematami linearyzacji (Molinari [136], Paquin et al. [155], Sabar et al. [181]) oraz z rozwiązaniem ścisłym znalezionym przy wykorzystaniu transformat Laplace'a. Stwierdzono, że zaproponowana metoda oraz modele z prac Paquin et al. [155] i Molinari [136] redukują się do rozwiązania ścisłego w przypadku materiałów nieściśliwych, natomiast przy założeniu ściśliwości sprężystej najkorzystniejszy wariant sekwencyjnej linearyzacji odpowiada modelowi zaproponowanemu przez Molinariego [136]. Wariant ten został wybrany do dalszych rozważań.

Koncepcja sekwencyjnej linearyzacji złożonej odpowiedzi materiału może być zastosowana w różnych schematach uśredniania bazujących na rozwiązaniu Eshelby'ego. Jej zastosowanie w modelu Mori-Tanaka [140] jest natychmiastowe (cześć 6.2.2). Trudniejsze jest zaadaptowanie proponowanego podejścia do schematu wewnętrznie-zgodnego. Jak pokazano w podrozdziale 6.3, konieczne jest wtedy oprócz rozważenia dwóch podproblemów: lepkiego i sprężystego, wykonanie tak zwanego kroku akomodacyjnego. Ponownie przewidywania zaproponowanego przejścia mikro-makro porównano z przewidywaniami innych modeli (Molinari [136], Paquin et al. [155]), jak również z dostępnym rozwiązaniem ścisłym podanym w Rougier et al. [174] w przypadku nieściśliwego, dwufazowego materiału o dużym kontraście we własnościach lepkich i sprężystych. Wykazano, że wykorzystując zaproponowaną metodą otrzymuje się zadowalające wyniki w stosunku do modeli konkurencyjnych. W części 6.3.3 przedstawiono próbę rozszerzenia stosowalności opracowanej metody do opisu nieliniowej lepkości. Opracowane rozwiązanie wymaga dalszych studiów w przypadku silnie nieliniowych związków konstytutywnych, ponieważ otrzymywane rezultaty są wtedy niewłaściwe. Na zakończenie, na przykładzie γ-TiAl, zaprezentowano możliwość zastosowania opracowanego podejścia do modelowania polikryształów metali o wysokiej wytrzymałości właściwej.